To the Graduate Council:

I am submitting herewith a dissertation written by Chang H. Lee entitled "Weldability and Microstructural Analysis of Nuclear Grade Austenitic Stainless Steels." I have examined the final copy of this dissertation for form and content and recommend that it be accepted in partial fulfillment of the requirement for the degree of Doctor of Philosophy, with a major in Metallurgical Engineering.

Carl D. Lundin, Major Professor

We have read this dissertation
and recommend its acceptance:

Domenic A. Canonico

John D. Landes

Charlie R. Brooks

R. A. Buchanan

Accepted for the Council:

Vice Provost
and Dean of The Graduate School

WELDABILITY AND MICROSTRUCTURAL ANALYSIS OF NUCLEAR GRADE AUSTENITIC STAINLESS STEELS

A Dissertation

Presented for the

Doctor of Philosophy

Degree

The University of Tennessee, Knoxville

Chang H. LEE

December 1988

DEDICATION

This dissertation is really dedicated to the author's God and parents. Without their support, this work would not have been possible. This great work is also dedicated to his wife, Eun, and his daughters, Ji-Hyun Ruth and Joo-Hyun Julie, for their patience and understanding.

ACKNOWLEDGEMENTS

The author would like to express his acknowledgement to his major advisor, Doc. Carl D. Lundin, for his patience and guidence throughout the course of this study. Deep gratitude is also extended to Dr. Charlie R. Brooks, Dr. Ray A. Buchanan, Dr. Dominic A. Canonico and Dr. John D. Landes for their kind help during this work. Dr. Seiji Katayama in The Japanese Welding Research Institute, Japan, is also acknowledged with respect for his helpful comments and encouragement while his staying at The Welding Research Group in UT.

The author wishes to express his appreciation to The J.A. Jones Applied Research, Sumitomo Metal Industries LTD, General Electric Company, Kraftwerk Union, New York Power Authority, Lawrence Livermore National Laboratories, Tennessee Valley Authority, Argonne National Laboratories and Mannesmann Anlagenbau, for financial support. The Tennessee Valley Authority, General Electric Company, Mannesmann Anlagenbau, Sumitomo Metal Industries, Kraftwerk Union and Teledyne Mckay are further appreciated for their donation of materials to conduct this investigation.

Last but not least, the author wishes to thank all staff members of the Dept. of Materials Science and Engineering, and Welding Research Group members, especially Mr. Klyan Khan and Mr. Paul Qiao, for their contribution and help to the success of this work.

ABSTRACT

This study evaluated the hot ductility response, and hot cracking susceptibility (fusion zone solidification cracking and HAZ liquation cracking) of modified nuclear grade and standard austenitic stainless steels. Extensive microstructural characterization using state-of-the art analytical electron microscopy (TEM and STEM) as well as SEM (EDAX) and OLM was performed to correlate the material behavior with metallurgical characteristics. In addition, studies of the effect of Si, N, and rare earth elements on hot cracking susceptibility, significance of the ductility dip phenomena and backfilled solidification cracks were also performed. Furthermore, based on the metallurgical evaluation, the possible mechanisms involved in solidification cracking and HAZ liquation cracking of the modified alloys are proposed. Finally, the optimized chemical specifications and requirements for nuclear grade stainless steels are also suggested.

The hot ductility and weldability behavior of the modified 316NG and 347NG alloys were found to be superior to, or at least equivalent to, the standard AISI 304, 316 and 347 alloys. Hot ductility response and hot cracking susceptibility of stainless steels were dependent upon major and minor element content (P, S, Si and Nb), ferrite content (potential), grain size, and solidification mode (Cr_{eq}/Ni_{eq} ratio). Among them, the primary solidification mode was the most important factor such that the primary ferritic alloy exhibited a better behavior than that solidified in a primary (fully) austenitic mode when other variables were constant. The influence of the primary

solidification mode was found to be more important for crack propagation than for initiation.

The effect of impurity level (P + S) on the extent of cracking was found to be dependent on the Cr_{eq}/Ni_{eq} ratio, such that when the ratio is greater than approximately 1.6, the P + S content can be as high as 0.06%. However, when the ratio is less than about 1.5, a P + S content as low as 0.02% can exert significant influence on solidification cracking. The relative amount of Nb to C and N (1/2 %Nb / (30 X %C + 50 X %N) appeared to be a predominant factor for the hot cracking in type 347. When this ratio is less than about 0.1, P, S and Si played a significant role in solidification cracking.

In order to predict material behavior more quantitatively and definitively, "new" parameters: critical strain temperature range (CSTR) and ductility recovery ratio (DRR) for Gleeble hot ductility testing and the cracked HAZ length (CHL) for the Varestraint base metal HAZ cracking, were developed and analyzed as a function of metallurgical variables and chemical composition. The correlation among these parameters indicated that when the CSTR is smaller than 70 $\pm$ 10 F^{o} and DRR is greater than 40 $\pm$ 5%, the material is less susceptible to HAZ liquation cracking (virtually zero CHL).

The ductility dip phenomenon occurs by fracture along original but embrittled grain boundaries (by melting and resolidification due to impurity element segregation) at temperatures above the equicohesive temperature but below the dynamic recrystallization temperature. Grain boundary embrittlement may be further enhanced by the precipitation of chromium rich carbides and an increased amount of

liquid formation by exposure to a higher peak temperature. The ductility dip phenomena may be characteristic of the testing method which involves significant deformation and dynamic recrystallization (under fast strain rate condition at high temperatures) and may not be likely to occur in the actual weld HAZ.

The addition of nitrogen to high silicon (1.25%) 304 decreases the solidification cracking susceptibility, when the primary solidification mode is maintained ferritic. The decreased cracking susceptibility was found to be due to a decrease in amount of low melting sulfides by the formation of high sulfur containing silicates. For a fully austenitic 316 stainless steel, the extent of solidification cracking decreased with an increase in the nitrogen content from 0.047% to 0.12%. The decrease in solidification cracking in a material containing higher nitrogen was due to a decrease in the solidification cell size and a narrower "brittleness temperature range" (BTR).

The extent of backfilled solidification cracks appeared to be a function of the primary solidification mode, length and width of the crack, location of crack in the weld and the applied strain level. The backfilling phenomenon is a result of capillary action of liquid. The liquid source for backfilling is that just ahead of solidification front which is enriched in Cr and/or Ni depending upon the solidification behavior and the liquid existing during the last stages of solidification.

TABLE OF CONTENTS

CHAPTER PAGE

I. INTRODUCTION ----------1

1. BACKGROUND ----------1

2. OBJECTIVES ----------7

II. LITERATURE REVIEW ----------9

1. MECHANISMS OF HOT CRACKING ----------9

2. SOLIDIFICATION MECHANICS OF STAINLESS STEEL ----------16

3. EFFECT OF COMPOSITION ON HOT CRACKING SUSCEPTIBILITY ----------45

4. HOT DUCTILITY TESTING AND CRITERIA FOR HOT CRACKING ASSESSMENT ----------59

5. VARESTRAINT TEST AND CRITERIA FOR HOT CRACKING ASSESSMENT ----------81

III. MATERIALS AND EXPERIMENTAL PROCEDURES ----------95

1. MATERIALS ----------95

2. EXPERIMENTAL PROCEDURES ----------99

a. Gleeble Hot Ductility Testing ----------99
b. Varestraint Hot Cracking Tests ----------102
c. Element Implant Technique ----------106
d. Solidification Study ----------108
e. Microstructural Evaluation ----------108

IV. RESULTS AND DISCUSSION ----------114

1. GLEEBLE HOT DUCTILITY EVALUATION ----------114

a. Hot Ductility Behavior of Standard and Modified Alloys ----------115
B. Development of New Parameters and Their Application ----------122
c. Metallurgical Behavior During Hot Ductility Testing ----------145

2. VARESTRAINT HOT CRACKING TESTS ----------188

a. Fusion Zone Solidification Cracking ----------190

b. Weld Metal HAZ Liquation Cracking ----------262
c. Base Metal HAZ Liquation Cracking ----------278

3. PREDICTION OF THE BASE METAL HAZ BEHAVIOR FROM THE GLEEBLE HOT DUCTILITY TESTS ----------299

V. EFFECT OF Si, N AND REM ON HOT CRACKING BEHAVIOR --------311

1. SI AND ITS SYNERGISTIC EFFECTS WITH N ----------311

2. EFFECT OF NITROGEN ----------323

3. EFFECT OF RARE EARTH METAL (REM) ----------338

VI. EVALUATION OF BACKFILLED SOLIDIFICATION CRACKS ----------347

1. INTRODUCTION ----------347

2. MATERIALS AND EXPERIMENTAL PROCEDURES ----------348

a. Materials ----------348
b. Test Evaluations ----------348

3. EXPERIMENTAL RESULTS ----------349

a. Solidification Cracking Susceptibility ----------349
b. Backfilled Solidification Cracks ----------352
c. Microstructural Evaluation of Backfilled Region --358

4. DISCUSSION ----------364

VII. WELDABILITY RECOMMENDATIONS ----------371

VIII. CONCLUSIONS ----------376

REFERENCES ----------392

APPENDIX ----------411

VITA ----------443

LIST OF TABLES

TABLE PAGE

1. Specifications of 316 stainless steel for nuclear application.----3

2. Specifications of 347 stainless steel for nuclear application.----4

3. Correlation between solidification process and room temperature ferrite morphology.----35

4. A summary of hot ductility testing parameters used in USA, German, France and Japan.----76

5. Chemical compositions of 316NG, AISI 304 and 316 materials investigated in this study.----96

6. Chemical compositions of 347NG and AISI 347 materials investigated in this study.----97

7. Hot ductility testing conditions and procedure.----101

8. Ranking of materials based on Gleeble hot ductility test.---124

9. Summary of hot ductility test results of current program materials.----134

10. Varestraint fusion zone solidification cracking test results of 316NG, AISI 304 and 316.----192

11. Varestraint fusion zone solidification cracking test results of 347NG and AISI 347.----197

12. Varestraint weld metal HAZ liquation cracking test results of 316NG, AISI 304 and 316.----265

13. Varestraint weld metal HAZ liquation cracking test results of 347NG and AISI 347.----267

14. Varestraint base metal HAZ liquation cracking test results of 316NG, AISI 304 and 316.----281

15. Varestraint base metal HAZ liquation cracking test results of 347NG and AISI 347.----282

16. Correlation among Gleeble hot ductility parameters (CSTR/DRR) and Varestraint HAZ cracking parameter (CHL).----304

17. Chemical compositions of materials used for Si effect study.----------313

18. Chemical compositions of materials used for N effect study.----------327

19. Extent of backfilled cracks in a) 316NG-D and b) 316NG-B at 4% strain.----------353

20. Extent of backfilled cracks in 347NG-E, a) 2% and b)4% strain.----------354

21. Suggested specifications for 316NG and 347NG.----------375

A-1. Chemical compositions of materials studied.----------413

A-2. Statistical analysis of on-heating hot ductility test results.----------425

A-3. Statistical analysis of on-cooling hot ductility test results.----------426

A-4. Effects of heating and cooling rates on hot ductility.------429

LIST OF FIGURES

FIGURE PAGE

1. Effect of consttsitutional features on cracking susceptibility in binary systems. ----------11

2. Schematic representation of mechanism for partial melting in a single phase alloy. ----------15

3. Schematic explanation of the origin of constitutional supercooling. ----------21

4. Schematic representation of the influence of the parameters on the pattern of solidification. ----------24

5. The Fe-Cr-Ni ternary phase diagram. ----------25

6. Schematic Fe-Cr-Ni pseudo-binary diagram at constant Fe content. ----------28

7. Schematic illustration of the chromium and nickel distribution across a subgrain following solidification. ----30

8. Schematic representation of solidification and solid state transformation behavior resulting in different characteristic morphologies of weld metal microstructure. ---36

9. Schematic pseudo-binary diagram of the Fe-Cr-Ni ternary system illustrating the effect of composition on austenite-ferrite morphology in austenitic stainless steel weldments. ----------38

10. Crack susceptibility chart in terms of ferrite content and P+S contents. ----------52

11. Liquation temperature as a function of the ratio of columbium content to the carbon and nitrogen contents. -------54

12. Effect of N on hot cracking susceptibility in fully austenitic stainless steel weld metal without Nb. ----------55

13. Classification of on-heating and on-cooling hot ductility behavior. ----------64

14. Schematic illustration of zero ductility range used as a crack sensitivity criterion. ----------68

15. Schematic illustration of mid-range ductility dip used as crack sensitivity criterion. ----------69

16. Factors contributing to hot ductility and hot strength.--------79

17. Schematic showing principle of varestraint testing procedure. ----------84

18. Schematic drawing of varestraint test samples for longitudinal and transverse modes. ----------89

19. Schematic representation for the determination of brittleness temperature range for cracking.----------92

20. Schematic explanation for the occurrence of solidification cracking from a view point of the relationship between ductility of alloys and deformation during welding. ----------93

21. A pictorial view of the Varestraint positioned in the longitudinal mode. ----------103

22. Schematic drawing of the Varestraint test device showing the manner in which a specimen is tested. ----------105

23. Schematic representation of the element implant technique.----------107

24. Schematic drawing of the way in which TEM thin foils are extracted from the Varestraint sample. ----------111

25. Typical Hot ductility behavior of AISI 304 (304-1).----------116

26. Typical Hot ductility behavior of AISI 347 (347-1).----------116

27. Typical hot ductility behavior of 316NG (316NG-D).----------118

28. Typical hot ductility behavior of 316NG (316NG-7).----------118

29. Typical hot ductility behavior of 347NG (347NG-1).----------119

30. Typical hot ductility behavior of 347NG (347NG-D).----------119

31. A pictorial view of the stainless studs and thermocouple attachment for simultaneous measurement of thermal and strain cycles.---------- --129

32. Typical insitu thermal and strain cycles in the full scale weld (24" dia. stainless steel pipe).----------130

33. Typical fracture strain recovery measured as a function of test temperature for 316NG (316NG-A).----------132

34. Typical fracture strain recovery measured as a function of test temperature for 347NG (347NG-D).----------132

35. A schematic drawing of the concepts of CSTR and DRR.---------135

36. Correlation between CSTR and DRR.----------136

37. Relationship between CSTR and ferrite potential.----------140

38. Correlation between DRR and 1/2 %Nb / (30 X %C + 50 X %N).---142

39. Correlation between CSTR and 1/2 %Nb / (30 X %C + 50 X %N).--142

40. Base metal microstructure of 347NG-E in the as-received condition. ----------147

41. Typical optical microstructure just adjacent to the fracture surface and SEM fractograph of the sample tested on-heating at 2100 °F, 347NG-E.----------148

42. Typical optical and SEM microstructures and fractograph of the sample tested on-heating at 2300 °F, 347NG-E.---------150

43. Typical optical microstructure and SEM fractograph of the sample tested on-heating at 2350 °F, 347NG-E.----------152

44. Typical optical and SEM microstructures and Fractograph of the sample tested on-heating at 2400 °F, 347NG-E. --------155

45. Typical optical and SEM microstructures and Fractograph of the sample tested on-heating at 2430 °F, 347NG-E.---------157

46. Typical optical and SEM microstructures and Fractograph of the sample tested on-heating at ZDT of 2480 °F, 347NG-E. ----158

47. Incipiently melted grain boundary and EDAX on the widened boundary.----------160

48. STEM analysis of white particles in Figure 47. ----------161

49. Typical optical and SEM microstructures near the fracture surface and fractograph, tested on-cooling at range from the ZDT to 2300 °F, 347NG-E.----------163

50. Typical optical and SEM microstructures, tested on-cooling at 2100 °F, 347NG-E.----------165

51. Typical optical and SEM microstructures near the fracture surface and fractograph, tested on-cooling at 1900 °F, 347NG-E.----------167

52. Typical optical and SEM microstructures near the fracture surface, tested on-cooling at 1700 °F, 347NG-E.----------168

53. A summary of microstructure changes during on-heating and on-cooling in 347NG-E.----------170

54. Typical SEM fractographs, tested at ZDT, 316NG-7.----------172

55. Typical microstructures near the fracture surface in the longitudinal section, tested at ZDT of 2475 ^{o}F, 316NG-7.-----173

56. Typical microstructure near the fracture surface, tested on -cooling a) at 2000 ^{o}F and b) at 1800 ^{o}F, 316NG-7.--------175

57. SEM micrograph of the ductility dip sample and EDAX analysis, tested on-cooling at 1800 ^{o}F.----------177

58. Typical TEM microstructures in a) thin foil and b) carbon extraction replica, near the fracture surface in the ductility dip sample, 316NG-7.----------178

59. STEM analysis on the particles in the Figure 58b.----------179

60. Typical optical microstructures, tested on-cooling at a) 1600 ^{o}F and b) 1500 ^{o}F, 316NG-7.----------180

61. Typical optical microstructure tested at 1800 ^{o}F on cooling from the ZDT - 50 F^{o}, 316NG-7.----------182

62. Comparison of fusion zone solidification cracking of 316NG materials with AISI 304 and 316.----------191

63. Relationship between total crack length and maximum crack length.----------193

64. Comparison of fusion zone solidification cracking of 347NG with AISI 347.----------196

65. Relationship between solidification mode and Cr_{eq} and Ni_{eq} using the Hammer and Svensson formula.----------200

66. Correlation among the P + S content, Cr_{eq}/Ni_{eq} and the extent of solidification cracking in 316NG, 304 and 316.-----202

67. Effect of P + S level on solidification cracking for a given Cr_{eq}/Ni_{eq} (1.6).----------203

68. Effect of Cr_{eq}/Ni_{eq} on solidification cracking as a function of P + S content.----------203

69. Relationship between fusion zone solidification cracking and 1/2 %Nb / (30 X %C + 50 %N) in type 347.----------207

70. Effect of P + S content on solidification cracking in 347 materials when 1/2 %Nb / (30 X %C + 50 X %N) is less than 0.1. ----------208

71. Synergistic effect of P and Si on solidification cracking in 347 materials when 1/2 %Nb / (30 X %C + 50 X %N) is less than 0.1.----------208

72. Effect of P + S content on solidification cracking in 347 materials when 1/2 %Nb / (30 X %C + 50 X %N) is greater than 0.1.----------209

73. Influence of room temperature ferrite content on solidification cracking in 304, 316, 316NG and 347NG.--------209

74. A schematic pseudo-binary section at 70 %Fe of the Fe-Cr-Ni ternary system.----------212

75. Macroscopic appearance of the rapidly quenched weld sample.----------214

76. Typical microstructures near the solidification front in the rapidly quenched samples, a) 316NG-7 and b) 316NG-1. ----215

77. Higher magnification microstructures in Figure 76a, a) just behind of the solidification front and b) some distance from the front.----------217

78. Higher magnification microstructures in Figure 76b, a) just behind of the solidification front and b) some distance from the front.----------218

79. TEM microstructure in 316NG-D, revealing a fully austenitic substructures.----------221

80. STEM chromium and nickel concentration profile across the cells through A-B in Figure 79.----------222

81. Liquidus surface of the Fe-Cr-Ni ternary diagram showing approximate solidification path of the primary austenitic 316NG-D.----------224

82. A higher magnification of the cell boundary area in Figure 79.----------226

83. TEM microstructure in primary ferritic 347NG-E.----------227

84. STEM chromium and nickel concentration profile across the primary dendrite ferrite through C-D in Figure 83.-------228

85. A typical TEM microstructure of the solidification grain boundary in 347NG-E.----------230

86. STEM analyses on the particles along the boundary in Figure 85.----231

87. Typical surface of an evaluated Varestraint sample showing the various crack location regions.----233

88. Solidification cracks typical of the fully austenitic sample extracted parallel to the Varestraint test surface, 316NG-7.----235

89. Higher magnification of the crack tip region in Figure 88.---236

90. SEM micrograph of the interdendritic region in the fully austenitic weld and EDAX analysis on the white microconstituents in the interdendritic region.----238

91. Typical solidification cracks in the primary ferritic weld (347NG-E) together with EDAX analysis on the microconstituents in the grain boundary and interphase boundary.----240

92. Nb(C,N) and Nb(C,N)-austenite eutectic in a) interphase boundary and b) grain boundary.----241

93. TEM micrograph on the carbon extracted sulfides and phosphides in the grain boundary in 347NG-E.----243

94. Typical solidification cracking in the low 1/2 %Nb / (30 X %C + 50 X %N) material of 347NG-F.----244

95. Optical microstructures near the weld fusion line region in 347NG-B.----245

96. The migrated grain boundaries typical of a) primary ferritic and b) fully austenitic.----247

97. Typical solidification crack surface in fully austenitic (316NG-D).----249

98. Higher magnification of a) region B and b) region C in Figure 97a.----251

99. Higher magnification of a) region D in Figure 97a and b) EDAX analysis.----253

100. Typical solidification surface in primary ferritic (347NG-E).----254

101. Schematic drawings of solidification substructure morphology and subsequent changes typical for a) fully austenitic and b) primary ferritic weld metal.----257

102. Comparison of liquation cracking behavior in the weld metal HAZ between 316NG and AISI 304 and 316 materials.----------263

103. Comparison of liquation cracking behavior in the weld metal HAZ between 347NG and AISI 347 materials.----------264

104. Typical weld metal HAZ liquation cracking in the fully austenitic 316NG-D.----------269

105. Typical weld metal HAZ liquation cracking in the primary ferritic 347NG-E.----------271

106. Nb(C,N) -austenite eutectic in the grain boundary in 347NG-E.----------272

107. Nb(C,N) - austenite eutectic at the ferrite and austenite interphase boundary in the weld metal HAZ in 347NG-E.---------274

108. Base metal HAZ liquation cracking behavior of 316NG materials.----------279

109. Base metal HAZ liquation cracking behavior of 347NG materials.----------280

110. Effect of Nb content on liquation cracking in the base metal HAZ of 347 materials.----------283

111. Correlation between base metal HAZ liquation cracking and 1/2 %Nb / (30 X %C + 50 X %N) in 347 materials.----------283

112. Effect of ferrite potential on the extent of liquation cracking in the base metal HAZ.----------285

113. Typical liquation cracks in the base metal HAZ and liquated grain boundaries near the fusion line in the fully austenitic 316NG (316NG-D).----------286

114. Partially melted region next to the fusion line in the primary ferritic base metal HAZ, revealing ferrite formation along the grain boundaries.----------288

115. Typical microstructures in the base metal HAZ of type 347 material (347NG-E), revealing a difference in the location of the segregation bands relative to the fusion line.---------289

116. Constitutional liquation of Nb(C,N) in grain boundary, (347NG-E).----------291

117. SEM fractograph of the base metal HAZ liquation crack surface and EDAX analysis in the fully austenitic (316NG-D).----------293

118. SEM fractograph of the base metal HAZ liquation crack surface in the primary ferritic (347NG-E), a) macroscopic appearance and b) higher magnification of region A in a).-----294

119. Higher magnification of a) region B in Figure 118a and b) EDAX analysis on Nb(C,N)-austenite eutectic.----------295

120. Correlation between MCL in the base metal HAZ in the Varestraint with CSTR in the Gleeble hot ductility testing.----------301

121. Correlation between MCL in the base metal HAZ in the Varestraint with DRR in the Gleeble hot ductility testing.----------302

122. Correlation between TCL in the base metal HAZ in the Varestraint with DRR in the Gleeble hot ductility testing.----------302

123. A schematic representation of the concept of the Cracked HAZ Length (CHL).----------306

124. The location of CHL relative to the instantaneous weld pool in the base metal HAZ.----------306

125. Correlation between CHL in the base metal HAZ cracking in the Varestraint and DRR in the Gleeble hot ductility testing.----------307

126. Correlation between CHL in the base metal HAZ cracking in the Varestraint and CSTR in the Gleeble hot ductility testing.----------307

127. Effect of silicon content on solidification cracking in 304.----------314

128. Typical solidification crack in the 1.25 %Si containing 304.----------316

129. STEM analysis on a) phosphide, b) sulfide and c) manganese silicate.----------317

130. Effect of nitrogen addition on solidification cracking in the high silicon containing (1.25 %) 304 weld metal.-------319

131. Solidification cracks in the primary ferritic high Si (1.25%) weld metal, 5 %N_2 + 95 %Ar shielding.----------320

132. Solidification cracks in the fully austenitic high Si (1.25%) weld metal, 20 %N_2 + 80 %Ar shielding.----------321

133. STEM analyses on manganese silicates a) type A and b) type B.----------324

134. Typical TEM micrograph of the high Si and N containing primary ferritic 304 weld metal.---------- 325

135. A schematic drawing of a groove weld deposited with three different N containing electrodes (SMAW) from which Varestraint samples were extracted.----------328

136. Effect of N content on solidification cracking in the fully austenitic type 316 stainless steel weld metal.----------330

137. Effect of N content on the maximum crack length in the fusion zone hot cracking of fully austenitic type 316 weld metal.----------330

138. Solidification cracks in the high nitrogen containing (0.12%) fully austenitic weld metal.----------331

139. Typical microstructures in a) 0.047 %N, b) 0.078 %N and c) 0.12 %N containing fully austenitic weld metals.----------333

140. Influence of nitrogen content on the solidification substructure size in the fully austenitic weld metal.---------334

141. Approximate solidification paths of 316N-A, 316N-B and 316N-C, a) Liquidus and b) Solidus surfaces of Fe-Ni-Cr ternary diagram.----------336

142. A schematic drawing of Temperature-Ni_{eq} diagram at constant Cr_{eq}, showing the effect of N addition on the Brittleness Temperature Range (BTR) of fully austenitic weld metal.----------337

143. A comparison of solidification cracking behavior of REM containing 347L and 347R with that of AISI 347.----------340

144. Typical fusion zone microstructures in the REM (0.008%) containing fully austenitic 347L.----------343

145. Typical fusion zone microstructures in the REM (0.017%) containing primary ferritic 347R.----------344

146. A comparison of liquation cracking behavior in the weld metal HAZ of the REM containing fully austenitic 347L (0.008 %REM) and primary ferritic 347R (0.017 %REM) with that of AISI 347.----------345

147. A comparison of liquation cracking behavior in the base metal HAZ of 347L and 347R with that of AISI 347.----------345

148. Schematic drawing of the hot cracked zone along the solid-liquid interface, divided into three equal regions.----------350

149. Comparison of fusion zone solidification cracking susceptibility of 316NG-B, 316NG-D and 347NG-E.----------351

150. Influence of primary solidification mode on the extent of backfilling.----------356

151. Effect of augmented strain level on the extent of backfilling.----------357

152. A typical backfilled solidification crack in 316NG-D.---------359

153. The chromium and nickel distribution across the backfilled crack in 316NG-D.----------360

154. A typical backfilled solidification crack in 347NG-E.---------362

155. The chromium and nickel distribution across the backfilled crack in 347NG-E. ----------363

156. A typical macrograph of hot cracked zone along the solidification interface in 347NG-E.----------365

157. A schematic drawing of the capillary rise.----------367

A-1. Hot ductility behavior of 316 L tested with a conventional cross wire thermocouple technique.----------415

A-2. Hot ductility behavior of 304 L tested with a conventional cross wire thermocouple technique.----------416

A-3. Hot ductility behavior of 347 tested with a conventional cross wire thermocouple technique.----------417

A-4. Schematic representation of the conventional thermocouple technique.----------419

A-5. Schematic representation of the separate wire thermocouple technique.----------420

A-6. Hot ductility behavior of 316 L tested with a separate wire thermocouple technique.----------422

A-7. Hot ductility behavior of 304 L tested with a separate wire thermocouple technique.----------423

A-8. Hot ductility behavior of 347 tested with a separate wire thermocouple technique.----------424

A-9. Effect of the strain rate(crosshead speed) on the on-heating hot ductility.----------433

A-10. Effect of hold time at test temperature on the on-heating hot ductility.----------435

A-11. Effect of hold time at test temperature on the on-cooling hot ductility.----------435

A-12. Effect of hold time at test temperature on the hot ductility response of the 304 L.----------437

A-13. Effect of hold time at peak temperature(ZDT) on the on-cooling hot ductility.----------437

CHAPTER I

INTRODUCTION

1. BACKGROUND

Intergranular Stress Corrosion Cracking (IGSCC) of weld sensitized 304 and 316 stainless steel piping in BWR systems has received serious consideration during the last decade. Many efforts have been undertaken at numerous research institutions aimed at the understanding of the mechanism involved in IGSCC and at finding preventive methods for mitigating the occurrence of IGSCC in BWR systems.

The essential conditions for IGSCC require the coincidence of three main factors at the same location (1): a susceptible microstructure (sensitization), a critical stress intensity, and a critical environment (O_2 content of high purity water). Recently, the U.S. Nuclear Regulatory Commission Piping Review Committee (2,3) recommended, after extensive review of IGSCC problems in the U.S., that at least two of the three causative factors should be altered to minimize the occurrence of IGSCC, although best practice would call for modification of all three factors. The NRC committee (2,3) stated that **" the preferred action to combat IGSCC, for the long term fixes, is to replace commonly used materials such as Types 304 and 316 stainless steel, which are prone to sensitization, with sensitization resistant materials such as Type 316 NG stainless steel."**

Recent research carried out in the U.S. and Japan (4,5) revealed that both 304 and 316 Nuclear Grade materials (304 NG and 316 NG), as

compared to the conventional 304 and 316, have performed well in a wide range of laboratory tests including full scale pipe tests, slow strain rate tests, simulated crevice corrosion tests, and cyclic crack growth tests. In addition, the higher nickel content and the molybdenum addition in 316 make it less susceptible to martensite formation during cold work and to pitting type corrosion as contrasted to 304. Thus, use of 316 NG provides an additional measure of protection against IGSCC and pitting corrosion. It is one of the materials which is being used by utilities in replacement programs and for new piping (2). A comparison of several chemical specifications for 316NG is given in Table 1.

Another material which has also received considerable attention as a replacement material is a modified 347 (347 Nuclear Grade) stainless steel. More than 20 years of experience in West Germany and extensive laboratory testing (4,6) have shown that the modified 347 material has a higher resistance to sensitization and IGSCC than that of the 304 and 316 stainless steels, and its resistance is essentially equivalent to 316 NG in these regards. The modified 347 materials are: TP 347 NG - West Germany, 347 LPN - Japan and ICL 473 Nb - France. The major modification of the alloy composition is in the niobium and carbon contents. Comparison of the chemistry for these modified alloys with AISI 347 is shown in Table 2. The Nb/C ratios of the modified alloys are considerably enhanced in comparison to AISI 347 (except ICL 473 Nb). The Japanese modification, 347 LPN, has an additional control on phosphorus and nitrogen contents to improve resistance to IGSCC as well as weldability and strength.

Table 1. Specifications of 316 stainless steel for nuclear application.

	AISI 316 (USA)	AISI 316 LN (USA)	316 NG (GE)	316 NG (EPRI)	316 NG (NYPA)	316 NG (Japan)
C	0.08 max	0.03 max	0.02 max	0.02 max	0.02 max	0.02 max
Si	1.0 max	1.0 max	1.0 max	0.75 max	0.50 max	0.75 max
Mn	2.0 max	2.0 max	2.0 max	2.0 max	2.0 max	2.0 max
P	0.045 max	0.045 max	0.045 max	0.03 max	0.015 max	0.025 max
S	0.03 max	0.03 max	0.03 max	0.005 max	0.015max	0.005 max
Ni	10.0-14.0	10.0-14.0	10.0-14.0	11.0-14.0	11.0-14.0	11.0-14.0
Cr	16.0-18.0	16.0-18.0	16.0-18.0	16.0-18.0	16.0-18.0	16.0-18.0
N	-	0.10-0.30	0.06-0.10	0.06-0.10	0.06-0.10	0.06-0.12
Nb	-	-	-	0.05 max	0.02 max	-
Mo	2.0-3.0	2.0-3.0	2.0-3.0	2.0-3.0	2.60-3.0	2.0-3.0
Co	-	-	-	0.25 max	0.10 max	0.20 max
G.S[a]	-	-	-	4 / 3/2[b]	4/2[c]	-
FN[d]	-	-	-	2.5	2-4	-

a: ASTM grain size
b: <0.75"/0.075 <t < 2"/>2" thickness
c: <0.75"/>0.75" thickness
d: Ferrite number according to Figure NB-2433 · 1 - 1 of ASME section III

Table 2. Specifications of 347 stainless steel for nuclear application.

	AISI 347 (USA)	347 LPN (Japan)	TP347 mod.[a] X 6 CrNiNb 18.10 (German)	ICL 473Nb (France)	NYPA	EPRI	TVA[b]
C	0.08 max	0.02 max	0.04 max	0.03 max	0.02 max	0.02 max	0.02 max
Si	1.0 max	0.5 max	1.0 max	0.75 max	0.5 max	1.0 max	0.6 max
Mn	2.0 max	1.4-1.9	2.0 max	2.0 max	2.0 max	2.0 max	2.0 max
P	0.045 max	0.015 max	0.035 max	0.033 max	0.015 max	0.035 max	0.030 max
S	0.03 max	0.005 max	0.02 max	0.015 max	0.015 max	0.02 max	0.015 max
Ni	9.0-13.0	9.0-9-7	9.0-11.5	≈9.0	9.0-13.0	9.0-12.0	9.0-12.0
Cr	17.0-19.0	18.05-18.85	17.0-19.0	≈18.5	17.0-20.0	17.0-19.0	17.0-19.0
N	-	0.05-0.11	-	0.09 max	0.1 max	-	0.02-0.1
Nb	-	0.22-0.32	0.65 max	0.5 max	0.6 max	-	0.6 max
Nb/C	≧ 10	≧ 15	≧ 13	≧ 8	≧ 13	≧ 13	≧ 13
G.S[c]	-	-	equal/finer,4	-	4/2[d]	4/3/2[e]	5/3/2[e]
FN[f]	-	-	4-8	-	≧ 2	3-7	2-10

a: DIN 1.4550 mod.
b: preliminary
c: ASTM grain size
d: <0.75"/ >0.75"thickness
e: <0.75"/ 0.75"<t<2"/ >2" thickness
f: Ferrite Number according to Figure NB-2433.1-1 of ASME Section III

Although the new stainless steels, 316 NG and modified 347, have been proven to be more resistant to IGSCC and sensitization, very little information about their weldability is available in the literature (5,7,8). The U.S. NRC Piping Review Committee (3) has mentioned in their recommendations that all modified alloys are more resistant to IGSCC than conventional Types 304 and 316 stainless steels. However, " One specific caveat applies. Although low carbon stainless steels with nitrogen additions such as 316 NG have been successfully fabricated and welded in Japan and Europe, United States experience with these materials is limited. It appears that greater care must be exercised in the control of composition and fabrication variables to limit cracking during hot forming or welding."

The interest in the weldability of 316 NG has been further prompted by some cracking incidents during the bending of the rolled and welded pipe (9). These incidents have caused hot ductility requirements to be incorporated in the ordering specifications for the pipe materials. Some utilities have taken steps to further specify weldability related hot ductility testing to pin-point marginally ductile heats of materials with the aim of enhancing weld fabrication of the BWR components. However to date there is no definitive guideline for proper testing methodology/conditions and acceptance criteria.

The hot ductility of the weld HAZ was related, in the early work (10,11), to the potential for hot cracking during fabrication in many high alloy and stainless steel materials. The relationship between hot ductility and hot cracking was empirically established by

behavioral comparisons between fabrication incidents and the base metal HAZ response, in terms of the ability of the material to tolerate welding restraint strains without rupture in the HAZ. Thus hot ductility and hot cracking are considered to be related, in that hot ductility must be adequate to plastically accommodate the contractional welding strain without rupture (hot cracking).

However, the test methods for assessing hot ductility of the base material HAZ are varied, and although the Gleeble has become a common tool in the assessment of hot ductility, not all investigators have utilized similar testing parameters. This lack of standardization of hot ductility test methods does not provide for the ready comparison of results from laboratory to laboratory, or even between researchers in the same laboratories over a period of time. Nonetheless there appears no other alternative to testing under the thermal conditions attendant upon welding because, if other than the transient welding conditions were employed, the response would be far from the realm of realistic duplication and in turn the behavior would not be indicative of actual fabrication practice.

While this testing methodology is fraught with vagaries in high speed and high heating rate evaluations, it is probably not viable to proceed apart from these constraints unless a direct HAZ hot cracking evaluation method is developed.

Recently, the Welding Research Group at the University of Tennessee (12) has modified the testing methodology of the Varestraint test. Modification of the moving torch sub-scale varestraint hot cracking tester and the test methods employed have been instituted to

obtain information on the hot cracking of the base metal HAZ, weld metal HAZ and the fusion zone of the as-deposited pass. Comparative data between hot ductility and direct hot cracking of the base material HAZ can be obtained which will provide the correlation link necessary to enhance the understanding of the hot cracking phenomenon.

Further, the several chemical specifications proposed by utilities (Table 1), in which the major difference are in the residual and minor alloying elements content (S, P, Si, N and Nb) and ferrite requirements, require a systematic and statistical testing of many lots with different ferrite potentials and chemistry in each grade, 316NG and 347NG, and then an optimization of the chemical specifications.

2. OBJECTIVES

This investigation comprises the following four major areas of endeavor, all interrelated and leading to a fundamental understanding of the fabrication behavior of the stainless steel materials used in BWR and other nuclear service,

a) Evaluation of weldability of nuclear grades using the standardized testing methodologies (Gleeble hot ductility and Varestraint hot cracking test))

   * comparative evaluation of hot ductility behavior and weldability (hot cracking) of modified alloys and standard AISI grades.

b) Development of parameters for acceptance criteria involving weldability,

   * develop new parameters which are definitive and have an

ability to discriminate material to material and heat to heat basis with the same nominal composition.

* correlate hot ductility behavior with base HAZ liquation cracking resistance.
* predict material's behavior (in actual fabrication practice) from the laboratory test results.

c) Evaluation of weld related microstructure and its relationship to weldability.

* identify major and minor elements which are most responsible for hot cracking occurrence in 316NG and 347NG.
* determine the role of solidification process and ferrite on solidification cracking and HAZ liquation cracking.
* investigate metallurgical changes and grain boundary chemistry changes during high temperature-strain cycles (during hot ductility testing).
* evaluation of ductility dip phenomenon and its influence on weldability.
* effect of Si, N and REM on weldability.
* investigate backfilled solidification crack and its effect on weldability of stainless steel.

d) Propose the optimized chemical specifications for Nuclear Grade alloys

CHAPTER II

LITERATURE REVIEW

1. MECHANISMS OF HOT CRACKING

Three major types of high temperature cracking are known in welded austenitic stainless steel (13,14);

* Solidification cracking -- cracks formed during solidification of the weld metal in the pass being deposited.
* Liquation cracking -- cracks developed in the base metal HAZ and in the underlying passes (weld metal HAZ) in multipass welding.
* Ductility dip cracking -- cracks formed in regions, in both base metal and weld metal HAZs, which occur at a temperature well below the solidus temperature.

Many theories have been proposed to explain the occurrence of these types of hot cracks. The hot cracking theories which deal with weld metal cracking (solidification cracking) are the most advanced. Those for base metal and weld metal HAZ cracking are mainly extensions of weld metal hot cracking theories. The proposed theories for weld metal hot cracking are the Shrinkage-Brittleness theory (15-17), the Strain theory (18,19), Generalized theory (20,21) and Prokhorov theory (22). Of these theories, the one which has been widely accepted and provides the best understanding of the various phenomena related to hot cracking, even though it still remains as a hypothesis due to the lack of experimental data, is the Generalized theory proposed by Borland (20,21).

The Generalized theory is a modification and extension of the Shrinkage-Brittleness theory and Strain theory and explains how the quantity of liquid and its distribution during freezing affects the cracking tendency.

Borland (20,21) proposed four solidification stages affecting the occurrence of cracking, as shown in Figure 1;

1. Stage I (Primary dendritic formation) -- The solid dendrites are freely dispersed in a continuous liquid and thus no cracks occur.
2. Stage II (Dendrite interlocking period) -- In this stage, both the solid dendrites and the liquid are continuous. Liquid healing is possible if cracks form.
3. Stage III (Critical solidification range) -- In this stage, grain boundaries start to develop and no healing of cracks is possible if accommodation strains are exceeded.
4. Stage IV (Completion of solidification) -- In this stage, the remaining liquid solidifies, thus no cracking occurs.

Therefore, this theory postulates that the critical solidification range and accommodation strain are the factors determining hot cracking susceptibility. When the amount of strain exceeds the accommodation strain during the critical solidification range, cracking occurs. Further, the distribution of liquid phase during solidification is related to the physical properties, particularly the interfacial energies of the liquid and solid phases concerned. The interphase and grain boundary energies are related to the dihedral contact angle that determines the shape and distribution

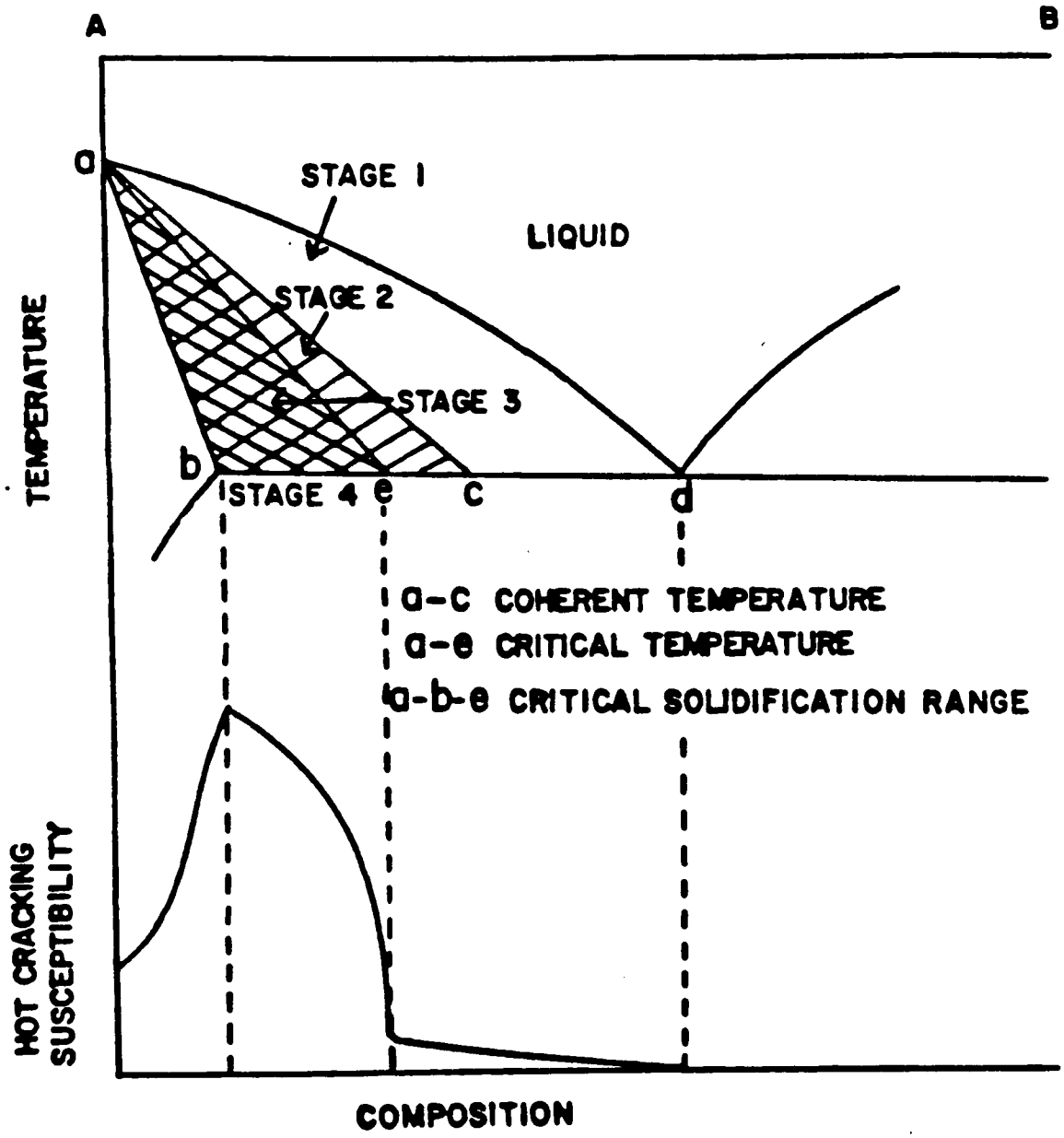


Figure 1. Effect of constitutional features on cracking susceptibility in binary systems.

Source: Borland, J., "Generalized theory of super-solidus cracking in welds (and casting)," British Welding Journal, (8), p. 508-512, (1961).

of the liquid and is often related to an interfacial surface energy ratio (τ);

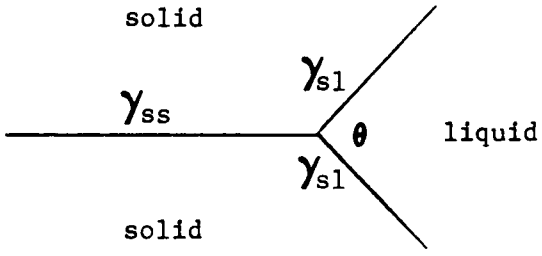
i.e., $\tau = \gamma_{sl}/\gamma_{ss} = 1/(2 \cos \theta/2)$

Where, : Surface energy

sl : Solid-Liquid interface

ss : Solid-Solid grain boundary

$0^o < \theta < 180^o$



In general, as the ratio τ increases above 0.5 the liquid progressively occupies less of the grain boundary edges and faces, and more of the grain corners. With τ below 0.5 ($\theta < 60^o$) the liquid phase can exist only as a continuous network along the grain boundary edges(and grain faces). Alloys which are most susceptible to cracking, according to the above model, should be those which contain a small amount of the solute element, and cracking may be prevented if the liquid phase composition can be modified so that it is much different from that of the solid (i.e., cracking can be prevented by increasing τ)

Many of the theories of HAZ hot cracking are initially derived from the liquation theories of weld metal cracking and the existence of a liquid film is essential in the occurrence of HAZ cracking (liquation cracking). According to Lundin (23), the mechanism of the

formation of liquid films in the HAZ during welding has been related to;

1. Liquation of grain boundary
2. Low melting segregates
3. Absorption of solute from the weld puddle
4. Constitutional liquation of inclusions and second phase constituents.

Grain boundary segregation aggravates liquation cracking by inducing melting of boundaries near the fusion line. The high dynamic stresses which occur as the weld cools tend to rupture these liquated or impurity-weakened boundaries. However, Easterling (24) noted that the origin of segregation in liquation cracking in the HAZ is quite different from that of solidification cracking. Melting of grain boundaries at the fusion line occurs at temperatures between the solidus and liquidus of boundaries. Since melting nucleates preferentially at high energy crystal defects such as grain boundaries, there is a gradual increase in melted boundary width as the fusion line is approached. Impurities having low solubility in the matrix or from melted inclusions near the fusion line tend to diffuse to the melted boundaries. On being cooled, these segregates tend to form films of low melting point grain boundary compounds or even low melting point eutectics. At this stage, if the strain imposed by the combined action of thermal and restraint stresses exceeds the strain tolerance of the microstructure cracking occurs.

Savage et al. (25,26) proposed that hot cracking in the HAZ initiates at liquated grain boundaries in the partially melted zone at

temperatures above or near the "effective solidus" and advanced an hypothesis to explain how the partial melting occurs. The partially melted region experiences peak temperatures between the liquidus and the effective solidus. Because of the segregation invariably present in a commercial alloy, the effective solidus is always significantly below the equilibrium solidus for the nominal composition of the alloy. In addition, interactions which may occur between certain types of inclusions and the matrix cause further depression of the effective solidus. Owczarski et al. (119) also found that a partially melted zone in the HAZ in the nickel base alloys was the most crack sensitive region of the base metal in the vicinity of the weld.

According to the mechanism concerning partial melting (25,26), the effective melting temperature in an alloy varies from point to point because of the localized variations in solute content as shown schematically in Figure 2. Note that the locations near the weld pool, when the instantaneous temperature is above the effective melting temperature, will experience localized melting (melted regions are shown by the cross hatched areas in Figure 2). At the high temperatures experienced near the fusion line rapid grain boundary migration would occur as a result of normal grain growth. However, the liquated regions, which have a composition similar to that of the matrix, readily wet any boundaries which intercept them and form molten films which arrest further grain migration. Pepe and Savage (27) indicated that constitutional liquation, which occurs under non-equilibrium heating in the weld HAZ, can further depress the effective solidus and create molten films on the grain boundaries, thus

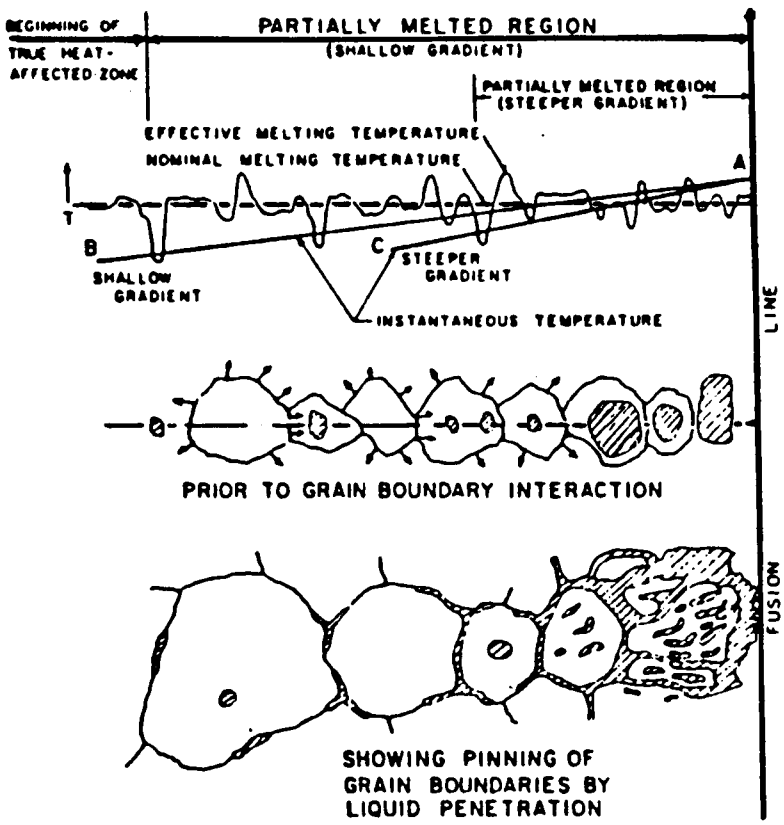


Figure 2. Schematic representation of mechanism for partial melting in a single phase alloy.

Source: Savage, W.F., Nippes, E.F. and Miller, T.W., "Microsegregation in partially melted regions of 70Cu-30Ni weldments," Welding Journal, 55(7), p. 181s-187s, (1976).

expanding the partially melted zone (i.e., increasing HAZ microfissuring susceptibility).

In multiple pass welds, the same mechanism can be applicable such that the microsegregation, which formed during solidification, in underlying beads tends to extend the partially melted region adjacent to the subsequent passes. Thus, microfissuring is often observed in the portions of underlying passes which have been reheated by subsequent passes.

Therefore, based on the proposed mechanisms for hot cracking in the fusion zone and heat affected zone, the basic requirements for the formation of a crack in a weldment are a susceptible microstructure and amount of strain imposed on. That is (23):

* The material compromising the weldment exhibits a phase or a combination of phases which possess a limited capacity to tolerate strain within some critical temperature range;
* The strain imposed upon by the combined action of thermal and restraint conditions within this critical temperature range exceeds the strain tolerance of the degraded microstructural region.

2. SOLIDIFICATION MECHANICS OF STAINLESS STEEL

a. General Theory

The formation of many types of weld metal defects such as solidification cracking (hot cracking), porosity, mechanical anisotropy, etc., is known to be closely related to the manner in which molten weld metal freezes and cools to room temperature. By

varying the welding conditions and composition of weld metal, the tendency toward hot cracking and other types of defects can be significantly changed. Similarly, segregation of alloying and/or residual elements can be substantially varied (58).

During the last two decades, considerable work has been conducted to investigate the basics of weld metal solidification mechanics and its effect on formation of defects and on the mechanical properties of weldments (25,58-65). During the usual solidification process, the transformation of a liquid phase to a solid normally occurs by a process of nucleation and growth, and solidification can proceed at a finite rate only if the system is undercooled below the equilibrium reaction temperature. In the fusion welding processes, however, the nucleation event is not significant since a solid-liquid interface is always present and direct growth from the unmelted base metal occurs. In other words, the existing solid grains at the solid-liquid interface in a fusion weld serve as ready made nuclei and the growth occurs with a minimum amount of supercooling. Such a process is known as "Epitaxial Growth". Further, in the normal case of a fusion weld, the molten metal and the base metal are usually similar in composition and possess the same crystalline form. Thus, if the solidifying weld assumes a crystallographic orientation identical to that of the adjoining solid grain at the fusion line, crystalline growth can occur without the necessity of expending surface free energy to create an additional grain boundary paralleling the fusion line (59-64).

Solidification usually proceeds along the easy growth direction which is oriented most closely to the direction of the maximum thermal gradient in the melt. In welding, the maximum thermal gradient in the weld pool is normal to the pool boundary at all points on the boundary and thus the form of the competitive growth process in a given material is uniquely controlled by the weld pool geometry. Furthermore, the grain orientation in the weld metal at the fusion boundary is determined by the orientations of the partially melted grains (epitaxial growth) and will therefore be most favorable for those grains growing from substrate grains with a <100> direction which is most closely aligned parallel to the direction of the normal to the pool boundary at the moment of solidification being considered.(64) (Both bcc and fcc materials have the same preferred easy-growth direction of <100>).

The most important consequence of non-equilibrium weld metal solidification (with a constitutional supercooling) is microsegregation which is uniquely important to weld hot cracking. Microsegregation is subdivided into cellular, dendritic and grain boundary segregations. The short-range effects, occurring when an interface is growing in a cellular form, produce compositional variations which although large, can be readily modified by heat treatment. Dendritic segregation either as coring or by the accumulation of solute in the interdendritic spaces is more difficult to eliminate by simple heat treatment (64). Grain boundary segregation occurs either by solute accumulation in grain boundary or by the impingement of two interfaces growing with an opposite growth

direction during the terminal-transient stage of solidification. The detailed nature of the segregation pattern is dependent on the growth conditions and morphology of the growing dendrites and is influenced by liquid flow in the semi-solid region.

In a pure metal, dendritic growth can only occur in the presence of a negative temperature gradient at the solid-liquid interface. However, in an alloy, the redistribution of solutes at the advancing solid-liquid interface can establish a condition known as constitutional supercooling which promotes dendritic solidification even in the presence of a positive temperature gradient at the solid-liquid interface. The cooling rates associated with weld solidification in the usual welding processes (except some high energy processes) are so rapid that the following boundary conditions can be assumed:

1. Diffusion in the solid phase is negligible,
2. Very little mechanical mixing of the liquid occurs in the immediate vicinity of the advancing interface,
3. Concentration changes in the liquid at the advancing solid -liquid interface occur by diffusion only,
4. Microscopic equilibrium exists between the solid and liquid phases in contact with one another at the moving solid-liquid interface.

Solidification under these conditions has been referred to as Case III solidification and is characterized by three distinct stages:

1. The initial transient stage
2. The steady state stage (dynamic equilibrium stage)

3. The terminal transient stage.

As the alloy cools through the solidification temperature range, solute is rejected at the solid-liquid interface. Since very little mechanical mixing of the liquid occurs in the immediate vicinity of the advancing interface, the rejected solute must be redistributed in the liquid only by diffusion (the initial transient stage). The freezing process is so rapid that diffusional processes can not effectively remove the excess solute near the moving interface until a dynamic equilibrium is reached (the steady state stage). The resulting dynamic equilibrium provides an excess of solute content decreasing to the nominal liquid composition at some distance from the interface. As a result, the effective liquidus temperature varies with distance from the interface (59-63). This phenomenon has been known as a "Constitutional Supercooling". Figure 3 provides a schematic explanation of how the concentration gradient in the liquid ahead of the advancing solid-liquid interface can cause constitutional supercooling. The concentration gradient is plotted in the upper left portion of the figure. The relevant portion of a hypothetical binary phase diagram is plotted at the lower right, using the same scale of concentration as was used for the ordinate at the upper left. By referring the concentration at a particular point on the diffusion gradient at the upper left to the plot of the binary phase diagram, the effective liquidus temperature at any location can be determinated.

The constitution of the liquid near the moving interface causes the effective liquidus to be depressed below that of the nominal

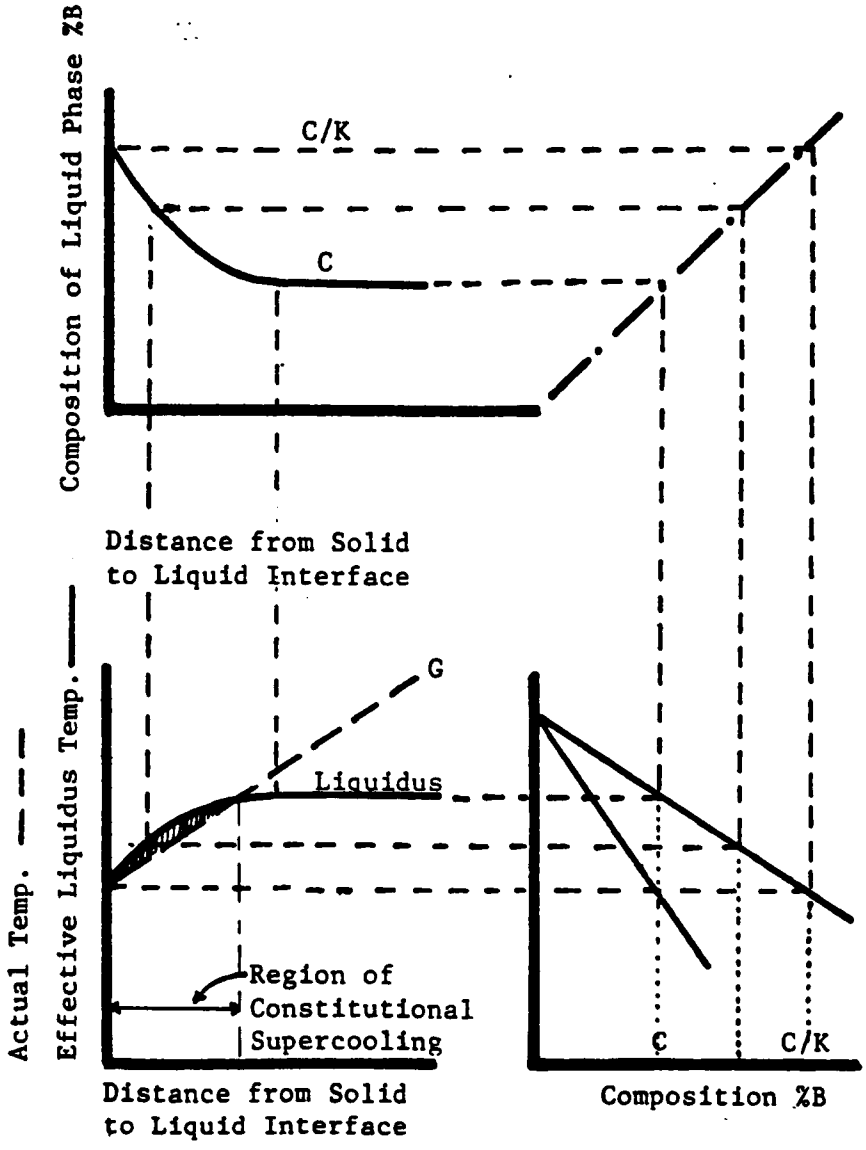


Figure 3. Schematic explanation of the origin of constitutional supercooling.

Source: Savage, W.F., "Solidification, segregation and weld imperfections," Welding in The World, 18(5-6), p. 89-114, (1980).

composition of the alloy. If the actual temperature gradient in the liquid ahead of the moving interface were to be shown by the dashed line, G, in Figure 3, the actual temperature would be below the effective melting temperature over a given distance. If by chance of protuberance was to form on the solid-liquid interface under these conditions, its tip would be in a region where the actual temperature was below the effective melting temperature of the surrounding liquid. Thus it could grow dendritically and reject the latent heat of fusion to the surrounding constitutionally supercooled liquid until it reached the point where the actual temperature in the liquid coincides with the effective liquidus (25).

The extent of constitutional supercooling in a given alloy depends on the following factors (25,59,63,64):

1. The temperature gradient in the liquid (G)
2. The rate of growth at the solid-liquid interface (R)
3. The nominal solute content of the alloy (C_o)
4. The diffusion coefficient of solute in the liquid (D).

As growth rate (R) increases, the constitutionally supercooled region in front of the solid-liquid interface increases. In turn, increasing in diffusion coefficient (D) of solute in the liquid and the temperature gradient in liquid (G), and decreasing in the solute content (C_o) decrease the extent of constitutional supercooling.

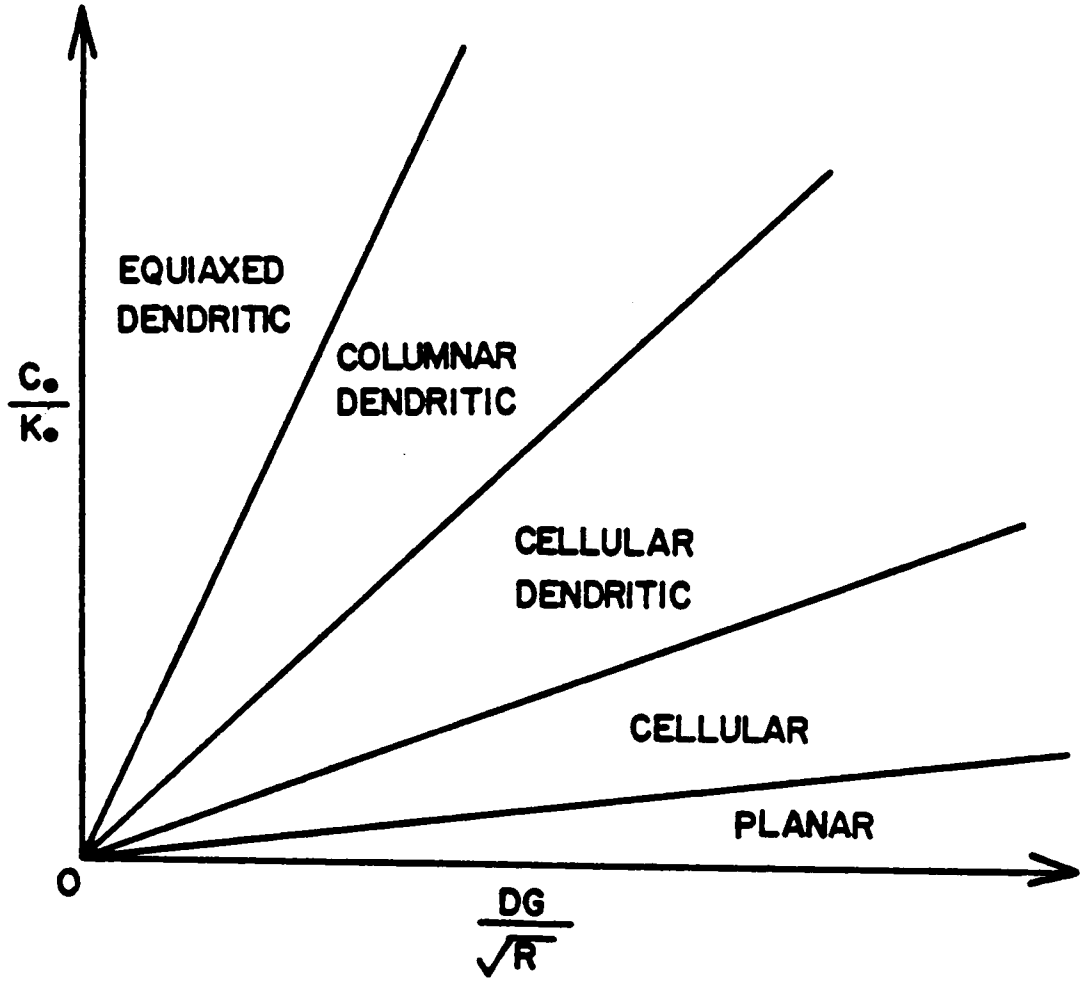
The extent of constitutional supercooling has a pronounced effect on the solidification mode and the resulting solidification substructure. The solidification pattern varies from being planar, through a cellular, a cellular dendritic and a columnar dendritic, to

being an equiaxed dendritic mode as the degree of supercooling increases, as shown schematically in Figure 4 (25,59,63).

b. Solidification Behavior of Stainless Steel Weld Metal

Since hot cracking in stainless steel occurs at or near the solidus temperature of the material, solidification behavior and high temperature microstructure during welding are significantly important to the understanding of hot cracking. Since the middle of the 1970^{s}, many investigators (33,66-95) have attempted to provide greater understanding of the mechanism of formation of the room temperature ferrite in the weld metals and its relationship to hot cracking. The presence of ferrite is related to reduced hot cracking susceptibility when its content is about 5-10% at room temperature. In addition, investigators have also attempted to correlate the hot cracking susceptibility of austenitic stainless steels with the primary solidification mode in addition to the room temperature ferrite content, and a good correlation between room temperature ferrite and the primary solidification mode has been established.

The solidification behavior of austenitic stainless steel welds is complicated by the occurrence of a variety of ferrite morphologies. The Fe-Cr-Ni ternary diagram shown in Figure 5 provides the basis for predicting phase equilibrium and solidification in austenitic stainless steels. The liquidus surface of the system as shown in Figure 5a, is represented by a series of isotherms which reach a minimum along a line running from the Fe-Ni peritectic reaction point, Fe-4 Ni, to the ternary eutectic point at 49 Cr-43 Ni- 8 Fe. The AISI 300 series alloy containing typically 60-70% Fe with Cr and Ni will be



C_o - NOMINAL SOLUTE CONTENT
K_o - DISTRIBUTION COEFFICIENT
D - DIFFUSION COEFFICIENT OF SOLUTE IN LIQUID
G - TEMPERATURE GRADIENT IN LIQUID
R - GROWTH RATE

Figure 4. Schematic representation of the influence of the parameters on the pattern of solidification.

Source: Lundin, C.D. and Chou, C.P.D., "Hot cracking susceptibility of austenitic stainless steel weld metals," Welding Research Council Bulletin 289, Nov.(1983).

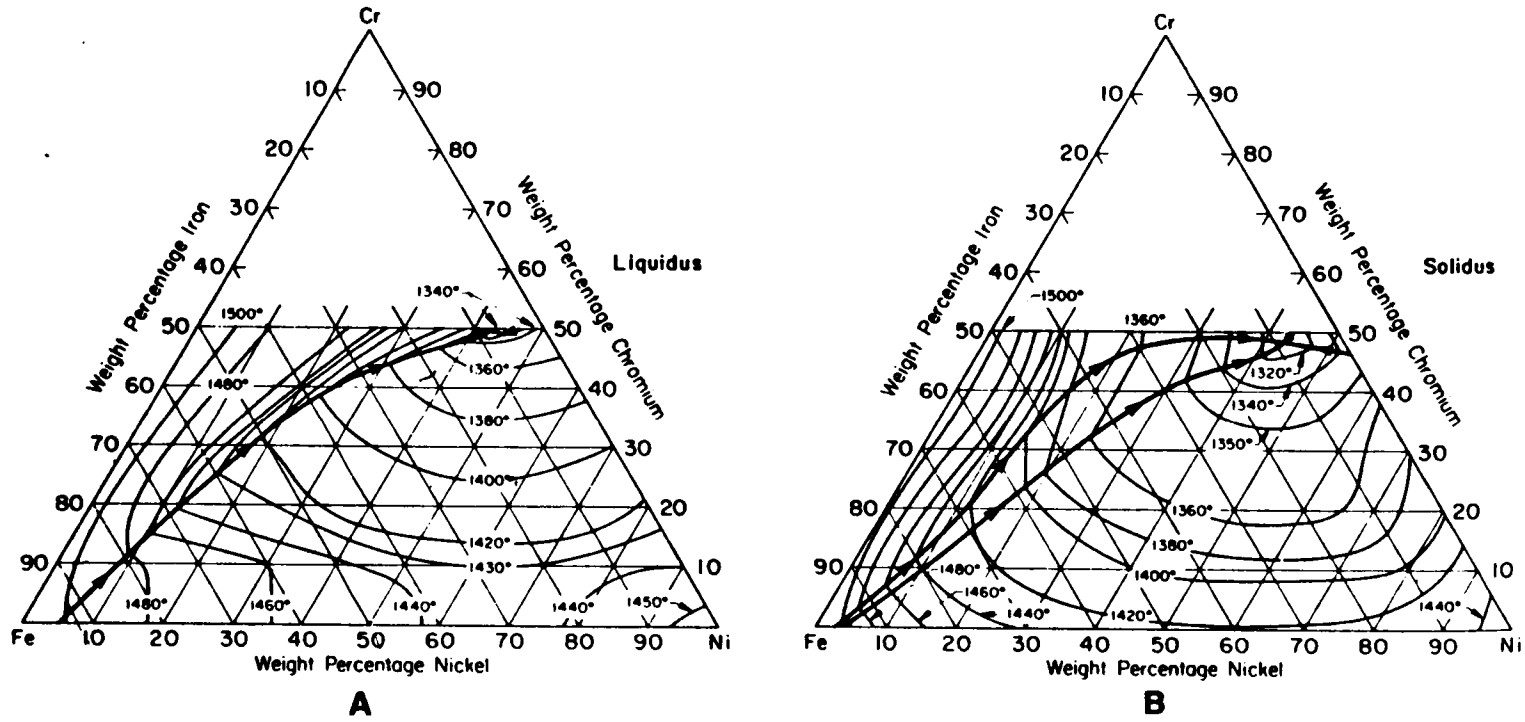


Figure 5. The Fe-Cr-Ni ternary phase diagram. a. Liquidus surface, b. Solidus surface.

Source: Metals Handbook, Vol. 8, p. 424, ASM, (1973).

close to the eutectic region of the diagram. Alloys having compositions on the Ni rich side of the eutectic liquidus will solidify as primary austenite while those on the Cr rich side of the eutectic through will solidify predominantly as a primary ferrite. However, depending upon the composition of the liquid in the last stage of the solidification, austenite or ferrite will form along the interdendritic regions.

The solidus surface as shown in Figure 5b shows that the isotherms in the delta ferrite and austenite regions are separated by the three phase isotherms which converge to a point at the ternary eutectic temperature of 2372°F (1300°C). The initial solidification phase is dependent only on the nominal composition of the liquid at the liquidus temperature. But segregation of alloying element during non-equilibrium solidification, as mentioned earlier, shifts the overall composition of the remaining liquid and alters the final solidification product. An increase in the concentration of austenite stabilizers in the remaining liquid leads to solidification as an austenite phase. On the other hand, local enrichment in ferrite forming elements ahead of the solid-liquid interface promotes solidification as delta ferrite (74).

Primary Austenitic Solidification Mode. Since most commercial AISI 300 series stainless steels are composed of 16-25% Cr and 8-20% NI, their compositions are localized in the iron-rich corner of the ternary phase diagram. Many investigators (67-70,72,74,75,80,83,85,95) have used a pseudo-binary diagram at a

constant iron content as shown in Figure 6, to predict the phase equilibrium during solidification and cooling to room temperature.

Although pseudo-binary diagrams such as in Figure 6 can be constructed at constant iron sections through the ternary diagram, the tie lines across the two and three phase fields do not necessarily fall on the constant iron plane. Therefore, it is rarely possible to predict either the initial solid composition or the equilibrium distribution coefficient accurately from the pseudo-binary diagram. It also has to be noted that other alloying elements, except Fe, Cr, and Ni, which are not considered in the diagram, can also significantly influence the phase equilibrium at a particular temperature. The prediction of compositional variation during non-equilibrium solidification of weld metal (Case III solidification) is even more difficult (74).

If the alloy composition is sufficiently far from the eutectic composition (for example C1 in Figure 6), solidification will occur completely as austenite and there will be no ferrite formation during the last stage of solidification. However, as the compositions approach the eutectic point (C2 in Figure 6), some ferrite can form during the final transient stage of solidification likely by the "eutectic reaction" (68-70). This ferrite will then be confined to the solidification cell boundaries. But according to Hoffmeister (96), the interdendritically formed ferrite, due to the segregation during solidification, may be either "proeutectic or eutectic" depending on the composition of the weld metal and the course of solidification. Lippold et al. (74) expressed another opinion to the

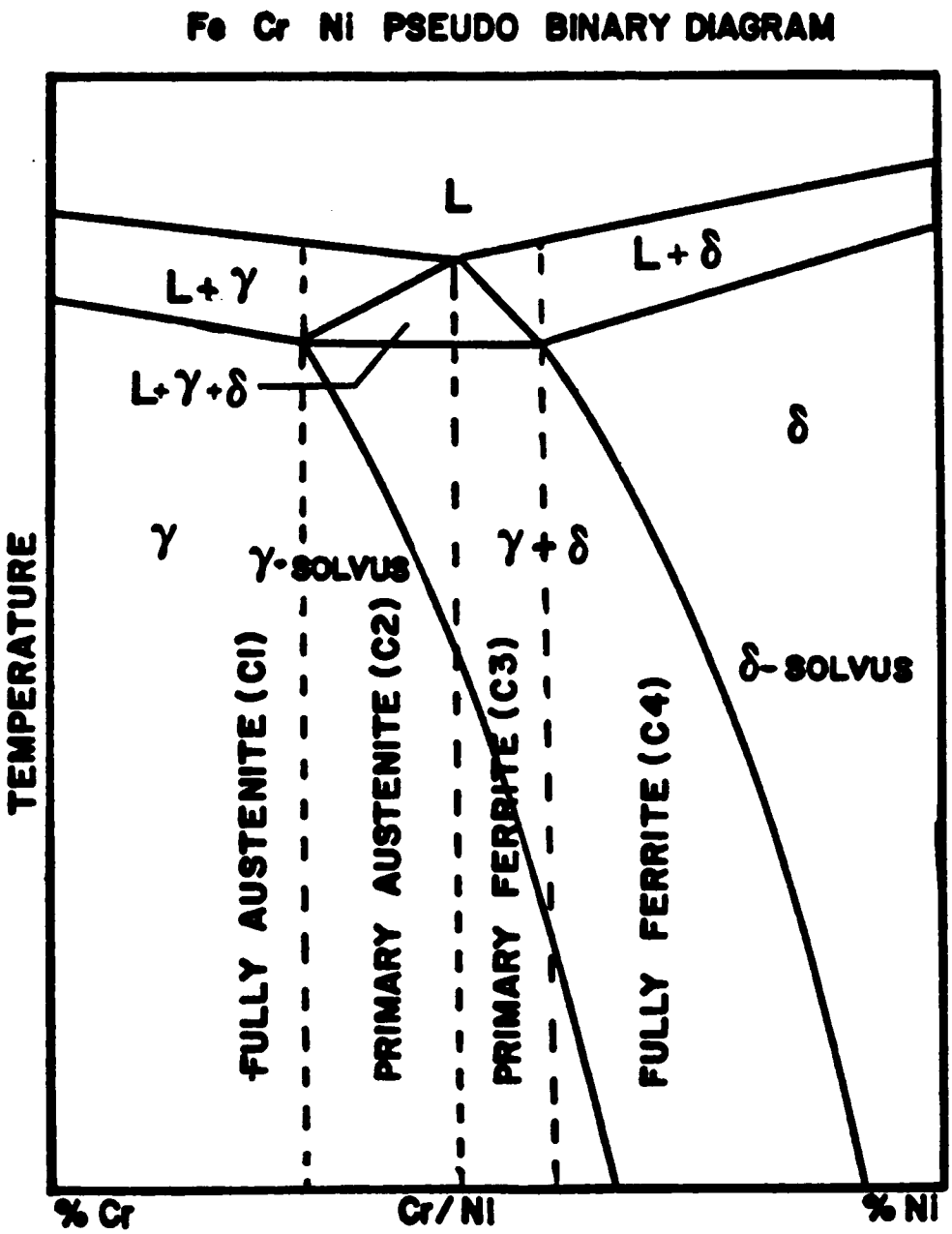


Figure 6. Schematic Fe-Cr-Ni pseudo-binary diagram at constant Fe content.

effect that the delta ferrite formed during the last stage of solidification is from the "divorced eutectic reaction", i.e., the delta ferrite is part of the divorced eutectic mixture of austenite and ferrite from the last liquid to solidify during the terminal transient stage. Lippold et al. further mentioned that since some divorced eutectic ferrite is observed at the grain and subgrain boundaries, the ferrite formed during the last remaining liquid is sufficiently enriched in ferrite formers and depleted in the austenite stabilizers to remain ferrite upon cooling to room temperature. However, a portion of the eutectic ferrite with a low Cr/Ni ratio probably transforms to austenite via a "massive transformation" although the primary austenite experiences no solid state transformation upon cooling to room temperature.

Therefore, according to Figure 6, during the initial transient period, alloys having a composition C2 will form austenite at the cores of the cellular dendrites and then it is surrounded by a region of nearly nominal composition (C2) formed during the steady state period. When the solute gradients in the liquid in advance of the adjacent solid-liquid interfaces impinge upon one another, the terminal stage begins and the solid formed is enriched in chromium and depleted in nickel as shown schematically in Figure 7a (74).

Primary Ferritic Solidification Mode. Since Masumoto et al. (67) observed that the hot cracking susceptibility of austenitic stainless steels is directly related to the primary solidification mode of material rather than the room temperature ferrite content, and the primary ferritic mode reduces or prevents hot cracking, many

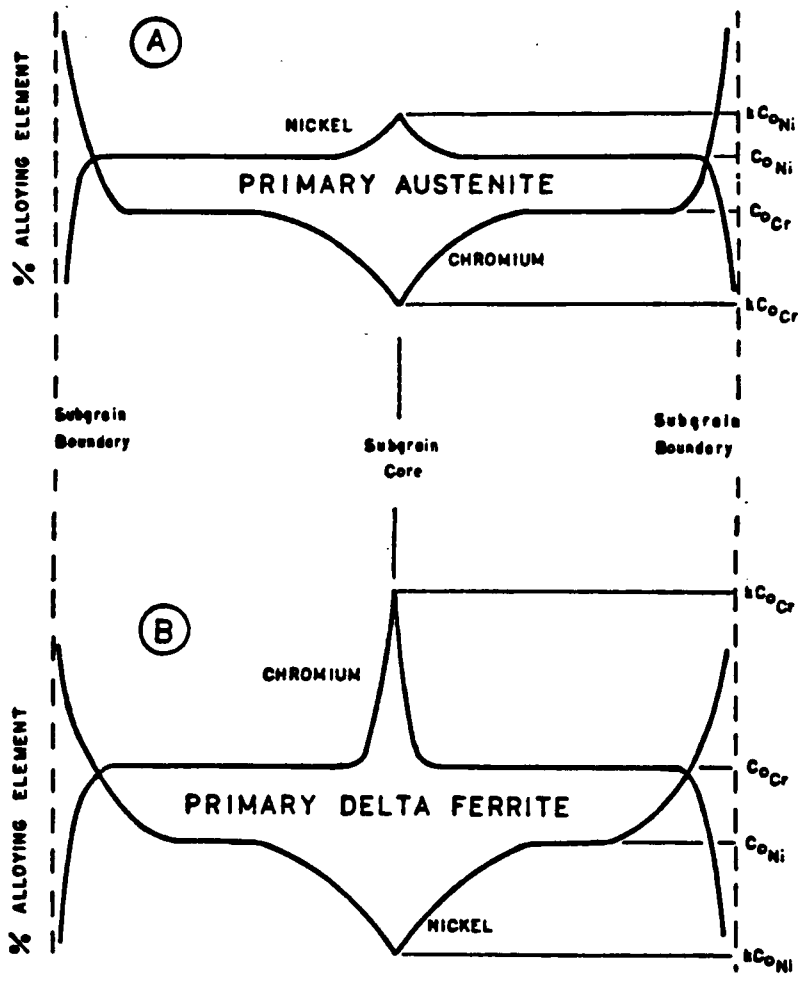


Figure 7. Schematic illustration of the chromium and nickel distribution across a subgrain following solidification. a. Primary austenite, b. primary ferrite.

Source: Lippold, J.C. and Savage, W.F., "Solidification of austenitic stainless steel weldments: Part I- A proposed mechanism," Welding Journal, 58(12), p. 362s-373s, (1979).

investigators (33,73,75-77,85,87,91,93-95) have paid enormous attention to the beneficial effects of the primary ferritic solidification mode on the hot cracking susceptibility of materials.

As in the case of the primary austenitic mode, the primary ferritic solidification behavior can be explained by utilizing the pseudo-binary diagram in Figure 6. Alloy having a composition on the Cr rich side of the eutectic liquidus (right side of the eutectic point in Figure 6) will solidify as a primary ferrite. If the composition is sufficiently far from the eutectic composition (C4 in Figure 6), solidification will occur completely as ferrite. As the compositions approach the eutectic point (C3 in Figure 6), some austenite can form during the terminal stage of solidification. However, segregation during solidification and variables in cooling rate can result in a different solidification process than that expected from the phase diagram.

Therefore, when the temperature reaches the liquidus of the material, the initial transient occurs at the cores of the dendrites, i.e., ferrite will first form in the cores of the cellular dendrites, and the portion of the ferrite subgrain that solidifies under steady state conditions forms a solid of nominal composition until the advancing interface impinges upon an adjacent solidification front. Once impingement occurs, the terminal transient stage begins and solidification is completed by the formation of austenite or ferrite depending on the composition of the last solidifying liquid. The distribution of chromium and nickel during solidification as a primary ferrite is schematically summarized in Figure 7b.

Lippold and Savage (74) insisted that as in the case of the primary austenitic mode, the terminal transient stage is completed by the formation of a divorced eutectic mixture of austenite and ferrite. However, David et al. (80), Fredriksson (66), Suutala et al. (92) and Brooks et al. (70) observed that after partial primary ferritic solidification, the ferrite is enveloped by austenite until solidification proceeds to completion, i.e., the terminal transient occurs by a peritectic reaction instead of eutectic reaction.

In summary, the primary solidification mode can be easily distinguished from examination of the room temperature microstructure. In general, when the ferrite is located along the cores of dendrites, the alloy is considered to have ferrite as a primary solidification phase. When ferrite is located along dendritic boundaries, the alloy solidified primarily as austenite. Further, based on the alloy composition, which is a main factor controlling the primary solidification mode, four solidification procedures can be distinguished using a pseudo-binary diagram (Figure 6).

1. Fully austenitic (composition C1): $L - L + \gamma - \gamma$
2. Primary austenitic (composition C2):

   $L - L + \gamma - L + \gamma + \delta - \gamma + \delta$
3. Primary ferritic (composition C3):

   $L - L + \delta - L + \delta + \gamma - \delta + \gamma$
4. Fully ferritic (composition C4): $L - L + \delta - \delta$

(Where, L = liquid, γ = austenite, δ = delta ferrite)

The primary solidification mode is also significantly sensitive to cooling rate and the solidification conditions. Recently, Vitek

and Dasgupta et al.(85) have observed the modification of microstructure of AISI 308, 310 and 312 austenitic stainless steels evaluated by rapid solidification technique (laser welding and splat quenching) when compared to the microstructures of materials welded by GTAW. They found that the microstructure of 310 stainless steel, which had a fully austenitic structure after GTA welding, was not changed by the faster cooling rate. However, the room temperature microstructures of 308 and 312 steels were very sensitive to the cooling rate. With a faster cooling rate, the microstructure of 308, which showed a duplex austenitic-ferritic structure (10% ferrite) after GTAW, showed a fully austenitic structure. That is, the solidification mode was shifted from primary ferrite to primary austenite by the faster cooling rate. They (85) further found that although 308 had a primary austenitic solidification mode after laser welding, its hot cracking resistance was not impaired when compared to the case when the same nominal composition showed a primary ferritic solidification mode.

c. Ferrite-Austenite Transformation and Ferrite Morphology

Arata et al. (94), David et al. (80) and Lundin et al. (97) have found that when materials have ferrite as a primary solidification phase, as much as 60-80% of the liquid in a common composition range of AISI 304, 308 and 303 stainless steels solidified by primary ferrite before austenite started to form from the remaining melt. However, when the weld metal cooled below the solidus temperature, the primary ferrite transformed to austenite by a solid state transformation mechanism. Therefore, at room temperature, only a

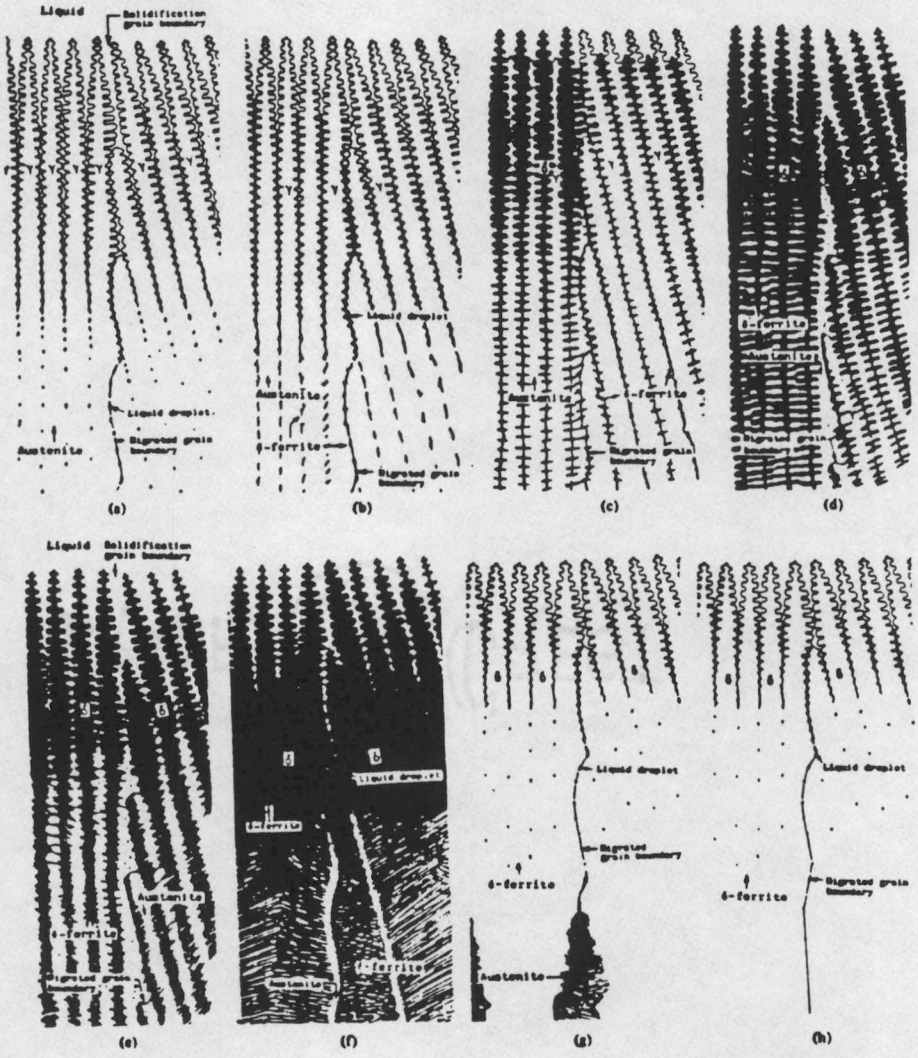
small portion of the primary ferrite will be observed as a residual ferrite resulting from partial ferrite-austenite transformation during solidification and subsequent solid state transformation.

The distribution and morphology of delta ferrite in the as-welded condition have been shown to be related to the primary solidification mode, which is principally influenced by the alloy composition and cooling rate, and the nature of the solid state ferrite-austenite transformation. In general, as the ratio of the Cr_{eq}/Ni_{eq} increases, the solidification mode changes, as shown earlier, from fully austenitic, to primary austenitic, primary ferritic and fully ferritic modes, and ferrite morphology also changes from interdendritic (eutectic) to vermicular, lacy, lathy (acicular) and widmanstatten austenite. However, different investigators use different names for the same type of ferrite as shown in Table 3. Schematic drawings of each type of ferrite are given in Figure 8 (by Katayama et al. (95)).

Vermicular Type Ferrite. The first study of solidification behavior and formation of vermicular type ferrite in a 304 austenitic stainless steel was conducted by Fredriksson (66), who used a controlled directional solidification technique. Fredriksson found that the advancing interface of the individual dendrites at the solidification front transformed to a lathy type ferrite morphology. However, in a region far behind the advancing tip, where the cooling rate is much slower, the ferrite morphology is of vermicular type. Thus, he concluded that the vermicular type ferrite was formed by a "diffusion controlled solid state transformation" with partitioning of

Table 3. Correlation between solidification process and room temperature ferrite morphology.

$Creq/Nieq$	Increase ⟶							
Solidification process (Type)	L → L+γ → γ (A)	L → L+γ → L+γ+δ → γ+δ (AE)	L → L+γ+δ → γ+δ (E)	L → L+δ → L+δ+γ → δ+γ (FE)		L → L+δ → δ → δ+γ (with δ→γ transf.) (F)		L → L+δ → δ (F)
Characteristic microstructure (Mode)	Fully austenite (FA)	Intercellular (eutectic) ferrite (IF)	Eutectic ferrite (EF)	Vermicular ferrite (VF)	Lacy ferrite (LF)	Acicular ferrite (AF)	Widmanstätten austenite (WA)	Fully ferrite (FF)
		Globular ferrite (GF) Island-like ferrite (IF)						
N Suutala T. Takalo T Moisio				(Vermicular ferrite)		(Lathy ferrite)	(Lathy austenite)	
J Lippold W Savage		(Intercellular ferrite)		(Vermicular ferrite)		(Acicular ferrite)	(Widmanstätten austenite)	
S. David				(Vermicular ferrite)	(Lacy ferrite)	(Acicular ferrite)		
J Brooks A Thompson J Williams	(Austenite)	(Eutectic ferrite)		(Skeletal ferrite)		(Lathy ferrite)	(Widmanstätten austenite)	



(a) Mode FA (fully austenite);
(b) Mode IF (intercellular eutectic ferrite);
(c) Mode EF (eutectic ferrite);
(d) Mode VF (vermicular ferrite);
(e) Mode LF (lacy ferrite);
(f) Mode AF (acicular ferrite);
(g) Mode WA (Widmanstätten austenite);
(h) Mode FF (fully ferrite).

Figure 8. Schematic representation of solidification and solid state transformation behavior resulting in different characteristic morphologies of weld metal microstructure.

Source: Katayama, S. et al., "Correlation among solidification process, microstructure, microsegregation and solidification cracking susceptibility in stainless weld metal," Transactions of JWRI, 14(1), p.123-138, (1985).

Ni to austenite and Cr to ferrite, leaving only a Cr enriched, Ni depleted ferrite core along the dendrite and this core becomes a stable ferrite at room temperature.

This type of ferrite was also found by many other investigators (68,70,82,88,89,94,95). These investigators also concluded that during cooling, a large fraction of the primary ferrite is "consumed" by austenite in the diffusion controlled solid state transformation as found by Fredriksson (66).

Lippold and Savage (75) have also found the vermicular type ferrite in an alloy having a composition near the eutectic composition which had a primary ferritic mode. The alloy composition range (region 2) found by Lippold et al. (75) as yielding a vermicular type ferrite is given in the schematic pseudo-binary diagram of Figure 9. Unlike what was found by other investigators (66,68-70,82,88,94,95), Lippold (75) and Lyman (84) have observed that the vermicular type ferrite is not formed by the "diffusion controlled mechanism", but by the "diffusionless massive transformation mechanism". Both(75,84) suggested that the vermicular ferrite is the result of a Cr-rich, Ni-depleted dendrite core formed during the initial transient stage of solidification and this is the only retained ferrite, even though at the elevated temperature a large fraction of the dendrite is ferrite. They further suggested that the bulk of the dendrite at nominal composition, which solidifies as primary ferrite (formed during the steady state stage), is stable austenite at room temperature, and that the ferrite-austenite boundary originally near the cell boundary moves inward until it reaches a point at which the compositional driving

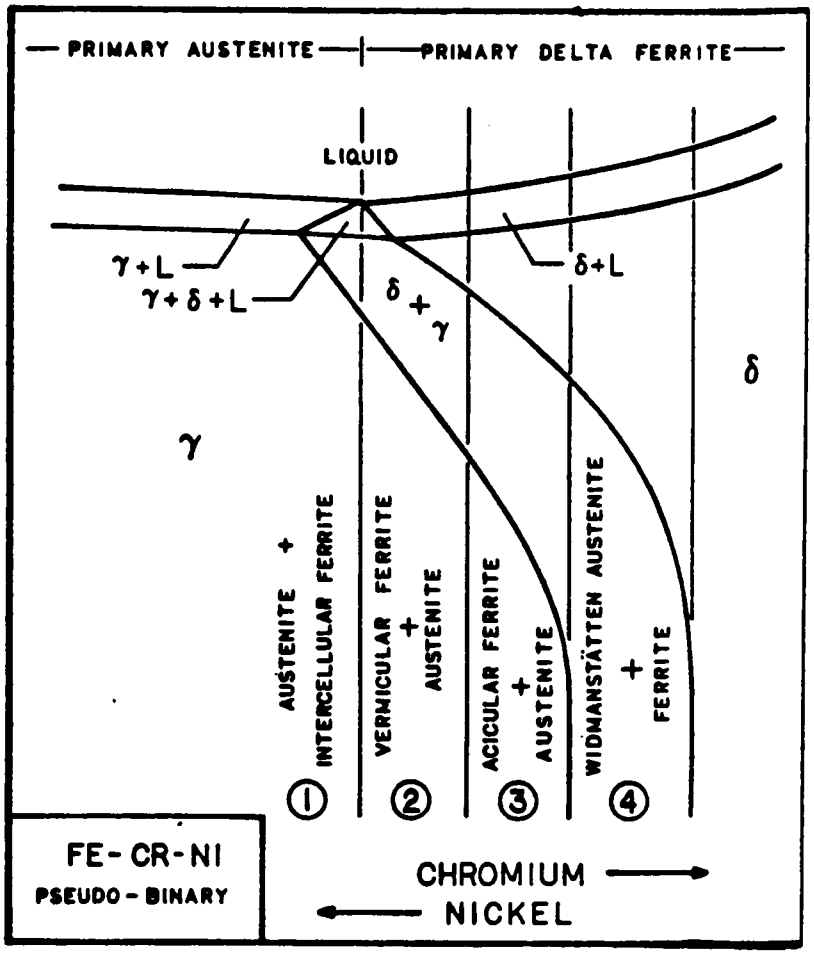


Figure 9. Schematic pseudo-binary diagram of the Fe-Cr-Ni ternary system illustrating the effect of composition on austenite-ferrite morphology in austenitic stainless steel weldments.

Source: Lippold, J.C. and Savage, W.F., "Solidification of austenitic stainless steel weldments: Part II- The effect of alloy composition on ferrite morphology," Welding Journal, 59(2), p. 48s-58s, (1980).

force is insufficient for further boundary motion. This position is located somewhere within the initial transient region at the subgrain core, leaving ferrite along the core of the solidification substructure at room temperature.

However, none of the other investigators except David (82), clearly defined the characteristic shape of vermicular morphology to distinguish from the other types of ferrite morphology. He characterized that vermicular ferrite appears as an aligned skeletical network or as a curved soft form depending upon the section viewed. The alignment is along the primary dendrite growth direction and ferrite is located at the cores of the primary and secondary arms, i.e., individual substructure (dendrite) and its growth direction are clearly distinguishable.

Lacy, Lathy and Acicular Type Ferrite. At higher Cr_{eq}/Ni_{eq} ratios and higher cooling rates, the ferrite morphology changes from vermicular type to the more complicated and needle-like ferrite: lacy, lathy and acicular. However, as shown in Table 3, names of the ferrite morphology applied by various investigators may be different .

The alloy composition range (region 3) which will have the complicated ferrite types at room temperature is given in Figure 9 by Lippold et al. (75). As Figure 9 reveals, in this composition range, the first ferrite-austenite transformation occurs at relatively low temperature when compared to the case of the vermicular type ferrite. That is, the rate of the partitioning of elements by diffusion is less. Here again, Lippold and Savage (75) and Lyman (84) suggested that acicular ferrite is formed by a diffusionless transformation

mechanism as in the case of the vermicular ferrite, whereas other investigators (68,70,82,88,94,95) suggest a diffusion controlled transformation.

Suutala et al. (88) found that the austenite formed between ferrite dendrites, by a peritectic or eutectic reaction, grows into the remaining liquid and already formed ferrite. Further, below the solidus temperature, the simultaneous or immediate growth of the austenite into the ferrite by an equiaxial or acicular mechanism results in a drastic decrease in the volume fraction of ferrite and in a partitioning of elements between the austenite and residual ferrite. The compositional difference is caused by a solid state diffusion controlled transformation and is greater than that generated by solidification. Brooks (68,70) has also found, after extensive STEM work, that the ferrite is enriched in Cr and depleted in Ni with respect to the austenite. This composition variation between the two phases can only result from a diffusion controlled transformation of ferrite to austenite. The Cr and Ni concentration profiles within each phase is also consistent with alloy partitioning during cooling through the two phase field. Brooks further noted that the Cr and Ni concentration profiles of the lathy and vermicular morphology are similar.

According to Lippold and Savage (75), the alloy composition within region 3 in Figure 9 will have ferrite as the primary solidification phase and this primary delta ferrite is stable over a relatively large temperature range (between the solidus and ferrite solvus) and thus a decreasing of the concentration gradients in the

initial transient region by diffusion occurs during cooling from the solidus to the ferrite solvus. However, the cooling rate through the two-phase region still suppresses the diffusion controlled transformation of ferrite and thus the microstructure exhibits an acicular morphology at room temperature.

As in the case of the vermicular type ferrite, an exact definition of the characteristic appearance and directionality of these types of ferrite is not available. As Table 3 shows, the lathy ferrite referred by Brooks et al. (68,70) and Suutala et al. (87-89) is named as acicular ferrite by Lippold and Savage (75). David (82) and Katayama et al. (95) divided lathy ferrite into lacy and acicular ferrite. David (82) has defined the metallographical appearance of the lacy and acicular ferrite. According to David (82), the lacy ferrite is characterized by long columns of interlaced ferrite network oriented along the growth direction in an austenite matrix and the ferrite is located within the cellular dendrites, i.e., each substructure can be easily distinguishable. However, the secondary and ternary arms can not be distinguished. David further suggested that the origin of the lacy type ferrite is likely to be by transformation of primary ferrite cells to widmanstatten austenite and ferrite. Acicular ferrite, as characterized by David, is needle-like ferrite randomly distributed in an austenite matrix. Unlike the vermicular and lacy ferrite, the structure has no directionality and also does not seem to conform to the solidification substructure in any way.

Widmanstatten Austenite. For alloys having a higher Cr_{eq}/Ni_{eq} ratio, ferrite transforms to austenite by the nucleation and growth of austenite within the ferrite, producing widmanstatten microstructure (68). The alloy composition range which will have a widmanstatten austenite is given as region 4 in Figure 9. According to Figure 9, for alloys in this range of composition, the ferrite and austenite should coexist in a near equilibrium mixture at room temperature. According to Lippold et al. (75), since the composition of the austenite formed in this composition range differs from the nominal composition, a massive transformation is impossible. Consequently, a diffusion controlled transformation of ferrite to austenite must occur upon cooling through the two-phase region. Thus, the as-welded microstructure consists of ferrite and widmanstatten austenite which nucleates at an austenite boundary and forms along a specific habit plane in the ferrite. For this type ferrite, the relatively large range of temperatures over which the ferrite is stable, extensive coarsening of the ferrite grains prior to transformation is allowed.

According to Brooks (70), the widmanstatten austenite also can form within the ferrite cell (along the cores) as well as along the austenite boundary at the grain boundary. He found that the austenite nucleated within the ferrite before the ferrite-austenite boundary receded and grew within the ferrite.

Interdendritic Ferrite (Eutectic). This type of ferrite usually forms in alloys having a composition close to the eutectic, especially toward the left side of the eutectic composition (region 1) in the pseudo-phase diagram of Figure 9. Alloys in this range solidify as

primary austenite and may form a limited amount of ferrite by a eutectic or peritectic reaction depending upon the composition of the remaining liquid during the last period of solidification. However, even at higher Cr/Ni ratios which have a primary ferritic solidification mode (composition within region 2 in Figure 9), ferrite can form interdendritically. Suutala et al. (88) observed that during primary ferritic solidification, the austenite forms between ferrite dendrites (interdendritic region) and grows into the last solidifying liquid and already formed ferrite. The growth into the remaining liquid causes segregation typical of austenitic solidification and may then enable the formation of interdendritic ferrite.

d. Effects of Ferrite on Hot Cracking

To minimize the possibility of hot cracking during welding of the austenitic stainless steels, it has been common practice to produce welding filler metals of such composition that the weld deposit contains a small amount (5-10%) of delta ferrite at room temperature. The amount of ferrite in the austenite matrix is known to be very dependent upon the specific composition of the weld deposit (43,98). Further, the amount of ferrite required to prevent or reduce hot cracking is also dependent upon the composition of material, especially impurity levels of P, S, Si etc.

However, as mentioned earlier, the hot cracking susceptibility of austenitic stainless steels is directly correlated with the primary solidification mode of the material being welded rather than the absolute ferrite content at room temperature. The primary ferritic

solidification mode leads to better hot cracking resistance than when material has a primary austenitic solidification mode.

The reasons why the primary ferritic solidification mode leads to a higher resistance to fusion zone cracking are not clear. However, it has been postulated in the literature (31,34,43,44,66,87,94,95,99-104) that:

1. Ferrite has a higher solubility for impurities; P, S, Si, etc than austenite and thus decreases microsegregation along the grain boundaries.

2. The generation of a substantial area of interphase boundaries between ferrite and austenite in addition to the austenite-austenite boundaries reduces the concentration of impurities at the austenite-austenite grain boundaries.

3. Grain refinement occurs in a two phase alloy.

4. Lowered potential for liquid wetting with two different crystal structures at the interphase boundaries.

5. Alloys having compositions which form some ferrite have a smaller solidification temperature range than those having fully austenitic compositions.

6. Cracks can be arrested because of the difficulty in propagation along a path of irregular ferrite-austenite boundaries rather than along single phase boundaries.

7. The ductility of ferrite at high temperatures is greater than that of austenite, allowing relaxation of thermal stresses.

8. Contraction stresses are reduced because of the smaller coefficient of thermal expansion of ferrite.

Unfortunately most of the above postulations are still subject to arguments among investigators. Recently, Brooks et al. (100) thoroughly examined each of the above postulations and found that which of them plays an important role in reducing hot cracking susceptibility is dependent upon the primary solidification mode, i.e., only some of the above postulations play an important role for a particular solidification mode.

Therefore, since in most cases hot cracking is a direct consequence of the formation of the low melting liquid films along the grain boundaries resulting from the microsegregation, any mechanism (primary solidification mode, ferrite content, grain refinement - increased grain boundary areas, etc.) which reduces the microsegregation along the grain boundaries during solidification and subsequent solid state transformation will reduce hot cracking susceptibility of austenitic stainless steels.

3. EFFECT OF COMPOSITION ON HOT CRACKING SUSCEPTIBILITY

In the previous section, theories of hot cracking proposed that the segregation of certain elements at grain boundaries and in interdendritic regions is closely linked to crack formation. As a whole, the experimental evidence indicates that more than one hot cracking mechanism can operate to produce microfissuring in weld metal and HAZs. Regardless of the uncertainty of the rupture mechanics, there has been good agreement on the residual elements which promote cracking. With the worst offending residual elements defined, it should be possible to ascertain the tolerable level of each. However,

this has proved impractical because the amount of any elements that can be tolerated is dependent upon the following principal factors which also control the formation of microfissures (28);

1. microstructure
2. composition
3. stress
4. hot ductility
5. presence of notches.

Unfortunately the extension of hot ductility and hot cracking results directly to chemical analysis alone is one of the most difficult aspects of translating the results to engineering practice. Therefore, some general observations in the literature (28-57) concerning the effects of composition are indicated below.

The summarized "general trends" of the influence of alloying elements and impurities on the weld metal and base metal HAZ cracking can be found from the works by Hull (29), Morishige et al. (30) and Linnert (28).

Hull (29) has evaluated quantitatively, by means of the cast pin tear test, the effects of 18 alloying elements on susceptibility to hot cracking in austenitic stainless steels. N, Mn, Mo, W and Cr decrease the susceptibility to hot cracking. On the basis of equal percentage by weight, Co, V, Al, Ni, Ta, Cu, Si, Nb, Ti, C, Hf, Zr, and B cause increasing amounts of cracking, in the order listed. From this observation, Hull recommended possible compositions for alloys resistant to hot cracking, emphasizing that Cr should be as high and Ni as low as possible without resulting in unacceptable levels of

delta ferrite, that Mn should be higher than normally used, and C and Si low.

A similar trend for the base metal HAZ cracking was also found by Morishige et al. (30) after extensive hot ductility and hot tear hot cracking tests. According to Morishige et al.,

$$\Delta H = -700\ \%C + 17\ \%Cr - 37\ \%Ni - 117\ \%Nb + 29\ \%Mo - 188$$

$$L = 299\ \%C + 8\ \%Ni + 142\ \%Nb - 105$$

When the hot ductility parameter ΔH of material is below 100 and the hot cracking parameter L value is positive, the alloy has a poor hot ductility and is susceptible to HAZ hot cracking. Thus for the austenitic stainless steels, C, Nb and Ni should be controlled to reduce hot cracking susceptibility.

In terms of the impurity elements, Linnert (28) found that, the most frequently dealt with offending elements, in approximate order of decreasing potency, are B, P, S, Se, Sn, Si, Cb and Ta.

a. Carbon and Silicon (31-42,57)

The effects of carbon and silicon on weld cracking are somewhat inter-related. However, the general opinion is that high carbon and silicon contents are harmful from the point of view of fissuring. Within certain limits, increasing the carbon content can compensate for the unfavorable influence of silicon, but with a further increase beyond certain limits, the crack tendency increases in many cases.

Of many theories about the influence of silicon on the crack susceptibility proposed in the literature, the following has been more or less accepted (35):

1. The formation of silicate films at the grain boundaries;

films having a low melting point can cause solidification cracks. High melting point silicates reduce the homogeneity of the structure and thereby the ability to withstand shrinkage stresses.

2. The formation of residual liquid enriched with silicon and having a low melting point.
3. The liquidus/solidus interval is widened.

However, the influence of silicon on the crack susceptibility is not the same in different chromium/nickel weld metals. When the material has a fully austenitic composition, it is highly sensitive to variations in the silicon content and can generally tolerate up to 0.6-0.7 %Max. However, when material has a partially ferritic composition, the silicon content can be tolerated up to 2-2.5% without increasing the crack susceptibility (35).

Ogawa et al. (39) found that increasing carbon content considerably improves the cracking resistance in austenitic stainless steels with a high niobium content (0.78%), but this effect is less pronounced when the niobium content is low (0.26%). Rozet, Campbell and Thomas (42) have also found a beneficial effect of carbon when silicate slag films are responsible for severe fissuring, the higher carbon levels lead to the greater fluidity of the molten pool accounting for the disappearance of the films.

Dahl et al. (37) have noted after extensive STEM microprobe analysis, of austenitic stainless steels containing niobium, as the silicon content increases there is an enrichment of the silicon content as well as the niobium and nickel contents in the fusion grain

boundary zones, resulting in a lowering of the solidification temperature of the molten grain boundary zones. Therefore, they report that a lower on-cooling zero ductility temperature (at which the ductility starts to recovery after exposure to a zero strength temperature) in the higher silicon containing materials (0.2 vs 2.15%) was attributed to the high silicon segregation along grain boundaries.

Lippold (38) also observed an increase in silicon, along with titanium, in grain boundaries in alloy 800. He found that the fusion zone cracking mechanism in alloy 800 involved the complex interaction of titanium, silicon, niobium and carbon along the solidification boundaries. He further showed that the silicon content had the greatest effect on the hot cracking susceptibility such that the heat with the highest silicon content was the most susceptible to fusion zone cracking.

Brooks et al. (40) also attributed hot cracking in A286 precipitation hardening superalloy to the Laves phase which is enriched in both silicon and boron in addition to titanium. Therefore, they recommended that decreases in both silicon and boron contents are extremely effective in reducing fusion zone cracking of alloy A286.

b. Phosphorus and Sulfur (31-34,37,39,41,43-53,57)

Most investigators indicate that both sulfur and phosphorus are the elements most detrimental in promoting hot cracking in the absence of ferrite during solidification of austenitic stainless steels. Sulfur and, to a lesser extent, phosphorus dissolve more readily in the ferrite, minimizing the segregation to the dendrite and/or grain

boundaries where strains imposed could cause microfissures. The effect of both elements on hot cracking is strongly dependent upon the primary solidification mode during welding and the mode in turn depends on chemistry and welding conditions. Astrom et als.(33) have observed that the main cause of hot cracking in 18-10 stainless steels is sulfur and, to a less extent, phosphorus segregation along the solidification boundaries, but their effects depend upon the primary solidification mode of the weld metal. In a fully austenitic weld metal, manganese largely remains in solution and is not available during the final stage of solidification to help "break up" the sulfide films. If the weld metal has a primary ferritic solidification mode, manganese which is not as soluble in ferrite is thus released to combine with sulfur resulting in decreased sulfur segregation along boundaries. Further, refinement of the two phase structure causes the sulfur and phosphorus to be more uniformly distributed throughout the solidified weld.

Similar results have also been found by Japanese researchers (46-48,52,54) in AISI 304 and 310S stainless steels. They observed that increasing both the phosphorus and sulfur contents led to an increase in the brittleness temperature range (BTR) of the materials. In case of type 304, the detrimental effect of increasing phosphorus and sulfur contents was slight because the segregation of both elements to grain boundaries was much less due to the primary solidification of delta ferrite in comparison with the primary solidification of austenite in type 310S stainless steel. They also observed that sulfur had a harmful effect but was not as harmful as

phosphorus because sulfides were formed with a granular morphology (-MnS) at a higher temperature than the temperature of the BTR. On the other hand, phosphorus was likely to segregate to form low melting eutectics with austenite and M_3P phosphides in the boundaries.

Brooks et al.(43,44,51) found that phosphorus and sulfur were the main culprits in producing cracking in austenitic stainless steel welds of type 309 and high nitrogen and high manganese containing alloys. They indicated that the ferrite level required to prevent cracking was found to be extremely dependent upon the sulfur and phosphorus contents in the weld metal. For very low levels of phosphorus + sulfur, little or no ferrite was required to prevent cracking. At low levels of ferrite and phosphorus + sulfur content, an increase of 0.01% phosphorus + sulfur required an increase of approximate 4 FN to maintain the same cracking resistance. For ferrite contents greater than 13-14 FN, large amounts of phosphorus and sulfur could be accommodated without cracking. The relationship between ferrite content and P + S content on the hot cracking sensitivity of type 309 stainless steel from the work by Lambert (51) is given in Figure 10.

Ogawa et al. (39) have also observed that in the fully austenitic weld metal, the hot cracking susceptibility increases remarkably for phosphorus and sulfur contents in excess of 0.015% and 0.01% respectively. Hot cracking resistance was significantly improved by reducing phosphorus and sulfur to less than 0.002% even in fully austenitic weld metal.

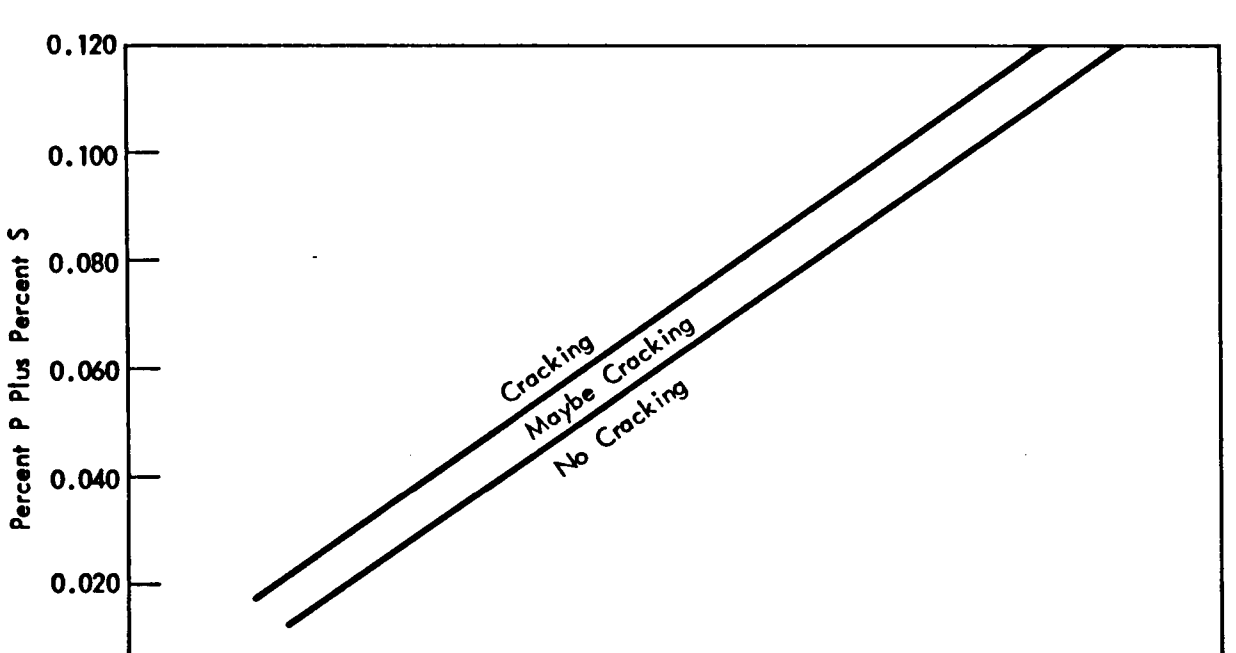


Figure 7. CRACK SUSCEPTIBILITY CHART.

Figure 10. Crack susceptibility chart in terms of ferrite content and P+S contents.

Source: Lambert, F.J., "Role of ferrite and phosphorus plus sulfur in the crack sensitivity of autogenously welded type 309 stainless steel," Y-2049, ORNL, July (1976).

German researchers (37) detected that with increasing sulfur content in niobium containing stainless steel, mixed inclusions consisting of sulfides and oxides as well as manganese sulfides were formed at grain boundaries. On heating to a zero strength temperature (ZST) during hot ductility testing, the mixed inclusions were fused into a constituent containing high portions of sulfur, chromium, manganese and silicon, and the liquid constituent did not solidify on cooling until a temperature about 200C^{o} below the ZST.

c. Nitrogen (31,39,41,44,47,48,53,55)

Since nitrogen is a strong austenizer and a strengthener, it may be expected that it would be harmful when added to stainless steels. This, however, does not appear to be the universal case. Borland et al. (31) mentioned that the nitrogen content of 18Cr-8Ni stainless steels is usually about 0.05-0.06% and in such amounts, it does not exert a harmful influence on the cracking potential of austenitic-ferritic welds.

A beneficial effect of nitrogen can be seen from the work done by Cullen and Freeman (53) who studied the effect of nitrogen on liquation due to the Cb(C,N) eutectic in type 347 steel, as shown in Figure 11. Figure 11 indicates that as the nitrogen content increases the liquation temperature of the eutectic increases producing a beneficial effect for nitrogen. Ogawa et al. (39) and Chou (165) have also found that the addition of nitrogen to the unstabilized fully austenitic weld metal (type 310S) lowers the cracking susceptibility as shown in Figure 12. Ogawa et al. attributed the beneficial effect of nitrogen to the fact that nitrogen inhibits the enrichment of

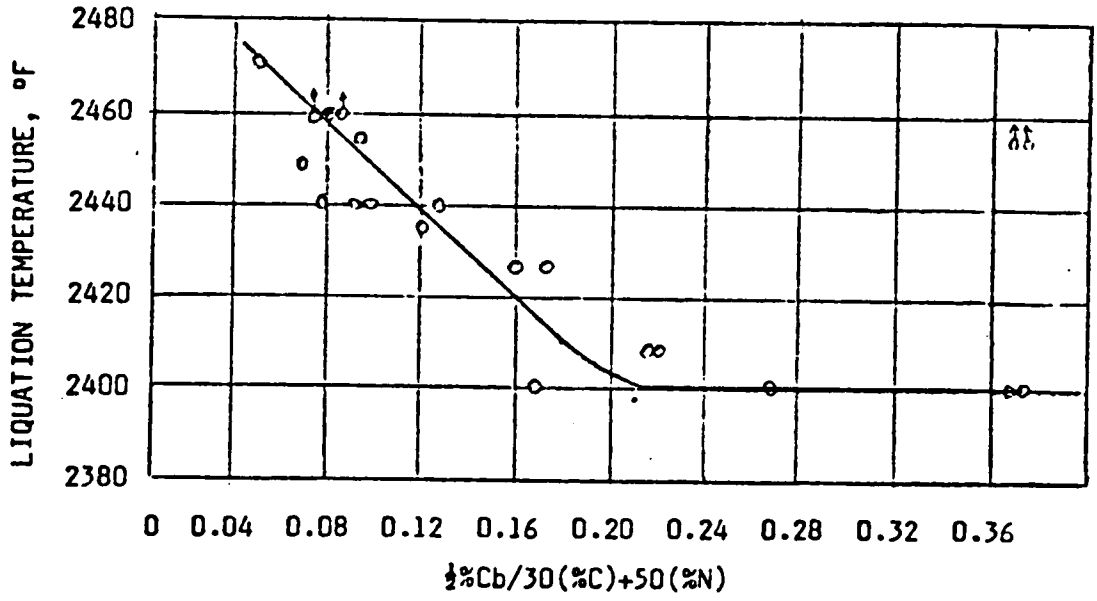


Figure 11. Liquation temperature as a function of the ratio of columbium content to the carbon and nitrogen contents.

Source: Cullen, T.M. and Freeman, J.W., "Metallurgical factors influencing hot ductility of austenitic piping at weld heat-affected zone temperatures," Journal of Engineering for Power, 85, p. 151-164, (1963).

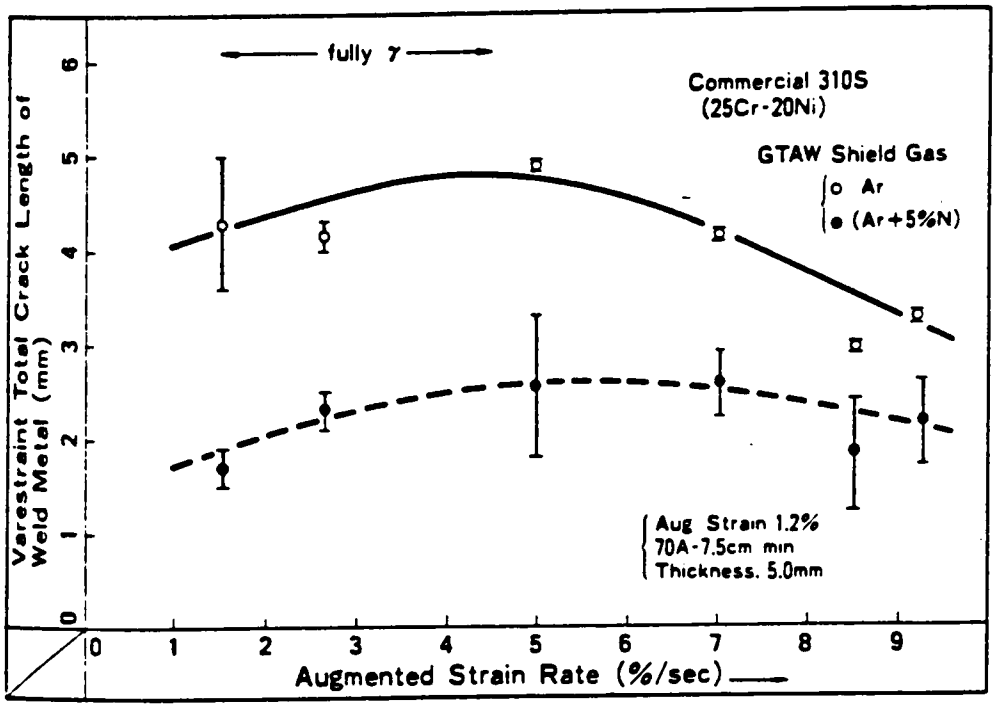


Figure 12. Effect of N on hot cracking susceptibility in fully austenitic stainless steel weld metal without Nb.

Source: Ogawa, T. and Tsunetomi, E., "Hot cracking susceptibility of austenitic stainless steels," Welding Journal, 61(3), p. 82s-93s, (1982).

silicon at grain boundaries. However, they found that nitrogen contents above 0.02% in niobium containing fully austenitic steels, decreased the hot cracking resistance significantly, but the resistance was slightly decreased in austenite-ferrite duplex weld metals containing niobium. They further noted a small increase in heat affected zone cracking with an increase in nitrogen from 0.02 to 0.06% in a fully austenitic 347 material having 0.015C and 0.3Nb.

Matsuda et al. (47) have observed that addition of 0.09-0.18% nitrogen to "18-8" stainless steels resulted in a decrease of primary delta ferrite content from 70-75% to 0-50%, and thus the 5% residual ferrite in the weld metal at room temperature was decreased to about 0-1.5%. They further noted that the degree of microsegregation of phosphides and sulfides (especially phosphides) was found to increase significantly with a reduction in primary delta ferrite content during solidification. That is, enhanced crack susceptibility due to nitrogen addition was attributed to the decreased primary ferrite content, the consequent decrease in residual ferrite content, and a concomittant increase in extent of microsegregation of phosphorus along the grain boundaries.

d. Niobium and Titanium (31,32,34,37-41,48,56,57)

The primary purpose of the addition of niobium and titanium to austenitic stainless steels is to increase resistance to intergranular corrosion, because these elements form stable carbides in preference to chromium. However, both elements are also responsible for improved creep properties in stainless steels and are frequently cited as

enhancing the propensity toward fusion zone and heat affected zone cracking.

As previously mentioned, Morishige et al. (30,32) assigned a negative coefficient to niobium in his cracking formula, indicative of its harmful effect on hot ductility and hot cracking. Ogawa et al. (39) have also observed that an increase in niobium content increases both fusion zone and heat affected zone hot cracking by enhanced segregation to grain boundaries. They (39) found that the grain boundaries of niobium containing steels were decorated with island-like reaction products that contained considerable quantities of niobium carbo-nitride. Further, they indicated that increasing the carbon content improved the hot cracking resistance considerably in steels with a high niobium content (0.78%), but the effect was less pronounced in low niobium steel (0.26%Nb).

Metallographic studies of hot cracking in weld deposits of niobium stabilized 18Cr-8Ni electrodes by Fredriks and Van der Toon (34) indicated that all weld deposits made with niobium stabilized electrodes displayed a greater tendency toward hot cracking than the corresponding unstabilized electrodes, and that an eutectic phase along grain boundaries promoted crack formation. Their microprobe analysis revealed that the eutectic phase contained relatively a high concentration of sulfur and silicon, and that the concentration of niobium was approximately 15 times as high as in the surrounding matrix.

Dahl et al.(37) have indicated that the influence of niobium and other elements (silicon, phosphorus and sulfur) on the hot cracking

resistance of type 347 alloy is strongly dependent on the material condition. In the as-cast condition, due to the high concentrations of niobium at some grain boundaries in the coarse grain structure, there is always a high susceptibility to hot cracking, and this can not be reduced by lowering silicon, phosphorus or sulfur contents. However, in the niobium stabilized weld metal, the susceptibility to hot cracking can be reduced at silicon contents of less than 0.5%, sulfur and phosphorus contents each less than 0.015%.

Lippold (38) has indicated that the fusion zone hot cracking of alloy 800 was associated with low melting liquid films which formed as a result of titanium, silicon, and niobium partitioning during solidification. These liquid films wet the boundaries producing preferential sites for hot crack formation. He further found that as grain boundary migration occurs in the HAZ, the carbides dissolve leaving a titanium rich solute which offers preferential sites for crack formation during cooling. If the carbides in the alloy are present as relatively large particles, less dissolution occurs than if the particles are small, causing less heat affected zone cracking. A similar observation by Brooks (40) showed that increasing the titanium content from 2.2% to 2.6% in A286 precipitation hardening superalloy decreased the zero strength temperature in hot ductility tests by almost $100F^{o}$. He further noted that the Laves phase (Fe_2Ti) which formed upon decomposition of the eutectic TiC provided liquation of grain boundaries, resulting in grain boundary weakness at temperatures far below the solidus temperature.

In contrast to the above observations, Matsuda et al. (56) found that an optimum amount of titanium (about 0.05%) in 0.024%P and 0.002%S containing fully austenitic stainless steel (310S) gave a beneficial effect by reducing the degree of cracking. They attributed the beneficial effect of titanium to raising the solidification temperature of the phosphide eutectic (resulting in a reduced BTR). However, when the titanium content was increased beyond the optimum, it exerted a harmful effect on hot cracking by increasing the amount of the low melting point eutectic which enriched in titanium.

4. HOT DUCTILITY TESTING AND CRITERIA FOR HOT CRACKING ASSESSMENT

a. General

Hot ductility testing has been used to evaluate the fabrication and service performance of austenitic stainless steels, since Sauveur used the hot twist test for determining the optimum temperature for hot working of various steels in 1929 (105). The direct welding related application of ductility testing was introduced shortly after the "Gleeble" was developed in 1949 by Nippes and Savage (10). The Gleeble was designed originally to simulate the time-temperature cycle to which various points in the base metal HAZ are subjected during the welding cycle. In the mid 1950's, the Gleeble was modified to permit straining specimens at temperature during the time-temperature cycle. The hot ductility measured for the simulated weld HAZ was related to the potential for hot cracking during fabrication in many stainless steels and high alloys (10,11). The relationship between hot ductility and hot cracking was empirically established by comparisons

between fabrication cracking incidents and the base material response, in terms of the materials ability to tolerates welding restraint strains without cracking in the HAZ. Thus, hot ductility and HAZ hot cracking susceptibility of materials are related, in that hot ductility of the HAZ must be adequate to plastically accomodate the contraction strains without hot cracking.

However, the test methods for assessing hot ductility of the base material HAZ are varied, and although the Gleeble has become a common tool in the assessment of hot ductility, not all investigators have used similar test parameters. In addition, the method of interpreting hot ductility test results also varies from laboratory to laboratory, in that the criteria for discrimination between materials have not been established.

The following literature review includes test parameters (conditions) and criteria for hot ductility testing as employed in the U.S., Europe and Japan.

b. Test Methodology and Criteria

The Gleeble is essentially a high speed, hot tensile tester, instrumented so that heating and cooling of the test specimens can be accurately programmed to reproduce the rapid temperature changes that occur during welding. The Gleeble can reproduce, with an accuracy of $\pm$ 15 F^{o}, a weld HAZ thermal cycle requiring a heating rate less than 3000F^{o}/sec and a cooling rate of less than 500 F^{o}/sec at 1000 ^{o}F on properly sized specimens. The test employs a cylindrical specimen which is clamped between two water cooled jaws separated a given distance from each other. In addition to serving as grips for tensile

testing, the cooper jaws also provide a means for introducing current into the specimen and insure rapid heat extraction (cooling) when the current flow is interrupted. The heating current is controlled electronically throughout the thermal excursion by means of a signal obtained from a fine wire thermocouple welded to the center of specimen gage length, the instantaneous temperature of the specimen is compared with a reference temperature and the current level is increased, decreased, or interrupted as required.

In testing methodology, the most important and critical factors to be considered are;

1. **Thermal cycle** which includes "heating and cooling rates" equivalent to those which are obtained in the weld HAZ.

2. **Peak temperature**, a temperature below the bulk melting temperature of the material being studied. However, for on-cooling tests, the peak temperature must be that experienced in the HAZ immediately adjacent to the fusion line. (characteristic of the region in which the HAZ hot cracking commonly occurs).

3. **Crosshead speed (strain rate)** for mechanical testing, must be rapid and is a variable related to the necessity to to test at constant temperature.

4. **Holding time** at testing temperature and/or at peak temperature.(consistent with the equipment used to insure constant temperature testing.)

5. **Thermocouple attachment technique** which is an important variable in controlling testing temperature (a prime source of temperature error).

However, it has been difficult to directly compare the work of various researchers (10,11,106-125) because of the differences in the above mentioned testing parameters (methodology) from investigator to investigator.

In the original and subsequent work by Nippes et al. (10,11), the heating and cooling rates used were chosen to represent weld thermal cycles (equivalent to those HAZ regions just adjacent to the fusion zone) in welds made with an energy input of 70 KJ/in in 1-1/2 inch thick stainless plate with 72 ^{o}F preheat (room temperature), i.e., for heating, rapid rise temperature to 950 ^{o}F and then an average heating rate of 240 ^{o}F/sec from 950 ^{o}F to a peak temperature. The tensile testing (loading) rate or crosshead speed was 5 in/sec. The peak temperature range used depended on the alloys but is in the 2200 ^{o}F-2500 ^{o}F range for stainless steels.

Soldan and Mayne (106,107), who correlated laboratory hot ductility tests with the fabrication and service performance of high temperature austenitic steel piping, used similar testing parameters. However, the criteria used were somewhat different. Soldan and Mayne (106,107) indicated that the ductility (reduction in area) on-cooling from 2400 ^{o}F to 2300 ^{o}F should be greater than 60% (reduction in area) for acceptable welding behavior. However, Nippes et al. (11), divised various classifications of hot ductility behavior for austenitic stainless steels and related these classifications to potential HAZ cracking problems. The basis for the anticipated behavior was on the amount of the ductility recovery and the recovery rate per temperature interval during on-cooling testing. The Nippes criteria are given

schematically in Figure 13. According to Nippes et al. (11), when a material has an H2 on-heating behavior, it should be rejected because of high HAZ cracking susceptibility, and when the material has an H1 on-heating class, on-cooling tests have to be conducted to further evaluate the HAZ cracking potential.

The C1, C2 and C3 on-cooling classifications are the most commonly encountered after an on-heating behavior equivalent to H1. The relative susceptibility of the HAZ to hot cracking of materials was ranked as follows. The material with behavior described as C1 is readily weldable without any tendency toward HAZ cracking. The C2 and C3 behaviors predict less desirable hot cracking tendency with C3 indicative of the highest susceptibility to HAZ cracking. They(10,11) further generalized that " **testing at 2300 ^{o}F on cooling from a peak temperature corresponding to the point where the on-heating ductility closely approximates zero provides the best method of testing**" They further stated, "..... **materials of known propensity for cracking have all exhibited on-cooling ductility values less than 40% of the on-heating reduction in area**".

The Nippes et al. (11) criteria, which utilize on-cooling behavior from the "zero ductility temperature (ZDT)", are more practical and flexible than that of Soldan and Mayne (106,107) who used on-cooling behavior from an arbitrary temperature of 2400 ^{o}F. The 2400 ^{o}F maximum temperature used by Soldan and Mayne during the test is not necessarily sufficiently high to evaluate the weld HAZ region near the fusion line which is the most susceptible to cracking in the austenitic stainless steels.

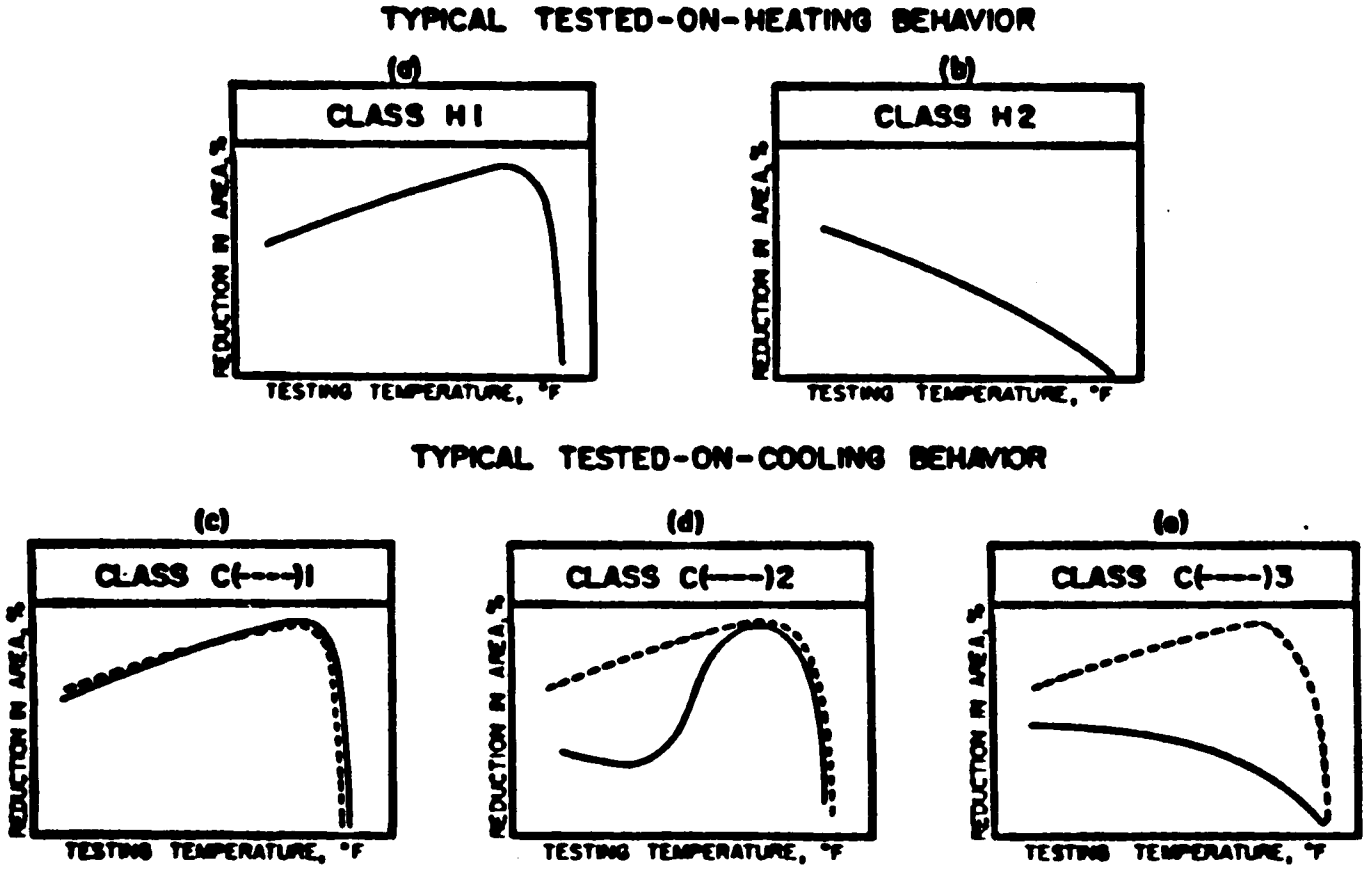


Figure 13. Classification of on-heating and on-cooling hot ductility behavior.

Source: Nippes, E.F., Savage, W.F. and Grotke, G., "Further study of the hot ductility of high temperature alloys," Welding Research Council Bulletin 33, Feb. (1957).

In the 60's and early 70's, many U.S. researchers (37,108-112,119,120) began to reconsider the concept of a zero ductility temperature. They (37,108-112,119,120) also considered the importance of the recovery of strength in addition to recovery of hot ductility, after the material has undergone a thermal excursion equivalent to that experienced in the weld HAZ.

Kreischer (109) commented after observing discrepancies between Gleeble hot ductility test results predictions and actual weld HAZ cracking incidents that " .....**that either the Gleeble hot ductility test can not be used with a high degree of reliability to predict crack susceptibility, that the test results are not being properly evaluated, or that the testing methods have to be altered**". Kreischer further suggested that recovery of tensile strength as well as ductility might have a significant effect on the tendency of a material to develop hot cracks during welding, i.e., the poorer the ductility of a material, the higher its tensile strength recovery would have to be for it to be crack resistant. He emphasized that in cases when the zero ductility temperature (ZDT) and zero strength temperature (ZST) are different, tests "should be" conducted on cooling from both of these temperatures.

For the criteria for hot cracking assessment, Kreischer used the rate and amount of the both ductility and strength recoveries. That is, when both hot ductility and strength recover well after exposure to the ZST, the material should be crack resistant. When both ductility and strength recoveries are poor, the material is crack susceptible. However, when either recovery is poor and the other is

"only moderately good", several factors such as a relative physical and mechanical properties of the weld metal and base metal have to be considered.

Williams (108), who used the same testing parameters as those of Nippes et al. (10,11) except a crosshead speed of 2 in/sec instead of 5 in/sec, also mentioned that the use of higher test temperature enhanced the capability of hot ductility test to discriminate between materials. In other words, tests utilizing the zero strength temperature (ZST) as a maximum temperature discriminated to a greater degree than did those using a lower maximum temperature.

A similar concept of using a high peak temperature (ZST) for the on-cooling tests also can be found in the work by Yeniscavich (110,111), Duval et al. (112), Musch (113) and Dahl et al. (37) in West Germany and Donati et al. (14) in France.

Duval et al. (112) claimed that the on-cooling testing from the nil strength temperature (NST) (equivalent to ZST) of material provided a more reasonably discriminating and sensitive test than testing from the nil ductility temperature (NDT)(equivalent to ZDT) for determining relative heat affected zone crack susceptibility. They further mentioned that the amount and rate of recovery of mechanical properties (ductility and strength) after exposure to the NST are the most important factors governing crack susceptibility as was indicated by Kreischer (109).

The work of Yeniscavich (110,111) indicated that the original microstructural condition and testing parameters significantly affect hot ductility test results. The parameters investigated by

Yeniscavich were: holding time at testing temperature (2-10 sec), crosshead speed (0.15-4 in/sec), cooling rates (20-100 F^{o}/sec) and peak temperature (ZDT-ZST). According to Yeniscavich, the most important factor was a peak temperature, for which the ductility response over the entire temperature range was lowered by cooling from the higher peak temperature. In addition, Yeniscavich showed that a slower crosshead speed (0.15 Vs. 4in/sec) did not significantly affected the on-heating and on-cooling ductility response. The longer holding time (10 Vs. 2 secs) at the testing temperatures did not affect on the on-heating behavior, but it decreased the zero ductility range (ZDR)(temperature range between bulk melting temperature and a on-cooling ZDT at which ductility starts to recover during cooling as shown in Figure 14) and the mid-temperature ductility dip during on-cooling as shown in Figure 15.

Yeniscavich (110,111) further found that the both high ZDR and the mid-temperature ductility dip can be used for a good hot cracking resistance assessment. He found that the alloy showing greatest fissuring in his investigation had a small mid-temperature ductility dip and attributed this result to the much higher stress levels present in the mid-temperature range. From this observation, Yeniscavich (110,111) indicated that, in addition to the high temperature ductility range (ZDR), the mid-temperature ductility dip is an important criterion and may be a more significant factor than the high temperature ZDR. Bruhl and Zschau (164) in West Germany have also found the ductility dip phonomenon in the 316NG materials. However, they found that ductility dip was not significant with regard

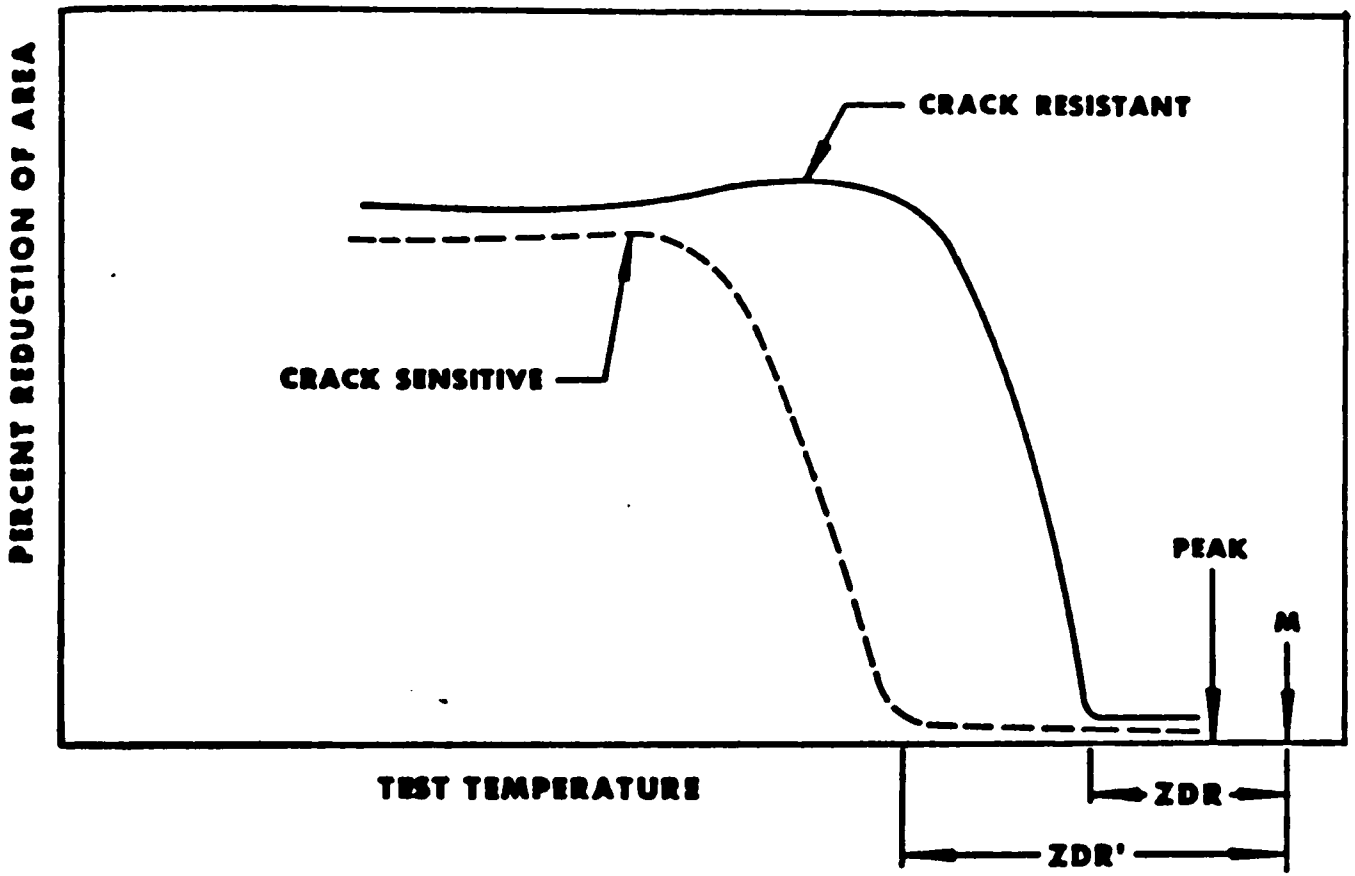


Figure 14. Schematic illustration of zero ductility range used as a crack sensitivity criterion.

Source: Yeniscavich, W., "Correlation of hot ductility curves with cracking during welding," Proceedings of symposium on methods of high-alloy weldability evaluation, sponsored by WRC, Apr. (1969).

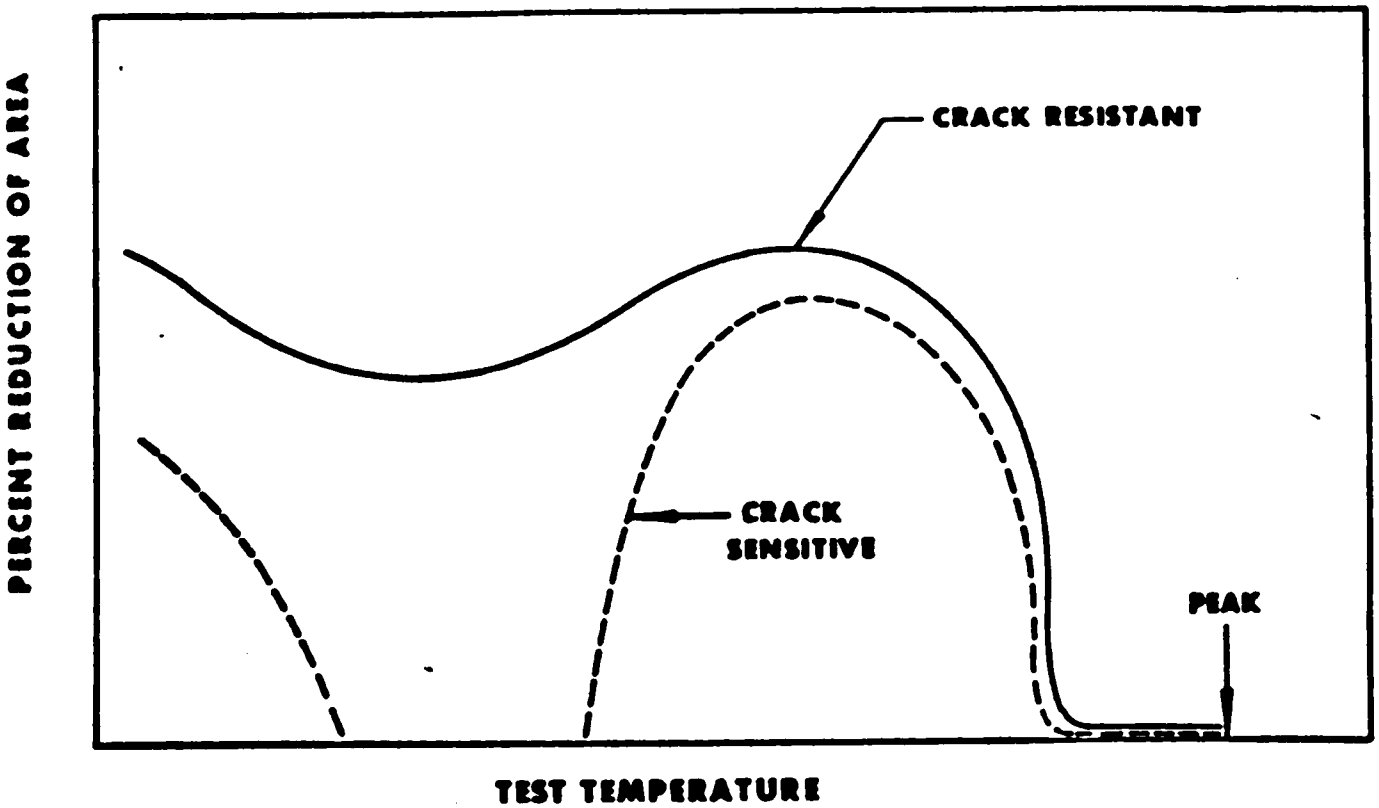


Figure 15. Schematic illustration of mid-range ductility dip used as crack sensitivity criterion.

Source: Yeniscavich, W., "Correlation of hot ductility curves with cracking during welding," Proceedings of symposium on methods of high-alloy weldability evaluation, sponsored by WRC, Apr. (1969).

to hot cracking susceptibility as long as the material has sufficient strength.

A concept similar to the zero ductility temperature range methodology can also be found from the work of Williams (108), and Musch (113) and Dahl et al. (37) in West Germany, Donati et al. (115) in France and Sumitomo Steel Co. in Japan (124).

Williams (108) indicated that the temperature difference between the ZST found during on-heating tests and the on-cooling ZDT, at which the ductility starts to recover after exposure to the ZST, can be used as a criterion for HAZ hot cracking assessment. The German researchers (37,113) also claimed that the difference between the zero strength temperature and the on-cooling zero ductility temperature defines the temperature range exhibiting a high susceptibility to cracking. From their test results, The German researchers derived a cracking factor (criterion) for the susceptibility to hot cracking in the HAZ of base metal and in the reheated zone of the weld metal in multipass welding;

Cracking Factor (%) = (ZST - ZDTC)/ZST X 100

where, ZST = Zero strength temperature found from the on-heating tests

ZDTC = Zero ductility temperature at which ductility starts to recover on cooling from ZST

That is, the larger the cracking factor, the greater is the susceptibility to cracking. However, in testing methodology, the German researchers (37, 113) used testing parameters different from those in the U.S. and the parameters changed with individual

researchers in the same laboratory over a period of time. In the earlier work (37), they used a thermal cycle with a heating time of 5 secs from room temperature to the peak temperatures, a cooling rate of 140F ^{o}/sec above 1832 ^{o}F and a crosshead speed of approximately 0.28 in/sec on 0.25" diameter specimens. However, in their later work (113), they utilized a heating time of 10 secs from room temperature to the maximum temperatures, a cooling rate of 86 F^{o}/sec above 1832 ^{o}F and a crosshead speed of 0.4 in/sec on 0.25 in. diameter specimens. This clearly shows that standard hot ductility test methodologies have not been used to derive the available literature data and ready comparisons of results from laboratory to laboratory, or even results from the same laboratories over a period of time can not be made.

French researchers (115) also used their own testing parameters: the crosshead speed was 110 MM/sec (4.3 in/sec), the applied thermal cycle corresponded to that experienced in the HAZ, welded with a welding energy of 20 KJ/Cm (50.8 KJ/in) on a 1-1/2" thick plate of stainless steel. This will give a faster cooling rate than that with standard U.S cycle (70 KJ/in in the same thickness stainless steel). However, they used a similar evaluation criteria to that employed by the German researchers (37,115), Williams (108) and Yeniscavich (110,111). They measured the tendency toward hot cracking by a characteristic called the "null ductility isotherm" (which is characteristic of what happens in the immediate vicinity of the fusion zone.) The null ductility isotherm is: T = Fusion line temperature (Bulk melting temperature) - ZDT on cooling after exposure to the ZST.

Thus, the larger the null ductility isotherm, the greater is the susceptibility to cracking.

Japanese researchers (30,32,124) have utilized induction heating equipment for hot ductility testing and conducted tests in argon atmospheres. However, researchers in different laboratories used different testing parameters as in the cases of the U.S. and West Germany. Morishige et al. (30,32) adopted a constant maximum temperature of 1350 ^{o}C (2462 ^{o}F) and linear heating and cooling rates. Further, they introduced a hold time of 15 secs at peak temperature and at test temperatures and used a crosshead speed of 0.04 in/sec. For assessing the hot cracking susceptibility of materials, Morishige et al. (30,32) correlated the hot ductility test results and the chemical composition of a material as follows;

$$\Delta H = -700\,(\%\,C) + 17\,(\%\,Cr) - 37\,(\%\,Ni) - 117\,(\%\,Nb) + 29\,(\%\,Mo) - 188$$

When ΔH is over 100, the material has an excellent hot ductility and is considered to be resistant to hot cracking.

However, Sumitomo Steel Co. (124) used a different holding time at peak temperature and at test temperatures, although they used similar linear heating and cooling cycles as that of Morishige et al. (30,32). In on-heating tests, a 10 sec holding time at test temperature was used, whereas for the on-cooling tests, a 5 sec holding at the test temperature after a 10 sec hold at peak temperature (ZST) was used. With regard to the criteria for hot cracking assessment, they used a concept of a brittle temperature range (BTR) which is equivalent to the zero ductility temperature

range (ZDR) used by Williams (108), Yeniscavich (110,111) and German researchers (37,113). They further found that when the BTR is greater than 70C^{o}, the material is crack sensitive.

Only one criterion is recognized in ASTM specifications (a supplementary requirement(S-7) in ASTM A 430 (117)). The ASTM A430 specification, like the majority of criteria, utilizes a hot ductility test and assesses the recovery of ductility upon cooling from a temperature in the HAZ near the fusion line. In the ASTM requirement, the peak temperature utilized is 50 F^{o} below the zero ductility temperature and testing is accomplished upon cooling 100 F^{o} below the ZDT - 50 F^{o}. Sixty percent reduction in area is required. Unfortunately, no test details are provided so that the test can be conducted in a similar manner by all parties. It is considered that this test is not discriminating, in that it will only reveal very poor material from the hot ductility standpoint. Like in the other cases (10,11,106,107), the critical region of the HAZ, the zero ductility region, is not evaluated and this is the region where the majority of HAZ cracks occurs.

Recently, some specifications have been promulgated and again required a peak temperature of 50 F^{o} below the zero ductility temperature for the on-cooling tests, and also specified that, "Gleeble tests shall be performed for every heat of material in accordance with buyer-approved procedures", resulting in the possibility of conducting tests in an arbitrary fashion which depends on the purchasers of the material. The further recommendations were that the maximum holding time at testing temperature be 60 secs and

test temperature should be between 2000 ^{o}F and 2300 ^{o}F (in 50 F^{o} increments). The criterion for acceptance is that the reduction in area in the range of 2000-2150 ^{o}F should not be less than 75% and in the range of 2200-2300 ^{o}F not be less than 60%. This specification did not mention the on-heating tests, i.e., no matter how the material behaves during the on-heating tests, if it meets the on-cooling test requirements, it can be considered to be resistant to cracking. The use of a peak temperature of 50F^{o} below the zero ductility temperature for the on-cooling tests can also be found in the recent work by Bruhl and Zschau (164)(required by another utility in the specification of their 316NG Replace BWR piping). Further the acceptance criterion specified by Commonwealth was the same as in the case of the NYPA specifications, materials should have a on-cooling ductility (reduction in area) of 75% below 2200 ^{o}F and 60% above 2200 ^{o}F.

The subject of standardization of the hot ductility test was first addressed by High Alloy Committee of the Welding Research Council in the early 70's (125). However, the work was never brought to fruition. The round robin testing involved in this project clearly showed the variation in laboratory-to-laboratory techniques. Even though the project pinpointed some of the critical aspects of the testing methodology and procedure, it did not try to set the criterion which is most important in interpreting the results and discriminating between materials.

In the light of the above review, it appears that the test methods for assessing the hot ductility of the HAZ are varied, and although the Gleeble has become a common tool in the assessment of hot

ductility, not all investigators have utilized similar testing parameters. A summary of the parameters by some of the U.S., West German, French and Japanese investigators is given in Table 4.

Therefore, the standardization of the Gleeble (or equivalent) hot ductility test procedure and testing parameters is strongly needed. The parameter study "must" include the followings as mentioned earlier; thermal cycle (heating and cooling rate), crosshead speed, peak temperature for the on-cooling tests, holding time at both peak and testing temperatures and thermocouple attachment technique.

In addition to the testing methodology, the methods of interpreting test results and the criteria for hot cracking assessment also vary significantly. The summary of different criteria used to date is the following

1. The amount and extent of ductility recovery during on-cooling tests when compared to that of the on-heating tests.
2. Incorporation of the recovery extent of hot ductility and tensile strength .
3. Zero ductility range on cooling (ZDR, BTR, etc.).
4. The mid temperature ductility dip.

c. Metallurgical Phenomena and Hot Ductility Testing

Hot cracking in stainless steels, nickel base alloys and other structural alloys occurs in the fusion zone (as deposited weld metal), base metal HAZ and weld metal HAZ in multipass welds. The problem of cracking in welds is difficult to deal with since the high temperatures and steep temperature gradients in the weld result in

Table 4. A summary of hot ductility testing parameters used in USA, German, France and Japan.

Parameters	Units	USA	German	French	Japanese
Thermal cycle	Kj/in	70	a	50.8	b
Initial temp.	°F	72	NS	NS	NS
Maximum temp.	°F	ZDT	ZST	ZST	2462
Cross head speed	in/sec	2.5	.37	4.3	.04
Hold time	sec	1	NS	NS	10
Gage length	in	.8	NS	NS	NS
Thermocouple diameter	mils	10	10	10	10

a = Heating rate, 5 secs from room temperature to peak temperature. Cooling rate, 140F°/sec

b = Linear heating and cooling

NS = No specified

ZDT = zero ductility temperature

ZST - zero strength temperature

temp. = temperature

unavoidable complex stress patterns and the formation of a variety of unique rapidly heated and cooled microstructures. Relatively simple metallurgical phenomena become complex under these non-equilibrium conditions (114).

However, since the Gleeble was introduced by Nippes et al. (10,11), an enormous amount of information has been generated concerning the microstructure and properties of the weld heat affected zone from synthesized specimens which have experienced a thermal history equivalent to that in the actual weld HAZ. The Gleeble, as shown in the previous section, also has been extensively used to study hot ductility response of materials during the on-heating and on-cooling portion of a thermal cycle. Hot ductility tests not only provide for determination of the relative crack sensitivity of different alloys, but also can permit differentiation of "good" and "bad" heats of the same nominal composition (11,114). However, only small number of investigators (108-112,114,116,119,123) have attempted to investigate the metallurgical changes that occur during hot ductility testing which are directly related to the final hot ductility test results, and which are also important to proper interpreting the results.

Weiss et al. (114) have presented a model to explain the interaction of various physical metallurgical phenomena during hot ductility testing of Inconel 600, and showed that the shape of hot ductility test result curve is strongly influenced by the initial microstructures and is a result of the interaction of strengthening and softening processes. They (114) separated three characteristic

temperature ranges in the on-heating ductility curve as shown in Figure 16. Figure 16 shows the factors contributing to hot ductility and hot strength, and the fracture mode for each characteristic temperature range.

* Region I: in this temperature region, the strengthening processes (work hardening and solid solution hardening) predominates over the softening process (recovery) resulting in high strength but lower ductility. The fracture mode is fully transgranular or mixed mode of transgranular and intergranular.

* Region II: in this temperature region, ductility increases and strength decreases as temperature increases, and the softening processes (recovery, grain migration and dynamic recrystallization) is predominant. There may be no strengthening. The fracture is exclusively by ductile rupture. The beginning of this region (ductility minimum) is strongly influenced by the initial microstructure.

* Region III: in this temperature region, the ductility and strength suddenly drop to very low values. The severe loss of ductility and strength is related to partial melting which results from the non-equilibrium heating and constitutional liquation of second phase particles or segregated regions. The fracture mode changes from ductile to intergranular. Typical microstructural observations on specimens heated to this temperature region include the presence of serrated grain boundaries and terrace like fracture surface topographies.

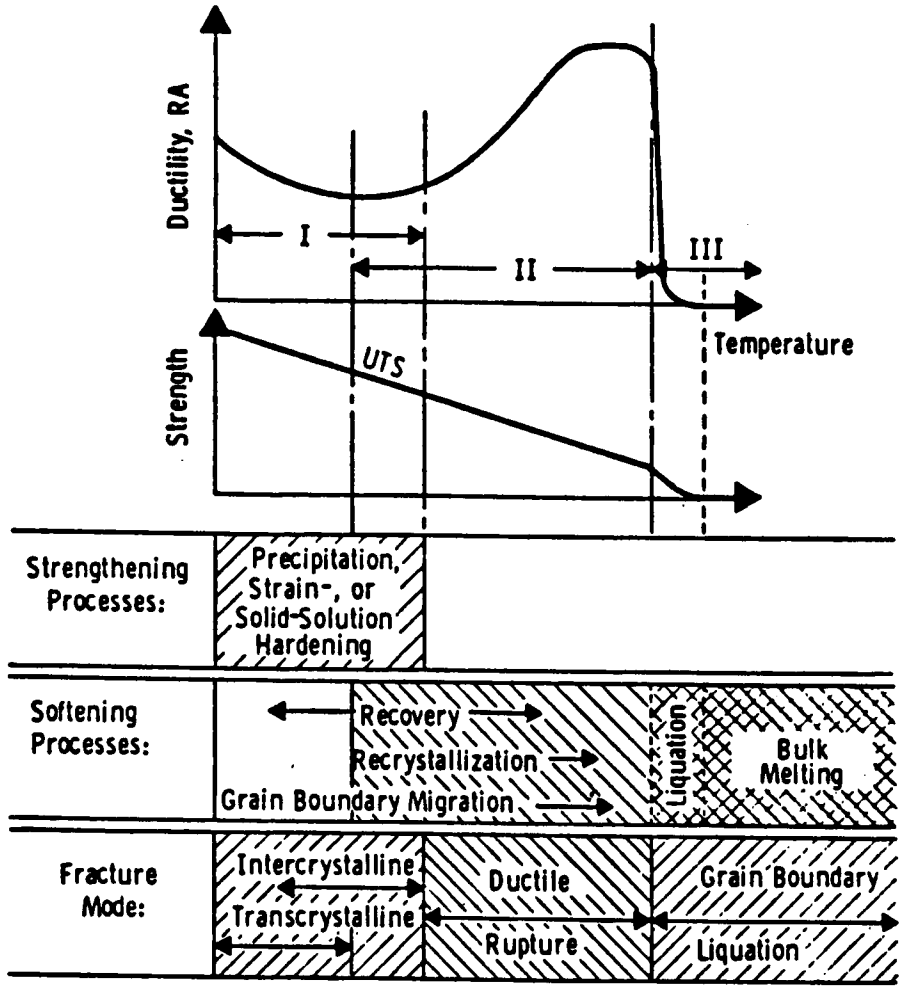


Figure 16. Factors contributing to hot ductility and hot strength.

Source: Weiss, B., Grotke, G.E. and Stickler, R., "Physical metallurgy of hot ductility testing," Welding Journal, 41(10), p. 471s-487s, (1970).

However, other investigators (108,110-112,119) have made different observations from samples heated to Region III. Williams (108) has found that under high strain hot ductility testing, the zero ductility temperature (ZDT) coincided with the temperature at which the first grain boundary melting occurred and the zero strength temperature (ZST) was where extensive grain boundary wetting occurred. Whereas Weiss et al. (114), as shown in Figure 16, found that liquation first starts at a temperature where both the ductility and strength suddenly drop.

Yeniscavich (110,111) postulated that liquation started at the temperature of the maximum in ductility, and that the zero strength temperature is the temperature at which a liquid film covered the entire grain boundary face. However, Duvall et al. (112) and Owczarski et al. (119) proposed that a shift in failure mode occurs at the temperature of the downturn in ductility (maximum ductility temperature), which is the same temperature as that found by Weiss et al. (114). But they (112,119) did not observe any evidence of grain boundary liquation until the temperature reached the zero ductility temperature.

Therefore, it can be seen that extensive metallographic work is needed to verify the metallurgical changes during testing and the relationship to the shape of the ductility curves in order to properly interpret the test results. No "detailed" study of metallurgical reactions during hot ductility testing in stainless steels is available in the open literature. In addition, the study of metallurgical changes during on-cooling, which is probably more

important than that during on-heating, in terms of HAZ cracking, is also strongly needed.

5. VARESTRAINT TEST AND CRITERIA FOR HOT CRACKING ASSESSMENT

a. General

Many test methods (126-135,153,159) have been developed and utilized since the 1950's to investigate hot cracking in austenitic stainless steels and other alloys. Most of these tests were devised to evaluate one particular type of cracking such as HAZ cracking, solidification cracking or reheat cracking. However, many of these testing methods give only a quantitative ranking of materials and could not be used to investigate the basic concepts and/or mechanisms of cracking.

Kammer et al. (127) claimed that a suitable test method has to meet the following requirements, which are those the "ideal" test should incorporate:

1. Ability to show a direct correlation with actual fabrication and service behavior,
2. Reproducibility of results with freedom for variation due to the human element,
3. Sensitivity to small changes in a test variable,
4. Ability to show the effects of several welding variables,
5. Economical preparation of specimens and running of tests.
6. Applicability to all welding processes.

However, not many of test methods developed meet the above requirements for the ideal test. Therefore, many investigators have

invented new test methods, and developed and modified the existing test methods.

In the early 1960's, Lundin and Savage (126) developed a new test method, VARESTRAINT, and claimed that it met the above requirements for the ideal test. It has also been proved that the varestraint technique can be successfully used in the following types of hot cracking studies (136):

1. The evaluation of the relative hot cracking sensitivity of different types of base materials.
2. The evaluation of heat-to-heat variations in hot cracking susceptibility
3. The evaluation of the hot cracking sensitivity of filler metals as deposited and modified by welding process
4. The evaluation of the effect of specific alloying elements on the hot cracking sensitivity of base metals
5. The determination of the hot cracking temperature range
6. The performance of fundamental studies of the mechanisms of hot cracking

After the initial development of the test by Lundin and Savage (126), a considerable number of changes were made in the design and methodology of the varestraint testing equipment. Like in the case of the Gleeble hot ductility test discussed in the previous section, many criteria have been developed for hot cracking assessment.

b. Varestraint Test Method

The varestraint method of testing for hot cracking has been utilized by researchers (126,130-132,136-158,160) world-wide for the

past two decades. The popularity of the test is due to its ability to synthesize the conditions necessary for hot cracking of a full scale weldment in a laboratory size sample. The test employs an actual weld bead to produce the thermal conditions characteristic of the welding process and representative heat inputs, thus producing microstructures which are virtually identical to actual production welds. Mechanical restraint is simulated by an externally applied augmented strain. The test shows considerable flexibility since the metallurgical and mechanical factors for hot cracking can be independently varied.

Although a considerable number of changes in the varestraint test technique have occurred during the past decades, the basic concept and advantages of the original version did not change. The design and methodology has been improved (A comprehensive review of developments is given in WRC bulletin 280 by Lundin et al. (137)).

These developments have primarily resulted in changes in the sample dimensions and equipment design, use of welding process and method of straining. In the original varestraint (126,136,138), the specimen is supported as cantilever at one end as shown in Figure 17, and weld is deposited parallel to the long specimen dimension, beginning near the unsupported end. When the arc approaches the point marked "A" in the Figure 17, the force is applied at the unsupported end and the specimen is bent downward rapidly to conform to the radius of curvature of the top surface of the interchangeable die-block "B". Meanwhile the arc travels steadily onward and is subsequently interrupted in the run off area "C". Two auxiliary "bending bars" are added in order to force the specimen to conform to the contour of the

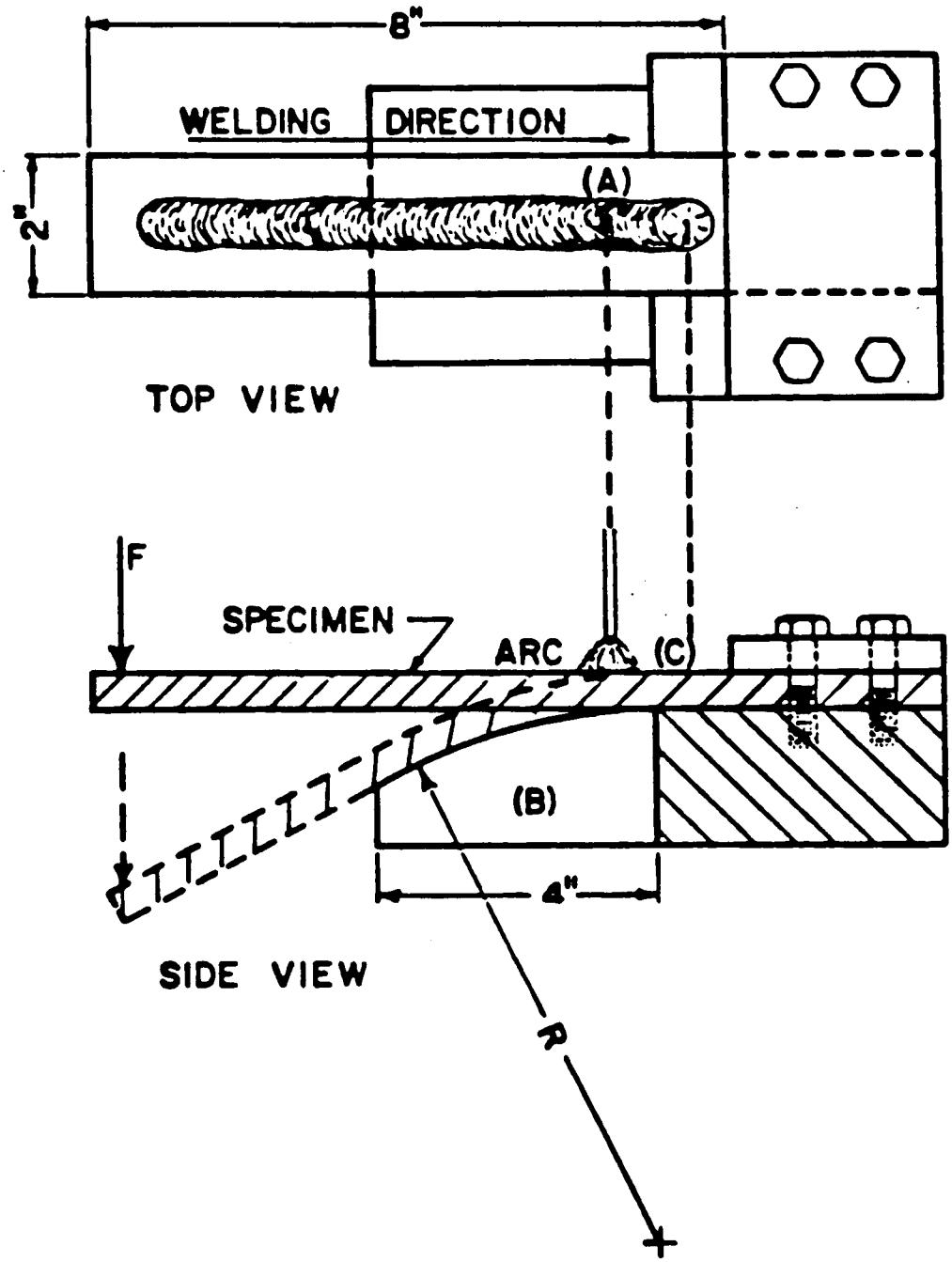


Figure 17. Schematic showing principle of varestraint testing procedure.

Source: Savage, W.F. and Lundin, C.D., "The evaluation of the weldability of structural alloys with the varestraint test," Technical Report AFML-TR-68-48, RPI, July (1968).

die block in use. From the known value of the radius of the die-block, the nominal value of the suddenly applied augmented longitudinal strain in the outer fibers of the test specimen can be determined,

$$\epsilon = t/2R$$

where, t: specimen thickness

R: radius of curvature of the die-block

A particular set of welding conditions can be chosen and the influence of various amounts of augmented strain on hot cracking can be evaluated. Alternatively, the magnitude of the augmented strain can be fixed and the welding conditions varied in order to determine the influence of welding variables on hot cracking behavior.

A radical change in testing methodology evolved from the efforts of Australian, European, and Japanese researchers and has been termed as the Transvarestraint test (143-149). The Murex test which predates the Varestraint, and Brockhurst and Muir's modified version of the Murex test were forerunners of the Transvarestraint test. In the Transvarestraint, the strain is applied transverse to the weld bead. Run-on and run-off tabs need to be used to assist in achieving steady state thermal conditions and minimize heat build up at the terminating edge.

The Transvarestraint test has been found to be best suited for the evaluation of the fusion zone cracking sensitivity. Both SMAW and GTAW processes have been used with the Transvarestraint. The Transvarestraint concept appears to complement the initial Varestraint test in application and utility. Primary interest in the

Transvarestraint test has been for filler metal evaluation, i.e., evaluation of the fusion zone.

A second generation of Varestraint testing evolved with the Spot-Varestraint test colloquially known as the Tig-A-Ma-Jig. The first concerted use of the Spot-Varestraint was by Goodwin (161), and Turner and Lundin (151). This test involves the placement of an autogeneous GTAW spot in the center of a specimen clamped securely at both ends. Normally, the face of the spot is bent in tension while fusion zone is still molten and the HAZ surrounding the spot is examined for cracking. Alternately, the timing of the strain application can be such as to enable testing of the solidified spot fusion zone. This test was originally developed to simplify the testing of sheet materials. The test permitted reduction in the specimen size and thus an inherent saving of high alloy materials (137,152).

The major conceptual difference between the Spot-Varestraint and the basic Varestraint test is related to the thermal history of the weld region. In the conventional test, the augmented strain is applied as an actual weld bead is being deposited. In the Spot-Varestraint, the strain is applied to a region surrounding a stationary spot. The Spot-Varestraint has been used successfully to rank various materials as regards their susceptibility to hot cracking in the fusion zone as well as the heat affected zone. However, the stationary spot used in the Spot-Varestraint concept produces a temperature distribution in and around the spot fusion zone which differs markedly from the distribution in production welds on the same

thickness material. This discrepancy was considered critical and although successful ranking of materials has been accomplished with the spot method, a weld bead produced by a moving torch was considered far more realistic (137).

Thus a moving torch version of the spot test was developed and used initially at Oak Ridge National Laboratories (137). The moving torch modification was simple and has been utilized by many researchers since its introduction. Basic device design improvements were made by Turner and Lundin(151) and remained the same until the recent modifications accomplished at the University of Tennessee (12).

Recently, Lundin et al. (12) have modified the conventional sub-scale moving torch Tig-A-Ma-Jig with adoption of Transvarestraint capability and improved test procedures and concepts. The modifications incorporated involve both design and concept. The design modifications permit testing to be accomplished in the transverse mode as well as the normal longitudinal mode with a simple rotation of the varestraint head. The concept changes involve simultaneous evaluation of the hot cracking susceptibility of the fusion zone, base metal HAZ and weld metal HAZ. This new methodology not only is more economical but also permits evaluations for all types of hot cracks in a single test sample, increasing the information available from each test sample.

In the equipment modifications, the moving torch assembly was designed so as to permit rotation of the transversing mechanism by 90 degree thus providing for welding transverse to the strain application by the radiused die-block. The incorporation of the transverse mode

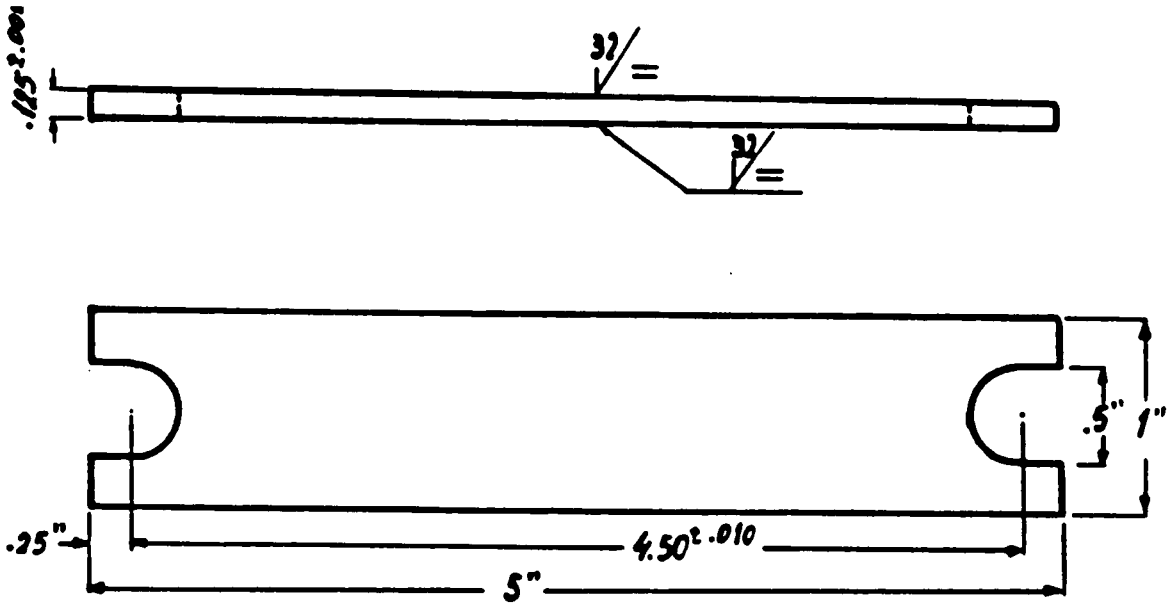
requires a slightly different sample preparation involving the use of run-on and run-off tabs. The longitudinal and transverse samples are shown in Figure 18. The tabs for run-on and run-off in the transverse sample are tack welded on the under side only at the center. The 1" wide X 5" long samples are slotted at the ends to accommodate alignment pins. The slotted design has been used by several researchers, as opposed to the holes originally employed, because it permits sample movement in the longitudinal direction upon straining. The longitudinal movement eliminates much of the longitudinal tensile strain component and primarily leaves the bending strain component as the test augmented strain.

Lundin (137) mentioned that the utilization and concepts of Varestraint is a valid method for hot cracking assessment. He further claimed that although no concerted attempt has been made to standardize the construction of procedures for Varestraint testing, "the quantitative assessment of a materials hot cracking sensitivity and the correlations between the test results and fabrication behavior has been good".

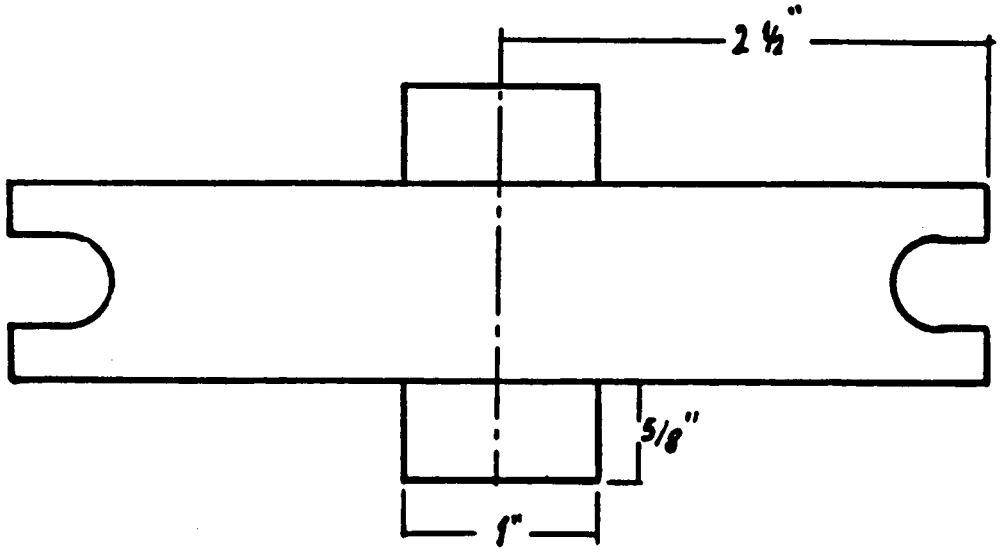
c. Criteria For Hot Cracking Assessment

The following several criteria have been used to evaluate and interpret the test results. However, in many cases, two or three criteria have been used in the same instance.

* Total (Combined) Crack Length (12,126,130-132,136-143,145-153,155,156,162): is the most commonly used criterion. It is obtained by adding the lengths of the cracks found in the weld deposit and the heat affected zone of each specimen and combining these totals to find



Varestraint test sample (longitudinal mode).



Varestraint test sample (transverse mode).

Figure 18. Schematic drawing of varestraint test samples for longitudinal and transverse modes.

the combined total crack length. According Lundin (136) and Lundin and Savage (126), the total combined crack length produced in the weld deposit and the heat affected zone will give the best quantitative index of the hot cracking sensitivity of the weld metal and the heat affected zone (both base metal and weld metal HAZs), respectively, for a given welding procedure. Miura (162) has found a good correlation between Y-groove self restraint crack test and varestraint. When the total crack length in varestraint test is 4 mm or longer, weld metal hot cracking occurs in the Y-groove self restraint test.

* Threshold Strain (12,126,136,138,148-151) is another criterion used by many investigators combined with a crack length criterion. This is the minimum augmented strain required to cause cracking in a particular material with a given set of welding variables. This criterion provides a quantitative method for comparing welding procedures.

* Maximum Crack Length (138,142,146,148-150,152) is also used as a qualitative index for preliminary rapid screening of materials tested at constant level of augmented strain. The maximum crack length is extensively used by the Japanese researchers (138,142,146) to derive their own criteria, such as Brittleness Temperature Range (BTR) and Critical Strain Rate for temperature drop (CST). Senda et al. (146) noted that the maximum crack length provides both an indication of the brittle temperature range for cracking and a rapid quantitative means of assessing solidification cracking susceptibility and is the most important index in the Transvarestraint test. Recent work by Lundin et al. (166) have also indicated that the maximum crack

length permits ranking several types of austenitic stainless steels in the same order as in the case of the total crack length, and that the maximum crack length can be used for a rapid screening of materials tested at comparable levels of applied strain.

* Brittle Temperature Range (BTR): the brittle temperature range can be measured by a combination of the maximum crack length and temperature distribution along the axis of weld bead. The distribution is measured along the centerline of the weld bead by plunging a thermocouple into the molten weld puddle directly behind the arc and allowing it to freeze into the weld as the arc moves forward. The schematic representation for the determination of the brittle temperature range for cracking is shown in Figure 19. Arata et al. (142) found that the BTR for solidification cracking exists "only within a certain temperature range for each stainless steel". This means that at a certain (critical) augmented strain, the maximum crack length reaches a critical value and it does not change with a increasing augmented strain.

Another criterion derived from the maximum crack length is the CST which is a critical strain rate for temperature drop (inch/^{o}F) during solidification of alloy. This is determined using the relationship between augmented strain and the length of the longest crack. A schematic representation for determination of the CST is given in Figure 20. The CST is measured by a tangential straight line drawn from the solidus temperature of the alloy to the ductility curve (augmented strain Vs. temperature). A solidification crack will form if the magnitude of the applied strain (deformation) exceeds the

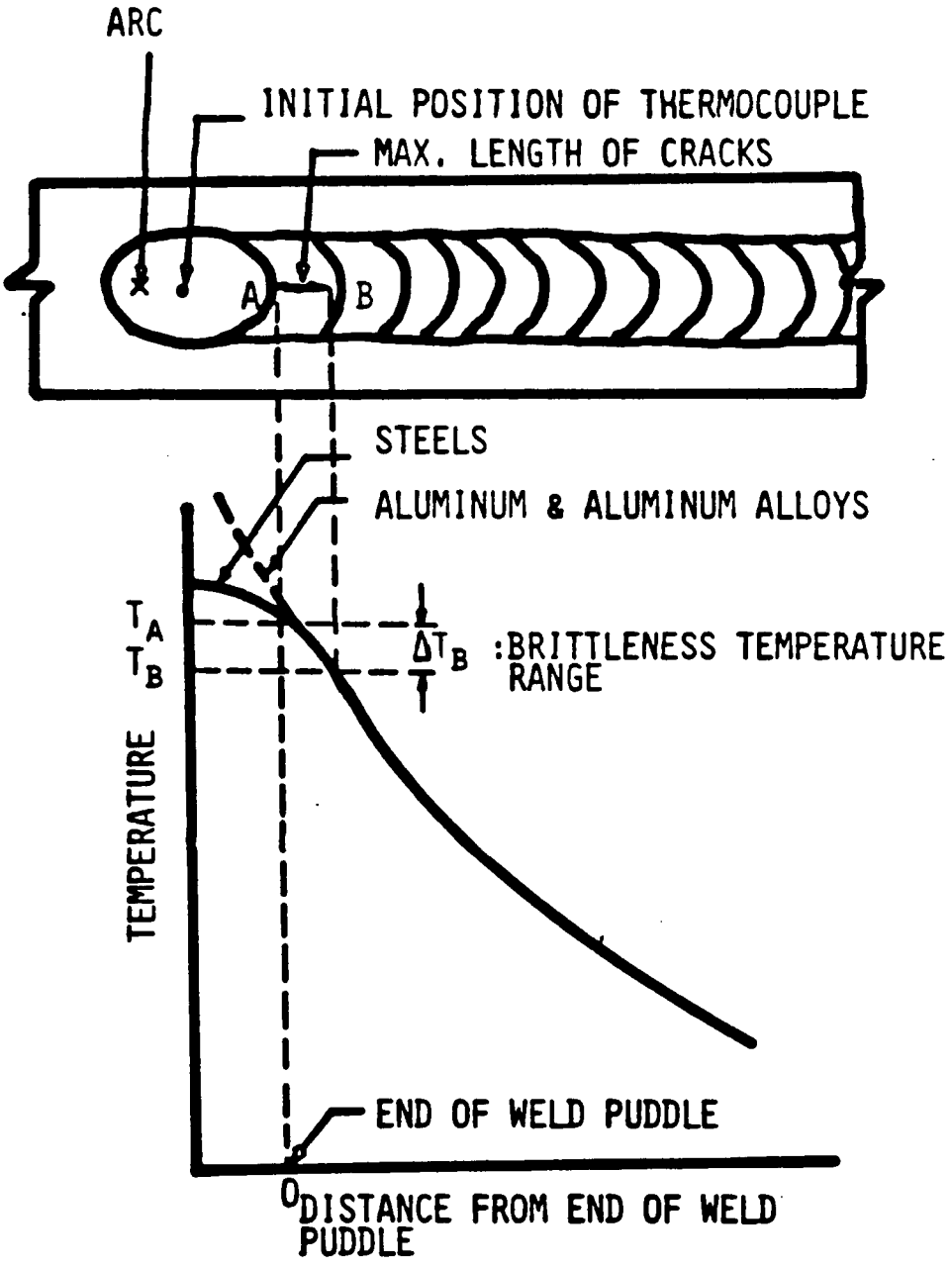


Figure 19. Schematic representation for the determination of brittleness temperature range for cracking.

Source: Lundin, C.D., "A new approach to the study of hot cracking in fusion welds," PhD dissertation, RPI, July (1966).

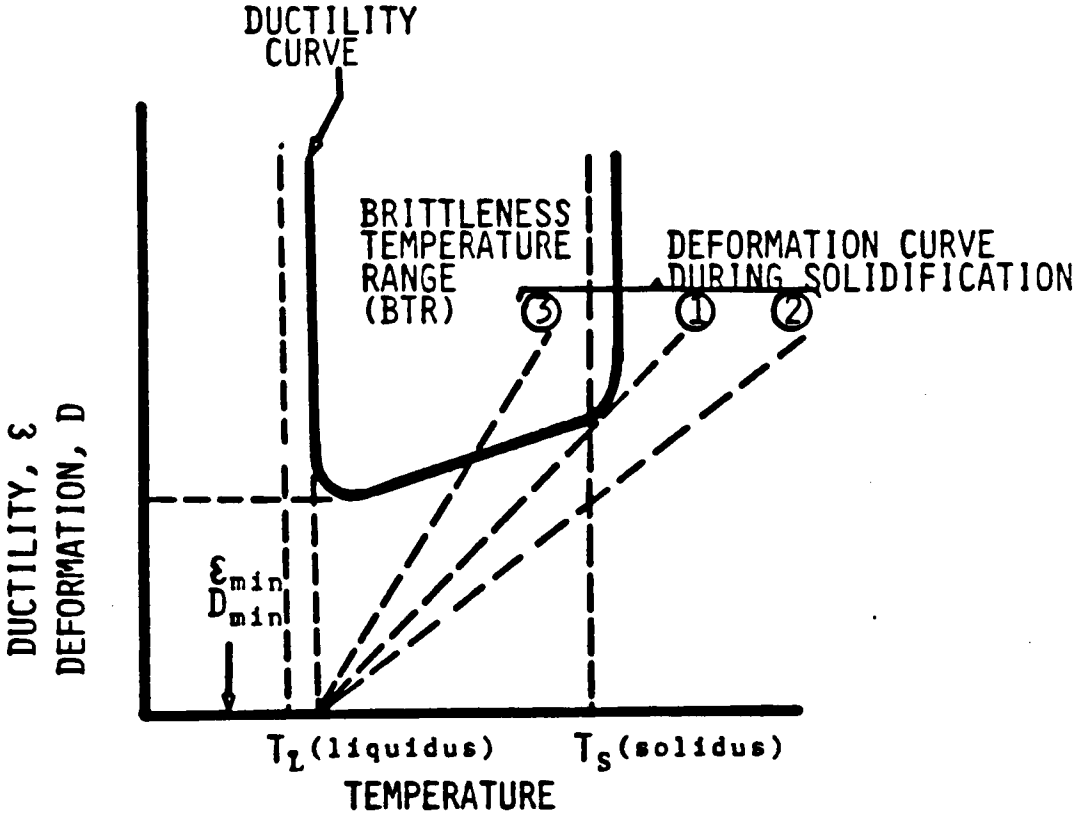


Figure 20. Schematic explanation for the occurrence of solidification cracking from a view point of the relationship between ductility of alloys and deformation during welding.

Source: Senda, T. et al., "Fundamental investigation on solidification crack susceptibility for weld metals with transvarestraint test," Transactions of JWRI, 2(6-7), p. 41-61, (1972).

ductility of the alloy in the brittle temperature range,--Curve (3) in Figure 20.

The above discussion reveals that several criteria have been used for ranking and understanding of the hot cracking susceptibility of materials, but no single criterion can rank all materials or explain the entire range of behavior. Lundin (137), in his discussion of interpretation of the Varestraint test results (criteria), concluded that "the data, especially the total crack length and cracking threshold strain criteria, has to be statistically related to the chemical analysis of the material, and then elements responsible for behavioral (cracking) differences can be uniquely identified", indicating the combined criteria of the total crack length and threshold strain is the best criteria for understanding hot cracking susceptibility of materials.

CHAPTER III

MATERIALS AND EXPERIMENTAL PROCEDURES

1. MATERIALS

The materials evaluated in this study included two types of alternate BWR materials, modified 347 varieties and 316 Nuclear Grade (NG) austenitic stainless steels. Three standard AISI 304, 316 and 347 steels were also evaluated for comparison with the alternate alloys. A summary of the complete chemical composition and ferrite content (average of 5 readings) measured on the autogenously melted fusion zone by Magne-Gage is given in Tables 5 and 6. For easy identification, each heat of material was assigned a Code number which is shown in the first column in Tables 5 and 6. There are two types of "suffixes" in the code number. The materials having an alphabetical suffix were tested in this current study, while, the materials having a numerical suffix were tested previously at UTK (166) and included in this study in order to provide a wide chemical range for statistical analyses.

Since one of the main goals of this study was a comparative evaluation of nuclear grade stainless steels with regard to hot ductility and hot cracking behavior, more than 10 heats each of 347NG and 316NG were evaluated (13 heats of 316NG and 11 heats of 347NG and 2 equivalents; 347 LPN and ICL 473Nb).

The 316NG specification has a maximum carbon content of 0.02% and a nitrogen content of 0.06-0.12% such that it meets the strength requirements of the nominal AISI 316 alloy. The 316NG also has

Table 5. Chemical compositions of 316NG, AISI 304 and 316 materials investigated in this study.

Code	Type	Heat No.	FN[a]	FN[b]	C	Si	Mn	P	S	Cr	Ni	Mo	N	Nb	Co	Cu
316NG-A	316NG	K30678	5.1	5.0	0.010	0.48	1.61	0.024	0.019	17.33	10.62	2.09	0.060	-	-	
316NG-B	316NG	32809	3.2	4.9	0.011	0.58	1.06	0.032	0.013	16.95	10.50	2.15	0.078	-	-	
316NG-C	316LN	D651205	4.2	3.2	0.010	0.46	1.09	0.021	0.001	17.40	11.50	2.88	0.105	-	-	
316NG-D	316LN	D4C1204	0.1	0.0	0.010	0.51	1.60	0.021	0.001	17.55	12.95	2.76	0.113	-	-	
316NG-1	316NG	32657	2.0	1.0	0.012	0.46	1.54	0.027	0.023	16.28	10.15	2.06	0-098	-	0.15	
316NG-2	316NG	27262	0.2	0.0	0.018	0.51	1.37	0.021	0.009	16.95	11.25	2.23	0.097	-	-	
316NG-3	316NG	27287	0.0	0.0	0.017	0.49	1.73	0.025	0.004	16.55	11.65	2.13	0.100	-	-	
316NG-4	316NG	69514	1.6	0.0	0.020	0.48	1.39	0.025	0.015	17.27	11.51	2.20	0.083	-	-	
316NG-5	316NG	D450904	0.2	0.0	0.006	0.51	1.71	0.021	0.001	17.35	13.02	2.49	0.096	-	0.20	
316NG-6	316NG	D440104	0.3	0.0	0.010	0.52	1.75	0.019	0.001	17.25	12.90	2.56	0.101	-	0.20	
316NG-7	316NG	D441103	0.0	0.0	0.011	0.51	1.70	0.020	0.001	17.25	12.85	2.47	0.094	-	0.20	
316NG-8	316NG	D472701	0.1	0.0	0.006	0.52	1.72	0.020	0.002	17.34	12.87	2.49	0.093	-	0.20	
316NG-9	316NG	D442604	0.1	0.0	0.009	0.52	1.73	0.020	0.001	17.30	12.90	2.50	0.099	-	0.20	
316-1	316ELC	S51493	4.0	3.0	0.016	0.47	1.66	0.024	0.011	16.30	10.13	2.11	0.054	-	0.20	0.18
304-1	AISI304	56072	2.4	4.0	0.065	0.51	1.54	0.030	0.025	18.39	8.60	0.21	-	-	0.13	-
304-2	AISI304	638731	4.4	5.0	0.058	0.68	1.62	0.020	0.029	20.32	9.16	0.24	-	-	0.16	-
304-3	304ELC	160143	3.5	5.0	0.015	0.54	1.43	0.026	0.008	18.19	9.17	0.29	0.078	-	0.18	0.27

a: Measured Ferrite content with Magne-Gage
b: Ferrite potential by Delong method

Table 6. Chemical compositions of 347NG and AISI 347 materials investigated in this study.

Code	Type	Heat No.	FN[a]	FN[b]	C	Si	Mn	P	S	Cr	Ni	Mo	N	Nb	Co	REM[c]
347NG-A	347NG	82546	2.2	4.0	0.022	0.32	1.51	0.025	0.004	17.68	10.48	0.24	-	0.40	-	-
347NG-B	347NG	172716	3.9	5.4	0.033	0.43	1.67	0.028	0.002	18.15	10.20	0.56	0.0035	0.43	-	-
347NG-C	347NG	174072	4.5	5.0	0.028	0.34	1.75	0.030	0.008	18.30	10.42	0.49	0.0279	0.41	-	-
347NG-D	347NG	161358	3.3	5.5	0.045	0.28	1.60	0.030	0.015	18.30	10.70	-	-	0.60	0.12	-
347NG-E	347NG	161286	4.4	3.0	0.050	0.53	1.93	0.029	0.005	18.10	10.50	-	-	0.56	0.14	-
347NG-F	347NG	173260	3.3	3.0	0.030	0.35	1.70	0.029	0.011	18.28	10.53	-	0.0259	0.36	-	-
347NG-G	347NG	316642	1.8	2.8	0.030	0.42	1.66	0.024	0.009	17.96	10.46	-	0.0236	0.33	-	-
347NG-H	347NG	173446	2.4	1.9	0.035	0.25	1.65	0.029	0.005	18.05	10.75	-	0.017	0.41	-	-
347NG-I	347LN	D632201	1.6	1.5	0.015	0.31	1.48	0.017	0.001	18.40	10.40	0.42	0.085	0.36	-	-
347NG-J	347NG	46112	3.0	3.0	0.014	0.31	1.21	0.024	0.013	17.12	9.65	0.16	0.066	0.23	0.07	-
347-1	AISI347	876195	3.0	5.5	0.045	0.54	1.60	0.032	0.007	17.80	9.71	-	-	0.67	-	-
347-2	347LPN	-	5.5	5.0	0.014	0.30	1.64	0.012	0.005	18.44	9.25	-	0.062	0.26	0.06	-
347-3	KCL473Nb	T6961	3.6	6.0	0.018	0.50	1.49	0.029	0.011	18.26	9.01	0.37	0.075	0.49	0.17	-
347-4	347NG	173268	4.0	3.0	0.025	0.34	1.74	0.033	0.006	18.25	10.77	-	0.022	0.37	-	-
347-5	347L	-	0.0	0.0	0.030	0.17	1.61	0.013	0.007	18.58	11.49	-	-	0.30		0.008
347-6	347R	-	3.5	3.0	0.020	0.51	1.43	0.019	0.012	18.22	10.14	-	-	0.74		0.017
347-7	TP347	869962	4.0	2.5	0.042	0.47	1.58	0.025	0.002	18.07	9.18	-	-	0.63	-	-
347-8	AISI347	S51493	3.0	4.0	0.049	0.59	1.73	0.024	0.013	17.26	9.41	0.21	0.026	0.61	-	-
347-9	AISI347	-	3.0	5.0	0.037	0.63	1.56	0.029	0.001	18.00	9.67	0.32	0.044	0.61	-	-

a: Measured Ferrite content with Magne-Gage
b: Ferrite Potential by Delong Method
c: Rare earth metals

controlled manganese and phosphorous contents to decrease IGSCC susceptibility and to aid in maintaining the required strength. The major chemistry alteration in the modified 347 alloys is the carbon and niobium contents, such that the Nb/C ratio of the modified alloy is higher in comparison to AISI 347 (>13 vs. >8). Although the Nb/C ratio has been significantly increased, the maximum amount of Nb in the modified alloys is lower than in AISI 347 because of lower carbon content. The Japanese modified, 347LPN, has additional control on phosphorous and nitrogen levels to improve resistance to IGSCC as well as to improve weldability and strength.

All of the 347 varieties evaluated, with an exception of 347L, have a positive ferrite content (1.6 to 5.5 FN) in the fused zone (austenite + ferrite duplex microstructure). There are two microstructure groups in the 316NG alloy. The first is a fully austenitic group: 316NG-D, 2, 3 and 5-9, the other is a ferrite containing group (1.6 to 5.1 FN): 316NG -A, B, C, 1 and 4. All standard AISI 304 and 316 grades have a ferrite content ranging from 2.4 to 4.4 FN.

It has to be noted that the carbon content of two heats of 347NG, -D and E, exceeds the nuclear grade requirement ($C_{max} < 0.04$). However, these heats were approved by manufacturer after satisfactory intergranular corrosion tests in accordance with DIN 17740. Furthermore, other heats of 347NG (F, G and H) have lower Nb/C ratio than required ($Nb/C \geq 13$)

Types 347L and 347R with rare earth additions (mixture of La, Se, etc.) have also been included to investigate the role of rare earth elements on the weldability of 347.

2. EXPERIMENTAL PROCEDURES

a. Gleeble Hot Ductility Testing

Hot ductility behavior of all program materials was evaluated using the Gleeble which is essentially a high-speed, hot-tensile tester, instrumented so that heating and cooling of the test specimen can be accurately programed to reproduce the rapid temperature changes that occur in the heat affected zone during welding. Therefore the technique provides the tensile properties of any microstructure which may evolve within the weld heat affected zone.

The test employs a cylindrical specimen, 0.25 in. in diameter and 4 in. long with a 1/4 - 20 thread on both ends. The samples were extracted in the longitudinal orientation with respect to rolling or forming direction. The specimen is clamped between water cooled copper jaws separated 0.8 in. from each other, which, in addition to serving as grips for tensile testing, provide a means for introducing the current to the specimen and insuring a rapid cooling when the current flow is interrupted. The current is controlled electronically throughout the desired thermal excursion by means of a signal obtained from a fine wire thermocouple percussion spot welded to the center of the specimen gauge length.

The thermal cycles utilized were characteristics in the HAZ of a 1-1/2 in. thick stainless steel plate welded with an energy input of

70 KJ/in.. Tests were conducted during on-heating and on-cooling conditions. The on-cooling tests were performed from the zero ductility temperature (ZDT), which is the temperature at which almost complete grain boundary liquation occurs and is the liquidus temperature of the segregated grain boundaries. The ZDT was determined by two methods. The first was the conventional way, that is, the ZDT was measured during the on-heating tests (on-heating tests were conducted until a ZDT was obtained). By the second method the ZDT was determined when a specimen separated under a small load (approximately 50 lbs) during rapid heating. In most cases, the ZDT for both methods was identical (within 5 F^{o}). When difference is more than 10 F^{o}, the higher temperature was considered as the ZDT and used for the on-cooling tests.

The data of interest in the test evaluation were, the percentage reduction in area, fracture load and strain. The summarized testing condition and parameters are given in Table 7. (The justification of the testing parameters in table 7 is described in detail in Appendix).

Hot ductility testing was conducted in the air. However, when a clean unoxidized fracture surface was needed for fractography, tests were conducted using argon shielding in an atmosphere chamber incorporated into the Gleeble. Alternate chamber evacuation and backfilling with argon provided a chamber atmosphere which resulted in clean fracture surfaces with no detectable oxidation.

Table 7. Hot ductility testing conditions and procedure.

PARAMETER	CONDITIONS
Sample	Cylindrical: Diameter; 0.25 ± 0.001 inch (6.0 ± 0.5 mm) Length; 4.0 + 0.125 inch (100 ± 5 mm) Thread; 1/4-20 on Both Ends
Thermocouple	Diameter: 0.010 inch Chromel-Alumel; <2475°F Noble Metal/Alloy; >2475°F Attachment Methods: Percussion/Spot Welding Cross Wire Technique Separate Wire Technique
Thermal Cycle	Characteristics for a Peak Temperature of 2400°F in 1-1/2 inch Stainless Steel 70 KJ/inch Energy Input, SMAW
Peak Temp.	Zero Ductility and Zero Strength Temperature
Hold Time	Test Temperature*; 1 - 2 secs Permitted Peak Temperature ; Not Permitted
Crosshead Speed	2.5 ± 0.5 inch/sec (63 ± 13 mm/sec)
Jaw Separation	0.8 ± 0.2 inch (20 ± 5 mm)
Testing	Minimum 2 Tests at Each Temp. A Difference of Greater Than 30% in R.A., Will Necessitate One More Test. 100 - 200°F Intervals Below ZDT/ZST - 100°F. 25°F Intervals between ZDT/ZST - 100°F and ZDT/ZST.

* Only when test temperature is below ZDT/ZST - 100°F

b. Varestraint Hot Cracking Tests

Hot crack testing of all program materials was conducted using the Varestraint method which was recently modified in terms of testing concepts and design by the Welding Research Group at The University of Tennessee (12). The main concept changes involve a multipass technique which provides for a simultaneous evaluation of the hot cracking tendency in the fusion zone, weld metal HAZ and base metal HAZ using one specimen.

Sample Preparation and Welding Conditions. All the samples that were extracted from the program materials had longitudinal orientations. The specimen dimension is 5 in. long, 1 in. wide and 1/8 in. thick. The surface finish is 32 rms. Samples were slotted at the ends to accommodate the alignment pins of the Varestraint device.

The welding conditions were chosen to give a circular weld pool shape and approximately half thickness penetration. The following welding parameters have shown to be optimum for the evaluation of austenitic stainless steels of 0.125 in. thickness.

Process.....Autogenous GTAW
Current.....100 Amp.
Voltage.....12 V.
Travel Speed.....10 ipm.
Shielding gas.....Argon-30 cfh.
(10 secs pre and post weld purge)
Electrode.....2 % thoriated tungsten
3/32 in. dia., 60^{o} tip angle
Arc length.....0.062 in.
Polarity.....DCEN
Interpass temperature.....room temp. ($72\ ^{o}F$)

Multipass Technique. A pictorial view of a Varestraint tester positioned in the longitudinal mode is shown in Figure 21. The multipass technique requires a minimum of three passes. A schematic

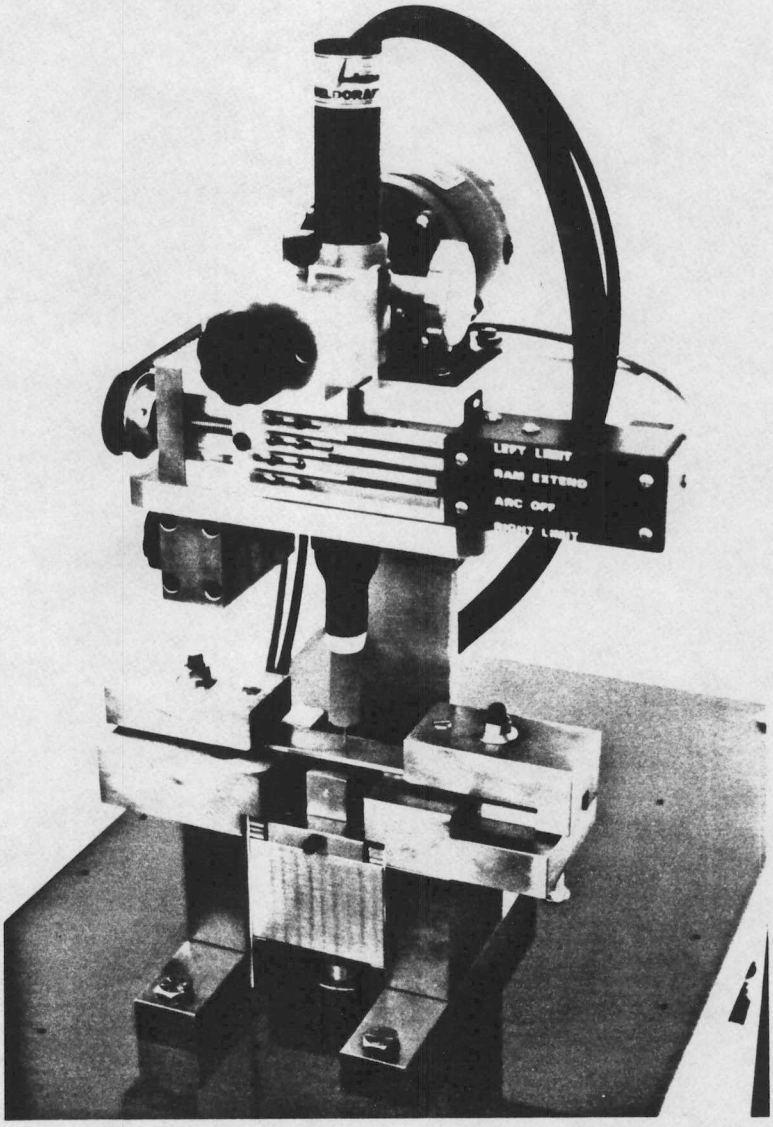


Figure 21. A pictorial view of the Varestraint positioned in the longitudinal mode.

drawing of the Varestraint test device showing the manner in which a specimen is tested, is illustrated in Figure 22. Figure 22 shows both the top and front views of the sample positioned in the device before and after testing. A macroscopic sketch of the tested region, revealing cracks and indicating the sequence of weld passes, is also shown in Figure 22.

The multipass technique for evaluation of the three zones is conducted as follows (with reference to Figure 22): After positioning the sample in the device, two 2 in. long parallel autogenous passes are made with a predetermined spacing between them (depending on material). A third pass was positioned so that it produces a base metal HAZ which overlaps the HAZ of the second pass and simultaneously produce a HAZ in the weld metal of the first pass. When the third pass is positioned, it is along the center of the specimen and overlaps 1/4 of the width of the first pass. The spacing between second and third pass is in the range of 1 - 1.5 mm. To enhance cracking in both the weld metal HAZ and the base metal HAZ, fourth and fifth passes are superimposed directly on the third pass. The total number of passes is restricted to five to avoid excessive distortion of the sample. The augmented strain is applied during the last pass just after the torch passes the center of the radius block, such that the augmented strain is applied to the solidifying interface at the center of the sample directly over the crown of the radius block. Therefore, four base metal HAZ and three weld metal HAZ exposures are strained together with the fusion zone of the test pass.

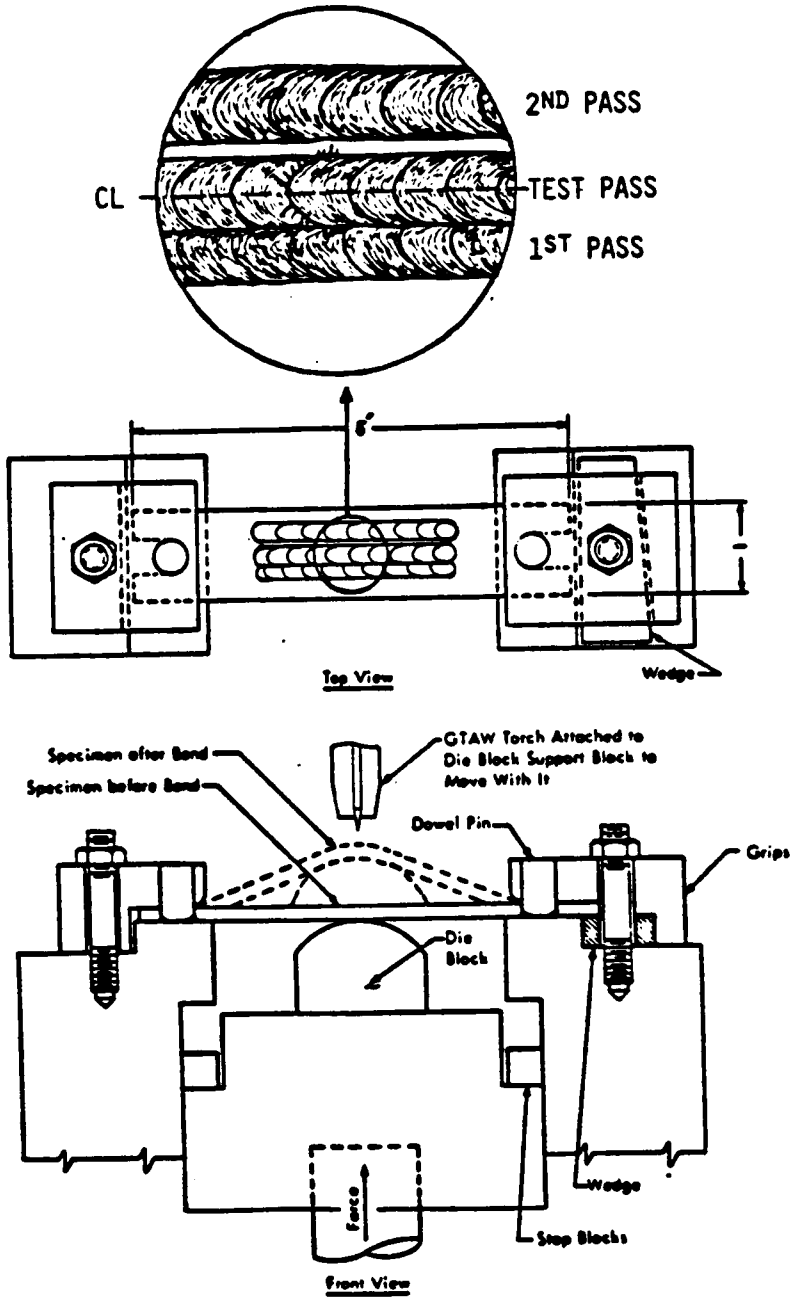


Figure 22. Schematic drawing of the Varestraint test device showing the manner in which a specimen is tested.

The range of augmented strains applied in this study was 0 - 4%. The cracking determination and measurement were accomplished on the as-welded surface at a magnification of 70X using a binocular microscope. The number of cracks, maximum crack length, total crack length and cracking threshold strain for each of the weld zones were measured and recorded. The ferrite content in the as-welded condition was also measured with a Magne-Gage.

c. Element Implant Technique

In order to investigate the influence of a particular element (Si, C) on solidification cracking susceptibility and the synergistic effect of N with Si, the composition of type 304 (Code 304-3) was modified using an element implant technique. In this technique, a thin sheet of material with the desired modifying element is cut to the appropriate size (to provide the desired composition in the weld zone) and spot welded to the test specimen. Then an autogenous GTA weld is made to fuse the implanted material and combine it with the base metal. With the knowledge of the chemical composition of the added material and the base material and the fusion zone cross section, the desired composition is obtained by controlling the size of the fused weld zone.

To modify the silicon content in the fusion zone, 12 mil thick Fe - 3.5% Si alloy was used. To obtain several different levels of silicon, different numbers of the same size pieces were inserted into a groove made on the specimen surface and then spot welded before fusing in an argon shielding GTA weld. A schematic representation of the implant technique is given in Figure 23.

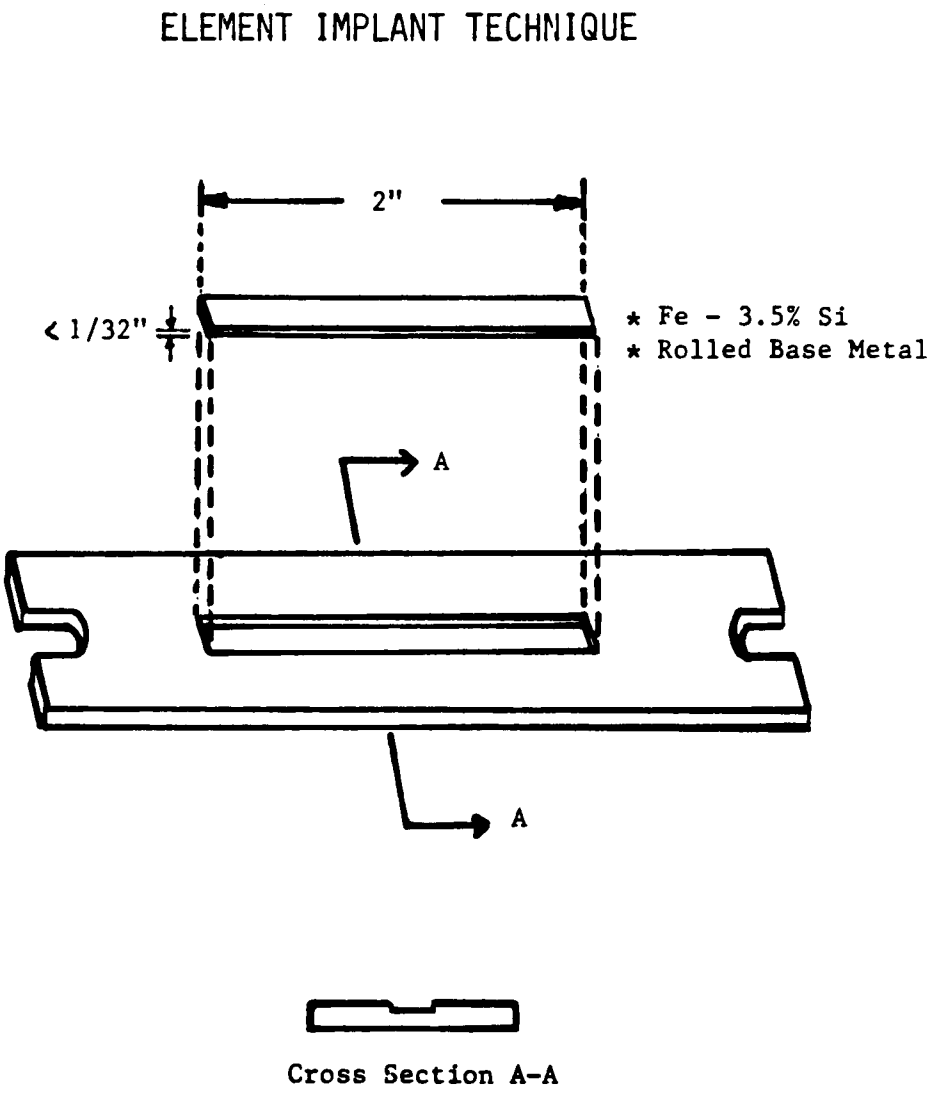


Figure 23. Schematic representation of the element implant technique.

Various N levels in the fusion zone were obtained by the addition of nitrogen to the argon shielding gas during autogenous welding. Since this technique involves only the addition of nitrogen to the shielding gas, the basic alloy composition is not be changed but the ferrite content and solidification mode (depending on the amount of addition) is altered. Therefore, when both N and Si were required, silicon implanted specimens were subsequently welded with nitrogen containing shielding gas.

d. Solidification Study

To investigate segregation behavior and high temperature microstructure, a rapid quenching technique was utilized for selected heats of 316NG and 347NG having a solidification mode of either primary ferrite or austenite. The technique utilized was a simple rapid quench method in which sample was quenched into ice water during autogenous GTA bead-on-plate welding. This resulted in a spectrum of microstructures from the high temperature solid-liquid interface microstructure to a normal welding induced microstructure. The welding parameters for the autogenous GTAW on 3" x 1 1/2" x 3/8" plate were; Current - 220A, Voltage - 13V, Travel Speed - 4 inches/min with argon shielding gas.

e. Microstructural Evaluation

Based on data analysis, hot ductility, hot cracking and rapidly quenched samples were selected for extensive metallurgical evaluation utilizing the high resolution analytical electron microscope (STEM and TEM), scanning electron microscope (SEM) and optical light microscope (OLM).

Mounted samples were polished to 0.05 um using alumina powder. Ferrite containing specimens were then etched in dilute aquaregia (1 part nitric acid, 3 parts hydrochloric acid and 1 part distilled water). Electrolytic etching in 10% oxalic acid was used for fully austenitic samples.

SEM fractography was conducted on the hot ductility samples tested in the argon atmosphere. For the fractographic examination of the Varestraint samples, the cracks were carefully excised (by a thin diamond slicing disc) and the crack faces were opened by fracturing samples through the crack at liquid nitrogen temperature. The opened surfaces were ultrasonically cleaned in acetone for 10 minutes before examination.

Selective Potentiostatic Etching by Electrolytic Dissolution (SPEED) Method. This method was developed by Japanese researchers (167-169) for the in situ morphological study of precipitates in steel. The principle of the SPEED method is to selectively dissolve the matrix by applying a potential adequate for retaining the precipitates on the etched surface in a non-aqueous solution of 10% acethylacetone - 1% teramethyl ammonium chloride - methanol.

In this study, the SPEED method was utilized for fractographic and metallographic examination of selected hot ductility and hot cracking samples. Samples were etched at room temperature for 25 - 30 sec at an applied potential of 300 - 350 mV Vs. SCE utilizing a EG&G Potentiostat, Model 273. The etched specimens were examined and analyzed using SEM and EDAX. The precipitates were further

characterized by carbon extraction replica technique utilizing STEM and TEM.

Preparation of Carbon Extraction Replicas. In addition to EDAX analysis of precipitates some selected metallographic samples and hot crack fracture surfaces were further characterized by a carbon extraction replica technique.

A thin carbon film (about 100 - 200 A thickness) was evaporated on a freshly etched sample or fractured surface in vacuum (10^{-4} mm of Hg). Then, the replica was scored with a sharp knife in a grid pattern (about 2 x 2 mm grid). For a fracture surface, the carbon coated surface was painted with Enamel except in the area of interest. The replica was then removed by etching the specimen in dilute Aqua regia to free the porous carbon film, followed by floating of the replica on the surface of distilled water. The floated replica was picked up on a copper grid, dried on filter paper and stored in a desiccator.

Preparation of Thin Foil Disc Samples. To analyze compositional distributions (mainly Fe, Cr and Ni) between ferrite and austenite, and to determine the level of segregated residual elements along dendrite and grain boundaries, thin foil disc specimens were extracted from selected varestraint samples.

To extract discs, a 3 mm dia. rod was machined from the weld as shown in Figure 24, and then about 200 um thick discs were sliced using a diamond cutting disc. The sliced discs were mechanically ground to about 125 um thickness before chemical thinning. Chemical thinning was accomplished in a dual-jet electropolishing unit

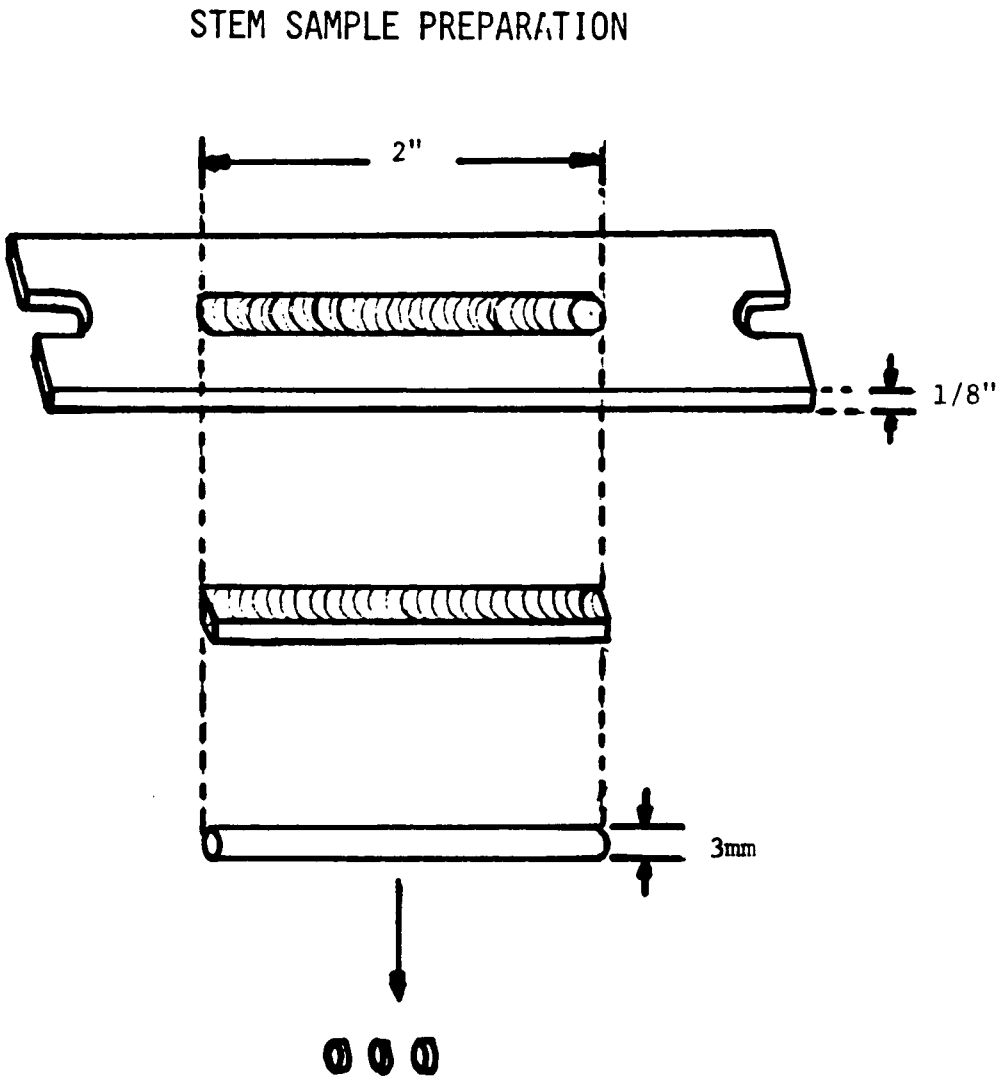


Figure 24. Schematic drawing of the way in which TEM thin foils are extracted from the Varestraint sample.

(Tenupol) using 5% perchloric acid in acetic acid at 13-15 ^{o}C, 70 V and 0.13-0.15 mA. Chemical thinning was terminated just before perforation. The final thinning/perforation and cleaning (chemical deposition during chemical thinning) was done by dual beam ion milling (Gatan Duomill - Model 6000) under a two beam condition with a beam angle of 15^{o} at 6 KV and 1 mA of total current (each beam at 0.5 mA).

Analytical Electron Microscopy (TEM & STEM). Thin foil discs and carbon extraction replicas were examined and analyzed with the Hitachi H-800 Transmission Electron Microscope (with a Gatan Model 607 - STEM unit) equipped with an energy dispersive X-ray spectrometer (Kevex Quantum detector) which was interfaced with a Delta 4 Processor - Kevex data aquisition program unit.

The Cliff-Lorimer technique (170) was used to calculate the composition (mainly Fe, Cr and Ni) from the integrated intensities. For this analysis, the intensities of only the K_{α} peaks were considered, because the K_{α} of Mn overlaps with the K_{β} of Cr. For the Fe-Ni-Cr ternary alloy, for example, the Cr content is:

$$C_{Cr} = I_{Cr}K_{Cr} / (I_{Cr}K_{Cr} + I_{Ni}K_{Ni} + I_{Fe}K_{Fe})$$

C_x : Content of x element
I_x : Peak intensity of x element
K_x : Correction factor of x element

The other two similar equations are available for Fe and Ni. Therefore, for the Fe-Ni-Cr alloy, $C_{Fe} + C_{Ni} + C_{Cr} = 1$. The Kevex data aquisition program calculates the correction factors (K_x) for each element. In this study, the presence of Mn was ignored (ignoring Mn did not significantly affect the measured intensity ratios).

Further, the computer generated background noise was subtracted from the spectrum before the analysis was conducted.

STEM elemental microprobe analysis was conducted at a 200 KV accelerating voltage. Although a spot size less than 3 nm can be used, spot size of 10 nm was used to get a sufficient counting rate for a 100 sec analysis time. The distance between each probe spot was maintained at about 0.1 - 0.2 um. When STEM analysis was conducted at and near a phase/grain boundary, the specimen was tilted so that the boundary was almost parallel to the beam direction.

CHAPTER IV

RESULTS AND DISCUSSION

1. GLEEBLE HOT DUCTILITY EVALUATION

The Gleeble device evolved because of the need to duplicate weld HAZ thermal histories and the concomitant necessity to test the resultant microstructures. The utilization of the Gleeble dates to the late 1950's, when it was used to investigate the hot ductility of high temperature alloys (11). The major advantage of using the Gleeble is that it provides one with the capacity to separate the effects of the mechanical factors from the metallurgical factors. The test not only proves to be invaluable in establishing the relative cracking tendencies of various stainless steels, but also provides the ability to differentiate between materials of the same nominal composition on a heat-to-heat basis.

The hot ductility measured in the simulated samples is normally related to the potential for hot cracking in the HAZ, and this is based on the fact that hot ductility of the HAZ must be adequate to plastically accommodate the weld contraction strains without cracking. Hot ductility testing on the laboratory simulated sample is an economical and efficient method to predict material behavior during fabrication, if a proper interpretation of the hot ductility test results is accomplished.

Discussion of the hot ductility test results for the program materials is divided into three sections. These sections discuss slightly different aspects, however, they are inter-related and lead

to a better understanding of the significance of hot ductility testing and relationship between material ductility and the microstructural changes during the high temperature - strain excursion. The three sections are:

a. Hot ductility behavior of standard and modified alloys

b. Development of new parameters and applications

c. Metallurgical behavior during hot ductility testing

Each sections begins with a brief introduction or summary.

a. Hot Ductility Behavior of Standard and Modified Alloys

In this section, the typical hot ductility behavior of the standard and modified grade stainless steels is briefly explained and compared using conventional parameters (criteria) which lead to the development of new parameters.

Standard AISI 304 and 347. The hot ductility behavior typical of AISI 304 and 347 is given in Figures 25 and 26, respectively. These particular hot ductility data are for 304-1 and 347-1. In each figure, the percentage reduction in area is plotted as a function of test temperature. The solid and dotted curves correspond to the on-heating and on-cooling behavior respectively. The ZDT for the on-cooling tests is also given in each figure. The vertical bars represent data spread at a given temperature. The absence of a bar indicates that the reduction in area for two or three tests at that temperature is essentially the same.

Both 304 and 347 have an almost identical on-heating behavior. The ductility gradually increases as temperature increases to approximately 2200 - 2300 ^{o}F and then dramatically decreases to a low

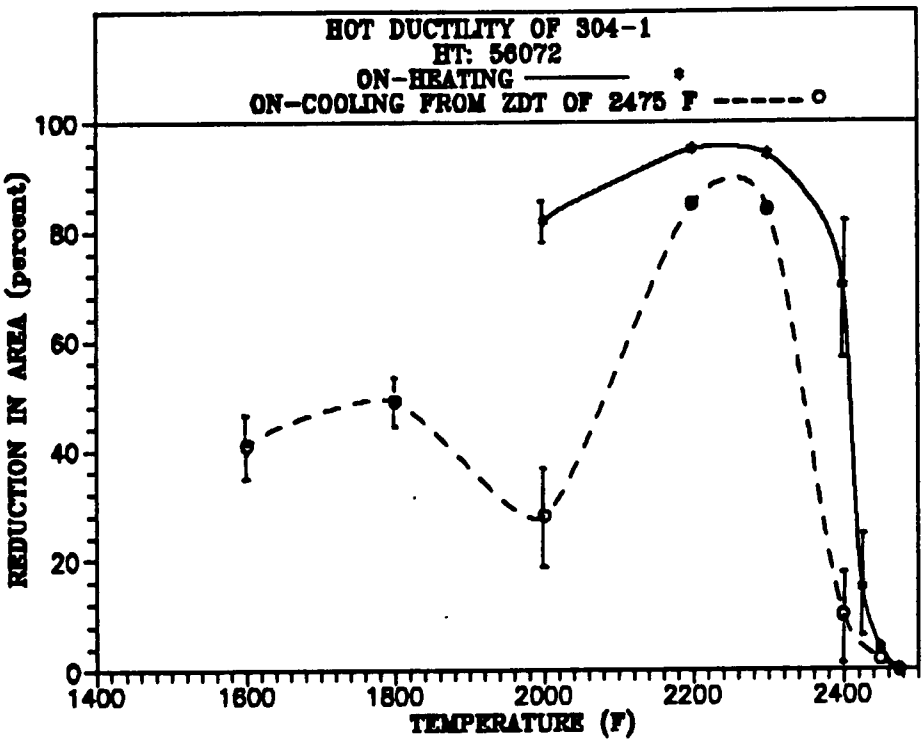


Figure 25. Typical Hot ductility behavior of AISI 304 (304-1).

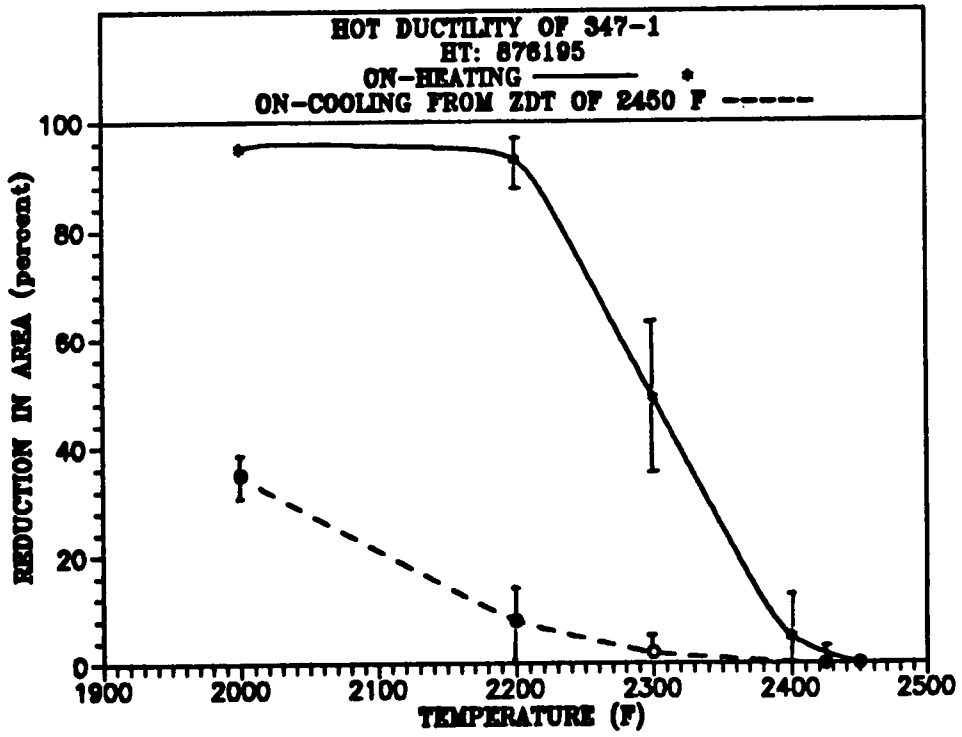


Figure 26. Typical Hot ductility behavior of AISI 347 (347-1).

value as the temperature approaches to the ZDT. In the case of 347, the sudden drop in ductility occurs over a wider temperature range as compared to 304 (250 vs. 150 F^{o}).

However, the on-cooling ductility response of both alloys is significantly different in terms of amount of ductility recovered (as compared to the on-heating level) and the approximate temperature at which the on-cooling ductility starts to recover to a nil amount. 304 shows a ductility recovery of approximately 90% of the on-heating ductility within 150 F^{o} of the ZDT of 2475 ^{o}F. However, AISI 347 reveals virtually no recovery in ductility until the on-cooling test temperature reaches 2200 ^{o}F, 250 F^{o} below the ZDT (2450 ^{o}F). Even at 2200 ^{o}F, the amount of ductility recovered is only approximately 10% of the on-heating ductility. 304-1 further reveals a shallow ductility dip behavior at approximately 2000 ^{o}F (after recovery to a maximum at about 2300 ^{o}F) during on-cooling. The significance of the ductility dip behavior will be discussed in detail in a later section.

Modified Alloys (316NG and 347NG). The typical hot ductility behavior of the modified alloys is presented in Figures 27 and 28 for the 316NG materials and Figures 29 and 30 for the 347NG materials. As in the case of AISI 304 and 347, four heats of the nuclear grades have virtually identical behavior during on-heating. However, the on-cooling ductility response is somewhat different from heat to heat and from alloy to alloy, in terms of the extent of ductility recovery relative to that on-heating and the approximate temperature range over which the on-cooling ductility is essentially zero.

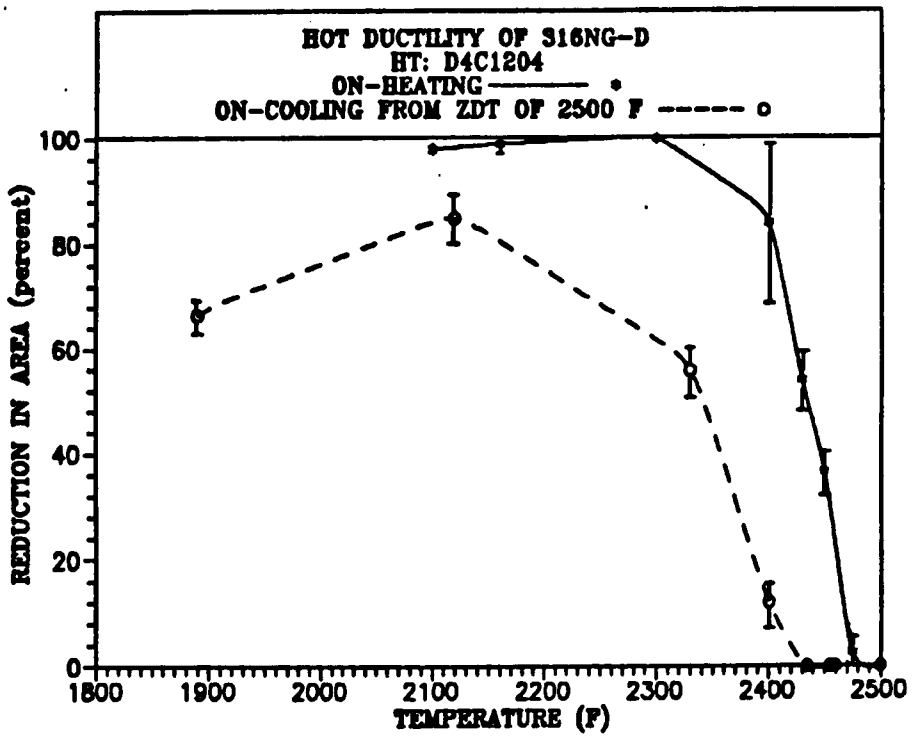


Figure 27. Typical hot ductility behavior of 316NG (316NG-D).

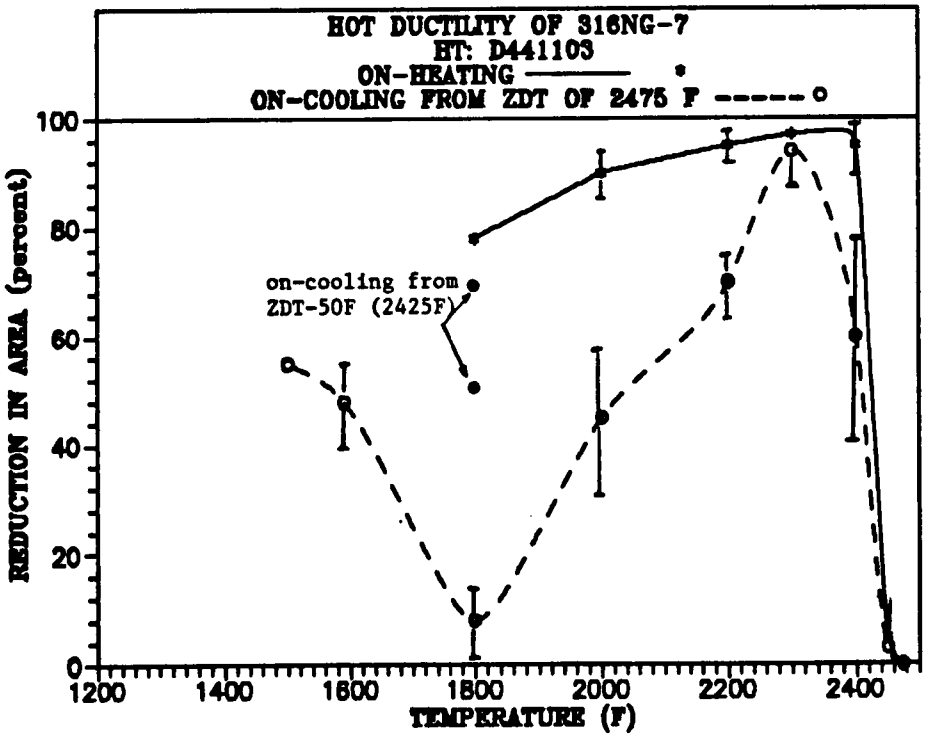


Figure 28. Typical hot ductility behavior of 316NG (316NG-7).

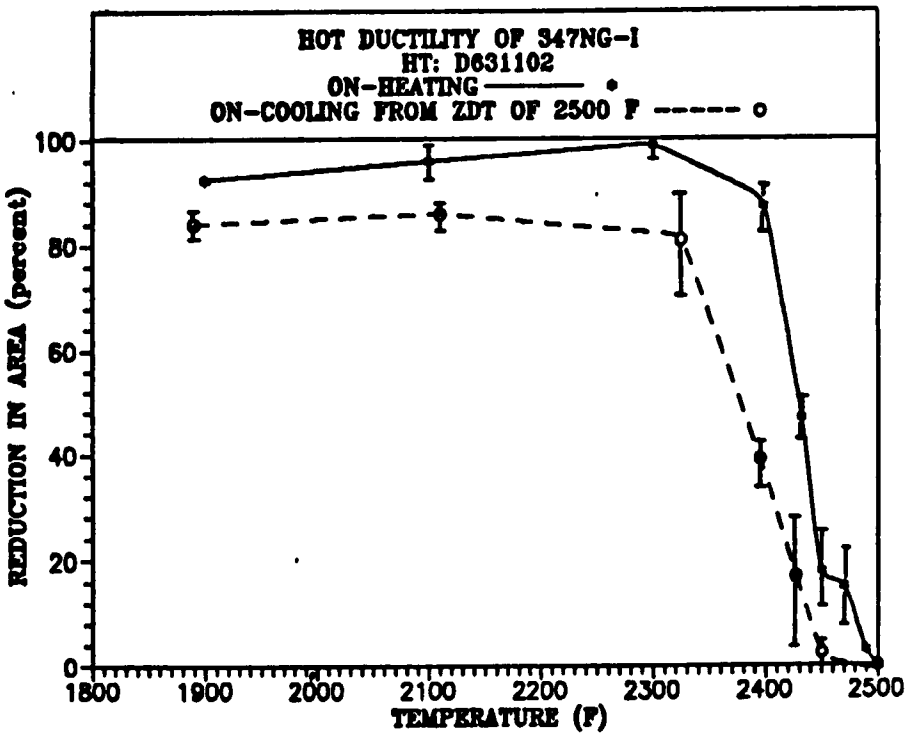


Figure 29. Typical hot ductility behavior of 347NG (347NG-1).

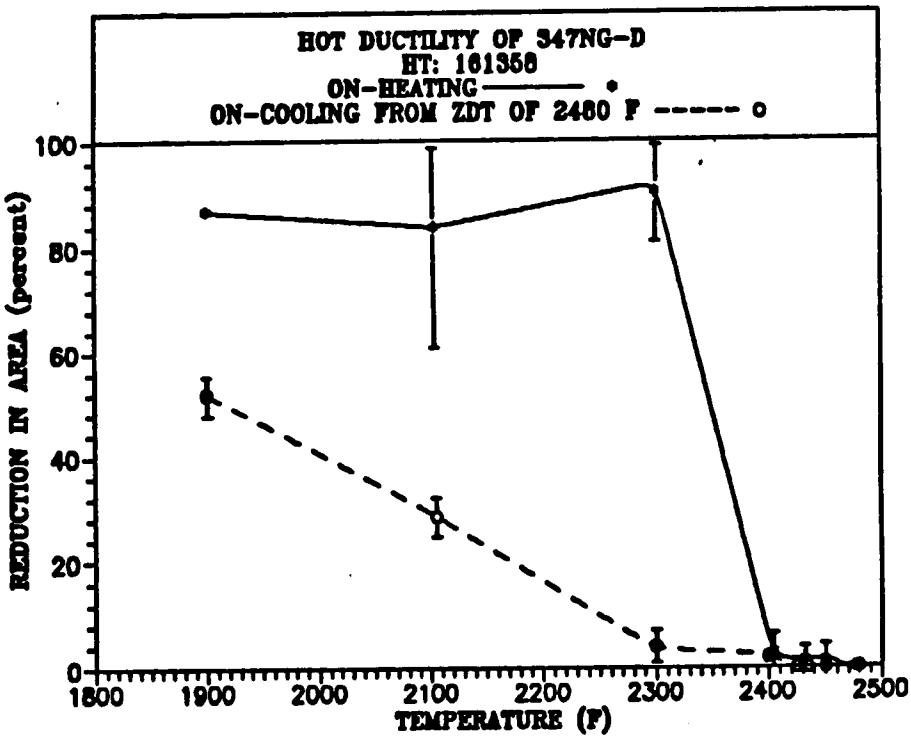


Figure 30. Typical hot ductility behavior of 347NG (347NG-D).

As far as the amount of ductility recovery is concerned, 316NG-7 has the best response among four nuclear grade alloys. The on-cooling ductility of 316NG-7 approximates 100% of the on-heating ductility within 100 F^{o} of the ZDT of 2475 ^{o}F. However, the ductility recovery gradually decreases as the temperature decreases below about 2200 ^{o}F and thus alloy shows a significant ductility dip at 1800 ^{o}F. 347NG-E (Fig 30) has the poorest ductility recovery as compared to the other NG grades and has virtually no recovery in ductility until the on-cooling test temperature reaches about 2300 ^{o}F; 200 F^{o} below the ZDT. The ductility behavior of 347NG-E is similar to that of AISI 347 (as shown in Figure 26). This is not an unexpected behavior when the chemical composition of 347NG-E is considered. The chemical composition of 347NG-E is similar to that of AISI 347. As mentioned earlier, the carbon content of 347NG-E exceeds the nuclear grade requirement of 0.04% max. and has a concomitantly higher Nb content to meet Nb/C ratio requirement.

The on-heating ductility drop temperature range varies from alloy to alloy and is somewhat wider in 347NG than in 316NG. Examination of the on-heating behavior of all program nuclear grade materials revealed that the on-heating ductility begins to drop approximately 200 F^{o} and 100 F^{o} below the ZDT for 347NG and 316NG, respectively. It is worthy to note that for both 347NG and 316NG, there are two stages in the on-heating ductility drop region. The first stage is a "rapid ductility decrease stage" and the second is a relatively "slow ductility dropping stage". It can also be noted that 316NG has a narrower second stage in comparison to 347NG. The reason

and significance of a wider ductility drop range and a wider second stage for 347NG will be discussed later in the section on metallographic examination. In 347NG, the metallurgical reaction between Nb(C,N) and the austenite matrix which occurs during on-heating may play an important role. It is generally believed that the on-heating ductility begins to decrease when low melting constituents liquate in the grain boundaries, by incipient melting and/or by constitutional liquation. The ductility may further decrease dramatically by a changing of the fracture mode from transgranular to intergranular and by an increased fraction of liquated grain boundaries as the temperature increases, during the first stage of the ductility drop region. At the end of the first stage, more continuously liquated grain boundaries may be formed. As the temperature approaches the ZDT, the grain boundaries will be almost completely wetted by liquid and thus the ductility is reduced to zero and the fracture stress is nil. This assumed/postulated metallurgical reaction will be further discussed in detail later.

When comparing the hot ductility behavior of AISI 304 and 347 with that of the modified alloys, the hot ductility response of 316NG is better or at least equivalent to that of AISI 304, but is superior to that of AISI 347. However, the behavior of 347NG is likely dependent upon the carbon and concomitant niobium contents. When C and Nb are well within the specification, the 347NG hot ductility response is superior to that of AISI 347 and is equivalent to that of AISI 304 and 316NG. In other instances, 347NG has the same behavior as that of AISI 347.

b. Development of New Parameters and Their Application

In this section, "new" criteria for the hot ductility test interpretation are developed and compared with the "conventional". The newly developed parameters are more quantitative and sensitive to the metallurgical variables so they allow differentiation on a heat-to-heat and alloy-to-alloy basis.

Conventional Methods. The relationship between the measured hot ductility and the susceptibility of a material to hot cracking was empirically established by comparisons between fabrication cracking incidents and the base material response on the basis that when a material has a sufficient ductility, it will not suffer from cracking by the weld thermal restraint strain. Thus, hot ductility and HAZ hot cracking susceptibility of materials are related. The hot ductility of the HAZ must be adequate to plastically accommodate contraction strains without cracking.

As reviewed in an earlier chapter, the methods of interpreting hot ductility test results (criteria) for HAZ cracking assessments vary significantly from investigator to investigator. The several criteria that have been used to date are:

1. The amount and extent of ductility recovery during on-cooling as compared to that on heating.

2. Incorporation of the extent of ductility recovery and tensile strength recovery.

3. Zero ductility range on-cooling (ZDR, BTR etc.,)

4. Mid temperature ductility dip range.

One of the most commonly used criteria is the generalized criteria by Nippes et al. (11), which is based on the above No.1 concept (the extent of ductility recovery during on-cooling from the ZDT as compared to the on-heating behavior). The Nippes criterion is schematically presented in Figure 13 (page 64). According to Nippes et al. (with reference to Figure 13), when a material has an H2 on-heating behavior, it should be rejected because of a high HAZ cracking susceptibility, and when it has an H1 on-heating class, on-cooling tests have to be conducted to further evaluate the HAZ cracking potential. The relative susceptibility of a material to HAZ hot cracking having an on-heating behavior equivalent to H1 is ranked as follow; with a behavior described as C1, the material is readily weldable without any tendency toward HAZ cracking. However, the C2 and C3 behaviors predict a less desirable hot cracking tendency with C3 indicative of the highest susceptibility to HAZ hot cracking.

Based on the Nippes generalized criteria, the hot ductility behavior of the many heats of program material (which have a numerical suffix in code number) were ranked at the University of Tennessee (166) and are summarized in Table 8. In Table 8, materials showing a similar behavior are grouped together in three different groups, I, II and III. Materials in groups I and III show the greatest and least susceptibility to HAZ cracking, respectively. Materials in Group II show a behavior between those of groups I and III. Group I materials have an H2 on-heating and a C3 on-cooling behavior or H1/H2 on-heating and a C3 on-cooling behavior. Group II materials have an H1 on-heating and C2/C3 on-cooling behavior or an H1/H2 on-heating and a C2

Table 8. Ranking of materials based on Gleeble hot ductility test.

(Using criteria of Nippes et al.)

Group	Code	Materials	Heat No.	On-cooling from a ZDT of (°F)
I	347-1	AISI 347	876195	2450
	347-7	TP 347	869962	2400
II	304-2	304	638731	2475
	316NG-1	316 NG	32657	2450
	316NG-2	316 NG	27262	2475
	347-3	ICL 473Nb	T 6961	2475
	316NG-4	316 NG	69514	2475
	347-4	347 NG	173268	2450
	316NG-7	316 NG	D-441103	2475
	304-1	304	56072	2475
III	316NG-5	316 NG	D-450905	2400
	316NG-8	316NG	D-472701	2450
	316NG-6	316NG	D-440104	2450
	316NG-9	316NG	D-442604	2475
	347-2	347 LPN	--	2500
	316NG-3	316NG	27287	2475

Group I: H2-C3 and H1/H2-C3 behavior
II: H1-C2/C3 and H1-C2 behavior
III. H1-C1 behavior

on-cooling behavior. Group III materials have an H1 on-heating and a C1 on-cooling behavior.

Table 8 reveals that AISI 347 falls into Group I, the most susceptible and 316NG and 347NG fall in Groups II and III. These materials were also tested for hot cracking susceptibility using the Varestraint test. The comparison between the hot ductility test results ranked by Nippes criteria shown in Table 8 and Varestraint HAZ hot cracking test results revealed some striking similarities and some contrasts. Materials in Group I were rated at the top of the sensitivity list in the Varestraint hot cracking tests. However, there was essentially no discrimination between Group II and III materials. Especially when the same type of alloy (316NG or 347NG) was considered, the generalized criteria failed in discriminating on a heat to heat basis as a function of chemical composition, ferrite potential, etc. The Nippes generalized criterion is considered to not be a quantitative criteria but a qualitative one such that only "bad" materials can be differentiated from the "good" materials with respect to HAZ hot cracking potential.

Another criterion which has been commonly used is the concept of the zero ductility range (ZDR) (37,108,110,111,113,115,124), and this has been considered to be more quantitative than the Nippes criterion (11). The zero ductility range is defined as the temperature difference between the peak temperature (ZDT or ZST) and the on-cooling ZDT at which the ductility recovery begins. Thus, when a material has a wide ZDR, it is considered to be more susceptible to the HAZ hot cracking. However, as shown in the typical hot ductility

curves in Figures 25-30, the determination of the exact on-cooling ZDT is difficult. When the absolute zero ductility range is considered, the variation in the ZDR for different heats and alloys is so small that the discrimination power of the ZDR criteria is limited.

Because a material shows a nil ductility over a certain temperature interval is also equally susceptible to cracking, many investigators (108,113,115) have used the on-cooling nil ductility temperature for determination of the ZDR (peak temperature - nil ductility temperature (NDT)), instead of the absolute zero on-cooling ductility temperature. Unfortunately, the level of nil ductility recovery for the measurement of the on-cooling NDT used by investigators, is arbitrary and varies from 3% to 20%.

Using the nil ductility range (NDR) concept and the temperature at which the on-cooling ductility recovers to an arbitrary value of 10% in reduction of area ($NDT_{10\%\ RA}$), the NDR for the AISI 304, 347, 316NG and 347NG (in Figures 25-30) varies from 35 to 300 F^{o}. AISI 347 shows the widest range (300 F^{o}), followed by 347NG-D (230 F^{o}), 316NG-D (90 F^{o}), 304-1 (75 F^{o}), 347NG-I (70 F^{o}) and 316NG-7 the narrowest range (35 F^{o}). The arbitrarily determined NDR appears to have a relatively good correlation with heat affected zone cracking susceptibility in the Varestraint test as will be discussed in the later section. Therefore, the concept of NDR gives a somewhat better discrimination than the Nippes generalized criteria. Further, the concept of NDR appears to be more quantitative and can discriminate between the relative susceptibility of different heats and alloys. However, it still requires continued evaluation in defining the exact

NDR of materials instead of using an arbitrary ductility recovery value.

Development of New Parameters. The basic requirements for the formation of a crack in a weldment are a susceptible microstructure and a specific magnitude of "strain". That is (23), when the strain imposed by the combined action of thermal and restraint conditions within the "critical temperature range" over which a material exhibits a phase or a combination of phases which possess a "limited capacity" to tolerate strain, a crack will form. Therefore, any criteria for the assessment of hot cracking susceptibility must have the ability to discriminate between materials as a function of the critical temperature range (microstructure) and the strain tolerance capacity.

It was shown in the previous section that the concept of a NDR is more quantitative and has a better heat to heat discrimination ability than the conventional criteria, but it requires continued evaluation to define the exact on-cooling NDT and NDR. Therefore, with a knowledge of the basic requirements of criteria for hot cracking susceptibility assessment, the concept of a nil ductility range is further evaluated and developed in this section.

In a continued effort, the fracture strain of material was evaluated as a function of test temperatures. The fracture strain measured in the hot ductility tests is then compared to the actual insitu weld thermal strains measured as a function of peak temperatures. This comparison is based on the fact that (as discussed previously) if the critical fracture strain of a material is less than

the thermal and/or restraint induced strain at a given temperature, the material may crack during welding.

The thermal strain data used in this comparison were determined at Battelle Pacific Northwest Laboratories (BPNL) where the actual thermo-mechanical (TM) history in a large scale weldment (24" dia. 304 stainless steel pipe) was measured pass-by-pass and analyzed by a computer based Data Retrieval and Analysis System (DRAS). The thermal strain was measured with modified MTS clip gages placed in the HAZ both parallel and perpendicular to the weld center line. Strain gages were attached to the surface through pairs of 1/8" dia. stainless studs which were spot welded to the counterbored surface. A set of "feet" with knife edges for clip gage attachment was secured to each pair of studs. Modified crack-opening-displacement clip gages were then placed between feet. Each modified clip gage consisted of a standard MTS clip gage with ceramic leg extensions for thermal and electrical isolation. Chromel-alumel thermocouples for temperature measurements (thermal history) were spot welded to the counterbore surface between the studs to allow simultaneous monitoring of the temperature with the strain. A pictorial view of the stainless studs and thermocouple attachment is shown in Figure 31. The detailed procedures and experiments to determine TM histories are given in the BPNL reports (171-173). Typical thermal and strain histories, taken parallel to the weld centerline on the counterbore surface at 0.2" from the weld centerline (0.08" from the weld fusion line) are given in Figure 32. In this study, only the thermal strains measured parallel to the weld centerline are utilized in comparison with the

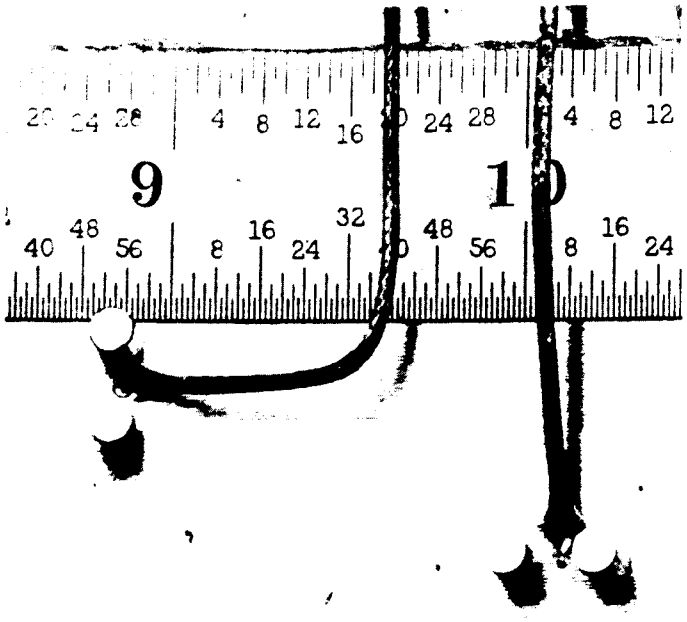


Figure 31. A pictorial view of the stainless studs and thermocouple attachment for simultaneous measurement of thermal and strain cycles.

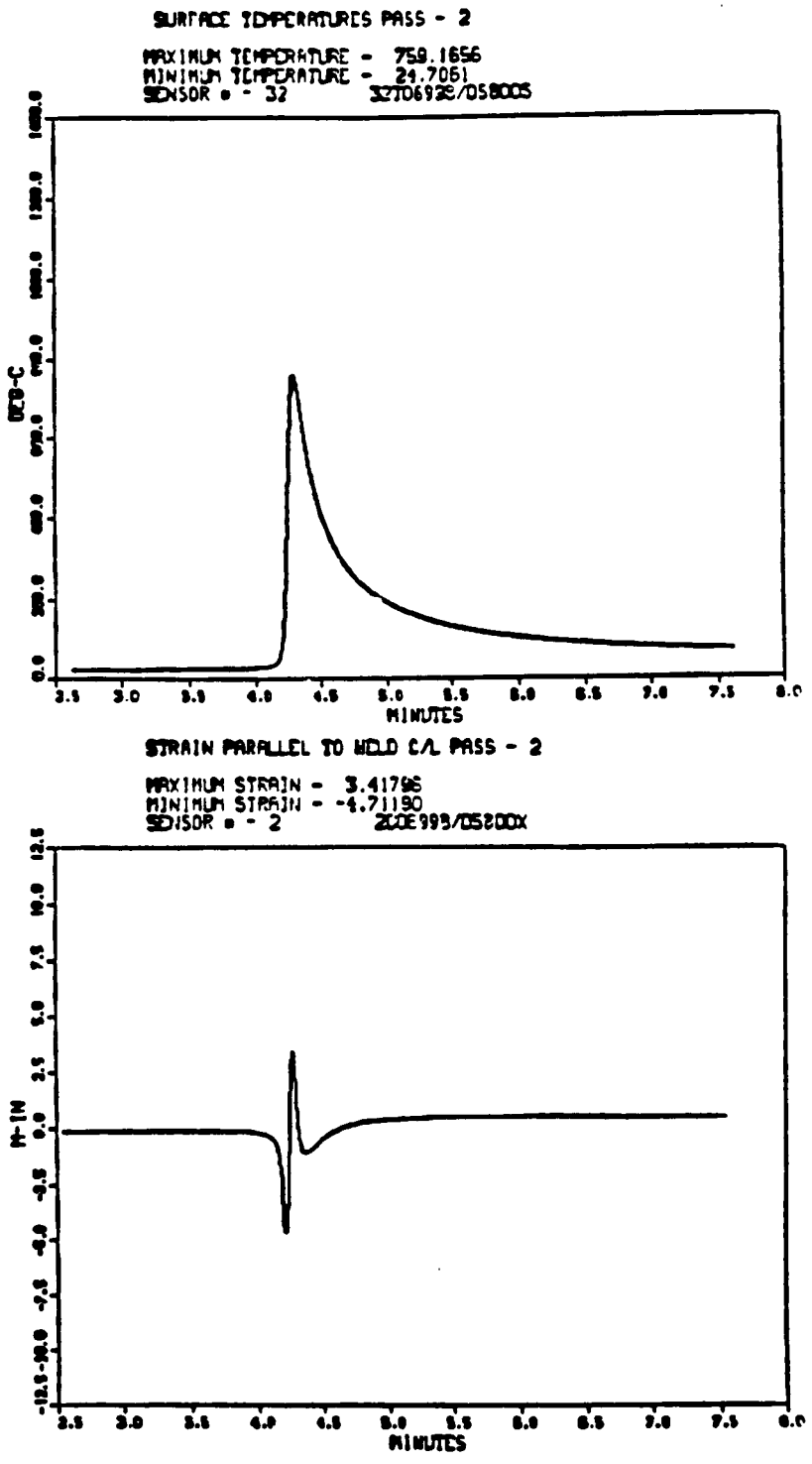


Figure 32. Typical insitu thermal and strain cycles in the full scale weld (24" dia. stainless steel pipe).

fracture strain in the hot ductility tests, because the majority of HAZ hot cracking occurs in the direction perpendicular to the weld fusion line. The strain parallel to the fusion line is more effective in crack formation. Further, as Figure 32 reveals, the thermal strain history is a combined compressive and tensile strain cycle. Only the tensile strain at a given peak temperature is considered in the comparison, because hot cracks form only under tensile stress (strain) conditions. Unfortunately, the thermal strain data are available only for temperatures below 1650 ^{o}F. Therefore, for comparison at the higher temperatures where hot ductility tests are conducted, the thermal strain data were extrapolated to the fracture temperature range.

Typical fracture strains for 316NG-A and 347NG-D during on-cooling testing from the ZDT are given in Figures 33 and 34, respectively. The extrapolated in situ thermal strain is also shown in each figure. The fracture strain for 316NG-A increases rapidly within a narrow temperature range on-cooling from the ZDT (2500 ^{o}F). However, the fracture strain for 347NG-D increases more slowly and over a wider temperature range. The intersection between the fracture strain curve and the in situ thermal strain curve gives the "Critical Fracture Strain". The temperature at this intersection is termed the "Critical Strain Temperature (CST)". At temperatures above the critical strain temperature, the material fracture strain is lower than the in situ weld thermal strain, and thus, the material may be susceptible to cracking due to the in situ thermal strain alone. Therefore, the temperature range between the ZDT and the critical

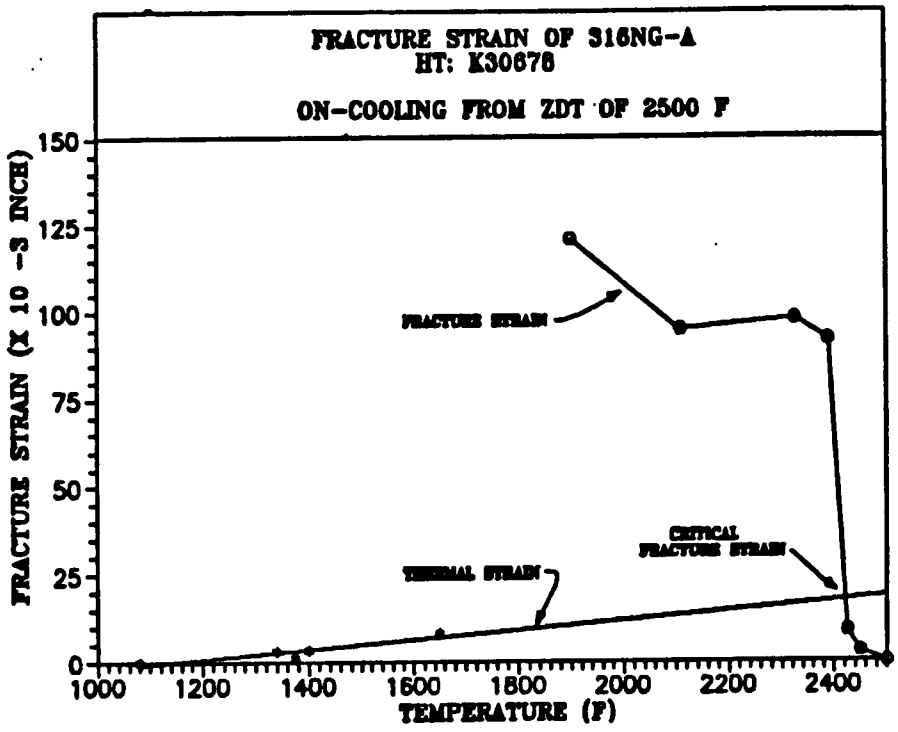


Figure 33. Typical fracture strain recovery measured as a function of test temperature for 316NG (316NG-A).

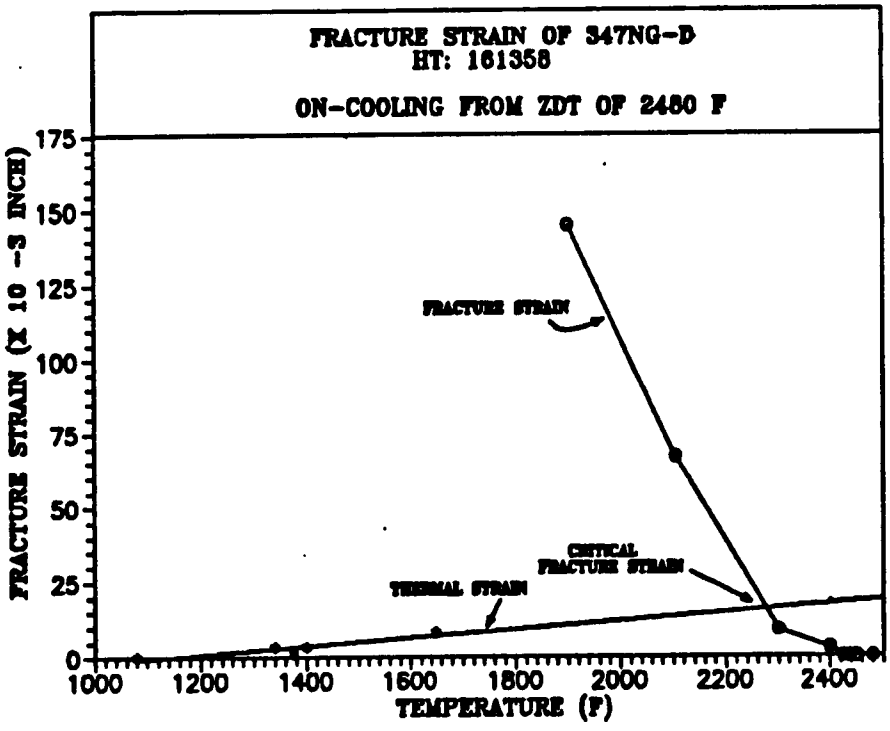


Figure 34. Typical fracture strain recovery measured as a function of test temperature for 347NG (347NG-D).

strain temperature (CST) is termed the "Critical Strain Temperature Range (CSTR)". As figures 33 and 34 show, the CSTR for 316NG-A and 347NG-D is 80 F^{o} and 200 F^{o} respectively. The CSTR for the other heats of 316NG and 347NG program materials is given in Table 9. The CSTR for the 316NG materials varies from 60 to 100 F^{o}. For 347, the CSTR ranges from 45 to 200 F^{o} revealing a wider heat-to-heat variation. The higher carbon and concomitantly higher niobium containing 347NG-D and E have the widest CSTR as compared to other heats of 347NG for which the composition is within the specification.

Further, it is interesting to note that when comparing the on-heating/on-cooling ductility data and the on-cooling fracture strain data, the temperature at which the on-cooling ductility starts to drop rapidly to a low value is about the same as the critical strain temperature (CST). Therefore, the ratio (percentage) of the on-cooling ductility to the on-heating ductility measured at the CST may also be a useful evaluation parameter. This ratio is termed the "Ductility Recovery Ratio (DRR)". The measured DRR together with CSTR for the program materials is given in Table 9. As in the case of the CSTR, there is also a wide range of variation in the DRR for the program materials. For 347NG, the DRR varies from 4% to 85%, on the other hand, 316NG has a narrower variation range from 43% to 100%. The relationship between the CSTR and DRR concepts, relative to the hot ductility and fracture strain curves, is schematically shown in Figure 35.

The correlation between CSTR and DRR for the current program materials is given in Figure 36. Figure 36 illustrates that with a

Table 9. Summary of hot ductility test results of current program materials.

Code	Type	ZDT(°F)[a]	CST[b] (°F)	CSTR[c] (°F)	DRR[d] (%)	NDR[e] (°F)	1/2Nb / (30C + 50N)
347NG-A	347NG	2500	2400	100	11	95	0.30
347NG-B	347NG	2500	2420	80	76	80	0.10
347NG-C	347NG	2485	2440	45	63	50	0.09
347NG-D	347NG	2480	2280	200	4	190	0.22
347NG-E	347NG	2480	2290	190	11	180	0.19
347NG-F	347NG	2500	2420	80	30	80	0.08
347NG-G	347NG	2485	2400	85	70	80	0.08
347NG-H	347NG	2475	2435	45	78	50	0.11
347NG-I	347NG	2500	2430	70	84	70	0.04
347NG-J	347NG	2500	2430	70	65	75	0.04
347-5	347L	2485	2420	65	35	60	0.17
347-6	347R	2450	2300	150	12	160	1.23
316NG-A	316NG	2500	2420	80	71	80	-
316NG-B	316NG	2500	2400	100	43	100	-
316NG-C	316NG	2500	2440	60	100	70	-
316NG-D	316NG	2500	2420	80	62	80	-

a: Zero Ductility Temperature
b: Critical Strain Temperature
c.: Critical Strain Temperature Range
d: Ratio of the on-cooling ductility to the on-heating ductility at CST
e: Nil Ductility Range (ZDT - temperature at which on-cooling ductility recovered to 7%)

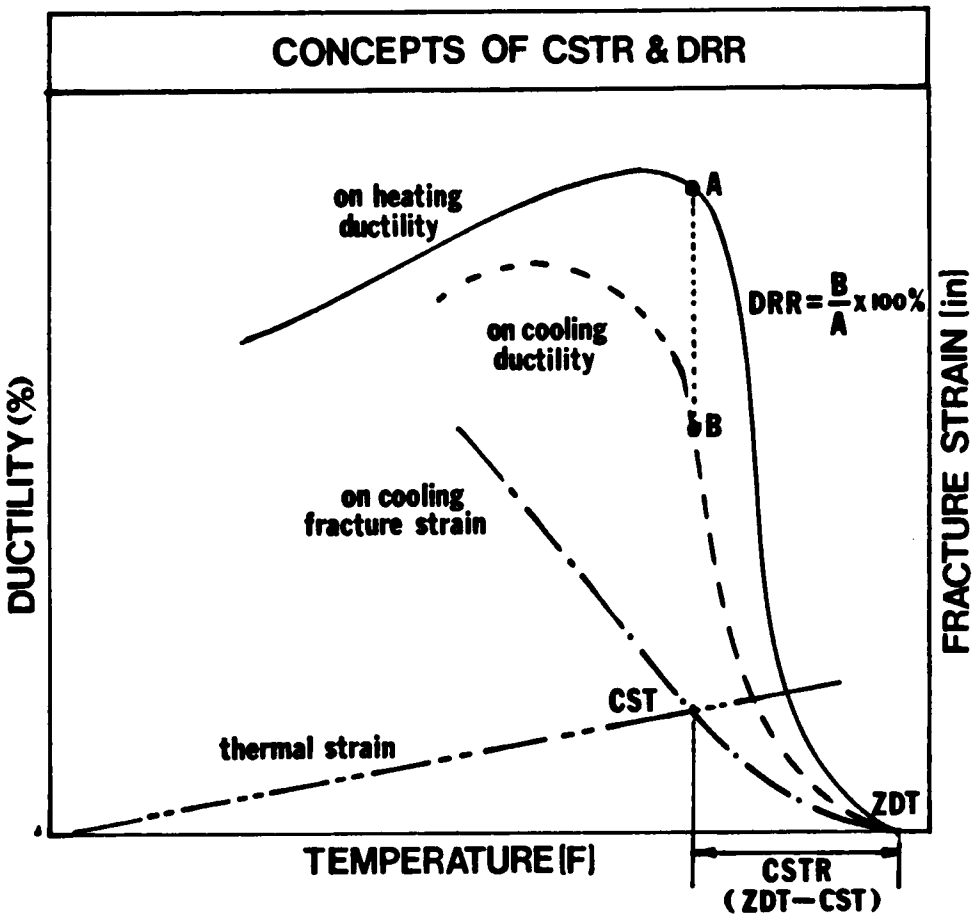


Figure 35. A schematic drawing of the concepts of CSTR and DRR.

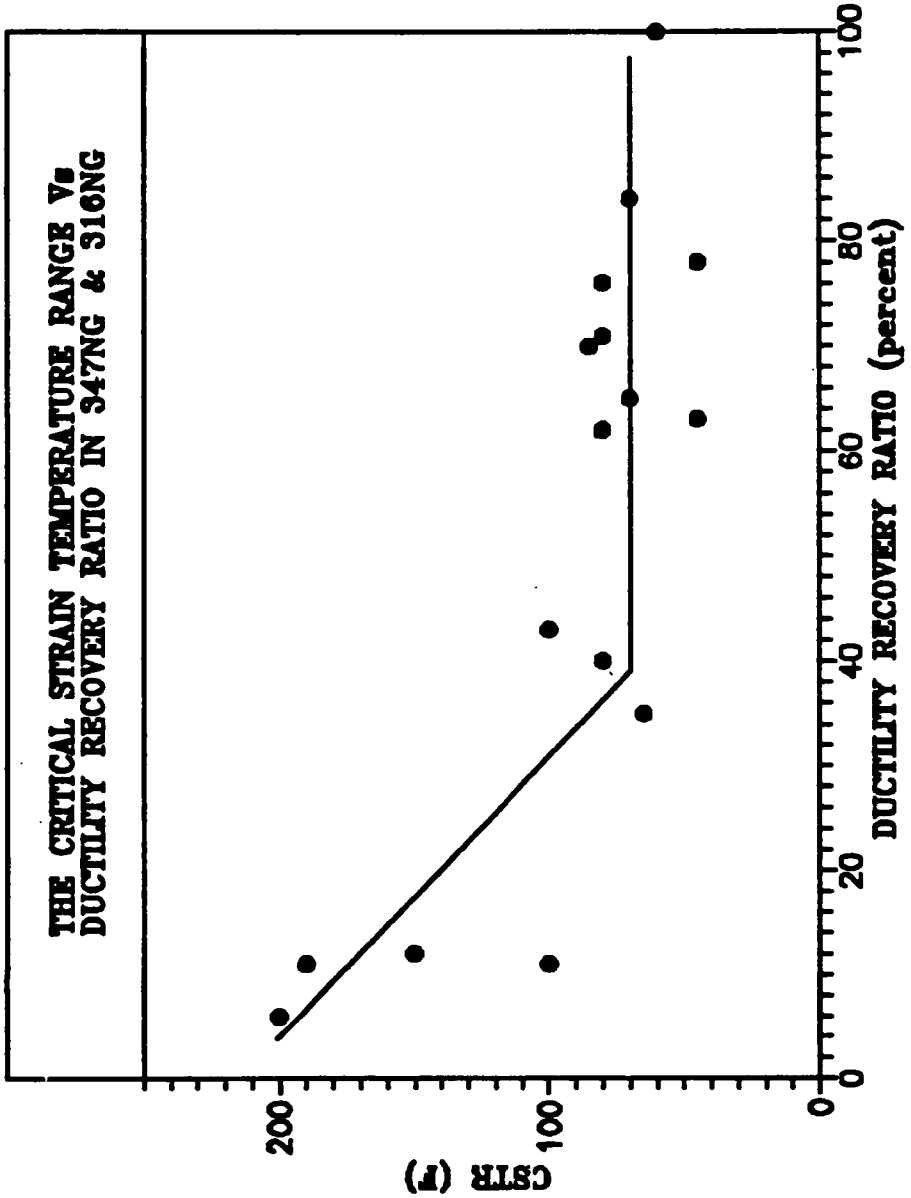


Figure 36. Correlation between CSTR and DRR.

decrease in the CSTR, the DRR gradually increases and when the DRR is greater than approximately 40 ± 05%, the CSTR appears to level off at about 70 ± 10 ^{o}F. This relationship may give an important clue in that when a material exhibits a CSTR smaller than about 70 ± 10 ^{o}F and the DRR is greater than 40 ± 5%, these may be a sufficient ductility to tolerate the welding restraint stress (strain) and thus the material will be resistant to the HAZ liquation cracking. However, it is probably not viable to proceed in developing the criteria into an indirect test method (Gleeble hot ductility testing) for cracking assessment unless a direct HAZ hot cracking evaluation is conducted and its results correlated with those in the indirect tests. Therefore, the criteria for hot ductility testing developed will be discussed after evaluation of the same materials with Varestraint HAZ cracking tests.

Analysis and Applications. In most instances, the actual in situ thermal strain data are not available which can be used to directly compare with the material fracture strain to determine the CSTR and DRR. A careful examination of the critical fracture strain in the program materials revealed that the critical fracture strain varied from 17 x 10^{-3} inch to 22 x 10^{-3} inch (expressed as an elongation over a fixed gage length corresponding to the standard hot ductility test method). Therefore, the average critical fracture extension is about 20 x 10^{-3} inch. Since about 90% of the specimen extension occurs within a 0.25 inch length in the center of specimen gage length and the temperature is essentially constant in this

region, the actual fracture strain (elongation) in the Gleeble hot ductility tests is as follows:

$$\frac{(20 \times 10^{-3}) \text{ inch} \times 0.9}{0.25 \text{ inch}} \times 100\ (\%) = 7\%$$

In a tensile test, the ductility in terms of reduction in area is usually identical to the ductility measured in terms of the elongation, when both values are small. Therefore, when the actual thermal strain data are not available, the temperature at which the on-cooling ductility recovers to approximately 7% of reduction in area can be used to define the CSTR and DRR. The measured CSTR using a 7% ductility recovery temperature is given in Table 9. Table 9 shows that both methods provide virtually almost the same temperature range over which the material fracture strain (ductility) is lower than the actual thermal restraint strain.

In the previous section, the CSTR and DRR were shown to be more quantitative than the conventional criteria and are sensitive to heat to heat variations. Further, the definition of the these criteria is not arbitrary. However, any criteria developed for hot cracking assessment has to be sensitive to the metallurgical variables. Therefore, an attempt was made to correlate the CSTR and DRR in terms of chemical composition, ferrite potential and other metallurgical variations.

The relationship between the ferrite potential and CSTR in Figure 37 reveals that the CSTR is not significantly influenced by ferrite potential. That is, for the limited ferrite potential range of the current program materials (FN 0 - 5.5), the variation in CSTR

is not a function of the ferrite potential. As will be discussed later, the "sudden" drop in ductility during on-heating and the ductility recovery rate within a given temperature range are a function of the fracture mechanism (intergranular or transgranular) and the amount of liquid formed during exposure to high temperature. The resolidification rate of the liquated grain boundaries (i.e, dependent on the amount of liquid formed) is a major factor for the extent of the ductility recovery temperature range (i.e., CSTR). Therefore, ferrite formed during exposure to the elevated temperature and existing ferrite in the as-received condition should provide a beneficial effects on the hot ductility (ferrite has a higher solubility for the impurity elements (P, S, Si, Nb, etc.) which are the main contributors for liquation at the grain boundaries). However, it is also well known that two phase structures which are subjected to extensive straining at high temperature have a lower ductility as compared to a single phase structure. Further, wrought stainless steel producers have been aware of the benefit to hot workability of keeping the alloy balanced to be free from ferrite (197). Morishige et al. (30) have also found, in their statistical study of more than 30 heats of commercial stainless steel, that there was no correlation between the ferrite forming tendency and hot ductility behavior. Therefore, these contradicting factors surrounding ferrite formation may result in a negligible influence on ductility and thus on CSTR and DRR as shown in Figure 37.

However, when considering the effect of ferrite on hot ductility, the effect of impurity elements should also be considered.

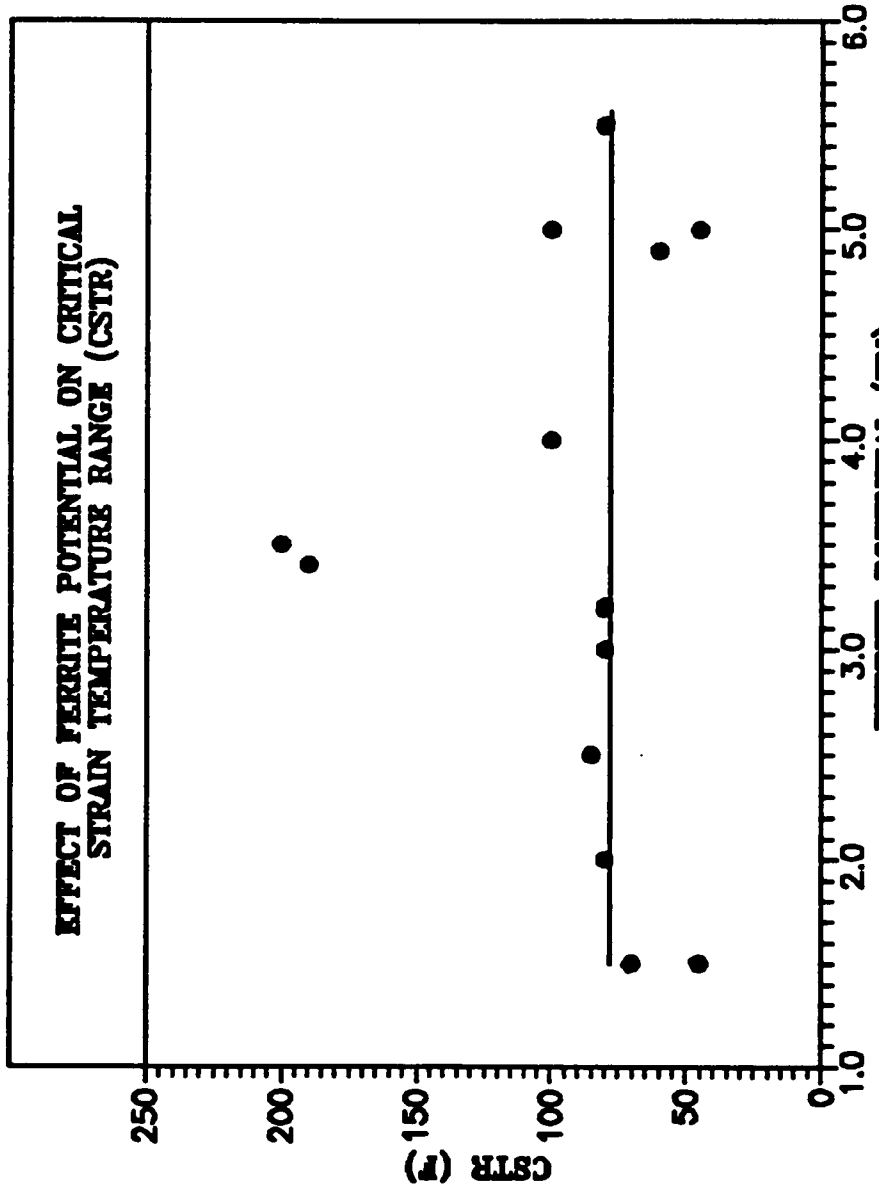


Figure 37. Relationship between CSTR and ferrite potential.

In the case of 316NG, the CSTR and DRR appear to be influenced by the P + S content, such that as P + S increases for a given ferrite potential, the CSTR increases and DRR decreases. For example, for a given ferrite potential (2-3 FN) of 316NG-A, B and C, as the P + S increases from 0.022% to 0.043% and 0.045%, the CSTR also increases from 60 F^{o} to 80 F^{o} and 100 F^{o}, respectively. The DRR also decreases from 100% to 43% with increase in the P + S from 0.022% to 0.045%. Further, for a given P + S (0.022%) for 316NG-C and D, the fully austenitic 316NG-D has a wider CSTR (80 vs. 60 F^{o}) and a lower DRR (62 vs. 100%).

For 347NG, the influence of impurity level (P + S) is not as clear as in the case of 316NG, but the ductility of 347NG appears to be influenced by the Nb, C and N contents. The correlations between CSTR and DRR and the ratio of niobium to carbon + nitrogen are given in Figures 38 and 39. In each figure, the CSTR and DRR is correlated with the ratio 1/2Nb / (30 x %C + 50 x %N). The significance of the 1/2Nb /(30 x %C + 50 x %N) ratio in type 347 was shown by Cullen and Freeman (53) who found that the grain boundary liquation temperature of 347 during exposure at high temperature was a function of 1/2Nb / (30C + 50N), such that when the ratio increased from 0.04 to about 0.2, the grain boundary liquation temperature due to Nb(C,N) - austenite eutectic reaction decreased significantly from 2470 ^{o}F to 2400 ^{o}F. However, when the ratio was above 0.2, no further decrease in the liquation temperature of the eutectic constituents along the grain boundaries was found (see Figure 11 (page 54)). The factors of 0.5 for Nb and 30 for C were taken from the Schaffler diagram and the

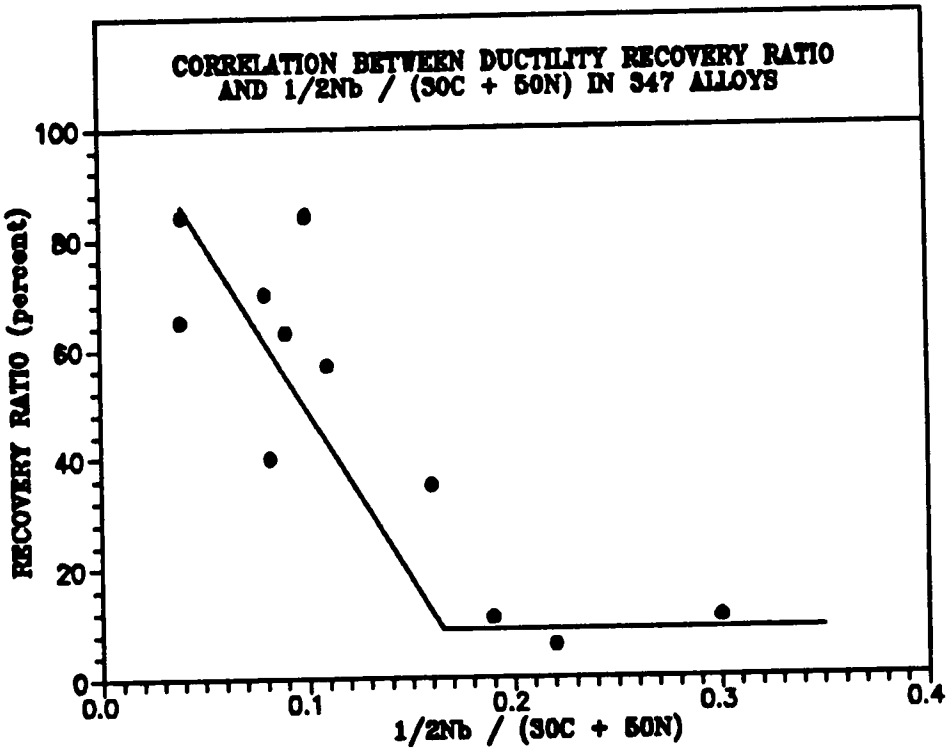


Figure 38. Correlation between DRR and 1/2 %Nb / (30 X %C + 50 X %N).

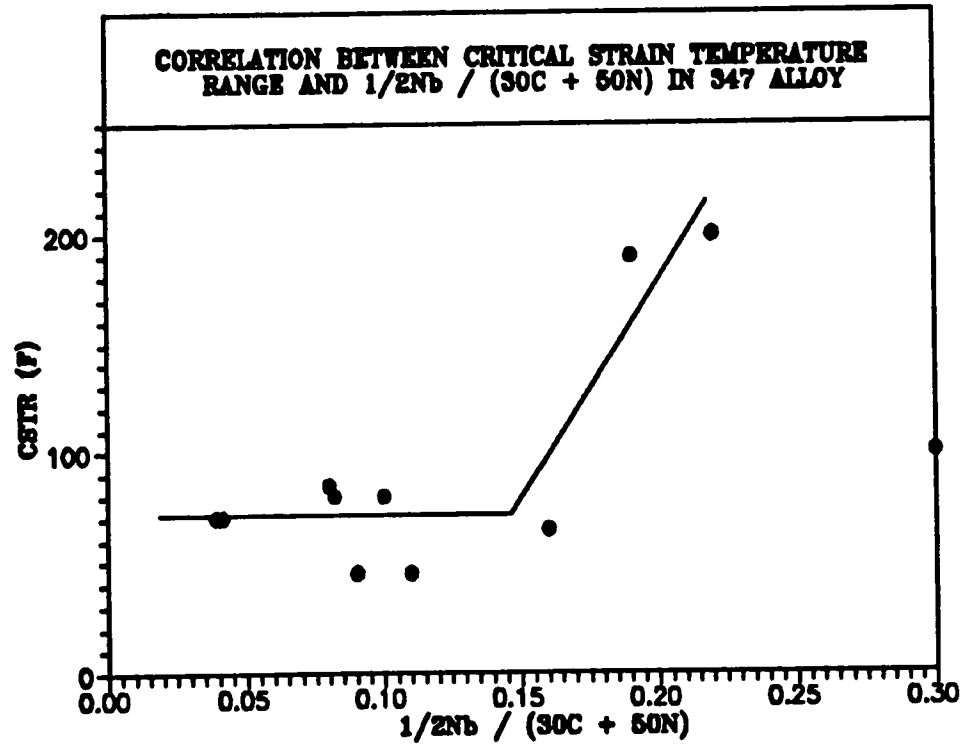


Figure 39. Correlation between CSTR and 1/2 %Nb / (30 X %C + 50 X %N).

factor of 50 for nitrogen was given by the fact that for given Nb and C contents, the N was approximately 60% more effective than C in raising the liquation temperature (53). As shown in Figure 38, as the value of 1/2Nb / (30C + 50N) increases the DRR gradually decreases. Figure 38 further indicates that when the ratio reaches about 0.15, the ductility recovery ratio no longer changes and levels off at approximately 10 $\pm$ 5%. The correlation between the CSTR and the ratio of 1/2Nb / (30C + 50N) (as shown in Figure 39) also depicts that like the case of the DRR, when the ratio is less than about 0.15, the CSTR is almost constant at 70 $\pm$ 10 ^{o}F. However, as the ratio increases beyond 0.15, the CSTR increases significantly. These correlations indicate that the hot ductility of 347, as may be expected, is influenced significantly by the niobium content and thus by the ratio of 1/2Nb / (30C + 50N). Further, when the chemistry of 347 is controlled so that the ratio of 1/2Nb / (30C + 50N) is less than approximately 0.15 with a low impurity level (P + S), the hot ductility response of 347 alloy may be improved significantly. The validity of the 1/2 / (30C + 50N) will be further discussed along with the Varestraint hot cracking results in a later section as to optimized the value and thus the optimized Nb content requirement for 347.

Figure 39 also shows that at a value 0.3 for the 1/2Nb / (30C + 50N) ratio, the CSTR is small. The reason, why the CSTR is small at this high ratio of Nb to C + N (347NG-A), is not clear. However, an influence of other residual elements and/or the grain size may also be involved (347NG-A has the finest grain size among all the program

materials). For a given concentration of residual elements and niobium level, the fine grain material has more grain boundary area and thus has a reduced concentration of the Nb rich phases along the grain boundaries, possibly resulting in a less continuous liquid network at high temperature and thus a smaller CSTR.

Summary. The above analyses reveal that the concepts of CSTR and DRR are more quantitative and appear to give a better discrimination on the heat-to-heat and alloy-to-alloy basis than the conventional criteria for hot cracking assessment. Further, these parameters are definitive and have a good correlation with the chemical composition (Nb, C and N), impurity level (P + S) and other metallurgical variables (ferrite potential and grain size). Thus, these newly developed criteria are sensitive to the metallurgical changes which may affect the cracking assessment.

In general, 316NG has a better hot ductility response than 347NG and is almost equivalent to that of 304 in terms of CSTR and DRR. However, when 1/2Nb / (30 x %C + 50 x %N) in 347 is less than approximately 0.15, the hot ductility response of 347NG is virtually equivalent to 316NG and 304. When the ratio is greater than 0.15, hot ductility of 347NG approaches that of AISI 347 in terms of CSTR and DRR.

The hot ductility of 316NG and 347NG is not a function of ferrite potential within the limited range studied in this investigation. However, for a given impurity level, a higher ferrite potential material generally has a better hot ductility response.

As mentioned earlier, the development of the acceptance criteria for the Gleeble hot ductility test will be further discussed after consideration of the evaluation of the HAZ cracking susceptibility of the same alloys by the Varestraint test. This is considered the only way in which the data necessary to provide reliable correlations between hot ductility test results and the behavior of material during welding can be obtained.

c. Metallurgical Behavior During Hot Ductility Testing

The previous section indicated that when using appropriate criteria, the hot ductility test not only provides the determination of the relative crack susceptibility of different alloys, but also can permit differentiation of "good" and "bad" heats of the same nominal composition. Therefore, it is necessary to investigate the metallurgical changes that occur during hot ductility testing which are directly related to the hot ductility test results, and which are also important to the proper interpretation of the results.

To correlate the hot ductility test results with the microstructural characteristics, metallographic and fractographic examinations were conducted principally on 347NG-E and 316NG-7, because 347NG-E has the poorest hot ductility response among the 347NG materials and 316NG-7 was the only heat out of more than 20 heats of nuclear grade material exhibiting a significant ductility dip behavior on cooling after exposure to the ZDT. However, whenever needed, metallography on other heats of material was also conducted and included in the following discussion.

On-Heating Behavior. A typical base metal microstructure for the as-received condition, from the 347NG-E, is given in Figure 40. The grains are more or less equiaxed and have an average diameter of 50 um with some grains as small as 30 um in diameter. Some residual ferrite, in bands elongated parallel to the sample (rolling) direction can also be noted. Furthermore, discrete niobium rich particles, aligned parallel to the rolling direction, also exist.

The typical optical microstructure just adjacent to the fracture surface and the fractography of the sample tested at 2100 ^{o}F on-heating are shown in Figure 41. All samples tested in the temperature range of approximately 1900 ^{o}F - 2300 ^{o}F have similar features. The fractograph indicates that at this temperature fracture occurred in a transgranular ductile mode. The fracture surface reveals dimples typical of ductile fracture. The microstructure shows equiaxed grains (about 10 um in diameter) which are much smaller compared to the as-received base metal, thus revealing evidence of a dynamic recrystallization which occurred during fracture (straining). Evidence for recrystallization can further be noted from morphology of the annealing twins straight in the fine equiaxed grains.

It is well known that the ductility (and strength) of a material during hot deformation is governed by the balance between work hardening and dynamic softening. If work hardening predominates, strength is high but ductility is low. When a softening process predominates, strength is low but ductility is high. Further, it is also known that austenitic stainless steel, which is a low stacking fault material, more likely undergoes dynamic recrystallization

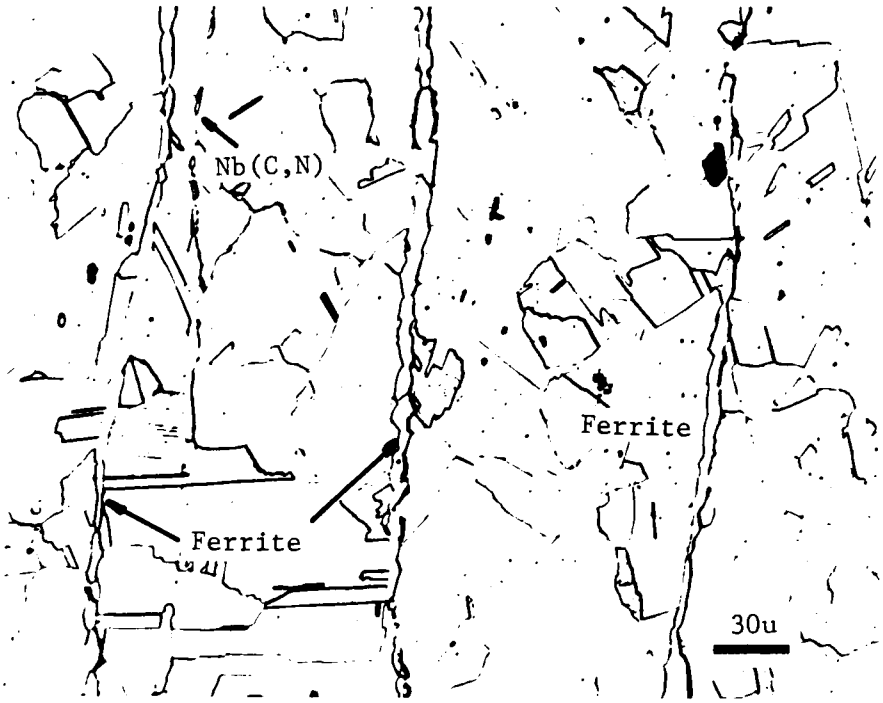


Figure 40. Base metal microstructure of 347NG-E in the as-received condition.

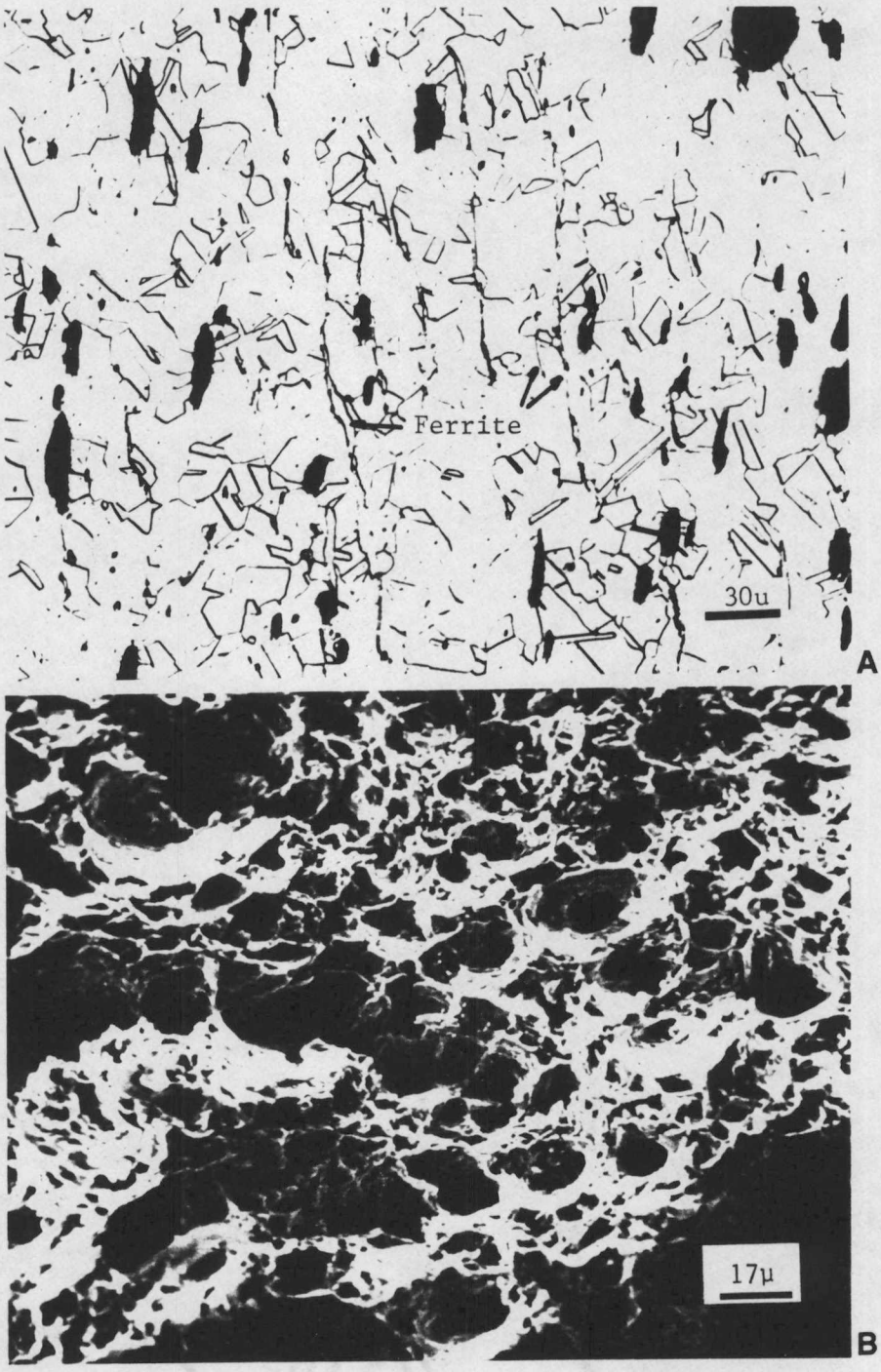


Figure 41. Typical optical microstructure just adjacent to the fracture surface and SEM fractograph of the sample tested on-heating at 2100 °F, 347NG-E.

instead of dynamic recovery as a softening process during hot deformation (174-175).

Therefore, in the case of the samples tested on-heating in the temperature range of 1900 - 2300 ^{o}F, the initially deformed grains are replaced by recrystallized equiaxed grains which nucleate at the original grain boundaries and recrystallization proceeds progressively with strain, resulting in a high ductility (more than 90%). Figure 41 further shows a significant number of cavity-like cracks formed parallel to the straining direction. These cracks have no obvious relationship to grain boundaries. These cracks may have formed on the initial grain boundaries in the early stage of the deformation (straining). However, with continued deformation at high temperature and with a high strain rate (2.5 in/sec in this case), any initially formed crack was immediately arrested and isolated from the original grain boundaries by the rapid recrystallization and the migration of newly formed grain boundaries. The isolation of initial cracks by dynamic recrystallization was also found in an Fe-Ni alloy (tested at high strain rate in a high temperature torsion test) by White et al. (176), who observed that crack formation and growth were dependent upon the rate of recrystallization and grain boundary migration.

The rate of dynamic recrystallization depends, at any given moment, on the extent of deformation and the temperature for a given material. At higher temperatures, recrystallization is extremely rapid and thus, the resultant grain size is larger than for a lower temperature as shown in Figure 42 (sample tested at 2300 ^{o}F at which the on-heating ductility begins to decrease). The equiaxed grain size

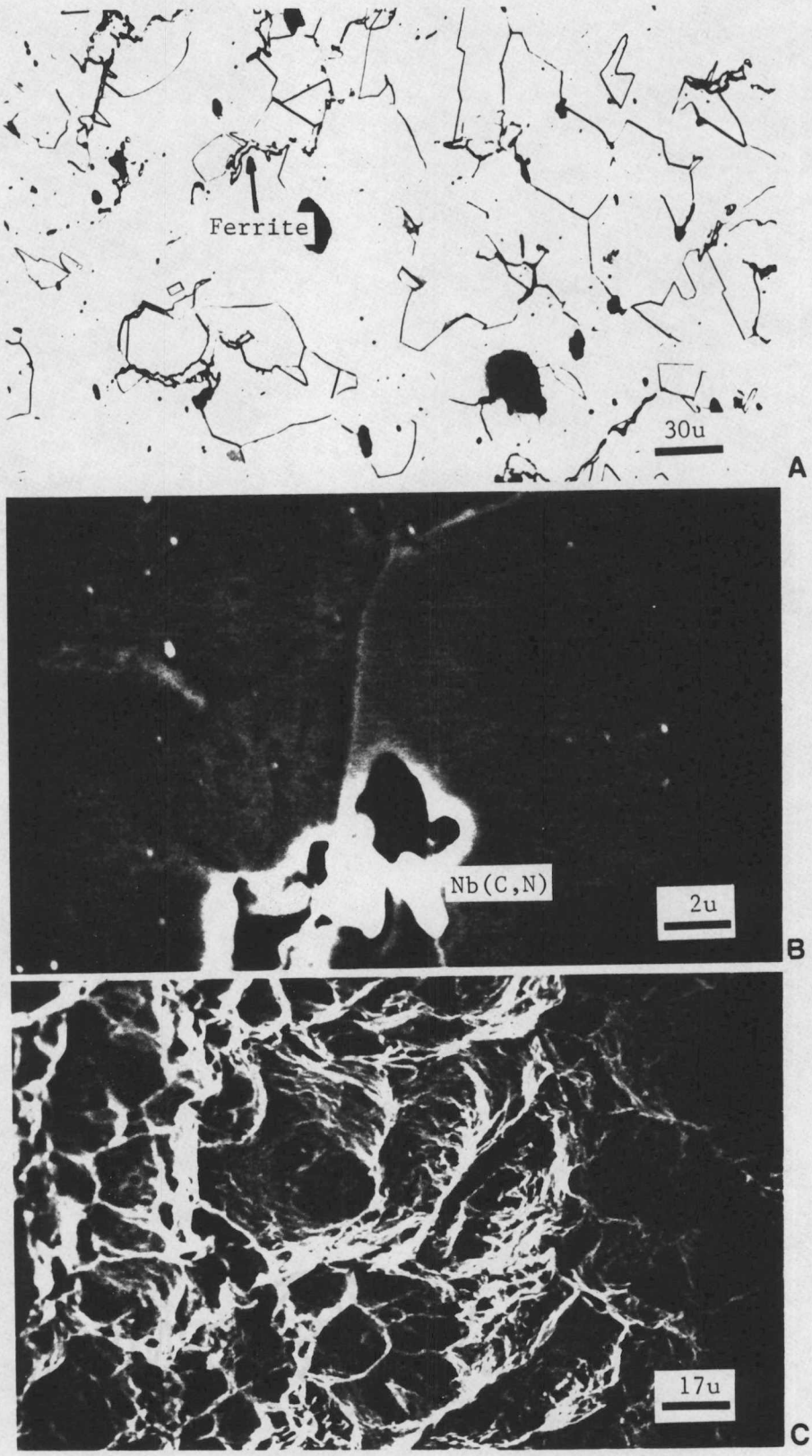


Figure 42. Typical optical and SEM microstructures and fractograph of the sample tested on-heating at 2300 °F, 347NG-E.

at this temperature is greater than that at 2100 ^{o}F and is almost the same as that in the as-received base metal. Therefore, at this temperature, the initially formed intergranular cracks must have been more rapidly blunted and isolated from the original grain boundaries, resulting in a more rounded crack tip and a smaller number of cavity-like cracks than at the lower temperature (see Figure 41). At 2300 ^{o}F, the original ferrite bands are broken and no longer continuous. Fractography reveals that although cracks were formed initially along original grain boundaries, fracture occurred in a transgranular mode relative to the new grains and is of a ductile type (microvoid coalescence mechanism).

Figure 42 further depicts that large niobium carbo-nitrides along the grain boundaries begin to react with austenite grain (constitutional liquation). However, the smaller carbo-nitrides in the grain matrix are intact with austenite. There is no evidence of incipient melting at the grain boundaries. Therefore, since the ductility at this temperature is greater than 90% (almost the same as that in the lower temperatures), the small amount of localized liquid formed by the constitutional liquation of Nb(C,N) does not appear to be significant.

The typical microstructure and fractography of the sample tested on-heating at 2350 ^{o}F, which has a 45% reduction in area and is approximately at the mid point of the first stage of the ductility drop region, is given in Figure 43. The grain size at this temperature is slightly larger and the ferrite bands are less continuous in comparison to that observed at 2300 ^{o}F. Significant

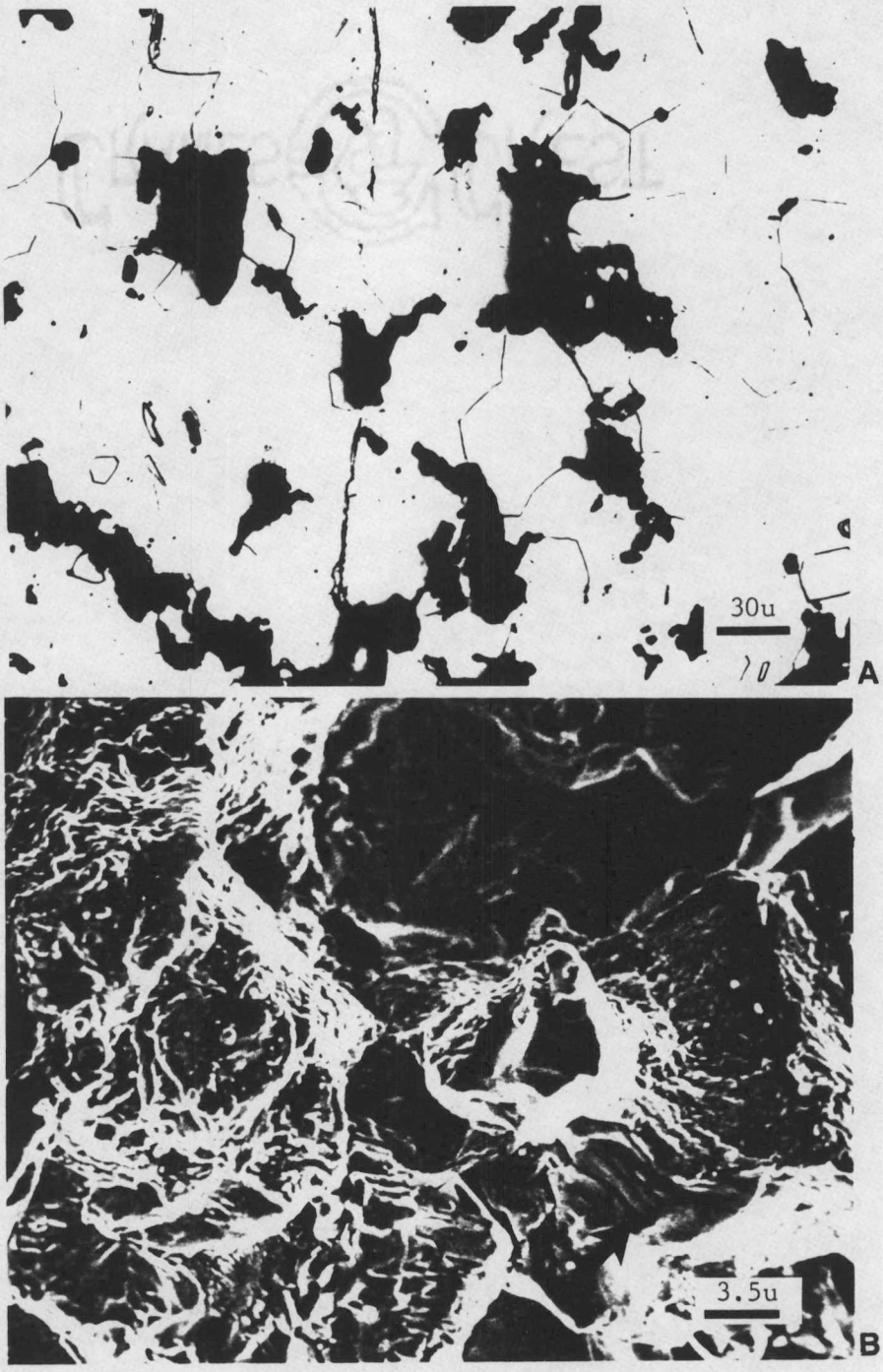


Figure 43. Typical optical microstructure and SEM fractograph of the sample tested on-heating at 2350 ^{o}F, 347NG-E.

cracking has formed and the cracks do not appear to have a clear relationship to the grain boundaries. However, the cracks appear to propagate in both parallel and perpendicular directions relative to the strain direction. The cracks which propagate perpendicular to the strain direction are generally related to the grain boundaries. Therefore, when straining a sample on-heating at this temperature, cracks formed at triple points and/or irregularities in the grain boundaries. Rapid recrystallization and migration at this high temperature immediately isolated these cracks from further growth. However, with continuous deformation, new cracks may have formed at the boundaries of the recrystallized grains and these, together with the portion of the initial cracks, may have grown by dragging moving boundaries to lengthen the cracks before the boundaries once again broke away from the crack surface "obstacles". Therefore, the crack paths are irregular in shape and show a mixture of transgranular and intergranular modes. The evidence of intergranular fracture is more clear on the fracture surface as shown in Figure 43. Fractographic evidence reveals more or less granular features, but with significant extent of ductile dimples on the grain faces. Evidence of liquid film which existed at a moment of fracturing can also be noted on the fracture surface (see arrow), but this is not clearly discernable in the cross section optical microstructure. The microstructural features therefore indicate that the sudden drop in the on-heating ductility may be attributable to fracture mode change from transgranular to intergranular, and is related to the formation of the liquid film along the grain boundaries.

Figure 44 shows microstructures for a sample tested at 2400 ^{o}F (the end of the first stage and start of the second stage of the ductility decrease range). At this temperature, the on-heating ductility is less than 10% and fracture occurred in a completely intergranular mode. The fracture surface is smooth, revealing the existence of the liquid film at the moment of straining. The optical and SEM microstructures also show evidence for liquid film formation along the grain boundaries, with cracks initiated in and propagated along these liquated and widened boundaries. Intergranular secondary cracks parallel to the fracture surface (perpendicular to the strain direction) can be clearly noted.

At this temperature, a Nb(C,N)-austenite eutectic liquid formed by constitutional liquation reaction starts to penetrate the grain boundaries. However, no dissolution or reaction between the Nb(C,N) particles in the grain matrix is evident. Figure 44 further reveals that the grain size is almost the same as that heated to 2350 ^{o}F but the ferrite content is significantly increased. It is not clear whether the grains are newly recrystallized grains or initial grains. As indicated earlier, when new grains form and replace the original grains the ferrite bands were broken and not continuous. Further, the cracks were not related to the grain boundaries. However, as shown in Figure 44, all cracks are clearly associated with the grain boundaries which are incipiently melted. Therefore, the grains at this temperature may be not the newly recrystallized grains but the initial grains. Further grain growth above 2300 ^{o}F may be restricted due to the obstacles including an increased ferrite content and liquid

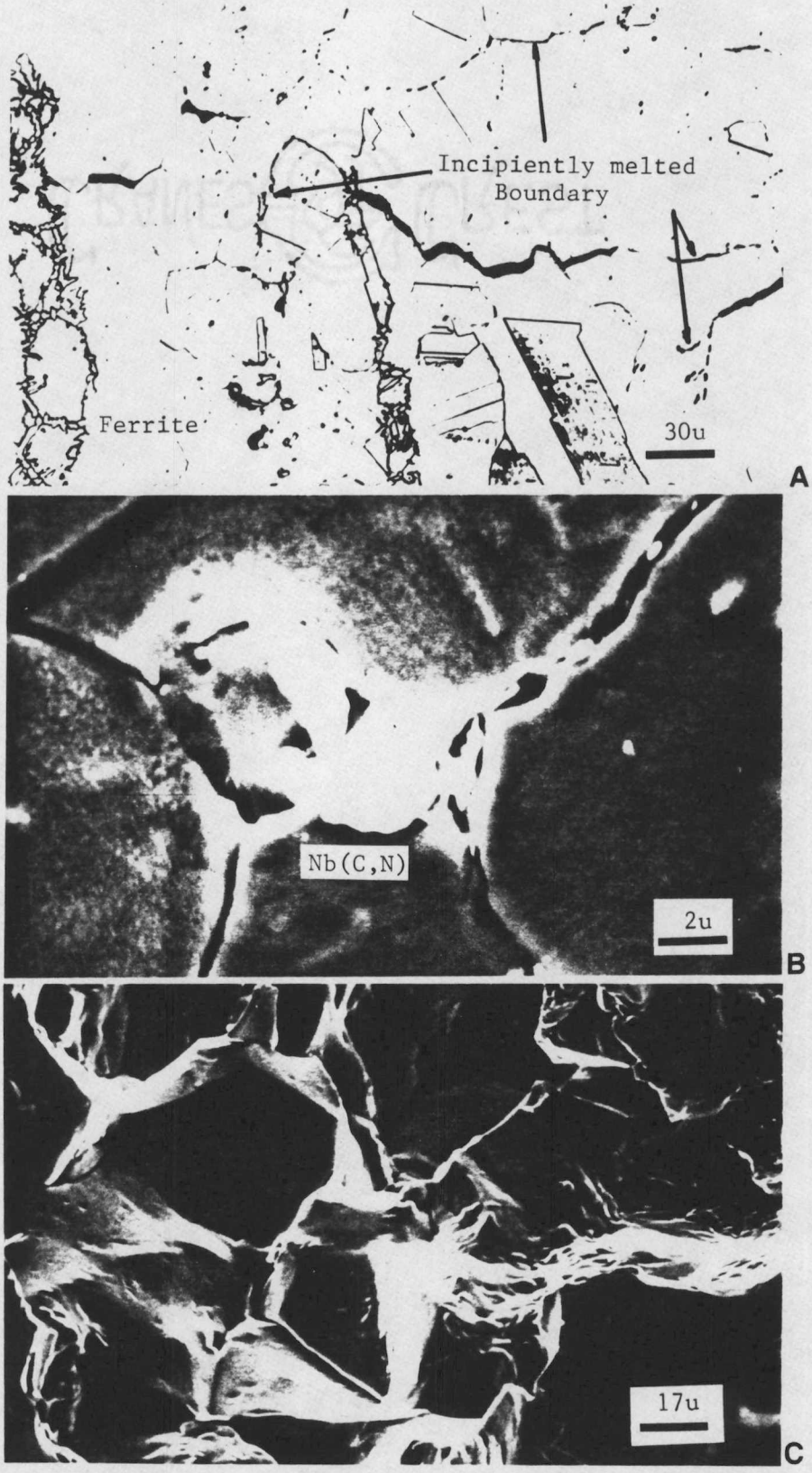


Figure 44. Typical optical and SEM microstructures and Fractograph of the sample tested on-heating at 2400 ^{o}F, 347NG-E.

drops/film formed by incipient melting and constitutional liquation of large Nb(C,N) at the grain boundaries.

It is also a well known fact that dynamic recrystallization in the low stacking fault energy materials occurs only when the strain (stress) is greater than a critical value (which is a function of temperature such that with an increase in test temperature, the critical strain (stress) for recrystallization is reduced (176-179)). Therefore, at 2400 ^{o}F, the critical strain and stress for the initiation of recrystallization may be higher than the fracture strain (stress) for 347NG-E. The significantly low fracture strain and stress are due to, as shown in Figure 44, the incipient melting of the segregated boundaries and beginning of Nb(C,N)-austenite eutectic liquid penetration along the grain boundaries.

The microstructures just adjacent to the fracture surface tested on-heating at 2430 ^{o}F in Figure 45 shows features almost identical to that at 2400 ^{o}F, except for more extensive incipient melting of the segregated boundaries and initiation of constitution liquation at the small Nb(C,N) with in the grains.

When the temperature approaches the ZDT, the grain boundaries becomes almost completely wetted as shown in Figure 46. Further, the extent of the Nb(C,N)-austenite eutectic increases and continuously penetrates along the grain boundaries. Fractography also reveals that the grain surface is almost completely wetted by a liquid at the moment of straining, resulting in zero ductility and nil strength. The above microstructural features at temperature of 2400 ^{o}F to the ZDT indicate that the second stage of the ductility decrease region is

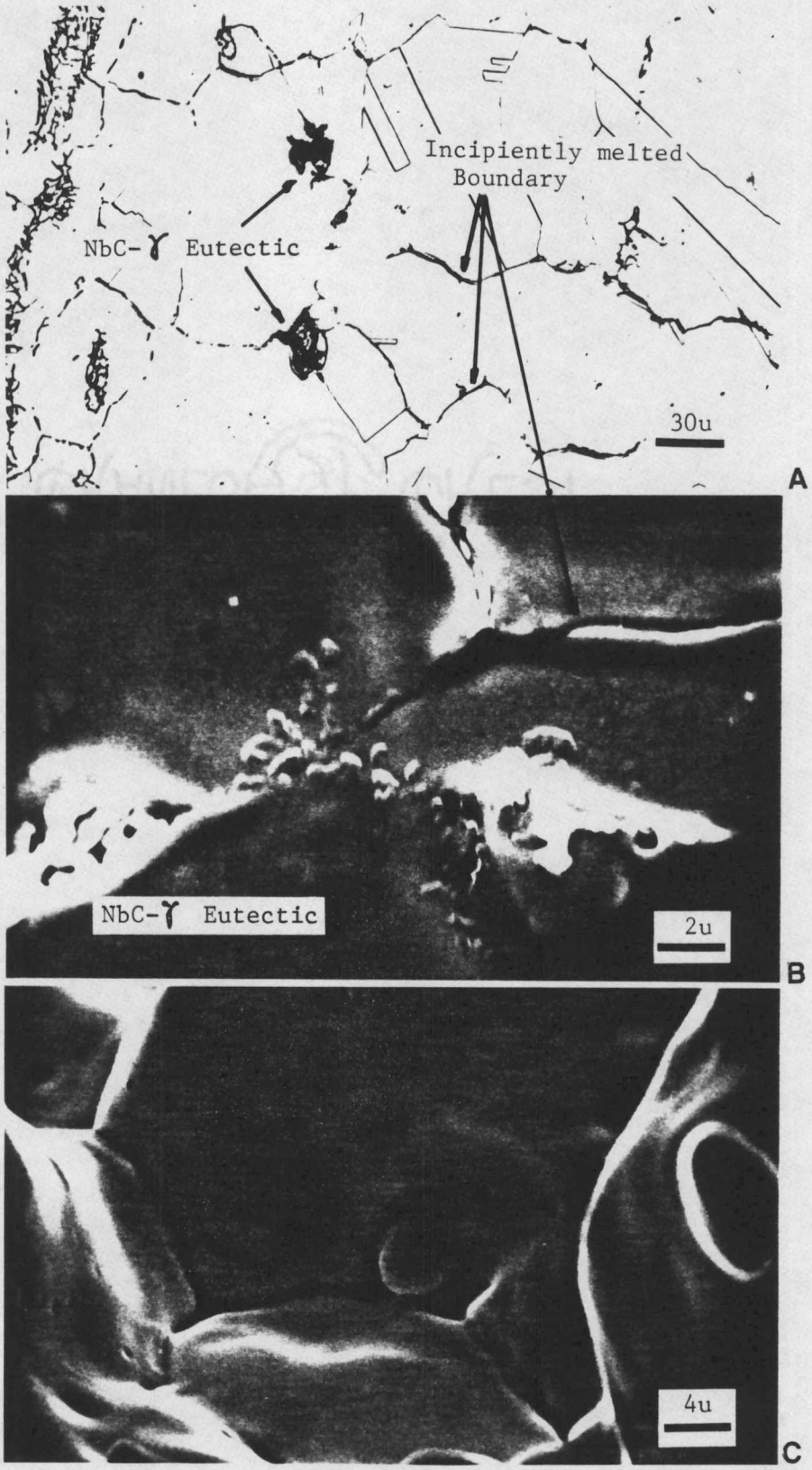


Figure 45. Typical optical and SEM microstructures and Fractograph of the sample tested on-heating at 2430 °F, 347NG-E.



Figure 46. Typical optical and SEM microstructures and Fractograph of the sample tested on-heating at ZDT of 2480 °F, 347NG-E.

controlled mainly by the extent of liquid formed and its continuity along boundaries.

Typical incipiently melted grain boundaries and EDAX analysis of a widened boundary are shown in Figure 47. Some small discrete particles along the melted and resolidified boundaries can be seen. EDAX analysis shows that the incipiently melted boundary is rich in silicon, niobium and sulfur. STEM analysis of the particles along the boundaries (Figure 48) reveals that these particles are Nb(C,N).

The above examination of the on-heating microstructures indicate that the on-heating hot ductility behavior is directly related to the metallurgical changes during the high temperature-strain excursion. The on-heating behavior can be divided into two regions, a) ductility increase region and b) ductility decrease region. The ductility decreasing region is further divided into 1) a first stage of rapid drop in ductility and 2)a second stage of slowly decreasing ductility.

The ductility increase region is mainly a result of dynamic recrystallization which occurs rapidly to reduce strain hardening and thus large strains can be accommodated by the repeatedly recrystallized material maintaining an equiaxed structure. Thus, although the cracks may form along the grain boundaries at early stages of deformation, rapid recrystallization and migration can blunt crack propagation and result in high ductility and a transgranular ductile fracture.

The first stage of the ductility drop region is governed by the fracture mode and localized liquid film formation. That is, the sudden drop in ductility is attributed to a fracture mode change from

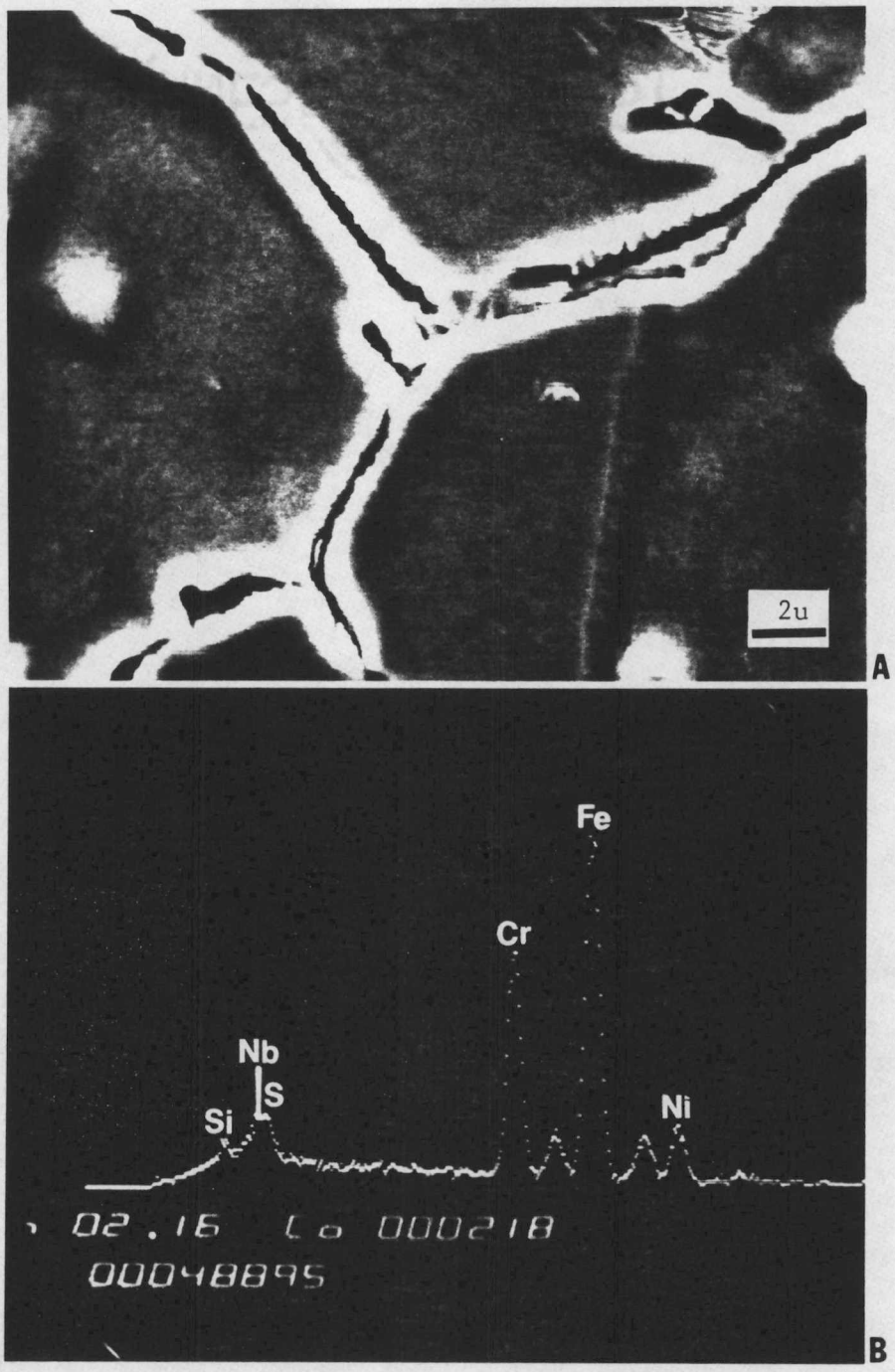


Figure 47. Incipiently melted grain boundary and EDAX on the widened boundary.

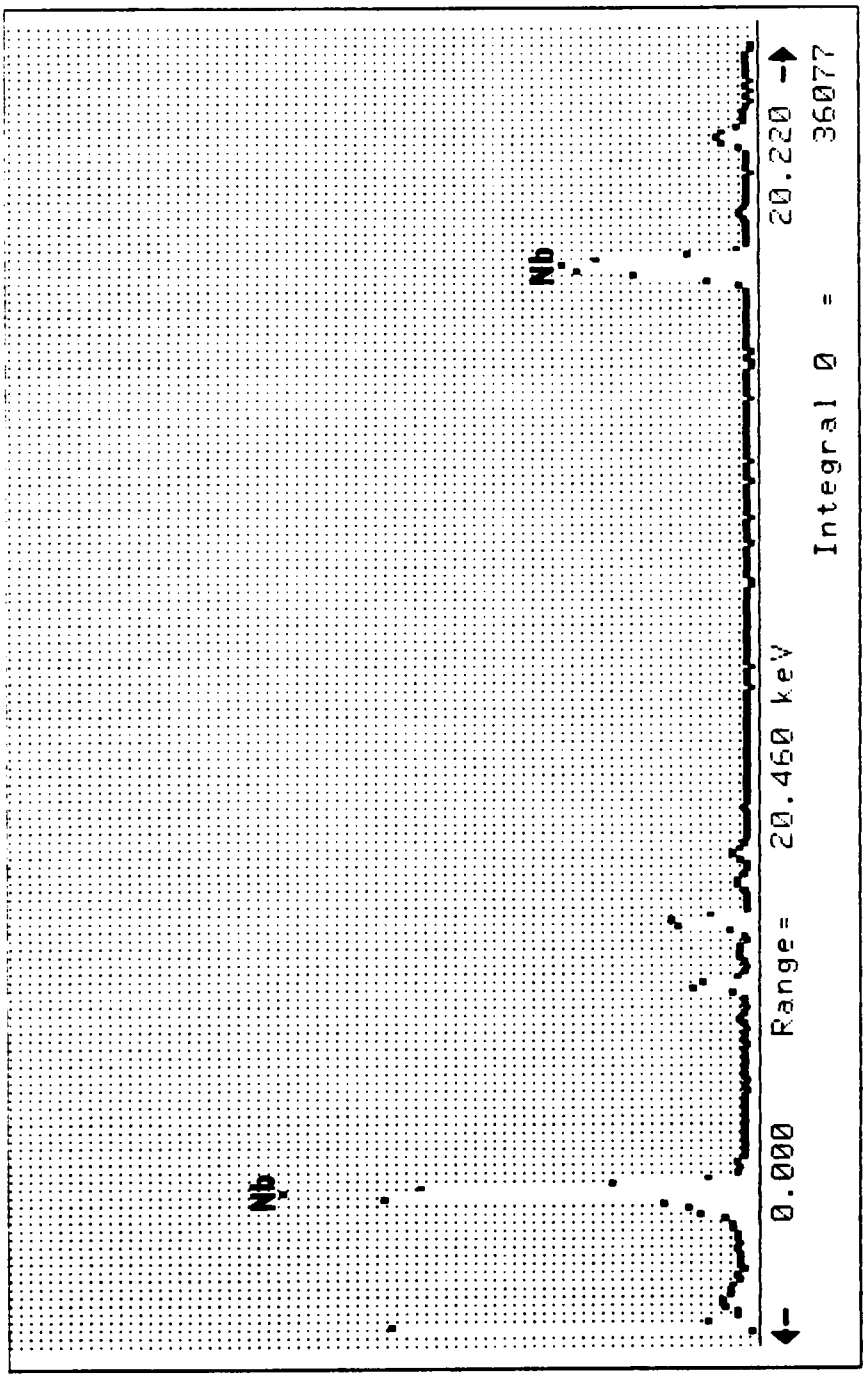


Figure 48. STEM analysis of white particles in Figure 47. (Carbon extraction replica).

transgranular to intergranular and is accelerated by the formation of localized liquid films along grain boundaries.

At the second stage of the ductility drop region, dynamic recrystallization does not appear to operate because of fracture strain lower than the critical strain for the initiation of recrystallization. Ductility at this stage is a function of the extent of the liquid formed by incipient melting at Nb, Si and S segregated boundaries and constitutional liquation of Nb(C,N) within the austenite matrix, and the continuity of liquid along the grain boundaries.

On-Cooling Behavior. Figure 49 shows the typical microstructures near the fracture surface and the fractography for sample tested on-cooling at 2300 ^{o}F. It is clearly evident that the microstructures are similar to those in the second stage of the on-heating ductility drop range. The basic difference is that the eutectic structure is more extensive than for on-heating, indicating the time spent near the ZDT controls the extent of liquid formation. The ferrite extent also increased. A careful examination reveals that most of the melted grain boundaries have started to resolidify. However, the boundaries penetrated by the Nb(C,N) eutectic liquid appear to be in a wetted condition at the moment of fracture. When the temperature decreases below 2300 ^{o}F, all of the boundaries which were incipiently melted or wetted by the eutectic liquid were completely resolidified before fracture.

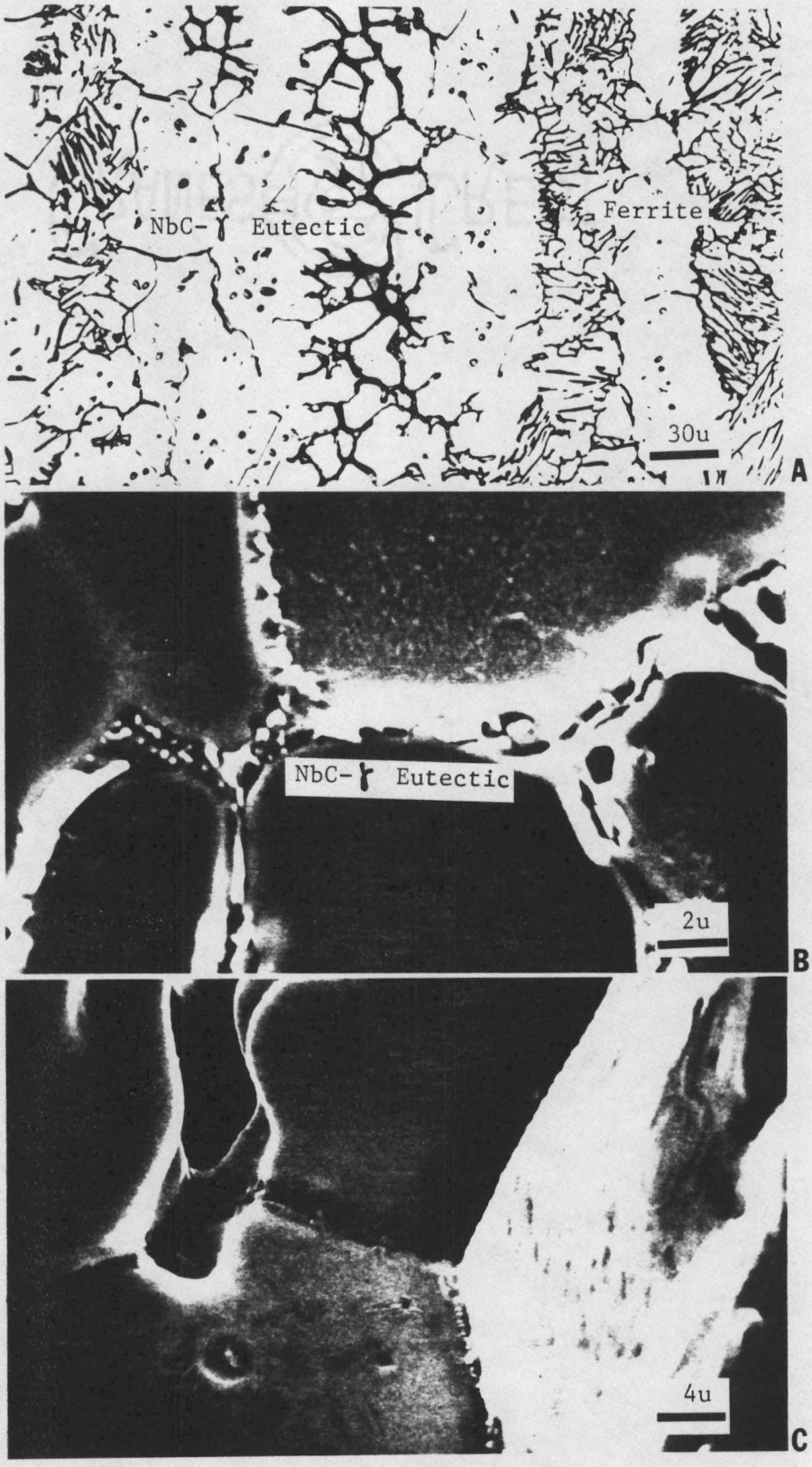


Figure 49. Typical optical and SEM microstructures near the fracture surface and fractograph, tested on-cooling at range from the ZDT to 2300 °F, 347NG-E.

With a further decrease in temperature (e.g., at 2100 ^{o}F), the microstructure has features almost identical to those developed on-heating at the same temperature as shown in Figure 50. The grains are completely recrystallized and are equiaxed. The initially formed cracks were apparently prevented from growing by rapid recrystallization and grain boundary migration. However, the important feature noted in these microstructures is the cavity like cracks formed at the prior melted and resolidified grain boundaries. These previously melted and resolidified grain boundaries are continuously decorated by Nb(C,N) particles as shown in the SEM micrograph in Figure 50. When compared to the microstructure of the samples tested on-heating at the same temperature (2100 ^{o}F), in which the initial boundaries had disappeared by recrystallization, the on-cooling microstructure clearly reveals both new boundaries and original boundaries. The prior melted and resolidified boundaries appear as "ghost boundaries" as shown in Figure 50. This feature further indicates that the prior melted and resolidified boundaries are enriched in solute elements as compared to the newly formed boundaries. It was shown previously that the melted boundaries were rich in Si, Nb and S. Therefore, the microstructural features strongly indicate that the prior melted and resolidified boundaries are significantly embrittled by the segregation of impurity elements and by precipitation of semi-continuous Nb(C,N) particles which are favored sites for crack initiation and subsequent propagation along boundary.

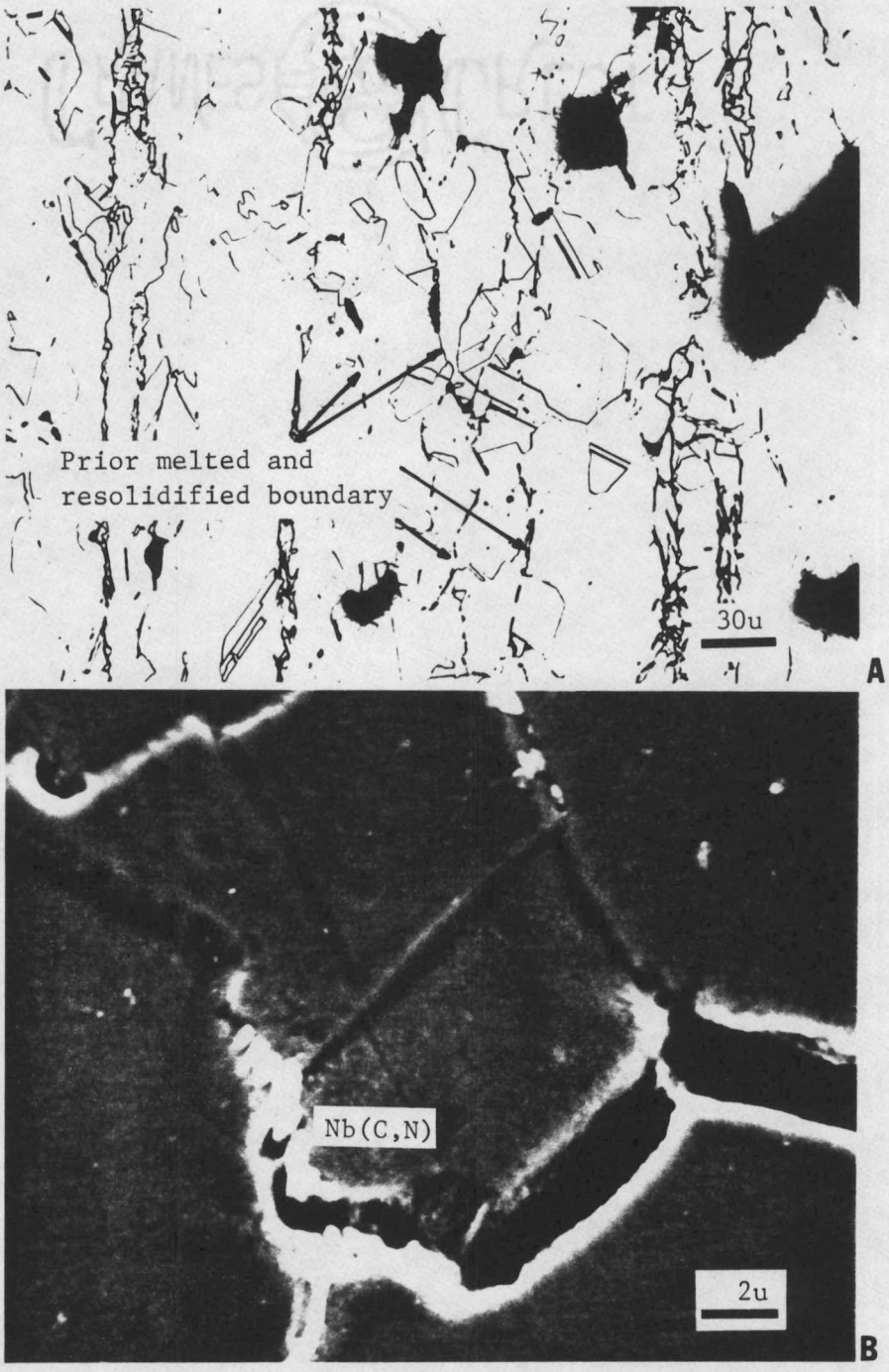


Figure 50. Typical optical and SEM microstructures, tested on-cooling at 2100 ^{o}F, 347NG-E.

Embrittlement of previously melted and resolidified boundaries is more evident in Figure 51. These features are from a sample tested on-cooling at 1900 ^{o}F. As shown in Figure 51, the prior boundaries are clearly defined at this temperature because recrystallization has just begun along the boundaries and is not completed at fracture. Small grains, recrystallized but not grown, are more clearly noted in the SEM micrograph. Because of incomplete recrystallization, the propagation of initially formed crack was not as completely blocked as was shown for 2100 ^{o}F, resulting in a longer cracks. Another different feature as compared to the on-heating fractographic appearance is that the fracture morphology is intergranular, even though a significant amount of ductile dimples exist on the grain faces.

At a fracture temperature of 1700 ^{o}F, no evidence of recrystallization can be found, as shown in Figure 52. The grains have grown significantly during exposure to the ZDT followed by cooling to low temperature (approximately 100-150 um in diameter). Fracture is still intergranular and along the prior melted and resolidified boundaries. Since the initially formed cracks were not "captured" by the newly formed grains, they are long and straight, resulting in a slightly decreased ductility. Further, at this temperature, the elongated grains indicate that the strength of grain boundaries is approaching that of grain interior. Thus, equicohesive temperature, above which the grain boundary strength is lower than that of the grain body, is close to 1700 ^{o}F. The dynamic recrystallization temperature of the 347NG-E is also between 1700 and

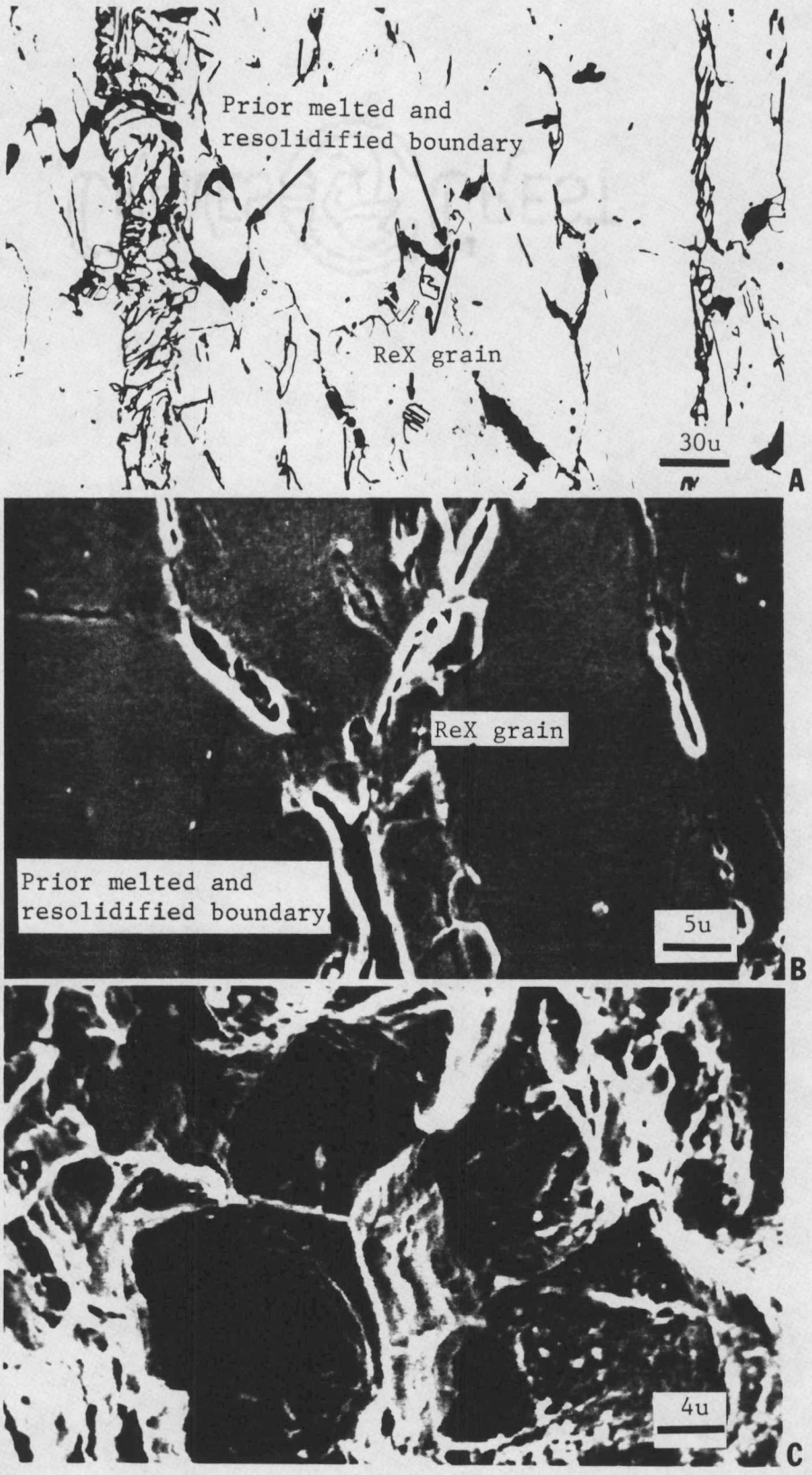


Figure 51. Typical optical and SEM microstructures near the fracture surface and fractograph, tested on-cooling at 1900 ^{o}F, 347NG-E.

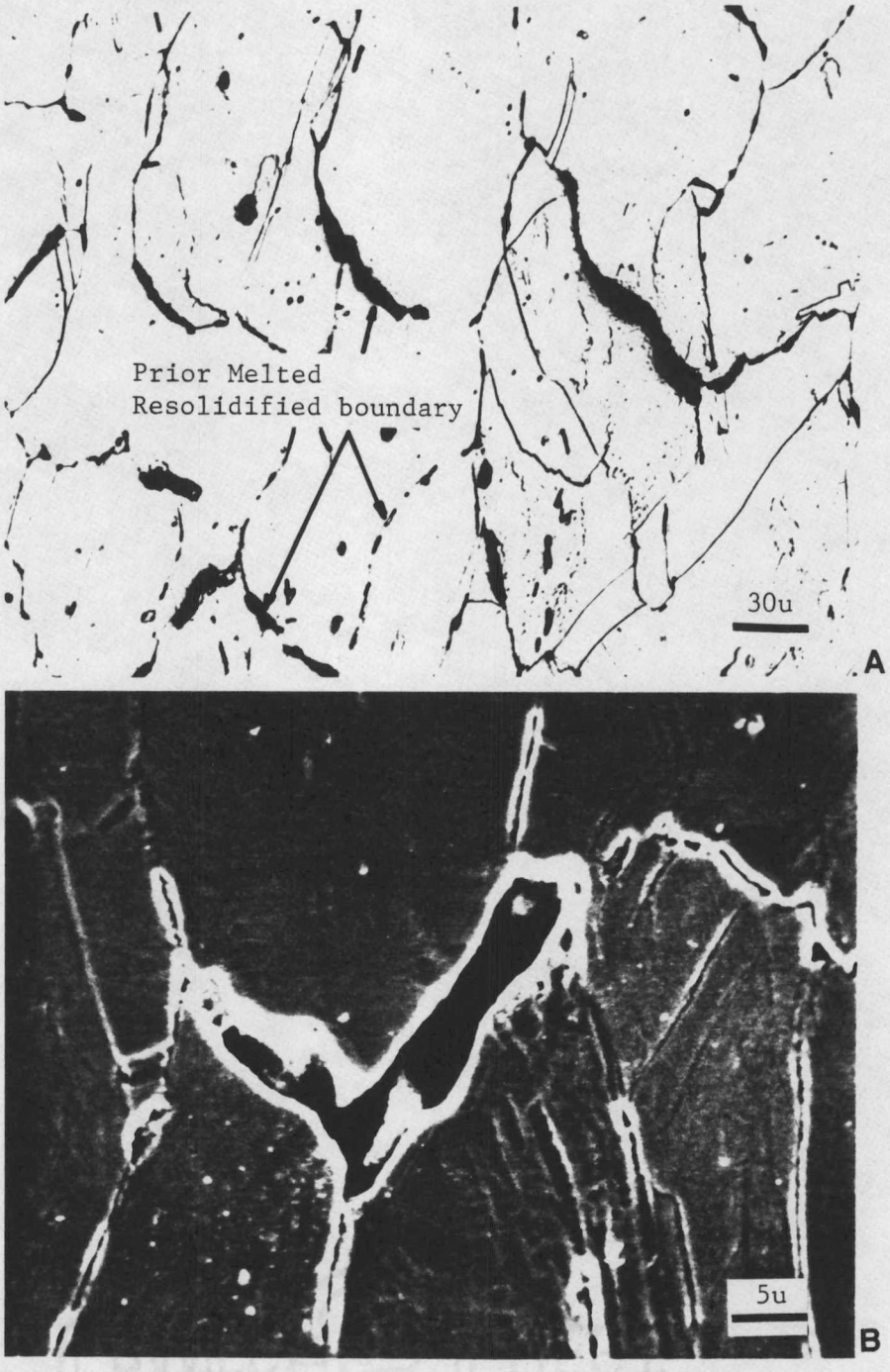


Figure 52. Typical optical and SEM microstructures near the fracture surface, tested on-cooling at 1700 ^{o}F, 347NG-E.

1900 ^{o}F, and thus the equicohesive temperature and the dynamic recrystallization temperature appear to be close. Therefore, the fact that when no recrystallization occurs the on-cooling ductility decreases as compared to the case for partial recrystallization, together with the above fact (equicohesive temp. _ recrystallization temp.), can be related to ductility dip phenomena.

In summary, the on-cooling microstructural and fractographic examination of 347NG-E strongly indicate that the on-cooling ductility is influenced not only by the deformation mechanism (balance between strain hardening and softening process of recrystallization) but also by the extent and distribution of the liquid formed at or near the ZDT and its rate of resolidification. Further, regardless of the test temperature between the ZDT and 1700 ^{o}F, fracture is intergranular and occurs along prior melted and resolidified boundaries which are rich in Si, Nb and S and decorated by the Nb(C,N)-austenite eutectic constituents. A summary of microstructural changes during on-heating and on-cooling for 347NG-E as related to the hot ductility curves is given in Figure 53.

Ductility Dip Phenomenon. Since Gleeble hot ductility testing was first conducted in the mid 1950's to determine material behavior during fabrication, many investigators (110, 111, 164) have observed a "ductility dip phenomenon" at a mid temperature range during on-cooling from the ZDT/ZST. However, the significance of the ductility dip behavior on the weldability (crack sensitivity) of material is not clear and contradictory. For example, Yeniscavich (110,111) has found that an alloy showing the greatest fissuring had a small mid

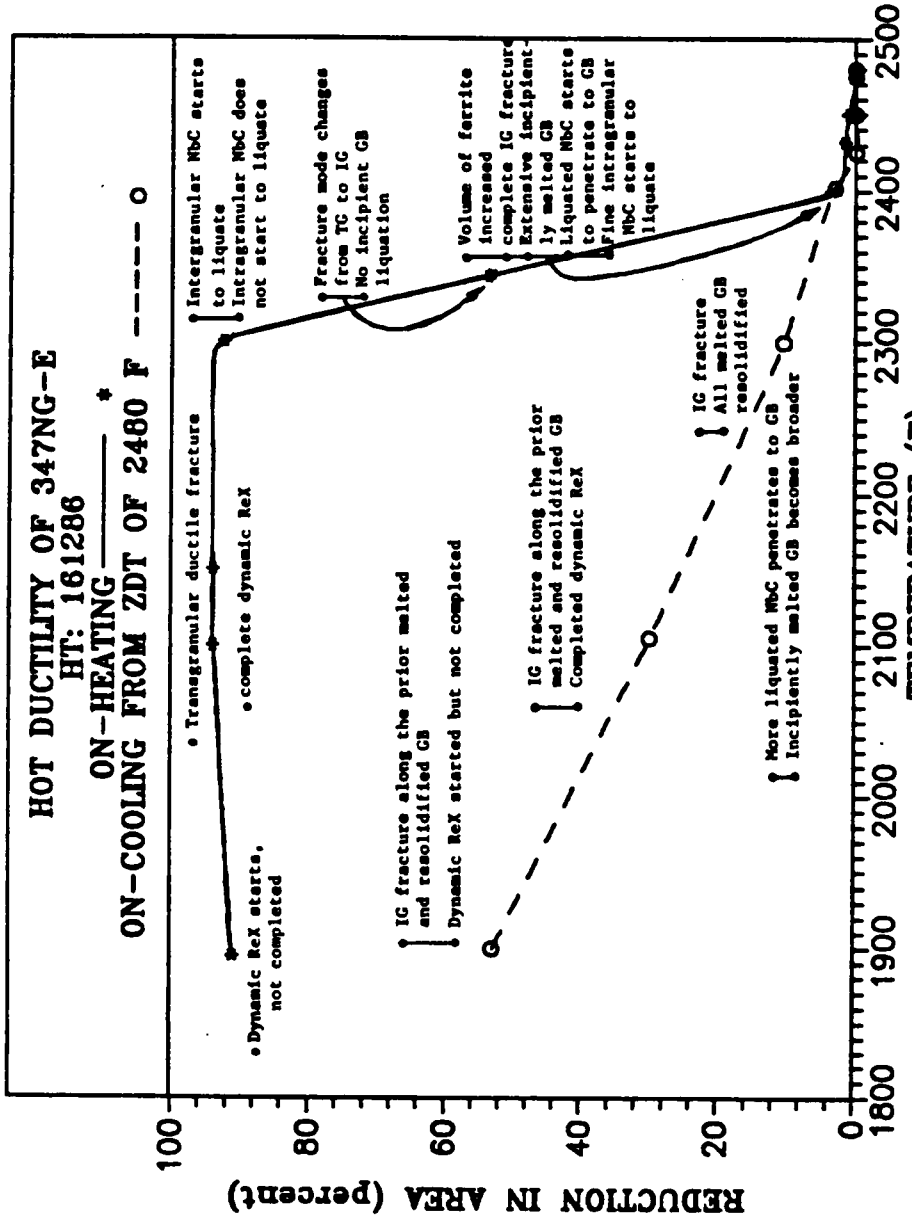


Figure 53. A summary of microstructure changes during on-heating and on-cooling in 347NG-E.

temperature ductility dip range, and he attributed this result to much higher stress for fracture in the mid temperature range. Further, Yeniscavich insisted that, in addition to the high temperature ZDR, the mid temperature ductility dip is an important criterion and may be a more important factor than the ZDR. On the other hand, Bruhl and Zschau (164) have also found the ductility dip phenomenon in 316NG and concluded that ductility dip is not significant with regard to hot cracking susceptibility as long as the material has sufficient strength.

Therefore, an hypothesis related to the ductility dip phenomenon is proposed in this section based on the microstructural changes discussed previously and in this section. For the microstructural evaluation of the ductility dip behavior 316NG-7 was chosen because this was the only heat out of more than 20 heats of nuclear grade 316 and 347 that exhibited a significant ductility dip at about 1800 ^{o}F during on-cooling from the ZDT. The evaluation was confined to the on-cooling microstructures, because the on-heating behavior is almost identical to 347NG-E and thus expected to show the similar microstructural features except for the constitutional liquation of Nb(C,N).

SEM fractographs and optical microstructural features of 316NG-7 tested at ZDT of 2475 ^{o}F are shown in Figures 54 and 55, respectively. Figure 54 shows an intergranular fracture surface typical of a specimen tested at the ZDT with grain facets showing a smooth structure indicating the existence of continuous liquid film along the grain boundaries at the moment of straining. EDAX analysis of the

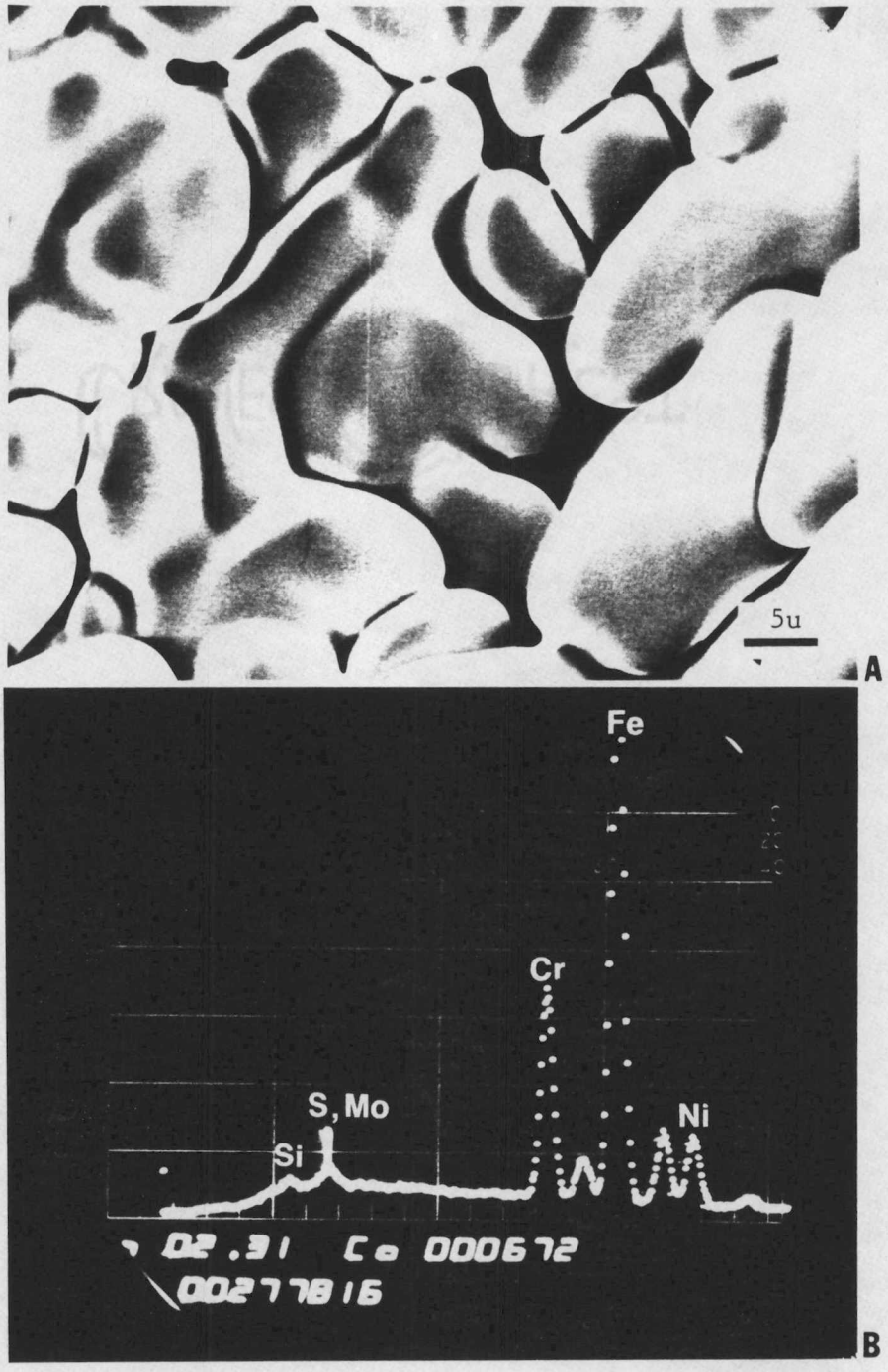


Figure 54. Typical SEM fractographs, tested at ZDT, 316NG-7.

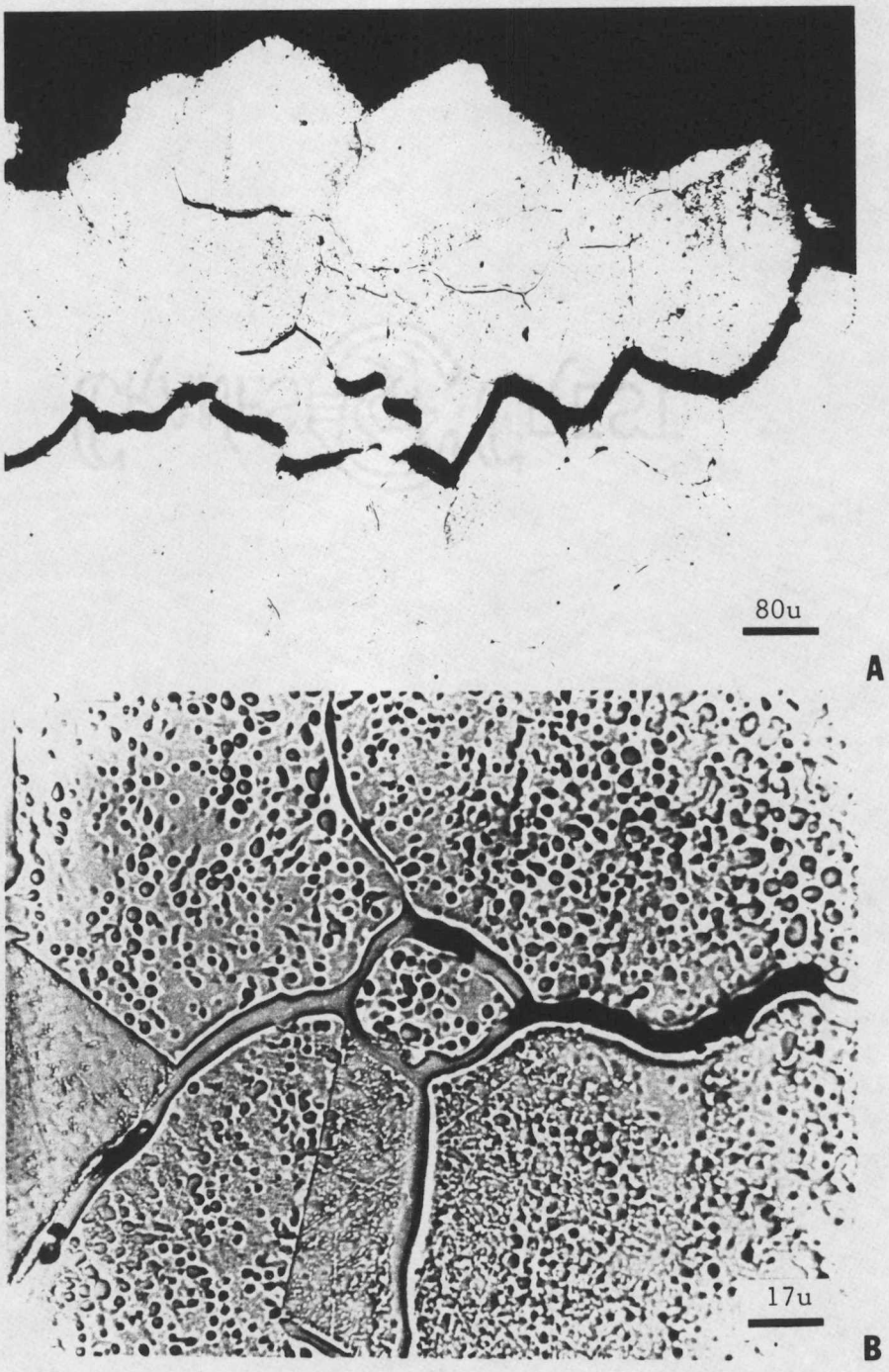


Figure 55. Typical microstructures near the fracture surface in the longitudinal section, tested at ZDT of 2475 ^{o}F, 316NG-7.

crack surface reveals grain faces are enriched in Si, Cr and S when compared to a room temperature fractured surface (grain matrix). The longitudinal section through the fracture plane in Figure 55 further reveals that the cracks formed at, and propagated along, the liquated and widened grain boundaries. Thus, as in the case of 347NG, the zero ductility intergranular fracture at the ZDT is related to a formation of liquid film along the segregated grain boundaries during on-heating to the ZDT. Therefore, it can be assumed that all the following samples tested on-cooling after exposure to the ZDT have experienced extensive liquid film formation along the grain boundaries.

The microstructure of a sample tested at 2000 ^{o}F on cooling from the ZDT is shown in Figure 56a. As expected, all grains have been dynamically recrystallized during deformation and fracture initiated along the original melted and resolidified grain boundaries. Prior grain boundaries can be seen as "ghost boundaries" in Figure 56a. The original grain size is five times larger than the newly recrystallized grains. Further, the original grains appear to have been elongated parallel to the strain direction before the cracks formed along the boundaries. The cracks formed on the sliding boundaries when the stress was sufficiently high, but the recrystallization and migration of the new boundaries was so rapid that initial cracks no longer propagated and no additional cracks formed at the new boundaries, resulting in relatively high ductility (50%).

The optical microstructure for samples tested at 1800 ^{o}F, at which the material shows a significant ductility dip, is shown in Figure 56b. As may be expected from the low ductility (< 10%), the

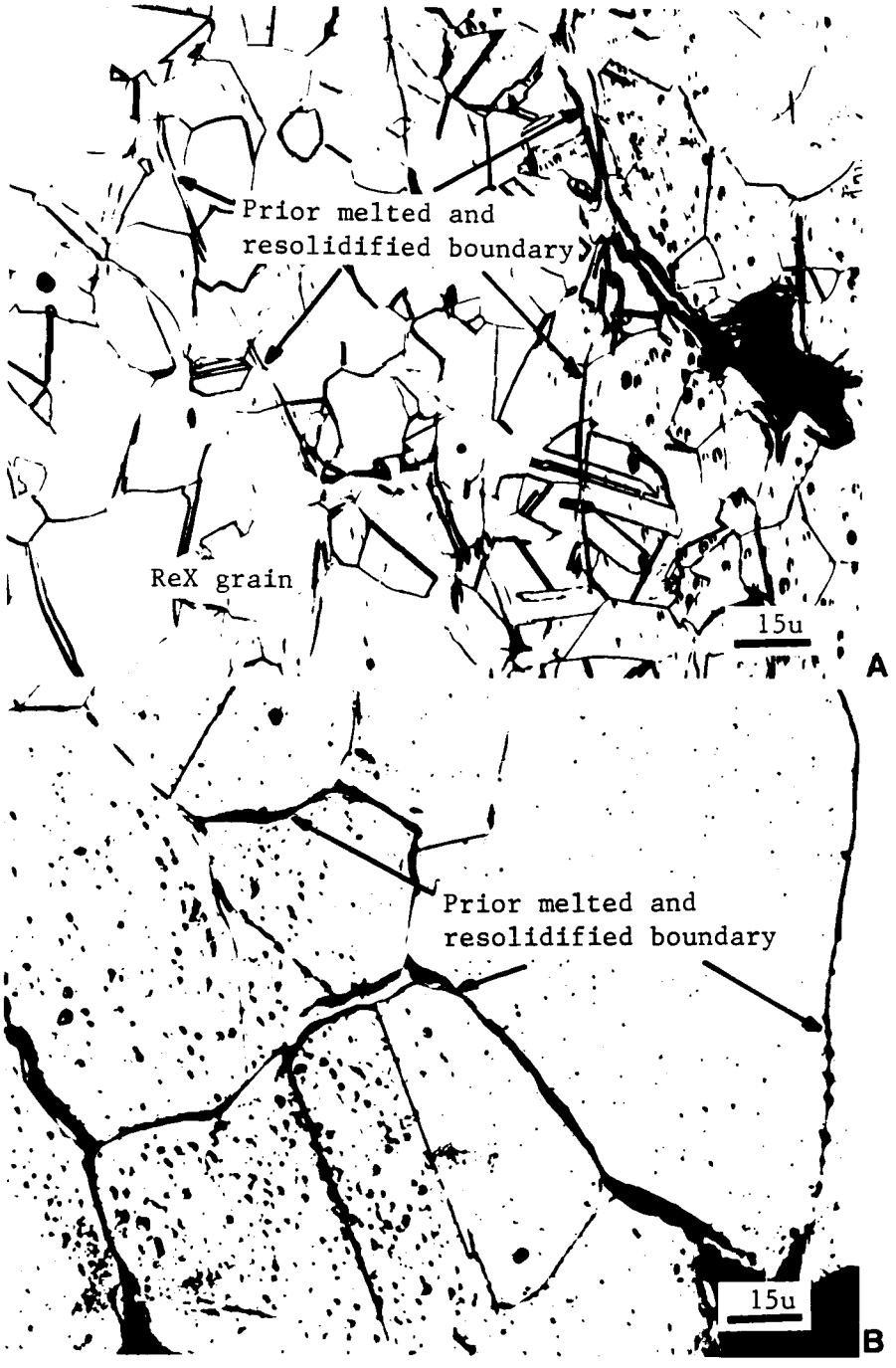
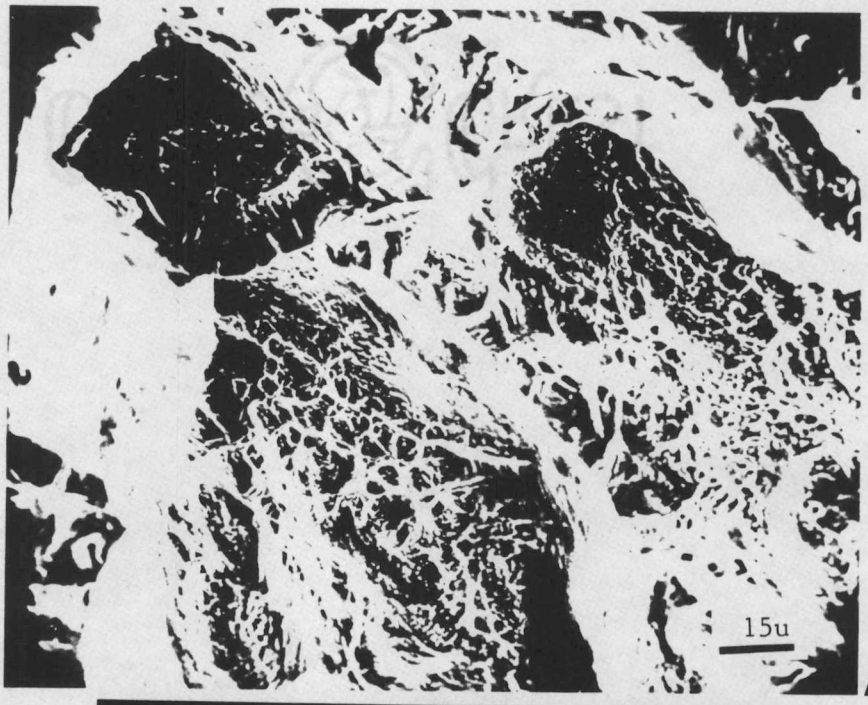
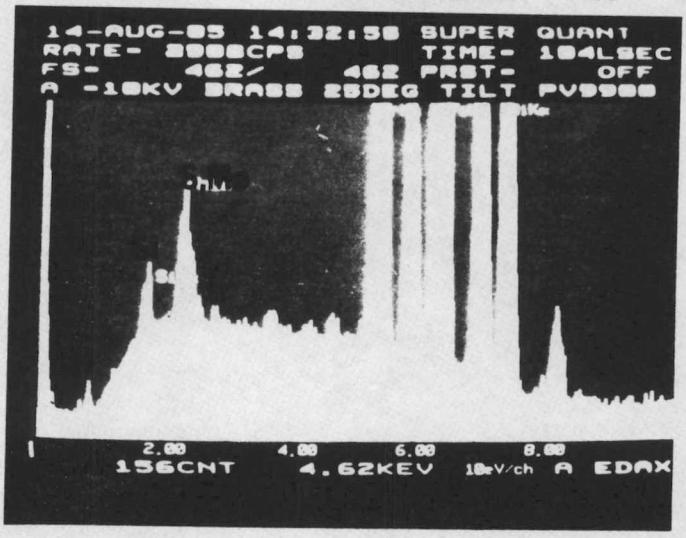


Figure 56. Typical microstructure near the fracture surface, tested on-cooling a) at 2000 ^{o}F and b) at 1800 ^{o}F, 316NG-7.

fracture is completely intergranular and propagated along the prior melted and resolidified boundaries. No evidence of recrystallization is seen. The fractography and EDAX analysis for the fracture surface (Figure 57) indicate that a significant extent of ductile dimples exists on the grain faces. Further, as other investigators (13,180-183) have observed, there is no evidence of a liquid film existing at the instant of fracture. EDAX analysis showed that the grain boundaries were rich in S and Si which were also detected in the liquid film remnants produced at the ZDT. Microstructure revealed by the thin foil TEM (extracted from a region just adjacent to the fracture surface) in Figure 58a shows a grain boundary triple point and reveals no evidence of any carbide precipitation in the grain boundary or the matrix. A TEM micrograph of the carbon extraction replica from the fracture surface (etched by the SPEED method to isolate precipitates from the matrix), and the STEM microprobe on the particles are given in Figures 58b and 59, respectively. Figures 58b and 59 show that some Cr, Fe and Mo rich carbides precipitated along the grain boundaries. No evidence of thermal facetings of the fracture surface (replica), which was detected by other investigators (13, 183), is noted.

Typical microstructures from samples tested on cooling at 1600 and 1500 ^{o}F are given in Figures 60a and b, respectively. At 1600 ^{o}F, small cracks formed along the prior grain boundaries which melted during exposure at and near the ZDT and resolidified during cooling. However, as compared to 1800 ^{o}F, the grain matrix is severely deformed and the grains are elongated with significant deformation bands.





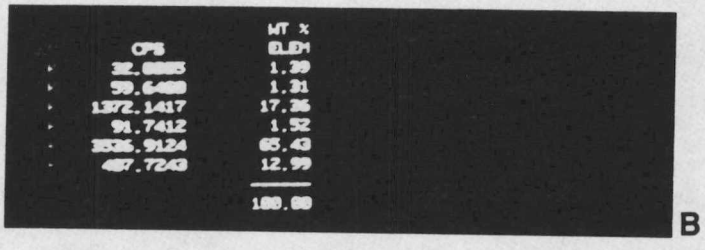


Figure 57. SEM micrograph of the ductility dip sample and EDAX analysis, tested on-cooling at 1800 ^{o}F.

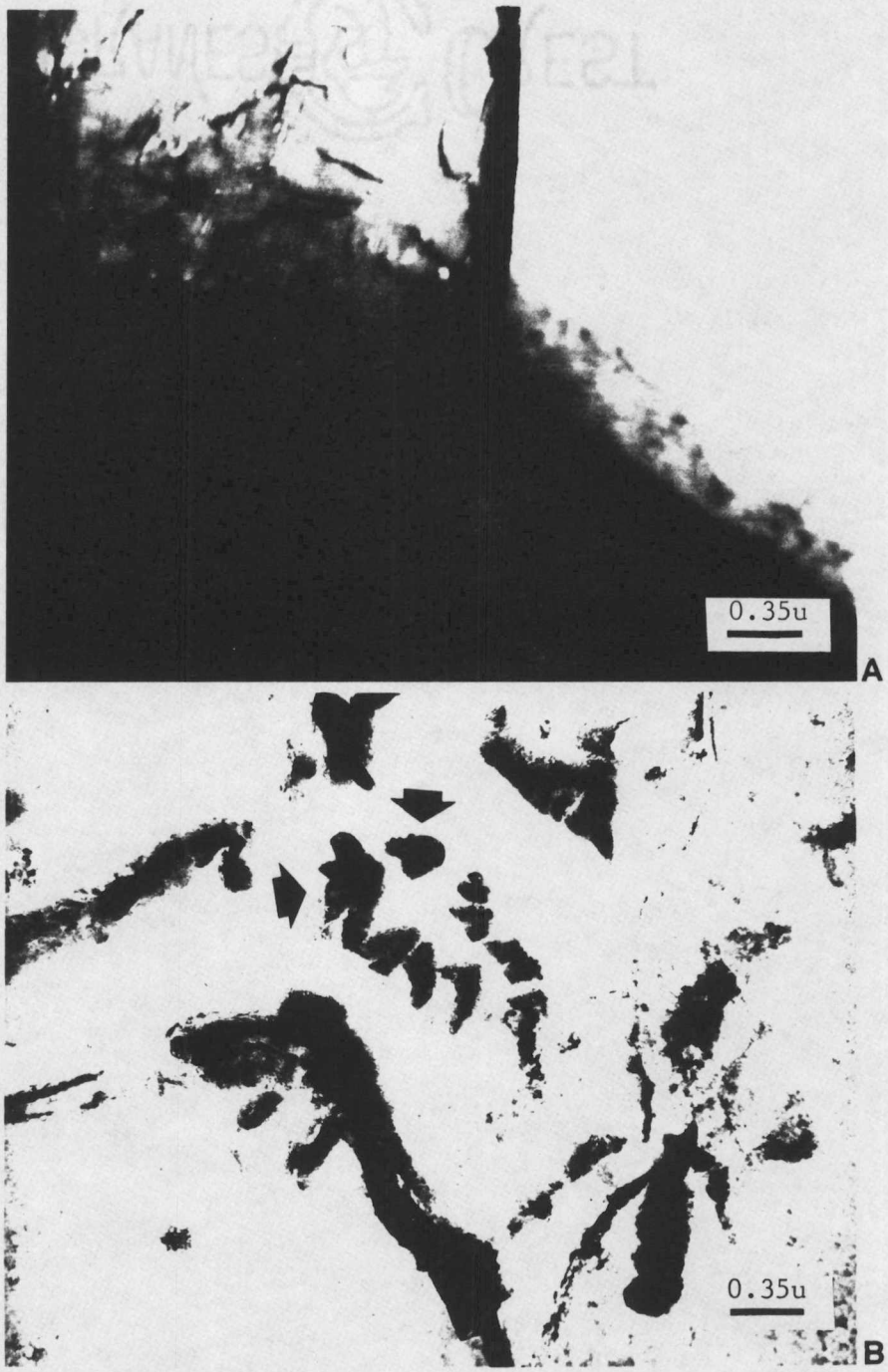


Figure 58. Typical TEM microstructures in a) thin foil and b) carbon extraction replica, near the fracture surface in the ductility dip sample, 316NG-7.

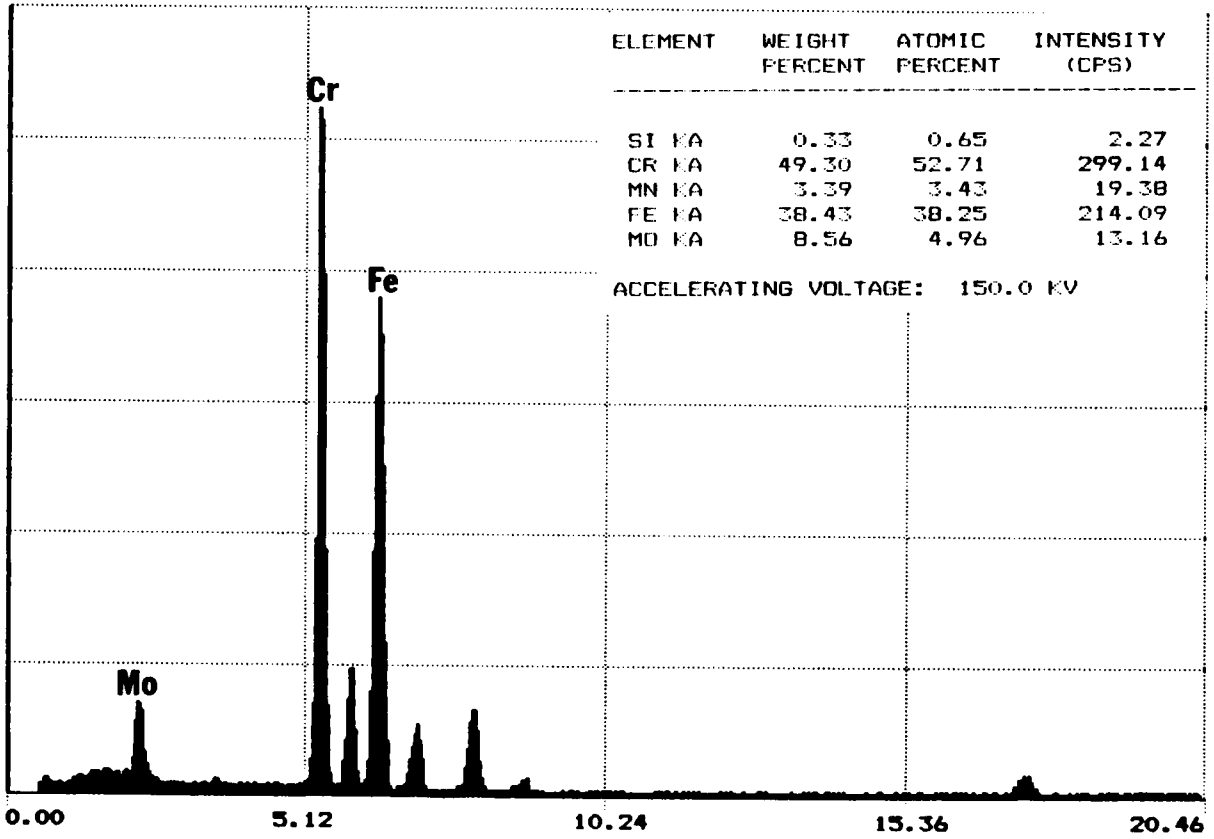


Figure 59. STEM analysis on the particles in the Figure 58b.

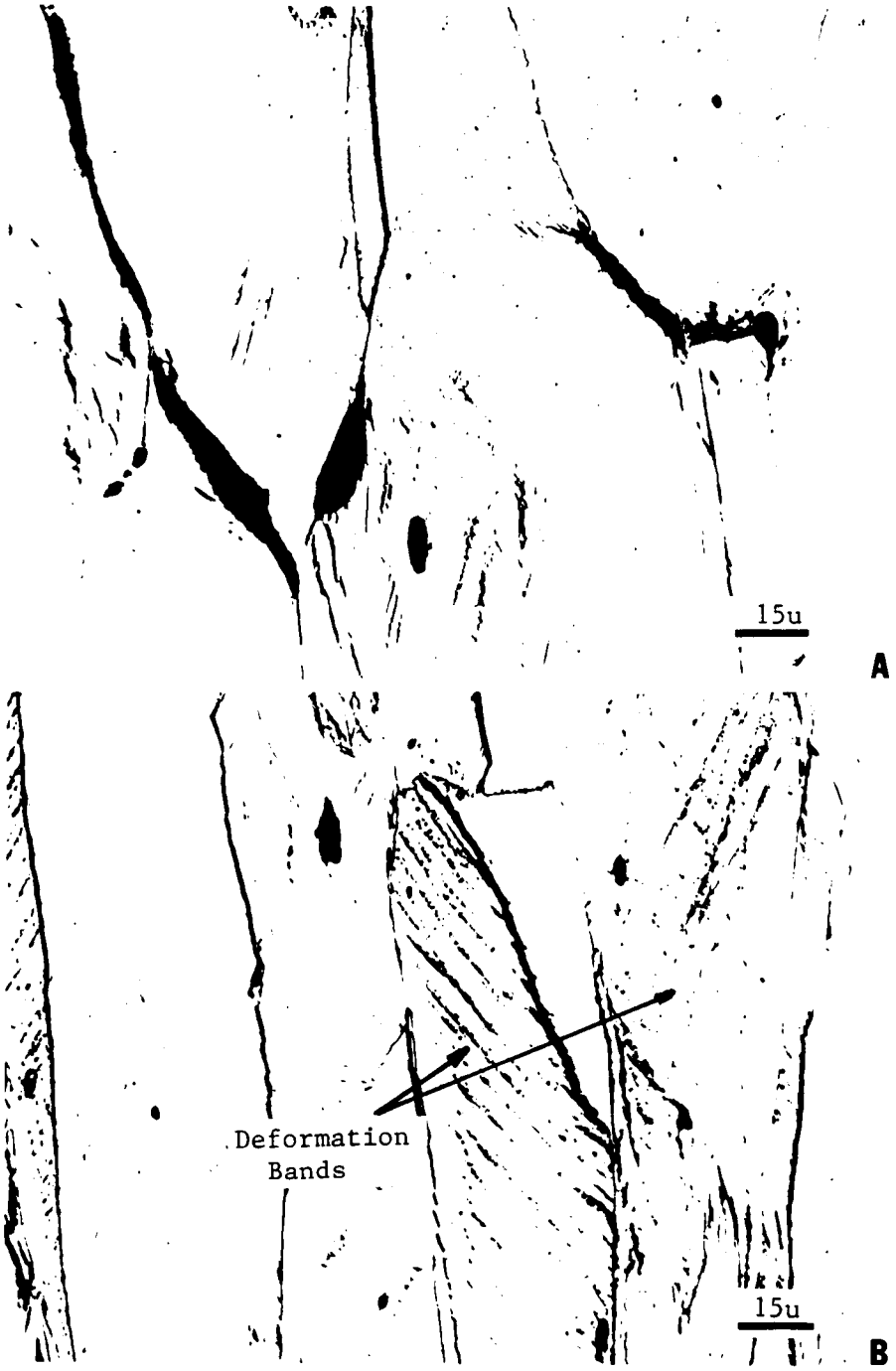


Figure 60. Typical optical microstructures, tested on-cooling at a) 1600 ^{o}F and b) 1500 ^{o}F, 316NG-7.

Thus, at this temperature, grain boundary strength appears to be almost the same as grain matrix and this temperature thus may be near the equicohesive temperature of 316NG-7. When the temperature decreased further to 1500 ^{o}F, no cracks are formed along the grain boundaries and the grains elongate to a greater extent. Fracture occurred in a completely transgranular mode. The grain matrix also has a considerable number of deformation bands revealing that the strength of the grain boundary is no longer lower than that of the grain body. Therefore, the ductility dip temperature is between the recrystallization temperature and the approximate equicohesive temperature.

An earlier study at UTK (166) showed that ductility dip behavior was significantly influenced by peak temperature for the on-cooling tests. Some examples are given in Appendix. Figures A-1 and A-7 show that when the on-cooling tests are conducted from the ZDT, both 316L and 304L reveal ductility dip behavior at about 2000 ^{o}F. However, when the on-cooling tests were accomplished during cooling from 50 F^{o} below the ZDT, the ductility dip for the both materials disappeared. Therefore, 316NG-7 was also tested at 1800 ^{o}F on cooling from the 50 F^{o} below the ZDT and revealed increased ductilities of 50% and 75%. When tested on-cooling from the ZDT, ductility at 1800 ^{o}F was less than 10% as shown in Figure 28 (page 118). Therefore, peak temperature (prior microstructure) plays a significant role in the ductility dip phenomenon. A microstructure of samples tested at 1800 ^{o}F after exposure to the ZDT-50 F^{o} is shown in Figure 61. As may be expected from the high ductility (75%), all grains are significantly



Figure 61. Typical optical microstructure tested at 1800 ^{o}F on cooling from the ZDT - 50 F^{o}, 316NG-7.

deformed and elongated in a direction parallel to the strain direction. Further, at this temperature, dynamic recrystallization has just begun and the new grains did not grow fully along the prior grain boundaries. However, as shown before, no recrystallization occurred at this temperature for material when tested on-cooling from the ZDT.

As the peak temperature decreases, the recrystallization temperature appears to shift to lower temperature. This may be due to the fact that an exposure to the lower peak temperature results in a reduced grain growth and thus more grain boundaries are available for the nucleation of the new grains. Further, it may be expected that when the peak temperature is lower, the extent of precipitation during cooling will be reduced, because heating to a higher temperature promotes dissolution. Thus, a lesser precipitation hardening effect on the grain matrix and lesser stress concentration along the grain boundaries resulting in intergranular fracture, can be expected. However, as previously shown, the ductility dip behavior of 316NG-7 does not seem to be influenced by precipitation hardening, because the TEM microstructure revealed no evidence of any carbides or compound precipitation in the grain matrix. On the other hand, some chromium rich carbides precipitated along the grain boundary which may reduce the grain boundary cohesive strength.

Another important effect of the exposure to the lower peak temperature is that the extent of liquid formed along the grain

boundaries is less, thus, grain boundary embrittlement may be decreased. Therefore, ductility recovery from the lower peak temperature is important and the ductility dip may not appear. Further, reduced grain boundary embrittlement due to exposure to the lower temperature may results in an increase in the equicohesive temperature which may then be higher than the recrystallization temperature, resulting in ductile transgranular fracture.

The above microstructural features strongly indicate that the ductility dip behavior is related to: 1). the extent of liquid formation during exposure at or near the peak temperature, 2). the relative recrystallization and the equicohesive temperatures, and 3). precipitation of the chromium rich compounds (carbides) along the grain boundaries. However, the hardening of the grain body by the precipitation of carbides, which many investigators postulated as one of the the main factors for the ductility dip phenomena, does not appear to be responsible for the phenomena in the case of 316NG. Furthermore, ductility dip behavior seems to require the simultaneous occurrence of all the above factors. Among them, the similarity of the recrystallization temperature and equicohesive temperature may be the most important factor. As discussed before, at temperatures above the ductility dip range (above the equicohesive and recrystallization temperatures), the fracture initiates at embrittled grain boundaries but growth is immediately arrested by newly recrystallized grains,

resulting in a relatively high ductility. On the other hand, at temperatures below the ductility dip temperature where the grain boundary strength is equivalent to that of the grain body, fracture does not initiate at the grain boundary and even if it initiates at discontinuities in the grain boundaries, fracture propagates transgranularly, resulting in a ductile fracture. **Therefore, the ductility dip appears to occur due to fracture along the original embrittled grain boundaries (by melting and resolidification due to impurity segregation) at temperature above the equicohesive temperature but below the recrystallization temperature. Grain boundary embrittlement may be further enhanced by the precipitation of chromium rich carbides and an increased amount of liquid formed by exposure to a higher peak temperature.**

Rhine et al. (184) and Dieter et al. (185) also found similar results in Inconel as the minimum elongation was associated with the occurrence of grain boundary shearing and associated intergranular rupture. Further, they (184) proposed that "the temperature at which the ductility minimum occurs must be above the temperature at which dynamic recovery begins, so that grain boundary shearing becomes active, and below the temperature for the rapid recrystallization, so the grain boundaries on which the shearing begins are not wiped out in the recrystallization process". However, this is based on the on-heating tests, i.e., the significance of grain boundary embrittlement

by melting and resolidification, occurring during exposure through the ZDT and cooling, is not considered.

Significance of Ductility Dip Behavior. Although several heats of materials evaluated in this study have shown ductility dip behavior, it is still not clear whether the behavior is a characteristic of the testing itself or that of material. There is no apparent differences in the chemical composition and metallurgical variables (ferrite potential, grain size) between the materials showing a ductility dip behavior and those free from the behavior. The previous section revealed that the ductility dip behavior is the result of the combination and/or competition between strain hardening and softening process of dynamic recrystallization, and the ductility dip occurs only below the recrystallization temperature and above the approximate equicohesive temperature. Below this temperature, fracture occurs in a ductile transgranular mode. One has to remember that the strain hardening and dynamic recrystallization processes are possible only under the "severe strain and high strain rate" conditions which are not likely to happen in the actual weld heat affected zone. Therefore, the ductility dip behavior of materials during Gleeble hot ductility testing "may be" the characteristic of the testing itself.

Although many investigators have found the ductility dip phenomenon, most incidences have required imposition of augmented

strains and further, very little is known about the significance of the ductility dip phenomenon in actual fabrication behavior. As mentioned earlier, Yeniscavich (110, 111) has found that the material which showed the greatest fissuring in his investigation had a small mid-temperature ductility dip upon Gleeble hot ductility testing. Unfortunately, he did not mention whether the fissures were really ductility type cracking or not. Recent unpublished investigations by the Welding Research Group at the University of Tennessee have found that alloy 316NG which had experienced cracking in field fabrication showed a significant scattering in the on-cooling data and also showed a ductility dip behavior in the Gleeble hot ductility test. Here again, whether the field cracking incident for this alloy was a characteristic of ductility dip cracking is not known.

Therefore, while rigorous correlations have not been made for the relationship of ductility dip behavior to the fabrication behavior, it should not be forgotten that various high temperature cracks may interact. For example, solidification and liquation cracks in the weld metal and HAZ may provide stress concentrations from which ductility dip cracks may propagate. Thus, when a material shows a ductility dip behavior in the Gleeble hot ductility testing, it must be subjected to careful evaluation after welding to verify the absence of fissuring.

2. VARESTRAINT HOT CRACKING TESTS

It has been a common practice to produce welding filler metals of such composition that the weld deposit contains a small amount (5 - 10%) of delta ferrite at room temperature to minimize the possibility of fusion zone hot cracking during welding of the austenitic stainless steels. The amount of ferrite required to prevent or minimize hot cracking is dependent upon the composition of material, especially the level of P, S, Si and other "harmful" elements (43). However, recent studies (67,75-77,85-87,91-95) have indicated that the solidification cracking susceptibility of austenitic stainless steels is directly related to the primary solidification mode rather than the absolute residual ferrite content at room temperature. A primary ferritic solidification mode leads to a better hot cracking resistance than when the material has a primary austenitic solidification mode.

Although delta ferrite is effective in reducing weld hot cracking, certain disadvantages occur with the presence of ferrite such as in applications where the ferromagnetic characteristic of ferrite is undesirable, increased stress corrosion cracking susceptibility in certain environments, transformation of ferrite to brittle sigma phase during elevated temperature service. Consequently, it is sometimes desirable to limit the residual ferrite content in the weld deposit.

The mechanism of the HAZ liquation cracking is slightly different from fusion zone solidification cracking, although the general causes are almost identical for both types of cracking. The most commonly known reasons for HAZ cracking are: grain boundary

liquation by incipient melting of the impurity segregates along grain boundaries, absorption of solutes from the weld puddle, and constitutional liquation of inclusions and second phase low melting constituents (23).

As mentioned earlier, many utilities have recently developed their own specifications in addition to those recommended by NRC, for materials and additional testing to insure that nuclear requirements would be attained and to provide for easy and trouble free fabrication. As a result, there are several different chemistry specifications for the nuclear grade stainless steels. The major difference is in S, P, Si, N and Nb contents and ferrite requirements. Further, although the new 347 materials have been successfully fabricated in Europe and Japan, because of earlier experience in the US with HAZ cracking during welding and HAZ stress relief cracking during long term service of 347 in the 1960's, some in this country are still reluctant to use the modified 347 (347NG) materials in welded piping systems.

Therefore, in this section, the weldability of 347NG and 316NG is thoroughly evaluated and compared to that of AISI 304, 316 and 347, using the multipass Varestraint technique which permits a simultaneous evaluation of the weld metal HAZ, the base metal HAZ and fusion zone of the deposited pass in a single specimen. The discussion of the weldability of program materials is divided into the three sections: a. fusion zone solidification cracking, b. weld metal HAZ liquation cracking and c. base metal HAZ liquation cracking. In each section, the behavior of nuclear grades is compared to the standard grades and

is analyzed in terms of chemical composition, impurity level (P, S, Si), solidification mode (Cr_{eq}/Ni_{eq}) and the ferrite content (potential). Based on data analyses and extensive metallographic examination, the possible mechanisms for hot cracking in each weld zone is discussed.

a. Fusion Zone Solidification Cracking

Varestraint Test Results. The behavior of all 316NG materials with respect to fusion zone hot cracking is compared with that of AISI 304 and 316 in Figure 62. The total crack length (TCL) versus augmented strain permits the ready comparison of behaviors of different alloys. The behavior of 316NG is devided into three groups based on the solidification modes; fully austenitic, primary ferritic and primary austenitic (austenite + eutectic ferrite), as shown in Figure 62. The primary solidification mode, as will be discussed later, were determined by careful examination of metallographic samples. The type of solidification mode was based on the location of delta ferrite within the dendritic structure. That is, in the primary ferritic solidification mode, retained ferrite is mainly distributed along the center of the dendrite core, while for the primary austenitic mode delta ferrite occurs in the interdendritic region. In the fully austenitic mode, no remnant ferrite exists in the room temperature microstructure. The solidification mode and maximum crack length (MCL) and total crack length (TCL) at the 4% augmented strain for all 316NG, 304 and 316 materials are given in Table 10. Figure 63 indicates that the TCL has an linear relationship with the MCL.

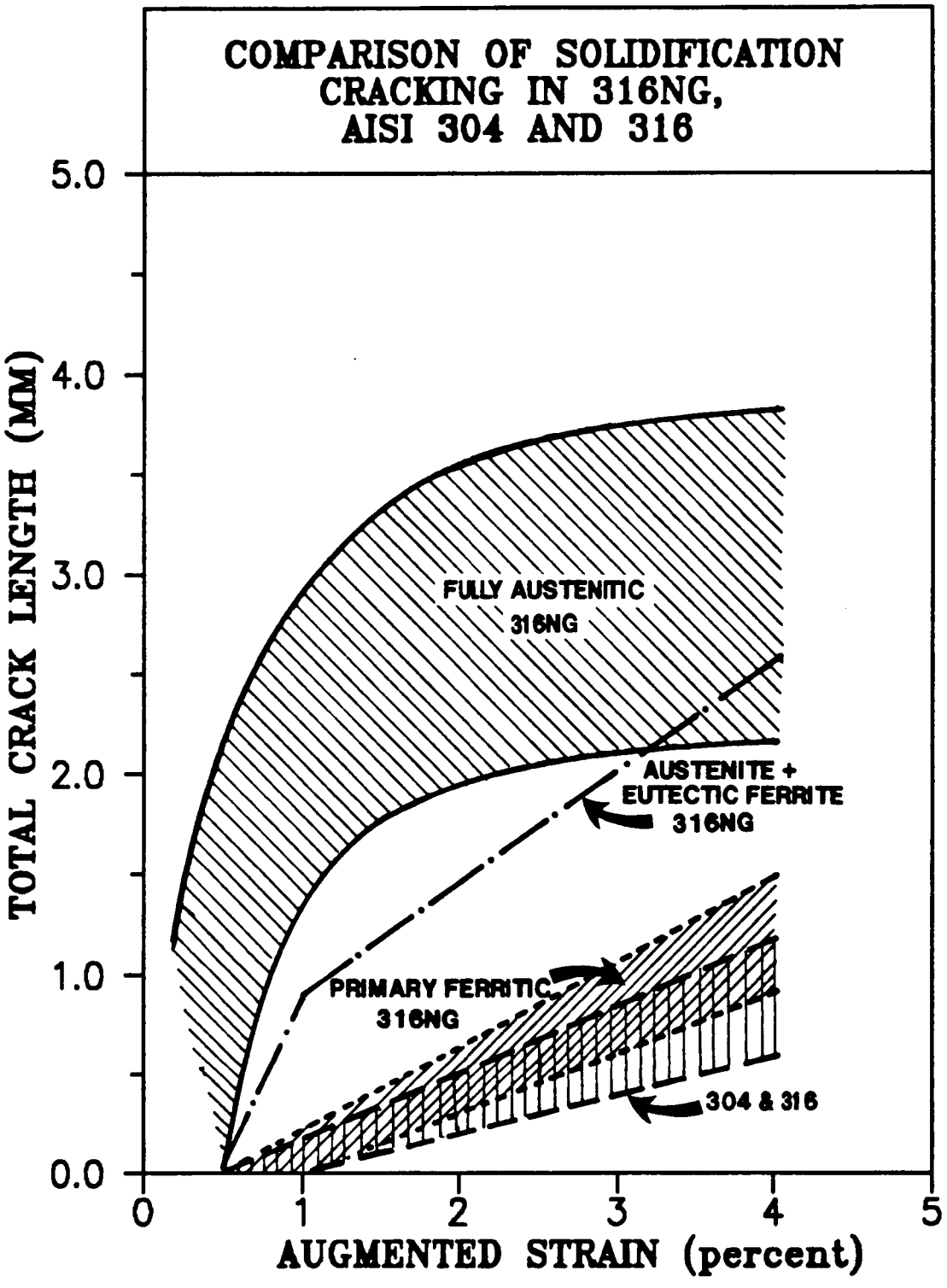


Figure 62. Comparison of fusion zone solidification cracking of 316NG materials with AISI 304 and 316.

Table 10. Varestraint fusion zone solidification cracking test results of 316NG, AISI 304 and 316.

Code	Type	FN[a]	P+S	N	Solidification Mode[b]	Cr_{eq}/Ni_{eq}[c]	G.S.	TCL[d]	MCL[e]
316NG-A	316NG	5.1	0.043	0.061	F	1.72	7.3	1.5	0.19
316NG-B	316NG	3.2	0.045	0.083	F	1.71	6.3	1.1	0.18
316NG-C	316LN	4.2	0.022	0.099	F	1.63	5.3	0.9	0.15
316NG-D	316LN	0.1	0.022	0.113	A	1.45	8.2	3.7	0.54
316NG-1	316NG	2.0	0.050	0.098	F	1.61	5.0	1.5	0.29
316NG-2	316NG	0.2	0.030	0.097	A	1.54	4.2	2.4	0.46
316NG-3	316NG	0.0	0.029	0.100	A	1.44	5.0	3.8	0.52
316NG-4	316NG	1.6	0.040	0.083	AF	1.55	5.9	2.4	0.33
316NG-5	316NG	0.2	0.022	0.096	A	1.43	3.5	3.1	0.47
316NG-6	316NG	0.3	0.020	0.101	A	1.43	3.3	3.0	0.53
316NG-7	316NG	0.0	0.021	0.094	A	1.43	3.2	3.1	0.43
316NG-8	316NG	0.1	0.022	0.093	A	1.45	3.8	2.7	0.50
316NG-9	316NG	0.2	0.020	0.099	A	1.43	3.8	2.2	0.34
316-1	316ELC	4.0	0.034	0.054	F	1.60		1.2	0.17
304-1	304	2.4	0.055	-	F	1.84	4.2	1.1	0.28
304-2	304	2.4	0.049	-	F	1.98	4.3	0.7	0.18
304-3	304ELC	3.5	0.034	-	F	1.71		0.6	0.11

a: Measured Ferrite content with Magne-Gage
b: F; primary ferritic, A; Fully austenitic, AF; primary Austenitic + Eutectic Ferrite
c: Hammer and Svensson Method
d: Total crack length (mm) at 4% Augmented strain
e : Maximum crack length (mm) at 4% Augmented strain

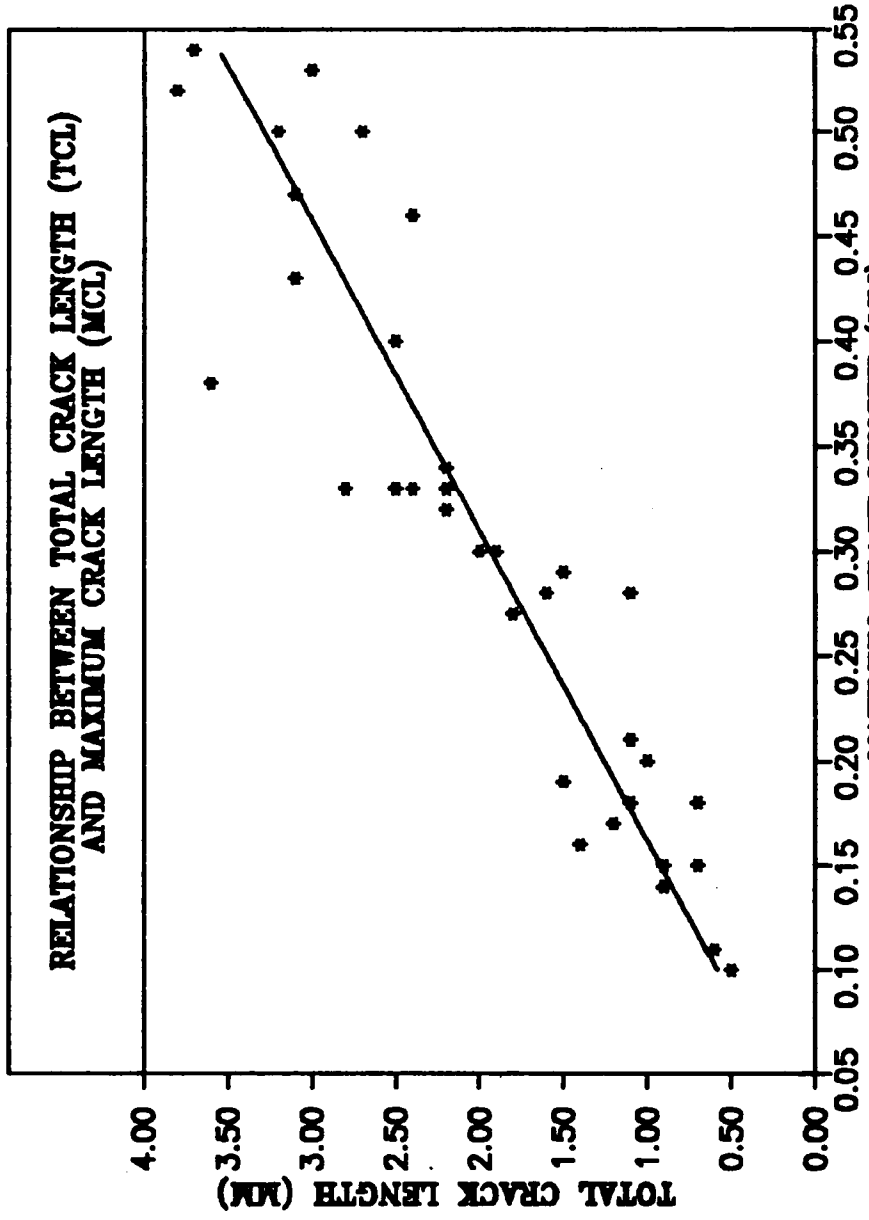


Figure 63. Relationship between total crack length and maximum crack length.

It is clear that the solidification cracking susceptibility of 316NG is predominantly a function of the primary solidification mode. Fully austenitic materials show a significantly greater TCL and MCL at all strain levels as compared to that of the materials which solidify in a primary ferritic mode. Fully austenitic materials also have a lower cracking threshold strain. Even at the lowest augmented strain level (0.25%) used in this study, the TCL of the primary austenitic materials is greater than that of the primary ferritics tested at the highest strain level (4%).

When 316NG has a primary ferritic mode, its susceptibility to solidification cracking is low and is virtually equivalent to that of standard grades of 304 and 316 which have also solidified in a primary ferritic mode. When 316NG solidifies as primary austenite with a formation of eutectic ferrite in the interdendritic region its susceptibility, in terms of TCL, is similar to that of the fully austenitic heats. However, the MCL appears to be lesser than that in the fully austenitic. This means that eutectic ferrite formation during the last stage of the solidification may have played a significant role in preventing the cracks from propagation rather than initiating. This will be discussed further later.

Figure 62 further reveals that in general, the TCL increases with an increase in the augmented strain level. The TCL/MCL of the primary ferritic 316NG and standard grades increases almost linearly as the applied strain increases. However, the TCL/MCL of the fully austenitic and primary austenitic 316NG increases rapidly with a small increase in the strain level and levels off beyond a certain value of

augmented strain. In other words, the hot cracks initiated in a fully austenitic material propagate easily to a maximum crack length with a relatively small increase in strain. On the other hand, the hot cracks initiated in a primary ferritic weld metal may not easily propagate and thus the maximum crack length at small augmented strains is low.

Further, because the TCL and MCL of the primary ferritic (hot cracking resistant) alloys increase almost linearly as the augmented strain increases, the CST (critical strain rate for temperature drop, see Figure 20 (page 93)) which requires a tangential line drawn from the liquidus can not be used as a criterion. Therefore, the combination of TCL, MCL and threshold strain and/or TCL/MCL at the constant strain of 4% is used for discriminating heat to heat variation in this study.

The fusion zone solidification cracking behavior of 347NG as well as AISI 347 is given in Figure 64. The metallographically determined solidification mode and the TCL and MCL measured on the as-welded samples tested at 4% strain level for all 347NG and AISI 347 materials are given in Table 11. The table reveals that all of the 347 materials, except 347NG-A, -B and 347L, solidify in a primary ferritic mode. 347NG-A and B have a mixed solidification mode, i.e., the primary ferritic and austenitic modes are mixed in the weld microstructure, while the 347L is fully austenitic. In Figure 64, the behavior of 347NG is separated into three groups depending on primary solidification mode and chemical composition. One group is defined for 347NG-D and E which have chemical compositions outside the

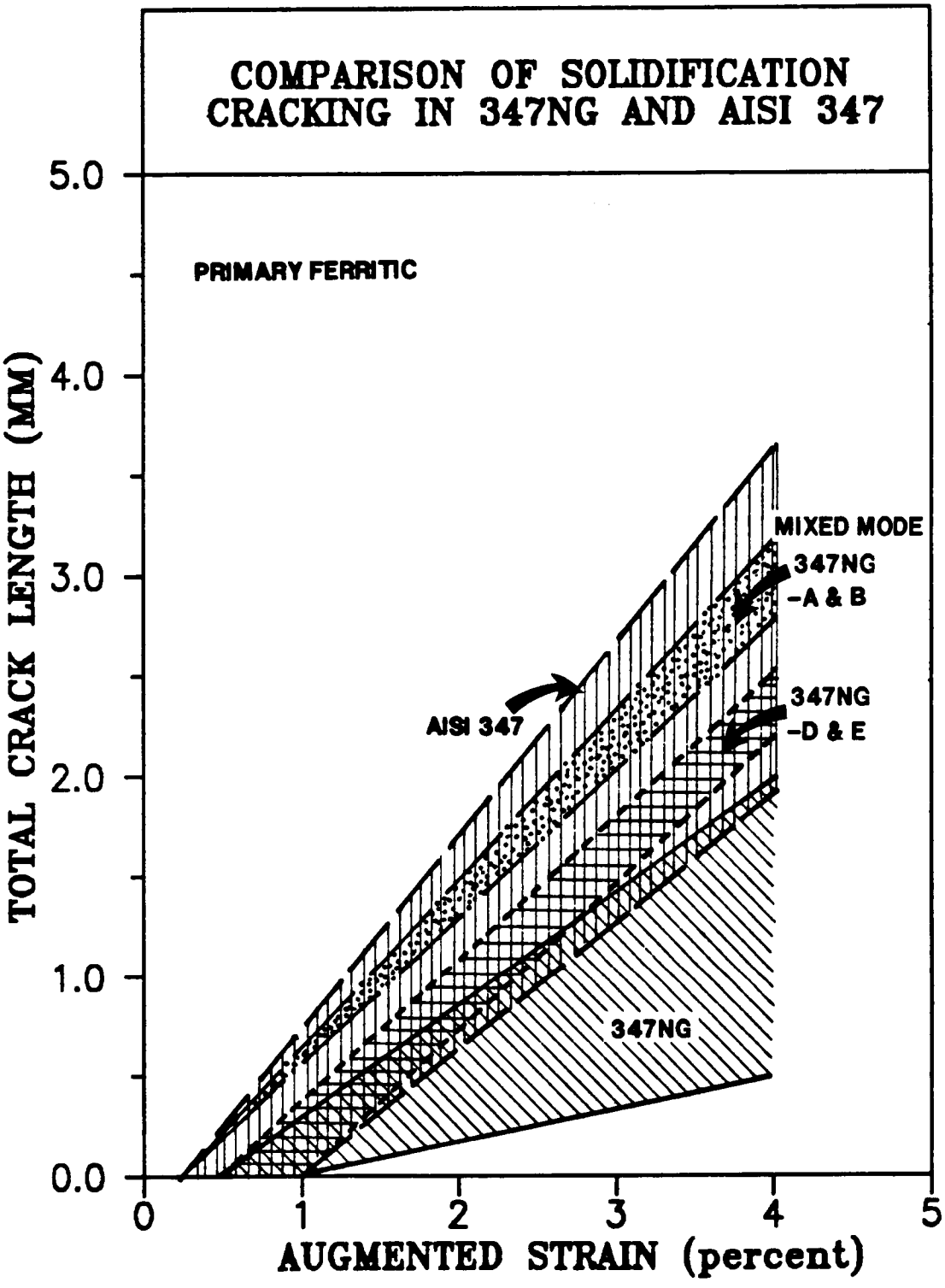


Figure 64. Comparison of fusion zone solidification cracking of 347NG with AISI 347.

Table 11. Varestraint fusion zone solidification cracking test results of 347NG and AISI 347.

Code	Type	FN[a]	P + S	G.S[b]	Nb	1/2Nb / (30C + 50N)	Cr_{eq}/Ni_{eq}[d]	Solidification Mode[c]	p*	TCL[e]	MCL[f]
347NG-A	347NG	2.2	0.029	11.0	0.40	0.30	1.69	Mixed	0.038	2.8	0.33
347NG-B	347NG	3.9	0.030	8.0	0.43	0.10	1.71	Mixed	0.045	3.2	0.50
347NG-C	347NG	4.5	0.038	6.0	0.41	0.09	1.70	F	0.044	1.6	0.28
347NG-D	347NG	3.3	0.045	7.0	0.60	0.22	1.63	F	0.041	2.2	0.33
347NG-E	347NG	4.4	0.034	7.0	0.56	0.19	1.64	F	0.050	2.5	0.40
347NG-F	347NG	3.3	0.040	3.0	0.36	0.08	1.62	F	0.046	0.7	0.15
347NG-G	347NG	1.8	0.033	6.2	0.33	0.08	1.61	F	0.041	1.4	0.16
347NG-H	347NG	2.4	0.034	6.0	0.41	0.11	1.57	F	0.030	1.8	0.27
347NG-I	347LN	1.6	0.018	5.2	0.36	0.04	1.63	F	0.029	0.9	0.14
347NG-J	347NG	3.0	0.037	5.0	0.23	0.04	1.62	F	0.036	1.1	0.21
347-1	AISI347	3.0	0.039	9.0	0.67	0.25	1.78	F	0.054	2.5	0.33
347-2	347LPN	5.5	0.017	8.0	0.26	0.04	1.77	F	0.024	0.5	0.14
347-3	KL473N b	3.6	0.040	9.2	0.49	0.06	1.88	F	0.049	2.0	0.35
347-4	347NG	4.0	0.039	5.0	0.37	0.10	1.60	F	0.047	01.0	0.25
347-5	347L	0.0	0.020	8.0	0.30	0.17	1.54	A	0.020	5.5	1.02
347-6	347R	3.5	0.031	6.2	0.74	1.23	1.86	F	0.044	2.2	0.32
347-8	AISI347	3.0	0.037	5.5	0.61	0.11	1.73	F	0.048	1.9	0.32
347-9	AISI347	3.0	0.030	5.5	0.61	0.09	1.78	F	0.054	3.6	0.38

a : Measured Ferrite content with Magne-Gage
b: ASTM Grain Size No.
c: F; primary ferritic, A; Fully austenitic, Mixed: Mixed ferritic and austenitic
d: Hammer and Svensson Method
e: Total crack length (mm) at 4% Augmented strain
f : Maximum crack length (mm) at 4% Augmented strain
P* = % P + 0.04 x % Si

specification limits; that is, these heats have carbon contents 0.045% and 0.05% and also have a concomitantly high niobium content as compared to the other heats of 347NG.

Figure 64 and Table 11 clearly indicate that as in the case of 316NG, fusion zone solidification cracking in 347NG is also strongly dependent upon solidification behavior. When 347 exhibits a fully austenitic microstructure (ie. 347L), even though its chemical composition is almost equivalent to other nuclear grade heats, its susceptibility to solidification cracking is significantly greater. The TCL and MCL (347L) at 4% augmented strain are more than 3 times greater than for the other 347NG lots.

When 347NG solidifies with ferrite as the primary phase and the chemical composition is within the specification, its hot cracking resistance in the fusion zone is superior to that of AISI 347, but in general, is slightly less resistant than AISI 304 and 316. However, the chemical composition of 347NG (especially C and Nb) is out of the nuclear grade limits, its susceptibility to solidification cracking is much greater than that of the AISI 304 and 316 grades and it is virtually equivalent to AISI 347. Further, although 347NG-A and B have a chemical composition well within the requirements, the fusion zone cracking is also similar to that of AISI 347, because they show a mixed primary austenitic/ferritic solidification mode. The significance of the mixed solidification mode will be discussed later. Therefore, it is apparent that fusion zone solidification cracking in types 316NG and 347NG is predominantly a function of the primary

solidification mode when the chemical composition is within nuclear grade requirements.

Data Analysis. In this section, the fusion zone solidification cracking results of the program materials are analyzed in detail as a function of impurity levels (P+S), chemical composition (Si, Nb, C and N), ferrite content and the Cr_{eq}/Ni_{eq} ratio.

Recently, Suutala et al. (88-90) have found that the primary solidification mode of a material can be predicted from the relative amount of Cr_{eq} and Ni_{eq}. When the ratio of Cr_{eq}/Ni_{eq} is less than about 1.48, the material will have a primary austenitic solidification mode and when the ratio is greater than 1.48, the material will solidify in a primary ferritic mode. Of the various equivalents cited in literature, Suutala et al. found that those developed by Hammer and Svensson (186) showed the correlation to the solidification mode.

The calculated Cr_{eq}/Ni_{eq} ratio using the Hammer and Svensson equivalents for all program materials is given in Tables 10 and 11. The tables reveal that the solidification processes determined by metallographic examination agree well with the Cr_{eq}/Ni_{eq} ratios such that when the ratio is less than 1.48, the material solidified in a fully austenitic mode. The graphical relationship between the solidification mode and the Cr_{eq} and Ni_{eq} is illustrated in Figure 65.

Although the primary solidification mode is a predominant factor for solidification cracking in 316NG and 347NG, the other metallurgical variables, especially impurity elements, can not be neglected. The significance of the primary solidification mode can be further noted by comparison of the behavior of 316NG-D (fully

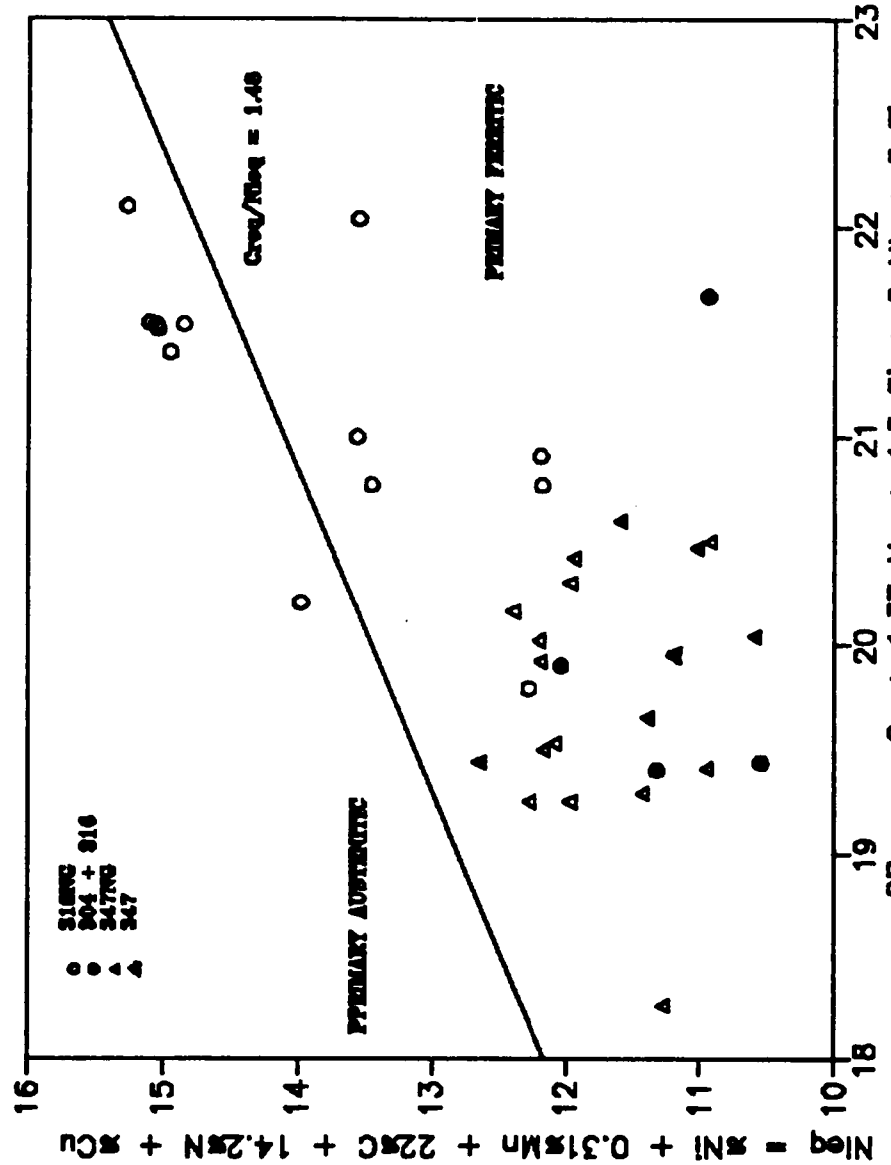


Figure 65. Relationship between solidification mode and Cr_{eq} and Ni_{eq} using the Hammer and Svensson formula.

austenitic) and 316NG-C (primary ferritic). Both heats have almost identical contents of "harmful" elements, P, S, C and Si. The main difference is the solidification behavior and the resultant room temperature ferrite content. The TCL at 4% strain of 316NG-D is almost 4 times greater than that of 316NG-C. Among heats 316NG-A, -B and -C, heat C has the smallest TCL and MCL, indicating a better resistance to solidification cracking. This may be due to the fact that heat 316NG-C has a lower P + S (0.022%) as compared to those of heats A and B (0.043 and 0.045%).

The effect of impurity content (P + S) and the solidification mode (Cr_{eq}/Ni_{eq}) on the extent of hot cracking in 316NG and 304 is summarized in Figure 66. The numerical numbers at each data point in Figure 66 are the TCL for 4% augmented strain. It is evident that crack susceptibility increases with a decrease in the Cr_{eq}/Ni_{eq} and with an increase in the P + S content. For a given Cr_{eq}/Ni_{eq}, the TCL linearly increases as the P + S content increases. At about 1.6 Cr_{eq}/Ni_{eq} ratio, when the P + S increases from 0.021% to 0.050%, the TCL almost doubles from 0.9 mm to 1.5 mm as shown in Figure 67. Further, as shown in Figure 68, solidification cracking decreases with an increase in the Cr_{eq}/Ni_{eq} ratio for a given P + S content. However, as may be expected, the effect of the Cr_{eq}/Ni_{eq} ratio depends upon the impurity level (P + S). Figure 68 reveals that for a given increase in the Cr_{eq}/Ni_{eq} ratio, the extent of cracking (TCL) decreases more rapidly when the impurity level (P + S) is low (0.03%) than when it is high (0.04%).

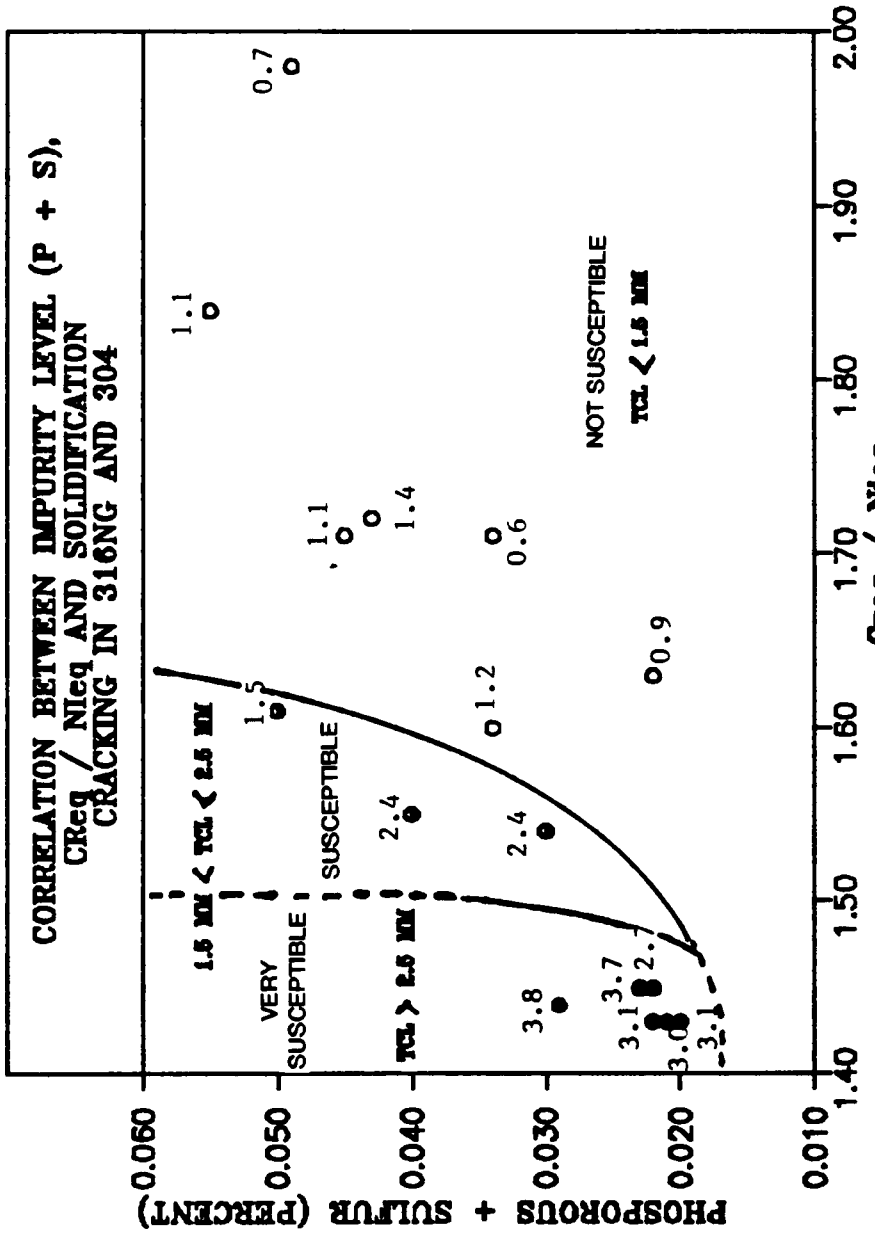


Figure 66. Correlation among the P + S content, Cr_{eq}/Ni_{eq} and the extent of solidification cracking in 316NG, 304 and 316.

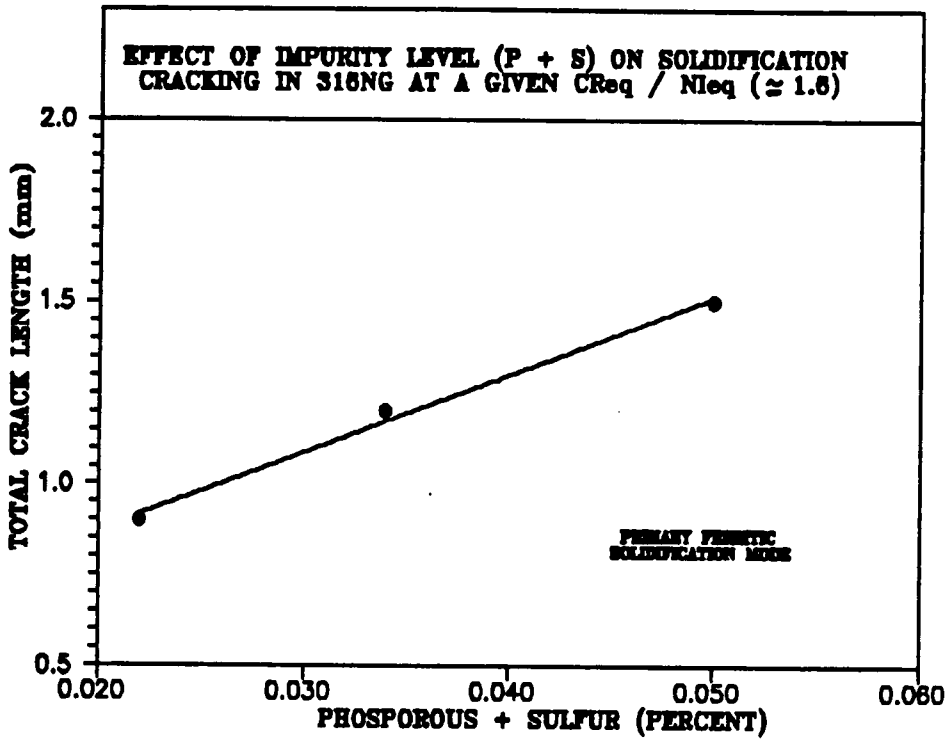


Figure 67. Effect of P + S level on solidification cracking for a given Cr_{eq}/Ni_{eq} (1.6).

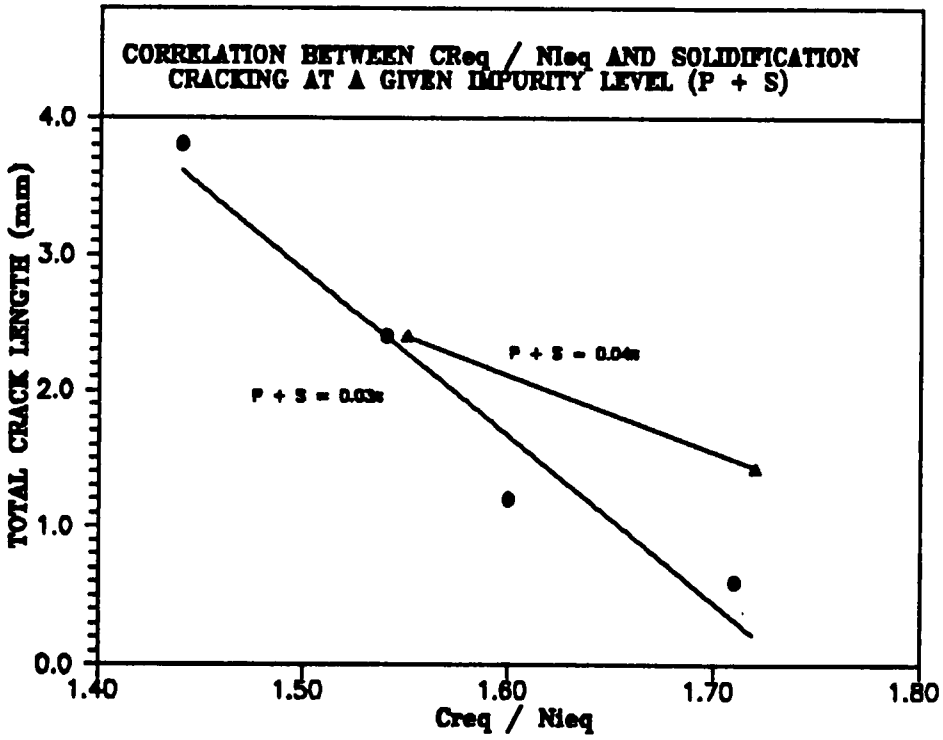


Figure 68. Effect of Cr_{eq}/Ni_{eq} on solidification cracking as a function of P + S content.

The significance of the Cr_{eq}/Ni_{eq} ratio is that the ratio can predict not only the primary solidification mode, but also the relative amount of the primary ferrite formation during solidification (187). In other words, within the primary ferritic solidification mode ($Cr_{eq}/Ni_{eq} > 1.48$), the higher Cr_{eq}/Ni_{eq} ratio material forms a greater amount of primary delta ferrite during solidification, which determines the relative extent of microsegregation of "harmful" elements to the last solidifying liquid in the dendritic and solidification grain boundaries. Matsuda et al. (47) have found that a nitrogen addition to "18-8" stainless steel decreased the primary ferrite content from 70 - 75% to 0 - 50%, resulting in an increase in the brittleness temperature range (BTR) of the 18-8 stainless steel. They attributed the enhanced crack susceptibility (increased BTR) to the increased degree of microsegregation of phosphides and sulfides in the intergranular region due to a reduced primary ferrite content. Therefore, the reduced cracking susceptibility in the higher Cr_{eq}/Ni_{eq} ratio material may be due to the decreased microsegregation of phosphides and sulfides in the interdendritic and solidification grain boundaries (by increased primary delta ferrite formation during the solidification process).

In Figure 66, the hot cracking susceptibility of the materials is grouped into three regions: the most susceptible, less susceptible and not susceptible, based on the TCL at the 4% strain level. Recently, the Welding Research Group at UT (188) has compared the external restraint type - Varestraint method with the semi-self restraint Finger test and the self-restraint type - Dummy weld test.

The comparison revealed that when the TCL at 4% strain in the Varestraint is smaller than about 1.5 mm, no cracking occurred in the Finger or the Dummy weld test. When the TCL is greater than 1.5 mm, the cracks appears in the Finger test, but no cracks were present in the completely self-restraint Dummy weld test. However, when the TCL in the Varestraint reached 2.5 mm, cracking also occurred in the Dummy weld test. Therefore, based on this comparison, the most susceptible materials are with TCL > 2.5 mm, the less susceptible materials are with 1.5 mm < TCL < 2.5 mm, and the least susceptible materials are TCL < 1.5 mm. It is interesting to note that when the Cr_{eq}/Ni_{eq} ratio of a material is less than about 1.5 (i.e. primary austenitic mode) it is most susceptible to hot cracking, even with a low P + S content (0.02 %). When the Cr_{eq}/Ni_{eq} is between 1.5 and 1.6, materials are somewhat susceptible and the behavior is strongly dependent on the P + S content. Further, when the Cr_{eq}/Ni_{eq} of material is greater than about 1.6 and the P + S is within specification (0.06% max.), the solidification cracking susceptibility appears to be very low.

Unlike types 304, 316 and 316NG, the hot cracking susceptibility of 347 does not "directly" correlate with the P + S and the Cr_{eq}/Ni_{eq} ratio, but appears to be mainly a function of the Nb, N and C contents. However, a higher carbon and thus a higher niobium content, does not necessarily give rise to a greater susceptibility to fusion zone solidification cracking, if it has a primary ferritic solidification mode. For example, heats 347NG-D and E, which have a higher C and Nb contents as compared to the other nuclear grades, have a slightly smaller MCL and TCL than that of the lower C and Nb

containing 347NG-A and B which have a mixed solidification mode. Further, 347L, which has a lower C and Nb as well as a lower impurity level (P + S) but has a fully austenitic solidification mode, has the greatest susceptibility to solidification cracking among all 347 lots.

No direct correlation between the Nb (and Nb/C) and the hot cracking susceptibility of 347 materials can be found. However, as in the case of hot ductility results, the value of 1/2Nb / (30 x C% + 50 x N%) shows an excellent relationship with the TCL and MCL (as shown in Figure 69). When the ratio increases, the TCL at 4% strain also gradually increases for all 347 materials which solidify in the primary ferritic mode. When 1/2Nb / (30C + 50N) is less than about 0.1, the TCL appears to be almost constant. When the ratio is small (< 0.1), other variables can play a significant role in the heat to heat variation. Figures 70 and 71 indicate that when 1/2Nb / (30C + 50N) is less than 0.1, solidification cracking in 347 materials is also strongly dependent upon the P + S (Figure 70) and Si (Figure 71), in addition to Nb, C and N. The TCL increases with an increase in the P, S, and Si contents. However, when 1/2Nb / (30C + 50N) is greater than 0.1, the effect of impurity level (P + S) appears to be minor as compared to that of the relative content of Nb to C and N as shown in Figure 72. Thus, Nb has the predominant influence.

Within the limited variation in ferrite content (1.5 - 5.5FN), the hot cracking susceptibility of all the primary ferritic materials is not a function of the room temperature ferrite content. Figure 73 shows that variation in the TCL at the higher ferrite level appears to

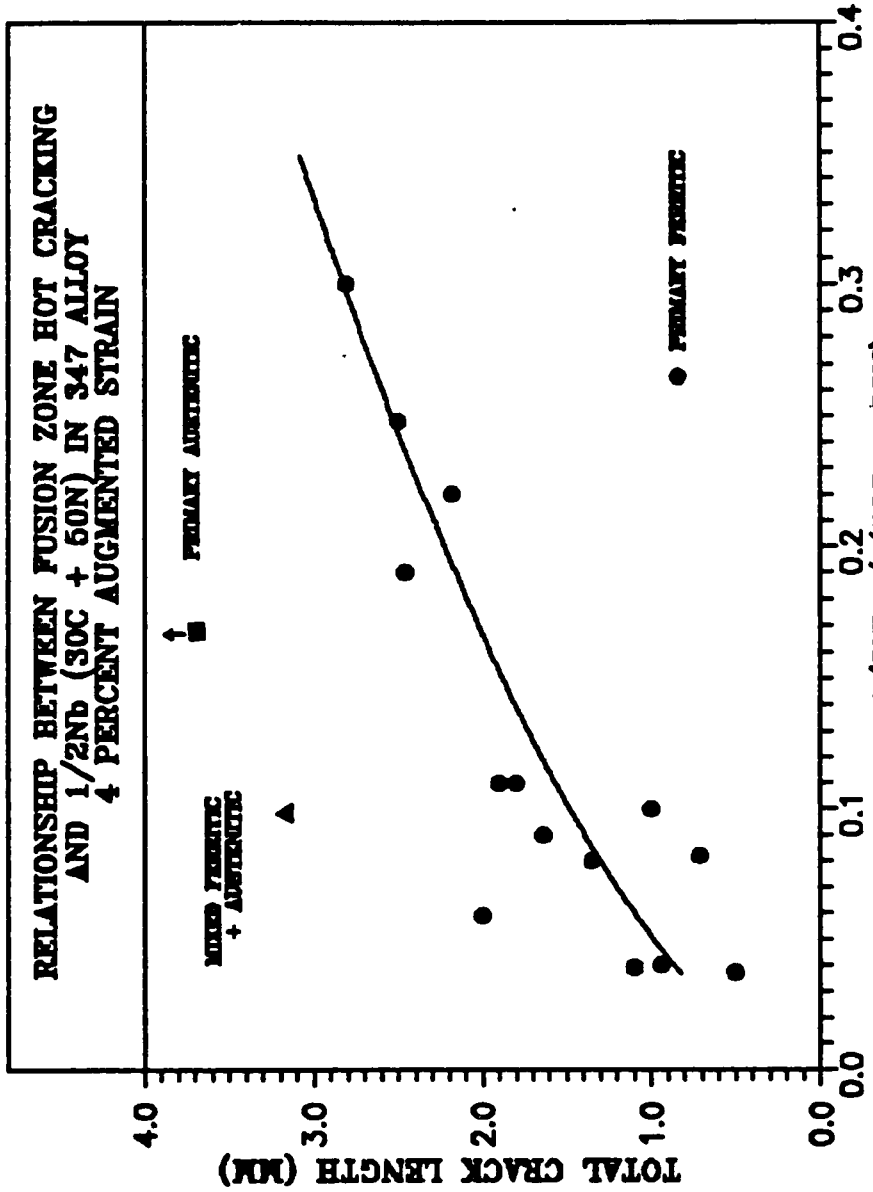


Figure 69. Relationship between fusion zone solidification cracking and 1/2 %Nb / (30 X %C + 50 %N) in type 347.

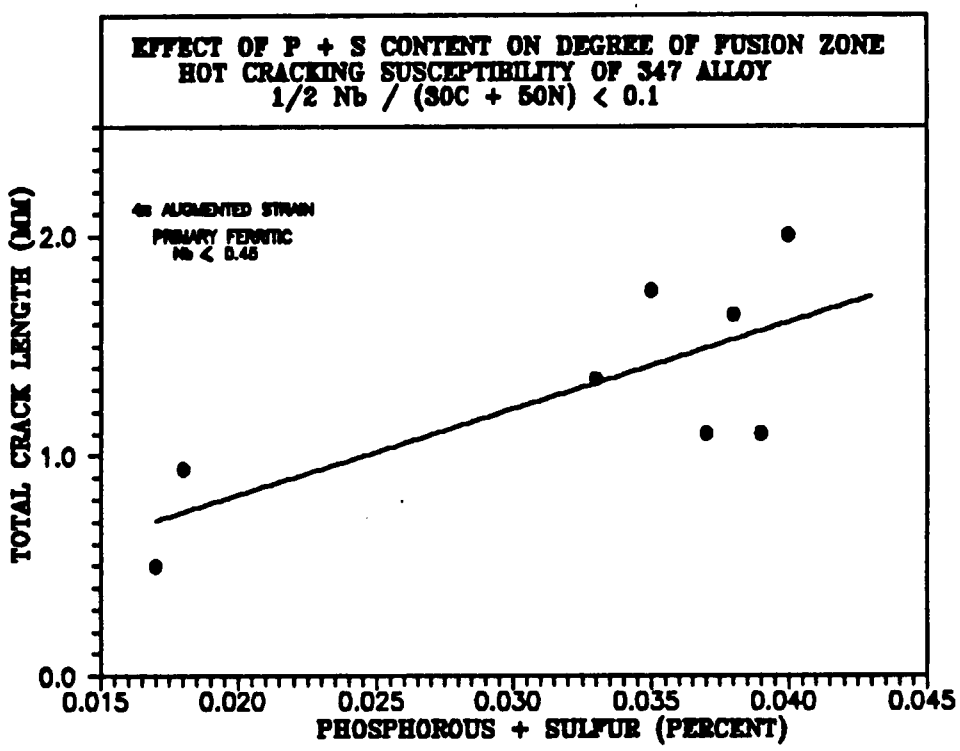


Figure 70. Effect of P + S content on solidification cracking in 347 materials when 1/2 %Nb / (30 X %C + 50 X %N) is less than 0.1

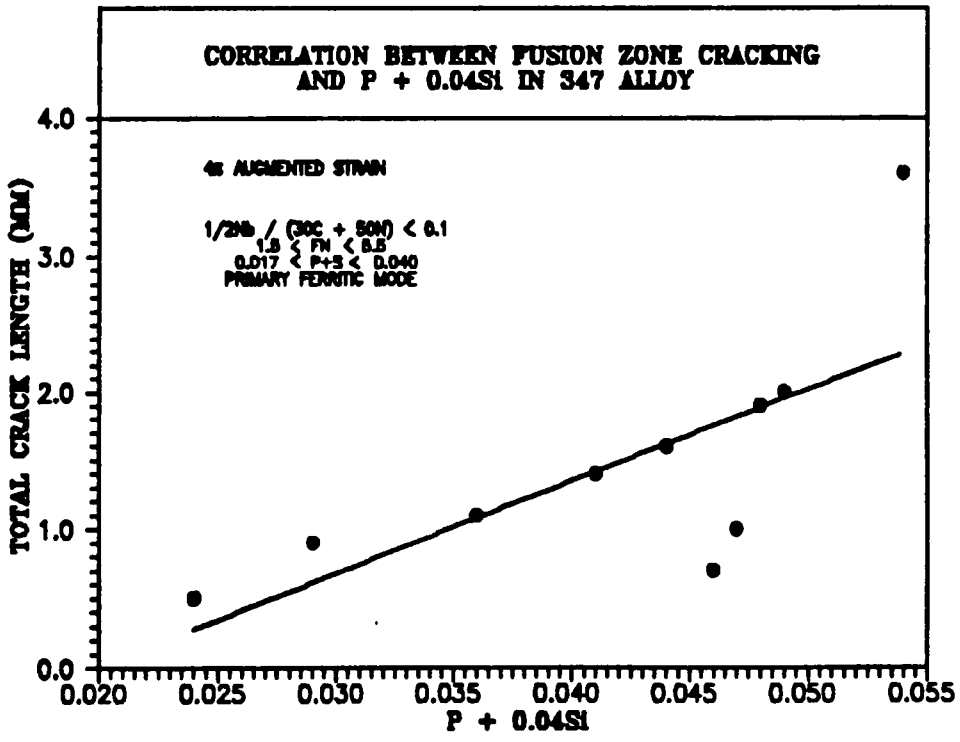


Figure 71. Synergistic effect of P and Si on solidification cracking in 347 materials when 1/2 %Nb / (30 X %C + 50 X %N) is less than 0.1.

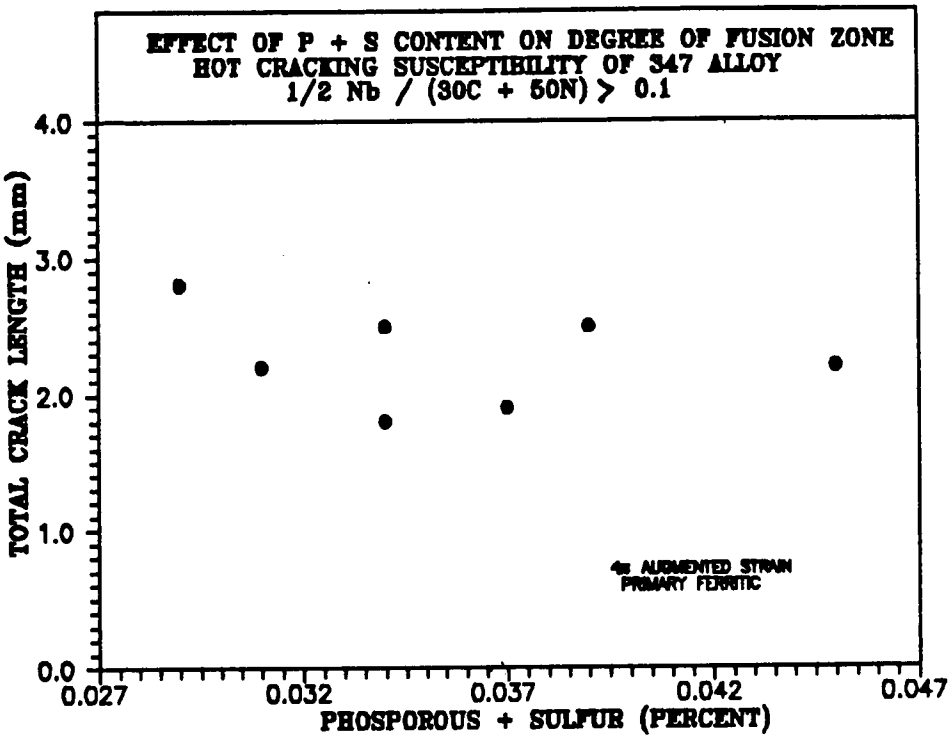


Figure 72. Effect of P + S content on solidification cracking in 347 materials when 1/2 %Nb / (30 X %C + 50 X %N) is greater than 0.1.

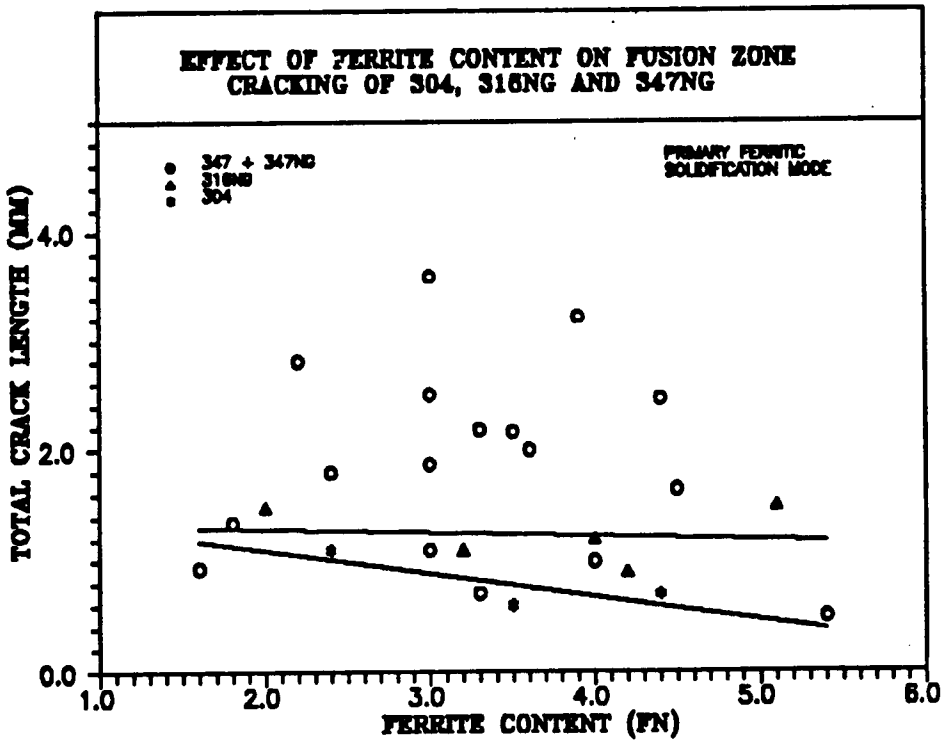


Figure 73. Influence of room temperature ferrite content on solidification cracking in 304, 316, 316NG and 347NG.

be slightly less than that at lower room ferrite, but it is considered negligible.

The above data analyses clearly indicate that solidification cracking susceptibility of austenitic stainless steels, regardless of alloy type, is predominantly a function of the primary solidification mode such that a material solidifying in a primary ferritic mode has a significantly greater resistance to hot cracking than an alloy which has a primary or fully austenitic solidification process. For primary ferritic 316NG, the susceptibility is influenced by the amount of the primary delta ferrite (Cr_{eq}/Ni_{eq}) and impurity level (P + S). However, the Nb to C and N ratio ((1/2Nb / (30 x C% + 50 x N%)) influence hot cracking in type 347. When it is less than 0.1, the "harmful" elements (P, S and Si) also play an important role in the heat to heat variations.

Solidification and Transformation Behavior. Before examining the room temperature microstructure of Varestraint samples, it is very important to understand the high temperature microstructure during solidification, because solidification cracking occurs at or near the solidus temperature. To observe the high temperature solidification microstructure, selected samples (316NG-1 and -7) were rapidly quenched in ice water during welding. The quenched weld metal enables the primary solidification mode to be defined and permits comparison of the high temperature microstructure with that at room temperature (ferrite content and morphology).

The solidification and subsequent solid-state phase transformation behavior of austenitic stainless steel is mainly a

function of the chemistry of the alloy being considered. The Fe-Cr-Ni ternary system is useful for predicting the solidification and transformation characteristics. A pseudo-binary section of the Fe-Cr-Ni ternary system at 70 %Fe (as shown in Figure 74) can be used to predict the behavior of a typical stainless steel upon cooling from the solidification range.

316NG-1 which lies to the right (Cr rich side) of the eutectic triangle solidifies primarily as ferrite when the temperature reaches the liquidus temperature. As the temperature decreases within the solidification range, ferrite formation increases and the remaining liquid is enriched in nickel. When the final stage of solidification begins, the Ni enriched liquid in the interdendritic regions forms austenite by the eutectic/peritectic reactions (depending upon the composition of the last solidifying liquid). Following solidification, 316NG-1 enters the single phase ferrite regime. Within this ferrite region, diffusion is rapid and much of the elemental partitioning resulting from solidification may be reduced to some extent. Upon further cooling below T1 (but above T2) in Figure 74, this alloy enters the austenite-ferrite two phase region and a gradual transformation of ferrite to austenite occurs by a solid-state diffusion controlled mechanism. When the temperature falls below T2, the untransformed ferrite will further transform to austenite which is the stable phase at room temperature according to the phase diagram. However, nonequilibrium solidification and the transformation typical of the weld metal microstructure will normally retain some residual ferrite at room temperature.

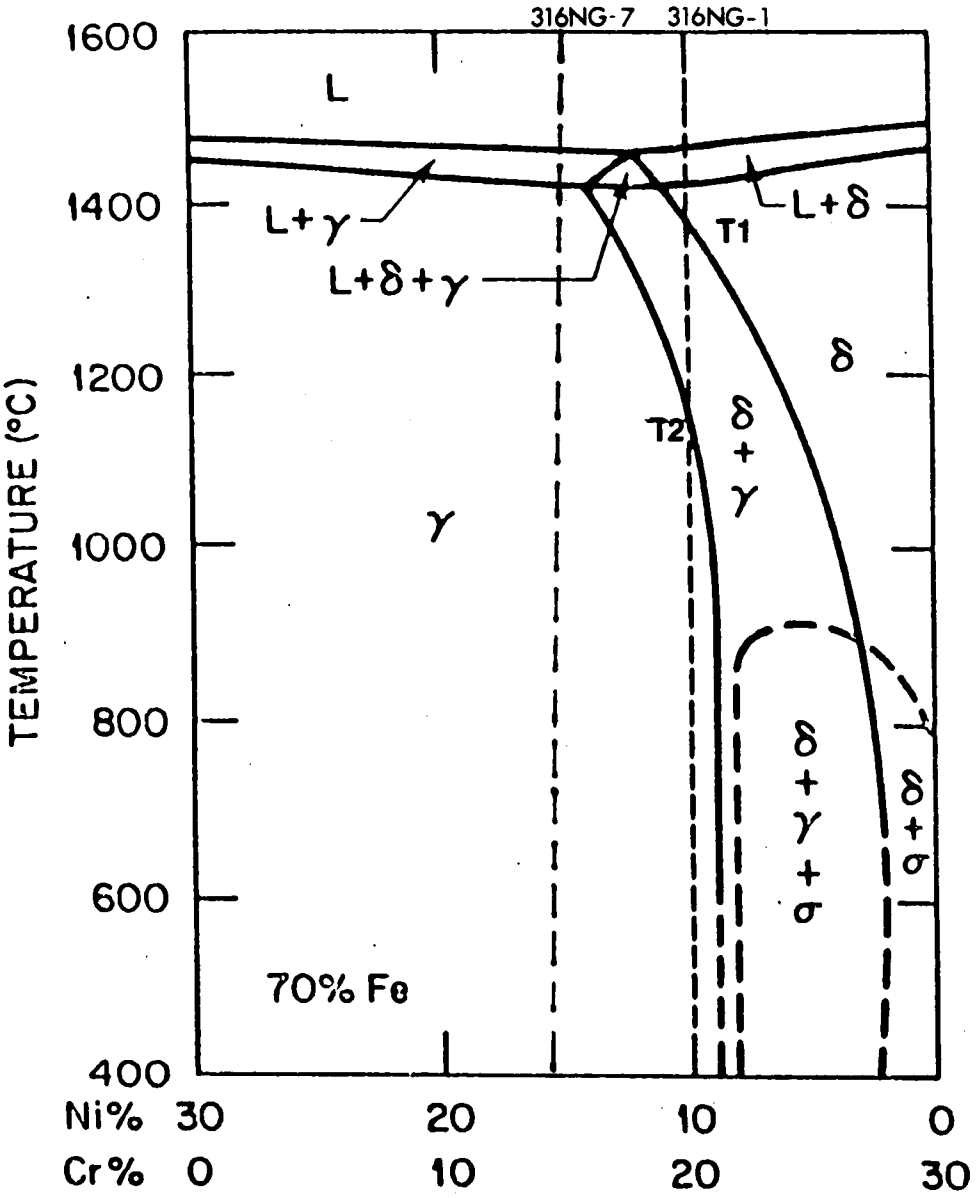


Figure 74. A schematic pseudo-binary section at 70 %Fe of the Fe-Cr-Ni ternary system.

316NG-7, which is on the high nickel side of the eutectic triangle, will solidify in a primary austenitic mode. However, as in the case of 316NG-1, the last solidifying liquid, which is enriched in chromium may form ferrite through the eutectic/peritectic reactions, depending upon the extent of segregation. Following solidification, interdendritic ferrite will transform to austenite, because below the solidus temperature, only austenite is stable. Upon further cooling below the solidus, segregated elements partitioned during solidification will be gradually reduced until temperature reaches a sufficiently low temperature where the diffusion rate is minimal. Therefore, from the pseudo-phase binary diagram, 316NG-1 is expected to have a duplex structure of mixture of delta ferrite at the core of dendrites and austenite in the interdendritic region. 316NG-7 will generally have a fully austenitic structure, if the last solidifying liquid is enriched sufficiently in Cr some eutectic delta ferrite may also be observed along the interdendritic region.

The macroscopic appearance of an as-quenched weld sample is shown in Figure 75. The instantaneous position of the solidifying solid-liquid interface at the moment of quenching is clearly seen. It also can be noted that the instantaneous liquid weld pool was expelled during rapid quenching. Higher magnification microstructures at the instantaneous solid-liquid interface regions of 316NG-7 and 316NG-1 are shown in Figure 76a and 76b, respectively. In the etched condition (diluted aqua regia), delta ferrite appears dark and austenite has a light appearance. 316NG-7 (Figure 76a) shows that the well defined lightly etched dendrite stems had advanced to the

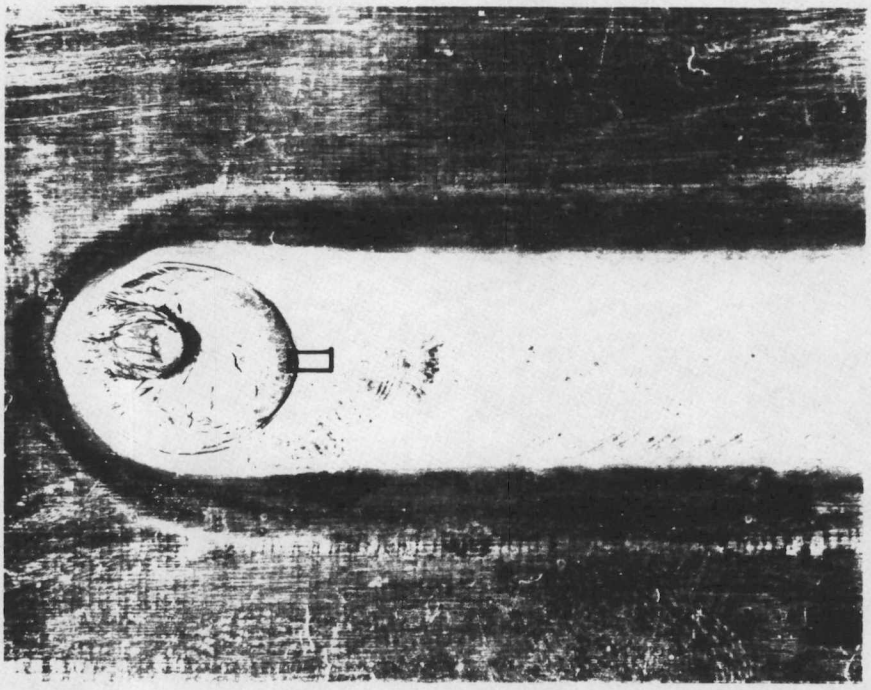


Figure 75. Macroscopic appearance of the rapidly quenched weld sample.

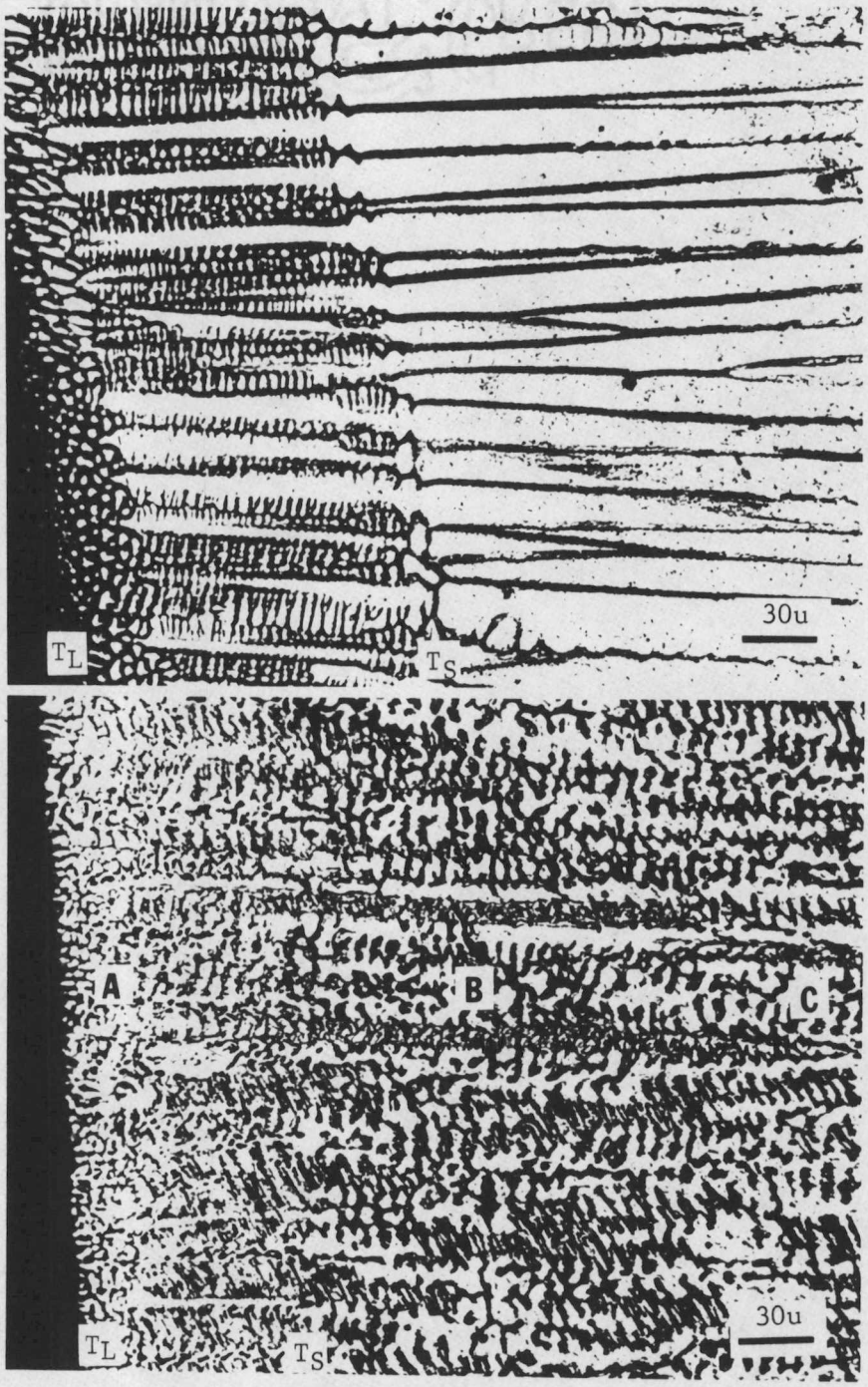


Figure 76. Typical microstructures near the solidification front in the rapidly quenched samples, a) 316NG-7 and b) 316NG-1.

solidification interface, indicating that the cellular dendrites solidified as austenite in the early stage of the solidification (primary austenitic mode). The darkly etched regions between primary and secondary arms adjacent to the S-L interface are not ferrite but are indication of the liquid at the moment of sudden quenching in ice water and have retained their own segregation pattern due to rapid cooling. However, for 316NG-1 (Figure 76b), the darkly etched dendrites are close to the solidification front revealing a primary ferritic solidification mode. Figure 76 further reveals that the solidification temperature range is wider for the primary austenitic 316NG-7 than that in the primary ferritic 316NG-1. The approximate solidification range is shown by T_L (liquidus) and T_S (solidus) in Figure 76.

At higher magnification, the microstructures near and slightly away from the solidification front for both 316NG-7 and 316NG-1 are shown in Figures 77 and 78, respectively. Figure 77 clearly shows that the last solidifying liquid drops which are enriched in phosphorous and sulfur rejected from the primary austenite phase during an earlier stage of solidification before quenching. The solute enriched "liquid drops" are indicated by arrows.

Figure 76 further reveals that the region near the solidification front (A) has a ferrite content greater than 60% at the high temperature at the moment of the quenching. In regions behind the solidification front (B and C), which were at lower temperatures than region A at the moment of rapid cooling, the ferrite level is less due to partial transformation of ferrite to austenite during

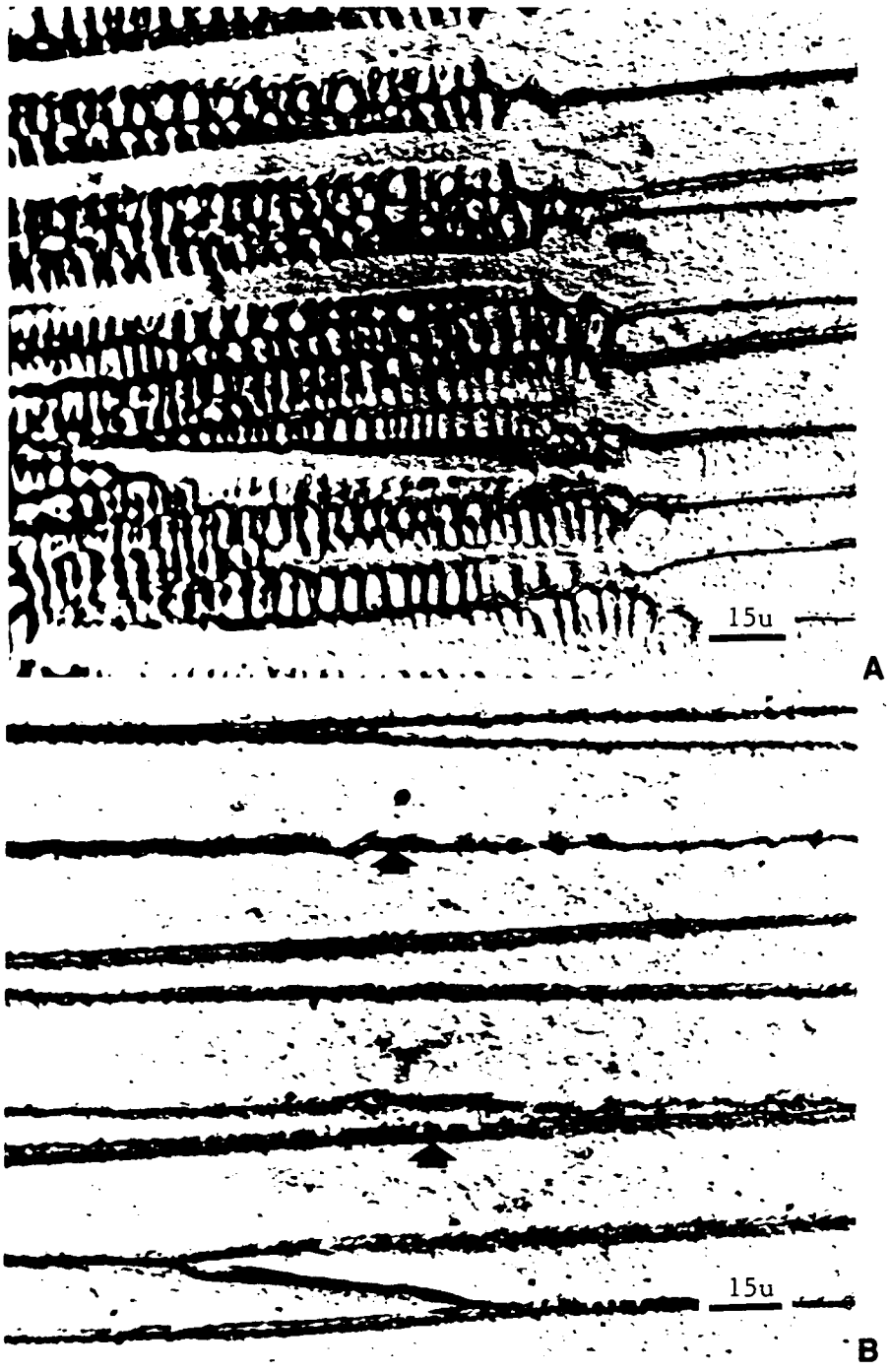


Figure 77. Higher magnification microstructures in Figure 76a, a) just behind of the solidification front and b) some distance from the front.



Figure 78. Higher magnification microstructures in Figure 76b, a) just behind of the solidification front and b) some distance from the front.

subsequent cooling after the solidification. Further the ferrite morphology also changed from a lacy type at high temperature during cooling to a vermicular type in the lower temperature regions, well away from the solidification front. In the as welded condition (normal cooling), only the vermicular morphology was observed in this heat.

The most important features found from examination of the quenched samples show that the solidification temperature range of the primary austenitic weld metal is wider than that for the primary ferritic alloy. Further, the low melting "liquid drops" which are enriched in phosphorous, silicon and sulfur are also more extensive and continuous in the austenitically solidified weld metal. Therefore the hot cracking temperature range (liquidus - effective solidus temperature) is more wider for the fully austenitic material. Further, the "liquid drops" in the interdendritic regions in the primary ferritic alloy appear to be confined to the austenite which formed during the last stage of solidification by eutectic/peritectic reactions, as found by Matsuda et al. (101).

STEM analyses were conducted on the thin foils which were obtained from heats 316NG-D and 347NG-E. The nominal compositions of 316NG-D and 347NG-E are almost identical to those of 316NG-7 and 316NG-1, except for the niobium in 347NG-E. Therefore, the solidification behavior of 316NG-D and 347NG-E can be assumed to be the same as that of 316NG-7 and 316NG-1 as shown in the pseudo-binary diagram in Figure 74 (page 212).

Before discussing STEM analysis, it has to be recalled that the data aquisition program in the STEM calculates the composition from the integrated intensities using the Cliff-Lorimer technique and the background noise was subtracted from the spectrum before the calculation was conducted. Further, the absorption effect and the thickness variation were not considered for chemical analysis. However, because the main concern in this study is the variation of concentration rather than the absolute values, a small deviation from the actual values can be tolerated. For a consistency, the bulk chemical composition measured by an "area" STEM analysis was used in comparison with the "spot" analysis.

Figure 79 shows the TEM microstructure from 316NG-D. The cell boundaries are clearly discernible with a dark appearance due to a mass absorption contrast resulting from the local thickness variation and piled-up dislocations. No delta ferrite can be found along the cell boundaries in this particular micrograph. However, other areas in the same foil, which are not shown here, revealed a small amount of eutectic ferrite. The STEM analysis was conducted across the cell, A to B as shown in Figure 79. The chromium and nickel distributions across the cell core and boundaries are given in Figure 80. The bulk (average) Cr and Ni concentrations measured by the "area" STEM analysis are also given with dotted lines.

The cell boundaries are enriched in Cr. The measured Cr content at the cell core is 17.2% and increases to 19% in boundaries. The Ni concentration is also enriched in the cell boundary, but to a lesser extent as compared to Cr. Ni increased from 14.8% at the cell core to

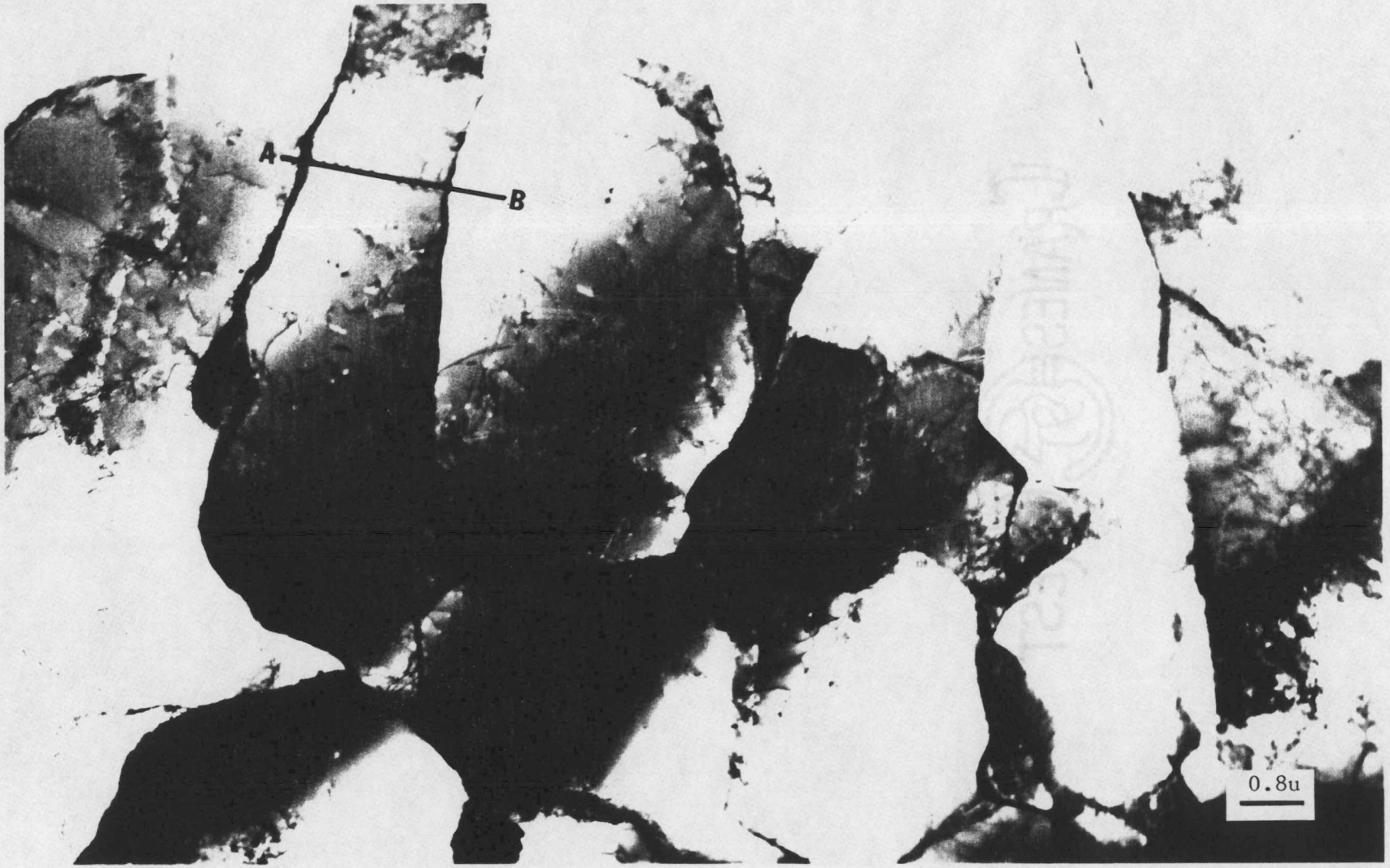


Figure 79. TEM microstructure in 316NG-D, revealing a fully austenitic substructures.

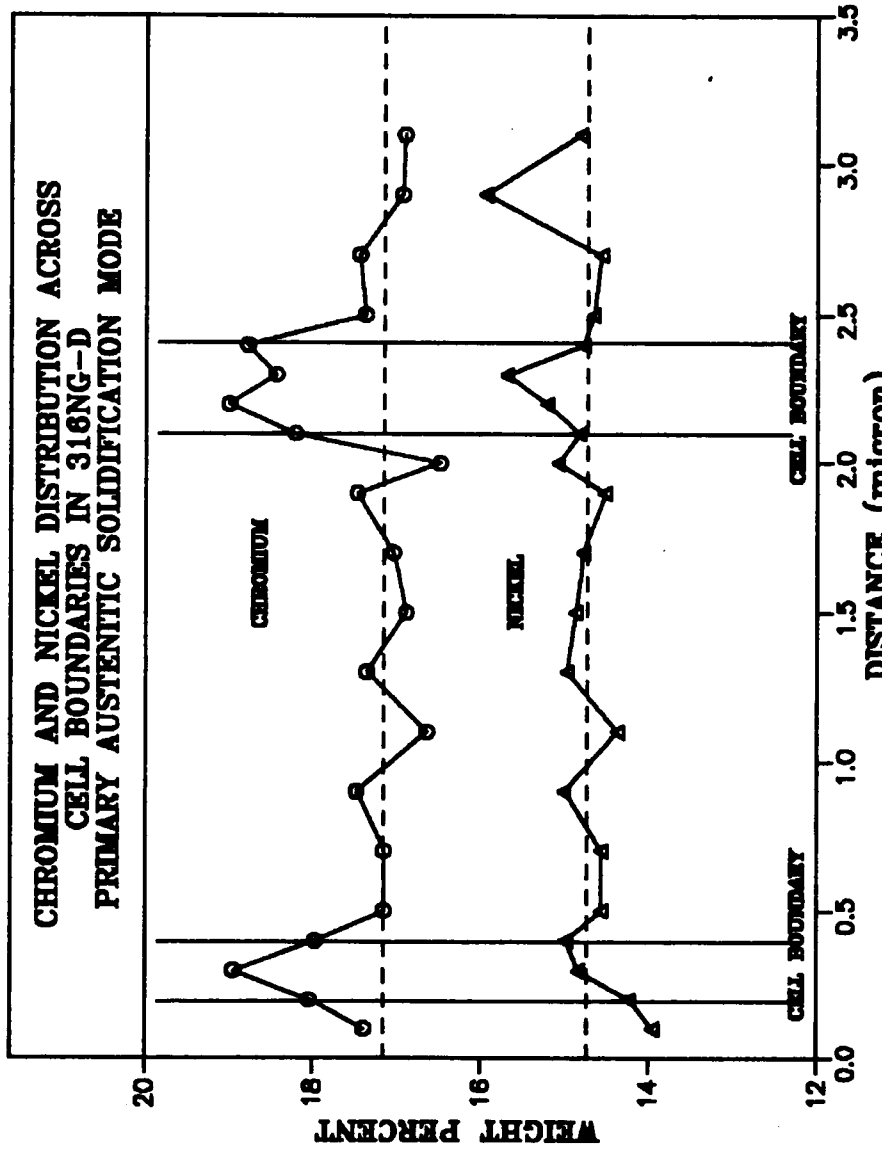


Figure 80. STEM chromium and nickel concentration profile across the cells through A-B in Figure 79.

15.8% in the cell boundary. It is interesting that this observed segregation pattern does not occur in the manner as that which is predicted from the constant Fe section of the pseudo-binary diagram. The diagram predicts Ni-enriched and Cr-depleted cell core, and Cr-enriched and Ni-depleted cell boundaries in 316NG-D. The Cr distribution is similar to the prediction that it is depleted within the cell center region and enriched in the cell boundary. However, the distribution of Ni has the same trend as Cr (although to a lesser extent), which is opposite to the prediction from the pseudo-binary diagram. The Cr and Ni distributions found in this study was also similarly observed by other investigators (69).

According to the Cr and Ni distributions, the Fe concentration is enriched in the cell core and depleted in the cell boundary, indicating a variation in Fe concentration across the dendrite. Therefore, the prediction of Cr and Ni distributions from the pseudo-binary diagram sectioned at a constant Fe can sometimes be misleading.

Further, from STEM analysis, it is possible to estimate the approximate solidification path of the primary austenitic 316NG-D. The composition of the initial and last liquid to solidify can be estimated from the measured composition within the dendrite cores and boundaries. The values of interest are the greatest and the least composition of each element. In the cell core, the Cr and Ni contents are 16.5% and 14.3% and the corresponding Fe concentration is 69.2%. While, the concentration in cell boundary is 19.2 %Cr, 15.8 %Ni and thus 65.2 %Fe. The initial and final liquid compositions are on the Fe-Cr-Ni ternary diagram in Figure 81. it is clear that the

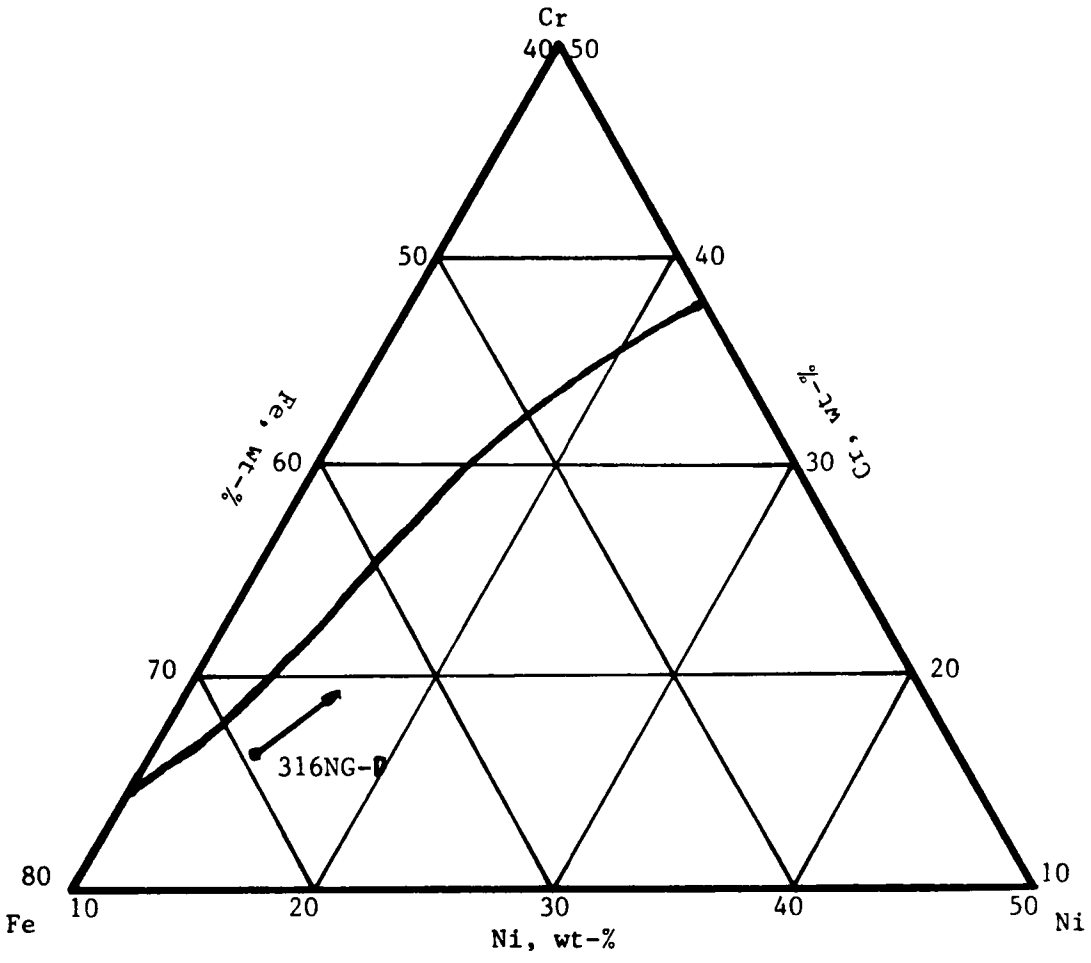


Figure 81. Liquidus surface of the Fe-Cr-Ni ternary diagram showing approximate solidification path of the primary austenitic 316NG-D.

solidification path of the primary austenitic weld metal extends away from the Fe corner and generally toward the Cr corner. It also extends toward the slightly increasing Ni region and it does not intersect the eutectic composition, resulting in a ferrite free fully austenitic microstructure at room temperature. However, as mentioned before, in some other areas in the same foil, a small amount of interdendritic ferrite was found, indicating localize variations in microsegregation.

A higher magnification micrograph of the cell boundary area in Figure 79 is shown in Figure 82. The cell boundaries are decorated with dislocations. A globular shaped particle at the cell boundary is noted and STEM analysis reveals that the particle is a phosphide $(Fe, Cr)_3P$. In this particular micrograph, precipitation of sulfide or other second phases can not be detected, as may be expected from the low sulfur content (0.001%) of 316NG-D. However, as will be shown later, some small globular sulfides were found in the interdendritic regions during SEM and EDAX evaluation.

Vermicular ferrite typical of all primary ferritic materials evaluated in this study is shown in Figure 83. This particular TEM microstructure is from a sample of 347NG-E. STEM analysis was performed across the primary dendrite stem (C - D) as shown in Figure 83. The Cr and Ni profiles across the dendrite are given in Figure 84. Within the austenite, the Ni is maximum at approximately 12% in the cell boundaries and decreases gradually as interface boundary is approached and reaches a minimum of about 9% adjacent to the interphase boundary. However, the significant Ni decrease region is

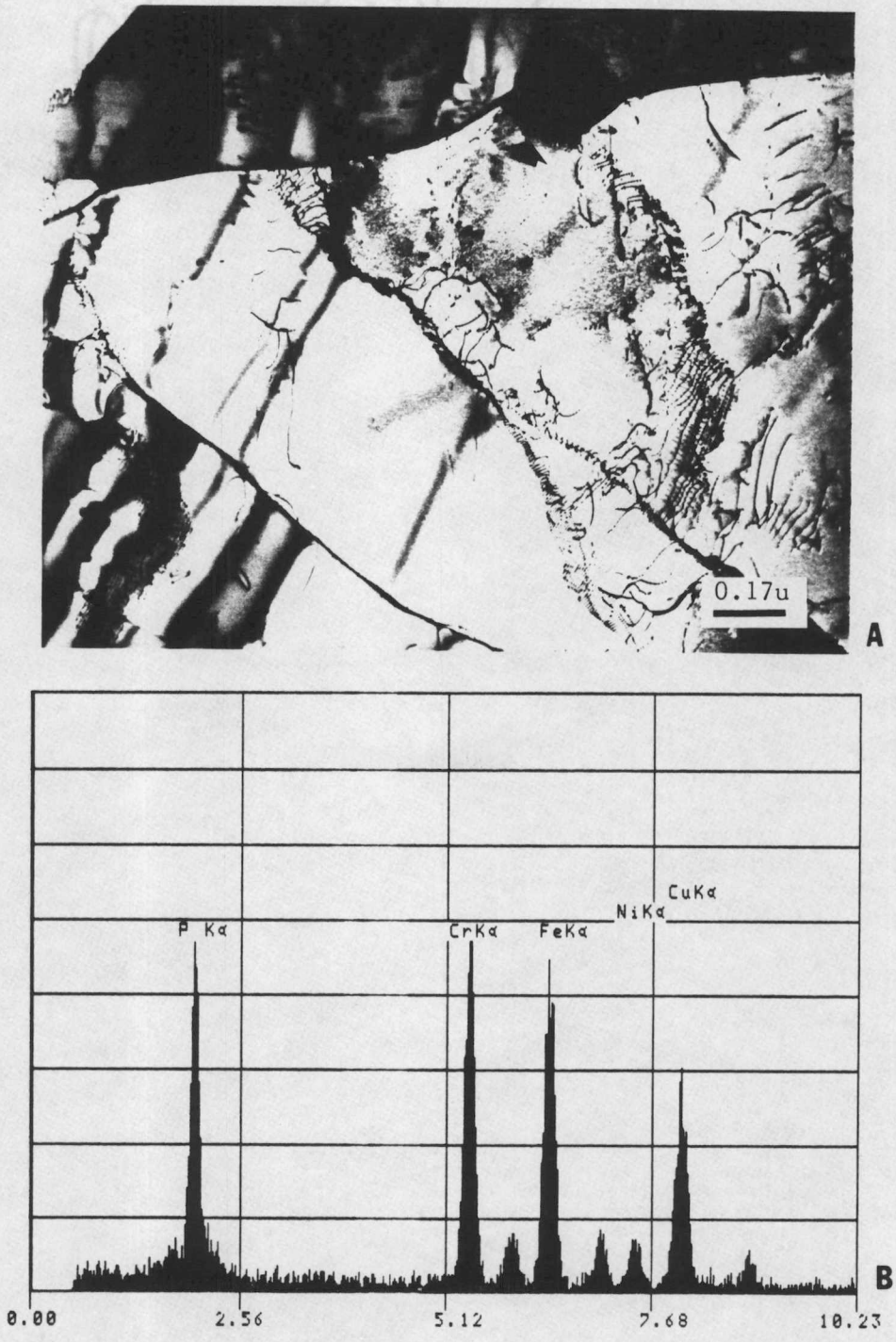


Figure 82. A higher magnification of the cell boundary area in Figure 79.

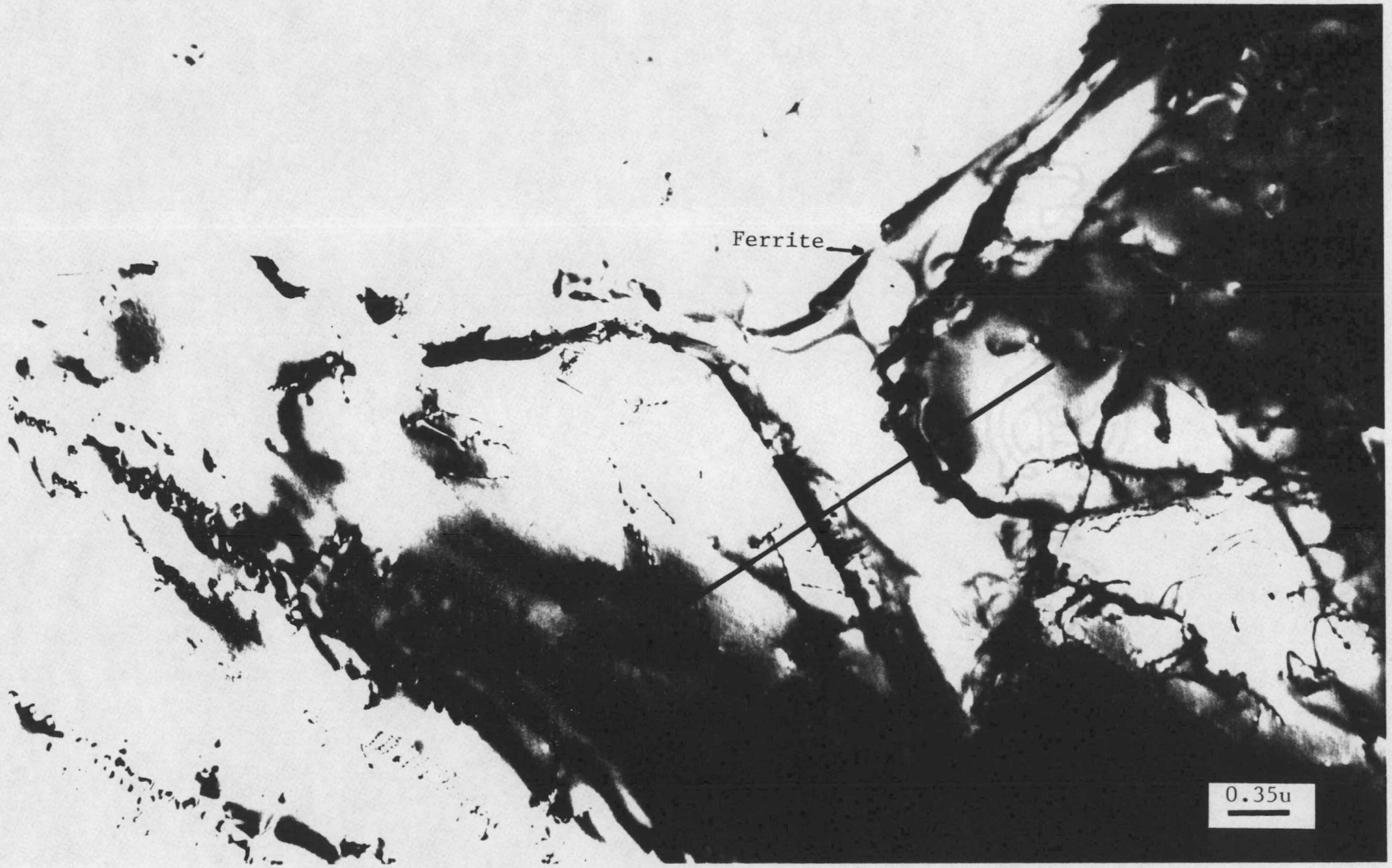


Figure 83. TEM microstructure in primary ferritic 347NG-E.

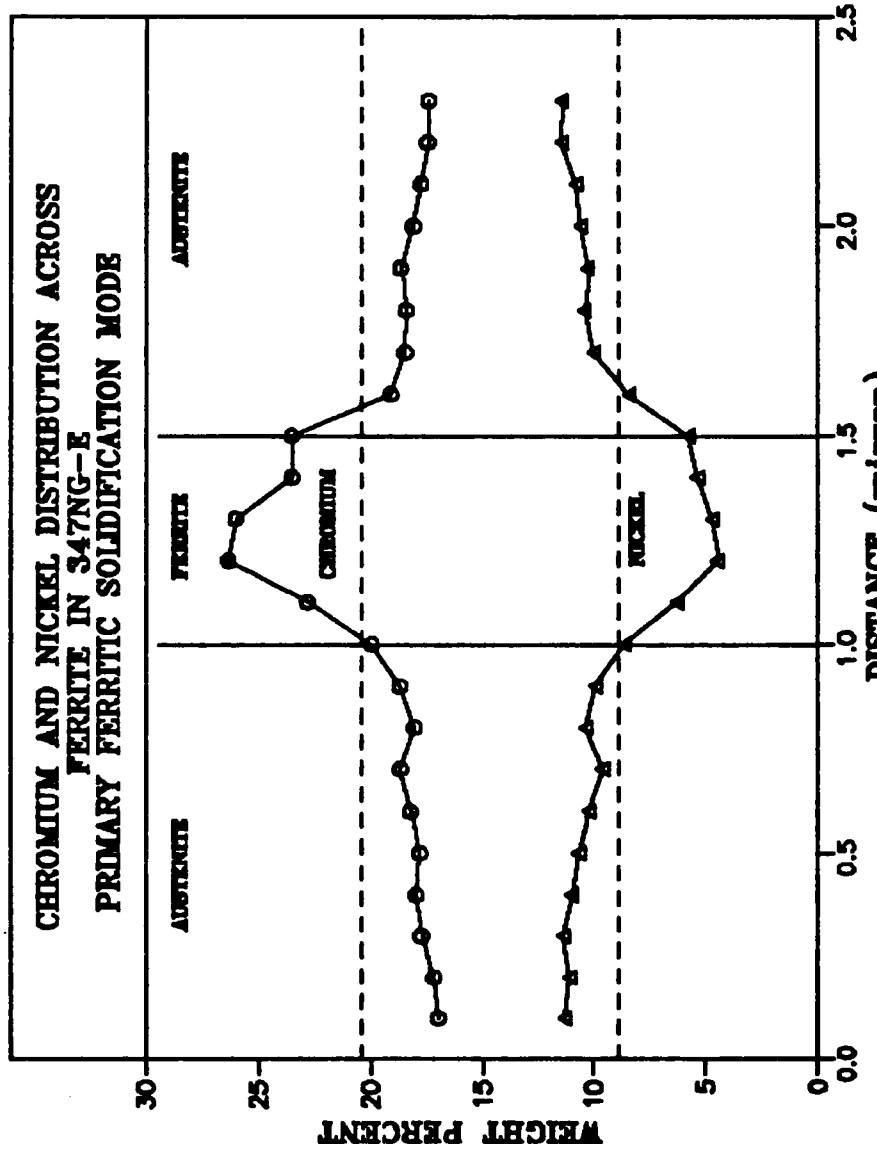


Figure 84. STEM chromium and nickel concentration profile across the primary dendrite ferrite through C-D in Figure 83.

within about 0.1 - 0.2um of the interphase boundary. In regions away from the boundary the Ni content is fairly uniform. The Cr concentration is a minimum of about 17% in the cell boundaries and reaches maximum of 20% near the austenite-ferrite interphase boundaries. Here again, as in the case of Ni, the Cr concentration is more or less uniform in austenite. The Cr content increases within 0.1 - 0.2um of the interphase boundary. Within the ferrite, composition gradients exist but are not symmetrical. The Ni content decreases from approximately 9% at one interphase boundary to a minimum of 5% at the center of the ferrite. The Cr concentration within the ferrite increases from about 20% at one boundary to the maximum content of approximately 26.5% at the center of the ferrite. Unlike the case for primary austenitic, the corresponding Fe concentration is uniform from the core of the dendrite to the dendrite boundary. Therefore, according to the STEM analysis, the solidification path of the primary ferritic 347NG-E extends in a increasing Ni and decreasing Cr direction with maintaining constant Fe. The STEM analysis agrees well with the prediction from the pseudo-binary diagram.

The higher magnification microstructure in Figure 85, which is from the same foil in Figure 83, reveals precipitates along the solidification grain boundaries and some lathy type ferrite at the bottom right of the micrograph. These precipitates are sulfides, phosphides and niobium carbo-nitrides as indicated by the STEM analyses shown in Figure 86. The phosphide and sulfide are smaller and of globular shape as compared to the niobium carbo-nitride which

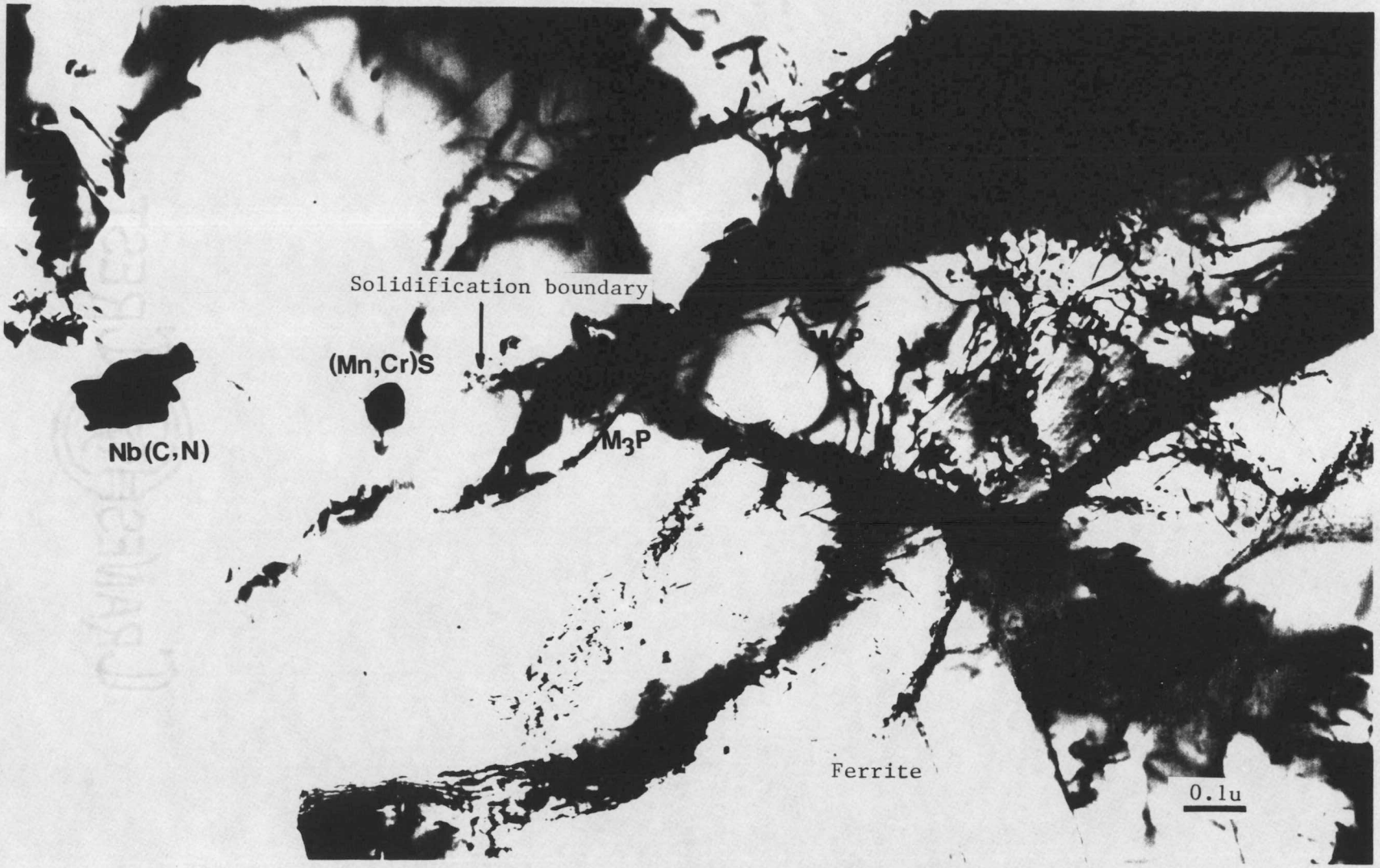


Figure 85. A typical TEM microstructure of the solidification grain boundary in 347NG-E.

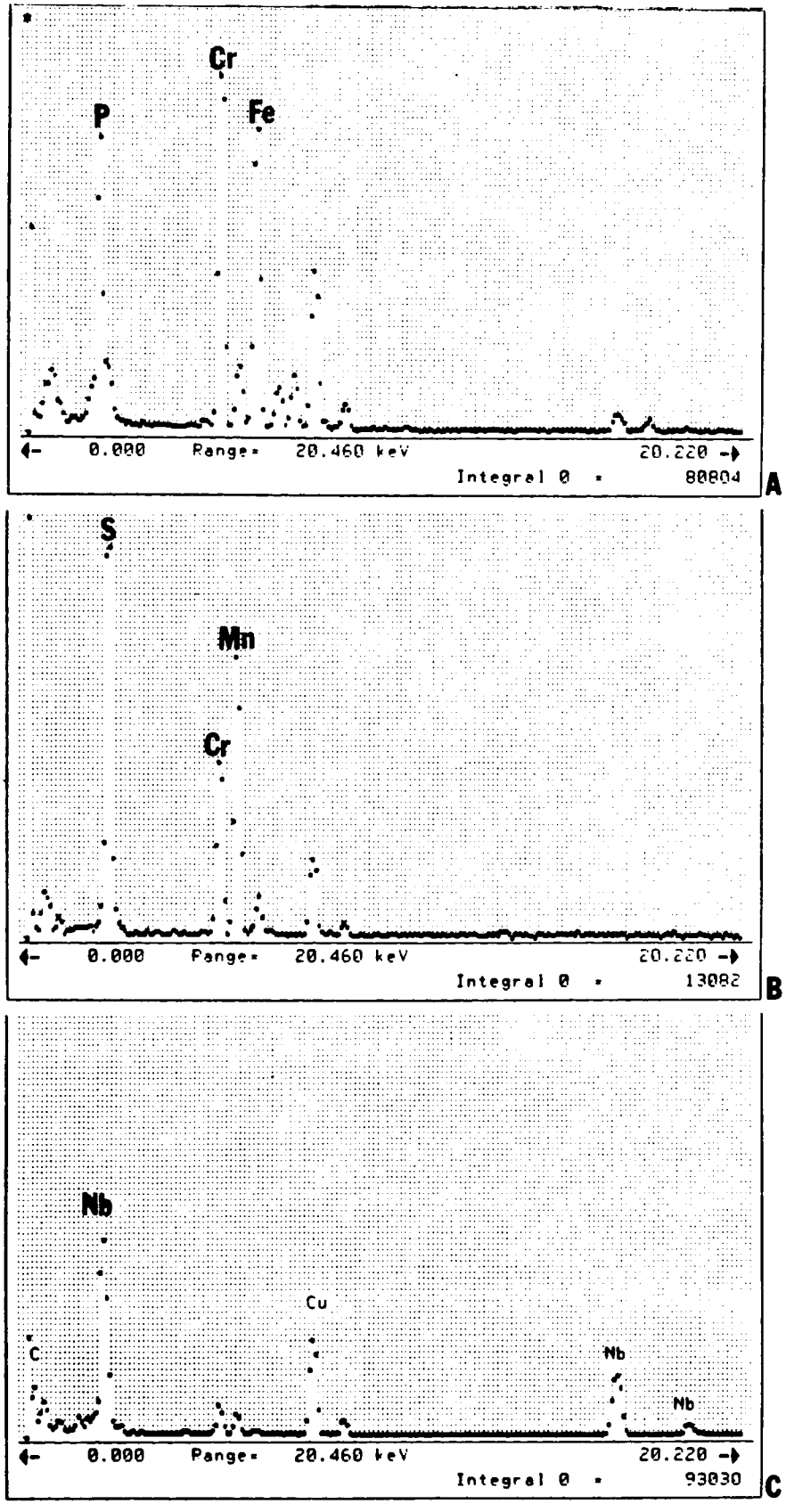


Figure 86. STEM analyses on the particles along the boundary in Figure 85.

has a blocky morphology. Therefore, although the primary ferrite scavenges some S, P and Nb due to their higher solubility in ferrite, these "harmful" elements still segregate into the dendrite and solidification grain boundaries, resulting in the formation of low melting second phases (sulfides, phosphides and Nb(C,N)-austenite eutectic), which in turn provide favorite sites for hot crack initiation and propagation.

Metallographic Characterizations

With a knowledge of solidification behavior and the segregation characteristics of a typical primary austenitic 316NG and primary ferritic 347NG, optical, SEM (EDAX), TEM (STEM) metallographic and fractographic examination of the Varestraint samples were performed. The micrographs and fractographs shown in the following figures are illustrative of the total effort made to characterize the occurrence and mode of cracking.

The location of cracking in a Varestraint tested sample, typical of those in this study, is illustrated in Figure 87: the various crack locations; fusion zone, weld metal HAZ and base metal HAZ are indicated. Many fusion zone solidification cracks are noted to be aligned perpendicular to the instantaneous position of the solidifying interface at the time of strain application and also along the columnar grain boundaries. However, small cracks in both the weld metal HAZ and base metal HAZ are not clear in this macrograph.

316 Nuclear Grade. Metallographic examination of 316NG was carried out on several heats, but heat 316NG-7 and 316NG-D revealed

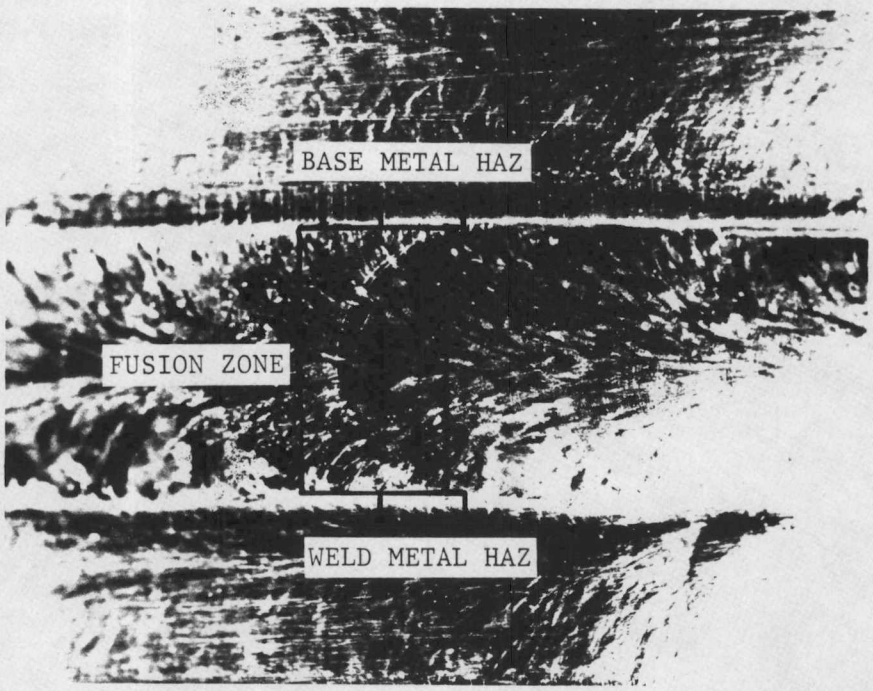


Figure 87. Typical surface of an evaluated Varestraint sample showing the various crack location regions.

the widest range of structures and received the majority of the attention.

Figure 88 illustrates the appearance of typical fusion zone hot cracks for the fully austenitic heat from a sample extracted parallel to the Varestraint test surface. The location of solid-liquid interface at the instant of straining is shown by the dashed line. It is clear that the cracking is intergranular and/or interdendritic (a fine cellular dendritic structure is present for the welding conditions used in this study). The grain boundaries can be distinguished by changes in the direction of the cellular dendritic structure as growth proceeds. However, the location of the room temperature grain boundaries may be different from the solidification grain boundaries which are defined by the cells and cellular dendritic orientation. This phenomenon is clearly shown in Figure 89 which is taken from the crack tip region in Figure 88. The solidification grain boundary migrated from the original position and is noted to cut across several cells. The exact reason for grain migration is not known, but it may be due to the reduction of total grain boundary energy by forming straighter grain boundaries (less boundary area). Kujanpaa et al. (89) postulated that grain boundary migration could be driven by plastic strain induced by residual stresses due to solidification shrinkage and thermal strains. Figure 89 further reveals that the migrated boundary seems to be pinned by a second phase which is location in the original solidification boundary. The second phase may be a low melting liquid phase at the time of grain boundary migration, such that when the augmented strain applied, the

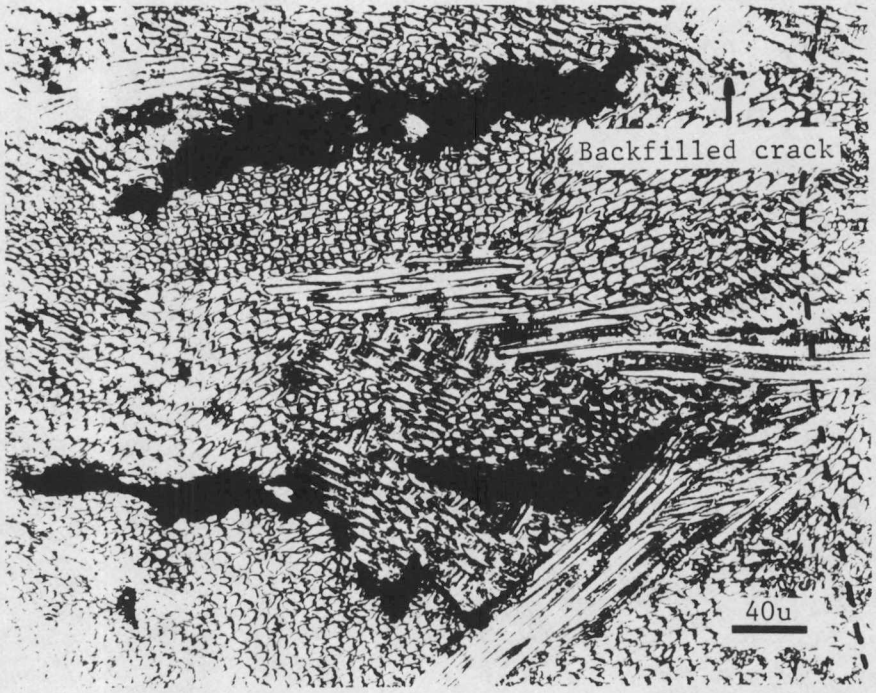


Figure 88. Solidification cracks typical of the fully austenitic sample extracted parallel to the Varestraint test surface, 316NG-7.

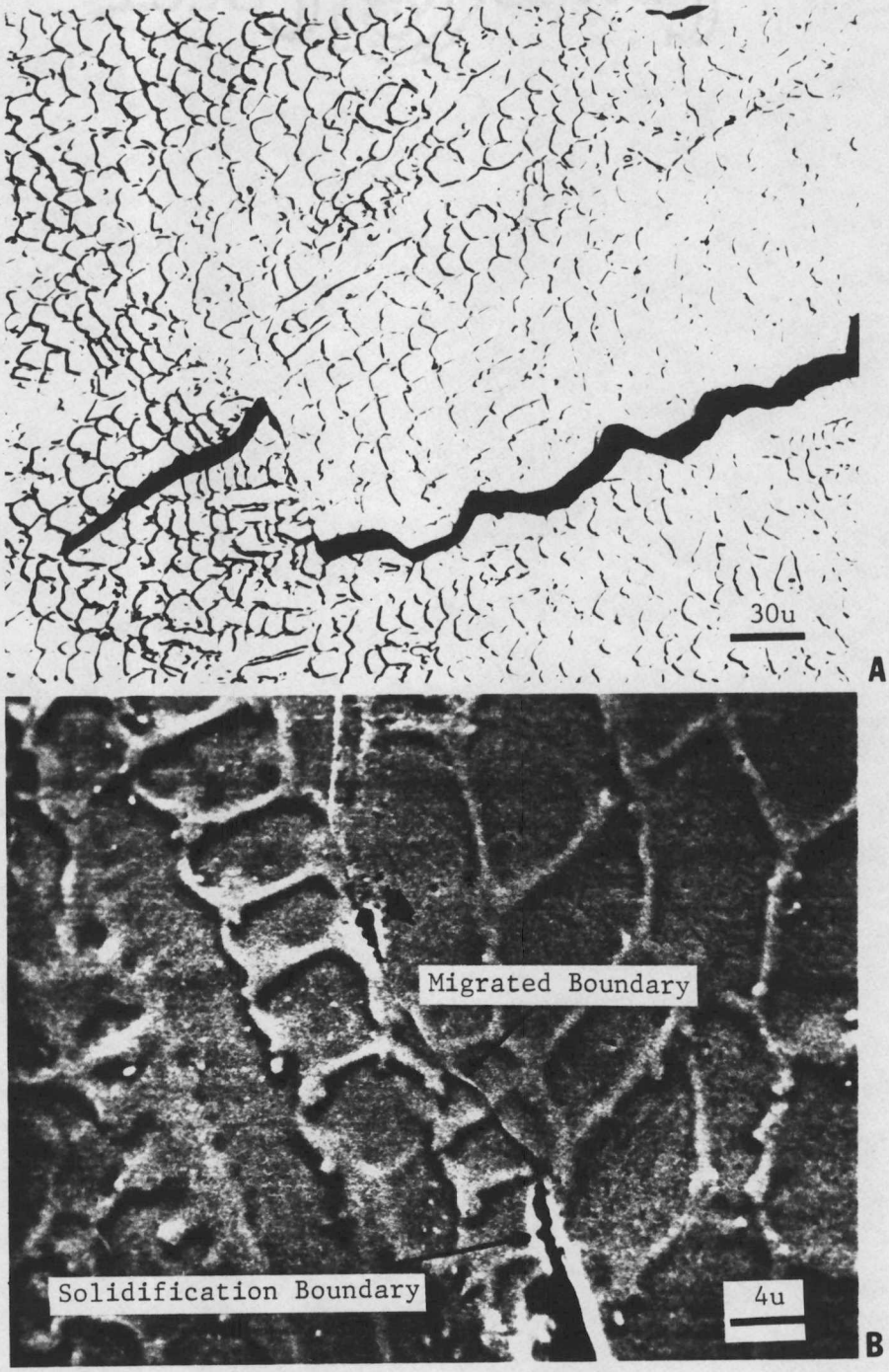


Figure 89. Higher magnification of the crack tip region in Figure 88.

grain boundary separation occurred at this small liquid film. Thus, at room temperature, only a small crack can be found as indicated in Figure 89. The solidification crack appears to have propagated along the migrated boundary which is more or less straight.

Figure 88 further reveals that the high temperature portion of hot cracks (near the instantaneous solid-liquid interface) appears to be backfilled. The detailed evaluation of backfilled solidification cracks in both the primary ferritic and austenitic solidification mode weld metals will be discussed later.

Figure 90 shows an SEM micrograph of the interdendritic region together with the EDAX spectra of the "white" microconstituents in Figure 90a. It is evident that these microconstituents are enriched in phosphorous and sulfur, confirmed as phosphides $(Fe,Cr)_3P$ and sulfides (Mn,Cr)S by STEM analyses of carbon extraction replica. Both phosphides and sulfides have a globular morphology and are about 0.4 - 0.5um in diameter. EDAX analysis in the regions away from the particles revealed that the interdendritic and grain boundary regions are also enriched in Si, Cr and Mo as compared to the grain matrix, indicative of microsegregation during solidification.

347 Nuclear Grade. All 347 materials, except 347L, evaluated in this study contained fusion zone ferrite at room temperature. 347NG-E experienced the greatest extent of cracking and thus best serves to illustrate microstructural features.

In general, cracking in 347 materials are similar in morphology to that of 316NG.

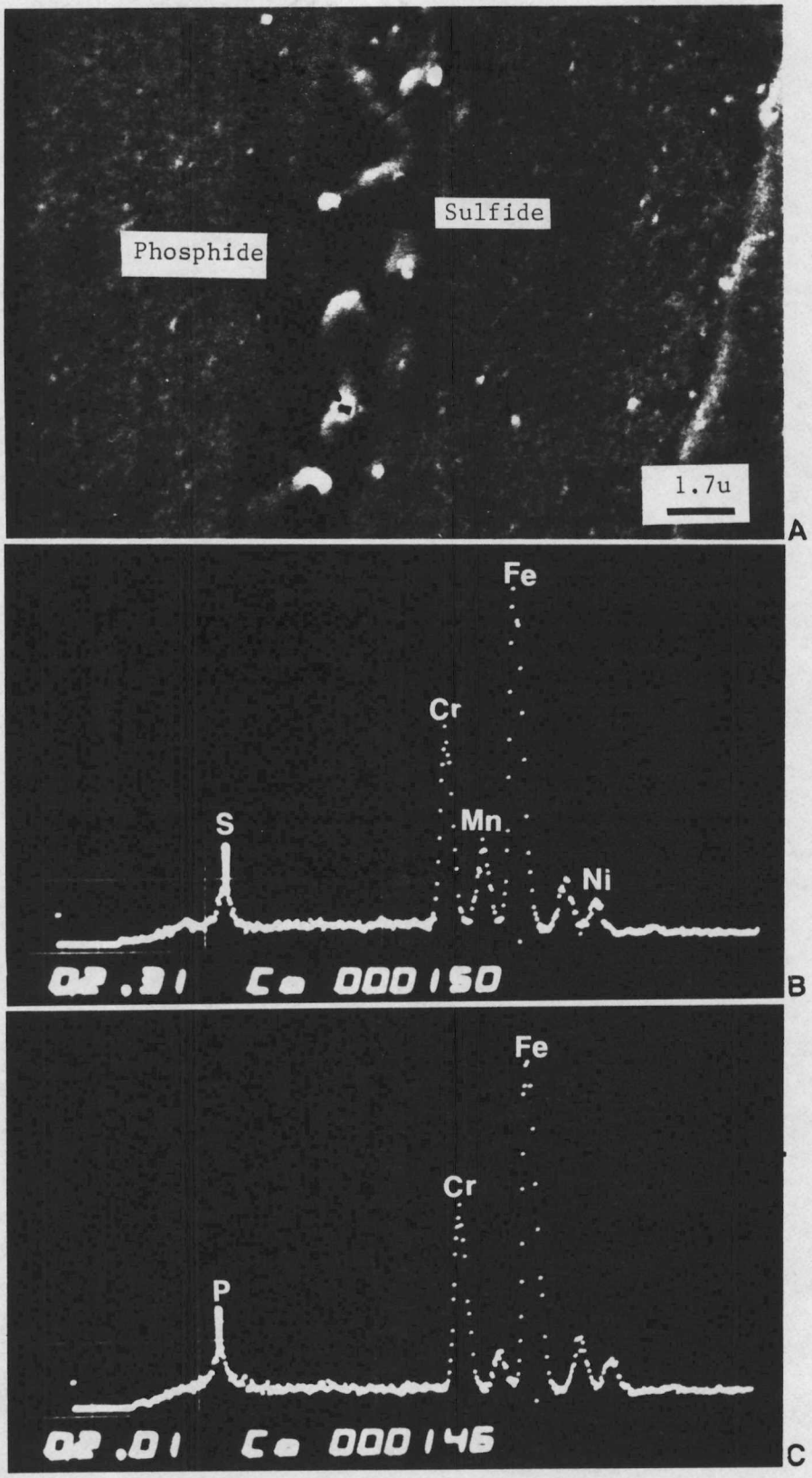


Figure 90. SEM micrograph of the interdendritic region in the fully austenitic weld and EDAX analysis on the white microconstituents in the interdendritic region.

Figure 91 shows fusion zone cracks in 347NG-E which are intergranular in a relatively fine austenite/ferrite matrix. The location of ferrite at the core of the dendrite arms indicates that this alloy solidified as ferrite during the early stage of freezing. As compared to the cracks in the fully austenitic microstructure (Figure 88), the cracks in the primary ferritic 347NG-E have a more pronounced branched morphology and are somewhat narrower. The microstructure at higher magnification (Figure 91b) shows that cracks propagated along migrated boundaries which coincides with interphase boundaries between austenite and ferrite. "White" appearing microconstituents along the edge of the crack and interphase boundaries can also be noted. EDAX analysis indicates that the "white" particles are enriched in Nb. The morphology of these constituents are shown in the carbon extraction replica TEM micrographs in Figure 92. The microconstituent in the grain boundary in Figure 92b has an eutectic type lamellar structure, indicating that these niobium carbo-nitrides are the product of Nb(C,N) - austenite eutectic formed during solidification of Nb enriched liquid, the last to solidify in the grain boundaries. The Nb(C,N) particles along the interphase boundaries (Figure 92a) have a rod type morphology. According to their position and morphology, these Nb(C,N) particles may have precipitated during the solid state transformation of ferrite to austenite after completion of solidification. When the ferrite is consumed by the austenite, the low Nb solubility in austenite results in rejection of Nb at the front of ferrite-austenite interface. Thus, the Nb enriched interphase boundaries will precipitate NbC and/or

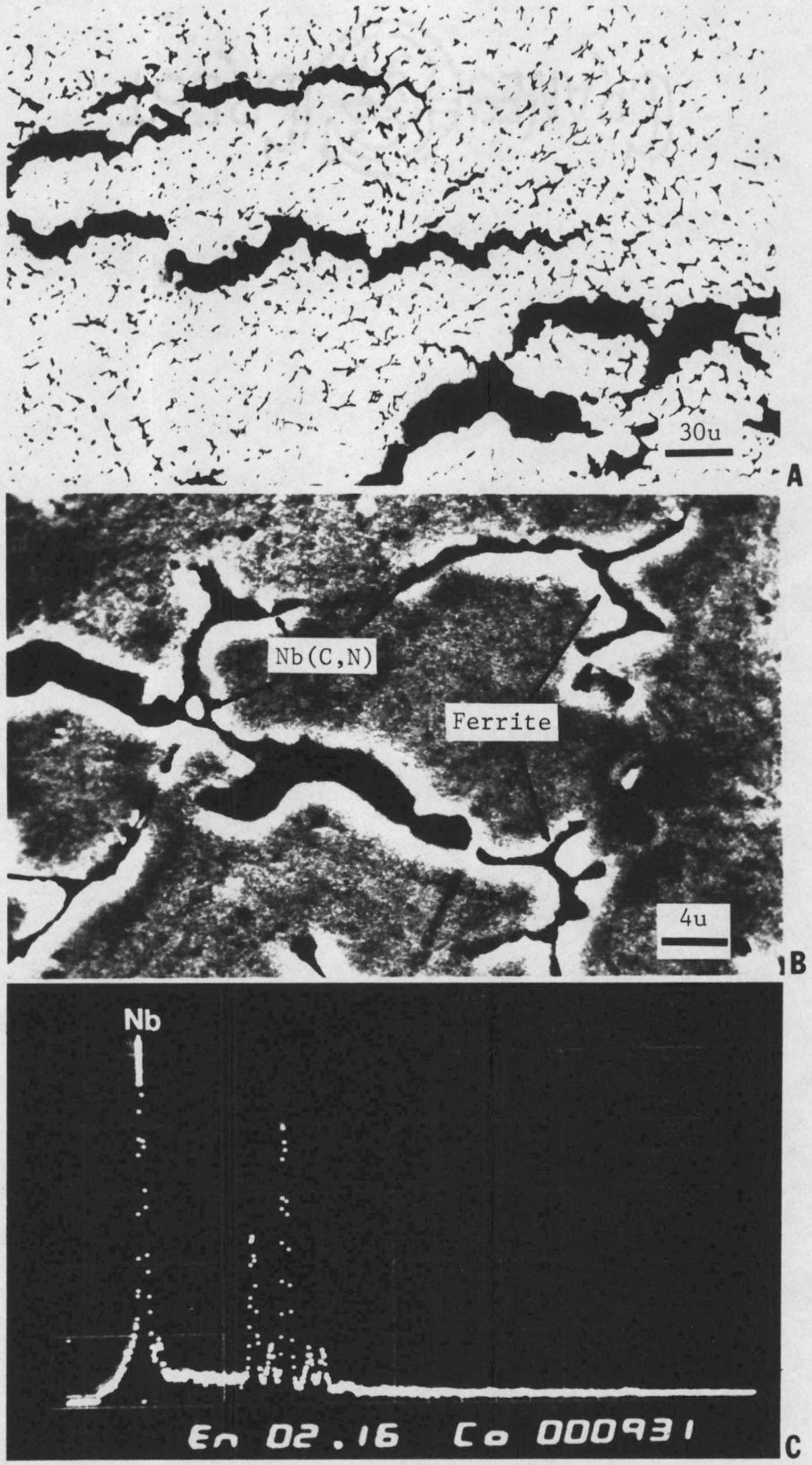


Figure 91. Typical solidification cracks in the primary ferritic weld (347NG-E) together with EDAX analysis on the microconstituents in the grain boundary and interphase boundary.



Figure 92. Nb(C,N) and Nb(C,N)-austenite eutectic in a) interphase boundary and b) grain boundary.

Nb(C,N) during cooling to room temperature. In addition to Nb(C,N) and Nb(C,N) - austenite eutectic constituents, sulfides and phosphides are also found along the grain boundaries as shown for 347NG-E in Figure 93. It has to be recalled that 347NG-E has a high Nb content (0.56%) and thus has a higher value of 1/2 Nb / (30 x C% + 50 x N%) (0.19) when compared to other 347NG lots.

In order to investigate the relationship between ratio - 1/2Nb / (30C + 50N) and the extent of precipitation of NbC and Nb(C,N) - austenite eutectic, 347NG-F, which has a low ratio value (0.08) (reduced solidification cracking susceptibility), was also metallographically examined as shown in Figure 94. Careful examination of Figure 94 reveals that very few different microconstituents can be found along the edge of the crack and within interphase boundaries, indicating that the formation of a low melting Nb(C,N)-austenite eutectic along the solidification boundaries did not extensively occur and is a function of 1/2Nb / (30C + 50N) which may be the primary factor for hot cracking in the fusion zone of type 347NG materials.

In an earlier section, 347NG-A and -B, which have chemical compositions well within the specification limits, showed a greater solidification cracking (equivalent to that of AISI 347). In particular, 347NG-B, which has a low 1/2Nb / (30C + 50N) ratio, showed the greater TCL and MCL in the Varestraint tests. The optical microstructures near the weld fusion line of 347NG-B (Figure 95) reveals that in addition to the center of the weld, significant cracking also occurred along the fusion line region. At higher

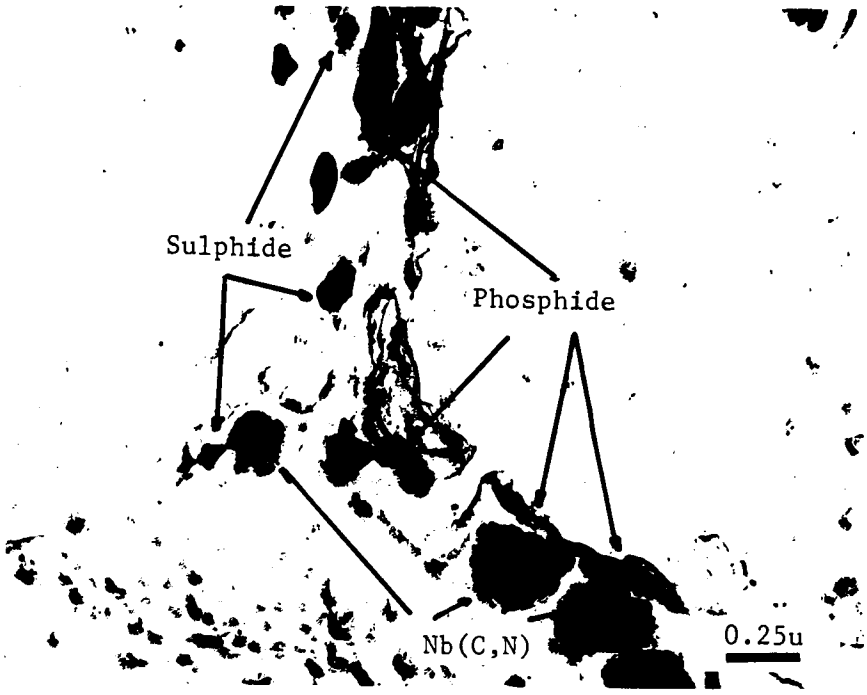


Figure 93. TEM micrograph on the carbon extracted sulfides and phosphides in the grain boundary in 347NG-E.

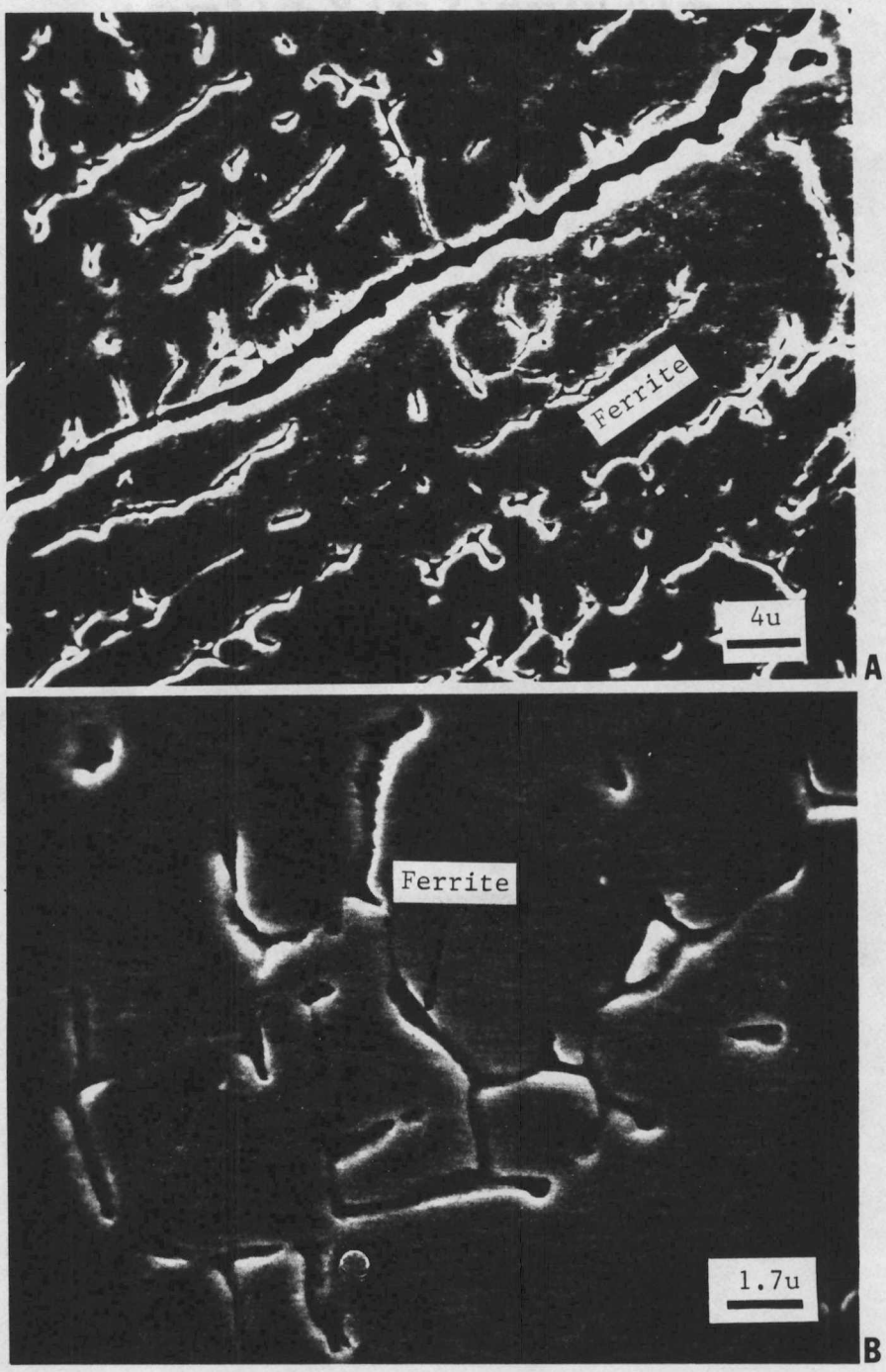


Figure 94. Typical solidification cracking in the low 1/2 %Nb / (30 X %C + 50 X %N) material of 347NG-F.



Figure 95. Optical microstructures near the weld fusion line region in 347NG-B.

magnification, it is revealed that the weld fusion line region solidified in a primary austenitic mode. Some eutectic delta ferrite along the cellular dendritic boundaries is evident. The cracks in the fusion line region are confined to the primary austenitic region. Therefore, it is now clear that the greater susceptibility of the 347NG-A and B with regard to solidification cracking is due to a primary austenitic solidification mode along the fusion line region.

The reason why the fusion line region in the 347NG-A and B solidified in a primary austenitic mode is not clear and can not be predicted from the chemical composition. It is may be due to a localized variation in microsegregation and/or cooling rates. The cooling rate at the fusion line region is generally faster than that in the center of the weld. It is known that a faster cooling rate sometimes can change the solidification mode from a primary ferritic to a primary austenitic mode (85). Brooks et al. (190) have found a nonuniform distribution of delta ferrite in the GTA welds of 309S stainless steels. However, their welds have more ferrite along the weld fusion line compared to the center region, as opposed to that found in this study.

Figures 96a and b show the crack tip regions typical of the primary ferritic (347NG-I) and the fully austenitic weld fusion zone (347L), respectively. As in the case of the primary austenitic 316NG discussed previously, the hot cracks propagated along migrated grain boundaries. The fully austenitic 347L has a straighter migrated boundary. Some fraction of the migrated boundaries coincide with the original solidification boundaries due to the pinning of movement by

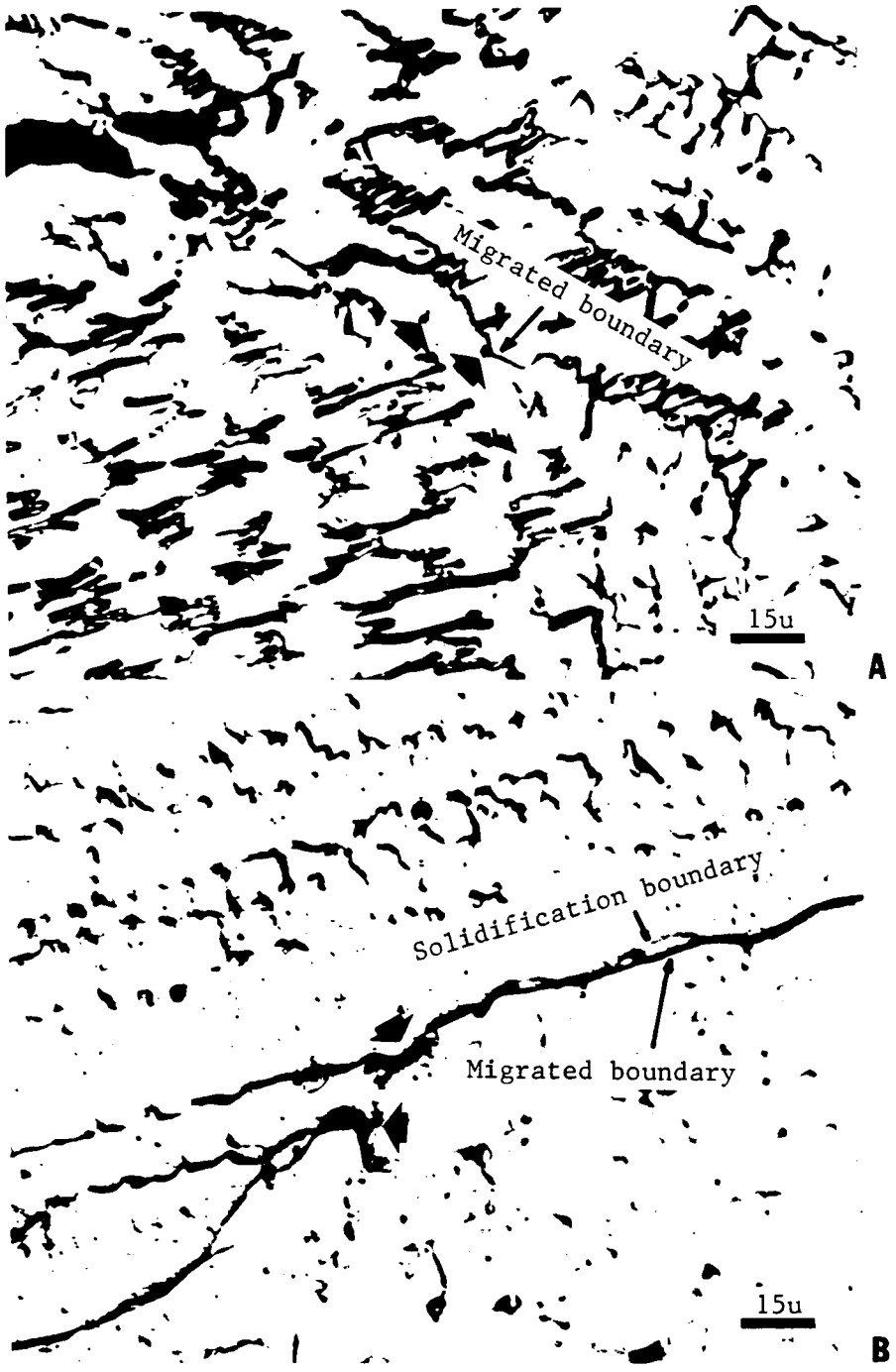


Figure 96. The migrated grain boundaries typical of a) primary ferritic and b) fully austenitic.

the low melting liquid drops at the solidification boundary. The liquid drop areas are expected to be enriched in phosphorous, sulfur and niobium based on the previous STEM and EDAX analyses. However, in the primary ferritic 347NG (Figure 96a), the amount of the phosphides, sulfides and niobium carbides-austenite eutectic along the original solidification boundaries is much less than for the fully austenitic (see arrows), therefore, most of the boundaries migrated easily and they were finally arrested at the primary delta ferrite and thus incorporated into the ferrite-austenite interphase boundaries. Because of the nature of the austenite-ferrite interphase boundaries, the migrated boundaries have a curved irregular shape. Therefore, it is apparent that it is difficult for cracks to propagate along the irregular boundaries as shown in Figure 96a. Difficulty in crack propagation may have played a significant role in the reduced MCL and result in a small extent of cracking in the primary ferritic fusion zone.

Fractographic Analysis

A typical solidification crack surface of the fully austenitic (316NG-D) is shown at low magnification in Figure 97a. The fracture surface reveals features of intergranular fracture aligned unidirectionally due to columnar grain growth. The microscopic features change gradually from the higher temperature region (top side in the micrograph) to the lower temperature region (bottom side). At a higher magnification of region A in Figure 97a (Figure 97b), the fine protuberances which correspond to the cellular dendritic primary and secondary arms can be clearly seen. The most interesting feature

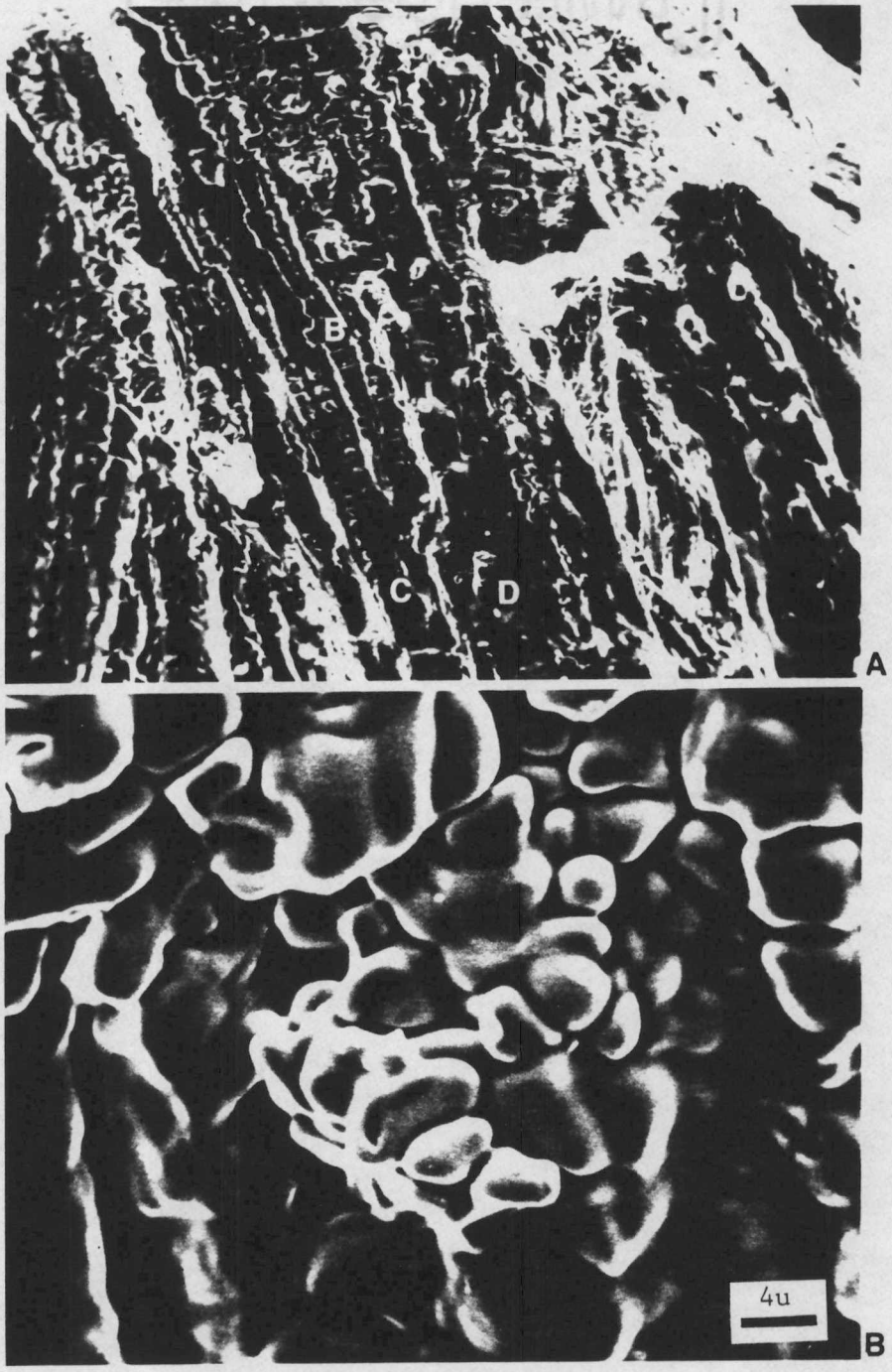


Figure 97. Typical solidification crack surface in fully austenitic (316NG-D). a) macroscopic appearance, b) higher magnification of region A in a).

of the highest temperature region adjacent to the crack initiation location is that the orientation of the fine protuberances is random (i.e., the growth direction of the dendrites is not evident). As shown before, the high temperature portion of a solidification crack just behind the trailing edge of the weld pool was backfilled by liquid. Therefore, the random orientation of dendrites in region A may have resulted from the backfilling phenomenon. In the slightly lower temperature region between A and B in Figure 97a, the growth direction of the primary and secondary arms is clear and it is parallel to the growth direction of the columnar grain (most commonly associated with a solidification related fracture surface). At the lower temperature crack region B (Figure 98a), the primary dendrites and the growth direction can still be observed but the protuberances become more obscure.

In region C at the lowest cracking propagation temperature, the fracture surface is of ductility dip type with a relatively smooth and flat appearance. The dendrite arms are not clearly evident as shown in Figure 98b. The fracture surface further reveals some "beach mark-like" wavy lines as shown in the right side of Figure 98b. The marks run from the top to the bottom of the micrograph, revealing the crack propagation direction. Some investigators (13,180,183) named these striation as thermal facets and indicated that they are evidence of the solid-state ductility dip cracking. This low temperature fracture surface may be due to crack extension along a more or less straight migrated grain boundary where no apparent liquid film existed, except when some portion of the migrated boundary was pinned by the low



Figure 98. Higher magnification of a) region B and b) region C in Figure 97a.

melting "liquid drops" in the original solidification boundary as shown before. Evidence for the existence of a small liquid film, which is enriched in sulfur, is shown in Figure 99.

EDAX analysis on the primary austenitic hot crack surface (316NG-D) revealed that as may be expected, the dendritic surface is enriched in Cr, S, P and Si and to a lesser extent in Ni as compared to the grain interior, indicating the formation of low melting liquid films is the prime reason for solidification cracking.

The macroscopic appearance of the fracture surface in a primary ferritically solidified alloy is almost the same as that of the primary austenitic weld metal as shown in Figure 100a. The hot crack surface is at the bottom left side in Figure 100a, and reveals the columnar grain pattern. At an increased magnification in Figure 100b, the entire crack surface from the high temperature region A to the low temperature side B has a dendritic appearance. The fine smooth protuberances of the primary and secondary dendrite arms running along the columnar grains provide evidence of liquid film existence at the instant of crack initiation and propagation. The size of the dendrite arms is somewhat finer than that in the fully austenitic 316NG. The most interesting fact is that no smooth and flat fracture surface can be found, unlike for the primary austenitic weld. This strongly indicates that crack propagation along the curved-irregular migrated grain boundaries, which are incorporated into the ferrite-austenite interphase boundaries, is difficult.

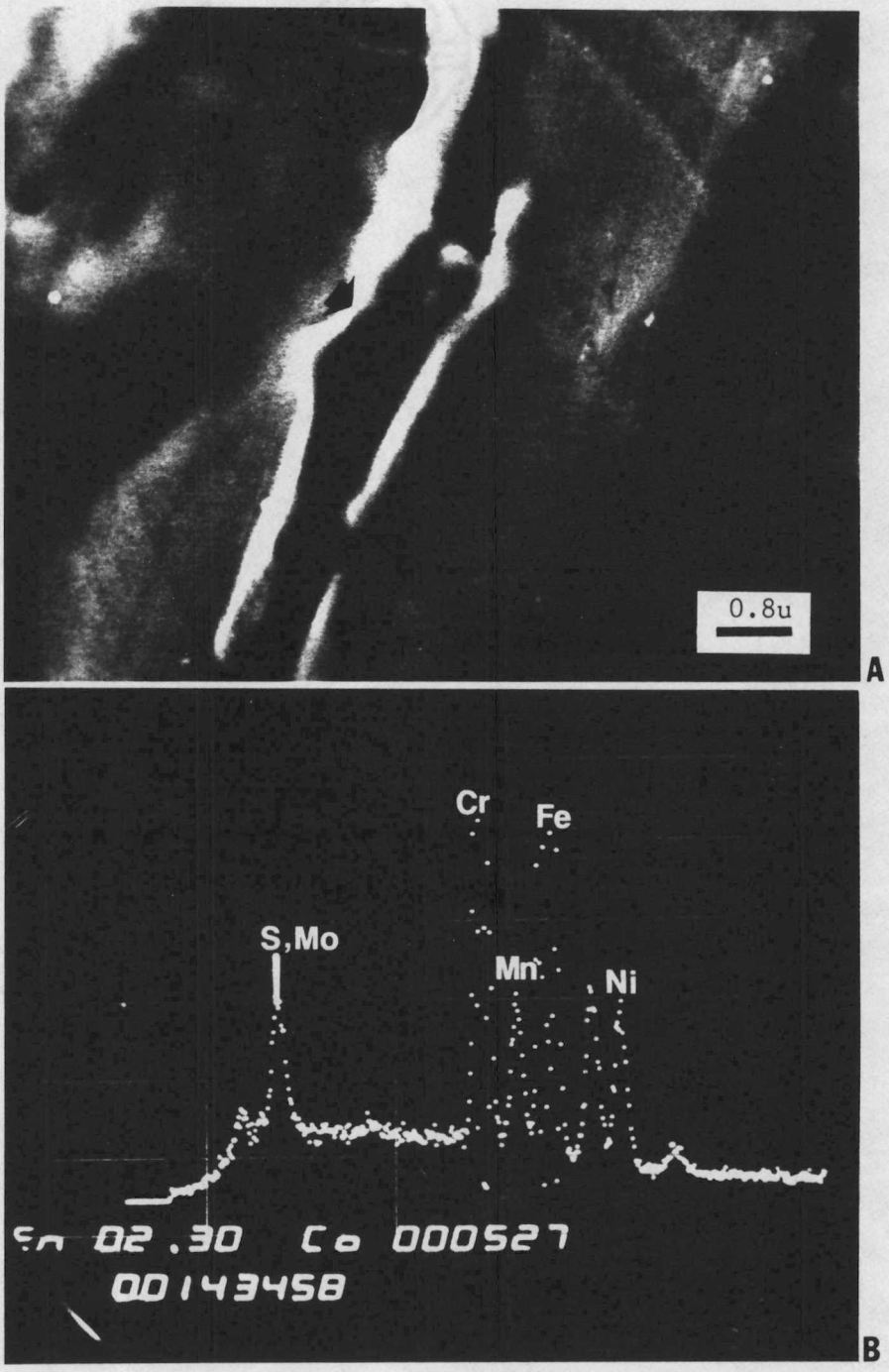


Figure 99. Higher magnification of a) region D in Figure 97a and b) EDAX analysis.

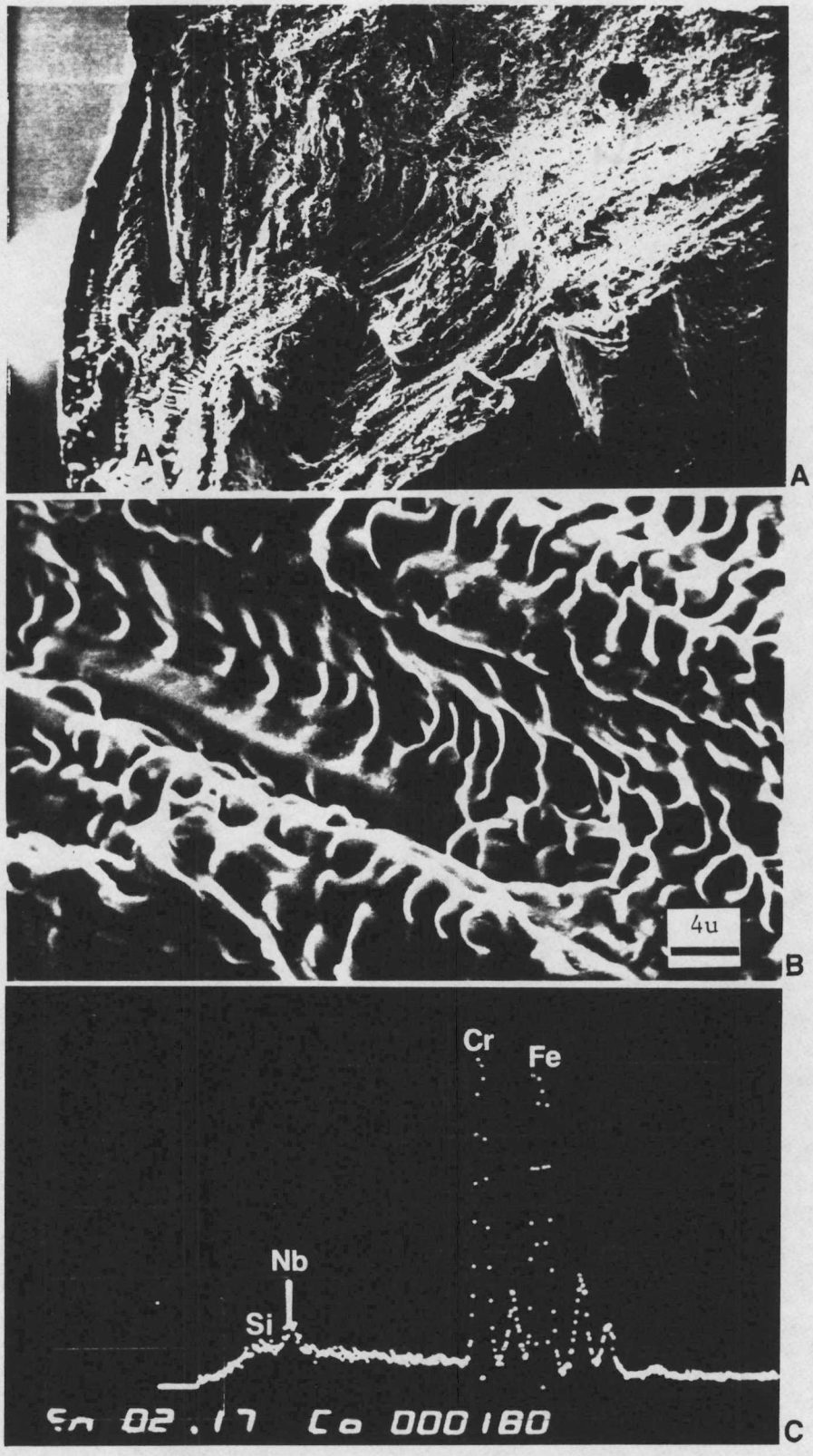


Figure 100. Typical solidification surface in primary ferritic (347NG-E). a) macroscopic appearance and b) higher magnification of a), c) EDAX analysis on dendrite surface.

Discussion

It is clear that the occurrence of solidification cracking in austenitic stainless steel is directly associated with existence of a low melting liquid film along the grain boundaries when the grain matrix regions have already solidified. Thus, when the combined strains of solidification shrinkage strain and thermal strain exceed the strain tolerance of the liquid film embrittled grain boundaries, hot cracks initiate and propagate.

The formation of low melting liquid films is mainly a function of the primary solidification mode and "harmful" element content of the alloy being welded. For a given "harmful" element content, the primary (fully) austenitic mode results in extensive segregation of these elements to the interdendritic and grain boundaries and thus forming more extensive and continuous low melting liquids, mainly because of the lower solubility of austenite for the "harmful" elements. Further, a low melting liquid more easily penetrates into austenite-austenite boundaries in fully austenitic weld metal than austenite-ferrite boundaries in primary ferritic welds (because of the a higher surface energy of boundary between crystal of the same structure). Thus, all of the above factors result in a greater extent of solidification cracking in a primary/fully austenitic material than in a primary ferritically solidified material.

The low melting constituents responsible for the formation of solidification cracking in 316NG and 347NG alloys are found to be sulfides (Mn,Cr)S, phosphides $(Fe,Cr)_3P$ and Nb(C,N)-austenite eutectics. Although no silicates or silicon rich phases were found in

this study, silicon segregation may have also influenced formation of low melting liquids along the solidification boundaries (based on EDAX analyses of fracture surfaces).

Although the reasons why hot cracking occurs and how the solidification mode and impurity elements play a significant role in solidification cracking in austenitic stainless steel are clear, it is not obvious whether the primary solidification mode is the more important factor for hot crack initiation or for propagation. Therefore, it is important to first consider where the hot cracks initiate and propagate. Based on quenched sample microstructure and the microstructural and fractographic examinations of normally solidified welds, the solidification morphology and subsequent microstructural changes for both fully austenitic and primary ferritic solidification modes are schematically summarized in Figure 101. A brief explanation of Figure 101 is as follows:

The solidification temperature range (T_L - T_S) in the fully austenitic material is wider than that for the primary ferritic weld fusion zone. The cellular dendritic morphology in fully austenitic gradually changes to a cellular substructure as temperature decreases. However, in the primary ferritic mode, delta ferrite forms at an early stage and the austenite subsequently forms along the interdendritic regions by an eutectic or peritectic reaction during the last stage of solidification. When the temperature decreases further, the original solidification grain boundaries migrate to minimize the total grain boundary area (i.e., surface energy). Because of "harmful" elements; sulfur, phosphorous, silicon and niobium, have a lower solubility in

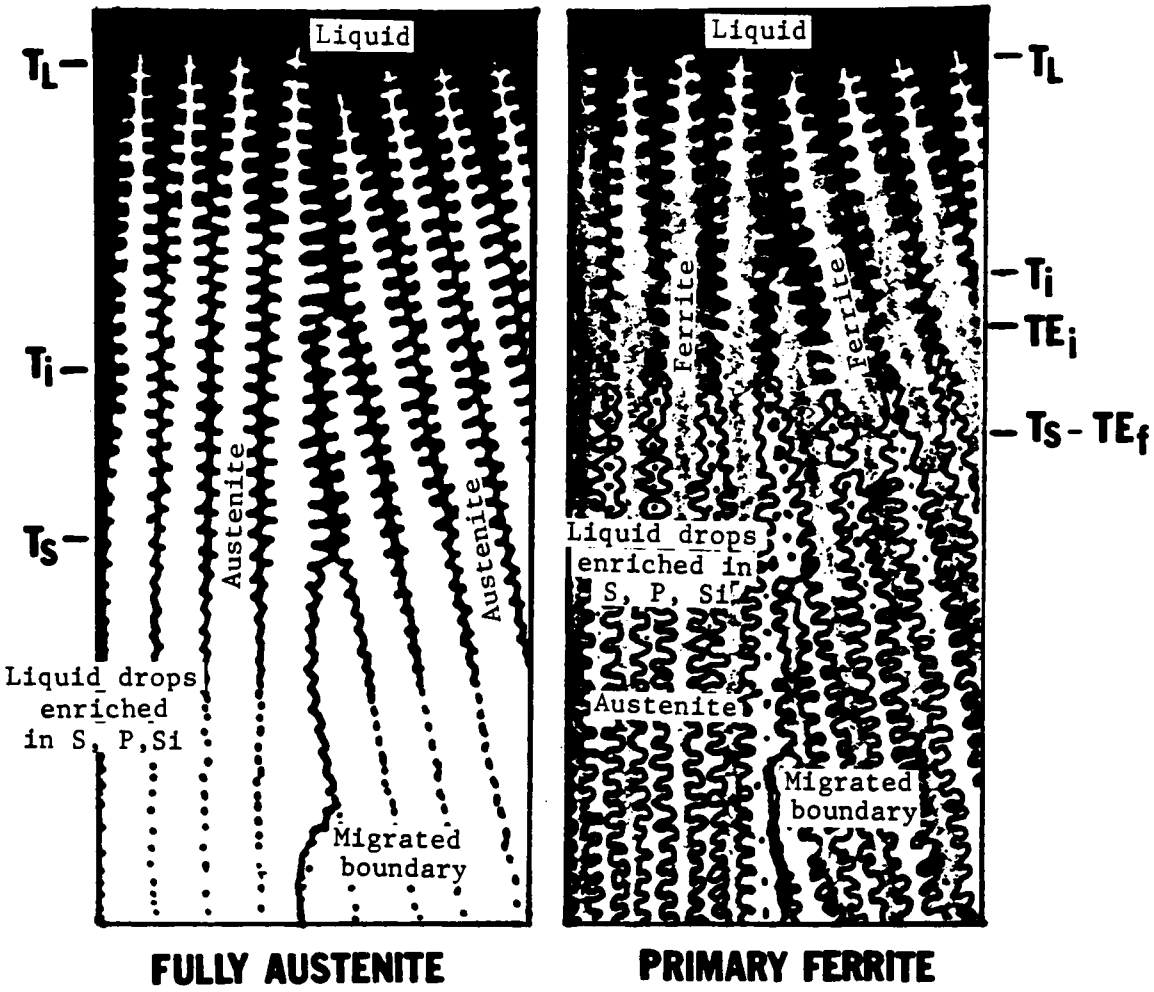


Figure 101. Schematic drawings of solidification substructure morphology and subsequent changes typical for a) fully austenitic and b) primary ferritic weld metal.

austenite than in ferrite, the last solidifying liquid is more highly enriched in these elements for the case of the fully austenitic than that for the primary ferritic mode. These impurities will lower the solidification temperature, thus at a temperature below the bulk solidus, a greater extent and a more continuous liquid phase may exist along the cellular dendritic and grain boundaries in the fully austenitically solidified fusion zone. Therefore, in the case of a fully austenitic solidification mode, the migrating grain boundaries are more or less arrested by low melting liquid drops over a wide temperature range, and some fraction of the migrating boundaries pull away from these obstacles and resides across several cells. Thus, the migrated grain boundaries in the fully austenitic weld metal are more or less continuously bridged by the liquid films and they are relatively straight (that is, for a wide temperature range, the migrating boundary coincides with the solidification boundary). In contrast, the primary ferritic materials have a reduced extent of liquid (drops) in the original solidification boundaries and thus the boundaries easily pull away from hindrances and more freely migrate. The boundaries are finally pinned by the ferrite-austenite interphase boundaries, resulting in irregularly curved barrier as shown schematically in Figure 101b. Further, because austenite forms during the last stage of solidification, most of the "liquid drops" are confined within the austenite and thus it is more difficult for migrated boundaries to be associated with the liquid drops.

Hot cracks usually form at temperatures between T_L and T_S, that is, just behind the solidification front regardless of solidification

mode. However, when hot cracks initiate at solidification grain boundaries at temperatures near the T_L, they will be immediately backfilled by the contiguous liquid which is continuous to the liquid in front of the instantaneous solid-liquid interface. Therefore, only the cracks initiated at temperatures not far T_S may survive and propagate into regions of lower temperature where significant low melting liquid films still exist. The probable hot cracking initiation temperature range over which the cracks will further propagate by an increasing shrinkage strain is designated as T_i in Figure 101. Although in this approximate crack initiation temperature range, the liquid is still continuous and connected to the liquid in the weld pool, the initiated cracks are at lower temperatures at the time the liquid is drawn into the cracks. Thus, complete healing is not possible and only a small high temperature portion of the crack is backfilled. (The evidence for the backfilling in the high temperature portion of cracks was shown previously.) Therefore, although the primary austenitic weld metal has a wider solidification range, the probable hot crack initiation/survival range may not be as wide as that in the primary ferritically solidified weld metal. Therefore, as far as the initiation of hot cracking is concerned, both solidification modes may have the same probability to form hot cracks.

However, propagation of initiated cracks appears to be strongly dependent on solidification mode. Fractographic examination reveals that the fracture morphologies change from more dendritic features in the high temperature regions to a flat surface in lower temperature regions for the fully austenitic weld metal. However, for the

fracture surface of the primary ferritically solidified alloy, a low temperature type flat morphology does not exist. Matsuda et al. (193) have attributed these transitions to a decrease in the amount of residual liquid in the interdendritic boundaries with decreasing temperature. Similar transitions in hot crack surface morphology have also been reported in duplex stainless steels (191) and in nickel base alloys (192).

The low temperature type fracture surface shows a smooth columnar appearance, indicating this region is associated with the propagation of hot cracks along the migrated boundaries on which almost no liquid film exists. In the fully austenitically solidification mode, due to grain boundary pinning by the continuous low melting liquid drops the majority of the migrated boundaries coincide with the original solidification boundaries over a wide temperature range. Therefore, the crack propagation is easy along a boundary which is decorated by a row of the liquid drops and eventually along the straight migrated boundaries in the fully austenitic materials.

However, in primary ferritically solidified weld metal, propagation along migrated grain boundaries is difficult due to the curved irregular morphology. Therefore, the majority of crack propagation in the primary ferritic weld may occur before solidification boundaries have fully migrated, that is, when some liquid drops still exist along the solidification grain boundaries (although the extent of liquid film is less). This propagation range may be between TE_i and TE_f (eutectic start and finish temperatures

between which austenite forms). At temperatures below TE_f, the low melting liquid drops are confined within the austenite as shown in Figure 101b. Therefore, there are no grain boundaries along the row of the residual liquid drops and thus it is difficult for a crack to propagate. Further, below the TE_f, the grain boundaries have fully migrated and been pinned by the ferrite-austenite interphase boundaries, resulting in further difficulty in crack propagation.

In the primary austenitic mode, ferrite forms during the last stage of solidification by eutectic/peritectic reactions. Unlike the case of eutectic austenite in the primary ferritic mode, the eutectic ferrite can not confine the liquid drops. Thus, the majority of the liquid drops exist along the solidification boundaries together with eutectic ferrite. Thus, grain boundary migration is limited by pinning by eutectic ferrite along the original solidification boundaries. However, the amount of low melting liquid films is significantly reduced by absorption of the "harmful" elements to the eutectic ferrite. Therefore, because of the existence of grain boundaries which connect rows of liquid droplets (although it is to lesser extent), an initiated solidification crack can propagate for a longer distance as compared to the primary ferritic solidification mode. However, due to the combined factors of a limited amount of liquid and the nature of the grain boundaries which have an irregular curved morphology by incorporation of the ferrite-austenite interphase boundaries, crack propagation is limited as compared with the fully austenitic fusion zone. The beneficial effect of eutectic ferrite formation on the crack propagation can be found from the Varestraint

results of 316NG-4 which solidifies in a primary austenitic mode with formation of eutectic ferrites along the interdendritic regions. The eutectic ferrite content at room temperature is 1.6 FN. The Varestraint results showed that the maximum crack length of this heat is greater than other primary ferritic 316NG lots but is less than that of fully austenitic lots. This result indicates that eutectic ferrite formation may not significantly influence crack initiation but effectively prevents the initiated cracks from easy propagation.

The above discussion shows that the primary solidification mode is important for both solidification crack initiation and propagation, but its influence appears to be more significant for crack propagation than initiation.

b. Weld Metal HAZ Liquation Cracking

Varestraint Test Results. The results of weld metal HAZ cracking susceptibility is summarized in Figures 102 and 103 for 316NG and 347NG, respectively. In these figures, the maximum crack length measured on the as-tested surface is plotted as a function of the augmented strain.

In Figure 102, the behavior of 316NG is compared with that of the standard 304 and 316 grades. The hot cracking behavior of 316NG in the weld metal HAZ is divided into two groups based on the solidification mode (fully (primary) austenitic and primary ferritic). The TCL and MCL at 4% strain for individual heats are summarized in Table 12. The measured ferrite content (FN), solidification mode, P + S content and Creq/Nieq ratio are also given in Table 12.

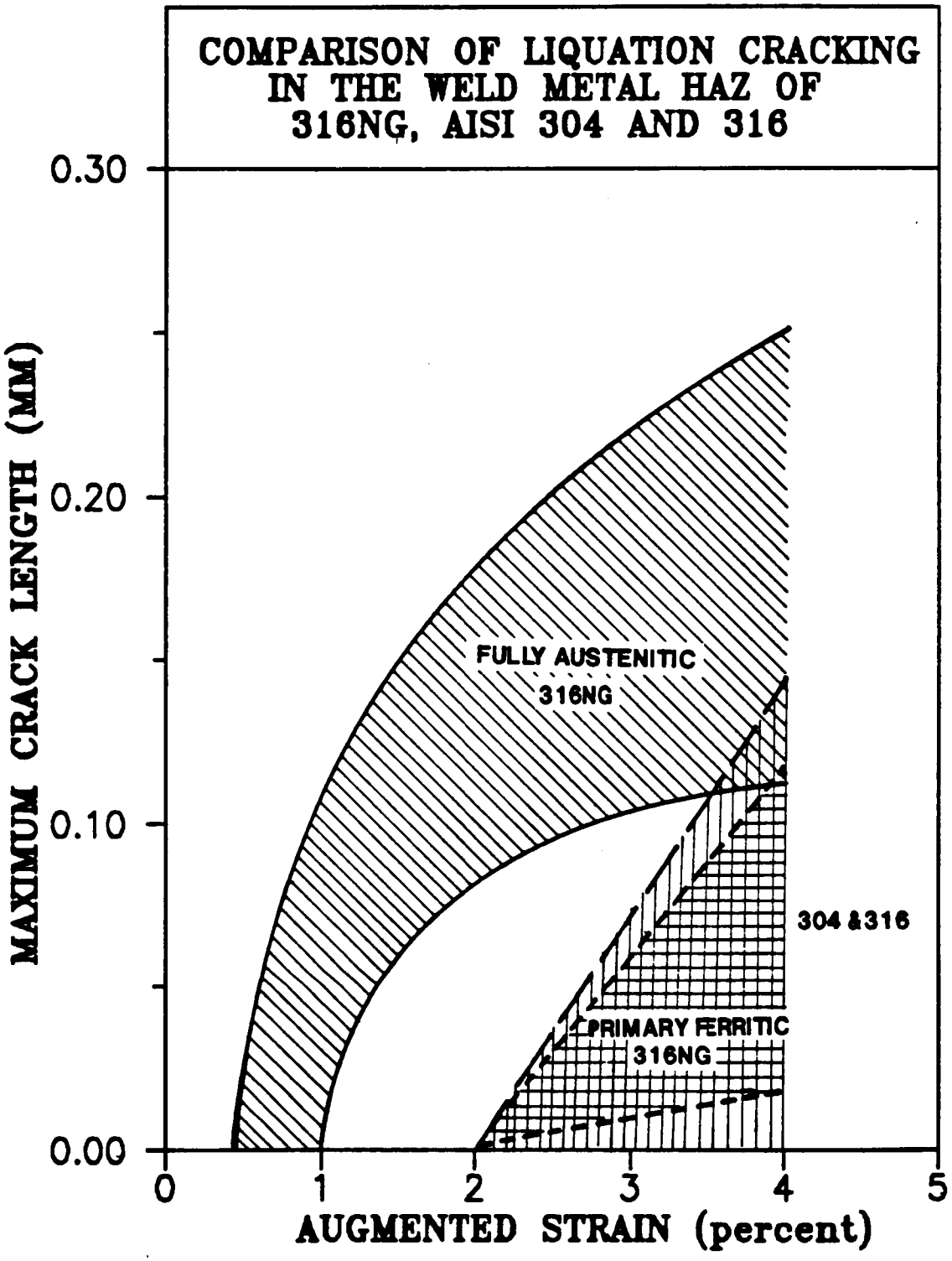


Figure 102. Comparison of liquation cracking behavior in the weld metal HAZ between 316NG and AISI 304 and 316 materials.

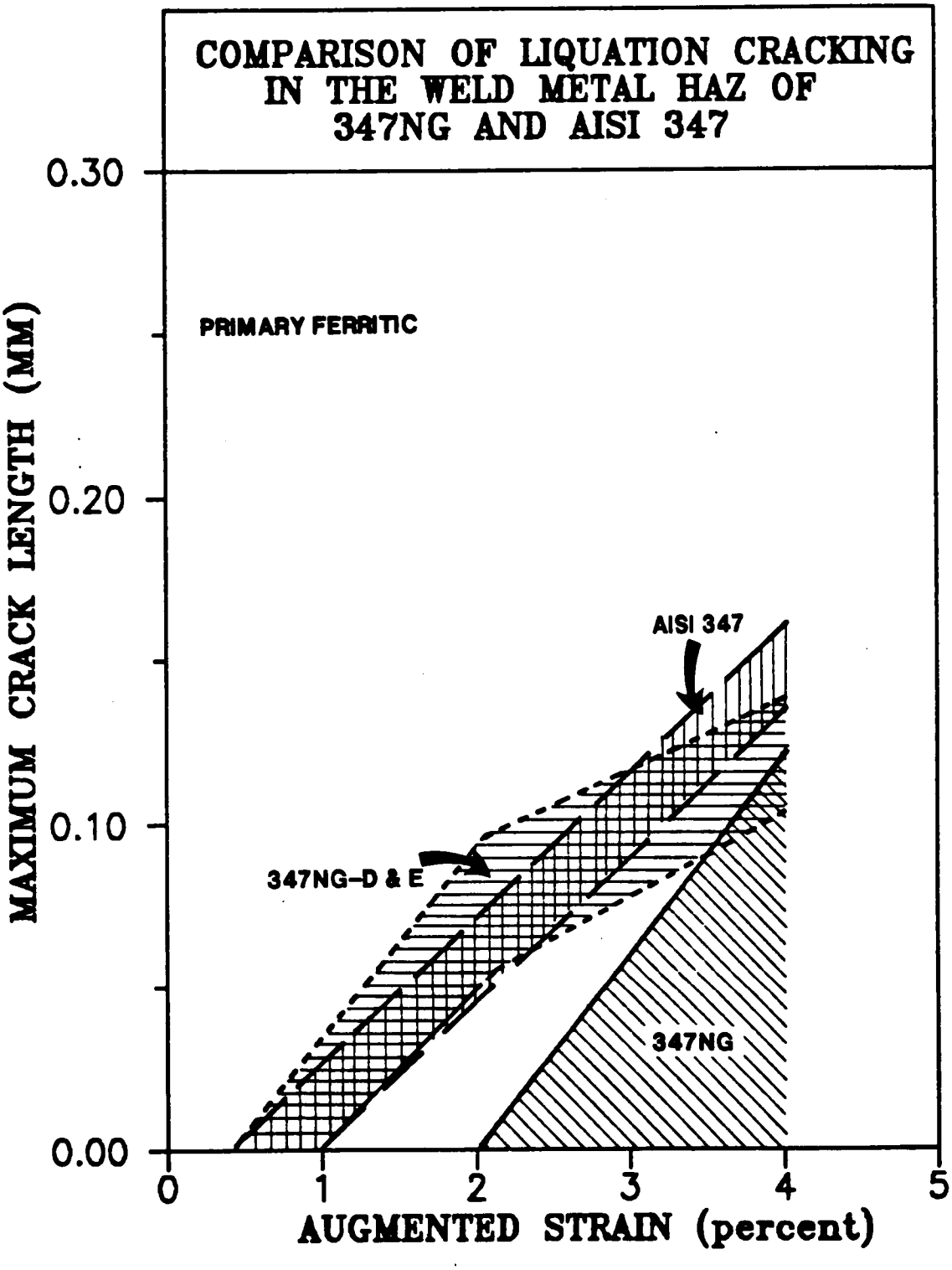


Figure 103. Comparison of liquation cracking behavior in the weld metal HAZ between 347NG and AISI 347 materials.

Table 12. Varestraint weld metal HAZ liquation cracking test results of 316NG, AISI 304 and 316.

Code	Type	FN[a]	P + S	N	Solidification Mode[b]	Cr_{eq}/Ni_{eq}[c]	G.S.	TCL[d]	MCL[e]
316NG-A	316NG	5.1	0.043	0.061	F	1.72	7.3	0.09	0.09
316NG-B	316NG	3.2	0.045	0.083	F	1.71	6.3	0.69	0.12
316NG-C	316LN	4.2	0.022	0.099	F	1.63	5.3	0.29	0.08
316NG-D	316LN	0.1	0.022	0.113	A	1.45	8.2	10.23	0.11
316NG-1	316NG	2.0	0.050	0.098	F	1.61	5.0	0.02	0.02
316NG-2	316NG	0.2	0.030	0.097	A	1.54	4.2	0.46	0.25
316NG-3	316NG	0.0	0.029	0.100	A	1.44	5.0	0.48	0.17
316NG-4	316NG	1.6	0.040	0.083	AF	1.55	5.9	0.51	0.21
316NG-5	316NG	0.2	0.022	0.096	A	1.43	3.5	0.21	0.18
316NG-6	316NG	0.3	0.020	0.101	A	1.43	3.3	0.21	0.21
316NG-7	316NG	0.0	0.021	0.094	A	1.43	3.2	0.37	0.19
316NG-8	316NG	0.1	0.022	0.093	A	1.45	3.8	0.08	0.05
316NG-9	316NG	0.2	0.020	0.099	A	1.43	3.8	0.40	0.14
316-1	316ELC	4.0	0.034	0.054	F	1.60		0.08	0.08
304-1	304	2.4	0.055	-	F	1.84	4.2	0.15	0.04
304-2	304	2.4	0.049	-	F	1.98	4.3	0.00	0.00
304-3	304ELC	3.5	0.034	-	F	1.71		0.25	0.14

a: Measured Ferrite content with Magne-Gage
b: F; primary ferritic, A; Fully austenitic, AF; primary Austenitic + Eutectic Ferrite
c: Hammer and Svensson Method
d: Total crack length (mm) at 4% Augmented strain
e: Maximum crack length (mm) at 4% Augmented strain

Figure 102 clearly indicates that as in case of the fusion zone solidification cracking, the susceptibility of 316NG with regard to weld metal HAZ liquation cracking is also a function of the primary solidification mode and thus the room temperature ferrite content. Nine heats of fully austenitic 316NG exhibit a longer MCL than those of the ferrite containing lots at all augmented strain levels. Further, the fully austenitic lots have a lower cracking threshold strain. However, when an alloy solidifies in a primary ferritic mode and thus has some residual ferrite (in the range of 2 - 5 FN), the weld metal HAZ cracking susceptibility is within the data spread of standard 304 and 316 grades, indicating the beneficial effect of ferrite on liquation cracking in the weld metal HAZ.

Because type 347 for which all heats, except 347L, solidify primarily as ferrite, the solidification mode is not a factor and further, the room temperature ferrite content does not appear to be the cause for the variation on a heat to heat basis as shown in Figure 103 and Table 13. In general, the 347NG lots which have chemical compositions within the specification limits, appear to have good cracking resistance. However, for 347NG with a high C and Nb content (heats D and E), the behavior is virtually equivalent to that of AISI 347. The cracking threshold strain for 347NG-D and E (0.5-1%) is much lower than those of the other 347NG lots (> 2%).

Unlike fusion zone hot cracking, the heats 347NG-A and B, which have a mixed solidification mode, show a low propensity to the weld metal HAZ cracking. This is because the primary austenitically solidified fusion line region is overlapped by the subsequent weld

Table 13. Varestraint weld metal HAZ liquation cracking test results of 347NG and AISI 347.

Code	Type	FN[a]	FN[b]	P + S	G.S.[c]	Nb	1/2Nb / (30C + 5 ON)	Cr_{eq}/Ni_{eq}[d]	Solidification Mode[e]	p*f	TCL[g]	MCL[h]
347NG-A	347NG	2.2	4.0	0.029	11.0	0.40	0.30	1.69	Mixed	0.038	0.28	0.07
347NG-B	347NG	3.9	5.4	0.030	8.0	0.43	0.10	1.71	Mixed	0.045	0.11	0.07
347NG-C	347NG	4.5	5.0	0.038	6.0	0.41	0.09	1.70	F	0.044	0.06	0.05
347NG-D	347NG	3.3	5.5	0.045	7.0	0.60	0.22	1.63	F	0.041	0.11	0.08
347NG-E	347NG	4.4	3.0	0.034	7.0	0.56	0.19	1.64	F	0.050	0.07	0.05
347NG-F	347NG	3.3	3.0	0.040	3.0	0.36	0.08	1.62	F	0.046	0.02	0.02
347NG-G	347NG	1.8	2.8	0.033	6.2	0.33	0.08	1.61	F	0.041	0.26	0.07
347NG-H	347NG	2.4	1.9	0.034	6.0	0.41	0.11	1.57	F	0.030	0.24	0.07
347NG-I	347LN	1.6	1.5	0.018	5.2	0.36	0.04	1.63	F	0.029	0.21	0.07
347NG-J	347NG	3.0	3.0	0.037	5.0	0.23	0.04	1.62	F	0.036	0.02	0.02
347-1	AISI347	3.0	5.5	0.039	9.0	0.67	0.25	1.78	F	0.054	0.75	0.15
347-2	347LPN	5.5	5.0	0.017	8.0	0.26	0.04	1.77	F	0.024	0.00	0.00
347-3	ICL473Nb	3.6	6.0	0.040	9.2	0.49	0.06	1.88	F	0.049	0.25	0.12
347-4	347NG	4.0	3.0	0.039	5.0	0.37	0.10	1.60	F	0.047	0.15	0.09
347-5	347L	0.0	0.0	0.020	8.0	0.30	0.17	1.54	A	0.020	0.20	0.08
347-6	347R	3.5	3.0	0.031	6.2	0.74	1.23	1.86	F	0.044	0.38	0.11
347-8	AISI347	3.0	4.0	0.037	5.5	0.61	0.11	1.73	F	0.048	0.92	0.17
347-9	AISI347	3.0	5.0	0.030	5.5	0.61	0.09	1.78	F	0.054	1.10	0.13

a: Measured Ferrite content with Magne-Gage
b: Ferrite potential by Delong Method
c: ASTM Grain Size No.
d: Hammer and Svensson Method
e: F; primary ferritic, A; Fully austenitic, Mixed: Mixed ferritic and austenitic
f: $p^* = \% P + 0.04 \times \% Si$
g: Total crack length (mm) at 4% Augmented strain
h: Maximum crack length (mm) at 4% Augmented strain

passes, thus only the primary ferritic weld metal is exposed to the weld HAZ thermal cycles.

There is no clear relationship between the extent of HAZ cracking and the ratio 1/2Nb / (30C + 50N), unlike that for fusion zone hot cracking. In general, however, heats with a higher the ratio and the higher P + S content show a greater susceptibility to cracking. The susceptibility to weld metal HAZ cracking may not be judged directly from the fusion zone behavior, although both zones have an identical solidification mode and similar room temperature ferrite content. Other metallurgical factors, such as the segregation behavior and the ferrite transformation to austenite which occurs during the subsequent multipass exposures, may have to be considered.

Comparing 316NG to 347NG, with the exception of the fully austenitic 347L and 347NG-D and E (high Nb and C), the resistance of 316NG is slightly better than that of 347NG, and is equivalent to that of the standard AISI 304 and 316 grades. However, fully austenitic 316NG and 347NG-D and E have a greater propensity to weld metal HAZ liquation cracking than 304 and 316 and are virtually identical to AISI 347.

Microstructural Characterization. The polished and etched metallographic section (parallel to the top surface of the test sample) from 316NG-D is shown in Figure 104. This shows a crack propagated intergranularly along grain boundaries in the HAZ. The crack appears to have been initiated at the fusion line and propagated to the lower temperature regions. Some cracks, which extended from the fusion zone solidification cracks across the weld fusion line,

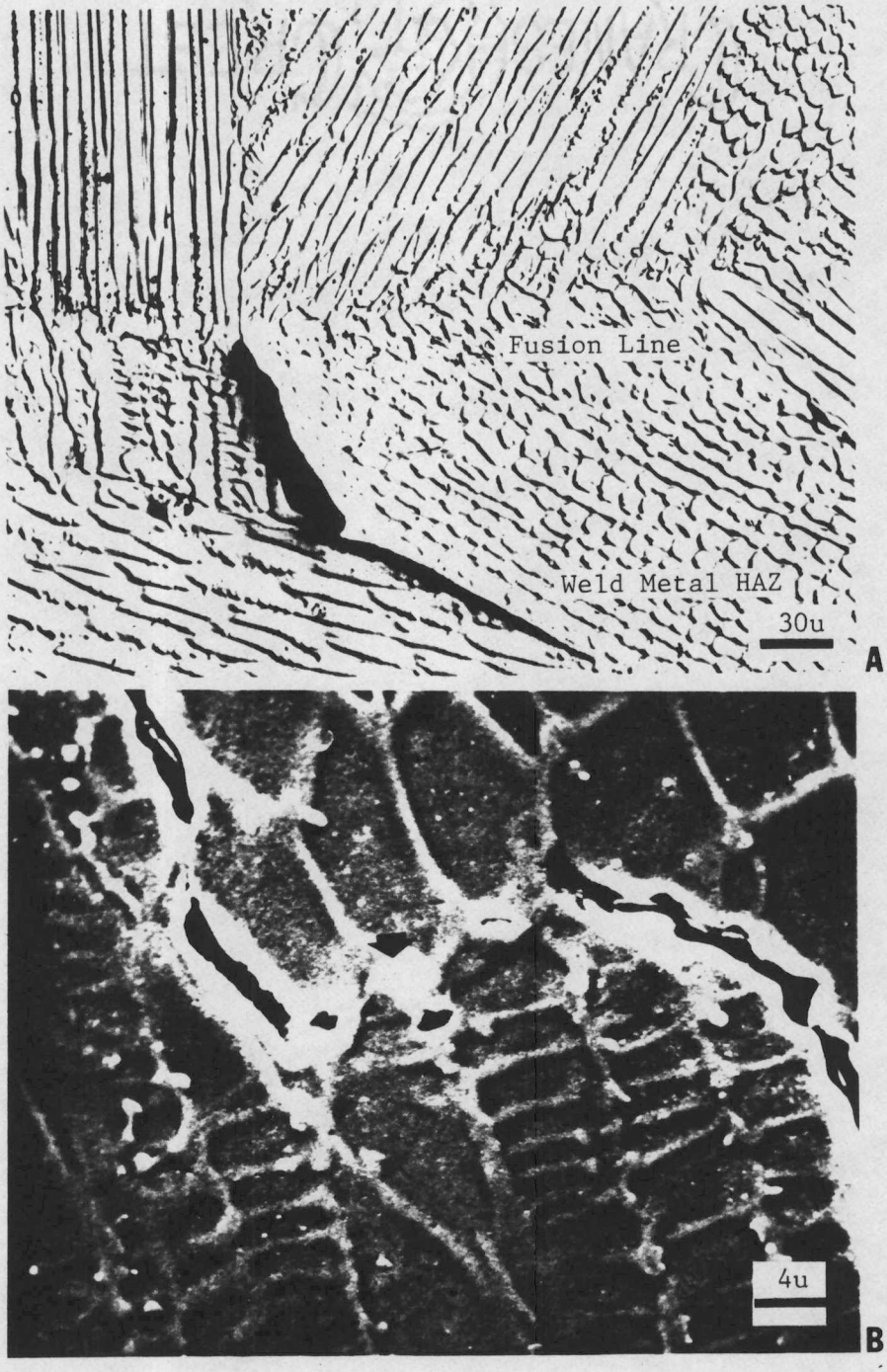


Figure 104. Typical weld metal HAZ liquation cracking in the fully austenitic 316NG-D.

were occasionally found as a consequence of the epitaxial nature of solidification in fusion welds. At an increased magnification in Figure 104b, which is from the region adjacent to the fusion line, the evidence of localized melting at the grain boundaries along which the crack propagated can be noted (the melted regions are indicated by the arrows). EDAX analysis revealed that the melted boundaries were enriched in S, P, Si and Mo as compared to the grain matrix. This can be expected from the previous TEM and STEM analyses of the fusion zone where the solidification boundaries were decorated by the (Mn,Cr)S and $(Fe,Cr)_3P$ microconstituents. Therefore, high peak temperatures near the fusion line promote incipient melting and/or constitutional liquation of these constituents with austenite matrix.

The weld metal HAZ cracks in ferrite containing weld metal have a slightly different crack morphology as shown in Figure 105. This particular microstructure is from 347NG-E, but is typical for the all ferrite containing weld metal HAZ's. The hot cracks are intergranular but are formed some distance away from the weld fusion line, in contrast to those in the fully austenitic weld HAZ, where cracks usually form at/near the fusion line. A careful examination of Figure 105a indicates that cracks formed in the lower ferrite regions. The hot cracked regions have a "globular" type ferrite while the surrounding area has vermicular ferrite. At higher magnification in Figure 105b the cracking is noted to be associated with the "white" microconstituents. A TEM micrograph of a carbon replica and the STEM spot analysis in Figure 106 show that these particles are enriched in Nb and have a lamellar eutectic structure, indicating that the hot

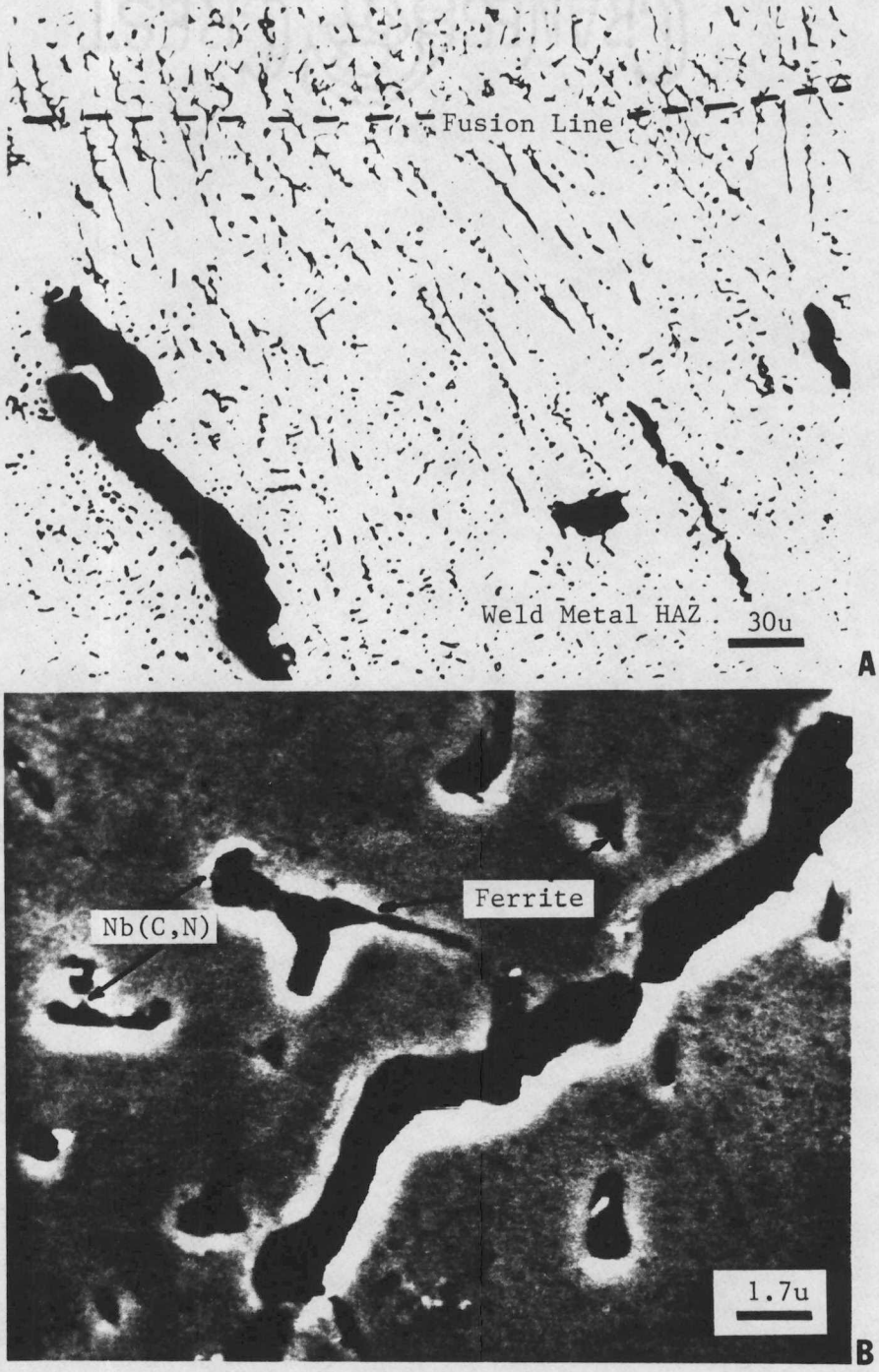


Figure 105. Typical weld metal HAZ liquation cracking in the primary ferritic 347NG-E.



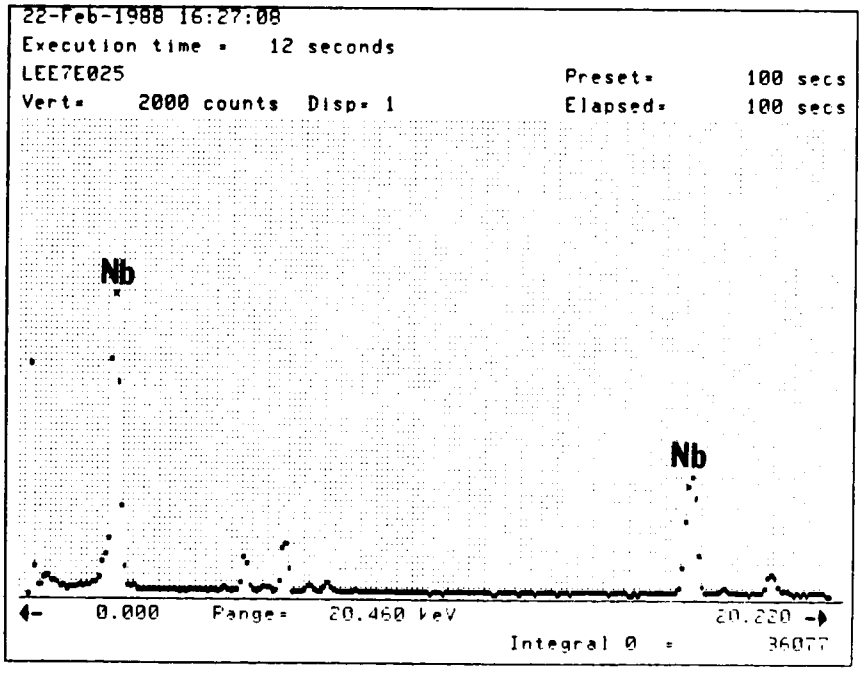


Figure 106. Nb(C,N) -austenite eutectic in the grain boundary in 347NG-E. a) carbon extraction replica and b) STEM analysis.

cracking is related to the Nb(C,N)-austenite eutectic liquid. Further, some (Mn,Cr)S sulfides are also found along the grain boundaries. Similar type particles are also noted in the ferrite-austenite interphase boundaries as shown in Figure 105b and 107. The TEM micrograph in Figure 107 clearly reveals that ferrite has a more or less rounded interphase boundary indicating that some partial transformation of ferrite to austenite has occurred during multipass welding (3 exposures in this sample). Constitutional liquation of the fine Nb(C,N) at the interphase boundary is indicated by the arrow.

Discussion. A prerequisite for liquation cracking in the weld metal HAZ is the formation of liquated regions within the solid metal HAZ adjacent to the fusion line. If this liquid promotes a least semi-continuous film along the grain boundaries and sufficient strain/stress are present, intergranular cracking will occur.

The results of the metallographic examination and TEM and STEM analyses have revealed that cracking in the weld metal HAZ of fully austenitic 316NG and primary ferritic 347NG occurs preferentially at intergranular sites and involves localized melting associated with an enrichment in S, P, Si for type 316NG and S, Si and Nb for 347NG. Most of the enrichment in these impurity elements along the grain boundaries had occurred during solidification before exposure to the subsequent passes. In the fully austenitic 316NG, because the above "harmful" elements have lower solubilities in austenite, the impurity elements are highly segregated in the last solidifying liquid in the interdendritic regions and form low melting microconstituents. In primary ferritic 347NG, in addition to microsegregation of these



Figure 107. Nb(C,N) - austenite eutectic at the ferrite and austenite interphase boundary in the weld metal HAZ in 347NG-E.

elements (although to a lesser extent), a significant amount of Nb(C,N) particles and Nb(C,N)-austenite eutectics form along the ferrite-austenite interphase and solidification grain boundaries. The segregation of impurity elements to the HAZ grain boundaries is further exacerbated when the weld metal is repeatedly reheated by the multipass welding cycles (3 cycles in this study).

When the fully austenitic weld metal is reheated to a high temperature by succeeding passes, grain boundary migration and growth easily occur because of no apparent hindrances of the movement by ferrite or other obstacles. The grain boundaries moving through the material during grain growth have a tendency to "sweep up" solutes and thus enhance the segregation of the "harmful " species and trap them in the grain boundaries. The "sweep up" effect is most pronounced in the region adjacent to the fusion line where the diffusivity of the solute atoms is high, allowing the atoms to diffuse with the moving grain boundaries. This "sweeping" effect of migrating boundary is suggested by several investigators (192,194-196). Therefore, during the last exposure to a weld cycle (third pass), the previous highly segregated grain boundaries will melt at temperatures above the liquidus temperature of boundaries. As the fusion line is approached there is a gradual increase in the width of the melted boundary. On cooling, the liquid film along grain boundary tends to form low melting point compounds and/or low melting eutectics. At this stage, if the strain imposed upon by combined action of thermal and restraint stresses (in this case, the augmented strain) exceeds the strain tolerance of the boundaries, cracking occurs. Thus, weld metal HAZ

cracking in the fully austenitic microstructure is extensive and forms in the region adjacent to the fusion line where most of the grain boundaries are continuously melted during weld thermal cycle exposure.

In contrast to the case of the fully austenitic weld metal HAZ, where the formation of liquid film was basically due to the impurity element segregation, in the ferrite containing weld metal of 347NG, enhanced segregation by the "sweeping" effect of migrating boundaries is minor due to the pinning effect of ferrite on boundary movement. Further, as shown in Figure 105, hot cracks form in the lower ferrite regions some distance away from the fusion line, instead of in the region next to the fusion line where more grain boundary liquation is probable. This region was termed the "Hazard HAZ" by Lundin and Chou (195) in their newly proposed theory of reheat hot cracking. They explained the formation of "Hazard HAZ" region using the pseudo-binary diagram similar to that in Figure 74 (page 212). During on-heating cycle, the residual ferrite in the Hazard HAZ region transforms to austenite by a solid state reaction. Ferrite, having a high solubility for "harmful" elements, releases these elements as it transforms to austenite. Thus, these released harmful elements are redistributed by diffusion to the grain boundaries, along which the "original" segregation was not significant, (due to the primary ferritic solidification mode). This redistribution of harmful elements to grain boundaries is more exacerbated by the multipass welding cycles as used in this study. In type 347 alloy, the solid state dissolution of fine Nb(C,N) particles further enhances microsegregation of Nb in grain boundaries. Therefore, when the peak

temperature reaches the melting point of the segregated boundaries, they will melt incipiently and become susceptible to boundary separation by thermal and restraint stresses during the cooling. Furthermore, the constitutional liquation of Nb(C,N) and the liquid penetration along boundaries increase more the extent of liquid film in boundary during on-heating cycles, and this Nb enriched liquid will form low melting Nb(C,N)-austenite eutectics during on-cooling and thus make 347 more susceptible to HAZ liquation cracking than type 316NG.

On the other hand, in the regions adjacent to the weld fusion line, where one may consider that higher peak temperatures exert an increased liquid formation effect at grain boundaries and thus greater susceptible to hot cracking, no cracks were found in this investigation. This may be, according to Lundin et al. (195), due to that in the high peak temperature regions (above the austenite solvus temperature), "new" ferrite forms at the existing ferrite, which has partially transformed to austenite expelling the "harmful" elements during on-heating below the austenite solvus temperature. This "new" ferrite "reabsorbs" the released harmful solutes. Thus, the resultant liquid films during on-cooling is reduced. Furthermore, the penetration of the Nb rich liquid formed by constitutional liquation of Nb(C,N) into the newly formed ferrite-austenite boundaries is difficult, because of the low surface energy of the boundary between the two phases. Therefore, crack initiation in the high ferrite region should be difficult. Further, the more or less continuous

ferrite network along the boundaries at higher temperature also make the propagation of cracks more difficult.

c. Base Metal HAZ Liquation Cracking

Varestraint Test Results. The behavior of the current program materials (316NG and 347NG) with respect to base metal HAZ hot cracking is shown in Figures 108 and 109, respectively. The extent of cracking at the 4% strain of the nuclear grade alloys is compared with that in the standard AISI grades in Tables 14 and 15.

As may be expected from the hot ductility tests, the behavior of 316NG is virtually identical to that of 304 and 316. The variation of 316NG on a heat to heat basis does not appear to be a function of the impurity level evaluated in this study. In general, however, the lower cracking susceptibility materials have lower impurity levels as shown in Table 14. 347NG has a more significant heat to heat variation as compared to 316NG. The base metal HAZ response seems to have a trend similar to the behavior in the weld metal HAZ. Here again, heats 347NG-D and E have a lower threshold strain compared to the other heats. Heat 347NG-D has the greatest TCL among the 347NG heats as the case of the weld metal HAZ. The resistance of 347NG to base metal HAZ hot cracking is superior to that of AISI 347. As in the case of 316NG, the HAZ response of 347NG does not have a clear relationship to the P + S content. However, as shown in Figures 110 and 111, the MCL of 347 increases with an increase in the Nb content and the ratio 1/2Nb / (30C + 50N). Although there is a significant scattering at the lower values, the ratio has a linear relationship with the extent of base metal HAZ cracking (MCL). As will be shown

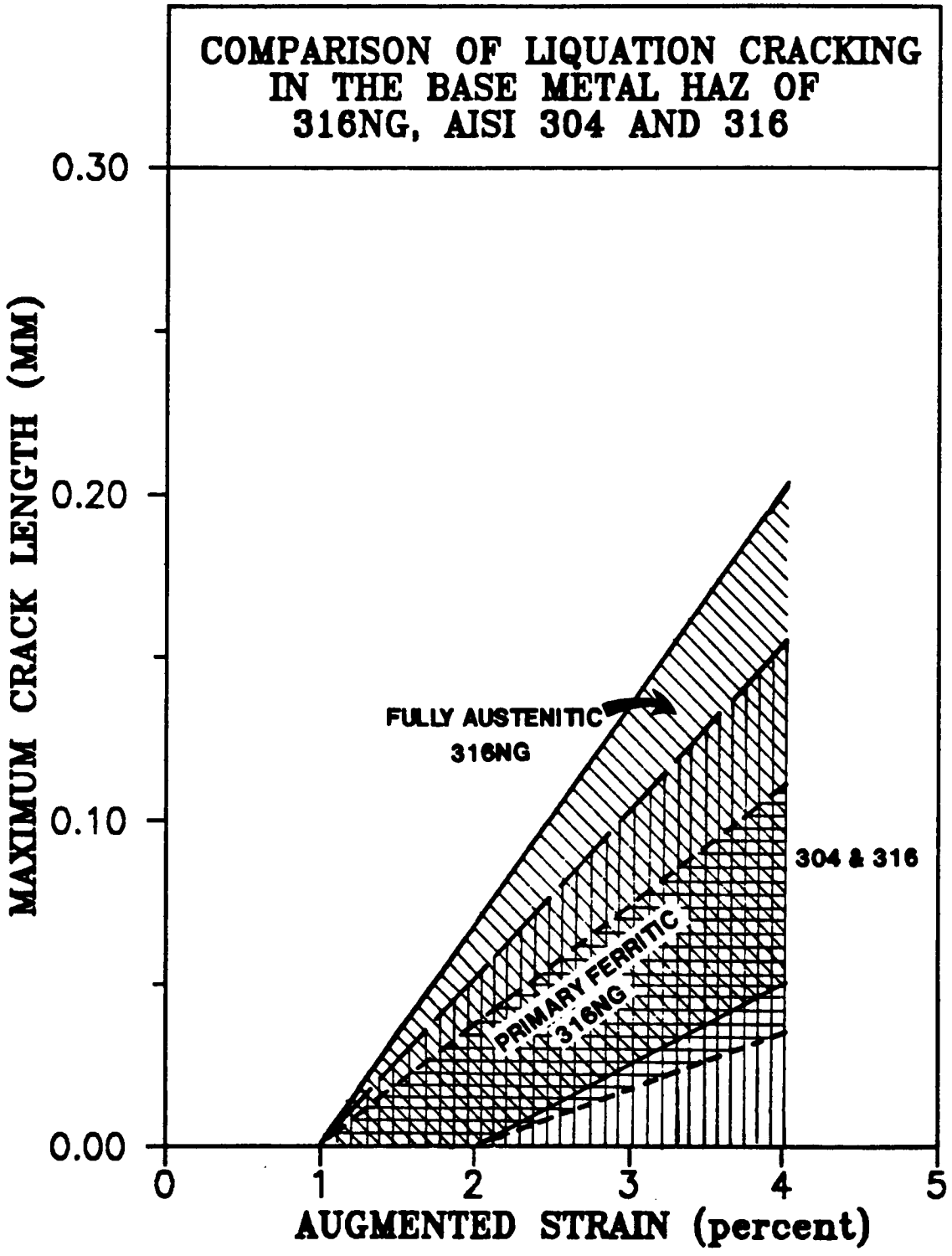


Figure 108. Base metal HAZ liquation cracking behavior of 316NG materials.

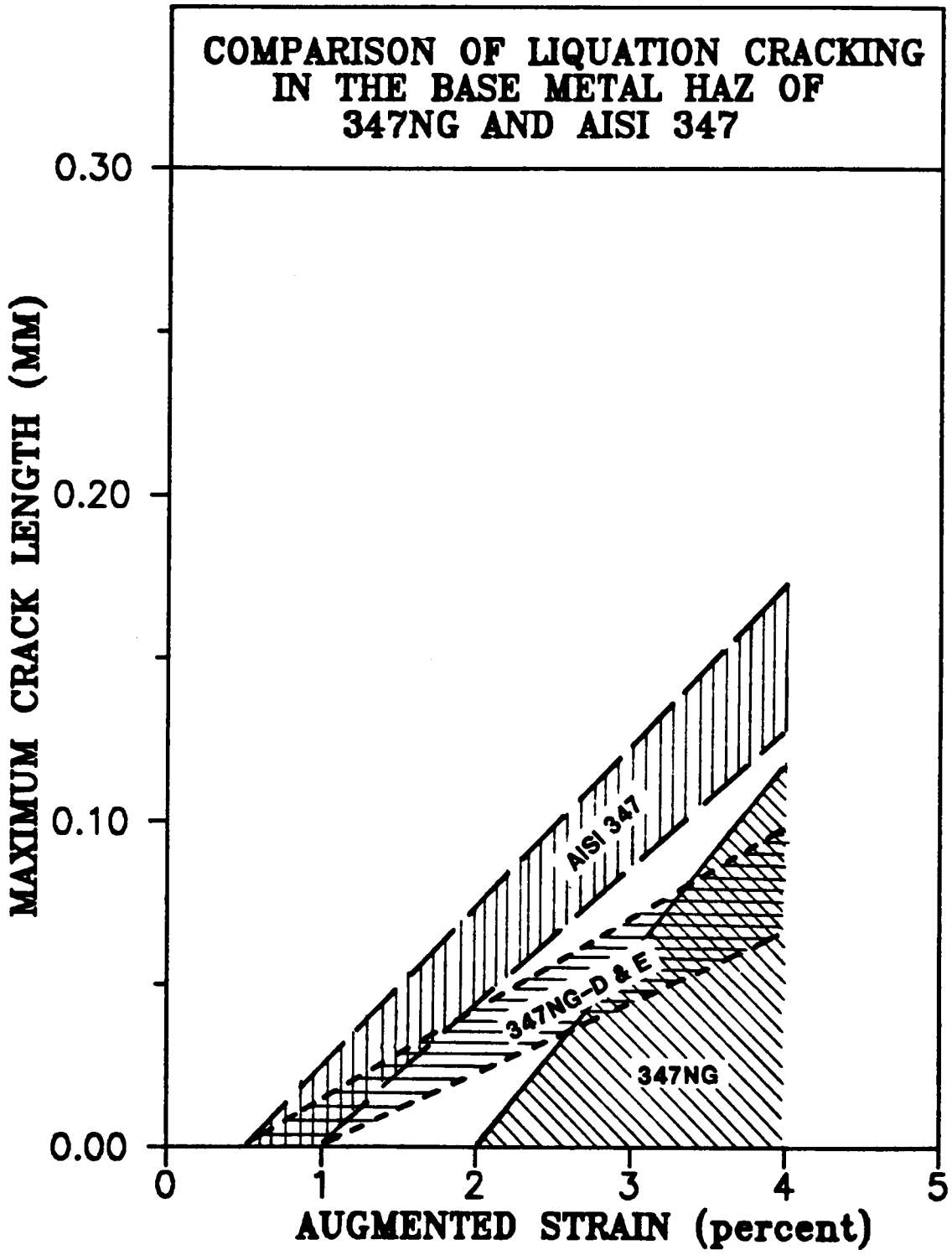


Figure 109. Base metal HAZ liquation cracking behavior of 347NG materials.

Table 14. Varestraint base metal HAZ liquation cracking test results of 316NG, AISI 304 and 316.

Code	Type	FN[a]	FN[b]	P + S	N	Solidification Mode[c]	Cr_{eq}/Ni_{eq}[d]	G.S.	TCL[e]	MCL[f]
316NG-A	316NG	5.1	5.0	0.043	0.061	F	1.72	7.3	0.13	0.06
316NG-B	316NG	3.2	4.9	0.045	0.083	F	1.71	6.3	0.63	0.12
316NG-C	316LN	4.2	3.2	0.022	0.099	F	1.63	5.3	0.32	0.09
316NG-D	316LN	0.1	0.0	0.022	0.113	A	1.45	8.2	0.48	0.13
316NG-1	316NG	2.0	1.0	0.050	0.098	F	1.61	5.0	0.17	0.05
316NG-2	316NG	0.2	0.0	0.030	0.097	A	1.54	4.2	0.17	0.14
316NG-3	316NG	0.0	0.0	0.029	0.100	A	1.44	5.0	0.08	0.05
316NG-4	316NG	1.6	0.0	0.040	0.083	AF	1.55	5.9	0.03	0.03
316NG-5	316NG	0.2	0.0	0.022	0.096	A	1.43	3.5	0.19	0.16
316NG-6	316NG	0.3	0.0	0.020	0.101	A	1.43	3.3	0.05	0.05
316NG-7	316NG	0.0	0.0	0.021	0.094	A	1.43	3.2	0.28	0.16
316NG-8	316NG	0.1	0.0	0.022	0.093	A	1.45	3.8	0.62	0.21
316NG-9	316NG	0.2	0.0	0.020	0.099	A	1.43		0.17	0.07
316-1	316ELC	4.0	3.0	0.034	0.054	F	1.60	4.2	0.25	0.12
304-1	304	2.4	4.0	0.055	-	F	1.84	4.3	0.10	0.04
304-2	304	2.4	5.0	0.049	-	F	1.98		0.00	0.00
304-3	304ELC	3.5	5.0	0.034	-	F	1.71		0.28	0.15

a: Measured Ferrite content with Magne-Gage
b: Ferrite potential by Delong Method
c: F; Primary ferritic, A; Fully Austenitic, AF; Primary Austenitic + Eutectic Ferrite
d: Hammer and Svensson Method
e: Total crack length (mm) at 4% Augmented strain
f: Maximum crack length (mm) at 4% Augmented strain

Table 15. Varestraint base metal HAZ liquation cracking test results of 347NG and AISI 347.

Code	Type	FN[a]	P + S	G.S.[b]	Nb	1/2Nb / (30C + 5 ON)	Cr_{eq}/Ni_{eq}[d]	Solidification Mode[c]	p*	TCL[e]	MCL[f]
347NG-A	347NG	2.2	0.029	11.0	0.40	0.30	1.69	Mixed	0.038	0.03	0.02
347NG-B	347NG	3.9	0.030	8.0	0.43	0.10	1.71	Mixed	0.045	0.06	0.04
347NG-C	347NG	4.5	0.038	6.0	0.41	0.09	1.70	F	0.044	0.00	0.00
347NG-D	347NG	3.3	0.045	7.0	0.60	0.22	1.63	F	1.041	0.57	0.10
347NG-E	347NG	4.4	0.034	7.0	0.56	0.19	1.64	F	0.050	0.81	0.13
347NG-F	347NG	3.3	0.040	3.0	0.36	0.08	1.62	F	0.046	0.00	0.00
347NG-G	347NG	1.8	0.033	6.2	0.33	0.08	1.61	F	0.041	0.05	0.05
347NG-H	347NG	2.4	0.034	6.0	0.41	0.11	1.57	F	0.030	0.00	0.00
347NG-I	347LN	1.6	0.018	5.2	0.36	0.04	1.63	F	0.029	0.25	0.09
347NG-J	347NG	3.0	0.037	5.0	0.23	0.04	1.62	F	0.036	0.05	0.03
347-1	AISI347	3.0	0.039	9.0	0.67	0.25	1.78	F	0.054	0.52	0.16
347-2	347LPN	5.5	0.017	8.0	0.26	0.04	1.77	F	0.024	0.16	0.12
347-3	ICL473Nb	3.6	0.040	9.2	0.49	0.06	1.88	F	0.049	0.49	0.17
347-4	347NG	4.0	0.039	5.0	0.37	0.10	1.60	F	0.047	0.14	0.07
347-5	347L	0.0	0.020	8.0	0.30	0.17	1.54	A	0.020	0.43	0.10
347-6	347R	3.5	0.031	6.2	0.74	1.23	1.86	F	0.044	0.02	0.02
347-8	AISI347	3.0	0.037	5.5	0.61	0.11	1.73	F	0.048	0.86	0.14
347-9	AISI347	3.0	0.030	5.5	0.61	0.09	1.78	F	0.054	0.62	0.13

a: Measured Ferrite Content with Magne-Gage
b: ASTM Grain Size No.
c: F; primary ferritic, A; Fully austenitic, Mixed: Mixed ferritic and austenitic
d: Hammer and Svensson Method
e: Total crack length (mm) at 4% Augmented strain
f: Miaximum crack length (mm) at 4% Augmented strain
p* = %P + 0.04 x % Si

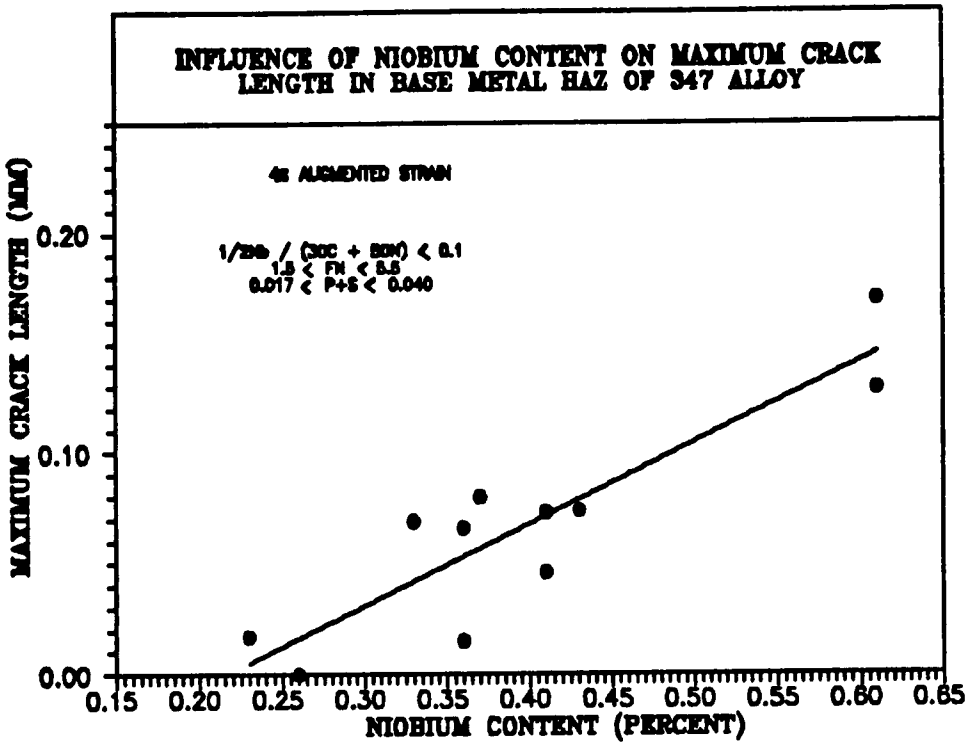


Figure 110. Effect of Nb content on liquation cracking in the base metal HAZ of 347 materials.

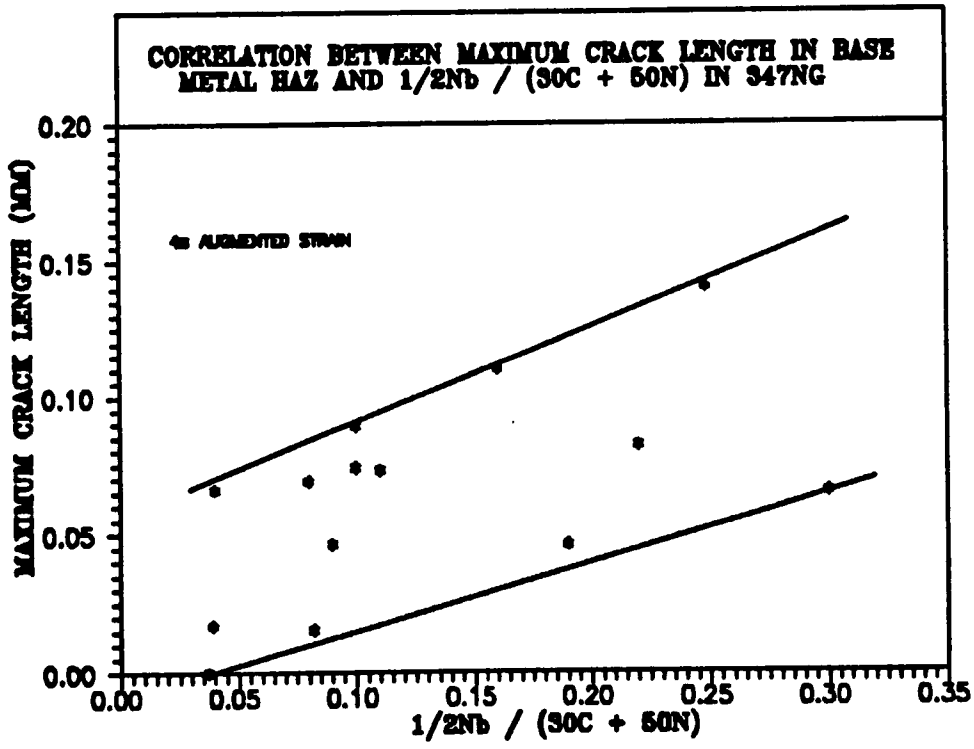


Figure 111. Correlation between base metal HAZ liquation cracking and 1/2 %Nb / (30 X %C + 50 X %N) in 347 materials.

later in this section, because liquation cracking in the base metal HAZ of 347 is directly related to the constitutional liquation of NbC and Nb(C,N), the ratio of 1/2Nb / (30C + 50N) (which gives an approximate liquation temperature of grain boundary due to the niobium carbo nitrides), may be a useful parameter to be employed for the evaluation of base metal HAZ behavior.

The effect of ferrite potential on the cracking extent of all materials is given in Figure 112. In general, as the ferrite potential increases, the MCL of decreases. However, the influence of ferrite appears to be slightly more effective for type 347 stainless steels than for 304, 316 and 316NG. That is, for a given increase in the potential, the decrease in the maximum crack length in type 347 is slightly greater than in the others. As Figure 112 shows, at lower ferrite potential, the extent of cracking in type 347 is greater than that of the other alloys, but as the potential increases, The 347 MCL approaches that of 316NG and 304 and when the ferrite potential reaches above about 3 FN, all materials have virtually identical cracking behavior (MCL).

Metallographic Characterization. A typical base metal HAZ crack in fully austenitic 316NG (316NG-D) is shown in Figure 113, which is characterized by intergranular fracture. The cracks appear to initiate near the weld fusion line and propagate into the HAZ about two grain distances and also extend to the fusion zone along the epitaxially related grain boundaries. One of the cracks at the left side of Figure 113 appears to be backfilled by liquid when the crack extends into the fusion zone. The backfilling of the crack occurred

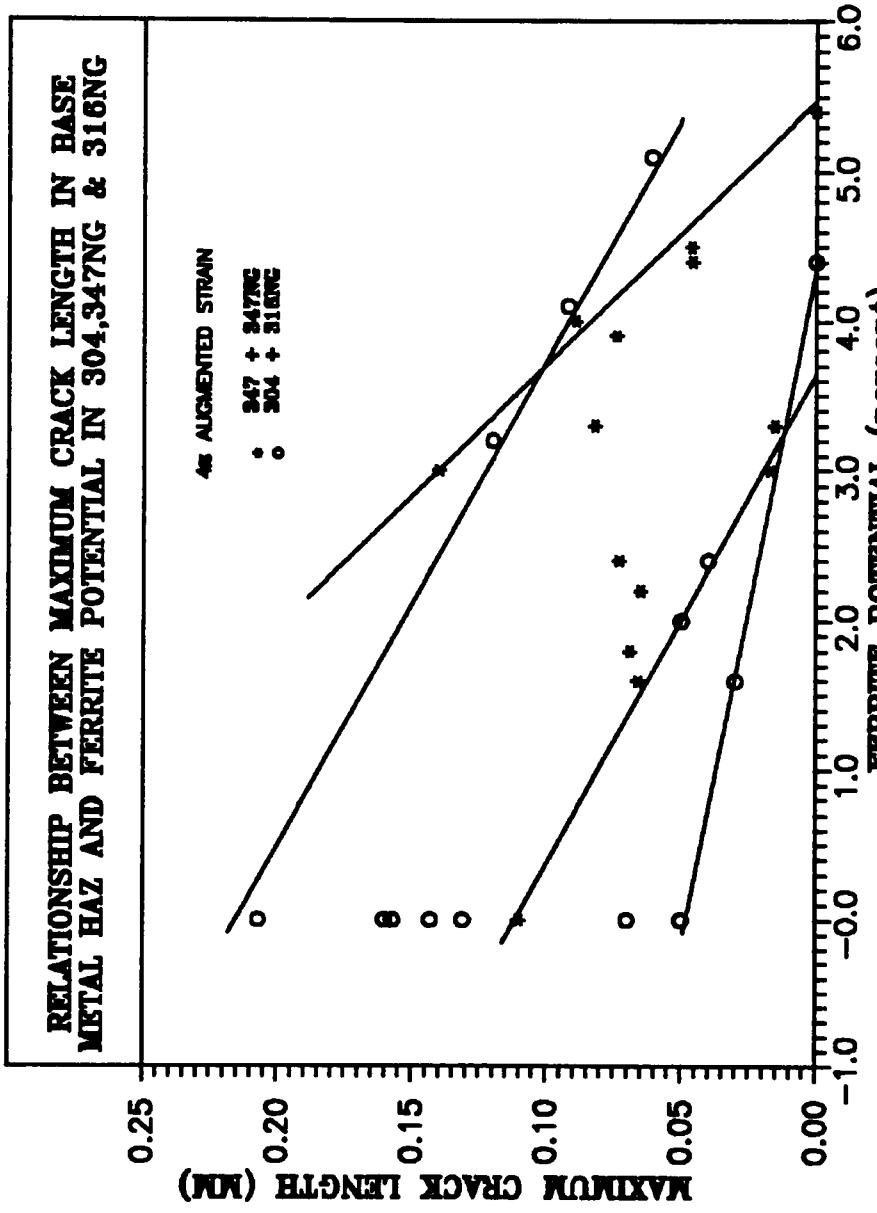


Figure 112. Effect of ferrite potential on the extent of liquation cracking in the base metal HAZ.

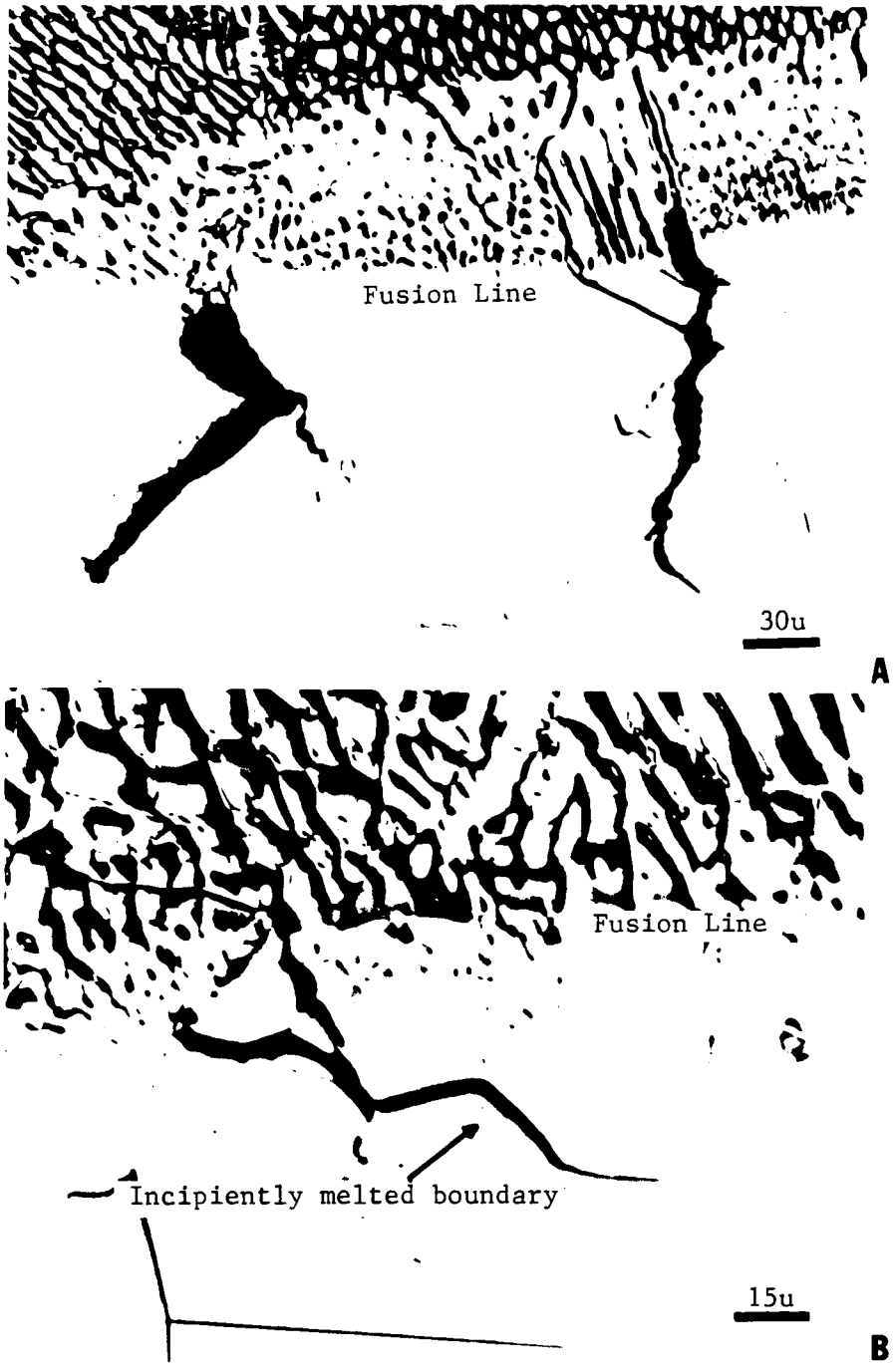


Figure 113. Typical liquation cracks in the base metal HAZ and liquated grain boundaries near the fusion line in the fully austenitic 316NG (316NG-D).

only in the portion which extended into the fusion zone. At higher magnification (Figure 113b), the region just adjacent to the fusion line experienced a significant melting along the grain boundaries. However, there is no clear evidence of the association of grain boundary liquation with any second phases or microconstituents.

Figure 114 reveals the fusion line regions that are typical of the positive ferrite potential 316NG material (also typical of the 304 and 316 materials). The transition from the true HAZ to the partially melted zone is characterized by the on-set of liquation along the grain boundaries. The extent of melting increases as the fusion line is approached. Careful examination reveals that almost continuous delta ferrite formed along the grain boundaries within about two grain diameters from the fusion line. Further, melting in the region surrounding the elongated ferrite band can also be noted. This ferrite exists in the as-received condition in a banded form but the morphology changed during elevated temperature exposure as expected. Because of the differences in solubility for the harmful elements, Si, S and P between ferrite and austenite in many instances the interphase boundary is found to be rich in these elements due to solid state diffusion (partitioning) during weld HAZ exposure. Thus, during on-heating, the ferrite-austenite interphase boundaries begin to melt first before melting of the less segregated austenite-austenite boundaries. This behavior is typical for all materials which have residual ferrite bands in the as-received condition.

Figure 115 shows the base metal HAZ microstructure typical of type 347. These microstructures in Figures 115a and 115b are from the

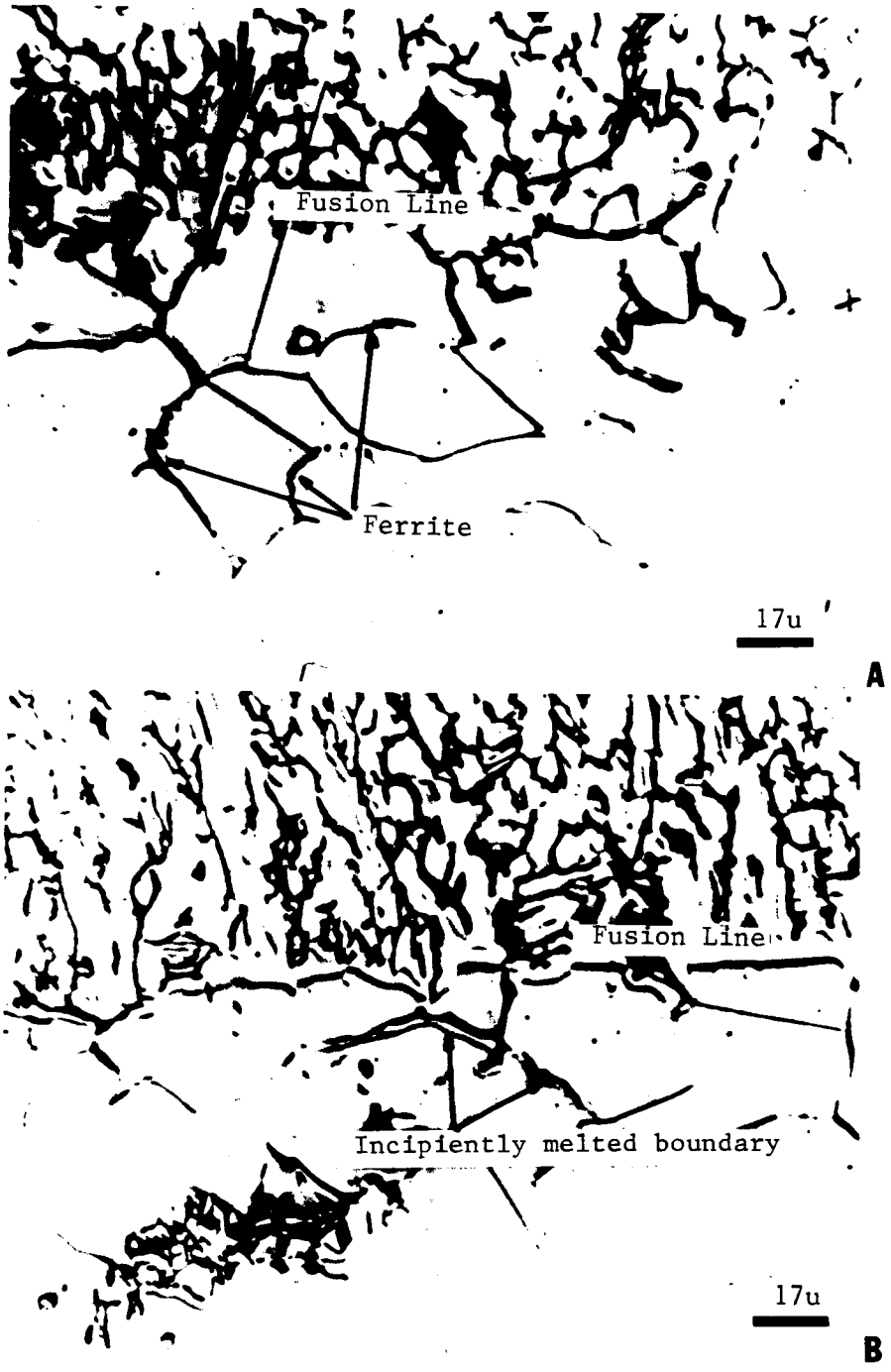


Figure 114. Partially melted region next to the fusion line in the primary ferritic base metal HAZ, revealing ferrite formation along the grain boundaries.



Figure 115. Typical microstructures in the base metal HAZ of type 347 material (347NG-E), revealing a difference in the location of the segregation bands relative to the fusion line.

same heat 347NG-E, but from different samples tested at 4% strain. In both microstructures, constitutional liquation of Nb(C,N) particles and segregation bands occurred within several grains from the fusion line and the extent increases as the distance to the fusion line decreases. However, careful examination reveals different microstructural characteristics between the two samples. The most apparent difference is that the location of the segregation bands relative to the fusion line is more closer in Figure 115b and thus a greater extent of constitutional liquation of Nb(C,N) has occurred, resulting in a longer liquation crack. However, the Nb(C,N) band in Figure 115a is away from the fusion line at which the peak temperature is not high enough to melt the segregated band by constitutional liquation. Thus, the segregate band remains intact and only Nb(C,N) particles near the fusion line melt and penetrates into the grain boundaries.

At higher magnification in Figure 116, constitutional liquation of Nb(C,N) and its association with HAZ cracking are evident. The liquid has more or less continuously penetrated into the grain boundaries and the niobium enriched liquid has resolidified as a Nb(C,N)-austenite eutectic.

Fractographic Analysis. For the fractographic examination of the Varestraint tested samples, the hot cracks in 316NG-D and 347NG-E were carefully excised by a thin cutting disc and the crack faces were opened by fracturing samples through the crack at liquid nitrogen temperature, and the opened surfaces were ultrasonically cleaned in

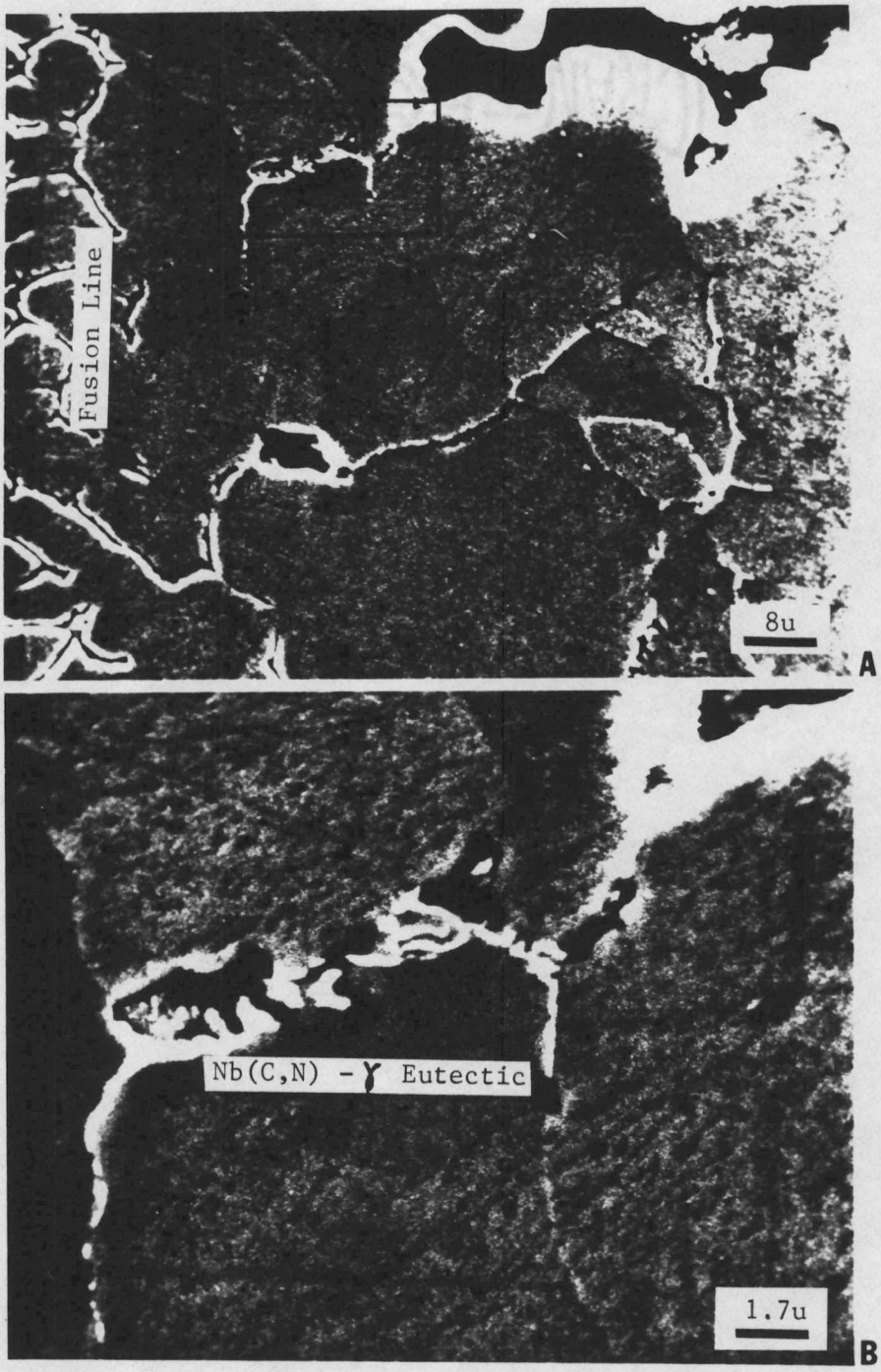


Figure 116. Constitutional liquation of Nb(C,N) in grain boundary, (347NG-E).

acetone for 10 minutes. The cleaned surface was then etched by the SPEED method to identify types and morphologies of second phases.

The fracture surface morphology of the region near the fusion line (316NG-D) as shown in Figure 117 reveals the intergranular nature of a crack. Careful examination reveals smooth and wavy patterns on the grain surface indicating the fracture is associated with a liquid film which is enriched in Si, S and/or Mo as shown in the EDAX analysis. However, no evidence of any second phases was found on the fracture surface.

Macroscopically, the fracture surface of the positive ferrite potential material (347NG-E) in Figure 118a has a rough appearance as compared to that in the fully austenitic base metal HAZ fracture surface. Approaching the fusion line, the fracture surface appears increasingly dendritic, indicative of more liquid at the grain boundaries in this region. The higher magnification microstructures in Figures 118b and 119 clearly show many dendritic/eutectic shape microconstituents on the surface. The EDAX analysis indicates that these constituents are enriched in niobium. Therefore, from the morphology, it can be expected that these are the products of the constitutional liquation of Nb(C,N) and its resolidification to the Nb(C,N)-austenite eutectics during cooling after grain separations.

Discussion. The results of Varestraint test, metallographic and fractographic inspection with SEM/EDAX have shown that hot cracking in the base metal HAZ of austenitic stainless steels occurs preferentially at intergranular sites and involves localized melting which is associated with an enrichment of S, Nb, S and/or Mo. The

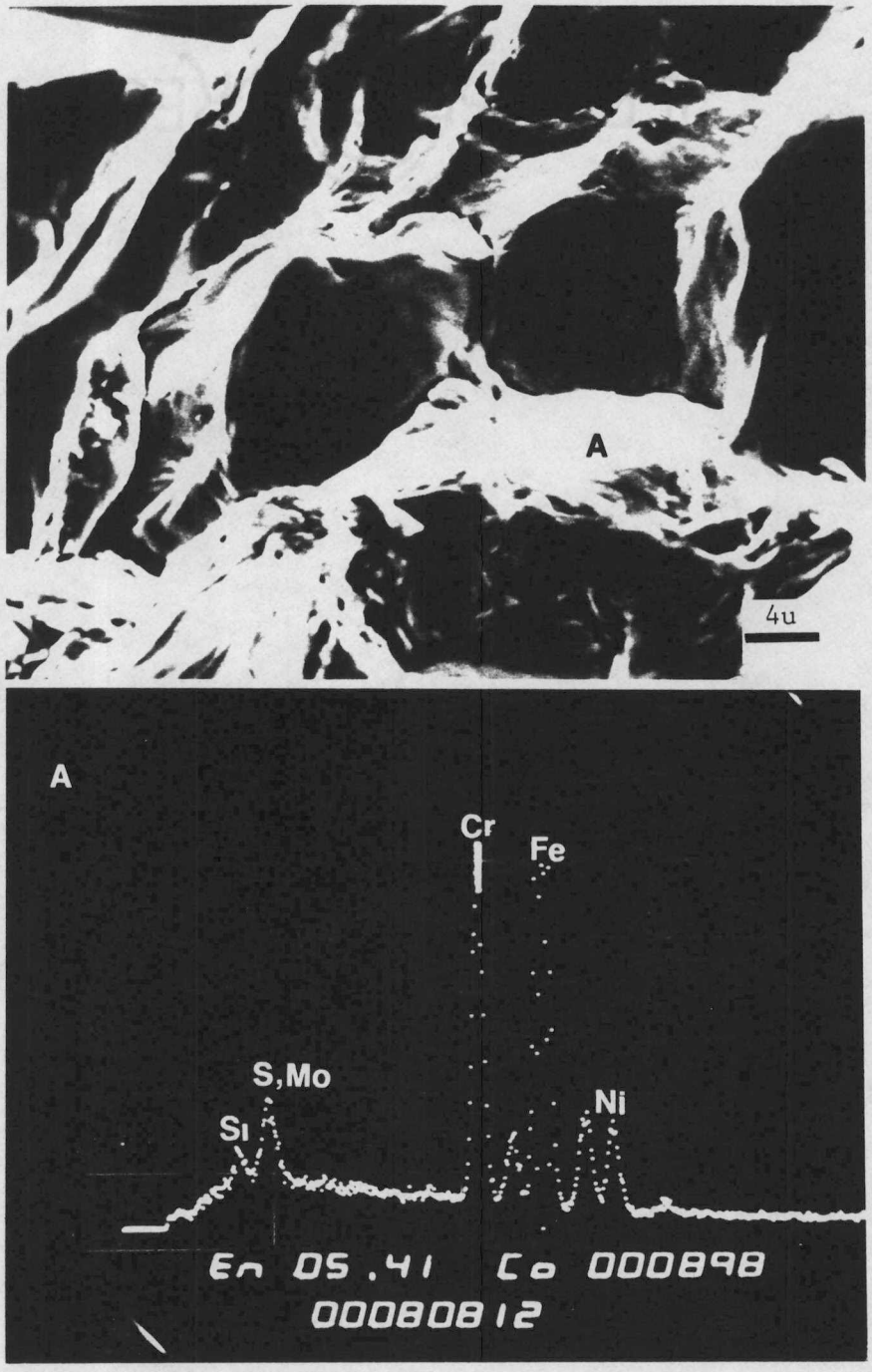


Figure 117. SEM fractograph of the base metal HAZ liquation crack surface and EDAX analysis in the fully austenitic (316NG-D).

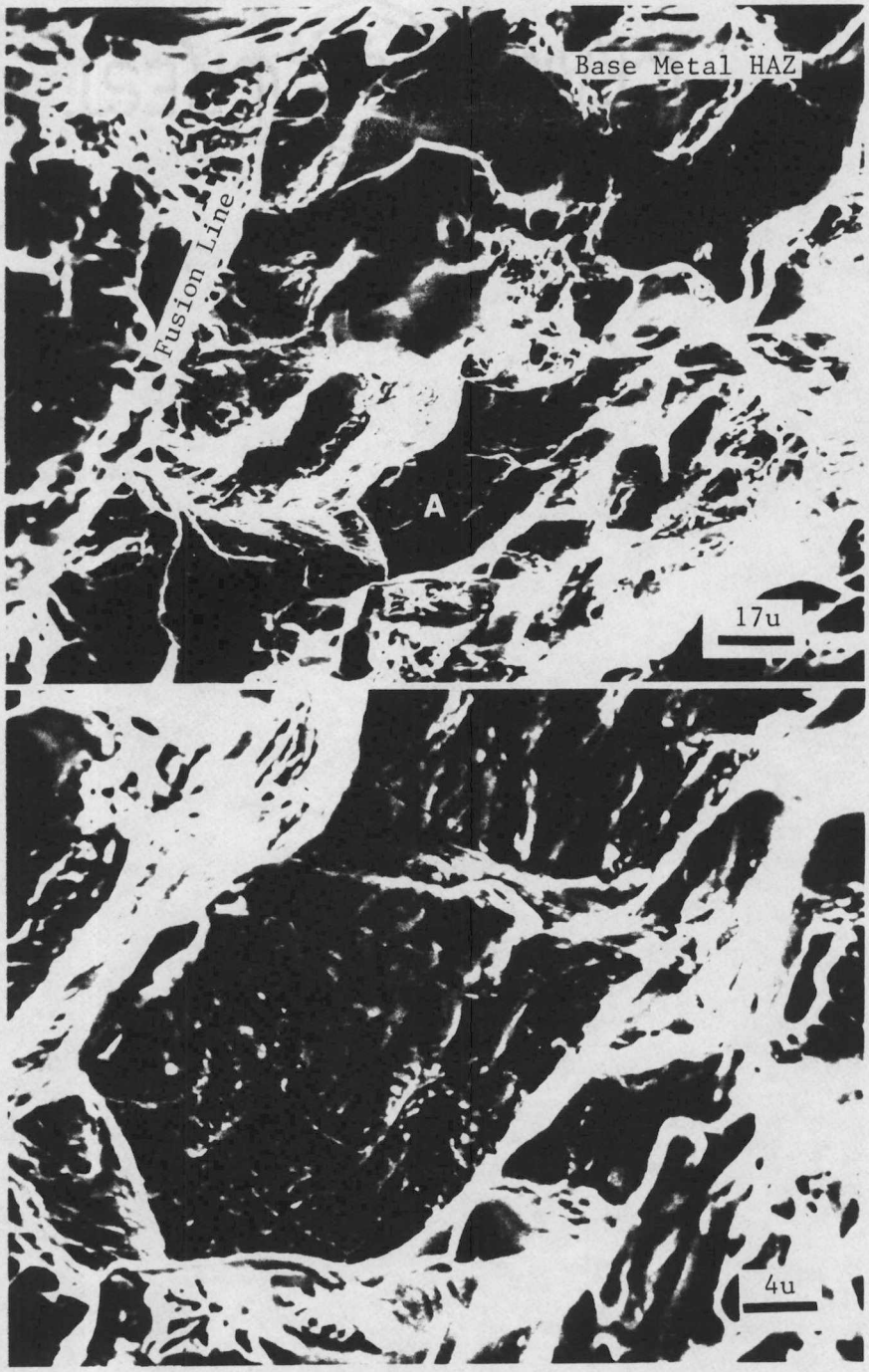


Figure 118. SEM fractograph of the base metal HAZ liquation crack surface in the primary ferritic (347NG-E), a) macroscopic appearance and b) higher magnification of region A in a).

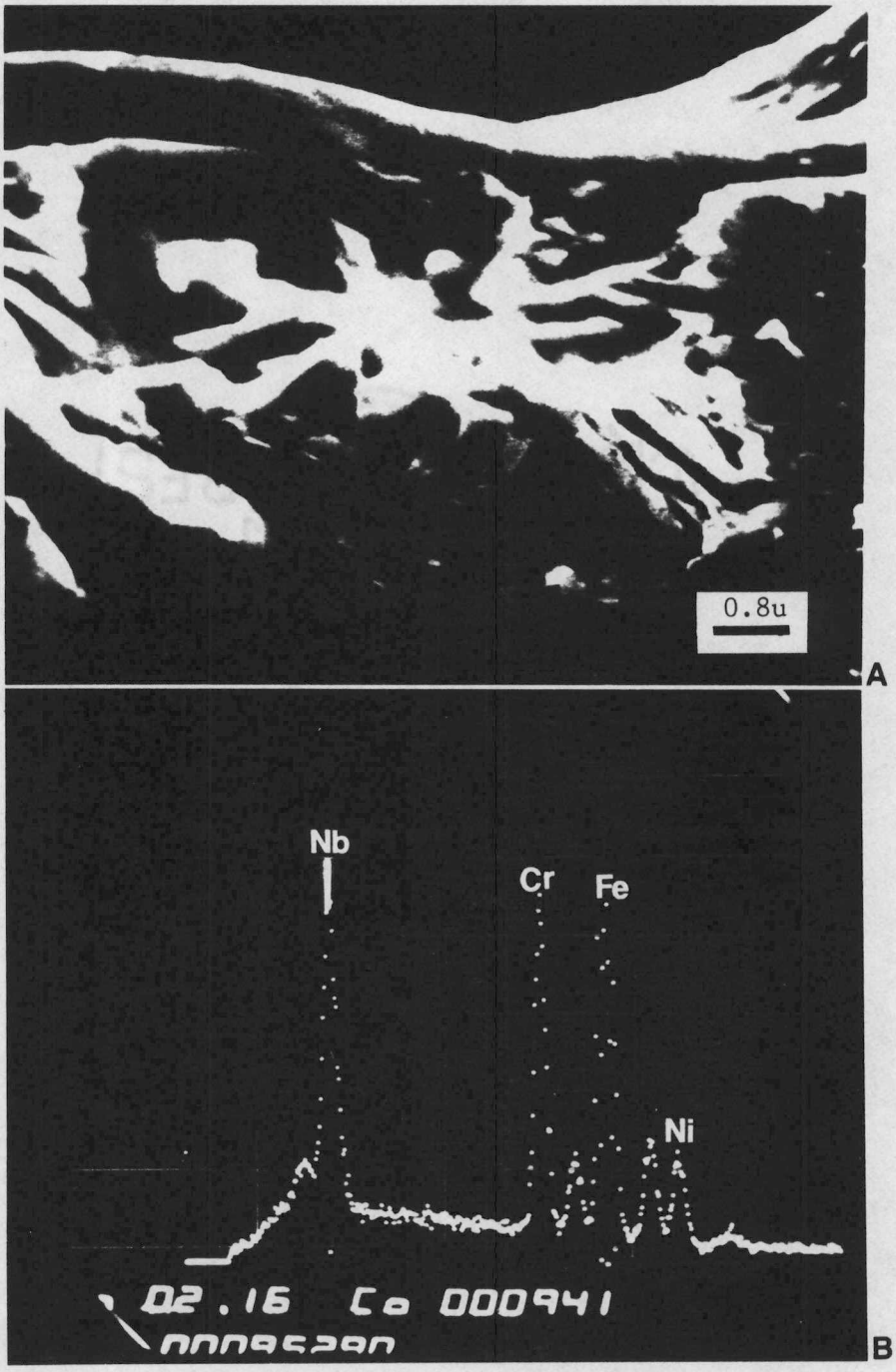


Figure 119. Higher magnification of a) region B in Figure 118a and b) EDAX analysis on Nb(C,N)-austenite eutectic.

grain boundary liquation in type 347 and 316NG is slightly different. In types 304 and 316NG materials, the liquation is mainly due to the "incipient melting" of the grain boundaries whose melting temperature was suppressed by the segregation of impurities. However, in 347, in addition to the incipient melting of the segregated boundary, constitutional liquation of Nb(C,N) particles and liquid penetration into the boundaries play a predominant role in crack formation. Thus, for given P, S and Si contents, 347 is slightly more susceptible to HAZ liquation cracking (longer MCL). The relatively longer MCL may be due to the wider liquation temperature range in 347. The earlier metallographic examination of Gleeble hot ductility tested samples indicated that the "incipient melting" of the segregated grain boundary occurred at about 2400 - 2450 ^{o}F (1315 - 1345 ^{o}C) for both 316NG and 347NG. However, the constitutional liquation of the large Nb(C,N) particles in the grain boundary begins at as low as 2300 ^{o}F (1260 ^{o}C) while the smaller particles in the grain matrix do not melt until temperature approaches about 2430 ^{o}F (1330 ^{o}C). Below 2430 ^{o}F (1330 ^{o}C), some small Nb(C,N) particles dissolve by a solid state reaction. Therefore, the wider localized melting temperature range in 347 may have resulted in a slightly longer MCL.

The Varestraint test results revealed that the heat to heat variation, within the same nominal chemical composition, was greater in 347 than in 304 and 316NG. The previous metallographic examination indicated that even within the same heat, there was a significant sample to sample variation, mainly due to the relative location of the segregation bands (Nb enriched bands) with regard to the weld fusion

line. That is, when a sample has segregation bands close to the fusion line, more constitutional liquation of Nb(C,N) and liquid penetration into the grain boundary occur, resulting in more extensive liquation cracking in the HAZ. However, when the segregation bands are located away from the fusion line, almost no or little liquation, depending upon the peak temperature experienced, was observed and thus a smaller MCL resulted. Therefore, significant heat to heat and sample to sample variations within the nominal composition in 347 alloy may be due to the variation in the density of the segregate bands and their location relative to the fusion line. However, in types 304 and 316NG, no segregation bands were observed near the fusion line so a reduced heat to heat cracking variation was evident. The significance of the segregation bands in HAZ liquation cracking can be found in the work by Tamura et al. (196), who observed that when the segregation bands do not exist, the migrating grain boundary can not "sweep up" enough solutes to cause extensive melting, resulting in a lower HAZ liquation cracking propensity.

The Varestraint test results also strongly indicate that although there is no clear correlation, the alloy having a higher content of harmful elements, in general, has a greater susceptibility. Further, the higher ferrite potential material has a better resistance to base metal HAZ liquation cracking than the fully austenitic alloys. The effects of ferrite was slightly more effective for type 347 than 304 and 316NG. Before considering the above observations, it is worthy to consider the generally accepted effects of ferrite formation during a thermal cycle. These are: 1. Delta ferrite has a higher

solubility for "harmful" elements such that these elements are less segregated in the austenite-austenite boundary. 2. Ferrite formation results in a more difficult grain migration and crack propagation, 3. The surface energy of the interphase boundary between ferrite and austenite is lower than that of austenite-austenite boundary and thus reduces liquid penetration.

The effectiveness of ferrite formation in the base metal HAZ on liquation cracking probably depends upon the manner in which the grain boundary liquid forms. Therefore, limited grain growth and difficulty of crack propagation due to ferrite formation are equally effective for types 347, 316NG and 304. As previously discussed, liquation in 316NG and 304 is mainly due to the "incipient melting " of a grain boundary whose melting point is depressed by segregation of impurity species. The possible sources of these "harmful" elements are a) the "original" segregation in the as-received condition during manufacturing processes and b) the "sweeping up" of solutes by a migrating boundary. These sources of segregation are significantly reduced by the above effects of delta ferrite (1 and 2). Thus, a reduced impurity segregation in the ferrite containing HAZ concomitantly results in a lesser extent of low melting liquid films along the grain boundary during on-cooling and then reduces extent of liquation cracking.

However, in type 347, in addition to the "incipient" melting of the segregated boundaries, constitutional liquation of Nb(C,N) and liquid penetration along the grain boundaries play a significant role. That is, the migrating boundaries are pinned by Nb(C,N) particles and

ferrite before the particles melt. When temperature reaches above 2300 ^{o}F (1260 ^{o}C), the particles in the boundaries begin to melt by constitutional liquation and the liquid penetrates along the grain boundaries as temperature increases. Unlike the grain boundary segregation of impurity atoms (which is more or less uniform), the Nb(C,N) particles along the grain boundary are not continuous and thus continuous wetting of grain boundary requires an easy penetration of liquid. Therefore, when ferrite forms along the grain boundary, the penetration of liquid into the ferrite-austenite boundary is difficult due to the high dihedral angle of the liquid in the low energy interphase boundary.

Therefore, in type 347 material, ferrite exerts all three beneficial effects. In contrast, types 304 and 316NG do not require the third effect of ferrite. However, it has to be remembered that at low ferrite potential (< 3 FN), the cracking sensitivity of 347, for a given impurity and ferrite potential, is "slightly" greater than that of 304 and 316NG, mainly due to the wider crack susceptible temperature range.

3. PREDICTION OF THE BASE METAL HAZ BEHAVIOR FROM THE GLEEBLE HOT DUCTILITY TESTS

This study has developed "new" quantitative and definitive criteria for hot ductility evaluation, by comparing fracture strain measured as a function of test temperature during the on-cooling tests to the actual in situ thermal strains measured as a function of peak temperature. These parameters are the Critical Strain Temperature

Range (CSTR) and the Ductility Recovery Ratio (DRR) measured at Critical Strain Temperature (CST) above which the fracture strain is smaller than the actual thermal strain and thus a material will crack by the assistance of thermal strain alone. These criteria are very sensitive to the metallurgical variables; ferrite potential, major and minor alloying elements and grain size in austenitic stainless steels, and thus can discriminate on a material to material or on a heat to heat basis for materials with the same nominal composition.

However, acceptance of these criteria as the hot cracking assessment criteria for the Gleeble hot ductility test has to be accompanied by comparison of these parameters with the HAZ cracking susceptibility of the same materials. This is the only way in which the necessary data to provide a reliable correlation between hot ductility response and the behavior of material during welding can be obtained. Therefore, in this section, the CSTR and DRR of the current program materials are compared with HAZ hot cracking susceptibility measured by Varestraint test.

Comparison of the hot ductility behavior with the Varestraint results is best accomplished using the base metal HAZ cracking potential, because both methods evaluate the same weld region. It is to be recognized, however, that to the extent that chemistry affects behavior, all three zones (fusion zone, weld metal HAZ and base metal HAZ) may be influenced in a similar manner.

The correlations between maximum crack length (MCL) and total crack length (TCL) from the Varestraint test with the CSTR and DRR from hot ductility test are given in Figures 120-122. Unexpectedly,

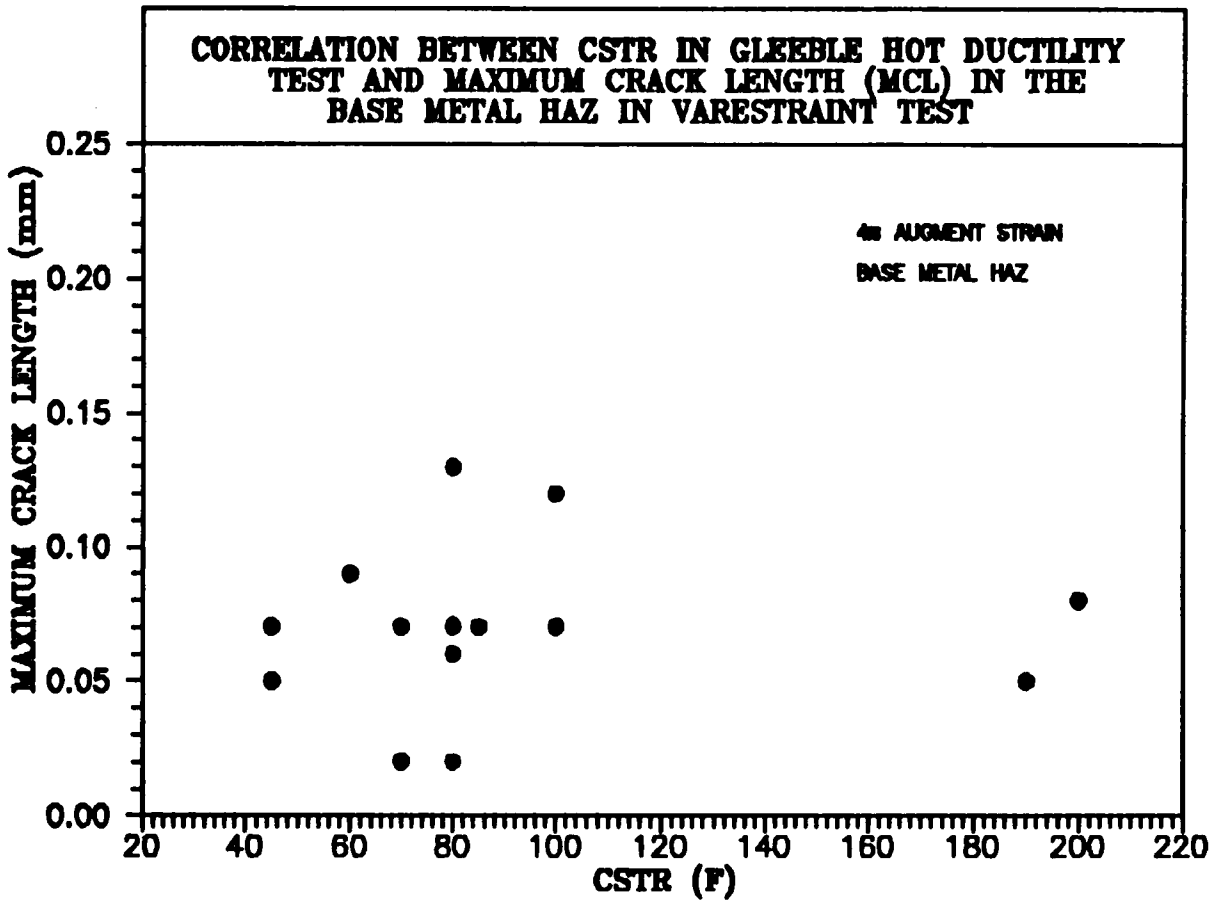


Figure 120. Correlation between MCL in the base metal HAZ in the Varestraint with CSTR in the Gleeble hot ductility testing.

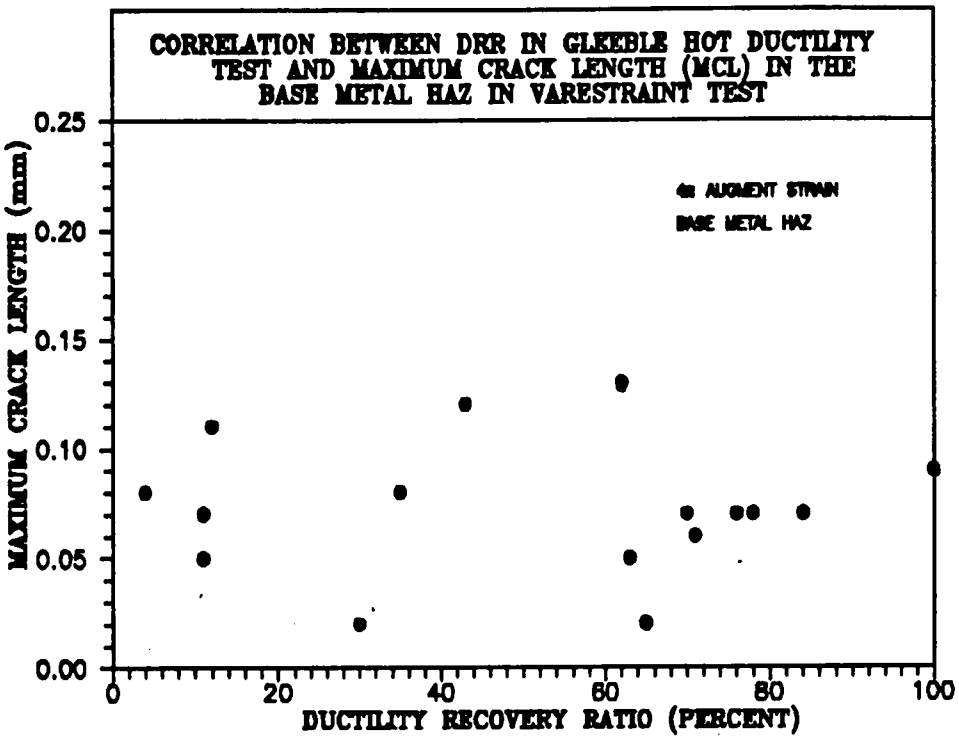


Figure 121. Correlation between MCL in the base metal HAZ in the Varestraint with DRR in the Gleeble hot ductility testing.

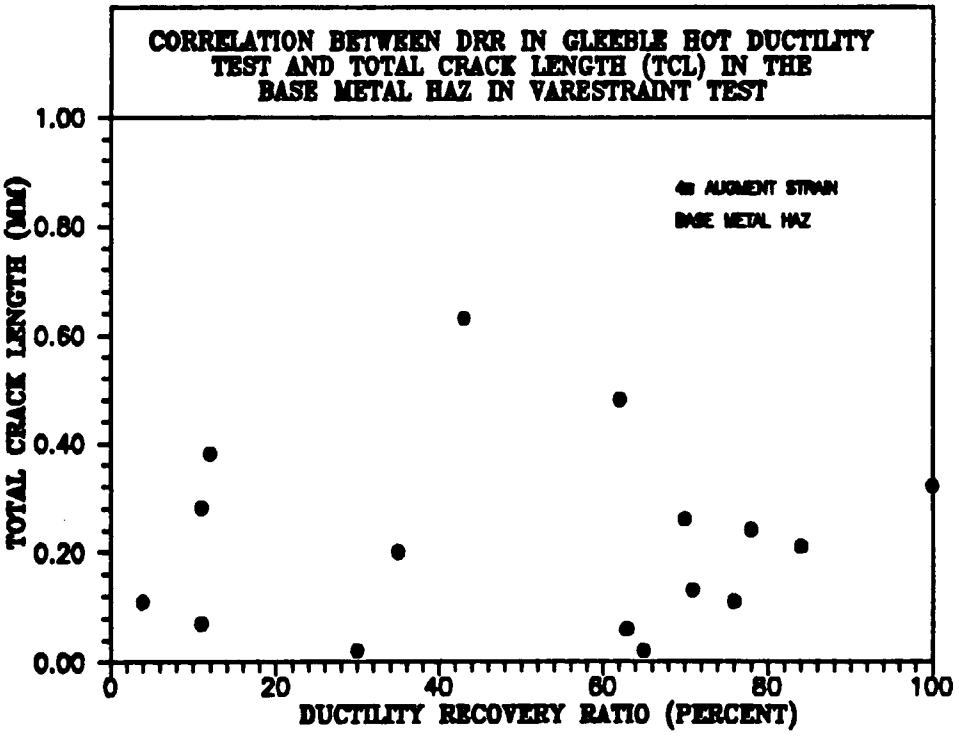


Figure 122. Correlation between TCL in the base metal HAZ in the Varestraint with DRR in the Gleeble hot ductility testing.

the CSTR and DRR in the hot ductility tests do not correlate well with MCL and TCL in the Varestraint test. No particular trend can be found in the MCL and TCL with the variation of CSTR from 45 F^{o} to 200 F^{o} and the DRR from 4 % to 100 %. When compared the DRR and CSTR with the cracking threshold strain, a slightly better correlation can be found as shown in Table 16. However, only the extremely susceptible materials (CSTR, > 150 F^{o} and DRR, < 10 %) can be distinguished and have a lower threshold strain as compared to the rest of the materials. For the majority of the materials, the threshold strain also does not vary with the CSTR and DRR.

It is evident that although the conventional criteria for the Varestraint test (MCL, TCL and threshold strain) have an ability to discriminate on a heat to heat basis as a function of the metallurgical variables as shown in the previous section, these criteria may not successfully be used in correlation with the hot ductility results. Because the on-cooling hot ductility testing, from which the CSTR and DRR were determined, is conducted during on-cooling from a "single" peak temperature (ZDT), the on-cooling hot ductility tests evaluate "only" the region which has experienced the ZDT peak temperature along and parallel to the fusion line. Therefore, the MCL and TCL, which are based on the measurement of crack length in direction perpendicular to the fusion line, may not give a good correlation with the hot ductility response. Thus, for a direct comparison of CSTR and DRR with the HAZ cracking susceptibility in the Varestraint test, a new criterion was developed. This criterion is termed the "Cracked HAZ Length (CHL)", which is measured along the

Table 16. Correlation among Gleeble hot ductility parameters (CSTR/DRR) and Varestraint HAZ cracking parameter (CHL).

Code	Type	ZDT(°F)	CSTR[a]	DDR[b]	CHL[c](mm)	Threshold strain (%)
347NG-A	347NG	2500	100	11	0.25	2
347NG-B	347NG	2500	80	76	0.07	2
347NG-C	347NG	2485	45	63	0.04	2
347NG-D	347NG	2480	200	4	0.54	0.5
347NG-E	347NG	2480	190	11	0.40	1
347NG-F	347NG	2500	80	30	0.22	2
347NG-G	347NG	2485	85	70	0.08	2
347NG-H	347NG	2475	45	78	0.11	2
347NG-I	347NG	2500	70	84	0.11	2
347NG-J	347NG	2500	70	65	0.10	2
347-5	347L	2485	65	35	0.26	1
347-6	347R	2450	150	12	1.46	1
316NG-A	316NG	2500	80	71	0.07	2
316NG-B	316NG	2500	100	43	0.19	1
316NG-C	316NG	2500	60	100	0.10	1
316NG-D	316NG	2500	80	62	0.12	1

a: Critical Strain Temperature Range
b: Ductility Recovery Ratio (%)
c: Cracked HAZ Length (CHL) in Base Metal HAZ

fusion line in the HAZ where hot cracks form. The location of the CHL relative to the instantaneous weld pool when the augmented strain is applied is schematically shown in Figure 123. The macroscopic hot cracked HAZ is also shown in Figure 124, which more clearly defines the location of CHL relative to the fusion line. The instantaneous weld pool is indicated by the dotted line.

The CHL is the length measured from the edge of the instantaneous weld pool (point A in Figure 123) to the last crack (point B) in direction opposite to the welding direction, where the HAZ is in the cooling portion of the thermal cycle when the augmented strain is applied. Some cracks in the HAZ in front of the instantaneous edge of the weld pool (point A) which experienced the on-heating cycles at the moment of straining, were also occasionally found. These cracks were not considered when measuring the CHL, because the CSTR and DRR were determined from the on-cooling ductility tests. From the practical standpoint, cracks do not form during on-heating cycles, during which the HAZ experiences compressive strains instead of tensile strains as shown earlier (actual TM cycles).

The measured cracked HAZ length (CHL) at the 4% strain level for the current program materials is given in Table 16 together with the CSTR and DRR. The graphical correlations of CHL with DRR and CSTR are given in Figures 125 and 126, respectively. These figures indicate that unlike the conventional criteria (MCL and TCL), the CHL has an excellent correlation with the CSTR and DRR. Figure 125 shows that with an increase in DRR, the CHL gradually decreases and when DRR is greater than about 40 $\pm$ 5%, the CHL appears to level off to a very low

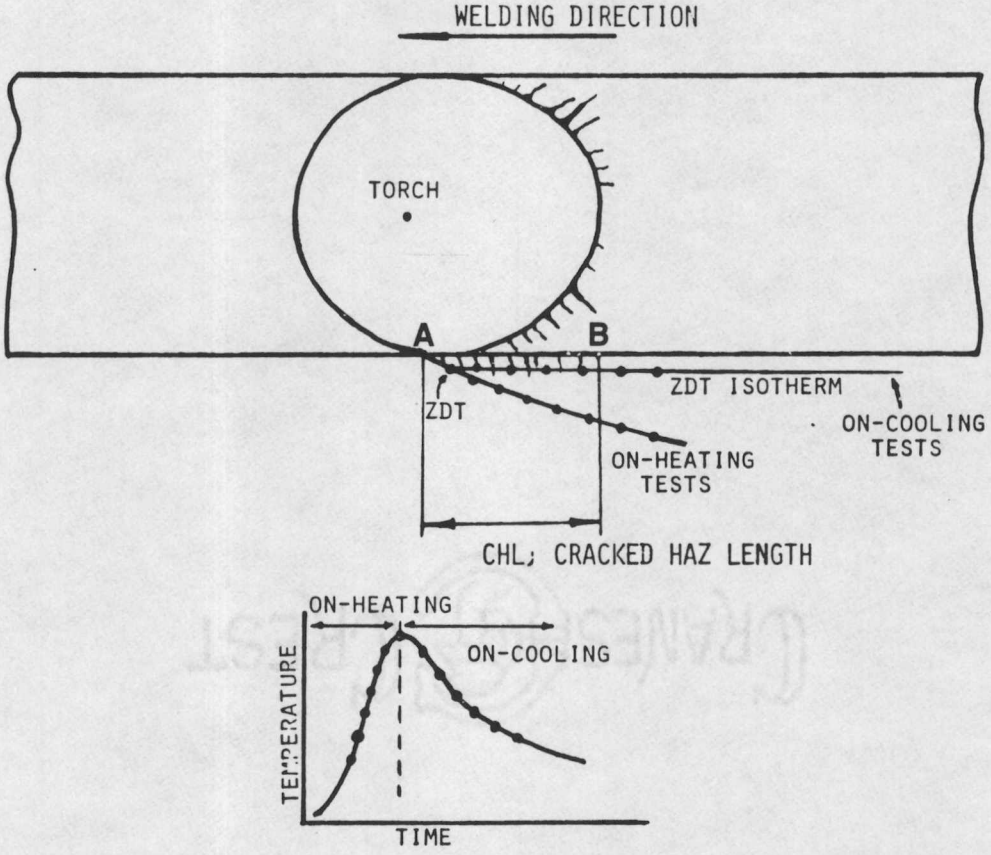


Figure 123. A schematic representation of the concept of the Cracked HAZ Length (CHL).

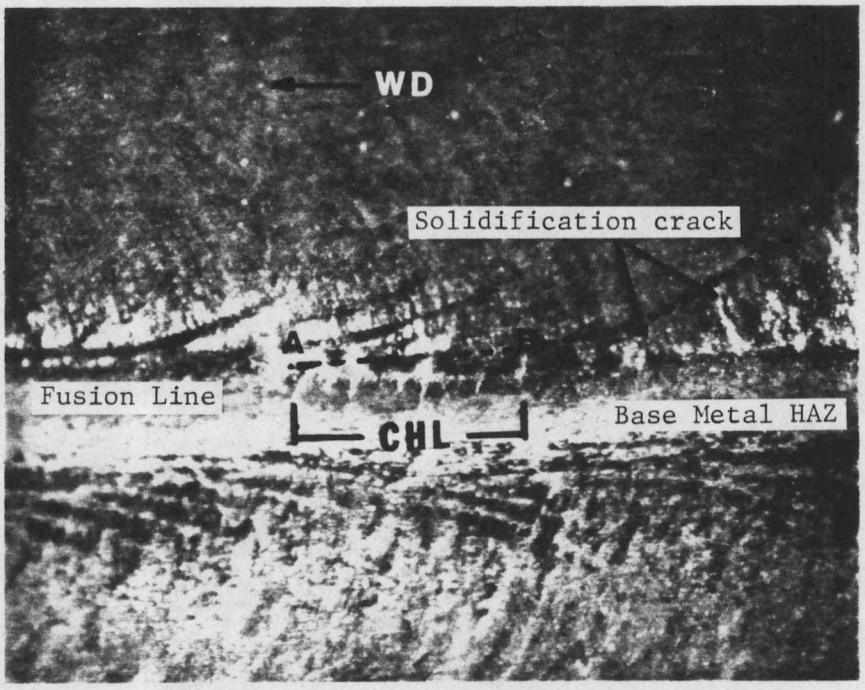


Figure 124. The location of CHL relative to the instantaneous weld pool in the base metal HAZ.

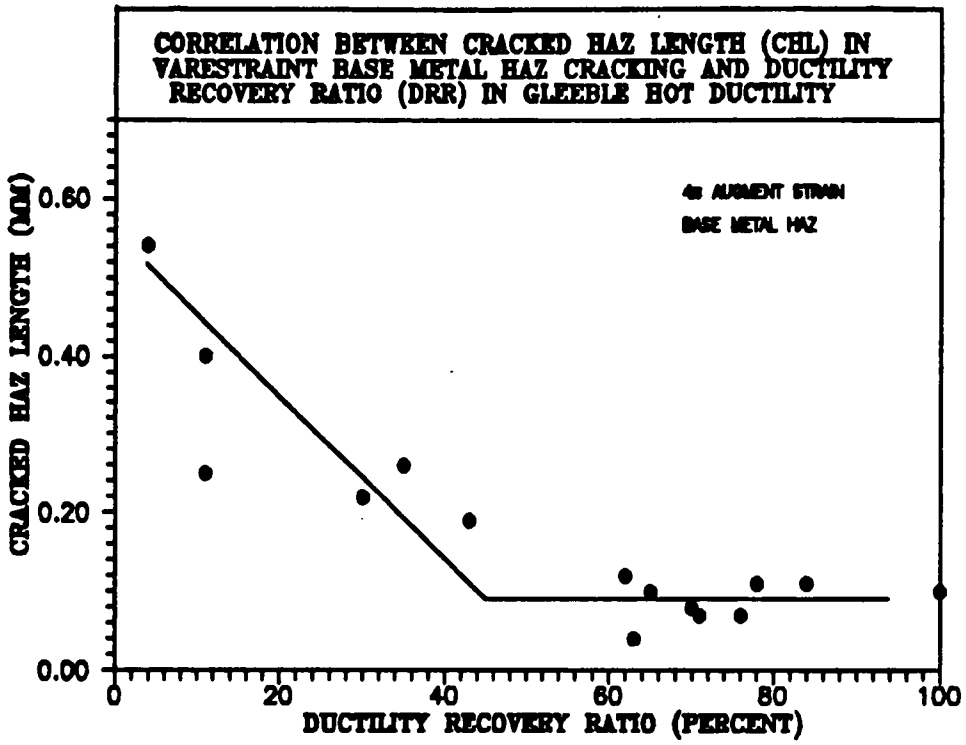


Figure 125. Correlation between CHL in the base metal HAZ cracking in the Varestraint and DRR in the Gleeble hot ductility testing.

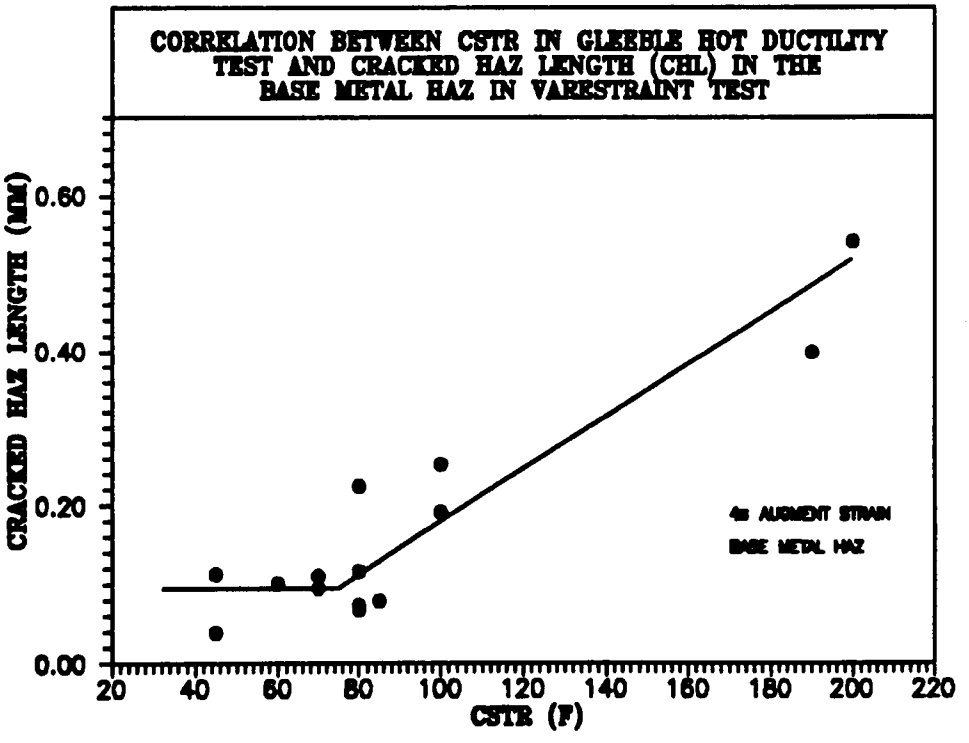


Figure 126. Correlation between CHL in the base metal HAZ cracking in the Varestraint and CSTR in the Gleeble hot ductility testing.

value of about 0.1 mm. In a similar way, Figure 126 reveals that when the CSTR is less than 70 ± 10 F^{o}, the cracked HAZ length is almost constant at 0.1 mm with variation in the CSTR. However, when the CSTR is greater than 70 ± 10 F^{o}, the CHL increases with an increase in the CSTR.

Therefore, when a material has the CSTR greater than 70 ± 10 F^{o} and DRR less than 40 ± 5%, the CHL is finite, indicating a higher susceptibility to base metal HAZ cracking. When the CSTR is less than 70 ± 10 F^{o} and the DRR is greater than 40 ± 5%, the CHL measured at 4% strain level is essentially zero and the material appears to be not susceptible to HAZ hot cracking. As mentioned earlier, the CSTR and DRR are very sensitive to metallurgical variables. Thus, from the above excellent correlations between CSTR, DRR and CHL, the "new" CHL criterion is also sensitive to the metallurgical variables and can thus discriminate on a material to material and heat to heat basis. Therefore, the critical values, 70 ± 10 F^{o} for CSTR, 40 ± 5% for DRR and 0.1 mm for CHL can be used successfully for acceptance criteria for Gleeble hot ductility testing and Varestraint base metal HAZ hot cracking. That is, when the hot ductility response of material during on-cooling from the ZDT is greater than 40 ± 5% in DRR and less than 70 ± 10 F^{o} in CSTR, the material will have a virtually zero CHL at the 4% strain level in the Varestraint test and thus be trouble free in actual field fabrication practice.

The next question, may be most important and difficult, "will a material having a CSTR greater than 70 ± 10 F^{o} and a DRR less than 40 ± 5% really cause difficulties in hot cracking when making a sound

weld in actual fabrication?" It must be remembered that the main purpose of hot ductility testing is to procure material with hot ductility properties which would be "suitable" for satisfactory weldability. A hot ductility requirement which is suitable for satisfactory weldability in certain conditions may not be necessarily suitable for other conditions.

The laboratory hot ductility testing on the simulated weld HAZ, for example, does not consider what kind of filler metals will be used in the welding of the particular materials being tested. It has been well known (106, 108 and 109) that when the weld metal is stronger than the heat affected zone (overmatched filler metal), a substantial amount of the necessary yielding due to the weld shrinkage stress, will occur in the HAZ. However, if the strength of the HAZ is equal to or greater than that of the weld (matched or undermatched filler metals), then it is possible that very little or no yielding would occur in the HAZ, resulting in a sound weld. Thus, the weld metal properties (ductility, strength and etc.) relative to that of HAZ determine, in many cases, whether the HAZ will suffer from cracking. Therefore, many investigators have considered that the criteria for the hot ductility test should be derived from the comparison of hot ductility data with the severely restrained weld test results as was done in this study. Further, the hot ductility and strength of the filler metal to be used should also be determined and then compared with that of the base material.

It has to be remembered that the CSTR and DRR were determined by using the actual insitu thermal strains which are the most realistic

values measured in an actual weld and the critical values of 70 ± 10 F^{o} for CSTR and 40 ± 5% for DRR were obtained from comparison with the results in the Varestraint test which is one of the most severe restraint type test methods (although the restraint is from an external source). When a self restraint type method is used for the determination of the critical values, the values may be greater than 70 ± 10 F^{o} for CSTR and be smaller than 40 ± 5% for DRR. Therefore, the critical values found in this study may be conservative but if the material passes the conservative criteria, it should be free from weld cracking. **Thus, it is strongly believed that if the welding conditions and weld joint designs are properly chosen, a material which has CSTR less than 70 ± 10 F^{o} and DRR greater than 40 ± 5% (in the Gleeble on-cooling hot ductility tests from the ZDT) will have a significantly reduced chance of cracking in the HAZ.**

CHAPTER V

EFFECTS OF Si, N AND REM ON HOT CRACKING BEHAVIOR

This chapter includes evaluation of the effects of some selected alloying and impurity elements on the hot cracking susceptibility of austenitic stainless steels. The elements evaluated are Si, N and rare earth metals. Although, in the earlier chapters, the effect of some of these elements on solidification and liquation cracking susceptibility of stainless steel was discussed, it is very important to understand how the individual elements behave in regard to hot crack formation. In order to systematically investigate, the weld fusion zones were designed to have different levels of each element investigated while maintaining other elements at a constant level by the element implant technique or by obtaining materials having different levels of specific elements.

1. SI AND ITS SYNERGISTIC EFFECTS WITH N

As reviewed in the literature review chapter, the general opinion is that a higher silicon content is harmful from the point of view of hot cracking. The influence of silicon is, however, known to be different in weld metals with different chemical compositions. When the material has a fully austenitic composition, it is highly sensitive to silicon content. The partially ferritic composition is not so sensitive to Si and it can be tolerated up to 1.5-2.5% without increasing hot cracking susceptibility (35).

In this section, the effect of Si level on solidification cracking is systematically evaluated. In order to modify the silicon content in the fusion zone of 304-3, the element implant technique using a Fe - 3.5% Si alloy was utilized as described earlier in the experimental procedure. The modified chemical composition with three different levels of Si are given in Table 17. The silicon content varies from 0.54% to 1.25%.

Further, in order to investigate the synergistic effect of Si with N, the highest Si implanted samples (1.25%) were subsequently fused under a N_2 containing Ar shielding gas. The various N levels in the fusion zone were obtained by the addition of different volume percent of nitrogen (0, 5%, 20%) to the Ar shielding gas during autogenous fusing. Since this technique involves the addition of N_2 to the shielding gas, the basic composition of the weld was not changed except its ferrite content (and solidification mode depending on the amount of the addition).

Varestraint Test Results and Discussion

The effect of silicon on solidification cracking susceptibility of type 304 stainless steel is illustrated in Figure 127. In this figure, the total crack length is plotted as a function of the silicon content. Each data point is the average of three tests at 4% augmented strain level. Figure 127 clearly indicates that as Si increases to 0.78%, the susceptibility to solidification cracking of 304 also increases. When the Si content is greater than 0.78%, no further increase in the extent of cracking can be noted. In fact, when the Si increases to 1.25%, the extent of cracking decreased

Table 17. Chemical compositions of materials used for Si effect study.

Code	Type	FN*	C	Si	Mn	P	S	Cr	Ni	Mo	N
304Si-A	304	3.0	0.015	0.54	1.43	0.026	0.008	18.19	9.17	0.29	0.078
304Si-B	304	4.0	0.032	0.78	1.32	0.026	0.008	18.19	9.17	0.29	0.078
304Si-C	304	8.0	0.050	1.25	1.25	0.026	0.008	18.19	9.17	0.29	0.078

a: Measured Ferrite content with Magne-Gage

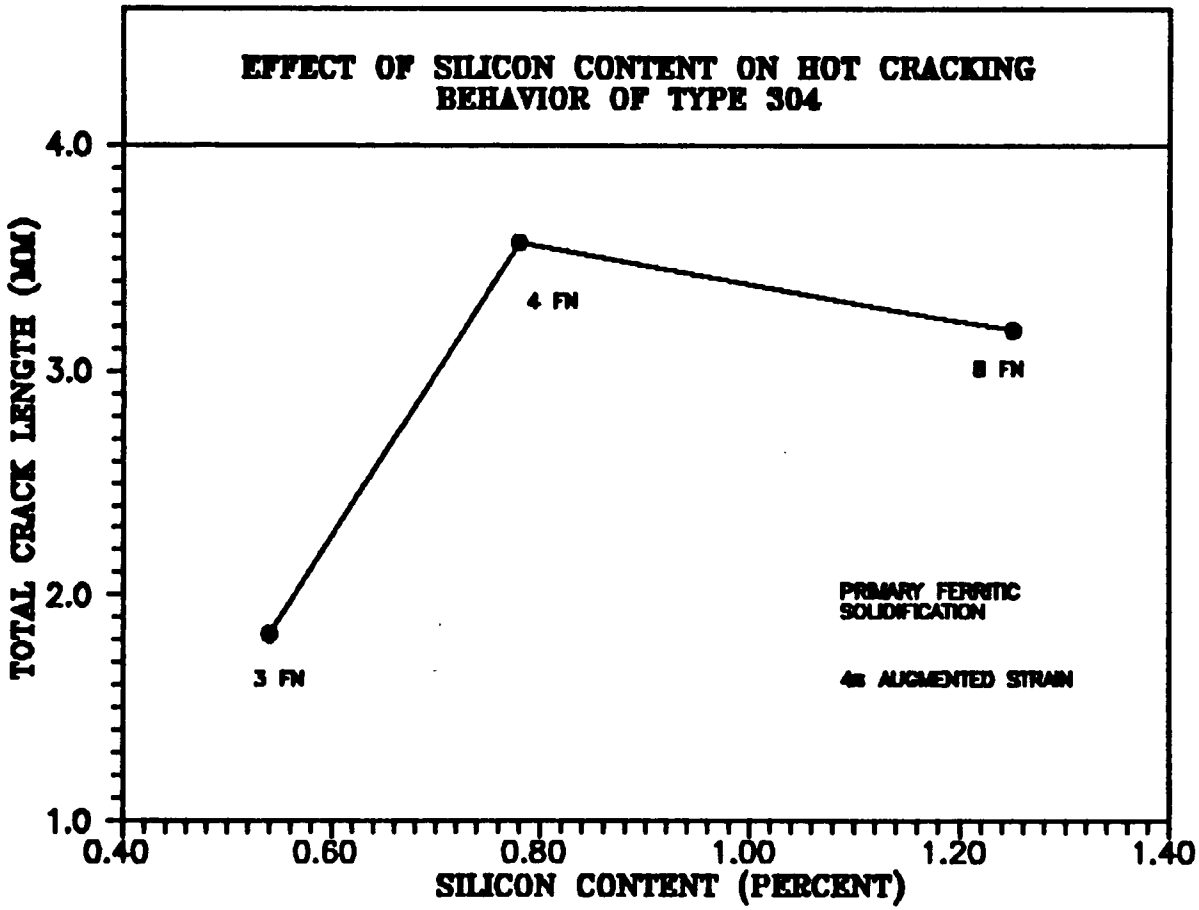


Figure 127. Effect of silicon content on solidification cracking in 304.

slightly as compared to that at 0.78%Si. However, the cracking is still much greater than that at 0.54%Si. The room temperature ferrite content at each Si level is also given in Figure 127. All materials have a primary ferritic solidification mode and the ferrite content increases as the silicon content increases due to the strong ferrite stabilizing effect of Si. When Si increases to 0.78% from 0.54%, there is almost no change in FN. However, when the Si content is raised to 1.25%, the room temperature residual ferrite content more than doubled (8 Vs. 3 FN). The slightly decreased solidification cracking in the high Si (1.25%) sample as compared to the 0.78 %Si sample may be due to an increased amount of primary ferrite during solidification (increased Cr_{eq}/Ni_{eq}) and thus concomitantly higher room temperature ferrite content.

The typical microstructure and crack morphology in the 1.25%Si weld metal is shown in Figure 128a. Cracking has occurred along solidification grain boundaries, along which a significant amount of silicates, phosphides and sulfides precipitated, as shown in the TEM micrograph from the carbon extraction replica in Figure 128b. Figure 128b reveals that the solidification grain boundary is continuously decorated by the fine sulfides, phosphides and larger manganese silicates (STEM analyses on these particles are given in Figure 129). Therefore, the greater solidification cracking in the higher Si alloy appears to be directly associated with segregation of Si in addition to S and P, which in turn form low melting silicates, sulfides and phosphides in the grain boundaries during cooling and provide favorite sites for crack formation.

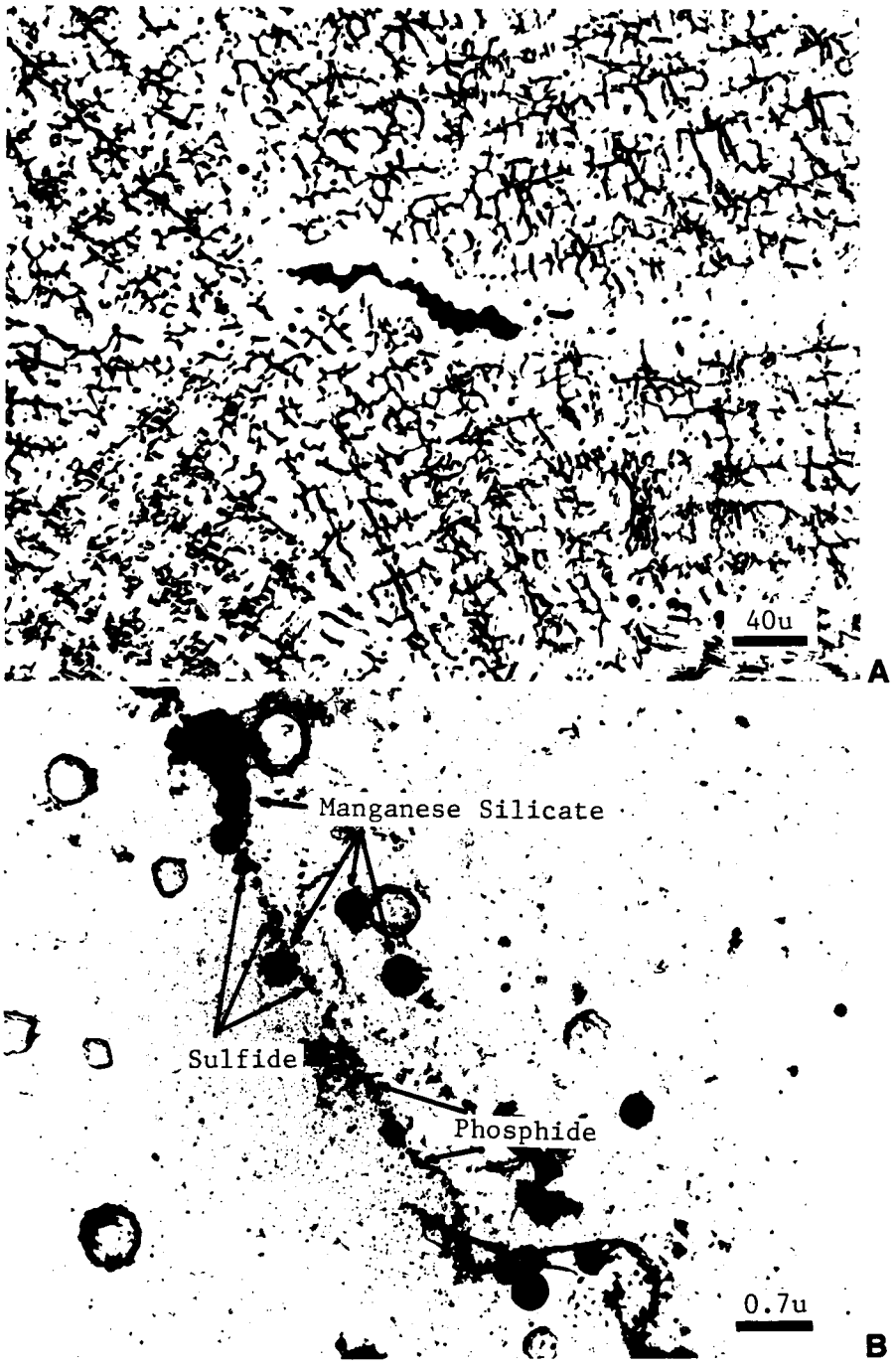


Figure 128. Typical solidification crack in the 1.25 %Si containing 304. a) OLM and b) TEM (carbon extraction replica).

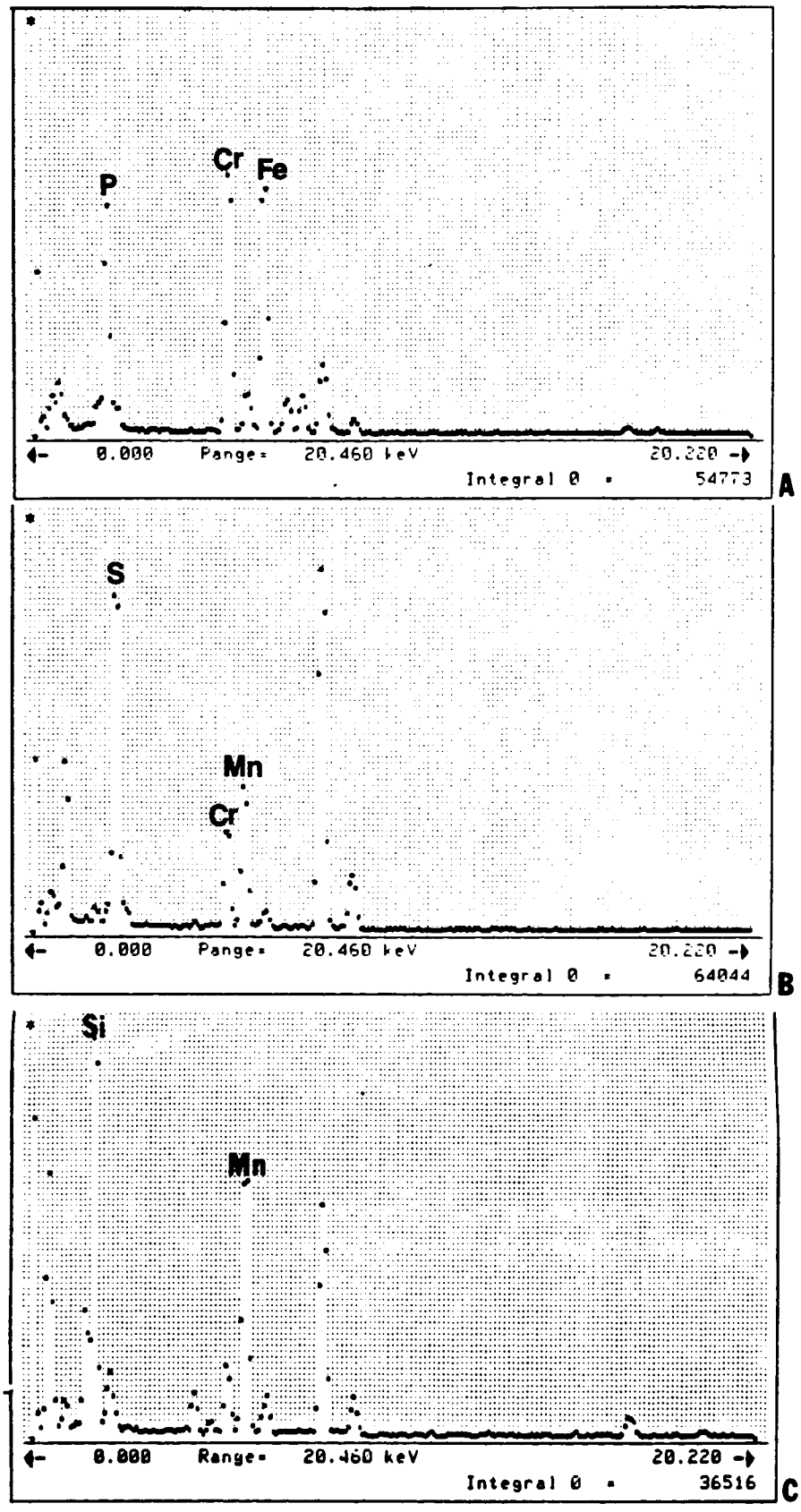


Figure 129. STEM analysis on a) phosphide, b) sulfide and c) manganese silicate.

Kakhovskii et al. (198) have found that when silicon increases, a highly Si-segregated, last solidifying liquid forms chromium-nickel-silicon eutectics along the interdendritic regions. The result of this is that the high temperature intergranular ductility and strength of the material decreases abruptly, causing a decreased resistance in welds to hot cracking. However, in this study, no evidence of formation of the Cr-Ni-Si eutectic was found.

The effect of nitrogen additions on fusion zone hot cracking behavior of the high Si containing (1.25%) 304 weld metal is given in Figure 130. The total crack length is plotted as a function of the volume percentage of N_2 in the Ar shielding gas. When 5% nitrogen is in the Ar shielding gas, the TCL, unexpectedly, decreased as compared to that welded with 100% Ar. However, when the nitrogen addition was increased to 20 vol%, the extent of cracking increased considerably. The room temperature microstructures for both the 5 vol% and 20 vol% additions are given in Figures 131 and 132 and reveal that the 5 vol% N_2 addition still results in a primary ferritic solidification mode and about 1 FN retained ferrite. On the other hand, the 20 vol% N_2 addition resulted in a solidification mode change from the primary ferritic to fully austenitic. Thus, the significant increase in cracking in the fusion zone when welded with the 20 vol% N_2 shielding gas is mainly due to fully austenitic freezing, which results in an increased amount of segregation of low melting temperature phosphides and sulfides along the dendritic boundaries as shown in Figure 132b.

Further, as long as the weld metal maintains the solidification mode as primary ferritic, the addition of N does not appear to have a

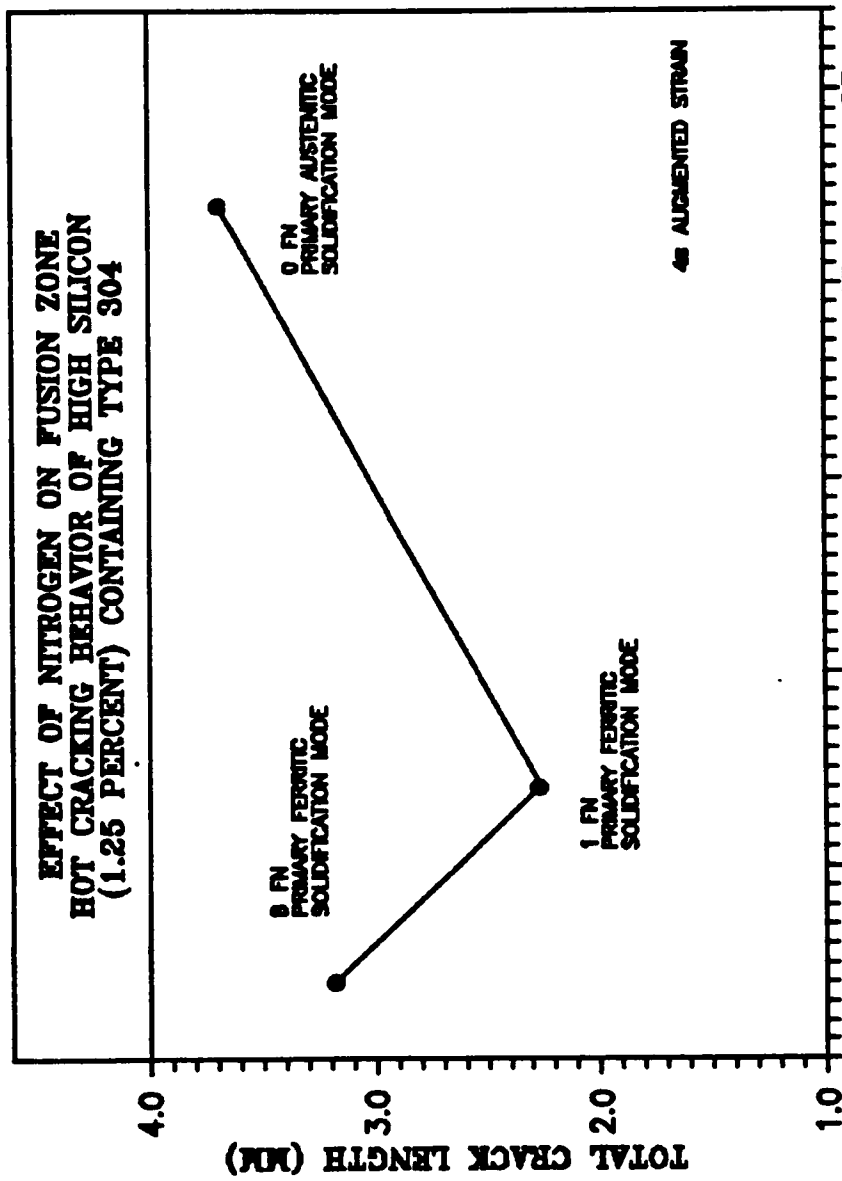


Figure 130. Effect of nitrogen addition on solidification cracking in the high silicon containing (1.25 %) 304 weld metal.



Figure 131. Solidification cracks in the primary ferritic high Si (1.25%) weld metal, 5 %N_2 + 95 %Ar shielding.

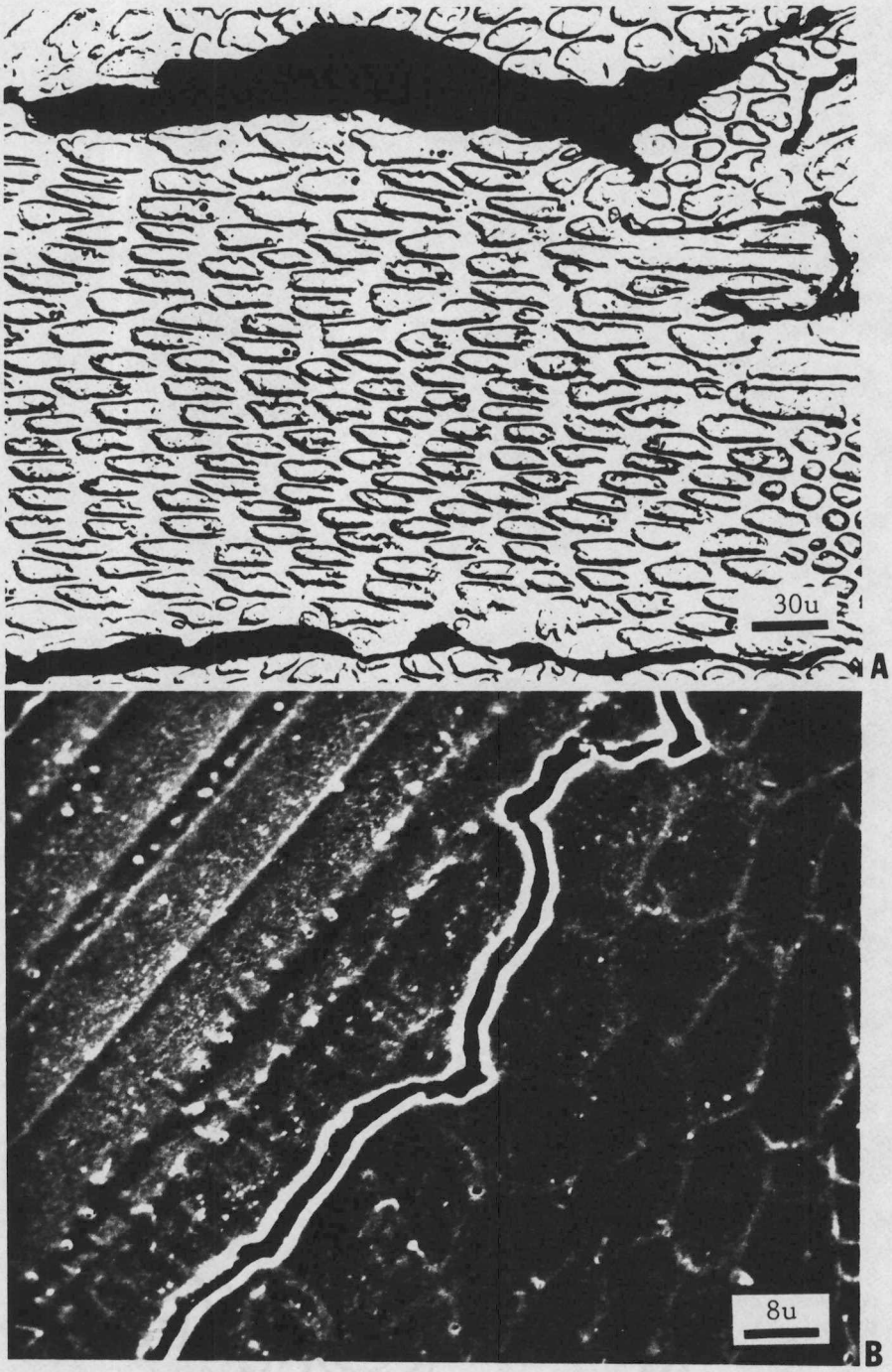


Figure 132. Solidification cracks in the fully austenitic high Si (1.25%) weld metal, 20 $\%N_2$ + 80 %Ar shielding.

harmful effect. In fact, it decreases the extent of cracking of the high silicon containing 304 (1.25%). A very similar result was reported by a Russian researcher (199); that an increase in the nitrogen content, at constant level of other alloying elements and with the ferritic-austenitic structure of weld metal unchanged, caused no harmful effects on hot cracking resistance, regardless of the reduction in the ferrite content were noted. Other Russian researchers (198) have found that when nitrogen is added to the weld metal, the permissible silicon content without causing solidification cracking is raised and the hot cracking susceptibility of the 0.4-0.45 %Si containing alloy was decreased by increasing the nitrogen content up to 0.1-0.12%. However, if the concentration is further increased beyond a critical amount, the resistance to cracking decreases. The researchers attributed the increased resistance of the nitrogen containing weld metal to the retardation of the polygonization process by the nitrogen atoms.

Ogawa et al. (39) have also found that the addition of nitrogen has lowered hot cracking susceptibility of the high silicon containing unstabilized fully austenitic weld metal. They attributed the beneficial effect to the fact that the nitrogen addition may inhibit the enrichment of silicon at grain boundaries. They (39) further suggested additional studies of precipitates at grain boundaries in order to understand the role of nitrogen.

Therefore, STEM analysis was conducted on the particles extracted in the carbon replicas. A careful examination of Figure 131b reveals that in addition to the sulfides and phosphides, two

other second phases can be seen; type A is relatively large and has a dark blocky morphology, in contrast to type B which is small and has a globular morphology with a bright appearance. The STEM analysis of these particles in Figure 133 reveals that both particles are basically Si-Mn oxides (silicates). However, the fine globular type B silicate contains a significant amount of S. As shown before, in the 1.25 %Si weld metal fused with 100% Ar shielding gas, only the type A silicates were found along the solidification boundary. Therefore, formation of the high sulfur containing silicates indicates that the decreased solidification cracking in the primary ferritic high Si and N weld metal may be due to the scavenging of S (and thus a reduced extent of low melting sulfides along grain/dendritic boundaries). The formation of the high S containing silicate is also found in the thin foil TEM microstructure as shown in Figure 134. The type A silicate (SiO_2-MnO) is trapped within the delta ferrite and the high sulfur containing globular silicate (type B) is at dendritic boundary.

It has to be noted that although the nitrogen addition appears to decrease hot cracking susceptibility of the high Si (1.25%) fusion zone in type 304, provided the primary solidification mode is ferritic, the susceptibility is still significantly greater than that of the low Si (0.54%) weld metal. Therefore, from the hot cracking standpoint, the silicon content should be kept as low as possible (<0.5%).

2. EFFECT OF NITROGEN

In general, nitrogen is known to decrease the hot cracking resistance of low ferrite austenitic stainless steels, simply because

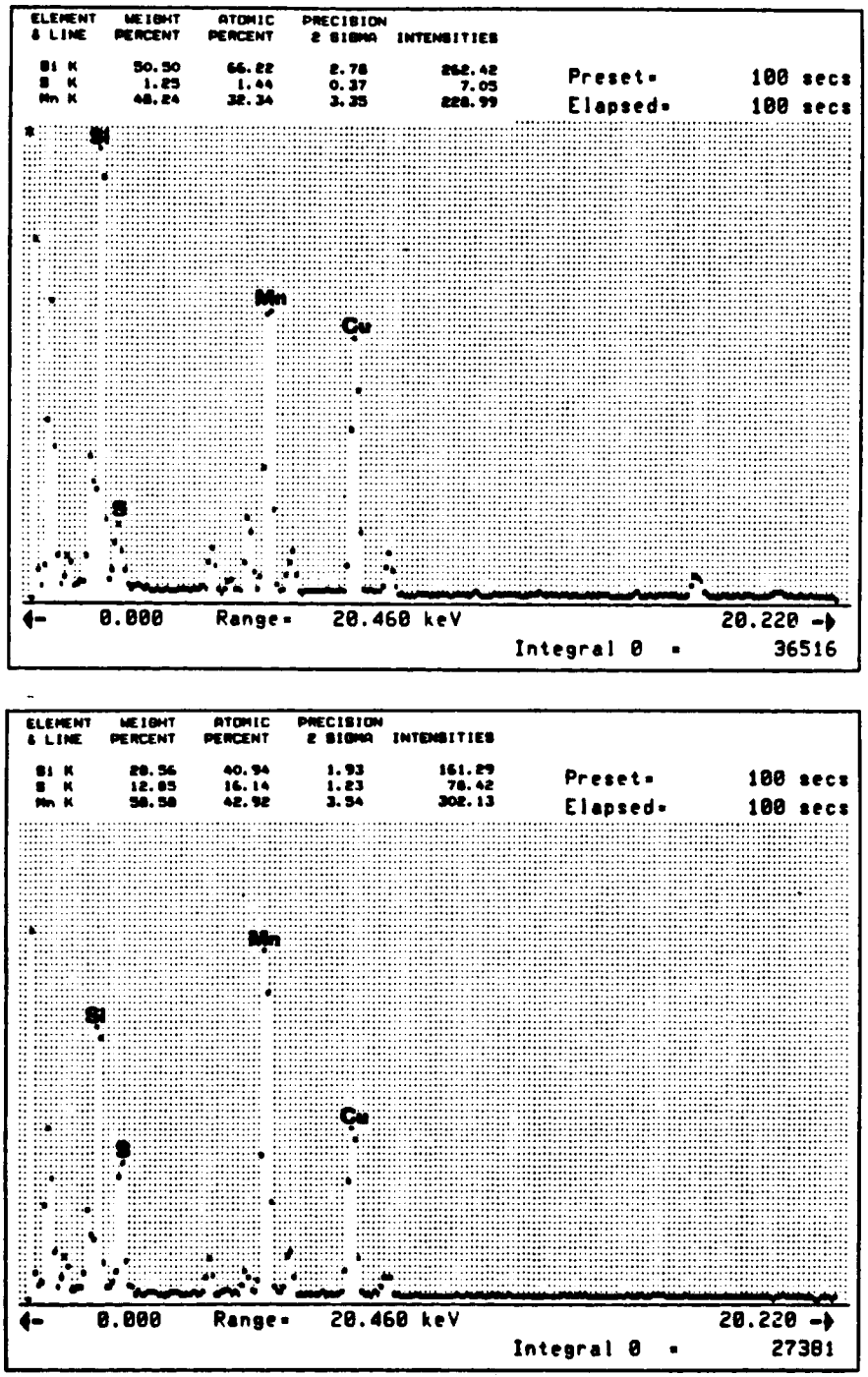


Figure 133. STEM analyses on manganese silicates a) type A and b) type B.

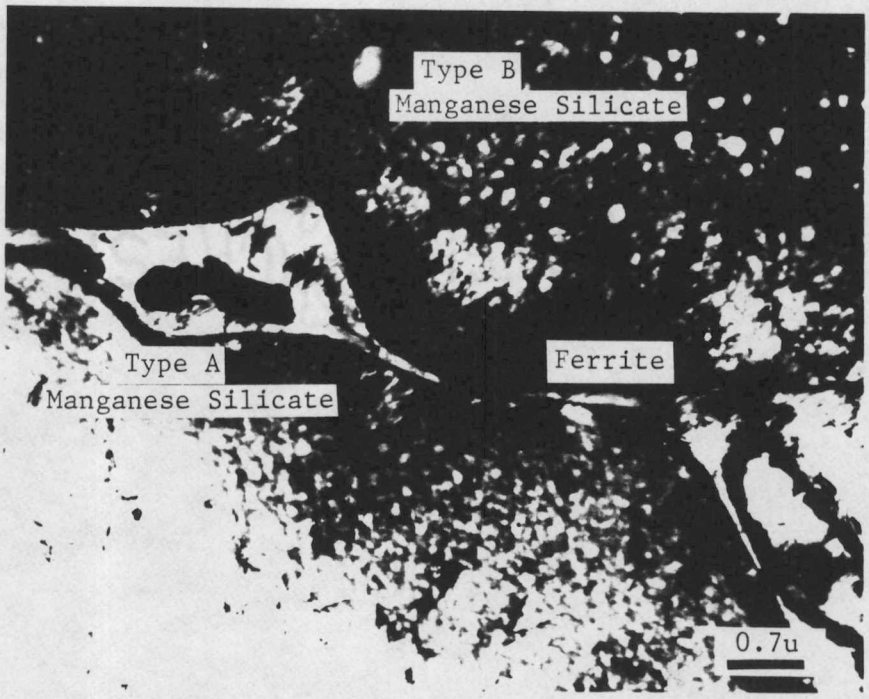


Figure 134. Typical TEM micrograph of the high Si and N containing primary ferritic 304 weld metal.

of its effect on the solidification mode (tendency toward austenitic) and thus reduced ferrite potential. Nevertheless, as shown in Table 1 (page 4), nitrogen has been introduced to the low carbon nuclear grade stainless steels to compensate for the strength reduction brought about by the reduced carbon content. The nitrogen addition has been linked to improved corrosion resistance, a more or less fortuitous effect. Further, the previous section indicates that nitrogen can be tolerated if the elemental balance is adjusted so as to ensure a primary ferritic solidification mode which will insure some residual ferrite in the room temperature microstructure.

However, an understanding of the role of individual elements and their influence on solidification cracking in stainless steels without an interference of the other parameters, is sometimes needed. In order to remove the factors of solidification mode and ferrite content, fully austenitic stainless steels with varying nitrogen levels were evaluated. Three different levels of nitrogen containing type 316 electrodes were deposited with SMAW as shown schematically in Figure 135. The welding conditions were; 160 A, 14 V, and 10 inch/min travel speed. The chemical composition of the as-deposited weld metals are given in Table 18. Nitrogen content varies from 0.047% to 0.12%. The other major and minor alloying elements are almost constant for the three welds. The ferrite content measured with Magne-Gage reveals that as planned, all three weld metals are fully austenitic. Four Varestraint samples were extracted from each weld deposit for hot cracking evaluation. The Varestraint tests were

Table 18. Chemical compositions of materials used for N effect study.

Code	Type	FN*	C	Si	Mn	P	S	Cr	Ni	Mo	V	Cb	Co	Cu	N
316N-A	316	0.0	0.042	0.34	3.23	0.016	0.012	17.59	13.80	2.15	0.11	0.01	0.07	0.35	0.047
316N-B	316	0.0	0.040	0.33	3.12	0.016	0.012	17.64	13.80	2.15	0.11	0.01	0.07	0.32	0.078
316N-C	316	0.0	0.041	0.29	3.08	0.016	0.011	17.62	13.78	2.16	0.11	0.01	0.08	0.26	0.12

a: Measured Ferrite content with Magne-Gage

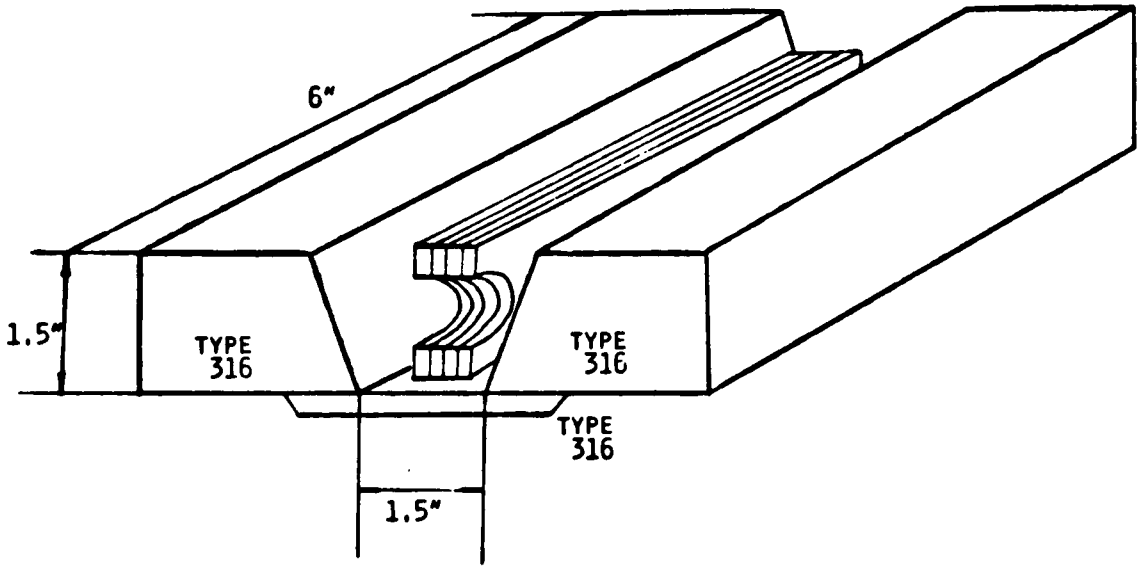


Figure 135. A schematic drawing of a groove weld deposited with three different N containing electrodes (SMAW) from which Varestraint samples were extracted.

conducted only at the 4% strain level because of the limitation in materials.

Varestraint Test Results and Discussion

The fusion zone hot cracking behavior of the fully austenitic type 316 stainless steels as a function of the nitrogen content is shown in Figure 136. Each data point is the average of three tests at 4% augmented strain level. It is evident that the hot cracking susceptibility (total crack length) continuously decreases with an increase in the nitrogen content from 0.047% to 0.12%. The maximum crack length data given in Figure 137 reveals that when the nitrogen increases from 0.047 to 0.12%, MCL is almost constant (in fact, slightly increased), but when the nitrogen content further increases to 0.12%, the MCL decreases as is the case for the total crack length. Typical solidification cracks found in the 0.12 %N sample are shown in Figure 138, which reveals that cracks form and propagate along the cellular dendritic/grain boundaries.

The reasons and mechanisms why the nitrogen addition to the fully austenitic weld metal exerts a beneficial effect with regard to solidification cracking is not clear. However, Kakhovsii (198) reported that the ability of nitrogen to retard the polygonization process in weld metal was regarded to be one of the reasons for the beneficial effect. Prosvirin et al. (201) and Zabolotskii (202) have further reported that in addition to inhibition of the polygonization processes by the clustering of nitrogen atoms, nitrogen addition increases the surface tension of the austenitic Cr-Ni melt which may have reduced the solidification cracking.

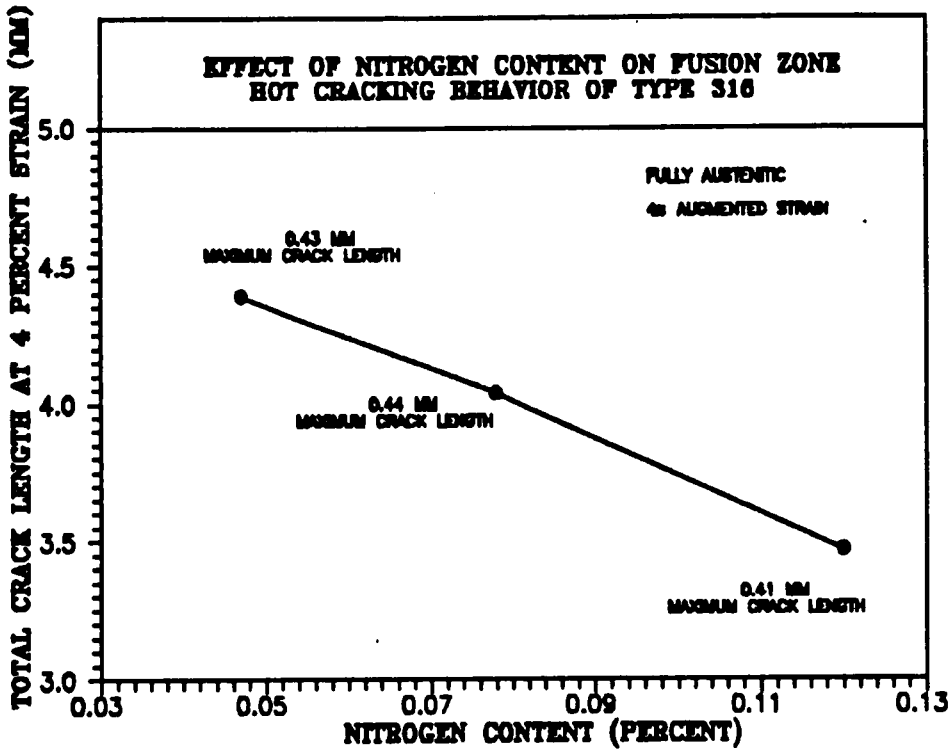


Figure 136. Effect of N content on solidification cracking in the fully austenitic type 316 stainless steel weld metal.

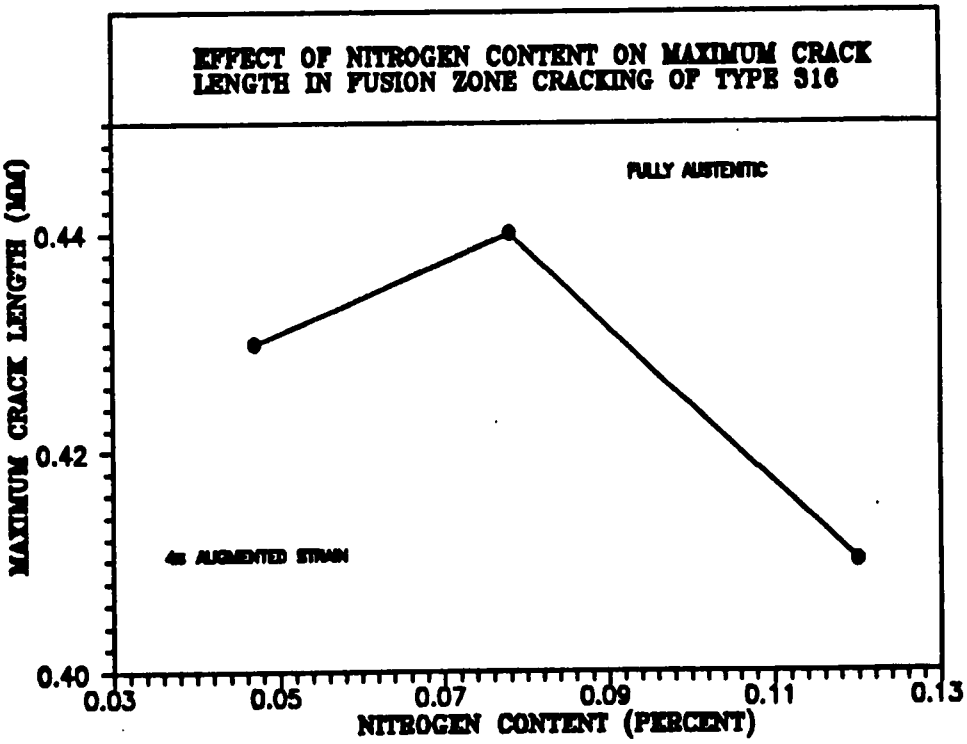


Figure 137. Effect of N content on the maximum crack length in the fusion zone hot cracking of fully austenitic type 316 weld metal



Figure 138. Solidification cracks in the high nitrogen containing (0.12%) fully austenitic weld metal.

Careful examination of the microstructures from the three weld metals shown in Figure 139 reveals that the highest N (0.12%) containing weld metal appears to have a smaller cellular dendrite size, with no apparent difference in the amount of precipitates in the boundaries. The average cell size measured in the five different locations in the fusion zone, as shown in Figure 140, clearly reveals that although there is a significant variation from location to location, the average cell size decreases from approximately 18 um to 14 um when the N increases from 0.047% to 0.12%. Mundt and Hoffmeister (203,204) have also found that an addition of 0.6% nitrogen to the ferritic weld metal resulted in a fully austenitic weld metal and also refined the grain size of the GTA weld metal. The decreased cell/grain size by the N addition may have partially resulted in a reduced of MCL and TCL, because the increase grain boundary area reduces the concentration of elemental segregation for a given amount of impurities.

Although the reason why the higher nitrogen content gives a smaller solidification substructure in the fully austenitic weld metal is not known, it may, however, be explained with the solidification process utilizing the Fe-Cr-Ni ternary diagram. The earlier solidification study showed that the solidification path of the fully austenitic weld metal extends away from the Fe corner, generally toward the Cr corner. It also extends in a slightly increasing Ni direction in the Fe-Cr-Ni diagram. Three weld metal compositions and the approximate solidification paths are plotted in the liquidus and solidus surfaces of the ternary Fe-Cr-Ni diagram as given in Figure

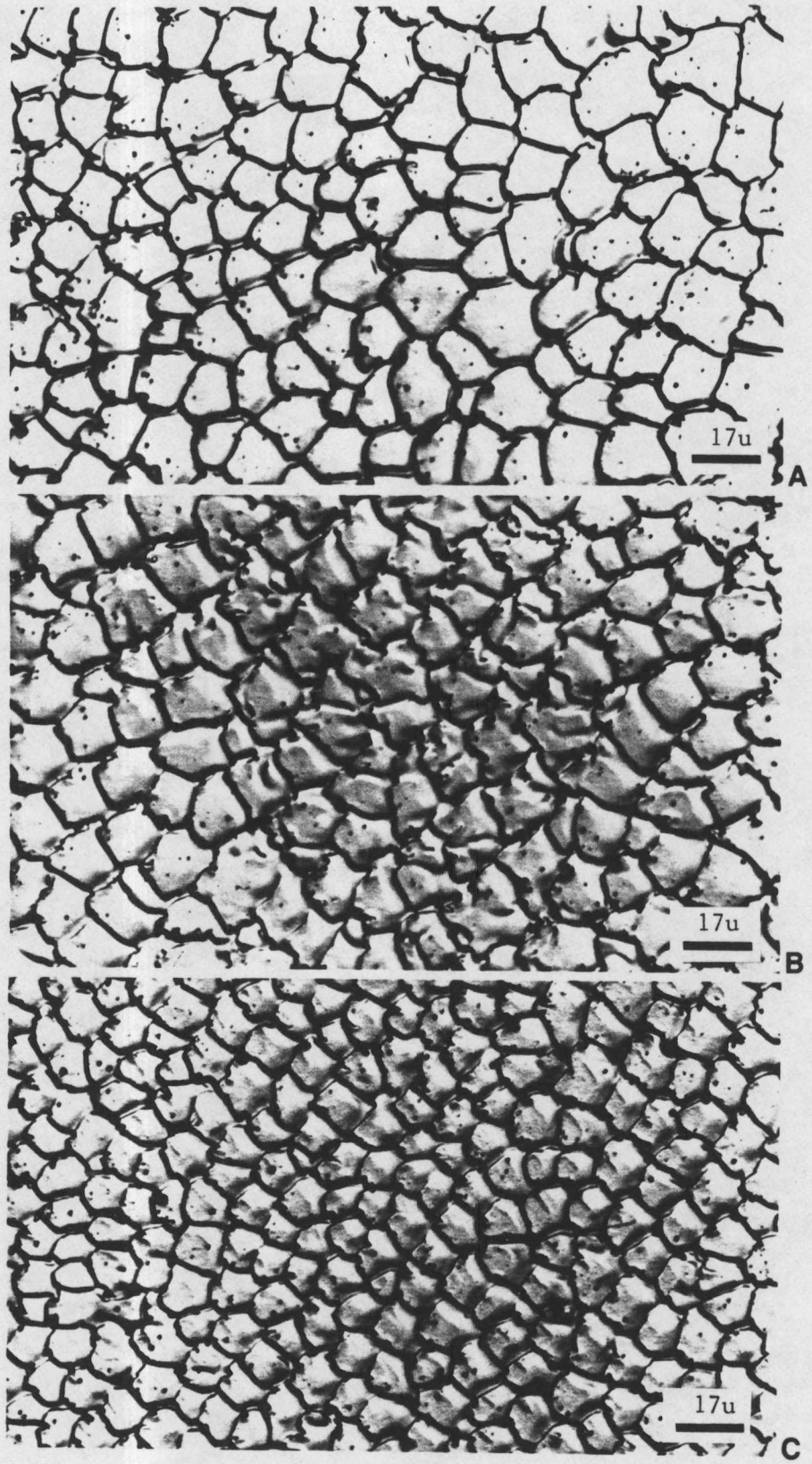


Figure 139. Typical microstructures in a) 0.047 %N, b) 0.078 %N and c) 0.12 %N containing fully austenitic weld metals.

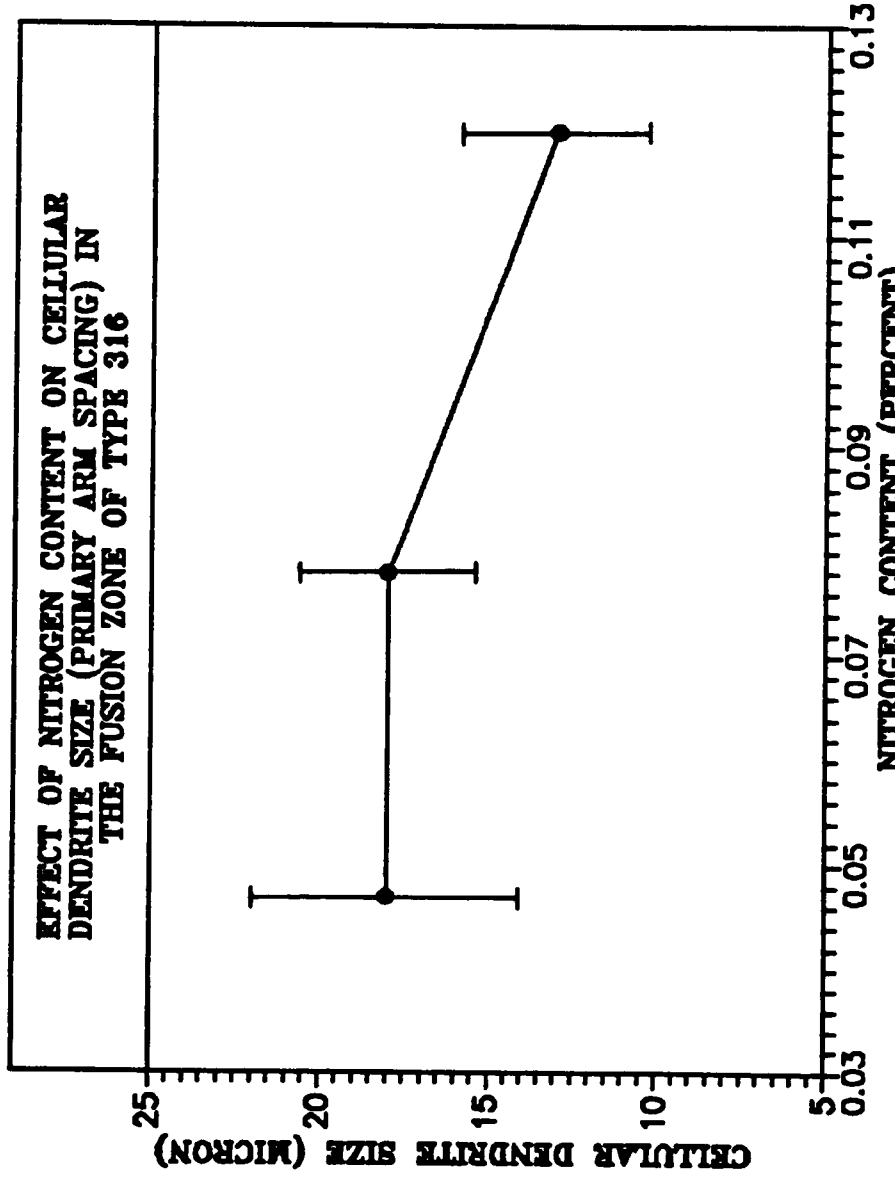


Figure 140. Influence of nitrogen content on the solidification substructure size in the fully austenitic weld metal.

141. The isothermal lines are also given in the diagram. In order to incorporate the effect of N, the N content is added to the Ni content by using a factor of 30 according to the Delong method (i.e., Ni + 30N). The locations of three compositions in the diagram clearly indicate that the liquidus and solidus temperatures decrease with an increase in N content when the other elements (especially Cr) are maintained constant. It is commonly known that when the freezing temperature of liquid (liquidus) is suppressed by an alloying element addition, the subgrain/grain size becomes smaller.

As shown before in the optical microstructures (Figure 139), there was no apparent difference in the amount of second phase precipitates (phosphides and sulfides) in cell boundaries as a function of nitrogen content. Medovar (205) also found that a nitrogen addition to fully austenitic stainless steels does not greatly affect the amount of second phases. Therefore, it can be assumed that the lower temperature limit in the brittleness temperature range (BTR), which is determined by the type and amount of low melting segregates, be constant for the three different N level bearing 316 weld metals. Thus, as shown in the schematic drawing (Figure 142), the BTR becomes narrower as the nitrogen content increases due to the decreased liquidus and solidus temperatures. This may have resulted in a decreased maximum crack length and thus the total crack length in the higher N weld metal.

However, it has to be remembered that although a higher N content decreases the cracking susceptibility of the "fully austenitic" stainless steel weld metal, when it is compared to that in

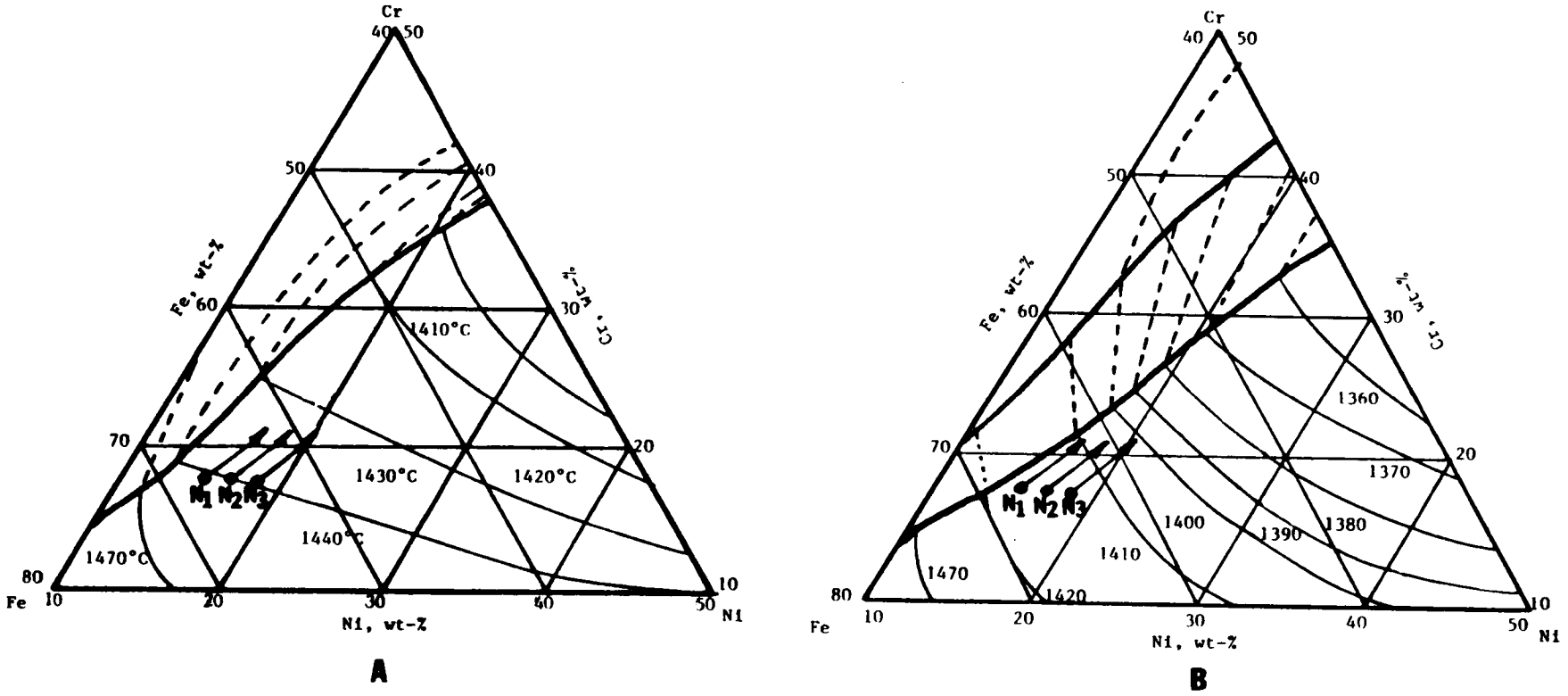


Figure 141. Approximate solidification paths of 316N-A, 316N-B and 316N-C, a) Liquidus and b) Solidus surfaces of Fe-Ni-Cr ternary diagram.

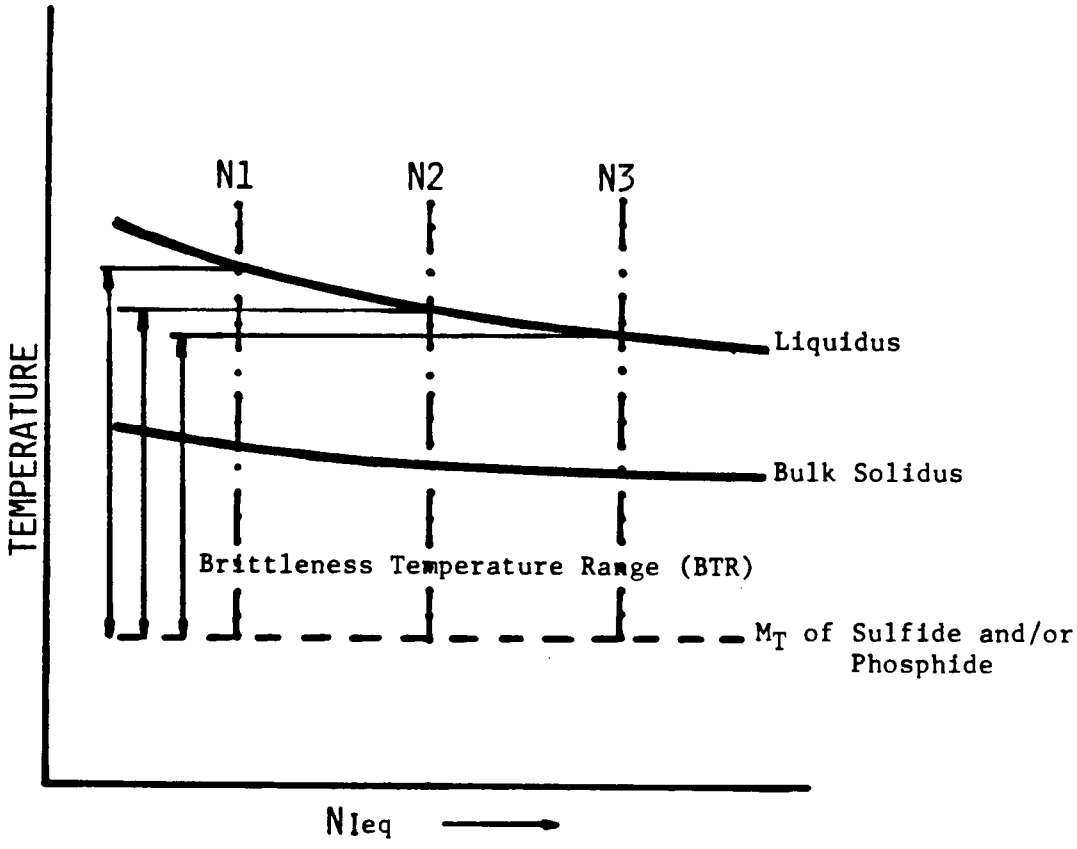


Figure 142. A schematic drawing of Temperature-Ni_{eq} diagram at constant Cr_{eq}, showing the effect of N addition on the Brittleness Temperature Range (BTR) of fully austenitic weld metal.

the primary ferritic weld metal which has the same level of nitrogen, hot cracking susceptibility of the fully austenitic alloy is still greater than the primary ferritic alloy. Therefore, when alloying with nitrogen to compensate for a lower carbon content in the nuclear grade materials, the compositional balance has to be adjusted such that it solidifies in a primary ferritic mode.

3. EFFECT OF RARE EARTH METAL (REM)

Rare earth metals (mixture of La, Ce, Nd and etc.) have been used conventionally for desulfurization and sulfide shape control in iron and steel making practice (206-209), due to the strong deoxidizing potential of REM. Recently, a number of Japanese researchers (32, 54) have investigated the potential beneficial effect of REM on solidification cracking in austenitic stainless steels. Matsuda et al. (54) have found that a La or REM addition improved solidification cracking resistance of fully austenitic stainless steel (310S). The main reason for the beneficial effect was the formation of high melting point La or REM containing phosphides and sulfides in stead of the low melting MnS type sulfide and M_3P type phosphide. Morishige et al. (32) have also recommended the addition of REM up to 0.02% in 347 to improve hot ductility and fusion zone cracking. Unfortunately, they (32) did not report the behavior of the REM containing materials in their report.

In this study, two heats of type 347 alloy having a REM addition have been evaluated and compared to that of AISI 347 which has a

similar chemical composition except REM addition. These two heats are 347L and 347R.

a. Varestraint Test Results and Discussion

The chemical compositions of 347L and 347R were given in Table 5 (page 97). The 347R has a REM content approximately twice (0.017%) that of 347L (0.008%). Unfortunately, a direct comparison may not be accomplished because of the significant difference in the chemical compositions and room temperature ferrite content (and solidification mode) of two heats. The 347L has a fully austenitic solidification mode, while the 347R solidifies in a primary ferritic mode and has a 3.5 FN residual ferrite in the (room temperature) microstructure.

A comparison of solidification cracking behavior of 347L and 347R to that of AISI 347-9, which has a chemical composition most similar to 347R among the 347 heats, is given in Figure 143. This figure clearly indicates that, as may be expected, the small addition of 0.008% REM in the fully austenitic 347L does not give any beneficial affect on the solidification cracking resistance. The total crack length of 347L is greater than that of 347R and AISI 347 (347-9) at all augmented strain levels. Matsuda et al. (54) have found that optimum level of La addition to remove S and P as high melting point La_2O_2S and LaP in the fully austenitic 310S is approximately La = 4.5P + 8.7S. Although they (54) did not give an approximate amount of REM required to effectively remove S + P, they found that the REM has a potential equivalent to La. Thus, the same amount of REM may be required. Therefore, approximately 0.12 %REM is required to remove S + P as the high melting point sulfide and

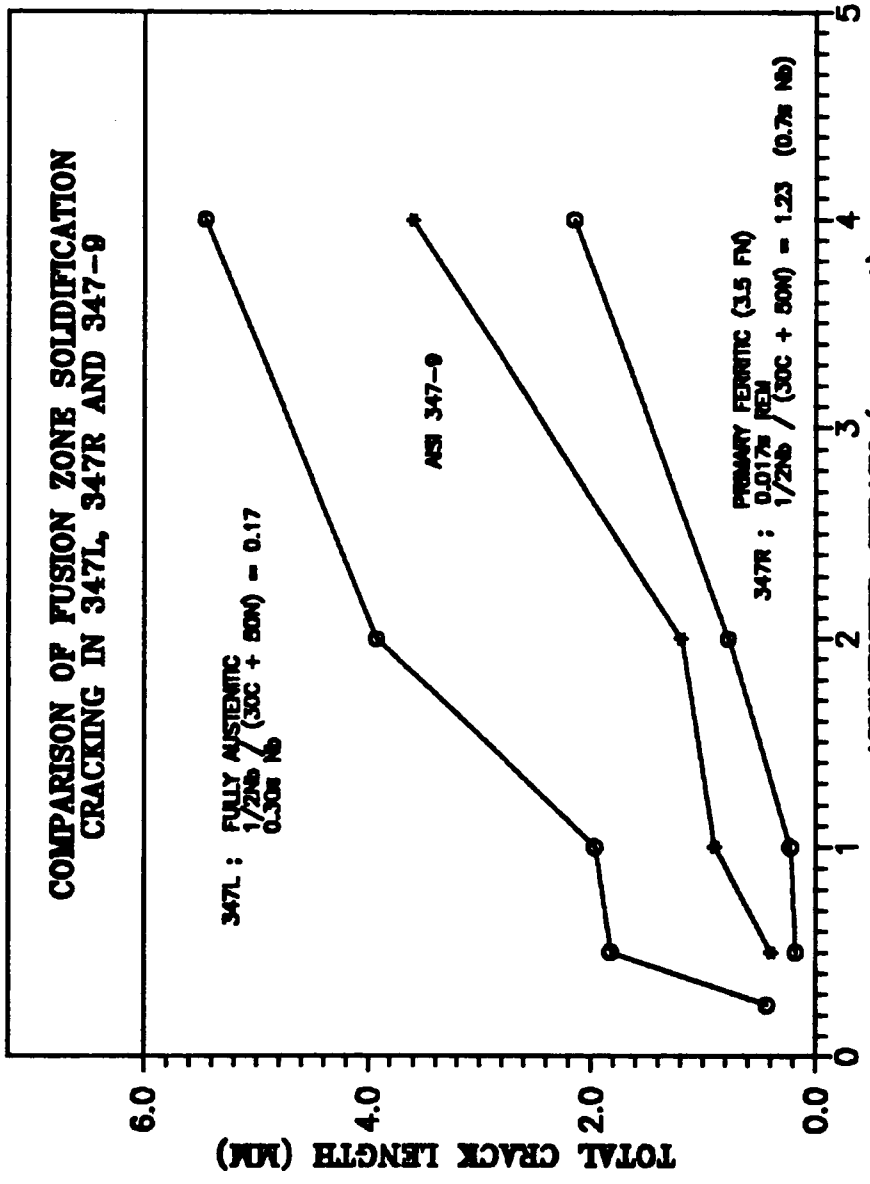


Figure 143. A comparison of solidification cracking behavior of REM containing 347L and 347R with that of AISI 347.

phosphide in the 347L. This may be the reason why the small addition of 0.008% REM does not influence hot cracking susceptibility. However, it has to be considered that although the P + S in 347L is completely removed by the addition of sufficient REM, the detrimental effect of Nb in the fully austenitic weld metal should not be ignored. Therefore, the greater cracking susceptibility of 347L is predominantly influenced by the fully austenitic solidification mode and Nb, in addition to the effects of S and P. 347L has a 1/2Nb / (30C + 50N) ratio of 0.17 which is considered to be high from the solidification cracking standpoint as was mentioned in the earlier section.

The 347R has a significantly high Nb relative to the C and N contents. The 1/2Nb / (30C + 50N) ratio is 1.23 which is highest among the 347 lots evaluated in this study. Based on the earlier results, this heat should have a great susceptibility to solidification cracking. However, the hot cracking susceptibility of the 0.017%REM containing 347R is, unexpectedly, lower than AISI 347 and much superior to that of the low REM (0.008%) fully austenitic 347L. Therefore, the 0.018% REM must have played a role in the reduction of susceptibility. There is no available data in the open literature regarding how much of a REM addition is required to effectively scavenge the P + S in the primary ferritic weld metal, as opposed to the case of fully austenitic alloy. However, REM requirement must be much smaller than that required for the fully austenitic, because the primary ferritic solidification mode gives a lower extent of S and P segregation. Thus, the 0.017 %REM may have

been sufficient enough to effectively scavenge the residual S and P, resulting in a reduced solidification cracking.

The typical fusion zone microstructures for both 347L and 347R are given in Figures 144 and 145. The 347L microstructure (Figure 144), which was etched with SPEED method, clearly reveals that the dark appearance microconstituents precipitate more or less continuously along the solidification boundaries. Higher magnification of the constituent from the carbon extraction replica in 144b shows that these microconstituents have a feathery/eutectic lamellar structure, revealing that as expected, these are Nb(C,N)-austenite eutectics. 347R in Figure 145 shows a duplex ferrite-austenite microstructure and the Nb(C,N) and Nb(C, N)-austenite eutectics precipitate along the interdendritic boundaries. There is no evidence of precipitates of the high melting point sulfides (Rare earth oxy-sulfide or Rare earth sulfide) and phosphide (Rare earth phosphide) in the microstructure. These constituents may have been removed as slag at the weld bead surface. Matsuda et al. (54) have found that a large amount of slag, which is enriched in La or REM, was observed on the bead surface of the GTA weld metal alloyed with La or REM.

The weld metal and base metal HAZ liquation cracking susceptibilities of 347L, 347R and AISI 347 are compared in Figures 146 and 147. The liquation cracking in the weld metal HAZ of 347L and 347R is similar to the fusion zone solidification cracking. Here again, the primary solidification mode is the predominant factor such that the primary austenitic 347L has the greatest crack susceptibility

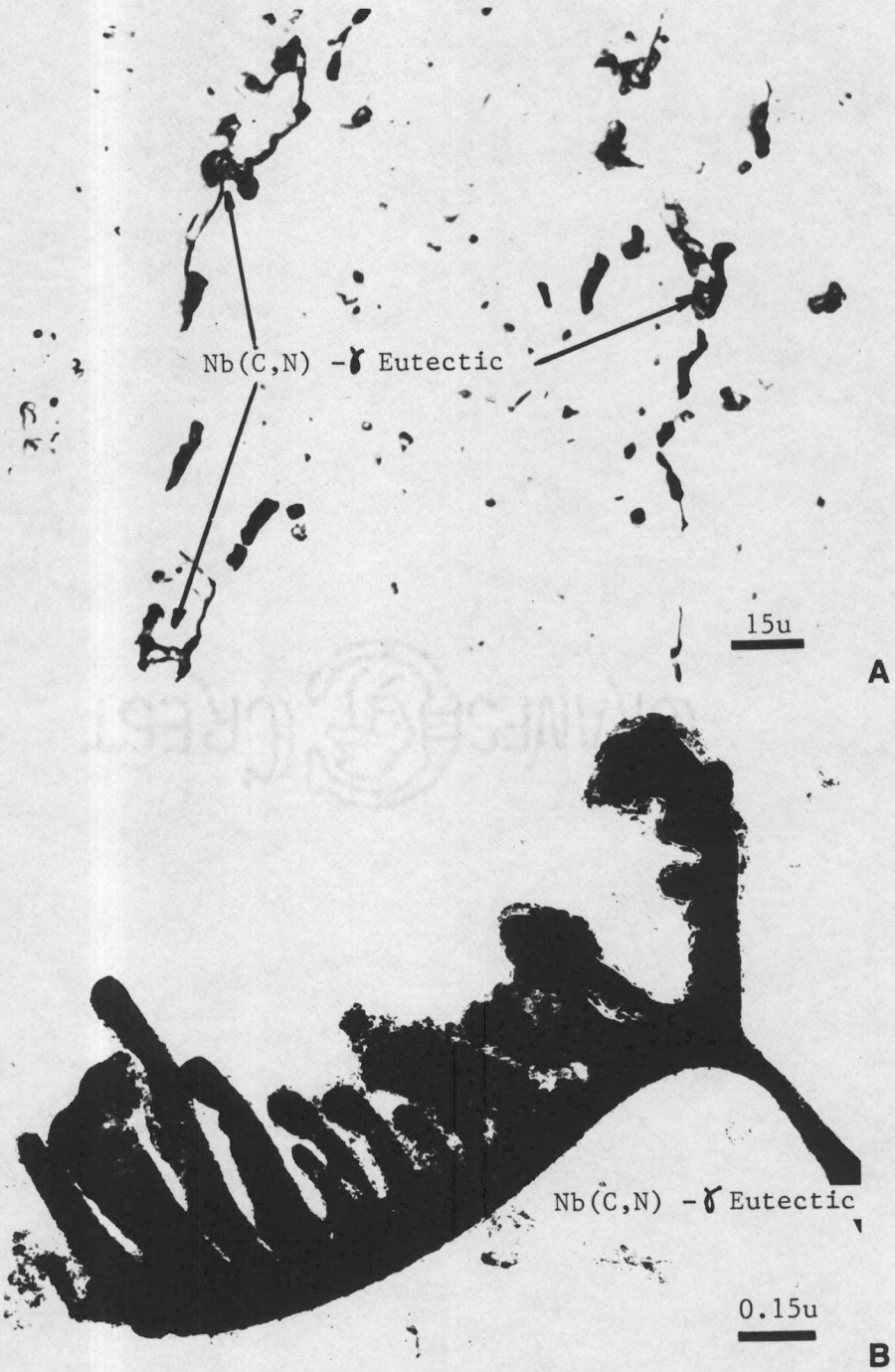


Figure 144. Typical fusion zone microstructures in the REM (0.008%) containing fully austenitic 347L. a) optical and b) TEM, Nb(C,N)-austenitic eutectic.

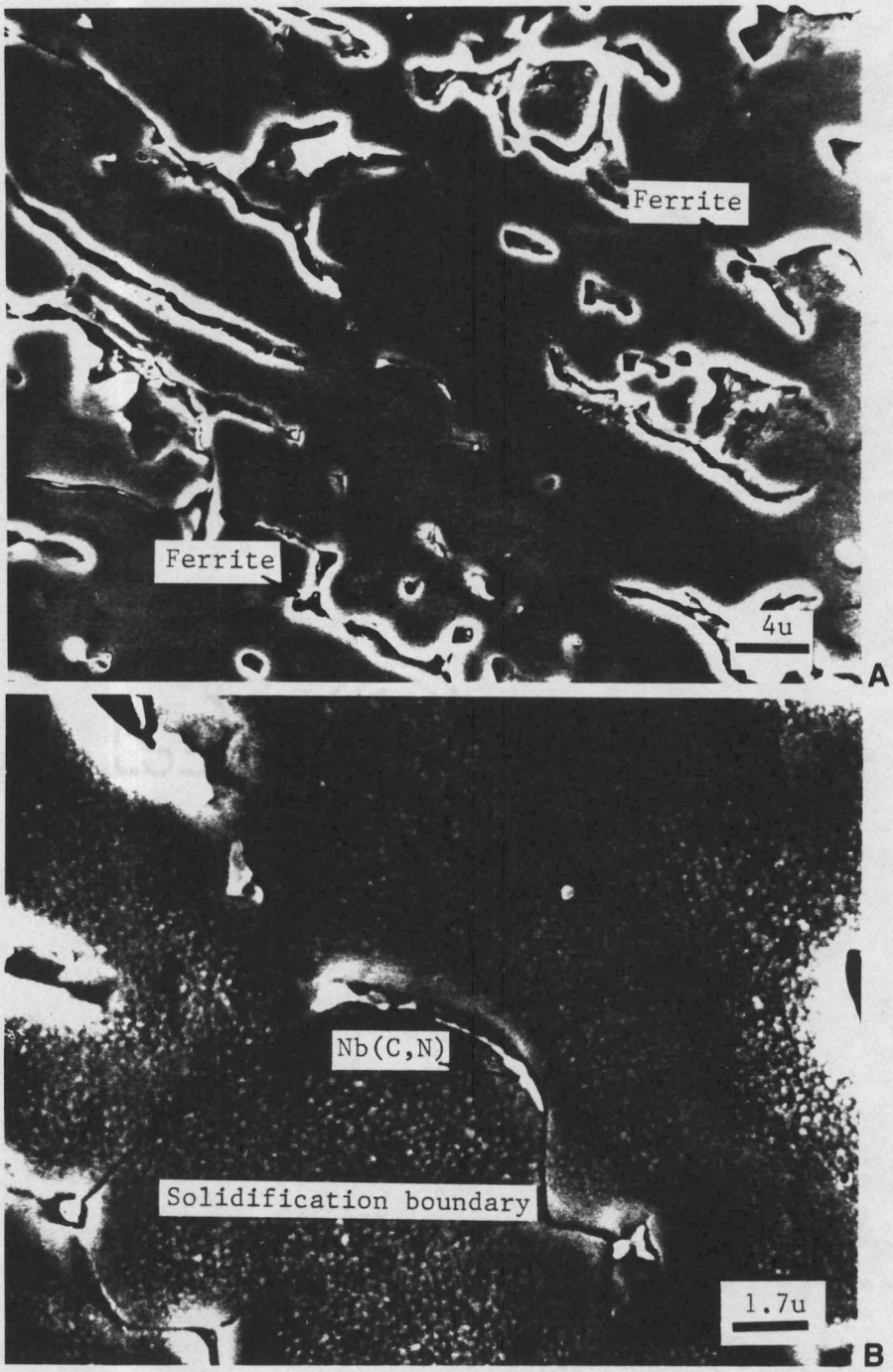


Figure 145. Typical fusion zone microstructures in the REM (0.017%) containing primary ferritic 347R.

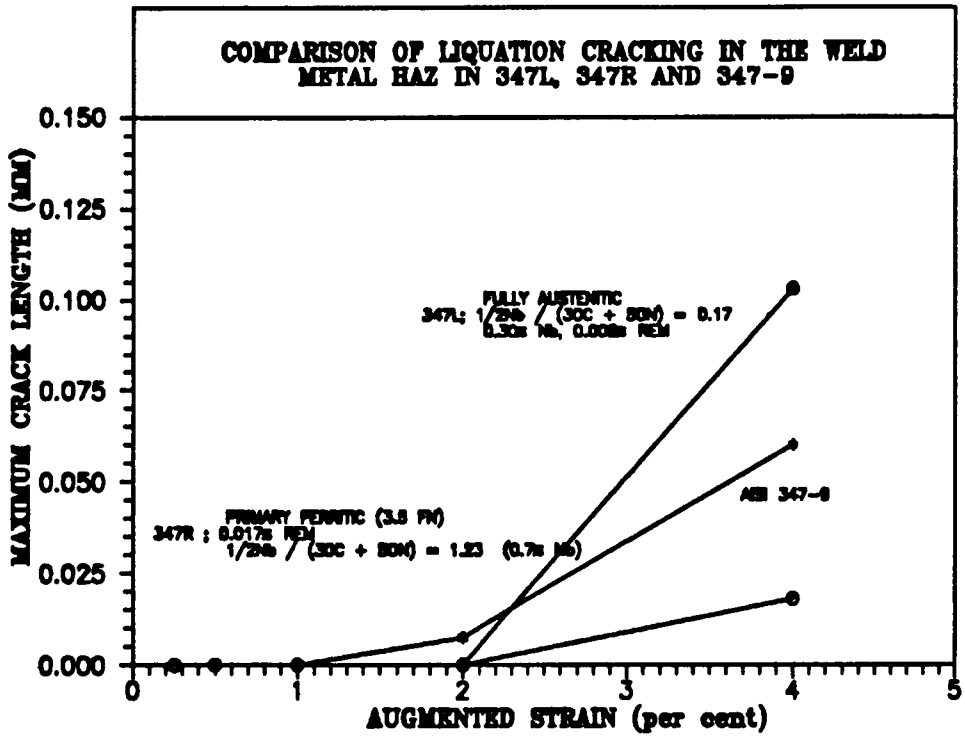


Figure 146. A comparison of liquation cracking behavior in the weld metal HAZ of the REM containing fully austenitic 347L (0.008 %REM) and primary ferritic 347R (0.017 %REM) with that of AISI 347.

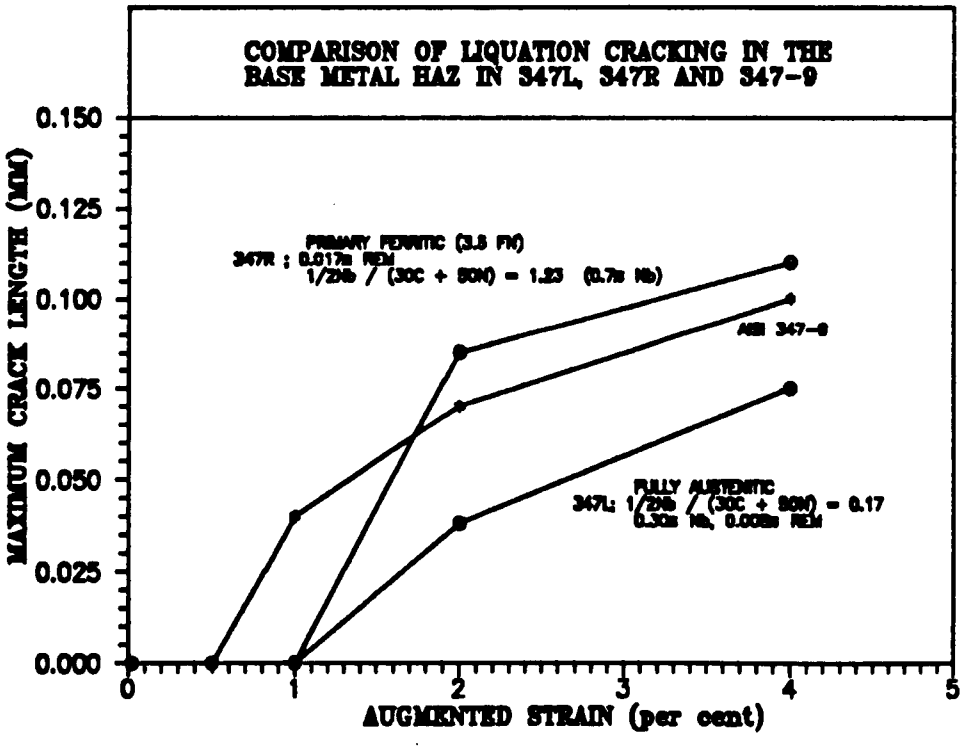


Figure 147. A comparison of liquation cracking behavior in the base metal HAZ of 347L and 347R with that of AISI 347.

among the three alloys. The addition of 0.017% REM to the primary ferritic 347 seems to have a beneficial effect on the weld metal HAZ liquation cracking as in the case of the fusion zone solidification cracking. However, the base metal HAZ hot cracking does not follow the same trend as shown in Figure 147. The lowest Nb containing 347L has a better resistance than the higher Nb containing 347R and AISI 347. At 4% strain, the highest Nb and largest 1/2Nb / (30C + 50N) (347R) has a greater cracking extent in the base metal HAZ. This fact seems to indicate that the REM addition may not influence constitutional liquation and melting of segregated grain boundaries, which are directly responsible for the HAZ liquation cracking. That is, the REM may scavenge the "harmful" elements (P + S) only during solidification. Therefore, when considering the hot cracking behavior in the all three weld zones, the reduction of the Nb, P and S contents appears to be the best practice, although a small addition of REM to the primary ferritic weld metal shows a beneficial influence.

CHAPTER VI

EVALUATION OF BACKFILLED SOLIDIFICATION CRACKS

1. INTRODUCTION

During welding of stainless steels, if a sufficient strain occurs, hot cracks initiate at the solid-liquid interface along the trailing edge of the weld pool and propagate along the liquated solidification boundaries and then along migrated grain boundaries. When hot cracks propagate, liquid just ahead of the solid-liquid interface is drawn into the cracks by capillary action and thus the high temperature end of the cracks are "backfilled". Because of unique segregation characteristics which depend upon the material solidification behavior, backfilled cracks are usually distinguishable from the solidification boundaries after etching.

The first reported observation of the backfilling phenomenon in solidification cracks in stainless steel weld metal is dated as early as the 1950's. Medovar (210,211) has found that when welding a high silicon containing austenitic stainless steel, extensive formation of the Ni-Si eutectic resulted in a reduced extent of hot cracking caused by healing of interdendritic cracks and refinement of the structure. The same researcher (212) in a later paper, further mentioned healing of cracks such that in the welding of 18-8 austenitic stainless steel which had a high Nb content (1-2%), the hot cracking resistance was improved, as compared to a medium Nb content of 0.6 - 0.8%. However, since the 1950s, not many investigators have reported on backfilling of hot cracks. Even if exists, only observation of backfilled cracks

was reported. Recently, some investigators (73,95,166,189) have begun to pay attention to the phenomena of backfilled solidification cracks. However, these investigators have examined only the microstructural characteristics and elemental distributions around the backfilled region in terms of the solidification mode without emphasizing the potential importance of backfilling on the evaluation of the weldability of materials.

Therefore, in this study, backfilled solidification cracks were systematically investigated in terms of: the primary solidification mode (ferritic vs. austenitic), applied strain levels, and types of stainless steel (316NG vs. 347NG). Further, the extent of backfilling is also evaluated as a function of the location in the weld and the temperature gradient in the weld HAZ.

2. MATERIALS AND EXPERIMENTAL PROCEDURE

a. Materials

The materials investigated in this study include 2 heats of 316 Nuclear Grade (NG) and 1 heat of 347NG austenitic stainless steel. These are 316NG-B, 316NG-D and 347NG-E. Lot 316NG-D has a primary austenitic solidification mode, while 316NG-B and 347NG-E have a primary ferritic solidification modes and thus have some residual ferrite at ambient temperature.

b. Test Evaluations

The Varestraint hot cracking tested samples were examined at 70X with a binocular microscope and each solidification crack was measured and recorded. In this study, only the fusion zone cracks were

considered. The backfilled crack length was measured on the metallographic samples tested at 2 and 4% augmented strain. The polished samples were etched in dilute aqua-regia (1 part of nitric acid, 3 parts of hydrochloric acid and 1 part of distilled water). To investigate backfilling as a function of solidification crack length and location in the weld, the solidification cracked zone along the instantaneous solid-liquid interface at the time of strain application was divided into 3 equal regions (A, B and C) as shown in Figure 148. Region A is in the center of the weld, region C is in the fusion line area and region B is an intermediate region between A and C. The solidification cracks found in each region were divided to four crack length groups: $L1 < 0.3mm$, $0.3mm < L2 < 0.5mm$, $0.5mm < L3 < 0.7mm$ and $L4 > 0.7mm$.

Some selected samples were examined further with SEM and EDAX / EPMA to characterize microstructure and compositional variation (Cr, Ni and residual elements) in and around the backfilled cracks.

3. EXPERIMENTAL RESULTS

a. Solidification Cracking Susceptibility

Although behavior of 316NG-B and -D and 347NG-E with respect to fusion zone solidification cracking was described in an earlier section, a brief comparison of the materials is shown as a function of augmented strain in Figure 149. (Recall that the total crack length is measured on the as-welded surface, where thin small cracks are usually not detectable). It is clearly noted that the fully austenitic 316NG-D shows the greater total crack length at all applied

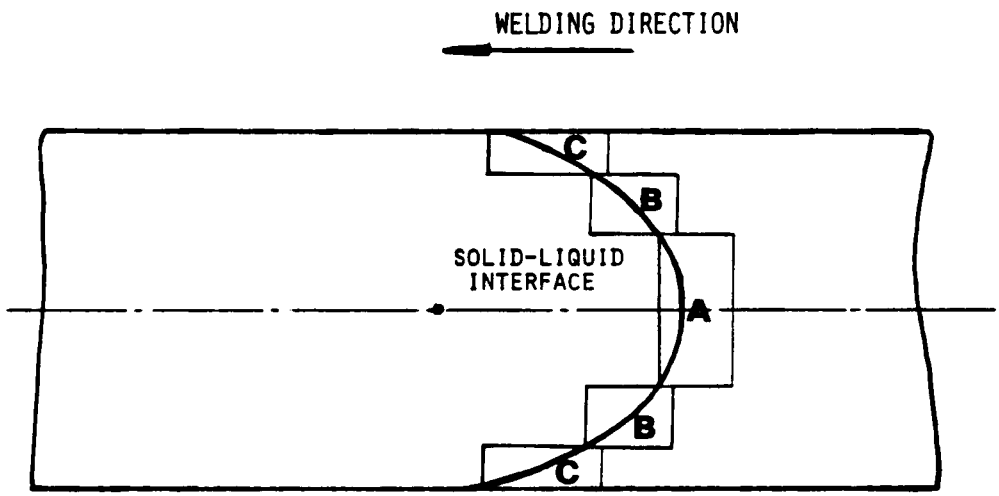


Figure 148. Schematic drawing of the hot cracked zone along the solid-liquid interface, divided into three equal regions.

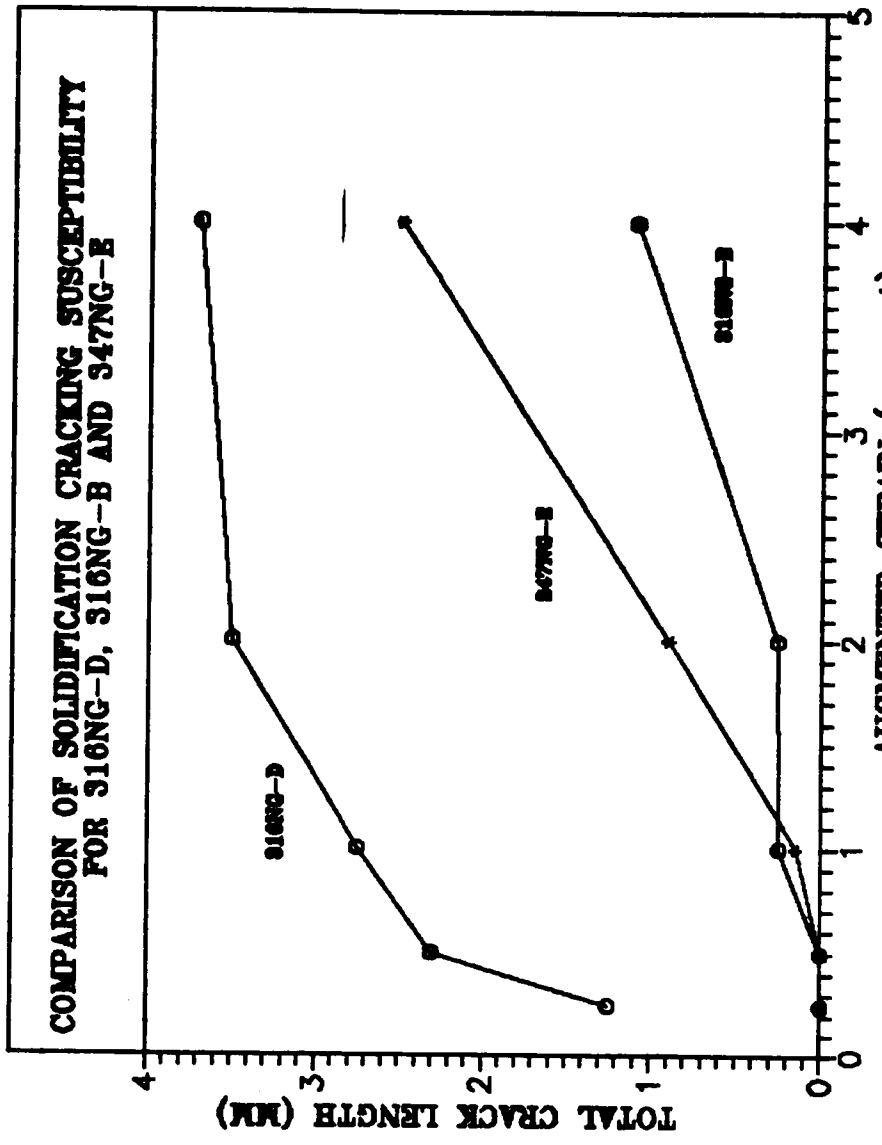


Figure 149. Comparison of fusion zone solidification cracking susceptibility of 316NG-B, 316NG-D and 347NG-E.

strain levels as compared to the other ferrite containing heats. Even at the lowest strain (0.25%) used in this study, the total crack length of 316NG-D is almost the same as that of 316NG-B tested at 4% strain. The total crack length in 316NG-D appear to reach a maximum at 2% strain.

347NG-E shows a behavior between 316NG-B and -D. At strain levels below 2%, both 316NG-B and 347NG-E have an almost identical behavior, however when the applied strain is increased to 4%, 347NG-E has a greater susceptibility to solidification cracking than 316NG-B, revealing the detrimental influence of niobium in the type 347 alloy.

Figure 149 further reveals the influence of the primary solidification mode on the extent of hot cracking. Weld solidifying in a primary austenitic mode (316NG-D) are more susceptible to solidification cracking than those solidifying in a primary ferritic mode (316NG-B and 347NG-E).

b. Backfilled Solidification Cracks

The extent of backfilling in each solidification crack was carefully measured using a calibrated scale at 100-200X OLM on the mounted samples tested at 2 and 4% strain. The measured average solidification crack length and backfilled crack length, number of cracks in terms of the solidification crack length groups (L1, L2, L3 and L4) and the positions in the weld (regions A, B and C), are given in Tables 19-20. The percentage of the average backfilled crack length to average solidification crack length is also given in the tables. The average of each column and row is given in the last column and row respectively.

Table 19. Extent of backfilled cracks in a) 316NG-D and b) 316NG-B at 4% strain.

Crack Length / Region	L1	L2	L3	L4	Average
A	-	NO 2 S: 0.33 mm B: 0.19 mm %: 57	NO 3 S: 0.61 mm B: 0.28 mm %: 46	NO 1 S: 0.92 mm B: 0.08 mm %: 9	S: 0.62 mm B: 0.18 mm %: 37
B	NO 3 S: 0.21 mm B: 0.13 mm %: 69	NO 2 S: 0.42 mm B: 0.19 mm %: 45	NO 2 S: 0.68 mm B: 0.28 mm %: 40	NO 2 S: 0.80 mm B: 0.35 mm %: 44	S: 0.53 mm B: 0.24 mm %: 45
C	NO 6 S: 0.19 mm B: 0.10 mm %: 51	NO 6 S: 0.37mm B: 0.11 mm %: 30	-	-	S: 0.28 mm B: 0.11 mm %: 41
Average	S: 0.20 mm B: 0.12 mm %: 60	S: 0.37 mm B: 0.16 mm %: 44	S: 0.65 mm B: 0.28 mm %: 43	S: 0.86 mm B: 0.18 mm %: 27	

A

Crack Length / Region	L1	L2	L3	L4	Average
A	NO 2 S: 0.28 mm B: 0.28 mm %: 100	NO 8 S: 0.36 mm B: 0.27 mm %: 77	-	-	S: 0.32 mm B: 0.27 mm %: 88
B	NO 4 S: 0.24 mm B: 0.16 mm %: 71	NO 7 S: 0.39 mm B: 0.21 mm %: 55	NO 2 S: 0.51 mm B: 0.25 mm %: 49	-	S: 0.38 mm B: 0.21 mm %: 58
C	NO 21 S: 0.13 mm B: 0.11 mm %: 86	NO 3 S: 0.37mm B: 0.18 mm %: 48	-	-	S: 0.25 mm B: 0.15 mm %: 67
Average	S: 0.22 mm B: 0.18 mm %: 86	S: 0.37 mm B: 0.22 mm %: 60	S: 0.51 mm B: 0.25 mm %: 49	-	

B

S: Average solidification crack length. B: Average backfilled crack length
%: (B/S) x 100 NO: Number of cracks
L1: < 0.3 mm 0.3mm ≤L2 ≤ 0.5mm 0.5mm ≤ L3 ≤ 0.7mm L4 > 0.7mm

Table 20. Extent of backfilled cracks in 347NG-E, a) 2% and b)4% strain.

Crack Length / Region	L1	L2	L3	L4	Average
A	NO 1 S: 0.29 mm B: 0.29 mm %: 100	NO 4 S: 0.36 mm B: 0.36 mm %: 100	-	-	S: 0.33 mm B: 0.33 mm %: 100
B	NO 1 S: 0.28 mm B: 0.28 mm %: 100	NO 4 S: 0.50 mm B: 0.27 mm %: 54	NO 3 S: 0.60 mm B: 0.33 mm %: 59	NO 2 S: 0.76 mm B: 0.22 mm %: 29	S: 0.54 mm B: 0.28 mm %: 63
C	NO 7 S: 0.19 mm B: 0.12 mm %: 68	NO 1 S: 0.42mm B: 0.20 mm %: 49	-	-	S: 0.31 mm B: 0.15 mm %: 59
Average	S: 0.25 mm B: 0.21 mm %: 89	S: 0.43 mm B: 0.28 mm %: 68	S: 0.60 mm B: 0.33 mm %: 59	S: 0.76 mm B: 0.22 mm %: 29	

A

Crack Length / Region	L1	L2	L3	L4	Average
A	NO 2 S: 0.29 mm B: 0.29 mm %: 100	NO 2 S: 0.39 mm B: 0.32 mm %: 78	NO 4 S: 0.64 mm B: 0.33 mm %: 49	-	S: 0.44 mm B: 0.32 mm %: 75
B	NO 3 S: 0.25 mm B: 0.21 mm %: 83	NO 2 S: 0.43mm B: 0.33 mm %: 77	NO 5 S: 0.57mm B: 0.33 mm %: 57	NO 6 S: 0.77 mm B: 0.28 mm %: 37	S: 0.51 mm B: 0.41 mm %: 63
C	NO 8 S: 0.15 mm B: 0.11 mm %: 90	NO 4 S: 0.37 mm B: 0.18 mm %: 51	-	-	S: 0.26 mm B: 0.15 mm %: 70
Average	S: 0.23 mm B: 0.20 mm %: 90	S: 0.40 mm B: 0.27 mm %: 69	S: 0.61 mm B: 0.33 mm %: 53	S: 0.77 mm B: 0.28 mm %: 37	

B

S: Average solidification crack length. B: Average backfilled crack length
%: (B/S) x 100 NO: Number of cracks
L1: < 0.3 mm 0.3mm ≤ L2 ≤ 0.5mm 0.5mm ≤ L3 ≤ 0.7mm L4 > 0.7mm

The tables clearly reveal that, in general, when the solidification crack length is small, the percentage of backfilled crack length to solidification crack length is higher. Further, the center of the weld (region A) shows the greatest extent of crack backfilling and thus the highest percentage of backfilled crack to solidification crack length as compared to regions B and C. All the above mentioned characteristics are true for all materials tested and at all strain levels.

The influence of solidification mode on the extent of backfilling is compared graphically in Figure 150. In all weld regions, the 316NG-B weld solidifying in the primary ferritic mode and has a longer absolute backfilled crack length and thus a greater ratio of backfilled to solidification crack length than the weld solidified in the primary austenitic mode (316NG-D). Figure 150 further illustrates that when the solidification crack length is smaller than 0.3mm, the primary ferritic solidification mode shows complete backfilling at the center of the weld (region A). As seen in tables 19-20, smaller solidification cracks (< 0.5mm) formed in the primary ferritic welds as compared to the primary austenitic weld.

Effect of the augmented strain level on the degree of backfilling in 347NG-E is given in Figure 151. There is almost no difference in the absolute backfilled length between 2 and 4% strain levels. However, the percentage of the backfilled length to the solidification crack length at the 2% strain level is slightly greater than that at the 4% strain level because the solidification crack length at the higher strain level is generally longer than that for

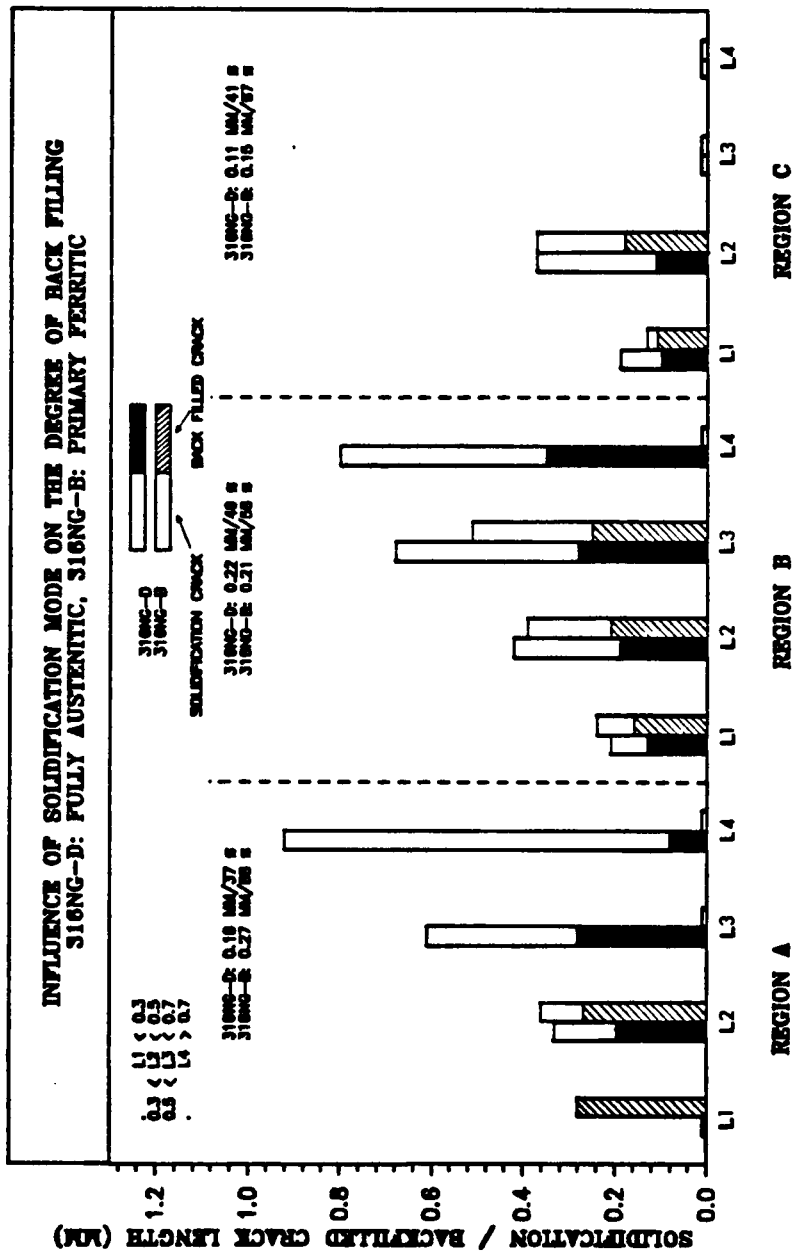


Figure 150. Influence of primary solidification mode on the extent of backfilling.

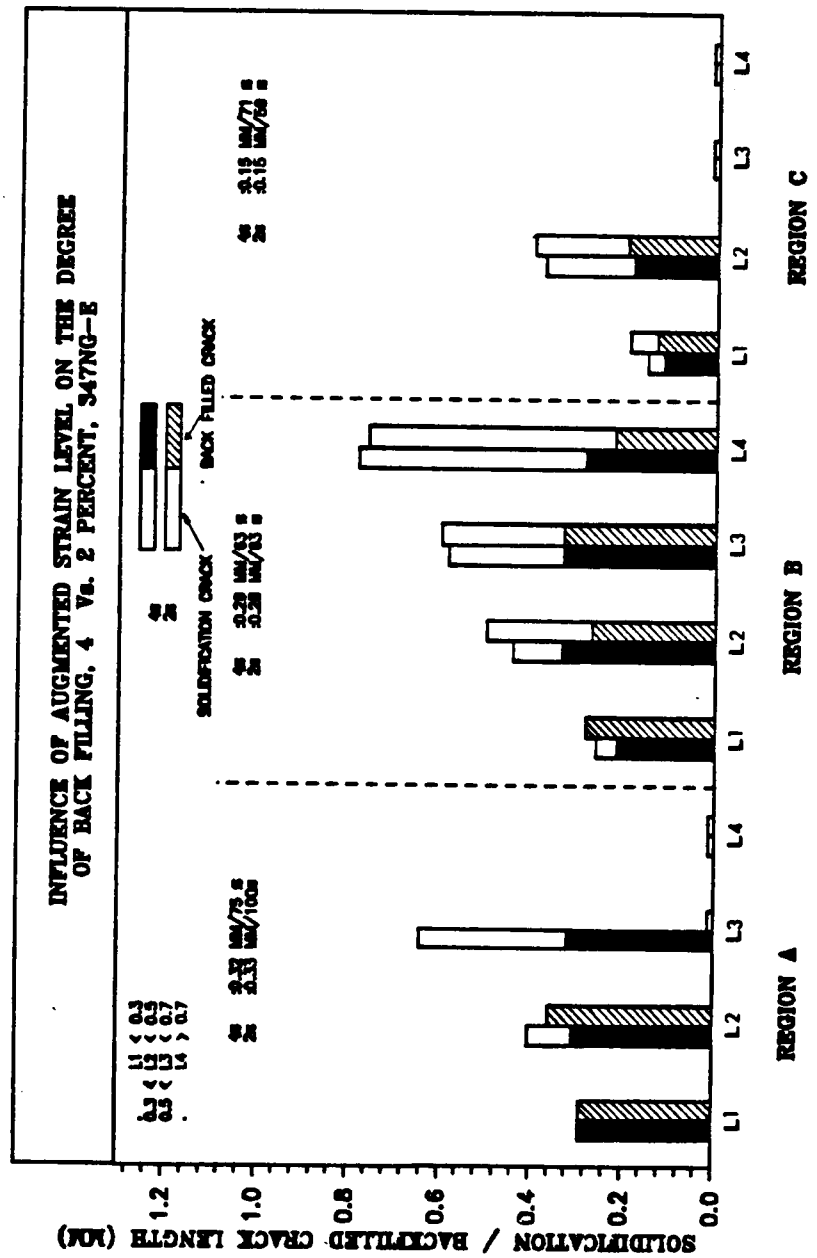


Figure 151. Effect of augmented strain level on the extent of backfilling.

the samples tested at lower strain levels.

c. Microstructural Evaluation of Backfilled Region

A typical backfilled crack in 316NG-D, which solidified in a primary austenitic mode, is shown in Figure 152a. The solidification crack occurred intergranularly. The grain boundary can be easily distinguished by the different cell orientation in the grains at either side of the grain boundary. The backfilled crack extends about 2 grain boundary lengths from the position of the instantaneous solid-liquid interface. The instantaneous solid-liquid interface position is shown by the dotted line. The distinctly different etching characteristics of the backfilled region gives easy discrimination from the adjacent regions and other grain boundaries. The backfilled cracks sometimes appears as narrow cracks at low magnification as shown in Figure 152a. However, at higher magnification, as shown in Figure 152b, it can be clearly seen that the crack was completely healed by a liquid. The width of this particular healed crack is approximately 8-10 um. Formation of delta ferrite along the center of the backfilled area can also be noted.

The different etching characteristics indicate that the elemental distribution along / across the backfilled crack may be different from the adjacent area. The chromium and nickel profiles across the backfilled crack at the region A-A in Figure 152b are given in Figure 153. The backfilled region is rich in chromium and slightly depleted in nickel as compared to the adjacent region. This is strong evidence of backfilling. Because 316NG-D has a primary austenitic solidification mode, during the solidification process Cr, the ferrite

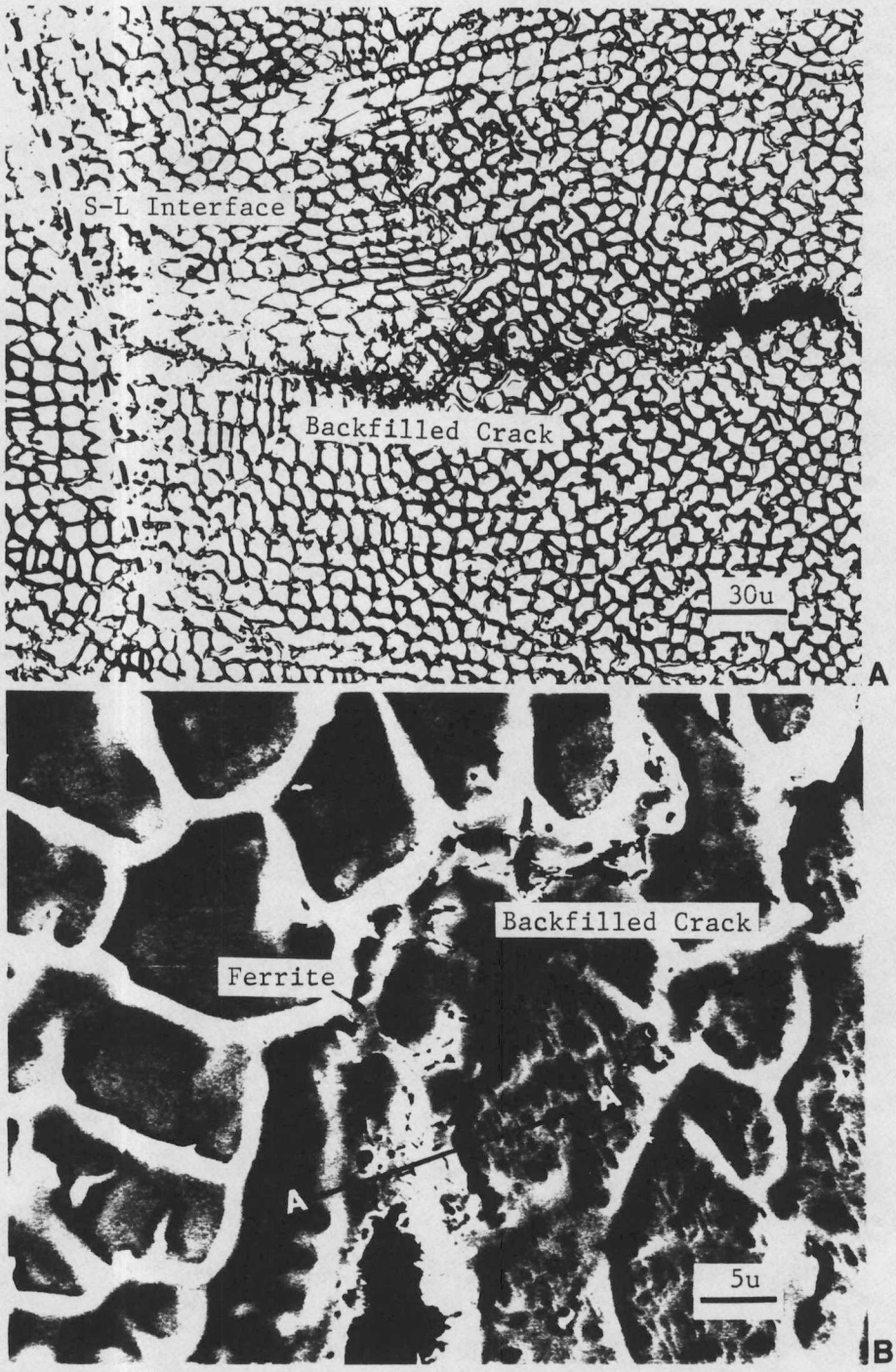


Figure 152. A typical backfilled solidification crack in 316NG-D. a) OLM and b) SEM.

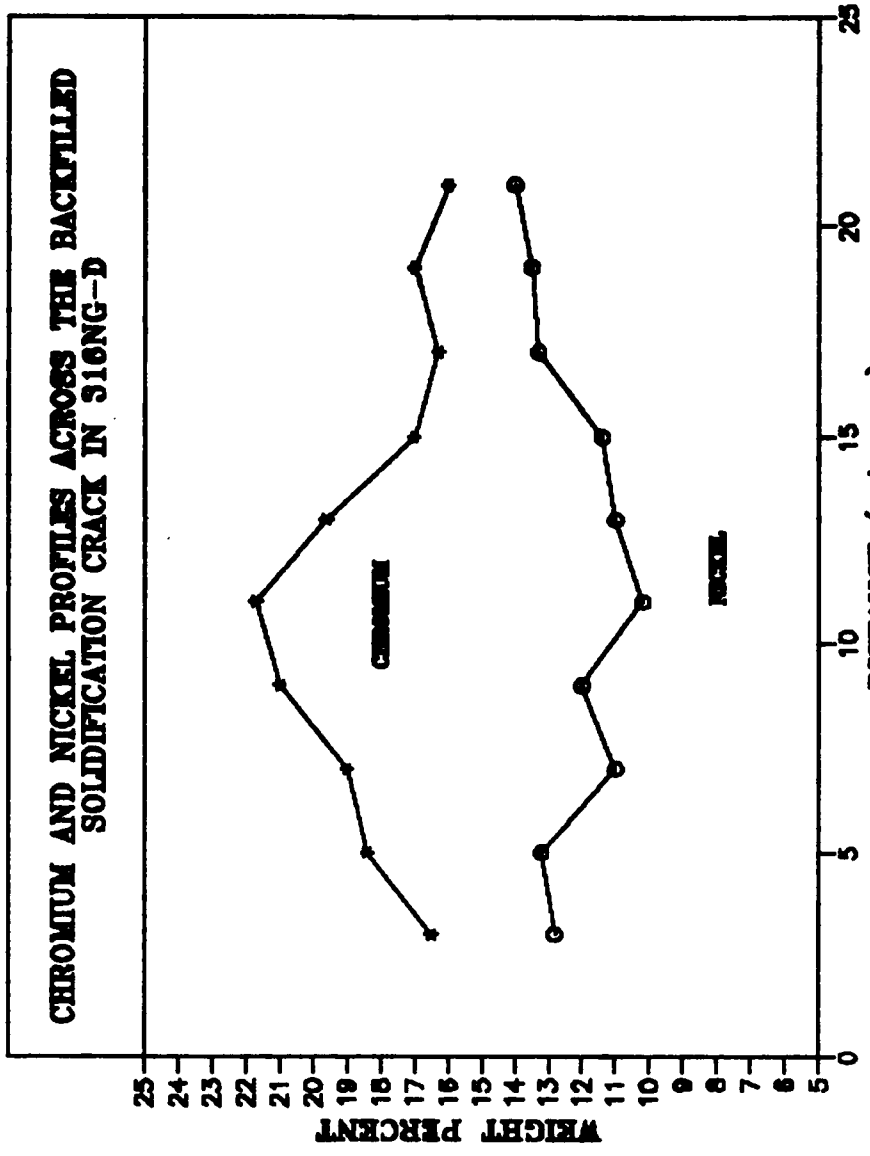


Figure 153. The chromium and nickel distribution across the backfilled crack in 316NG-D. (through A-A in Figure 152).

stabilizer, and to some less extent Ni were rejected into the liquid at the dendrite interstices and grain boundaries and into the liquid in forward of solidification front (as shown in earlier STEM analyses). Further the impurity elements (P, S, Si etc.,), which have a lower solubility in austenite and a small distribution coefficient ($k << 1$), will also segregate to the remaining liquid. Therefore the effective solidus temperature of the remaining liquid along the grain boundary is depressed below the bulk solidus temperature. If a sufficient strain is present or applied, hot cracks then form and when cracking initiates and a crack propagates, the Cr enriched liquid just ahead of the advancing solid-liquid interface is drawn into and fills the crack. Therefore the formation of delta ferrite along the backfilled crack is a product of solidification of Cr enriched liquid. No evidence of S and P segregation in the backfilled region was found in this study with EDAX. Only small extent of Si segregation was detected.

A typical backfilled crack in 347NG-E which solidified in a primary ferritic mode is shown in Figure 154. The chromium and nickel distribution across the backfilled area (region B-B) is given in Figure 155. The average chromium and nickel contents near, and in the backfilled area, is higher than in the surrounding regions. Since the primary solidification mode is ferritic, the liquid remaining during the final stage of solidification is enriched in nickel. Thus, the liquid will solidify as an eutectic mixture of austenite and ferrite during subsequent freezing. This can be noted in Figure 155, in which the chromium content at the center of the backfilled boundary is

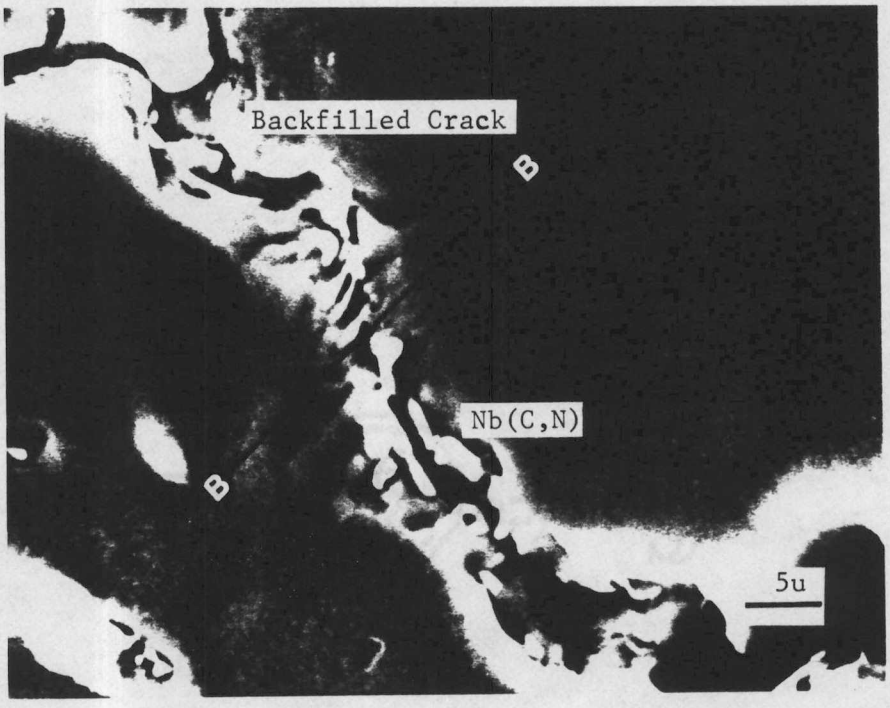


Figure 154. A typical backfilled solidification crack in 347NG-E.

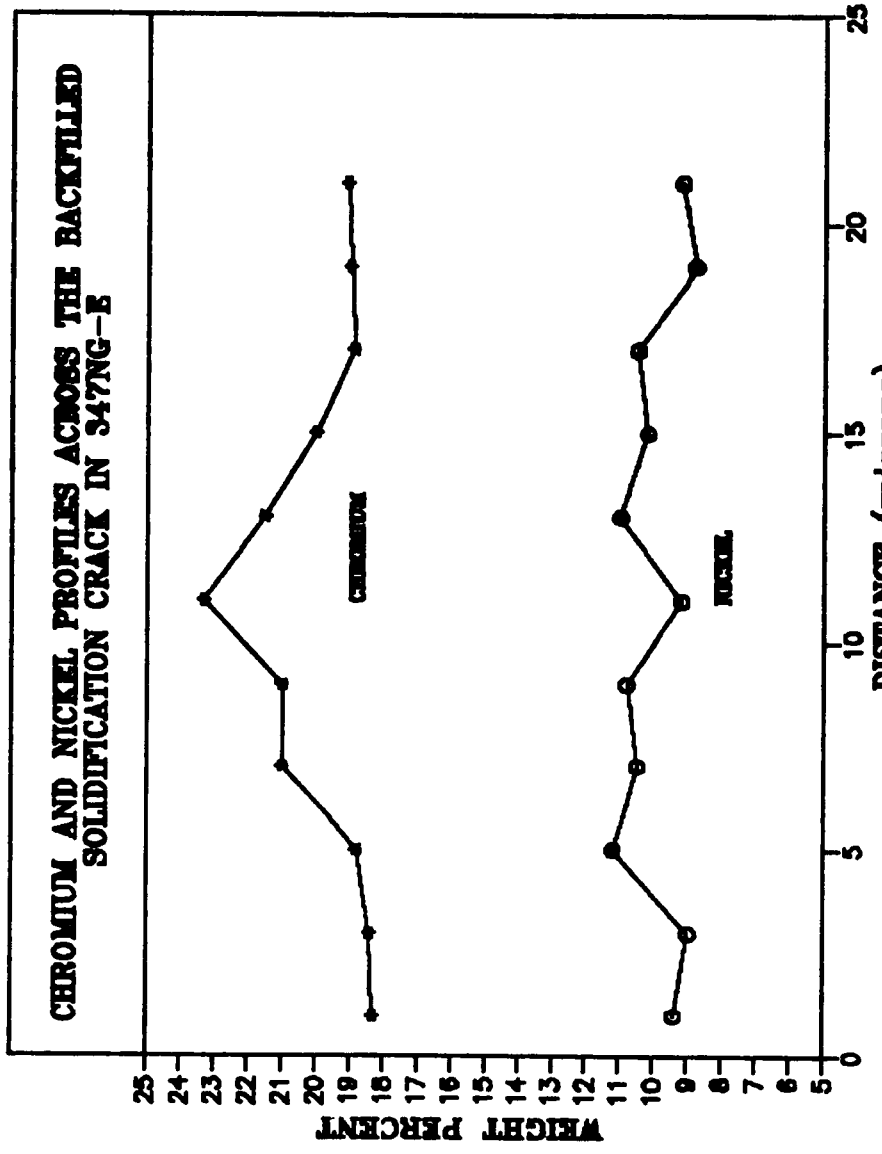


Figure 155. The chromium and nickel distribution across the backfilled crack in 347NG-E. (through B-B in Figure 154).

higher than in the adjacent backfilled area and at the same location the nickel content is slightly lower than in the surrounding matrix. However, there is no clear evidence of formation of ferrite in the center of the backfilled boundary as shown in figure 154. Figure 154 further shows formation of an almost continuous NbC or NbC-austenite eutectic along the backfilled crack, revealing that the formation of a low melting temperature NbC-austenite eutectic may have also played an important role in backfilling in the 347NG alloy.

4. DISCUSSION

Tables 19-20 show that the extent of backfilling is a function of location in the weld. The central region of the weld has the greatest extent (percentage and absolute length) of backfilled solidification cracks. This result indicates that the backfilling is also a function of the temperature gradient, because the weld center has the shallowest temperature gradient as compared to the other regions. A macrograph of the weld zone shown in Figure 156 clearly illustrates that the width of the backfilled region is greatest at the center of weld and becomes narrower close to the fusion line. The macrograph further reveals that when a crack is shorter, it is also thinner.

The backfilling of solidification cracks occurs by the liquid absorption into the cracks by capillary action (from liquid just ahead of the advancing solid-liquid interface). Therefore the backfilling phenomenon may be explained by capillary action theory. Capillary "rise" is a function of liquid density/viscosity, column



Figure 156. A typical macrograph of hot cracked zone along the solidification interface in 347NG-E.

radius/length, and surface energy (tension)(212). A schematic drawing of capillary rise is given in Figure 157. The height (h) of the liquid drawn into the column and the velocity (V) of liquid drawing are:

$$h = \frac{2\gamma_{lv}\cos\theta}{D_l g R} \qquad V = \frac{\gamma_{Lv}\cos\theta}{n}\cdot\frac{R}{4L}$$

where:

D_l - density of liquid
n - viscosity of liquid
R - radius of column
L - length of column
γ_{lv} - surface tension
θ - contact angle between liquid and column

To apply this equations, it has to be assumed that for a given material, there is no temperature gradient in the weld pool and no localized variation in the liquid viscosity and density (because an increase in temperature reduces γ_{lv}/n and improves penetration (213)). This is a reasonable assumption because the liquid drawn into the cracks is only from the thin stagnant liquid layer just ahead of solid-liquid interface along the trailing edge of the weld pool. Therefore, for a given material, capillary liquid drawing is only a function of crack width (column diameter) and length of the crack (column length). (The surface energy term in the both equations is identical for different cracks in a given material). That is, when a crack is thinner (usually the smaller crack is thinner), the capillary drawing is longer. It is also known that finer pores and flaws produce a greater "suction" (213). This may be the reason that the shorter/thinner crack has a greater extent of backfilling.

Figure 150 reveals that when a weld has a primary ferritic solidification mode (316NG-B), the degree of backfilling is somewhat

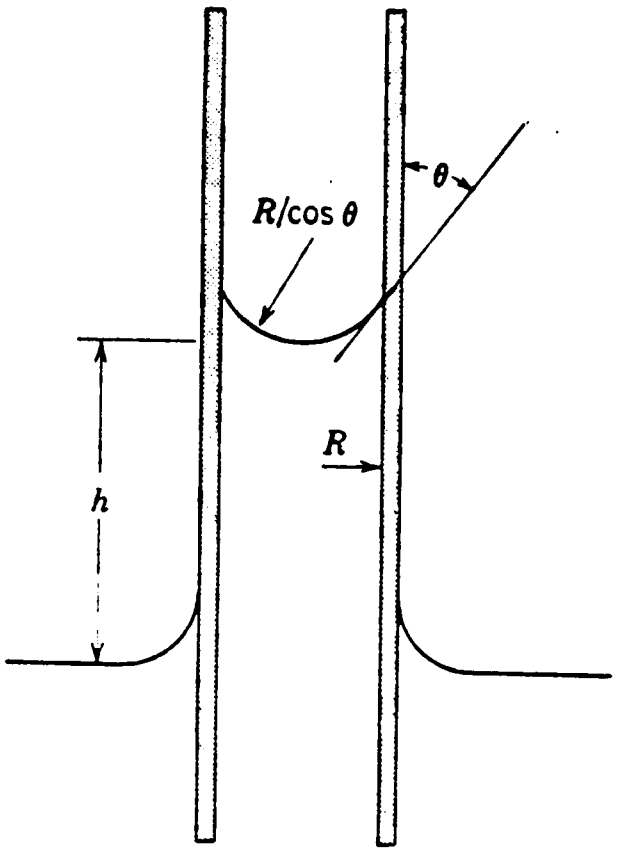


Figure 157. A schematic drawing of the capillary rise.

greater than that for a weld solidified in a primary austenitic mode (316NG-D). The above equations may also be applicable with the same assumptions. However, in this comparison, the surface tension and liquid contact angle have to be considered. It is known that the surface energy is greater and thus the liquid contact angle is smaller for an austenite-austenite boundary than for an austenite-ferrite boundary (214,215). Before considering the surface energy term in the equations, the weld metal freezing process has to be considered. As mentioned earlier, weld solidification cracking and the backfilling of cracks occur during the final stage of solidification just above or at the solidus temperature. Thus, the phases and type of interfaces existing during the final stages of solidification are more important than that at the earlier stages of freezing (primary phases and interfaces). In general, when a weld has a composition close to the eutectic through of the ternary Fe-Cr-Ni diagram and solidifies as ferrite, nickel and other austenite stabilizing elements segregate into the remaining liquid along the dendrite subgrain boundaries. During the last stage of the solidification, a mixture of austenite and ferrite forms along the boundaries by an eutectic reaction (in room temperature microstructure, only austenite can usually be observed due to transformation of ferrite to austenite during cooling to room temperature or by formation of a divorced eutectic). Likely, in the case of primary austenitic welds, during the final stages of freezing the remaining chromium enriched liquid will form a mixture of ferrite and austenite by an eutectic reaction along the dendrite interstices. Therefore, at the moment when liquid is drawn into the

crack by capillary action, a mixture of ferrite and austenite exists along the boundaries. In other words, a mixture of ferrite-austenite interfaces and austenite-austenite interfaces co-exist for both solidification modes. Therefore, it is reasonable to assume that both 316NG-D and 316NG-B have an equal extent of the mixture of austenite-austenite and austenite-ferrite interfaces at a moment when liquid is drawn into the crack. Thus, the terms of surface energy and contact angle (γ_{lv} Cos) in the capillary action equations can be assumed identical for both solidification modes. Therefore, the extent of backfilling in both solidification modes (316NG-D and -B) is again a function of crack length and width only. Tables 19 and 20a indicate that the average solidification crack length for the entire weld is longer in the primary austenitic 316NG-D than in the primary ferritic 316NG-B. Therefore, it is now clear that, a greater extent of backfilling in the primary ferritic weld may not be because of the solidification mode but because of the shorter average crack in the primary ferritic weld metal.

Comparing the extent of backfilling between 316NG-B and 347NG-E, both solidifying in a primary ferritic mode, 347NG-E shows a slightly longer absolute backfilled crack length for a given solidification crack length and location in the weld. However, the percentage of backfilled length to solidification crack length is almost identical for all regions in the weld, because the average solidification crack length in 347NG is greater than that in 316NG. The formation of a high Nb containing liquid along the boundaries, which forms a low melting Nb(C,N)-austenite eutectic during subsequent cooling and

solidification, may have also played an important role in the extent of backfilling in 347NG-E. The evidence for the NbC-austenite eutectic formation along the backfilled crack is shown in Figure 154.

The above results indicate that when a hot cracking resistant material is required, it is important to control the chemical composition so that the solidification mode is primary ferritic. In such cases, even if a solidification crack forms, it will be shorter and be healed to a greater extent. Further, when evaluating the weldability of stainless steels by measuring the solidification crack length in terms of maximum crack length (brittleness temperature range) and/or total crack length, the extent of the backfilling may also have to be measured and considered.

CHAPTER VII

WELDABILITY RECOMMENDATIONS

In order to evaluate weldability more consistently and efficiently, this study has standardized and modified the conventional testing methodology and conditions for the Gleeble hot ductility test and Varestraint hot cracking test. Further, to interpret the test results properly, new criteria, CSTR and DRR, have been developed and analyzed as a function of major and minor alloying elements, metallurgical variables (ferrite potential, grain size) and type of material. The acceptance criteria for hot ductility tests were derived, based on the comparison of the hot ductility response to HAZ liquation susceptibility in the highly restraint hot cracking test (Varestraint) on the same materials. Therefore, it is strongly recommended that when the proposed methodology and testing conditions are used, the data scatter can be significantly reduced and as it is easier to discriminate among behavior on a material to material or heat to heat basis, employing the new acceptance criteria. It is further suggested that the proposed testing conditions for the Gleeble hot ductility test and Varestraint test, together with the acceptance criteria (CSTR of 70 $\pm$ 10 F^{o} and DRR of 40 $\pm$ 5%), be incorporated into the supplementary test requirement in the material specification / weldability guide.

This investigation began with the question concerning the relative weldability of the new austenitic stainless steels, 316NG and 347NG, as compared to the standard AISI grades. (The alloys have shown

to have a superior corrosion resistance to the conventional AISI 304 and 316 grades). The answer to the question is clear that the commercial Nuclear Grade stainless steels have a weldability at least equivalent to that of standard grade stainless steels, provided the followings are considered and incorporated into the chemical specifications.

In the chemical specification for the nuclear grade stainless steels, the range of the Cr_{eq}/Ni_{eq} ratio (solidification behavior) may have to be specified in addition to the room temperature ferrite potential. That is, the chemical composition should be balanced to ensure that the material has a primary ferritic solidification mode. Based on the this investigation, the Cr_{eq}/Ni_{eq} of material should be greater than 1.60. Although a ratio between 1.5 and 1.60 may give no unlikely acceptable weldability, behavior is found to be strongly dependent upon the P + S level, even within the current available chemical specification limits. Further, although a P + S content less than 0.06% does not result in significant cracking if the Cr_{eq}/Ni_{eq} is greater than 1.60, the P + S content has to be minimized, and it is recommended that the P + S content be less than 0.03 %. (ie., P < 0.015%, S < 0.015%).

While the hot ductility behavior and hot cracking resistance in the fusion zone and weld metal HAZ for 316NG and 347NG did not show a clear relationship to the room ferrite content, the base metal HAZ cracking was found to be somewhat reduced by an increased ferrite potential. When the ferrite potential is greater than 3FN, HAZ liquation liquation cracking in both 316NG and 347NG was minimal.

Therefore, it is recommended that the ferrite potential of 316NG and 347NG be 3-5 FN (according to Figure NB-2433.1-1 of ASTM Section III (Delong method)).

The silicon content must also be controlled, although a certain combination of high silicon and nitrogen may give an acceptable hot cracking behavior, provided the primary ferritic solidification is maintained. The recommended silicon content is 0.5 %max.

The most important elements to be controlled in 347NG are Nb, C and N. The hot ductility test results indicate that when the ratio 1/2Nb / (30 x %C + 50 x %N) is less than 0.15, the material has a CSTR less than 70 ± 10 F^{o} and DRR greater than 40 ± 5%, showing good hot ductility response. However, for a high resistance to fusion zone solidification cracking requires that the ratio be lower than 0.1, indicating that a slightly lower Nb content can be allowed for the weld metal than for the base metal HAZ. Therefore, considering the behavior of all three weld zones, the ratio should be less than 0.1. Therefore, corrosion resistance and weldability are considered together, the optimum recommended Nb content is;

* Sensitization/IGSCC; $Nb_{min.}$ > 13 x %C

* Weldability; 1/2 %Nb / (30 x %C + 50 x %N) < 0.1

For 0.03 $\%C_{max.}$, 0.03 %N (residual)

> 13 x %C = > 0.39%

[1/2 %Nb / (30 x %C + 50 x %N) < 0.1] < 0.48%

Thus, Nbmax < 0.48%

However, in 347 austenitic stainless steels, not all the C and N are tied up with Nb (C and N in the solid solution within the

solubility limits). There is also no clear reason for the Nb to be greater than 13 times C for optimum sensitization resistance. To tie up all carbon as NbC, a stoichiometry of about 8 times Nb should be sufficient. Based on the above considerations, it is recommended that the Nb_{max} be less than 0.4% (Nb_{min} > 8 X C). Further, the Nb_{max} should be given in chemistry specifications in addition to Nb_{min} requirement.

This study has also shown that the nitrogen addition for 316NG and in some varieties of 347NG does not appear to have a detrimental effect with regard to hot ductility and hot cracking resistance. In contrast, the nitrogen addition was found to be beneficial in the scavenging of silicon and sulfur (minimizing segregation effects). Therefore, nitrogen can be added up to 0.1-0.12%, provided it does not change the solidification mode to primary austenitic and thus reduces the room temperature ferrite content (potential) significantly.

The other major and minor alloying elements may be within the ASTM specifications. However, it should be considered that in order to control the Cr_{eq}/Ni_{eq} to greater than 1.60, some specific elements limits should be considered.

Based on the above considerations, a suggested chemical specification for 316NG and 347NG is given in Table 21.

Table 21. Suggested specifications for 316NG and 347NG.

	C	Si	Mn	p	S	Ni	Cr	N	Mo	Nb	Co	G.S[a]	FN[b]	Cr_{eq}/Ni_{eq}[c]	Nb/C
347NG	0.03 max	0.5 max	1.5 -2.0	0.015 max	0.015 max	10.0 -14.0	16.0 -18.0	0.12 max	-	0.40 max	0.20 max	>4	3-5	>1.6	≥8
316NG	0.02 max	0.5 max	1.5 -2.0	0.015 max	0.015 max	10.0 -14.0	16.0 -18.0	0.06 -0.12	2.0 -3.0	-	0.20 max	>4	3-5	>1.6	-

a: ASTM grain size No.
b: Ferrite Number according to Figure NB-2433.1-1 of ASME Section III (Delong Method)
c: Hammer and Svensson Method

Cr_{eq} = %Cr + 1.37 x % Mo + 1.5 x % Si + 2 x % Nb + 3 x % Ti

Ni_{eq} = % Ni + 0.31 x % Mn + 22 x %C + 14.2 x % N + %Cu

CHAPTER VIII

CONCLUSIONS

1. HOT DUCTILITY TESTS

a. Development of New Criteria

1. New criteria - CSTR (Critical Strain Temperature Range) and DRR (Ductility Recovery Ratio) were developed for Gleeble hot ductility testing, based on the comparison between the fracture strain in the hot ductility test and the actual in situ HAZ thermal strain measured as a function of peak temperature.

2. The wider the CSTR (ZDT - CST (critical strain temperature), the greater potential for HAZ cracking

3. DRR is the ratio (percentage) of the on-cooling ductility to the on-heating ductility measured at the CST (almost the same temperature at which the on-heating ductility abruptly decreases).

4. CSTR and DRR posses a better discrimination capability and are more definitive than the traditional criteria.

5. CSTR and DRR are sensitive to metallurgical variables (ferrite potential and grain size), chemical composition (Nb, C and N) and impurity level (P + S) and can discriminate between materials and allow heat to heat delineation for materials with the same nominal composition.

b. Metallurgical Changes During Hot Ductility Testing

a). On-Heating

1. The on-heating behavior can be divided into two regions a) ductility increase region and b) ductility decrease region - these

regions are further divided into: i) first stage of rapid ductility decrease and ii) second stage of slowly decreasing ductility.

2. The ductility increase region is mainly a function of the extent of dynamic recrystallization and grain boundary migration which operate rapidly to reduce strain hardening, thus large strains can be easily accommodated and the ductility (%RA) remain high.

3. In the ductility increase region, although cracks formed along the original grain boundaries at the early stage of deformation, rapid recrystallization and migration prevents crack propagation and a high ductility results with a transgranular ductile fracture mode.

4. The first stage of the ductility decrease region is governed by the fracture mode and localized liquid film formation. The sudden drop in the on-heating ductility is attributed to a fracture mode change from transgranular to intergranular and it is accelerated by the formation of localized liquid films along grain boundaries with increasing temperature.

5. In the second stage of the ductility decrease region, dynamic recrystallization does not appear to operate because fracture strain lower than the critical strain for the initiation of recrystallization.

6. The lowered ductility in the second stage is a function of the extent and distribution of the liquid films formed by "incipient melting" of the segregated boundaries rich in Nb, S and Si and constitutional liquation of Nb(C,N) in austenite matrix.

7. Constitutional liquation of relatively large Nb(C,N) particles in the grain boundaries begins at temperatures as low as

2300 ^{o}F. However, fine Nb(C,N) particles within grains do not melt by the constitutional liquation reaction until the temperature reaches about 2430 ^{o}F. However, below this temperature, some of the fine carbo-nitrides dissolve by the solid-state dissolution mechanism.

8. "Incipient melting" of the segregated boundaries starts at about 2400 - 2450 ^{o}F for both 316NG and 347NG.

b). On-Cooling

1. The on-cooling ductility is influenced not only by the deformation mechanism (balance between strain hardening and the softening process of dynamic recrystallization) but also by the extent and distribution of liquid formed during exposure at and near the ZDT.

2. Liquid films completely resolidify when temperature reaches the CST, and the on-cooling ductility begins to fully recover below the CST. Therefore, the CSTR (ZDT - CST) gives an approximate indication of resolidification temperature for liquid formed at the ZDT. A faster resolidification temperature (narrower CSTR) provides a better ductility recovery rate.

3. Regardless of test temperatures between the ZDT and 1700 ^{o}F, the on-cooling fracture mode is intergranular and propagates along prior melted and resolidified grain boundaries which are rich in Si, S and Nb and decorated by the product of the Nb(C,N)-austenite eutectic reaction.

4. The prior melted and resolidified grain boundaries appear as "ghost boundaries" and are distinguishable from the recrystallized boundaries in the room temperature microstructure (due to

segregation). However, during on-heating tests, the original grain boundaries can not be discriminated from new boundaries.

c. Comparison of Nuclear Grades with Standard AISI Grade

1. The hot ductility response of 316NG is better or equivalent than that of AISI 304 and is superior to that of AISI 347.

2. The behavior of 347NG is dependent upon the carbon and niobium contents. When C and Nb are well within the specification limits, the response is superior to that of AISI 347 and equivalent to that of AISI 304 and 316NG. Otherwise, 347NG has a behavior similar to that of AISI 347.

3. The ferrite potential, within the range evaluated in this study (0-6FN), does not appear to influence the ductility response of 347NG and 316NG. However, for a given impurity level (P + S), the higher ferrite potential provides a slightly better ductility response.

4. The hot ductility response of type 347 is mainly a function of the Nb, C and N, in the form of 1/2Nb / (30 x %C + 50 x %N). When the ratio is less than 0.15, hot ductility behavior is adequate and CSTR is less than 70 F^{o}.

d. Ductility Dip Behavior

1. The typical microstructural characteristics of a material which undergoes the ductility dip behavior are: intergranular fracture along the prior melted and resolidified boundaries, existence of chromium rich carbide precipitates along the grain boundaries, a fracture surface enriched in Si and S, and no evidence of recrystallization.

2. Ductility dip behavior is sensitive to the peak temperature experienced in the HAZ. Ductility dip behavior disappears when the HAZ peak temperature lower(ZDT - 50 F^{o}).

3. Ductility dip behavior seems to be related to fracture along the original embrittled (by melting and resolidification due to impurity segregation) grain boundaries at temperature above the equicohesive temperature and below the recrystallization temperature. Grain boundary embrittlement may be further enhanced by the precipitation of chromium rich carbides and an increased amount of liquid formation by exposure to higher peak temperatures.

4. There is no apparent difference in the chemical composition and metallurgical variables (ferrite potential, grain size and etc.) between a material showing ductility dip behavior and one free of the behavior. The reason is not known.

5. A ductility dip in the on-cooling ductility may be a characteristic of the testing method itself which involves significant deformation at a fast strain rate at high temperature. This scenario of changes does not occur in an actual weld heat affected zone.

2. HOT CRACKING SUSCEPTIBILITY

a. Fusion Zone Solidification Cracking

a). General

1. The solidification cracking susceptibility of austenitic stainless steels, regardless of the alloy type, is predominantly a function of the primary solidification mode such that a material solidifying in a primary ferritic mode has a significantly greater

resistance than an alloy which has a primary or fully austenitic solidification mode.

2. The most "harmful" elements responsible for the solidification cracking were found to be S, P, and Si for 316NG, Nb, S, P and Si for 347NG. These elements are enriched in the last solidifying liquid and can form low melting microconstituents and/or eutectics along the solidification/interdendritic boundaries during cooling below the solidus. The constituents found in this study are (Mn,Cr)S, $(Fe,Cr)_3P$, SiO_2-MnO and the Nb(C,N)-austenite eutectic.

3. Hot cracks initiated at temperatures just above the solidus temperature appear to propagate along the rows of low melting liquid drops in the solidification boundaries and eventually extend along migrated grain boundaries. However, hot cracks initiated at temperatures near the liquidus (just behind advancing solid-liquid interface) are found to be backfilled with liquid from weld pool as soon as they occur.

4. In fully austenitic weld metal, the initiated cracks easily propagate along the solidification boundaries which are more or less continuously bridged by the low melting liquid drops and also extend to migrated boundaries.

5. In primary ferritically solidified weld metal, propagation along the migrated grain boundaries is considered to be difficult due to the curved irregular morphology incorporated into the ferrite-austenite interphase boundaries. Thus, the major extent of crack propagation may happen before the solidification boundary completely migrates (that is, some liquid drops still exist along the

solidification boundaries). The propagation temperature range may be between the solidus and the eutectic reaction temperature. At temperature below the solidus temperature, the low melting liquid drops are confined within the eutectic austenite and thus there is no grain boundary existing along the row of liquid drops, resulting in difficult crack propagation.

6. The primary solidification mode is closely associated with solidification cracking, but it appears to be more important for crack propagation than for crack initiation.

b). Behavior of Nuclear Grades

1. When 316NG and 347NG have a chemistry within the specification and have a primary ferritic solidification mode, their resistance to solidification cracking is virtually equivalent to that of AISI 304 and 316 and much superior to that of AISI 347. However, when they exhibit a primary austenitic solidification mode and the Nb and C contents in 347NG are out of specification limits, their susceptibility to fusion zone hot cracking is the same as that of AISI 347.

2. The susceptibility to solidification cracking of AISI 304, 316 and 316NG alloys is influenced significantly by the Cr_{eq}/Ni_{eq} ratio as well as P + S content. When the Cr_{eq}/Ni_{eq} is less than 1.5, the material is most susceptible, even with a low P + S, (0.02 %). When the ratio is between 1.5 and 1.6, the material is somewhat susceptible and the susceptibility is strongly dependent upon the P + S content. However, when the Cr_{eq}/Ni_{eq} ratio is greater than 1.6 and the P + S is within the specification limits ($\simeq$ 0.06 %), the

susceptibility to solidification cracking is considered to be negligible.

3. The effectiveness of a higher Cr_{eq}/Ni_{eq} ratio strongly depends on the P + S content. For a given increase in the ratio, the extent of cracking decreases more rapidly when the P + S level is low.

4. Unlike the case for 304, 316 and 316NG, the solidification cracking behavior of 347NG does not "directly" correlate with the P + S content and the Cr_{eq}/Ni_{eq}.

5. Hot cracking resistance of type 347 is a function of the ratio of 1/2Nb / (30C + 50N) such that when the ratio increases, the extent of solidification cracking also increases. When the ratio is smaller than about 0.1, heat to heat variations are influenced by the P + S and Si contents as well as the Nb content. However, when the ratio is greater than 0.1, solidification cracking is mainly a function of the Nb content relative to C and N.

6. For all of the ferritically solidified 347NG and 316NG, the room temperature ferrite content (within the limited range tested in this study; 1 - 5.5FN) was not a significant factor in heat to heat hot cracking variations.

b. Weld Metal HAZ Liquation Cracking

a). General

1. Although, both the fusion zone and the weld metal HAZ have an identical solidification mode and ferrite content, the susceptibility to weld metal HAZ liquation cracking may not be predicted from fusion zone behavior. Other factors; grain growth, segregation behavior and

transformation of ferrite to austenite (during the subsequent weld passes) have to be considered.

2. Liquation cracking in the weld metal HAZ involves localized melting associated with grain boundary enrichment in S, P, Si for 316NG and S, Si and Nb for 347NG. Most of the enrichment of these harmful elements occurs during solidification before exposure to subsequent weld passes. However, the segregation can be enhanced by the "sweeping" of solutes by a migrating boundary, solid state dissolution of solute rich particles and transformation of ferrite to austenite which releases solute by partitioning.

3. In the fully austenitic weld metal HAZ, a liquation crack usually initiates at or near the fusion line and propagates into the true HAZ and sometimes into the fusion zone. However, in the ferrite containing weld metal HAZ, cracks usually form in a low ferrite region (globular ferrite morphology) some distance from the fusion line, where the original ferrite has transformed to austenite and thus released the "harmful" elements to be redistributed at grain boundaries during subsequent passes.

4. The region adjacent to the fusion line in the ferrite containing weld metal HAZ is relatively immune to the cracking due to the formation of "new" ferrite in addition to the existing ferrite which has partially transformed to austenite expelling harmful elements during the on-heating portion of the thermal cycles below the austenite solvus. The "new" ferrite "reabsorbs" the released "harmful" solutes. Thus the possibility of liquid film formation is

less and the film may not be continuous. Thus, if cracks form, their propagation is difficult.

b). Behavior of Nuclear Grades

1. When 316NG is compared with 347NG, with the exception of the fully austenitic and the high C and Nb lots, the susceptibility is found to be slightly better than that of 347NG and is essentially equal to that of standard AISI 304 and 316.

2. The fully austenitic 316NG and the high C and Nb 347NG have a greater propensity toward weld metal HAZ liquation cracking than 304 and 316, and are identical to AISI 347.

3. There is no clear relationship between the extent of weld metal HAZ cracking and the ratio, 1/2Nb / (30C + 50N), unlike that found for fusion zone cracking. However, in general, a higher ratio and a higher P + S content results in a relatively greater susceptibility.

4. The primary solidification mode is the predominant factor for weld metal HAZ liquation cracking. Therefore, the as-welded microstructure (i.e., the extent of segregation) is the most important factor.

c. Base Metal HAZ Liquation Cracking

a). General

1. Similar to the case of weld metal HAZ cracking, liquation cracking in the base metal HAZ occurs preferentially at intergranular sites and involves localized incipient melting which is associated with an enrichment of Si, S and/or Mo for 316NG and Si, S and Nb for 347NG.

2. The primary sources for segregate enrichment in the grain boundaries may be the interaction of migrating grain boundaries (sweeping effect) with preexisting base metal segregation bands and solid state dissolution of the solute rich particles (for example, NbC and Nb(C,N)).

3. The density and location of the base metal segregation bands relative to the fusion line are found to be a main contributor to liquation and heat to heat variations in behavior. That is, when the segregation band is located near the fusion line, a considerable amount of constitutional liquation and more solutes segregation by sweeping in the migrating boundaries can occur, resulting in increased extent of cracking.

4. The higher ferrite potential provides a greater resistance to the liquation cracking.

b). Behavior of Nuclear Grades

1. In 304 and 316NG, liquation is due to "incipient" melting of the grain boundaries whose melting temperature has been suppressed by the segregation of impurities.

2. In type 347, in addition to the incipient melting of the segregated boundaries, constitutional liquation of Nb(C,N) particles and the liquid penetration into the boundaries play the predominant role in crack formation. Thus, for given P, S and Si contents, 347 is slightly more susceptible to HAZ liquation cracking (longer MCL) than 316NG.

3. The beneficial influence of ferrite formation appears to be slightly more effective for 347 than for 304 and 316NG. That is, for

a given increase in the ferrite potential, a decrease in the extent of cracking is greater in 347 than for 316NG and 304.

4. At low ferrite potential, the extent of cracking in 347 is greater than that in 304 and 316NG, but as the ferrite potential increases, the extent of cracking in 347 approaches that of 304 and 316NG and when the ferrite potential reaches 3 FN, all alloys show virtually identical behavior.

5.The base metal HAZ cracking behavior of 316NG is almost the same as that of AISI 304 and is superior to that of AISI 347.

6. The base metal HAZ cracking response of 347NG does not show a clear relationship to the P + S content. However, the MCL increases with an increase in the Nb and the ratio of 1/2Nb / (30C and 50N).

3. CORRELATION BETWEEN HOT DUCTILITY AND BASE METAL HAZ BEHAVIOR

1. For "direct" comparison of the Gleeble hot ductility tests (CSTR and DRR), a new criteria - the Cracked HAZ Length (CHL) was developed for Varestraint base metal HAZ cracking. The CHL is measured along the fusion line in the HAZ where hot cracks form.

2. The conventional criteria (TCL, MCL and threshold strain) for the Varestraint test do not show a sufficient correlation with the hot ductility test results (CSTR and DRR), because during on-cooling hot ductility testing, from which the CSTR and DRR were derived, is conducted from a "single" peak temperature, the ZDT. Thus, the on-cooling hot ductility tests evaluate "only" the region which has experienced the ZDT along and parallel to the fusion line. Therefore, the MCL and TCL, which are based on the measurement of crack length in

the direction perpendicular to the fusion line may not provide a good correlation with the CSTR and DRR.

3. The CHL shows an excellent correlation with the hot ductility test results. When a material has a CSTR greater than 70 ± 10 F^{o} and DRR less than 40 ± 5%, the CHL is finite and increases with changes in as indicated for the CSTR and DRR, thus revealing a higher susceptibility for base metal HAZ cracking.

4. When the CSTR is less than 70 ± 10 F^{o} and DRR is greater than 40 ± 5%, the CHL is essentially zero and the material appears to be very resistant to the HAZ liquation cracking.

5. Therefore, it is strongly believed that because the above critical values of CSTR and DRR are based on the comparison with the severe restraint hot cracking tests on the same materials (Varestraint), the CSTR of 70 ± 10F^{o} and DRR of 40 ± 5% can be used as the hot cracking assessment criteria for the Gleeble hot ductility test. Further, if a material has passed the Gleeble hot ductility screening tests using the above critical values, it should not suffer from any difficulties in actual fabrication practice, provided the joint design, filler metals and the other welding conditions are chosen properly.

4. EFFECTS OF SI, N AND REM ON HOT CRACKING

a. Effect of Si (0.5-1.25%) and Synergistic Effect with N

1. As the Si content increases to approximately 0.75%, susceptibility to fusion zone solidification cracking of 304 stainless steel increases. When the Si content is greater than 0.75%, no

further increase in cracking sensitivity occurs. In fact, when the Si content is raised to 1.25%, cracking is decreased slightly as compared to 0.75 %Si.

2. The decreased solidification cracking in a high Si containing material (1.25%) as compared to the 0.75 %Si may be due to an increased amount of primary ferrite occurring during solidification and concomitantly a higher room temperature ferrite content (8FN Vs. 4FN).

3. While maintaining a primary ferritic solidification mode, a nitrogen addition of 5 vol% in the Ar shielding decreased the fusion zone hot cracking for the high Si (1.25%) material. However, when the nitrogen addition was increased to 20 vol% in the shielding gas such that the solidification mode changes from primary ferrite to primary austenite, fusion zone cracking susceptibility increased significantly.

4. The decreased solidification cracking in primary ferritic high Si and N containing welds may be due to a scavenging of S and thus reduced low melting sulfide formation along the grain/dendrite boundaries by the formation of high sulfur containing manganese-silicates.

5. The Si content should be limited to less than 0.5%, although a certain combination of Si and N can reduce cracking.

b. Effect of N (0.047-0.12%)

1. For a fully austenitic 316 stainless steel, solidification cracking decreased with an increase in the nitrogen content from 0.047 to 0.12%.

2. The decreased solidification cracking in the higher nitrogen containing material is due to a decreased solidification substructure size. The cell size decreased from an average of 18 um to 14 um when the nitrogen content increased from 0.047 to 0.12%.

3. The decreased hot cracking susceptibility in the higher N material may be also due to the decreased brittleness temperature range (BTR), because of decreased liquidus and solidus isothermals with an increase in nitrogen in the fully austenitic weld metal.

4. With the same amount of nitrogen (for a primary ferritic solidification), the susceptibility to solidification cracking is lower than when the material has austenite as a primary solidification phase.

c. Effect of Rare Earth Metal (Mish Metals)

1. Addition of REM (0.017%) to 347 appears to have a beneficial effect on weld metal solidification cracking and weld metal HAZ liquation cracking, provided the weld metal solidifies in a primary ferritic mode.

2. Unlike the cases in the fusion zone and weld metal HAZ behavior, a REM addition was found to be ineffective for reducing liquation cracking in the base metal HAZ.

5. EVALUATION OF BACKFILLED SOLIDIFICATION CRACKS.

1. The extent of backfilling is a function of location in the weld and the temperature gradient. Thus, more extensive backfilling occurs at the center of the weld because the temperature gradient is shallowest at the centerline.

2. The extent of backfilling is also a function of solidification crack length and width such that the smaller and thinner the solidification crack, the greater is the backfilling regardless of the location in the weld.

3. A weld solidifying in a primary ferritic mode, as compared to the primary austenitic mode, exhibits a larger ratio backfilled crack length to solidification crack length due to the occurrence of smaller and thinner cracks

4. The applied strain level does not significantly influence backfilled crack length but at lower strains a slight increase in the ratio of backfilled crack length to solidification crack length at a given location in the weld was found.

5. For the same strain level and a primary ferritic solidification mode, 347NG has longer backfilled cracks than 316NG at a given location in the weld. However, the ratio of backfilled crack length to the solidification crack length is similar because the average solidification crack length is longer in 347NG than in 316NG.

6. The formation of Nb enriched liquid which subsequently forms low melting NbC-austenite eutectics along grain boundaries may play an important role in the extent of backfilling in 347NG.

7. Backfilling is a result of capillary action. The liquid source for backfilling is the liquid remaining during the final stages of solidification and the liquid ahead of the advancing solid-liquid interface along the trailing edge of the weld pool, which is rich in chromium or nickel depending on the solidification process.

REFERENCES

REFERENCES

1. Hanneman, R.E., Danko, J.C., Giannuzzi, A.J. and Riccardella, P.C., "Cause of Cracking-Evaluation of Performance Margin Between Different Diameter Type 304 Stainless Steel Piping Systems," EPRI NP-944, Dec.(1978).

2. U.S. Nuclear Regulatory Commission Pipe Crack Task Group, "Investigation and Evaluation of Stress-Corrosion Cracking in Piping of Boiling Water Reactor Plants," NUREG-1061, Mar.(1984).

3. U.S. Nuclear Regulatory Commission Piping Review Committee, "Report of the U.S. Nuclear Regulatory Commission Piping Review Committee: Summary-Piping Review Committee Conclusions and Recommendations," NUREG-1061, Vol. 5, Apr.(1985).

4. Alexander, et al., "Alternative Alloys for BWR Piping Applications," EPRI NP-2671, Oct.(1982).

5. Kobayashi, et al., "Stress Corrosion Cracking Resistance, Mechanical Properties and Weldability of Nuclear Grade 316 Stainless Steel," EPRI WS-79-176, May (1980).

6. Lundin, C.D., Lee, C.H., Menon, R. and Stansbury, E.E., "Sensitization of Austenitic Stainless Steels; Effect of Welding Variables on HAZ sensitization of AISI 304 and HAZ behavior of BWR Alternative Alloys 316 NG and 347," Welding Research Council Bulletin No. 319, Nov.(1986).

7. Ogawa, T. and Abe, S., "Weldability of Type 347 Stainless Steel with Improved Resistance to Intergranular Stress Corrosion Cracking," Proceedings-The Golden Gate Metals and Welding Conference, San Francisco, California U.S.A., (1979).

8. Lundin, C.D., Lee, C.H. and Menon, R., "Weldability Evaluations of Modified 316 and 347 Austenitic Stainless Steels : Part I. Preliminary Results," Welding Journal, 67(2), p. 35s-46s, (1988).

9. Cargill, R.L., "Materials Issues in BWR Piping Replacement," Nutech Engineers INC., San Jose, CA., June (1984).

10. Nippes, E.F., Savage, W.F., Bastin, B.T., Mason, H.F. and Curran, R.M., "An Investigation of the Hot Ductility of High Temperature Alloys," Welding Journal, 34(4), p. 183s-196s, (1955).

11. Nippes, E.F., Savage, W.F. and Grotke, G., "Further Studies of the Hot Ductility of High Temperature Alloys," Welding Research Council Bulletin, No.33, (1957).

12. Lundin, C.D., Menon, R., Lee, C.H. Osorio, V., "New Concepts in VARESTRAINT Testing for Hot Cracking," Welding Research. The State of the Art, Proceedings of the JDC University Symposium, Edited by Nippes, E. and Ball, D.J., 1985 International Welding Congress, ASM, Toronto, Canada, Oct.(1985).

13. Hemsworth, B., Boniszewski, T. and Eaton, N.F., "Classification and Definition of High Temperature Welding Cracks in Alloys," Metal Construction and British Welding Journal, 1(2), p. 5-16, (1969).

14. Haddrill, D.M. and Baker, R.G., "Microcracking in Austenitic Weld Metal," British Welding Journal, 13(1), p. 43-51, (1966).

15. Pumphrey, W.I. and Jennings, P.H., "A Consideration of the Nature of Brittleness at Temperature Above the Solidus in Castings and Welds in Aluminum Alloys," Journal of Institute of Metals, 75, p. 235-256, (1948).

16. Toropov, V.A., "On the Mechanism of Hot Cracking," Metallovedenie I Obrabotka Metalloy, 6, p. 54-58, (1957).

17. Medovar, B.I., "On the Nature of Weld Hot Cracking," Avtom. Svarka., 7(4), (1954).

18. Pellini, W.S., "Strain Theory of Hot Tearing," The Foundry, 80(11), p. 125-133, (1952).

19. Puzak, P.P., Apblett, W.R. and Pellini, W.S., "Hot Cracking of Stainless Steel Weldments," Welding Journal, 35(1), p. 9s-17s, (1956).

20. Borland, J.C., "Generalized Theory of Super-solidus Cracking in Welds (and Casting)," British Welding Journal, 7(8), p. 508-512, (1960).

21. Borland, J.C., "Suggested Explanation of Hot Cracking in Mild and Low Alloy Steel Welds, " British Welding Journal, 8(11), p. 526-540, (1961).

22. Dixon, B.F., and Phillips, R.H., "Cracking in the Transvarestraint Test, Part 3," Metal Construction, 4, p. 232-237, (1984).

23. Lundin, C.D., "A New Approach to The Study of Hot Cracking in Fusion Welds," Ph.D Dissertation, RPI., (1966).

24. Easterling, K., Introduction to the Physical Metallurgy of Welding, BMM Pub., (1983).

25. Savage, W.F., "Solidification, Segregation and Weld Imperfections," 1980 Houdremont Lecture. Welding in The World, 18(5-6), p. 89-114, (1980).

26. Savage, W.F., Nippes, E.F. and Miller, T.W., "Microsegregation in Partially Melted Regions of 70Cu-30Ni Weldments," Welding Journal, 55(7), p. 181s-187s, (1976).

27. Pepe, J.J. and Savage, W.F., "Effects of Constitutional Liquation in 18-Ni Maraging Steel Weldments," Welding Journal, 46(9), p. 411s-422s, (1967).

28. Linnert, G.E., "Weldability of Austenitic Steels as Affected by Residual Elements," ASTM STP 418, p. 105-119, (1967).

29. Hull, F.C., "Effects of Alloying Additions on Hot Cracking of Austenitic Chromium-Nickel Stainless Steels," Trans. ASTM, 60, p. 667-690, (1960).

30. Morishige, N., Kuribayashi, M. and Okabayashi, H., "Effects of Chemical Composition of Base Metal on Susceptibility to Hot Cracking in Austenitic Stainless Steel Weld," I.I.W.-Doc. IX-1114-79, (1979).

31. Borland, J.C. and Younger, R.N., "Some Aspects of Cracking in Welded Cr-Ni Austenitic Steels," British Welding Journal, 7(1), p. 22-59, (1960).

32. Morishige, N., Kuribayashi, M. and Okabayashi, H., "Study of Weldable 18Cr-10Ni-Nb Stainless Steels," IHI Engineering Review, 15(2), p. 1-6, (1984).

33. Astrom, H., Loberg, B., Bengtsson, B. Easterling, K.E., "Hot Cracking and Micro-Segregation in 18-10 Stainless Steel Welds," Materials Science, 7, p. 225-234, (1976).

34. Fredriks, H. and van der Toorn, L.J., "Hot Cracking in Austenitic Stainless Steel Weld Deposits," British Welding Journal, 15(4), p. 178-182, (1968).

35. Polgary, S., "The Influence of Silicon Content on Cracking in Austenitic Stainless Steel Weld Metal with Particular Reference to 18:8 Chromium-Nickel Steel," Metal Construction, 1(2), p. 93-97, Discussion in p. 130-141, (1969).

36. Potapov, N.N., Bobrikov, Y.V. and Volobue, Y.S., "Effects of Silicon on the Susceptibility of Austenitic-Ferritic Metal to Hot Cracking During Welding," Automatic Welding, (3), p. 40-42, (1982).

37. Dahl, W., Duren, C. and Muesch, H., "Susceptibility of Austenitic Welded Joints to Hot Cracking," I.I.W.-Doc.II-660-73, 27, (1973).

38. Lippold, J.C., "An Investigation of Weld Cracking in Alloy 800," Welding Journal, 63(3), p.91s-103s, (1984).

39. Ogawa, T. and Tsunetomi, E., "Hot Cracking Susceptibility of Austenitic Stainless Steels," Welding Journal, 61(3), p. 82s-93s, (1982).

40. Brooks, J.A. Krener, R.W., "Progress Toward a More Weldable A-286," Welding Journal, 53(6), p. 242s-245s, (1984).

41. Thomas Jr, R.D., "HAZ Cracking in Thick Sections of Austenitic Stainless Steels - Part II," Welding Journal, 63(12), p. 355s-368s, (1984).

42. Rozet, D., Campbell, H. and Thomas Jr, R., "Effect of Weld Metal composition on the Strength and Ductility of 15 Chromium-35 Nickel Welds," Welding Journal, 27(10), p. 481s-491s, (1948).

43. Brooks, J.A. and Lambert, F.J., "The Effect of Phosphorus, Sulfur, and Ferrite Content on Weld Cracking of Type 309 Stainless Steel," Welding Journal, 57(5), p. 139s-143s, (1978).

44. Brooks, J.A., "Weldability of High N, High Mn Austenitic Stainless Steel," Welding Journal, 54(6), p. 189s-195s, (1975).

45. Kujanpaa, V.P., "Effect of Steel Type and Impurities in Solidification Cracking of Austenitic Stainless Steel Welds," Metal Construction, 17(1), p. 40R-46R, (1985).

46. Arata, Y., Matsuda, F. and Katayama, S., "Solidification Crack Susceptibility in Weld Metals of Fully Austenitic Steels," Transactions of JWRI, 6(1), p. 46-57, (1977).

47. Matsuda, F., Nakagawa, H., Katayama, S. and Arata, Y., "Solidification Crack Susceptibility in Weld Metals of Fully Austenitic Stainless Steels; Effect of Nitrogen on Cracking in SUS 304 Weld Metal," Transactions of JWRI, 12(1), p. 89-95, (1983).

48. Matsuda, F., Nakagawa, H. and Katayama, S., "Effect of Alloying Elements on Solidification Crack Resistance of Austenitic Stainless Steel Weld Metals," I.I.W.-Doc. IX-1315-84, (1984).

49. Makin, S.M., Alcock, C.B., Arkell, D.R. and Pfeil, P.C.L., "Distribution of Phosphorus and Sulfur in Fully Austenitic Stainless Steel Welds," British Welding Journal, (10), p. 595-599, (1960).

50. Kujanpaa, V. and Moisio, T., "Effect of Phosphorus and Sulfur on Solidification Cracking in Austenitic Stainless Steel," Proceedings-Solidification Technology in The Foundry and Cast House, p. 372-375, The Metal Society, Univ. of Warwick, Coventry, Sept.(1980).

51. Lambert, F.J., "Role of Ferrite and Phosphorus and Sulfur in the Crack Sensitivity of Autogenously Welded Type 309 Stainless Steel," Y-2049, ORNL, (1976).

52. Arata, Y., Matsuda, F., Nakagawa, H. and Katayama, S., "Solidification Crack Susceptibility in Weld Metals of Fully Austenitic Stainless Steels; Effect of Decreasing P and S on Solidification Crack Susceptibility of SUS 310S Austenitic Stainless Steel Weld Metals, " Transactions of JWRI, 7(2), p. 21-24, (1978).

53. Cullen, T.M. and Freeman, J.W., "Metallurgical Factors Influencing Hot Ductility of Austenitic Piping at Weld Heat Affected Zone Temperature," Journal of Engineering for Power, 85, p. 151-164, (1963).

54. Matsuda, F., Nakagawa, H., Katayama, S. and Arata, Y., "Solidification Crack Susceptibility in Weld Metals of Fully Austenitic Stainless Steels; Effect of La or REM Addition on Solidification Crack Resistance," Transactions of JWRI, 11(1), p. 79-94, (1982).

55. Sadwski, E.P., "Modification of Cast 25Cr-20Ni for Improved Crack Resistance," Welding Journal, 53(2), p. 49s-58s, (1974).

56. Matsuda, F., Katayama, S. and Arata, Y., "Solidification Crack Susceptibility in Weld Metals of Fully Austenitic Stainless Steels; Effect of Titanium on Solidification Crack Resistance," Transactions of JWRI, 12(2), p.87-92, (1983).

57. Savage, W.F. Nippes, E.F. and Goodwin, G.M., "Effect of Minor Elements on Fusion Zone Dimensions of Inconel 600," Welding Journal, 56(4), p. 126s-132s, (1977).

58. Thielsch, H., "The Sense and Nonsense of Weld Defects; Relation of Defects to Weld Solidification," Welding Engineering, (11), p. 47-49, (1965).

59. Savage, W.F., Lundin, C.D. and Aronson, A.H., "Weld Metal Solidification Mechanics," Welding Journal, 44(4), p. 175s-181s, (1965).

60. Savage, W.F. and Aronson, A.H., "Preferred Orientation in the Fusion Zone," Welding Journal, 45(2), p. 85s-89s, (1966).

61. Garland, J.G., "Weld Pool Solidification Control," Metal Construction and British Welding Journal, 6(4), p. 2-8, (1974).

62. Savage, W.F., Lundin, C.D. and Chase, T.F., "Solidification of Fusion Welds in Face-Centered Cubic Metals," Welding Journal, 47(11), p. 522s-526s, (1968).

63. Savage, W.F., Nippes, E.F. and Erickson, J.S., "Solidification Mechanisms in Fusion Welds," Welding Journal, 55(8), p. 213s-221s, (1976).

64. Davies, G.J. and Garland, J.G., "Solidification Structures and Properties of Fusion Welds," International Metallurgical Reviews, 20, Review 196, p. 83-106, (1975).

65. Loper Jr, C.R., Shideler, L.A. and Devletian, J.H., "The Effect of Heat-Affected Zone Structure on the Structure of the Weld Fusion Zone," Welding Journal, 48(4), p. 171s-178s, (1969).

66. Fredriksson, H., "The Solidification Sequence in an 18-8 Stainless Steel, Investigated by Directional Solidification," Metallurgical Transactions A, 3(11), p. 2989-2997, (1972).

67. Masumoto, I., Takami, K. and Kutsuna, M., "Hot Cracking of Austenitic Steel Weld Metal," Journal of the JWS, 41(11), p. 1306-1314, (1972).

68. Brooks, J.A., "Solidification and Solid State Transformations of Austenitic Stainless Steel Welds," Proceedings-Trends in Welding Research in the United States, Edited by David, S., p. 331-357, Metal Park, Ohio, ASM (1982).

69. Brooks, J.A., Williams, J.C. and Thompson, A.W., "STEM Analysis of Primary Austenite Solidified Stainless Steel Welds," Metallurgical Transactions A, 14(1), p. 23-31, (1983).

70. Brooks, J.A., Williams, J.C. and Thompson, A.W., "Microstructural Origin of the Skeletal Ferrite Morphology of Austenitic Stainless Steel Welds," Metallurgical Transactions A, 14(7), p. 1271-1281, (1983).

71. Brooks, J.C., West, A.J. and Thompson, A.W., "Effect of Weld Composition and Microstructure on Hydrogen Assisted Fracture of Austenitic Stainless Steels," Metallurgical Transactions A, 14(1), p. 75-84, (1983).

72. Kou, S. and Le, Y., "The Effect of Quenching on the Solidification Structure and Transformation Behavior of Stainless Steel Welds," Metallurgical Transactions A, 13(7), p.1141-1151, (1982).

73. Lippold, J.C., "Weld Cracking Mechanisms in Austenitic Stainless Steels," Proceedings-Trends in Welding Research in the United States, Edited by David, S., p. 209-241, Metal Park, Ohio, ASM, (1982).

74. Lippold, J.C. and Savage, W.F., "Solidification of Austenitic Stainless Steel Weldments: Part I - A Proposed Mechanism," Welding Journal, 58(12), p.362s-373s, (1979).

75. Lippold, J.C. and Savage, W.F., "Solidification of Austenitic Stainless Steel Weldments: Part II - The Effect of Alloy Composition on Ferrite Morphology," Welding Journal, 59(2), p. 48s-58s, (1980).

76. Lippold, J.C. and Savage, W.F., "Solidification of Austenitic Stainless Steel Weldments: Part III - The Effect of Solidification Behavior on Hot Cracking Susceptibility," Welding Journal, 61(12), p. 388s-396s, (1982).

77. Cieslak, M.J. and Savage, W.F., "Weldability and Solidification Phenomenon of Cast Stainless Steel," Welding Journal, 59(5), p. 136s-146s, (1980).

78. Cieslak, M.J., Ritter, A.M. and Savage, W.F., "Solidification Cracking and Analytical Electron Microscopy of Austenitic Stainless Steel Weld Metals," Welding Journal, 61(1), p.1s-8s, (1982).

79. Ritter, A.M., Henry, M.F. and Savage, W.F., "High Temperature Phase Chemistries and Solidification Mode Prediction in Nitrogen-Strengthened Austenitic Stainless Steels," Metallurgical Transactions A, 15(7), p. 1339-1351, (1984).

80. David, S.A., Goodwin, G.M. and Braski, D.N., "Solidification Behavior of Austenitic Stainless Steel Filler Metals," Welding Journal, 58(11), p. 330s-336s, (1979).

81. Goodwin, G.M., Cole, N.C. and Slaughter, G.M., "A Study of Ferrite Morphology in Austenitic Stainless Steel Weldments," Welding Journal, 51(9), p. 425s-429s, (1972).

82. David, S.A., "Ferrite Morphology and Variations in Ferrite Content in Austenitic Stainless Steel Welds," Welding Journal, 60(4), p. 63s-71s, (1981).

83. Leone, G.L. and Kerr, H.W., "The Ferrite to Austenite Transformation in Stainless Steel," Welding Journal, 61(1), p. 13s-21s, (1982).

84. Lyman, C.E., "Analytical Electron Microscopy of Stainless Steel Weld Metal," Welding Journal, 58(7), p. 189s-194s, (1979).

85. Vitek, J.M., Dasgupta, A. and David, S.A., "Microstructural Modification of Austenitic Stainless Steels by Rapid Solidification," Metallurgical Transactions A, 14(9), p. 1833-1841, (1983).

86. Suutala, N., "Effect of Manganese and Nitrogen on the Solidification Mode in Austenitic Stainless Steel Welds," Metallurgical Transactions A, 13(12), p. 2121-2130, (1982).

87. Kujanpaa, V.P., Suutala, N.J., Takalo, T.K. and Moisio, T.J.I., "Solidification Cracking - Estimation of the Susceptibility of Austenitic and Austenitic-Ferritic Stainless Steel Welds," Metal Construction, 12(6), p. 27-30, (1980).

88. Suutala, N., Takalo, T. and Moisio, T., "Ferritic-Austenitic Solidification Mode in Austenitic Stainless Steel Welds," Metallurgical Transactions A, 11(5), p. 717-725, (1980).

89. Takalo, T., Suutala, N. and Moisio, T., "Influence of Ferrite Content on its Morphology in Some Austenitic Weld Metals," Metallurgical Transactions A, 7(10), p. 1591-1592, (1976).

90. Suutala, N., Takalo, T. and Moisio, T., "The Relationship Between Solidification and Microstructure in Austenitic and Austenitic-Ferritic Stainless Steel Welds," Metallurgical Transactions A, 10(4), p. 512-514, (1979).

91. Takalo, T., Suutala, N. and Moisio, T., "Austenitic Solidification Mode in Austenitic Stainless Steel Welds," Metallurgical Transactions A, 10(8), p. 1173-1181, (1979).

92. Suutala, N., Takalo, T. and Moisio, T., "Single-Phase Ferritic Solidification Mode in Austenitic Stainless Steel Welds," Metallurgical Transactions A, 10(8), p. 1183-1190, (1979).

93. Molian, P.A., "Solidification Behavior of Laser Welded Stainless Steel," Journal of Materials Science Letters, 4, p. 281-283, (1985).

94. Arata, Y., Matsuda, F. and Katayama, S., "Solidification Crack Susceptibility in Weld Metals of Fully Austenitic Stainless Steels; Fundamental Investigation on Solidification Behavior of Fully Austenitic and Duplex Microstructures and Effect of Ferrite on Microsegregation," Transactions of JWRI, 5(2), p.35-51,(1976).

95. Katayama, S., Fujimoto, T. and Matsunawa, A., "Correlation Among Solidification Process, Microstructures, Microsegregation and Solidification Cracking Susceptibility in Stainless Steel Weld Metals," Transactions of JWRI, 14(1), p. 123-138, (1985).

96. Hoffmeister, H., "Microsegregation and Delta-Ferrite Formation in Austenitic Weld Metal," Schweissen Und Schneiden, 25(5), p. 164-166, (1973).

98. Lundin, C.D., Delong, W.T. and Spond, D.F., "Ferrite-Fissuring relationship in Austenitic Stainless Steel Weld Metals," Welding Journal, 54(8), p. 241s-246s, (1975).

99. Hull, F.C., "Effect of Delta Ferrite on the Hot Cracking of Stainless Steel," Welding Journal, 46(9), p. 399s-409s, (1967).

100. Brooks, J.A., Thompson, A.W. and Williams, J.C., "A Fundamental Study of the Beneficial Effects of Delta Ferrite in Reducing Weld Cracking," Welding Journal, 63(2), p. 71s-83s, (1984).

101. Matsuda, F., Nakagawa, H., Uehara, T., Katayama, S. and Arata, Y., "A New Explanation for Role of Delta-Ferrite Improving Weld Solidification Crack Susceptibility in Austenitic Stainless Steel," Transactions of JWRI, 8(1), p. 105-112, (1979).

102. Lundin, C.D. and Spond, D.F., "The Nature and Morphology of Fissures in Austenitic Stainless Steel Weld Metals," Welding Journal, 55(11), p. 356s-367s, (1976).

103. Lundin, C.D. and Chou, C.P.D., "Hot Cracking Susceptibility of Austenitic Stainless Steel Weld Metals," Welding Research Council Bulletin, No. 289, (1983).

104. Lundin, C.D., Lee, C.H. and Menon, R., "Hot Ductility and Weldability of Free Machining Austenitic Stainless Steel," Welding Journal, 67(6), P.119s-130s, (1988).

105. Bloom, F.K., Clarke, W.C. and Jenning, P.A., "Relation of Structure of Stainless Steel to Hot Ductility," Metal Progress, 59(2), p. 250-256, (1951).

106. Soldan, H.M. and Mayne, C.R., "Ductility related to Service Performance of Heavy-Wall Austenitic Pipe Welds," Welding Journal, 36(3), p. 141s-150s, (1957).

107. Soldan, H.M. and Mayne, C.R., "Cracking Tendency in Heavy High Temperature Steam Piping," Metal Progress, p. 78-85, (1957).

108. Williams, C.S., "Steel Strength and Ductility Response to Arc.-Welding Thermal Cycles," Welding Journal, 42(1), p. 1s-8s,(1963).

109. Kreischer, C.H., "A Critical Analysis of the Weld Heat-Affected Zone Hot Ductility test," Welding Journal, 42(2), p. 49s-59s, (1963).

110. Yeniscavich, W., "A Correlation of Ni-Cr-Fe Alloy Weld Metal Fissuring With Hot Ductility Behavior," Welding Journal, 45(8), p. 344s-356s, (1966).

111. Yeniscavich, W., "Correlation of Hot Ductility Curves With Cracking During Welding," Proceedings-Symposium on Methods of High-Alloy Weldability Evaluation, Welding Research Council, N.Y., N.Y., April (1969).

112. Duvall, D.S. and Owczarski, W.A., "Further Heat Affected Zone Studies in Heat Resistant Nickel Alloys," Welding Journal, 46(9), p. 423s-432s, (1967).

113. Muesch, H., "Welding of Material Grade TP 347 Mod." Technical Report of Mannesmann, Anlagenbau, West Germany, March (1984).

114. Weiss, B., Grotke, G.E. and Stickler, R., "Physical Metallurgy of Hot Ductility Testing," Welding Journal, 49(10), p. 471s-487s, (1970).

115. Donati, J.R. and Zacharie, G., "Evaluation of Tendency Toward Hot Crack in the Welding Heat-Affected Zone of Austenitic 18-10 Stainless Steels; Discussion of a Cracking Criterion," Revue de Metallurgie, 71(12), p. 905-915, (1974).

116. Thompson, R.G. and Genculu, S., "Microstructural Evolution in the HAZ of Inconel 718 and Correlation with the Hot Ductility," Welding Journal, 62(12), p. 337s-345s, (1983).

117. ASTM SA-430, "Specification For Austenitic Steel Forged and Bored Pipe for High Temperature Service," p. 553-557

118. Pitcairn, D.R., "Pipe Replacement Materials, Issues and Lessons Learned," Nutech Engineers, San Jose, California, Aug.(1984).

119. Owczarski, W.A., Duvall, D.S. and Sullivan, C.P., "A Model for Heat-Affected Zone Cracking in Nickel-Base Superalloys," Welding Journal, 45(4), p. 145s-155s, (1966).

120. Puzak, P.P. and Rischall, H., "Further Studies on Stainless Steel Hot Cracking," Welding Journal, 36(2), p. 57s-61s, (1957).

121. Capeletti, T.L., Jackman, L.A. and Childs, W.J., "Elevated Temperature Toughness and a Dimensionless Parameter Involving the Zero-Ductility Temperature," Welding Journal, 51(12), p. 602s-605s, (1972).

122. Duvall, D.S. and Owczarski, W.A., "Heat Treatments for Improving the Weldability and Formability of Udimet 700," Welding Journal, 50(9), p. 401s-409s, (1971).

123. Macpherson, B.M., "Effect of Minor Elements on the Weldability of High-Nickel Alloys," Proceedings of a Symposium Sponsored by WRC, Houston, Texas, Oct.(1967).

124. Sumitomo Steel Corporation, Private Communication, July (1986).

125. Avery, H.S. and Gerkin, J.M., "Experience with Standardizing Gleeble Controlled Hot Tensile Tests," WRC High-Alloy Committee, (1975).

126. Savage, W.F. and Lundin, C.D., "The Varestraint Test," Welding Journal, 44(10), p. 433s-442s, (1965).

127. Kammer, P.A., Masubuchi, K. and Monroe, R.E., "Cracking in High-Strength Steel Weldments - A Critical Review," DMIC Report 197, Feb. (1964).

128. Lundin, C.D., Delong, W.T. and Spond, D.F., "The Fissure Bend Test," Welding Journal, 55(6), p. 145s-151s, (1976).

129. Borland, J.C., "Cracking Tests for Assessing Weldability," British Welding Journal, (10), p. 623-637, (1960).

130. Wilken, K. and Schonherr, W., "Description of Four Hot Cracking Tests Without Self-Restraint," Welding in the World, 13(9/10), (1975).

131. van Lent, P.H. and Masetti, F., "Report of the Collaborative Program on Hot Cracking Tests," I.I.W. Doc.II-752-75, (1975).

132. The Japanese Welding Engineering Society, "Hot Cracking Susceptibility Evaluation of Austenitic Stainless Steel Weld Metals," I.I.W. Doc. IX-1395-86, (1986).

133. Boudreau, J.S., "A Weld Cracking Susceptibility Test for Sheet Materials," Welding Journal, 35(4), p. 164s-168s, Discussion p. 498s-500s, (1956).

134. Brockhurst, P.J. and Muir, H., "Hot Cracking of Welds," Welding Design and Fabrication, 9(1), p. 80-86, (1965).

135. Matsuda, F. and Nakata, K., "A New Test Specimen for Self-Restraint Solidification Crack Susceptibility Test of Electron-Beam Welding Bead : Fan-Shaped Cracking Test," Transactions of JWRI, 11(2), p. 87-94, (1982).

136. Savage, W.F. and Lundin, C.D., "Application of the Varestraint Technique to the Study of Weldability," Welding Journal, 45(11), p. 497s-503s, (1966).

137. Lundin, C.D., Lingenfelter, A.C., Grotke, G.E., Lessman, G.G. and Matthews, S.J., "The Varestraint Test," Welding Research Council Bulletin, No. 280, August (1982).

138. Savage, W.F. and Lundin, C.D., "The Evaluation of the Weldability of Structural Alloys with The Varestraint Test," Technical Report AFML-TR-68-48, July (1968).

139. Grotke, G.E., "Varestraint Weldability Testing of A508 Class 2 and A533 Grade B, Class 1 Pressure-Vessel Steels," Research Report 73-1D4-WELST-R1, Westinghouse Research Laboratories, Feb. (1973).

140. Kihara, H. and Matsuda, F., "Varestraint Test for Hot Crack Susceptibility of HY-Type High Strength Steels," Transactions of JWRI, 2(2), p.83-94, (1973).

141. Cieslak. M.J. and Savage, W.F., "Hot Cracking Studies of Alloy CN-7M," Welding Journal, 64(5), p. 119s-126s, (1985).

142. Dickinson, D.W., "Republic Steel Integrated Varestraint - Tig-A-MaJig Testing Procedures," PR-12, 055-76-1, Republic Steel Research Center, Mar. (1976).

143. Mckeown, D., "Versatile Weld Metal Cracking Tests," Metal Construction and British Welding Journal, 2(8), p. 351-352, (1970).

144. Bailey, N. and Refelous, G.R., "Recent Developments in Transvarestraint Testing," The Welding Institute Research Bulletin, (8), p. 201-204, (1976).

145. Farrar, C.M. and Garland, J.G., "Developments in the Transvarestraint Test for Solidification Crack Susceptibility of Weld Metals," The Welding Institute Research Bulletin, M/77/73, (12), p. 1-11. (1973).

146. Senda, T., Matsuda, F., Takano, G., Watanabe, K., Kobayashi, T. and Matsuzaka, T., "Fundamental Investigations on Solidification Crack Susceptibility for Weld Metals with Trans-Varestraint Test," Transactions of JWS, 2(2), p. 41-61, (1971).

147. Morris, G.J., "Solidification Cracking in Thick-Walled Tubular Welds and Application of the Modified Transvarestraint Test," Australian Welding Journal, p. 9-13, Summer (1981).

148. Dixon, B.F., Phillips, R.H. and Ritter, J.C., "Cracking in the Varestraint Test : Part I - A New Procedure for Assessment of Cracking," Metal Construction, (2), p.86-90, (1984).

149. Kujanpaa, V., Suutala, N., Takalo, T. and Moisio, T., "Correlation Between Solidification Cracking and Microstructure in Austenitic and Austenitic-Ferritic Stainless Steel Welds," Welding Research International, 9(2), p. 55-73, (1979).

150. Arata, Y., Matsuda, F. and Saruwatari, S., "Varestraint Test for Solidification Crack susceptibility in Weld Metal of Austenitic Stainless Steels," Transactions of JWRI, 3(1), P.2-11, (1974).

151. Turner, P.W. and Lundin, C.D., "Effect of Iron on the Hot Cracking of Uranium Weld Metal - Part I," Welding Journal, 49(12) p. 579s-587s, (1970).

152. Matthews, S.J., "Weldability Studies on High Performance Alloys in Thin Sheet Form," Welding Journal, 54(9), p. 281s-287s, (1975).

153. Lessmann, G.G. and Gold, R.E., "The Varestraint Test for Refractory Metals," Welding Journal, 50(1), p. 1s-8s, (1971).

154. Lingenfelter, A.C., "Varestraint Testing of Nickel Alloys," Welding Journal, 51(9), p. 430s-436s, (1972).

155. Leclou, A. and Soulat, P., "Methods Developed to Determine the Tendency for Different Types of Weld Cracking in Austenitic Stainless Steels," BNWL-TR-89, Battelle Northwest Laboratories, Sept. (1973).

156. Thompson, R.E., "A Study of Hot Cracking in Welded High Strength Steels Using the Varestraint Test," MEL R&D Phase Report 13/67, U.S. Navy Marine Engineering Laboratory, Mar. (1967).

157. Dixon, B.F., Phillips, R.H., Malmgren, C.O. and Ritter, J.C., "Cracking in the Transvarestraint Test: Part 2 The Pattern of Solidification Cracking," Metal Construction, (3), p. 154-160, (1984).

158. Dixon, B., "Tests for Weld Metal Solidification Cracking - A Review," Australian Welding Journal, p. 16-21, Summer (1983).

159. Rabensteiner, G. and Tosch, J., "The Metallurgy of Welding Fully Austenitic CrNiMo Stainless Steels - An Update," Welding Journal, 64(4), p. 33-38, (1985).

160. Matsuda, F., Nakagawa, H., Ogata, S. and Katayama, S., "Fractographic Investigation on Solidification Crack in the Varestraint test of Fully Austenitic stainless steel; Studies on Fractography of Welded Zone," Transactions of JWRI, 7(1), p.60-70, (1978).

161. Goodwin, G.M., "The Effect of Minor Elements on the Hot Cracking Tendencies of Inconel 600," Ph.D. Dissertation RPI, (1968).

162. Miura, M., "Weldability of Austenitic Stainless Steel Tubes," Journal of Sumitomo Metal, 34(1), (1981).

163. Lundin, C.D., Chou, C.P.D. and Sullivan, C.J., "Hot Cracking Resistance of Austenitic Stainless Steel Weld Metals," Welding Journal, 59(8). p. 226s-232s, (1980).

164. Bruhl, F. and Zschau, M., "Fabrication of Components Manufactured in the Material: TP 316(NG) for Nuclear Power Plants," Technical Report of Mannesmann, Anlagenbau, West Germany, (1986).

165. Chou, C.P.D., Private communication, Dept. of Mechanical Engineering, National Chiao Tung University, Hsinchu, Taiwan, R.O.C., April (1986).

166. Lundin, C.D., Lee, C.H., Osorio, V. and Menon, R., "Weldability of Nuclear Grade Stainless Steels," Final Report, Tennessee Valley Authority Contract No.TV 64853A, September (1986)..

167. Yamaguchi, S., Kurosawa, F. and Abe, S.,"Hot Ductility and Grainboundary Precipitates in Austenitic Stainless Steels", Industrial Heating, Vol. LIII, No.9, p. 54, September (1986).

168. Saeki, M., Kurosawa, F. and Matsuo, M., "Micro and State Analysis as the Basis for Microalloying Techniques", Transactions ISU, Vol.26, p. 1017-1035, May (1986).

169. Kurosawa, F., Taguchi, I. and Matsumoto, R., Journal of Japanese Ins. Metals, Vol.43, p. 1068, (1979).

170. Cliff, G. and Lorimer, G.W., "Quantitative Analysis of Thin Metal Foils Using EMMA-4, the Ratio Technique", Proc. 5th European Conf. on Electron Microscopy, Manchester, Institute of Physics (London) p. 140-141, (1972).

171. Atteridge, D.G., Bruemmer, S.M. and Page, R.E., "Evaluation and Acceptance of Welded and Repair-Welded Stainless Steel for LWR Service", NUREG/CR-3613, PNL-4941, Annual Report, (1983).

172. Atteridge, D.G., Bruemmer, S.M. and Page, R.E., "Evaluation of Welded and Repair-Welded Stainless Steel for LWR Service", NUREG/CR-3613, PNL-4941, Annual Report, (1984).

173. Atteridge, D.G., Bruemmer, S.M. and Page, R.E., "Evaluation of Welded and Repair-Welded Stainless Steel for LWR Service", NUREG/CR-3613, PNL-4941, Semi-Annual Report, (1985).

174. Tegart, W.J.McG., "The Role of Ductility in Hot Working", p. 133-177, DUCTILITY, ASM, (1967).

175. Reynolds, R.A. and Tegart, W.J.McG., "The Deformation of Some Pure Irons by High-Speed Torsion Over The Temperature Range 700-1250 ^{o}C", Journal of I.S.I, p. 1044-1059, December (1962).

176. White, F.E. and Rossard, C., "A Mechanism For The Fracture of Steel in High-Temperature Torsion and Its Relation to Structural Changes", DEFORMATION UNDER HOT WORKING CONDITIONS, Proceedings, p. 14-20. at Dept. of Met., Univ. of Sheffield, England, July (1966).

177. Keane, D.M., Sellars, C.M. and Tegart, W.J.McG., "High-Temperature Deformation of Iron", DEFORMATION UNDER HOT WORKING CONDITIONS, Proceedings, P.21-28, At Dept. of Met., Univ. of Sheffield, England, July (1966).

178. Luton, M.J. and Sellars, C.M., "Dynamic Recrystallization in Nickel and Nickel-Iron Alloys During High Temperature Deformation", Acta Metallurgica, Vol.17, p. 1033-1043, August (1969).

179. McQueen, H.J., "Metallography and the Mechanisms Related to Hot Working of Metals", MICROSTRUCTURAL SCIENCE, Vol. 7, Proc. 11th Annual Technical Meeting of the International Metallographic Society, p. 71-86, (1979).

180. King, B.L., "Weld Metal and Heat Affected Zone Hot Cracking in Wrought Austenitic Stainless Steels", BWRA Report, C139/A/2/65, February (1966).

181. Honeycombe, J. and Gooch, T.G., "Effects of Microcracks on Mechanical Properties of Austenitic Stainless-Steel Weld-Metals", Metal Construction and British Welding Journal, p. 46-53, April (1973).

182. Honeycombe, J. and Gooch, T.G., "Microcracking in Fully Austenitic Stainless Steel Weld Metal", BWRA Report, M39/3/69, February (1970).

183. Honeycombe, J. and Gooch, T.G., "Microcracking in Fully Austenitic Stainless Steel Weld Metal", Metal Construction and British Welding Journal, p. 375-380, September (1970).

184. Rhines, F.N. and Wray, P.J., Transactions ASM, Vol. 54, p. 117-128, (1961).

185. Dieter, G.E., Mullin, J.V. and Shapiro, E., "Fracture of Inconel Under Conditions of Hot Cracking", DEFORMATION UNDER HOT WORKING CONDITIONS, Proceedings, p. 7-13, at Dept. of Met., Univ. of Sheffield, England, July (1966).

186. Hammar, O. and Svensson, U., "Influence of Steel Composition on Segregation and Microstructure During Solidification of Austenitic Stainless Steels", SOLIDIFICATION AND CASTING OF METALS, Proceedings, p. 401-410, The Metals Society, London, England, (1979).

187. Katayama, S. Private Communication, Japanese Welding Research Institute, Osaka, Japan (1988).

188. Lundin, C.D., Lee, C.H. and Qiao, P., "Comparative Evaluation of Four Hot Cracking Test Methods (Varestraint, Sigmajig, Finger and Dummy Weld Test)", Unpublished research, University of Tennessee, Knoxville, (1988).

189. Kujanpaa, V.P., David, S.A. and White, C.L., "Formation of Hot Cracks in Austenitic Stainless Steel Welds - Solidification Cracking", Welding Journal, 65(8), p. 203s-212s, (1986).

190. Brooks, J.A., Thompson, A.W. and Williams, J.C., "Weld Cracking of Austenitic Stainless Steels - Effects of Impurities and Minor Elements", PHYSICAL METALLURGY OF METAL JOINING, Edited by Kossowsky, R. and Glicksman, M.E., The Metallurgical Society of AIME, (1980).

191. Nelson, D.E., Baeslack III, W.A. and Lippold, J.C., "An Investigation of Weld Hot Cracking in Duplex Stainless Steels", Welding Journal, 66(8), p. 241s-250s, (1987).

192. Lippold, J.C., "An Investigation of Heat-Affected Zone Hot CRacking in Alloy 800", Welding Journal, 62(1), p. 1s-11s, (1983).

193. Matsuda, F., Nakagawa, H., Ogata, S and Katayama, S., "Fractographic Investigation on Solidification Crack in the Varestraint Test of Fully Austenitic Stainless Steel", Transactions of JWRI, 7(1), p. 59-70, (1978).

194. Baeslack III, W.A., Lata, W.P. and West, S.L., "A Study of Heat-Affected Zone and Weld Metal Liquation Cracking in Alloy 903", Welding Journal, 67(4), p. 77s-87s, (1988).

195. Lundin, C.D. and Chou, C.P.D., "Fissuring in the "Hazard HAZ" Region of Austenitic Stainless Steel Welds", Welding Journal, 64(4), p. 113s-118s, (1985).

196. Tamura, H. and Watanabe, T., "Mechanism of Liquation Cracking in weld Heat-Affected Zone of Austenitic Stainless Steels", Transactions of JWS, 4(1), p. 30-42, April (1973).

197. Kawasaki, T., Takada, I., Ohtsubo, H. and Suzuki, S., "Hot Workability of Austenitic Stainless Steels Containing Delta-Ferrite", Kawasaki Steel Technical Report, No. 14, p. 50-60, March (1986).

198. Kakhovskii, N.I., "Effects of Silicon, Nitrogen and Manganese on Chemical Heterogeneity in Type OKh23N28M3D3T Weld Metals and Their Resistance to Hot Cracking", Avt. Svarka, No. 8, p. 11-14, (1971).

199. Zhitnikov, N.P., "The Hot Cracking Resistance of Austenitic CrNi Weld Metal and Weld Zone in Relation to Nitrogen", Svar. Proiz, No. 3, p. 14-16, (1981).

200. Zhitnikov, N.P. and Zaks I.A., "Influence of Nitrogen on austenitic Weld Metal Structures", Svar. Proiz, No.8, p. 5-7, (1971).

201. Prosvirin, V.I., "The Effect of Nitrogen on The Phase Composition and Properties of a CrNiMo Austenitic Steels", Problems of the Physical Metallurgy of Austenitic Steels, Book No. 52, Moscow, Mashgiz, (1952).

202. Zabolotskii, V.M., "The Mechanism of Formation of Solidification Cracks in the Welding of Metals", Welding, No. 12, Leningrad, Sudostroenie, (1969).

203. Mundt, R. and Hoffmeister, H., "Effect of Chemical Composition and Weld Thermal Cycles on Phase Transformation and Microstructures of Ferritic-Austenitic Steels", Stainless Steel '84, Proceedings, Goteborg, Sweden, September (1984), p. 315-322, Institute of Metals, London.

204. Hoffmeister, H. and Mundt, R., "Investigation of the Effects of Carbon and Nitrogen and the Welding Conditions on the Structure of the Weld Metal in High-Alloy ferritic Austenitic NiCr Steels", Schweissen und Schneiden, Translation 11/1981, P. E198-E200.

205. Medovar, B.I., "The Welding of High Temperature Steels and Alloys", Mashinostroenie, Moscow, (1966).

206. Wilson, W.G., Kay, D.A.R. and Vahed, A., "The Use of Thermodynamics and Phase Equilibria To Predict The Behavior of the rare Earth Elements in Steel", Proceedings of 103rd TMS-AIME Annual Meeting, p. 132-140. Dallas, Texas, February (1974).

207. Wilson, W.G. et al., "The Use of Thermodynamics and Phase diagrams to Predict the Behavior of Rare Earths in Steel", Journal of Metals, p. 14-23, May (1974).

208. Likhanosov, V.N. and Sytnik, N.M., "Special Features of the Inoculation of Iron With Rare Earth Metal Oxides in Arc Welding Using Cored Wire", Automatic Welding, p. 42-44, May (1985).

209. Wilson, W.G. and Mclean, A., DESULFURIZATION OF IRON AND STEEL AND SULFIDE SHAPE CONTROL, The Iron and Steel Society of AIME, (1980).

210. Medovar, B.I., Avtom Svarka, Vol. 8, p. 79-90, (1955).

211. Medovar, B.i., Paton Commemoration Volume Mashgiz, p. 150-161, (1956).

212. Kingery, W.D., Bowen, K.H. and Uhlmann, D.R., INTRODUCTION TO CERAMICS, 2nd Edition, p. 177-216, John Wiley & Son Pub., (1976).

213. Reed, J.S., INTRODUCTION TO THE PRINCIPLES OF CERAMIC PROCESSING, p. 17-27, John Wiley & Sons Pub., (1988).

214. Smith, C.S., "Grains, Phases and Interfaces: an Interpretation of Microstructure", Trans. American Institute of Mining and Metallurgical Engineers, Vol. 175, p. 15-51, (1948).

215. Smith, C.S., INTERPHASE INTERFACES. IMPERFECTIONS IN NEARLY PERFECT CRYSTALS, John Wiley & Sons Pub., p. 377-401, (1952).

APPENDIX

PROPOSED METHOD FOR HOT DUCTILITY TESTING (PROCEDURE AND EXPERIMENTAL JUSTIFICATION)

PROPOSED METHOD FOR HOT DUCTILITY TESTING
(PROCEDURE AND EXPERIMENTAL JUSTIFICATION)

INTRODUCTION

To investigate standardization of the hot ductility test methodology, 0.25 inch (6 mm) diameter stainless steel rod stock has been obtained. The material conforms to the 304NG and 316NG specifications currently in use. Type AISI 347 rod stock has also been included for statistical testing and test standardization. Complete chemical analysis and the ferrite potential estimated by the Delong method is given in Table A-1.

Part 1 deals with the statistical evaluation and analysis whereas part 2 provides the suggested procedure for the "hot ductility" testing. The statistical evaluation of the testing parameters includes the following variables;

1 Thermocouple attachment technique; a conventional cross wire technique and separate wire techniques,

2 Thermal cycle including heating and cooling rates,

3 Peak temperature for the on-cooling tests,

4 Cross-head speed (strain rate),

5 Hold time at test temperature and at peak temperature,

6 Reproducibility, the data spread.

For the initial evaluation, tests were conducted on all three materials using the "standard" U.S. parameters. That is; the test

Table A-1. Chemical compositions of materials studied.

Type	Heat No.	C	Mn	P	S	Si	Cr	Ni	Mo	Cu	N_2	Nb	Co	FN[a]
304L	A2719	0.013	1.38	0.029	0.028	0.45	18.3	9.18	0.42	0.35	0.068	-	0.13	2
316L	9A2755	0.012	1.59	0.03	0.03	0.54	17.27	11.68	2.09	0.32	0.071	-	0.11	6
347	A16142	0.05	1.69	0.03	0.002	0.84	17.76	10.68	0.17	0.26	-	0.80	0.05	5

(a) calculated ferrite content according to Delong Method

employs a cylindrical specimen 0.25 inch in diameter and 4-1/4 inches long. The thermal cycle is that for a peak temperature of 2400°F in a 1-1/2 inch thick stainless steel plate welded with an energy input of 70 KJ/in (SMAW). Both on-heating and on-cooling tests were conducted. The on-cooling tests were conducted during the cooling portion of the cycle after exposure to the zero ductility temperature (ZDT) which was determined during the on-heating tests.

1. STATISTICAL ANALYSIS

Figures A-1 to 3 show the Gleeble hot ductility response for the 316L, 304L and 347 materials tested using the U.S. standard parameters. In each figure, the reduction in area is plotted as a function of test temperatures. The on-heating response of all the materials is similar. As the test temperature is raised, ductility is also increased, followed by a rapid loss in ductility over a narrow range of test temperatures. However, the on-cooling behavior shows material-to-material variation. Both 304L and 316L exhibit a ductility dip at approximately 2000 °F on cooling from the ZDT of 2475 °F and 2450 °F respectively. The 316L shows the best ductility recovery which approximates 100% of the on-heating ductility within 100F° of a ZDT (2450 °F). The 304L also shows a relatively good ductility recovery to approximately 70% of the on-heating ductility within 100F° of ZDT (2475 °F). However, AISI 347 reveals virtually no recovery in ductility until the on-cooling test temperature reaches about 2100 °F, 300 F° below the ZDT (2400 °F). The above ductility behavior of the three alloys tested with "standard" U.S. parameters

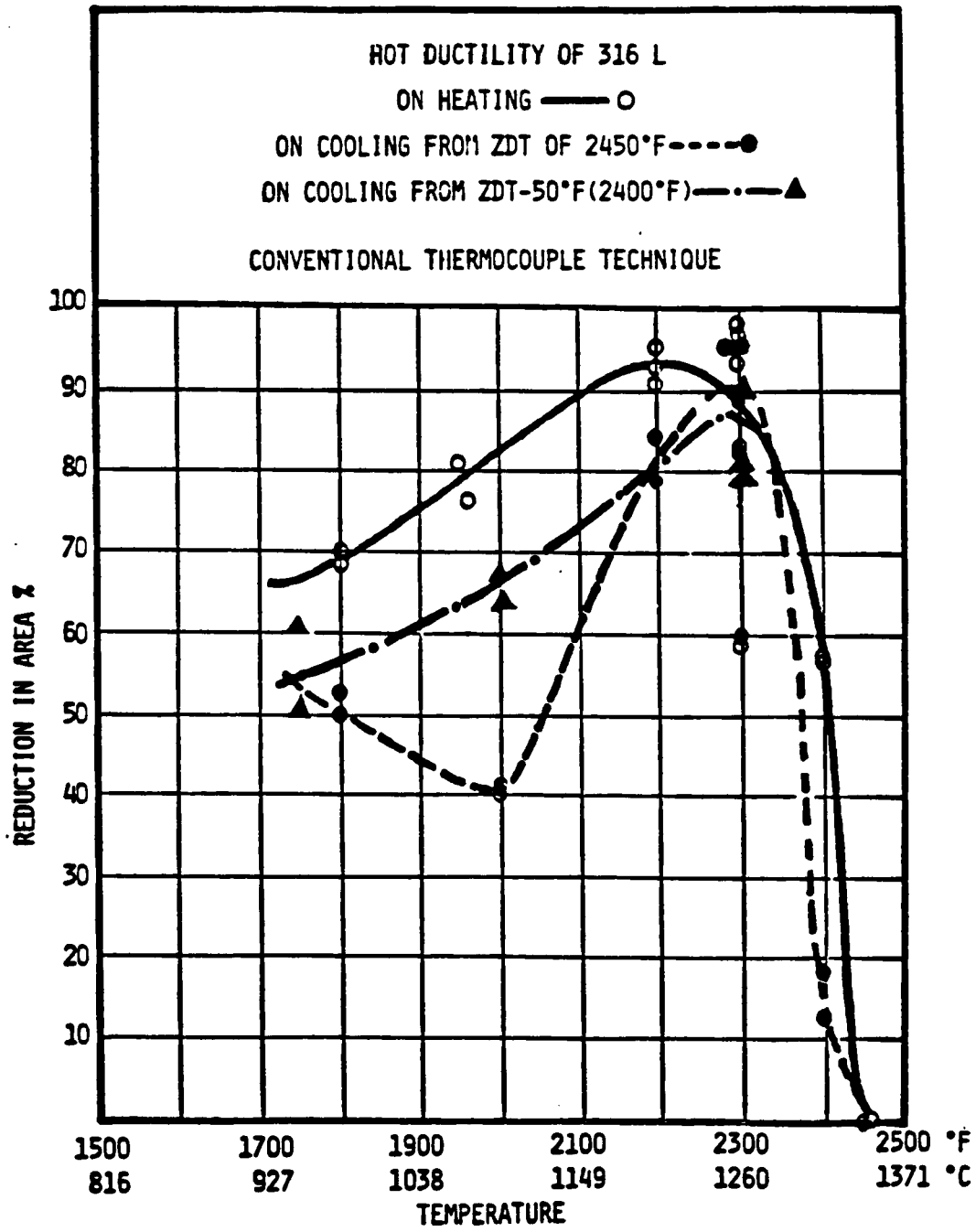


Figure A-1. Hot ductility behavior of 316 L tested with a conventional cross wire thermocouple technique.

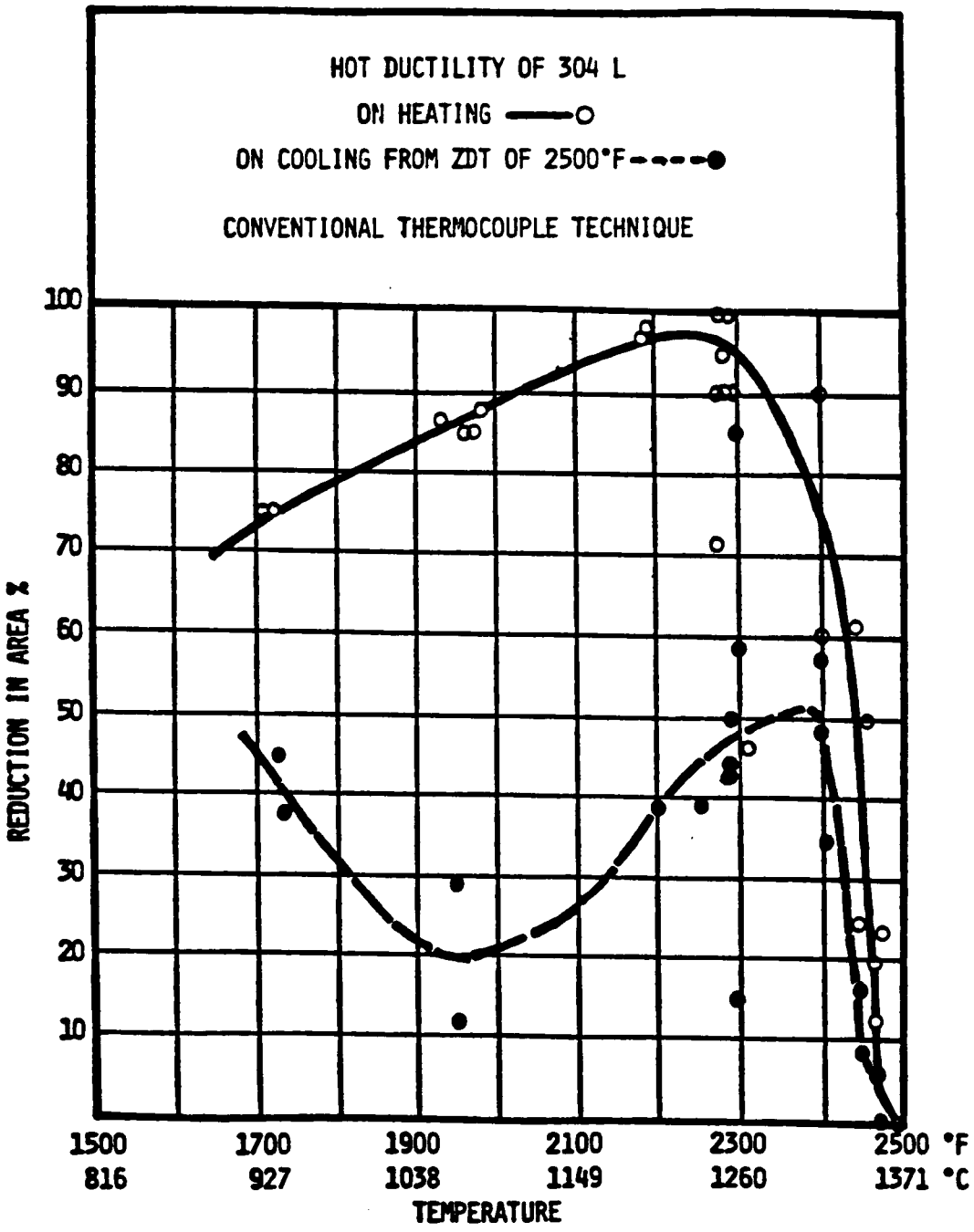


Figure A-2. Hot ductility behavior of 304 L tested with a conventional cross wire thermocouple technique.

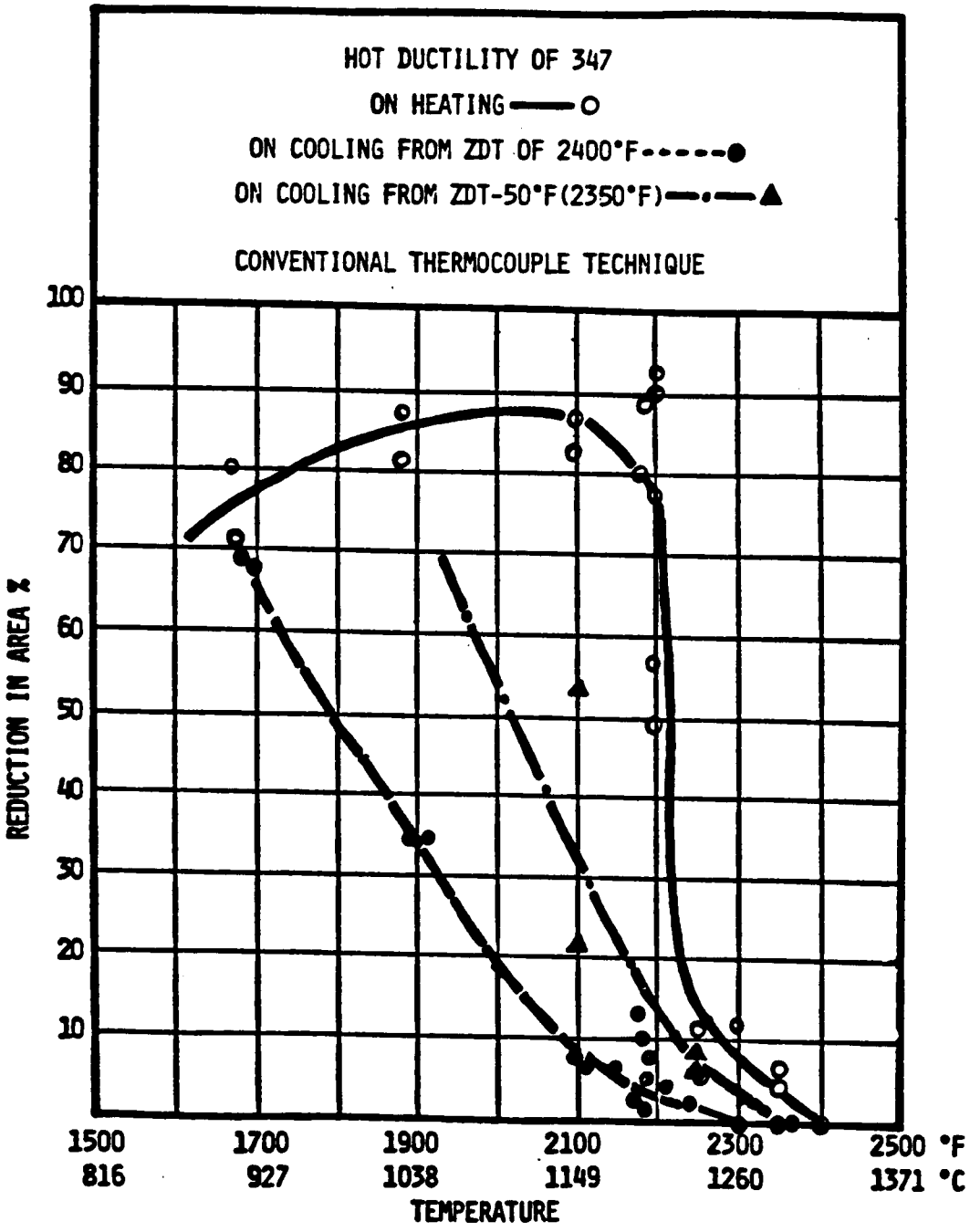


Figure A-3. Hot ductility behavior of 347 tested with a conventional cross wire thermocouple technique.

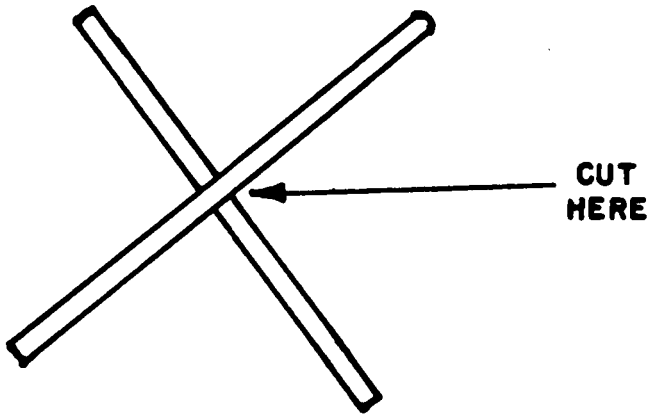
will be compared to that tested with the parameters discussed in the following sections.

a. Thermocouple Attachment Technique

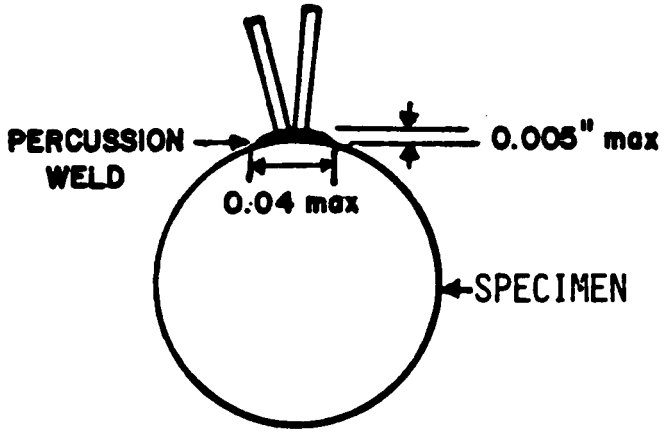
The temperatures are measured and controlled during the tests by means of a chromel-alumel (cross wire) thermocouple percussion welded to the center of the specimen gauge length. During testing, the instantaneous temperature of the specimen is compared with a reference temperature and the current flow is increased, decreased or interrupted as required. However, the temperature measurement and control through the thermocouple (pyrometry) have been recognized as an important source of experimental error, since the hot junction of the thermocouple is subject to air cooling despite its intimate attachment to the surface of specimen. (the hot junction of the thermocouple is usually at or above the surface of the specimen.) Thus, the instantaneous temperature reading can be different from that of sample surface. The conventional cross wire thermocouple method is shown schematically in Figure A-4. A junction is made by resistance welding the wires, then trimming the end with a sharp clipper or other sharp tool as shown in Figure A-4a.

Recently, the Gleeble 1500 has incorporated a new thermocouple attachment method. In this method, the thermocouple wires are individually percussion welded to surface of the specimen in a plane perpendicular to the axis of the specimen. Approximately a 1-2 mm spacing between the wires is recommended. A schematic representation of the separate thermocouple attachment technique is given in Figure

CONVENTIONAL CROSS WIRE THERMOCOUPLE TECHNIQUE



A. CROSS WIRE RESISTANCE WELDING



B. THERMOUPLE ATTACHMENT

Figure A-4. Schematic representation of the conventional thermocouple technique.

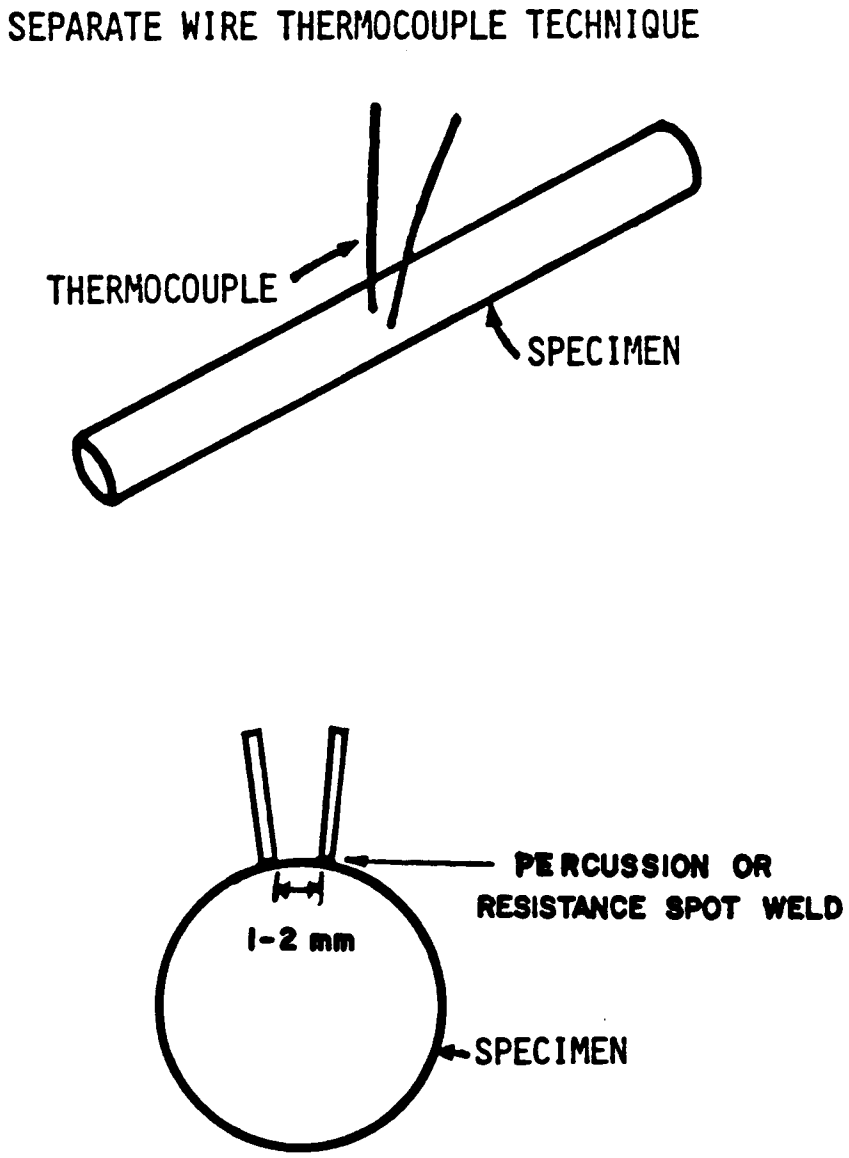


Figure A-5. Schematic representation of the separate wire thermocouple technique.

A-5.(In this study, thermocouples were attached by percussion welding (304L) and resistance spot welding (316L and 347)).

The hot ductility response of the three alloys, tested with the separate thermocouple method using the U.S. standard parameters, is given in Figures A-6 to 8. All three alloys reveal a behavior similar to that when tested with the conventional cross wire thermocouple method. That is, the thermocouple technique does not significantly influence the measurement of the overall ductility response of the materials. However, there is a slight difference in the ZDT of the 316L for the two thermocouple techniques. With the cross wire thermocouple method, 316L has a 2450 ^{o}F (ZDT), but with the separate wire method ZDT is 2475 ^{o}F. The zero strength temperature (ZST) for both methods was identical (2475 ^{o}F). While, in the case of the 304L and 347, the both ZDT and ZST were identical for the two thermocouple techniques.

The statistical analysis of the multiple tests at selected temperatures during on-heating and on-cooling, using both thermocouple methods is given in Tables A-2 and 3. Tables A-2 and A-3 reveal that the actual test temperature is seldom identical to that specified regardless of the thermocouple methods. The greatest 1 (standard deviation) value for all of the test temperatures is approximately in the order of 10^{o}F for both thermocouple methods, which is far less than 1% of the average temperature (coefficient of variation). In terms of the hot ductility variation, again there is no significant difference between methods. The standard deviation ( ) for both techniques is in the range of 10 to 15%.

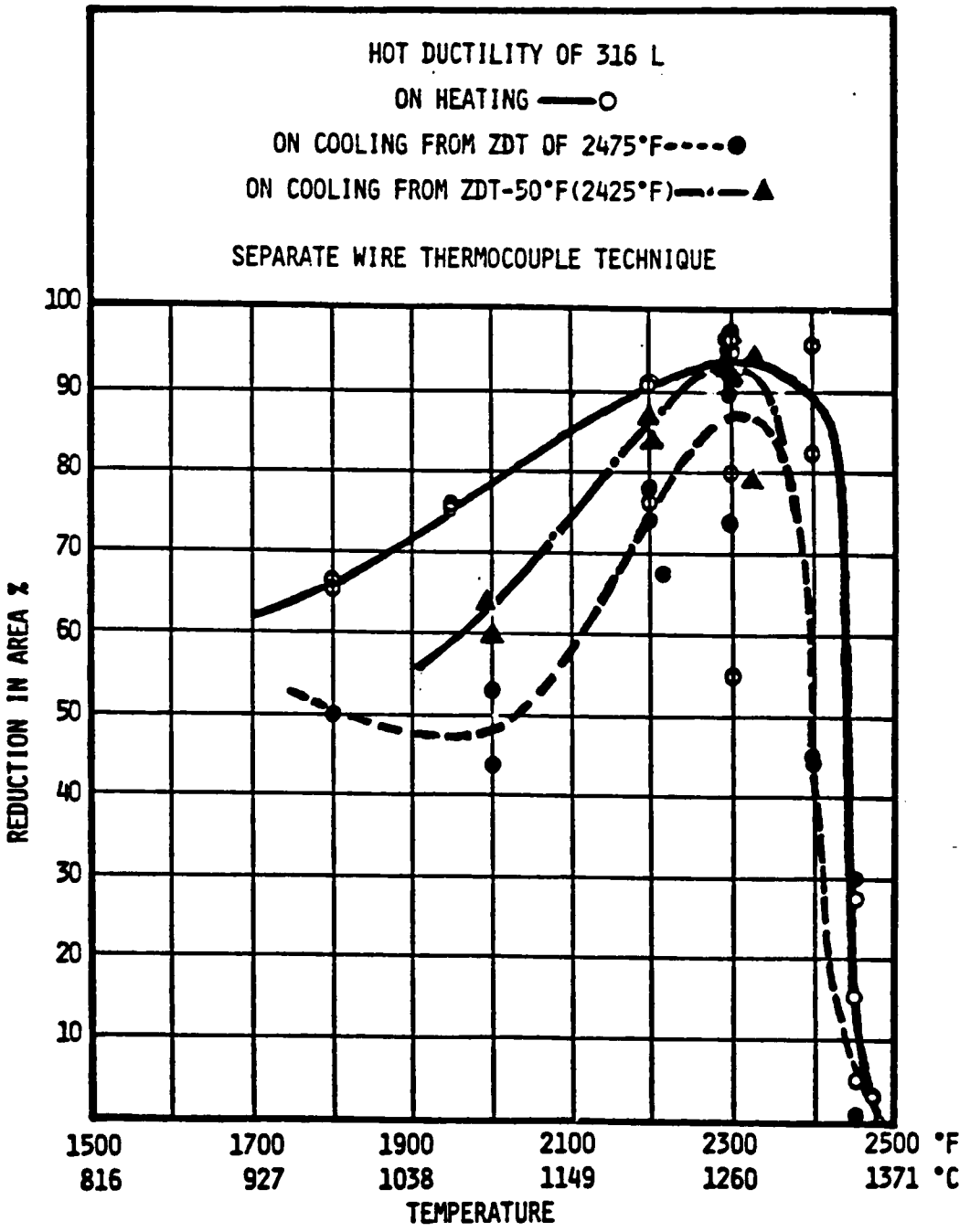


Figure A-6. Hot ductility behavior of 316 L tested with a separate wire thermocouple technique.

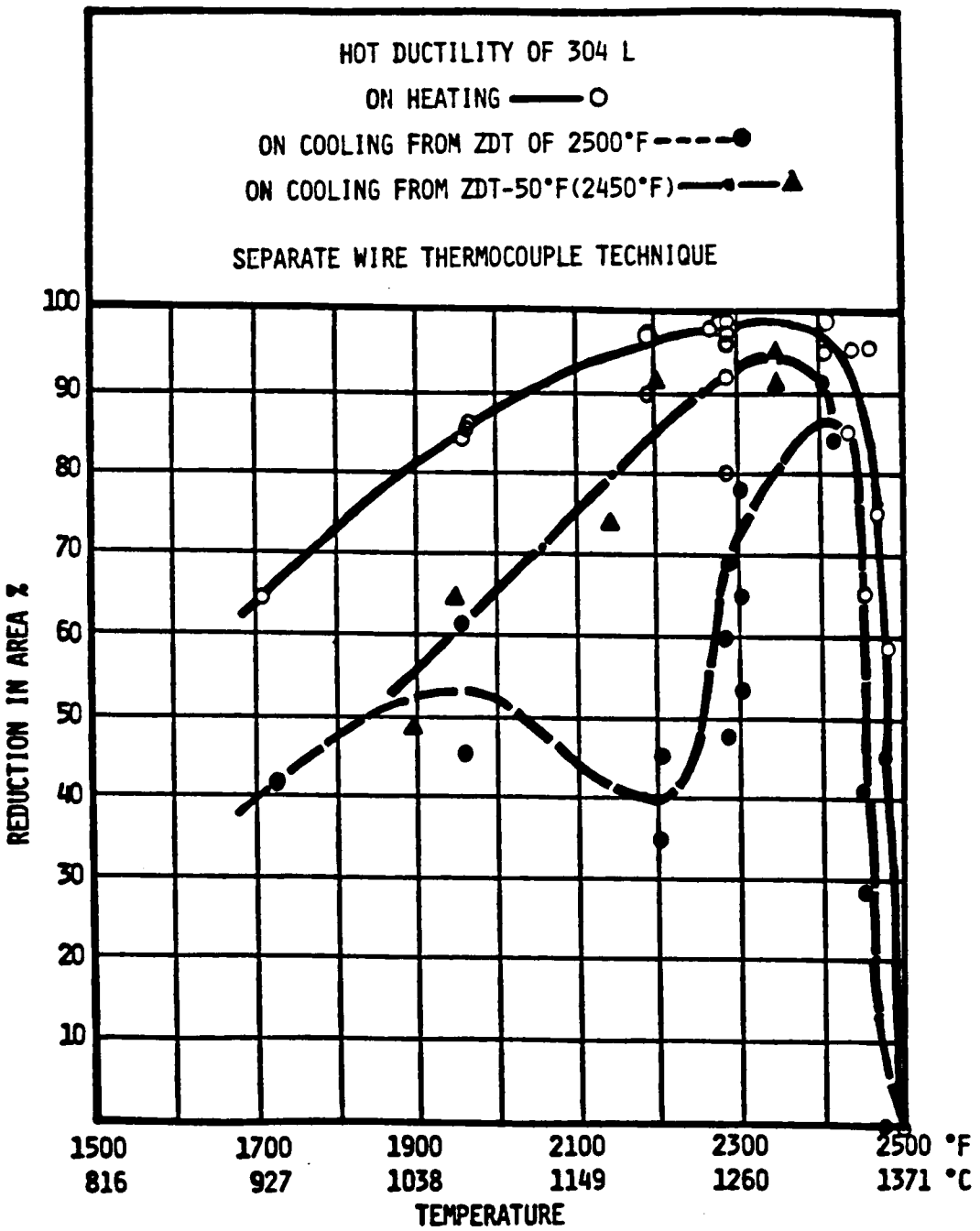


Figure A-7. Hot ductility behavior of 304 L tested with a separate wire thermocouple technique.

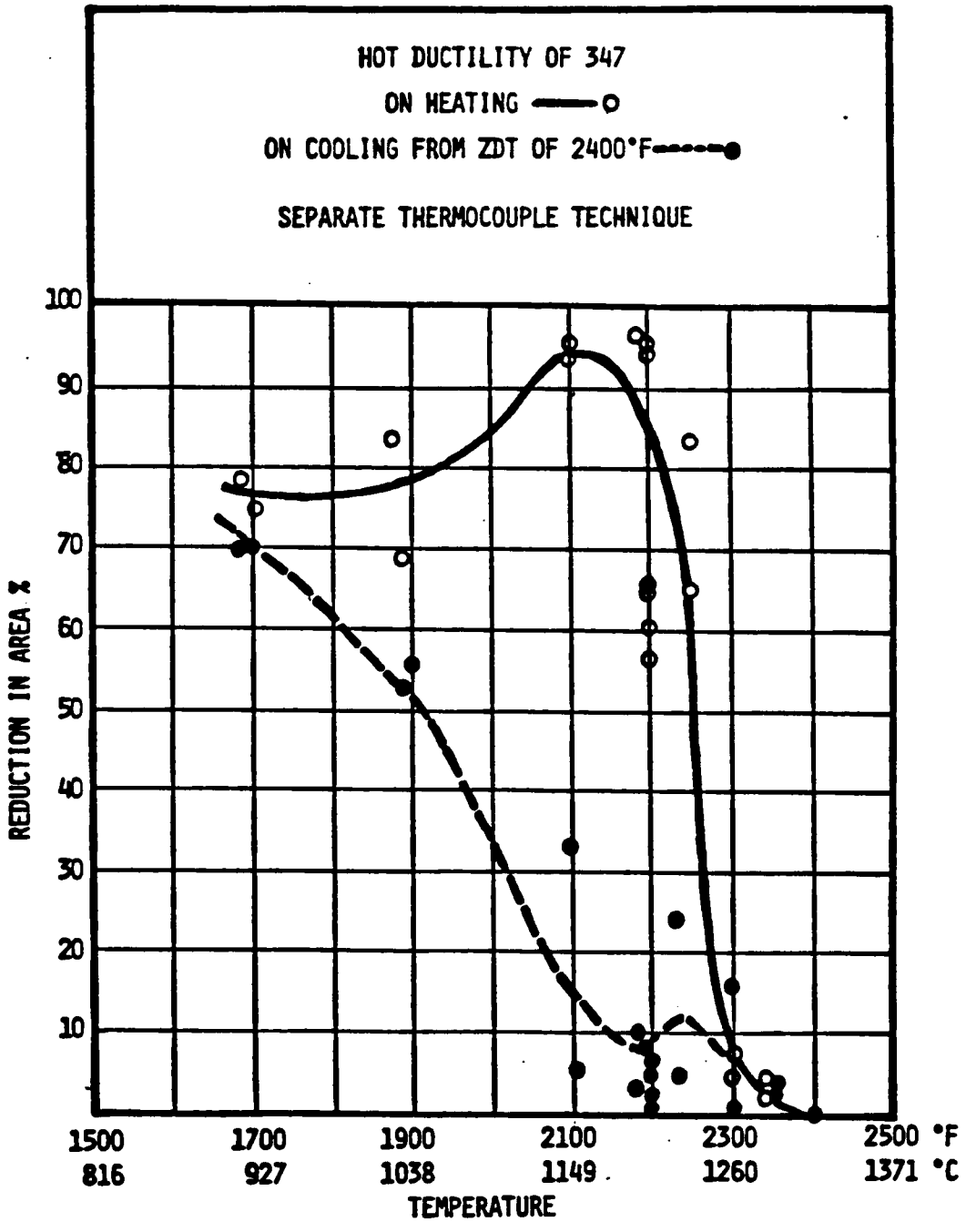


Figure A-8. Hot ductility behavior of 347 tested with a separate wire thermocouple technique.

Table A-2. Statistical analysis of on-heating hot ductility test results.

On-Heating

Material	Test Temperature[a] (°F)	Thermocouple[b] Technique	Number of Tests	Reduction in Area (%)					Strength (psi)					Actual Temperature Variation (°F)[c]				
				Avg.	Range		Std. Deviation[d]	Coeff. Variation[e] (%)	Avg.	Range		Std. Deviation[d]	Coeff. Variation[e] (%)	Avg.	Range		Std. Deviation[d]	Coeff. Variation[e] (%)
					Max	Min				Max	Min				Max	Min		
304L	1975	A	3	86.3	88	85	1.10	1.27	18,700	19,000	17,800	700	3.74	1968	1975	1960	5.67	0.29
		B	3	85.3	86	85	0.63	0.50	18,500	19,000	17,800	900	4.62	1975	1975	1975	0	0
	2300	A	7	90.7	99	72	5.96	6.57	8,600	9,200	7,100	610	7.00	2294	2298	2275	3.29	0.14
		B	7	95.6	99	88	4.90	5.14	9,000	10,000	8,000	370	3.94	2287	2295	2285	7.00	0.31
	2450	A	7	42.6	58	19	10.94	25.68	5,500	6,300	4,500	490	8.91	2446	2460	2430	8.14	0.33
		B	7	76.0	95	58	13.10	17.24	6,100	7,600	5,500	486	7.97	2443	2460	2430	7.57	0.31
316L	2300	A	7	88.0	98	59	9.71	11.04	8,900	10,000	5,300	1900	15.72	2300	2300	2300	0	0
		B	7	88.4	97	95	11.83	13.38	10,000	11,000	10,200	430	3.98	2300	2300	2300	0	0
347	2200	A	7	76.1	91	48	13.34	17.48	11,600	12,600	10,600	710	6.23	2197	2200	2185	4.14	0.19
		B	7	76.9	97	57	15.14	19.69	12,900	14,300	11,500	548	4.21	2199	2200	2195	1.43	0.06

a. Specified temperature
b. Thermocouple attachment technique; A: conventional cross wire technique
B: separate wire technique
c. Actual temperature from record
d. Standard deviation: calculated from the range
e. Coefficient of variation: the standard deviation as percent of the average

Table A-3. Statistical analysis of on-cooling hot ductility test results.

On cooling from ZDT

Material	Test Temperature[a] (°F)	Thermocouple[b] Technique	Number of Tests	Reduction in Area (%)					Strength (psi)					Actual Temperature Variation (°F)[c]				
				Avg.	Range		Std. Deviation[d]	Coeff. Variation[e] (%)	Avg.	Range		Std. Deviation[d]	Coeff. Variation[e] (%)	Avg.	Range		Std. Deviation[d]	Coeff. Variation[e] (%)
					Max	Min				Max	Min				Max	Min		
304L	2300	A	7	47.3	85	15	13.84	29.3	7,000	9,200	4,700	1,700	24.28	2296	2305	2285	5	0.22
		B	7	61.7	78	56	5.96	9.66	8,100	8,800	7,600	400	4.94	2295	2300	2285	5	0.22
	2450	A	7	8.7	23	2	6.16	70.80	2,700	4,700	1,000	1,200	44.44	2446	2450	2435	6.29	0.18
		B	7	35.1	41	23	9.41	26.81	5,500	8,000	3,900	900	16.36	2441	2445	2440	1.43	0.06
316L	2300	A	7	87.1	95	80	5.53	10.94	8,500	9,000	8,000	300	3.16	2300	2300	2300	0	0
		B	5	88.2	93	76	10.80	12.24	10,400	11,400	8,200	800	7.60	2300	2300	2300	0	0
347	2300	A	7	6.7	18	2	2.86	42.69	7,200	8,600	6,500	800	11.11	2186	2215	2175	10.20	0.47
		B	7	6.4	10	1	2.77	62.95	8,100	9,000	7,300	500	5.10	2196	2200	2190	3.57	0.16

a. Specified temperature
b. Thermocouple attachment technique; A: conventional cross wire technique
B: separate wire technique
c. Actual temperature from record
d. Standard deviation: calculated from the range
e. Coefficient of variation: the standard deviation as percent of the average

Therefore, the above statistical analysis of the multiple hot ductility tests reveals that both thermocouple methods can be used successfully. Simply, the conventional cross wire method requires more caution in making the cross wire resistance weld and trimming the junction prior to percussion welding.

b. Thermal Cycle

The thermal cycle that has been used for the hot ductility test in the U.S. is that representative of the heat affected zone just outside of the fusion zone in a weld made with an energy input of 70KJ/in. in 1-1/2 inch thick stainless steel plate (which gives a heating rate of approximately 240 F^{o}/sec and a cooling rate of 80 F^{o}/sec.) However, as pointed out in the technical literature review, many laboratories in Europe and Japan have used different thermal cycles for Gleeble (and other equipment) hot ductility testing. Therefore, in this standardization study, three different heating and cooling rates have been evaluated.

For simplicity, a linear heating and cooling cycle was utilized only with the 304L material. The heating rates investigated were 446 F^{o}/sec, 223 F^{o}/sec and 112 F^{o}/sec (which are equivalent to 5, 10 and 20 second heating times from room temperature to the 2300 ^{o}F of test temperature). The cooling rates, after exposure to the ZDT (ZST) of 2500 ^{o}F, were 200 F^{o}/sec, 40 F^{o}/sec and 20 F^{o}/sec (which are 1,5 and 10 second cooling times from the peak temperature (2500 ^{o}F) to the 2300 ^{o}F test temperature). The heating rate for the on-cooling tests was 223 F^{o}/sec.

The effect of the heating and cooling rates on the on-heating and on-cooling ductility of 304L is given in Table A-4. Table A-4 indicates that the on-heating and on-cooling hot ductility responses do not vary significantly as a function of the heating and cooling rates studied. The maximum variation in ductility is about 5% for the three heating rates and is about 20% for the different cooling rates, (a slightly higher sensitivity to cooling rates). When compared to the results obtained with the U.S. standard thermal cycle (240 F^{o}/sec heating rate and 80 F^{o}/sec cooling rate), the on-heating response is similar. The on-cooling ductility did not indicate any particular trend as the cooling rate was varied. Therefore, it can be noted that even for a particular heating and cooling rate, in the range evaluated in this study, the results do not yield significant variation in hot ductility. However, the heating and cooling rates may exert an influence on the hot ductility response of AISI 347 which has been known to be susceptible to constitutional liquation of the niobium carbide, a phenomenon which is sensitive to the heating rate.

For the direct comparison of the results from different laboratories, it is considered necessary to specify a standard thermal cycle. The thermal cycle should be representative of the heat affected zone of a weld to be most relevant. The thermal cycle should also be representative of the region near the peak temperature of the zero ductility range(in which the majority of the HAZ cracking occurs).

Table A-4. Effects of heating and cooling rates on hot ductility.

	On Heating								
	1	2	average	1	2	average	1	2	average
Heating rate (F°/sec)	446	446	446	223	223	223	112	112	112
RA (%)	98	99	98.5	99	99	99	86	99	92.5
Temperature (°F)	2,300	2,300	2,300	2,300	2,300	2,300	2,300	2,310	2,305
Strength (psi)	9,800	9,400	9,600	9,400	9,800	9,600	9,600	9,000	9,300

	On Cooling								
	1	2	average	1	2	average	1	2	average
Cooling rate (F°/sec)	200	200	200	40	40	40	20	20	20
RA (%)	96	98	97	88	68	78	89	95	92
Temperature (°F)	2,300	2,300	2,300	2,300	2,300	2,300	2,300	2,300	2,300
Strength (psi)	9,800	9,800	9,800	10,600	9,000	9,800	9,800	10,600	10,200

c. Peak Temperature For The On-Cooling Testing

Since the Gleeble has been utilized to assess the hot cracking susceptibility of stainless steel and other alloys, approximately four different peak temperatures have been used, for the on-cooling tests; an arbitrary temperature of 2400 ^{o}F, a 50 F^{o} below the ZDT, a ZST and most extensively a ZDT.

As discussed earlier, the use of an arbitrary peak temperature of 2400 ^{o}F is not discriminating, in that it will only reveal very poor material from the hot ductility standpoint. The most critical region of the HAZ, the zero ductility region, is not evaluated and this is the region where the hot cracking potential is greatest. Further, depending upon types of material and/or heats of the same nominal composition, a peak temperature of 2400 ^{o}F may be within or far below the zero ductility range. Thus, discrimination between different types of material and heats of the same nominal composition is arbitrary.

Another frequently used peak temperature is the "50 F^{o} below zero ductility temperature", which is required by ASTM specification A430. This is not as arbitrary as a peak temperature of 2400 ^{o}F, but it still represents a region generally outside the critical zero ductility region. The on-cooling tests from a peak temperature of the ZDT-50F^{o} for 304L, 316L and 347 alloys, together with those tested from the respective ZDT's, are compared in Figures A-1, -3, -6 and -7. These figures clearly indicate that selection of the peak temperature for the on-cooling tests is critical to hot ductility response. The hot ductility on cooling from the ZDT-50F^{o} shows a better recovery

when compared to that determined on cooling from the ZDT. For the 304L and 316L materials (Figures A-1, -6 and -7), the on-cooling ductility recovers to more than 90% within 50 F^{o} of the peak temperature when tested on cooling from the ZDT-50 F^{o}. In the case of 347 (Figure A-3), the on-cooling ductility shows a poor recovery from the ZDT-50 F^{o} as compared to 304L and 316L. However, when compared with the recovery when tested from the ZDT, ductility recovery is better than when tested from a 50 F^{o} below the ZDT, revealing again the importance of the peak temperature for the on-cooling tests.

The zero strength temperature has also been extensively used by many investigators, and it has been shown that the use of ZST for the on-cooling tests provides better discrimination than from the ZDT. However, as shown before, in many cases, the zero ductility temperature and zero strength temperature are virtually identical and when they are different, the difference is usually less than about 50 F^{o} (on-heating tests are conducted at 25 ^{o}F intervals within 100 F^{o} of the zero ductility temperature). If the testing intervals near the ZDT are greater than 25 ^{o}F, a difference of more than 50 F^{o} is occasionally found. Unfortunately, determination of the ZST is sometimes extremely difficult, because of the small fracture strength (load) (minor difference between ZDT and ZST load) and the day-by-day variation in the inertia and friction load of the system (which has to be subtracted from the measured load). Usually, for well lubricated loading systems, the friction and inertia load for a crosshead speed of 2.5 in/sec is in the order of 100 - 200Lb. (depending on type of test equipment). Further, the friction load may change by $\pm$ 50Lb

during a testing session or day by day if the loading system is not properly lubricated before each use. Thus it is difficult to discriminate between ZDT and ZST.

However, in cases where the ZDT and ZST are easily discriminated and decidedly different (50 F^{o}), tests should be conducted on cooling from both temperatures.

d. Cross-Head Speed (Strain Rate)

Crosshead speed is a variable related to the necessity to conduct the test at constant temperature. Therefore, it has been considered that the crosshead speed must be rapid because of the rapid change in temperature upon heating and cooling in a weld thermal cycle because specimen loading should occur as soon as the test temperature is reached and fracture should ensure at the beginning of the crosshead travel. In some systems the crosshead speed may be a function of specimen breaking strength. In such cases the crosshead speed should be set for low load (high temperature condition) since this test region is most critical. As noted below the strain rate does not significantly affect ductility.

In order to determine the sensitivity of the hot ductility response to variation in crosshead speed, three crosshead speeds, 0.5, 2.5 and 5 in/sec, have been evaluated. Tests were conducted on heating at 2300 ^{o}F (304L and 316L) and 2200 ^{o}F (347) using the U.S. parameters (except crosshead speed which was varied). To maintain the specimen at a constant temperature during the duration of the test (especially 0.5 in/sec low speed), the temperature was held constant. Test results for the three alloys are given in Figure A-9, where the

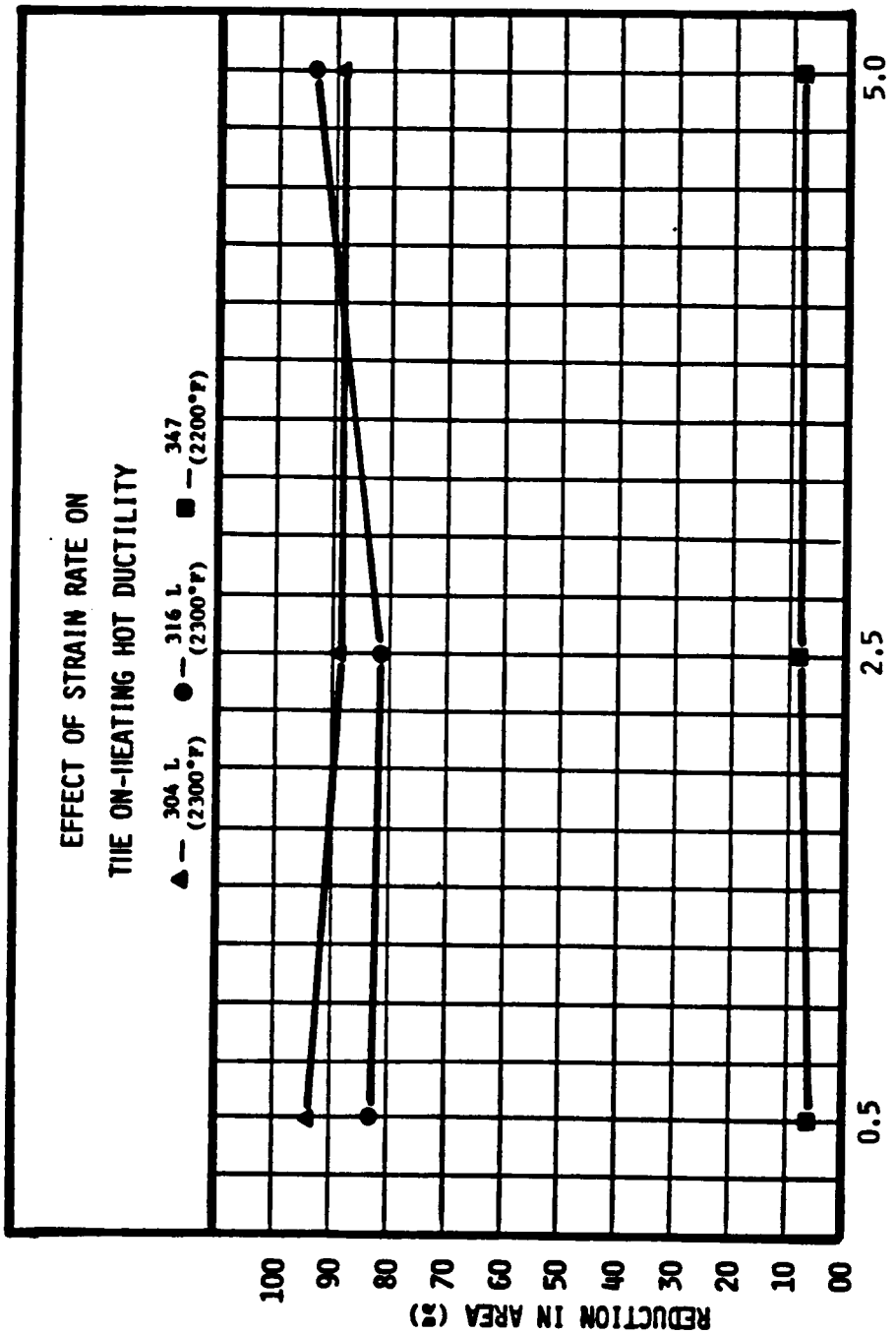


Figure A-9. Effect of the strain rate(crosshead speed) on the on-heating hot ductility.

ductility at a given temperature is plotted as a function of crosshead speed. The ductility response does not appear to be significantly affected by a change in the crosshead speed. The maximum variation in ductility for the range of the crosshead speeds studied is approximately 15% which is well within the test reproducibility as discussed earlier. However, as will be noted later for the slower crosshead speeds, the effect of hold time at test temperature has to be considered.

e. Hold Time

As in the case of the crosshead speed, a hold time at test temperatures and/or at peak temperature for the on-cooling tests is also a variable related to ensuring constant temperature testing.

Tests were conducted to evaluate the sensitivity of the hot ductility response to hold time at test temperature and hold time at peak temperature. In order to separate the effects of hold time and crosshead speed on the ductility response, tests were conducted at a constant crosshead speed of 2.5 in/sec. Hold times of 1, 10, 50, and 100 secs were evaluated. The hot ductility as a function of the hold time at test temperatures is given in Figure A-10 for the on-heating tests and in Figure A-11 for the on-cooling tests after exposure to the ZDT without a hold at peak temperature. Figures A-10 and A-11 reveal that during both on-heating and on-cooling, hold times up to 100 secs at test temperatures does not significantly influence on the ductility response when test temperatures are not close to the ZDT. However, when tests are conducted at higher temperatures close to the zero ductility temperature (150 F^{o}), the hold time at test temperature

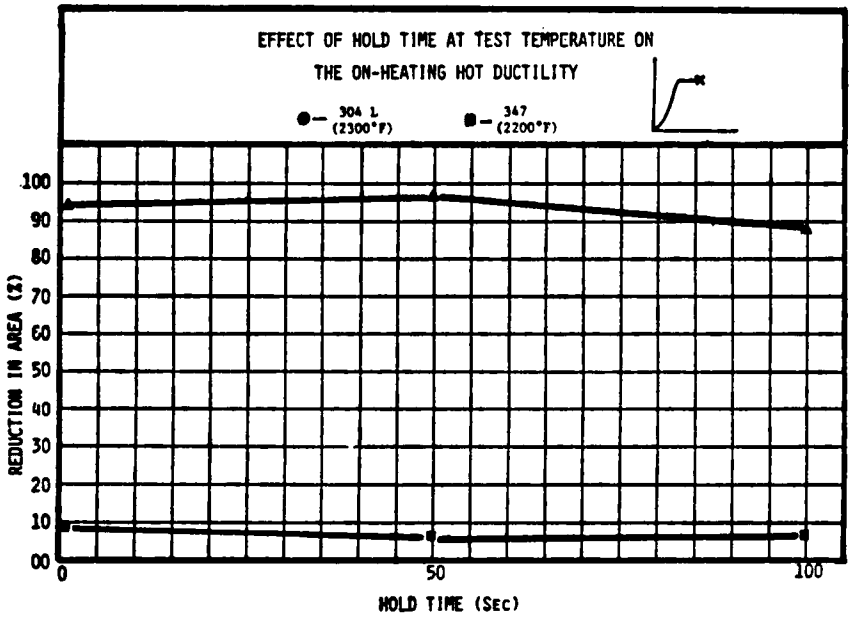


Figure A-10. Effect of hold time at test temperature on the on-heating hot ductility.

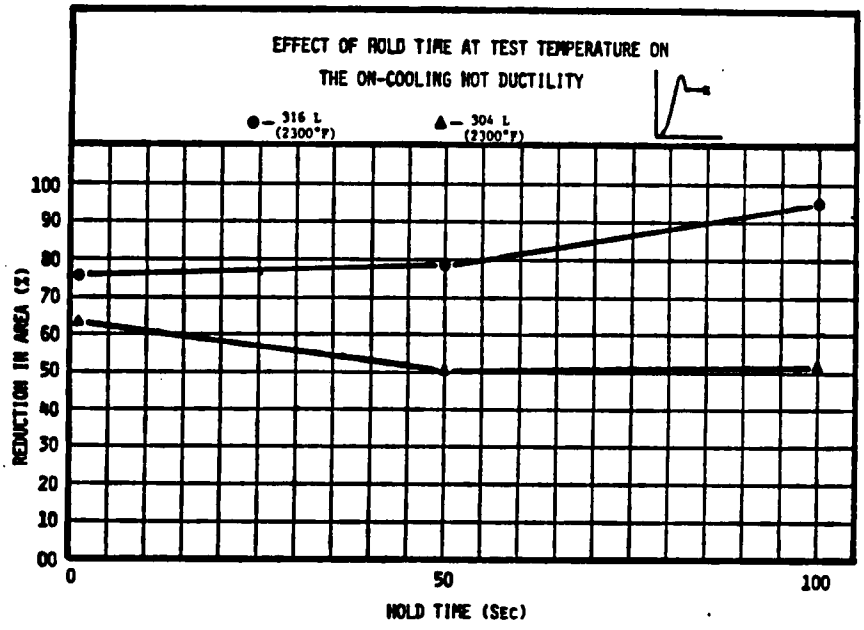


Figure A-11. Effect of hold time at test temperature on the on-cooling hot ductility.

exerts a significant effect on the hot ductility response as shown in Figure A-12. This figure shows that the on-heating ductility at 2450 ^{o}F decreases as the hold time increases. After 100 secs holding, the ductility decreased from 70% (for 1 sec holding time) to below 20%. Therefore, it is noted that the effect of the hold time at test temperature depends upon the test temperature.

The effect of the hold time at the peak temperature on the on-cooling ductility is shown in Figure A-13. (No hold time was used at test temperature.) Figure A-13 indicates that the on-cooling ductility of the three materials decreases as the hold time at peak temperature is increased. (The effect is more significant when hold time is used at peak temperature than when used at test temperature). Thus, in order to evaluate a material's natural response to the weld thermal cycle, a hold time at the peak temperature should not be used. In fact, a hold at test temperature and peak temperature is not the case actually experienced in the HAZ. It is most important to recognize that conducting hot ductility tests using thermal conditions and temperature which do not approximate the HAZ near the fusion zone is not realistic. If a hold time is necessary for the equipment to ensure constant temperature testing, a maximum 2 sec hold may be allowable.

2. SUGGESTED PROCEDURES FOR HOT DUCTILITY TESTING

The following suggested hot ductility test procedure is based on the extensive literature review in Chapter II and the statistical analysis of the test parameters discussed herein.

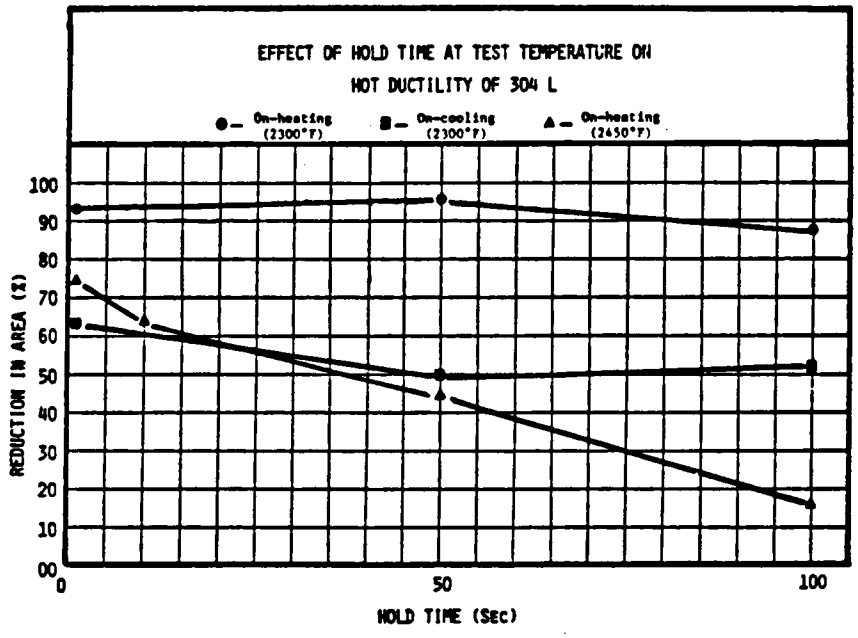


Figure A-12. Effect of hold time at test temperature on the hot ductility response of the 304 L.

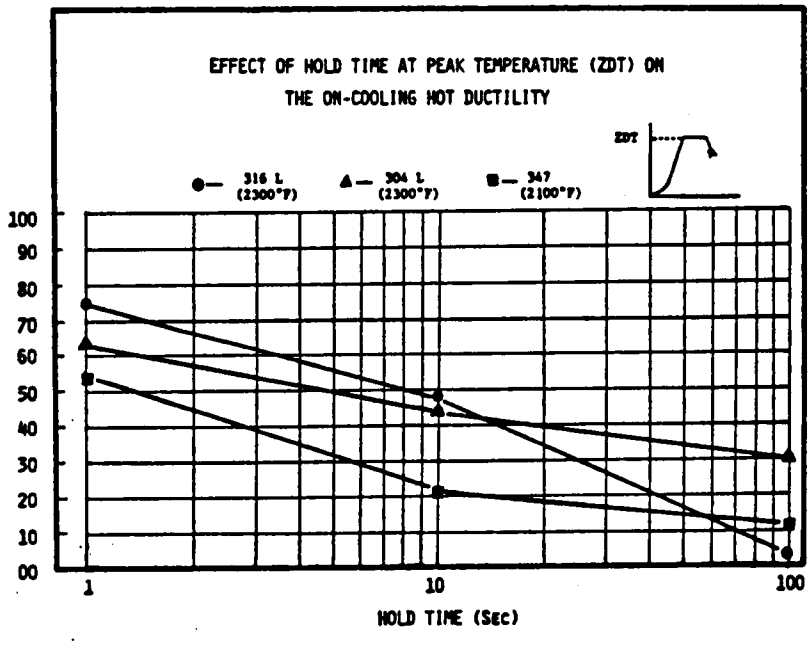


Figure A-13. Effect of hold time at peak temperature(ZDT) on the on-cooling hot ductility.

The reliability of hot ductility tests depends on the proper calibration of the equipment and performance of tests following a standard operating procedure such that results can be compared directly between laboratories. Before conducting tests, calibration of equipment should be done following the manufacturer's procedure. The calibration should include; loading system (and load), temperature, recording equipment, potentiometer, etc.

a. Specimen

The recommended specimen dimension is that for a cylindrical specimen 0.25 $\pm^{0.001}$ inch (6 $\pm^{0.5}$ mm) in diameter and 4 $\pm^{1/8}$ inch (100 $\pm^{5}$ mm) long with a 1/4-20 thread on both ends. The surface finish should be 10um or finer. However, other dimensions, which the equipment manufacturer recommends, can also be used.

The sample shall be extracted from the final product form of the material in the longitudinal orientation with respect to rolling or forming direction. For material thickness greater than 1/2 inch the samples must be marked as to the location within the thickness and for material thickness equal to and greater than 3/4 inch, the sample shall be extracted in equal numbers from both 1/4t locations.

b. Thermocouple

A Chromel-Alumel thermocouple of 0.010 inch wire diameter having a certified calibration (minimum of ± 3/4 of 1% of indicated temperature) should be used for most of the testing. However, for test temperatures exceeding 2475 ^{o}F, a noble thermocouple (Pt-PtRh, etc.,) should be used to prevent the thermocouple from reacting with

and detaching from the specimen or to eliminate an erroneous temperature recording if the thermocouple remains attached.

Two types of thermocouple attachment methods can be used; a conventional cross wire thermocouple percussion welded and a separate wire percussion or resistance spot welded. When the conventional cross wire technique is used, the junction should be made by resistance cross wire welding and trimming carefully as shown in Figure A-4. When the separate wire technique is used, thermocouple wires must be attached individually to the surface of the specimen in a plane perpendicular to the axis of the specimen (as shown in Figure A-5). A suitable space between the two thermocouple wires is approximately 1-2mm.

The thermocouples should be attached at the center of the specimen gauge length (within 0.01 inch). If percussion welding equipment is not available resistance spot welding is also an acceptable attachment method.

c. Thermal Cycle

A recommended thermal cycle is that which corresponds to the characteristics of a thermal cycle for a peak temperature of 2400 ^{o}F for 1-1/2 inch thick austenitic stainless plate welded by the SMAW process with an energy input of 70 KJ/in and a 72 ^{o}F (room temperature) preheat. A linear thermal cycle which has heating and cooling rates equivalent to that of the recommended thermal cycle can also be used. The peak test temperatures may be obtained by scaling the thermal cycle at equivalent times based on the ratio of peak temperatures.

Hold time at test temperature for the on-heating and on-cooling tests is allowed provided the test temperatures are not within approximately the 150 F^{o} of ZDT. When the test temperature is within 150 F^{o} of ZDT a hold time should not be used. In order to maintain constant conditions for all tests the hold time should not be incorporated. However, if a hold time is necessary for the equipment to obtain a stable test temperature, a maximum hold time of 2 secs may be used. A hold time at the peak temperature for the on-cooling tests is very critical and should not be employed.

d. Peak Temperature

The peak temperature for the on-cooling tests should be at least that of the zero ductility temperature. The recommended peak temperature is the zero ductility temperature (ZDT) which is found during on-heating tests. However, if it is possible to discriminate between the ZST and the ZDT and their difference is greater than $50^{o}F$, ZST on-cooling tests are also recommended. For maximum information, on-cooling tests from both ZDT and ZST should be conducted.

e. Crosshead Speed (Strain Rate)

The recommended crosshead speed is 2.5 $\pm$0.5 inch/sec (63 $\pm$13 mm/sec). A slower speed (as low as 0.5 inch/sec (13 mm/sec)) can also be used, but a hold time must be considered to maintain the test temperature constant during loading. However, for simplicity and consistency, the strain should be fast enough to ensure constant temperature testing without a hold time.

f. Tests

Hot ductility tests shall be conducted on all heats of austenitic stainless steel to be used for welded fabrication. The test results shall determine the acceptability of the material for welded fabrication. Tests should be conducted during both on-heating and on-cooling after exposure to the peak temperature (ZDT/ZST).

The free span (gauge length) between the water cooled copper jaws holding the specimen shall be 0.8 ±0.2 inch (20 ±5 mm).

The ductility of the material is determined by heating to temperatures in the range from 1800 °F to the peak temperature (ZDT/ZST), as measured by the reduction in area of the tested sample. A minimum of two samples should be tested at each test temperature. If the difference in reduction in area between two tests is more than 30%, one additional test should be conducted at the same temperature and the test results should be averaged. Tests shall be conducted at 100-200 F° intervals to within the 100 °F of the ZDT and then at 25 F° intervals up to ZDT/ZST. If the ZDT is not identical with the ZST, tests should be continued at higher temperature until the ZST is determinated. Load should be initiated as soon as the test temperature is reached (hold time is not recommended).

Once the peak temperature (ZDT/ZST) has been determined tests should be conducted on cooling from the peak temperature (ZDT/ZST) to 1800°F. The thermal cycle and peak temperature remain fixed for the on-cooling testing sequence. Within 100 F° of the peak temperature, the on-cooling test temperature interval should be 25 F°, and then in 100-200 F° intervals to 1800 °F. If the ductility at lower

temperatures is required, tests shall be continued to the lower temperatures of interest. A minimum of two tests should be conducted at each test temperature and if the ductility difference is more than 30%, another test must be conducted and the results averaged.

For both the on-heating and on-cooling tests, at completion of each test, the location of fracture in relation to the thermocouple shall be measured and if the distance is greater than 1/8 inch (3 mm) the result will be discarded. A summarized hot ductility test conditions is given in Table 7 (page 101).

g. Note

At the completion of each test the breaking load (strength), strain and actual test temperature should be measured and recorded for information. When measuring the breaking load (strength), the inertia and friction load produced by the system should be subtracted from the measured value.

VITA

The author was born and grown in Daegu, South Korea. He attended high school in his hometown and graduated from The Kei Seong High School in January, 1974. He entered The Han Yang University, Seoul, Korea in March, 1975. After finishing his sophomore year, he joined military service in May, 1977 and rejoined university in 1980 after completion of his three years service. He received a B.S degree in metallurgical engineering in February, 1982. Study toward a M.S. degree in metallurgical engineering at The University of Tennessee, Knoxville began in June, 1982 and awarded in March, 1985. The Ph.D. degree was awarded in December, 1988.

The author is a member of the American Society for Metals, the Metallurgical Society of AIME, the American Welding Society, and the National Association of Corrosion Engineers.